



HAL
open science

Thermodynamics of ultracold Bose and Fermi gases

Nir Navon

► **To cite this version:**

Nir Navon. Thermodynamics of ultracold Bose and Fermi gases. Atomic Physics [physics.atom-ph]. Université Pierre et Marie Curie, 2011. English. NNT: . tel-01081100

HAL Id: tel-01081100

<https://theses.hal.science/tel-01081100>

Submitted on 7 Nov 2014

HAL is a multi-disciplinary open access archive for the deposit and dissemination of scientific research documents, whether they are published or not. The documents may come from teaching and research institutions in France or abroad, or from public or private research centers.

L'archive ouverte pluridisciplinaire **HAL**, est destinée au dépôt et à la diffusion de documents scientifiques de niveau recherche, publiés ou non, émanant des établissements d'enseignement et de recherche français ou étrangers, des laboratoires publics ou privés.

Département de physique
École Normale Supérieure

Laboratoire Kastler Brossel



THÈSE de DOCTORAT de l'UNIVERSITÉ PARIS VI

Spécialité : Physique Quantique

présentée par

Nir Navon

pour obtenir le grade de DOCTEUR de l'UNIVERSITÉ PARIS 6

Thermodynamics of ultracold Bose and Fermi gases
Thermodynamique des gaz de bosons et fermions ultrafroids

Soutenue le 9 septembre 2011

devant le jury composé de :

M. Tin-Lun Ho	Rapporteur
M. Nir Davidson	Rapporteur
M. Wolfgang Ketterle	Examineur
M. Roland Combescot	Président
M. Werner Krauth	Membre invité
M. Frédéric Chevy	Membre invité
M. Christophe Salomon	Directeur de thèse

Contents

Introduction	9
I Methods to Probe the Thermodynamics of Quantum Gases	15
1 Thermodynamics of quantum gases	17
1.1 Ideal Quantum gases	17
1.1.1 Quantum Statistics	17
1.1.2 Bose-Einstein Condensation	18
1.1.3 Fermi Degeneracy	20
1.2 Short-Range Interactions	21
1.2.1 Reminder of scattering theory: <i>s</i> -wave scattering	21
1.2.2 The Scattering Length <i>a</i> and Universality	23
1.2.3 Feshbach Resonances	24
1.3 Probing the Equation of State of Quantum Gases	27
1.3.1 Dealing with the Trapping Potential: Local Density Approximation	28
1.3.2 Direct measurement of the EoS in low dimensions	30
1.3.3 In 3D: Trapped Gas EoS and Inverse-Abel Transform	31
1.3.4 Our Method: the Direct Measurement of the Local Pressure	33
2 The Lithium Machine	37
2.1 Trapping and Cooling the Lithium Isotopes	37
2.1.1 The Laser System	37
2.1.2 The Dual Species ⁷ Li- ⁶ Li Magneto-Optical Trap	39
2.2 Magnetic Trapping	40
2.2.1 Quadrupole Trap and Magnetic Transport	40
2.2.2 The Ioffe-Pritchard Trap	41
2.3 The Hybrid Magnetic-Optical Trap	43
2.3.1 Loading the Optical Trap	43
2.3.2 Bias Flip and Magnetic Axial Curvature	45
2.3.3 Spin-mixture preparation in a Fermi gas	46
2.3.4 Evaporation in the dipole trap	47
2.3.5 The Feshbach Field	50
2.4 Imaging	54
2.4.1 Resonant Absorption Imaging	54

2.4.2	Probe Beams Setup	55
2.4.3	Probe Frequencies	56
II Bosons		59
3	The Ground State of an Interacting Bose Gas	61
3.1	A Bose-Einstein Condensate with Tunable Interactions	61
3.1.1	Obtaining a Bose-Einstein Condensate of ${}^7\text{Li}$	61
3.1.2	Mean-Field Equation of State of a Bose-Einstein Condensate	62
3.1.3	Increasing the interactions in a Bose-Einstein Condensate	64
3.2	The Feshbach Resonance	65
3.2.1	A rough localization of the resonance	66
3.2.2	Radio-frequency association of Feshbach molecules	66
3.3	Measurement of the Equation of State	69
3.3.1	Determination of the global chemical potential	69
3.3.2	Pressure Calibration	70
3.3.3	Observation of beyond mean-field effects in a Bose gas	71
3.3.4	Quantitative determination of the Lee-Huang-Yang correction	72
3.3.5	Comparison to Quantum Monte-Carlo calculations	77
4	Dynamics of a Bose Gas with Tunable Interactions	79
4.1	In quasi-equilibrium	79
4.1.1	Cloud size measurements	79
4.1.2	Simple Theoretical Approaches	81
4.1.3	Three-body recombination	82
4.1.4	Consistency check of the Lee-Huang-Yang Equation of State	86
4.2	Towards the Feshbach resonance	87
4.2.1	Atom losses close to the Feshbach resonance	88
4.2.2	Radii Measurements	89
4.2.3	A Lower Bound on ξ_B	90
III Fermions		93
5	The Strongly Interacting Fermi Gas	95
5.1	Universal Thermodynamics of the Unitary Fermi Gas	95
5.1.1	Thermometry of the Strongly Interacting Fermi Gas	96
5.1.2	Determination of the chemical potential μ_0	98
5.1.3	Comparison to Many-body Theories	100
5.1.4	High-temperature Limit: Virial Expansion	102
5.1.5	Low-Temperature I: Fermi-liquid type behavior	104
5.1.6	Low-Temperature II: Normal to Superfluid Phase Transition	113
5.1.7	Equation of State of the Trapped Unitary Gas	115
5.1.8	Comparison with the Tokyo Canonical Equation of State	117
5.2	The Low-Temperature Fermi Gas with Tunable Interactions	118
5.2.1	The Equation of State of a Fermi gas in the BEC-BCS crossover	119
5.2.2	Comparison with many-body theories	120

5.2.3	Asymptotics I: the BCS-limit of a Weakly Interacting Fermi Gas	123
5.2.4	Asymptotics II: the Unitary Limit	124
5.2.5	Asymptotics III: the BEC-limit of a Weakly Interacting Bose Gas	127
5.2.6	Universality of the Lee-Huang-Yang correction	129
5.3	Finite Scattering Length Corrections	130
5.3.1	The virial coefficients b_2 and b_3 in the BEC-BCS crossover	130
5.3.2	Tan Contact at Finite Temperature	131
5.3.3	Estimate of the Correction for the Equation of State $h(\zeta)$	133
6	The Spin-Polarized Fermi Gas	137
6.1	Overview of the Phase Diagram	137
6.1.1	The Clogston-Chandrasekhar Limit	137
6.1.2	The $N + 1$ body problem: the Fermi Polaron	138
6.1.3	A Qualitative Phase Diagram	140
6.1.4	Experimental investigations	141
6.2	Measurement of the Equation of State	142
6.2.1	Pressure Calibration and Determination of the Chemical Potentials	143
6.2.2	The Equation of State of the Spin-Imbalanced Gas in the BEC-BCS crossover	144
6.2.3	The Normal/Superfluid Phase Transition	147
6.2.4	A Gas of Polarons	150
6.2.5	Comparison to other experiments	152
	Conclusion	159
	A Technical details	165
A.1	Testing the self-consistent determination of μ_0 on a Bose gas	165
A.2	Padé approximants	166
A.2.1	Relation between ξ and h	166
A.2.2	The BCS side	167
A.2.3	The Contact	167
A.2.4	The BEC side	168
A.2.5	Parameters for the Padé approximants	169
A.3	The Magnetic Circuit	170
	B Publications	173
B.1	Collective Oscillations of an Imbalanced Fermi Gas: Axial Compression...	175
B.2	Exploring the thermodynamics of a universal Fermi gas	180
B.3	The Equation of State of a Low-Temperature Fermi Gas with Tunable...	186
B.4	The equation of state of ultracold Bose and Fermi gases: a few examples	191
B.5	Fermi-Liquid Behavior of the Normal Phase of a Strongly Interacting...	206
B.6	Dynamics and Thermodynamics of the Low-Temperature Strongly...	211
B.7	Condensation energy of a spin-1/2 strongly interacting Fermi gas	216
	References	223

Remerciements

Ecrire des remerciements une année après la fin de la thèse n'est pas un exercice facile. Au-delà du plaisir scientifique, cette thèse fut une aventure humaine pour moi dont les bienfaits m'ont marqués. A l'occasion de mes années passées au Laboratoire Kastler-Brossel, j'ai eu l'occasion de côtoyer plusieurs personnalités, auprès de qui j'ai appris de la physique, mais surtout après de qui j'ai forgé des souvenirs qui vont au-delà de la science, et c'est ce que j'estime le plus.

Tout d'abord, je remercie Christophe, qui a supervisé ma thèse. Son intuition expérimentale nous a bien souvent guidé. Son enthousiasme et de son optimisme en fait quelqu'un avec qui c'était un grand plaisir de travailler. L'importante liberté (et les responsabilités afférentes) qu'il nous a laissée sur le choix d'expériences à réaliser correspondait particulièrement à mon tempérament et je lui en suis très reconnaissant. Je n'oublierai pas de sitôt cette discussion de physique inspirée à la plage de la Palombaggia, ou ces superbes courses en glacier où il m'a initié aux plaisirs de la montagne en crampons, lors de l'école d'été aux Houches sur la physique à N corps avec les atomes froids, à l'été 2010. Fred, mon co-directeur de thèse, a joué un rôle central dans mon parcours. C'est à la suite de mon stage de l'X avec lui au printemps 2005 que j'ai décidé de faire ma thèse en physique expérimentale. C'est grâce à lui que j'ai réalisé qu'il est possible d'être un expérimentateur et un théoricien de qualité simultanément. Et puis, comment ne pas mentionner le plaisir (et la surprise) d'avoir partagé avec lui ce penthouse de 150 m² à Cairns. Ou encore la gratitude qu'il ait relu et corrigé à une telle vitesse (et en vacances !) mon manuscrit de thèse, toujours disponible pour discuter de physique sur Google Talk à 1h du matin.

Je tiens à remercier les membres de l'équipe Lithium qui m'ont introduit à la psychologie complexe de cette expérience. Martin Teichmann, Leticia Tarruell, et Jason McKeever. Un remerciement très particulier à Florian Schreck, avec qui j'ai beaucoup interagi, bien que l'on ait été séparé par deux générations de thésards sur cette expérience. Son aide dans les premiers mois de ma thèse (combiné à son inégalable vitesse de réponse par e-mails) m'a été très utile. Après deux ans d'interactions par mail, je l'ai enfin rencontré et nous sommes depuis lors devenus amis. Sa présence à ma soutenance de thèse malgré un calendrier chargé n'a été qu'une preuve de plus de sa personnalité hors norme.

Cette thèse n'aurait pas eu cette forme sans Sylvain, son inspiration de la formule de la pression de Sant Feliu 2009 ayant été un tournant sur la manip. Travailler avec quelqu'un d'aussi talentueux a été une source de stimulation, et sans aucun doute l'un des plus grands plaisirs de ma thèse. Et malgré cela, le plus enrichissant aura été d'avoir transformé cette entente scientifique en une véritable amitié. Les événements les plus joyeux de la thèse (obtention du premier superfluide de fermions déséquilibré, acceptation de certains papiers) ont toujours été fêtés avec excès, comme j'aime, au point que nous n'avons conservé qu'une mémoire parfois parcellaire de certains événe-

ments.

Même si nous n'avons pas travaillé longtemps ensemble, je tiens à remercier Grainne, Kaijun, Kenneth, Trong Canh et Ulrich, pour leurs contributions à ce travail. Merci à la nouvelle génération, Igor, Benno et Andrew, avec qui j'ai pris du plaisir à travailler, et à qui je souhaite beaucoup de succès sur une expérience bien capricieuse. Durant ma thèse, j'ai beaucoup apprécié d'interagir avec les théoriciens, Yvan, Félix, Antoine Georges, Xavier et Roland, mais aussi les italiens Stefano Giorgini et Sebastiano Pilati, toujours disponibles, ou encore à la fin de ma thèse, avec les Monte Carlites Werner et Swann. Leur motivation et leur disponibilité a été une source d'enthousiasme pour moi. Merci aux membres du secrétariat, qui ont toujours été si sympathiques, disponibles, Dominique, Christophe (merci d'avoir toujours rempli la moitié des formulaires à ma place...), Thierry, Monique. Un grand merci à Yo pour sa disponibilité électronique permanente, et aux services de l'atelier. Je tiens à remercier tous les membres du groupe Atomes Froids pour l'excellente atmosphère au labo, remerciement particulier à Jean, pour avoir influencé, par son opinion tranchée, mon chemin après-thèse. Mon premier dîner à la High Table de Trinity lui donne pour le moment raison.

I feel honoured to have had such a remarkable PhD committee. First, I would like to thank Jason Ho, and Nir Davidson for accepting the task of reviewing my thesis. I would like to thank Nir for inviting me to spend a very interesting year at the Weizmann Institute, which led me to meet Roe and the world of trapped ions. I am very grateful to Wolfgang Ketterle for accepting to sit on my PhD committee despite a very busy schedule, and for his comments on my manuscript. The discussion we had before, and after my defence were very inspiring. Un grand merci à Roland d'avoir présidé le jury, et à Werner d'avoir accepté d'y siéger comme membre invité.

Un remerciement particulier à ceux qui ont relu ce manuscrit, et qui m'ont permis d'avoir le luxe de presque trois couches de corrections successives, et ce, dans un temps très limité (merci qui ?): Christophe, de m'avoir même fait parvenir ces corrections depuis la Chine, Fred, depuis ses vacances, Sylvain, Andrew (que j'ai mis à rude épreuve pour l'anglais), Benno, Igor, Ulrich, Takis (pour la petite partie supra haute- T_c) et Félix pour son incroyable marathon de lecture le dernier week-end avant la remise.

Et tout ce beau monde, qui m'aura donné tant de plaisir à vivre et travailler à Paris, Armix, dont l'enthousiasme et la joie de vivre sont quasiment inégalables et Maya, pour le calmer, les potes du quantum gang (et affiliés), Clémix, Jean, El Juli, Tartex, Tobo, Carles, Thibs, François et Judy, Ariane, Haim le grimpeur ou Christof-le-beau-gosse. J'ai été touché que la famille de Laura, Xavier, Kien, Florent, Martin, Thibs, Yo Zaouter et Matteo aient fait spécialement le déplacement pour fêter ma soutenance. Last but (certainly) not least, mes parents pour leur soutien permanent et indéfectible, mon frère et ma soeur pour leurs encouragements sous forme de plaisanteries permanentes sur le monde des physiciens, et enfin celle qui m'aura soutenu au quotidien et qui remet de l'équilibre dans ma vie, Laura. Cette thèse n'est pas le résultat du travail d'un homme seul, et j'en suis bien heureux.

Nir

15 octobre 2012

Introduction

As summarized by Philip W. Anderson in his famous quote “More is different”, the behavior of a quantum many-body system cannot be reduced to the understanding of its isolated constituents [1]. This idea is already illustrated in the few-body problem. While the two-body problem can be easily solved, the three-body system proved to be the source of spectacular new phenomena, ranging from chaos in classical mechanics, to the Efimov effect [2], the appearance of three-body bound states with universal properties, in the quantum-mechanical problem. The four-body problem poses formidable challenges, let alone the N -body system. The quantum (non-relativistic) many-body problem is easy to pose. Let us consider a quantum system composed of particles interacting via a binary interaction potential $V_{\text{int}}(\mathbf{r}_i - \mathbf{r}_j)$ immersed in an external potential $V(\mathbf{r})$. One can write the Hamiltonian of the N -body system:

$$\hat{H} = \sum_{i=1}^N \frac{\mathbf{p}_i^2}{2m} + \sum_{i<j} V_{\text{int}}(\mathbf{r}_i - \mathbf{r}_j) + \sum_{i=1}^N V(\mathbf{r}_i). \quad (1)$$

The problem then reduces to solving the Schrödinger equation for the many-body wavefunction $\Psi(\mathbf{r}_1, \mathbf{r}_2, \dots, \mathbf{r}_N)$:

$$\hat{H}\Psi_{\alpha}(\{\mathbf{r}_i\}) = E_{\alpha}\Psi_{\alpha}(\{\mathbf{r}_i\}) \quad (2)$$

to extract the energy spectrum E_{α} and the eigenstates Ψ_{α} , with the additional constraint of the (anti)-symmetry of the wavefunction Ψ with respect to the permutation of two particles, depending if the system is composed of indistinguishable fermions or bosons. Obviously, writing down the Schrödinger equation (2) doesn't bring us any closer to a solution. Except in very rare cases, this problem cannot be solved analytically. And even when it can¹, it is often difficult to use the many-body wavefunction and the energy spectrum to compute quantities that can be directly compared to experiments.

If the system is composed of weakly interacting particles, mean-field approximations or perturbative expansions can provide accurate descriptions. However, these approaches are insufficient for many of the major open problems in modern physics that deal with ensembles of strongly correlated particles such as neutron stars, the quark-gluon plasma, superfluid ^3He and ^4He , and high- T_c superconductors. These physical systems are extremely subtle: for instance the electron gas in cuprate superconductors is immersed in a notoriously daunting lattice structure, while the neutron-neutron interactions in neutron stars are very complex. However, simple models have been proposed to encapsulate the most important phenomena. The Fermi-Hubbard model for example describes particles in a periodic potential with on-site interactions and is thought to be one of the simplest models to describe high- T_c superconductivity. In a similar fashion, the Hamiltonian (1) with short-range interactions has been proposed as an elementary description of strongly correlated

¹A notable example being the Bethe ansatz to solve exactly some one-dimensional problems.

neutron matter [3]. Despite their apparent simplicity, there is no generic method to solve these models to date for large particle numbers and without uncontrolled approximations: it is thus unknown whether they represent faithful models. For example, though the phase diagram of the Fermi-Hubbard Hamiltonian has been studied for numerous years, its exact nature is still hotly debated.

If classical computers are unable to solve these quantum many-body problems, we can turn to analogic reasoning. If one can prepare a system that is accurately described by one of the above models, performing a measurement on it would amount to solving analogically the model: this is the idea of *quantum simulation*, originally proposed by R. Feynman in 1982 [4]. The advent of ultracold dilute quantum gases of neutral atoms, starting by the experimental production of gaseous Bose-Einstein condensates in 1995 [5,6], followed by degenerate Fermi gases in 1999 [7], has opened a new era in quantum simulation. These quantum gases can be manipulated with an unprecedented degree of control. First, the atoms can be placed in well-controlled external potentials of various shapes: harmonic or box-like traps, or multiple wells. Using interfering standing waves it is possible to subject the atoms to periodic potentials mimicking the potential experienced by electrons in the ion-crystal lattice structure of solid materials. This analogy [8] resulted in the experimental implementation of the Bose- and Fermi-Hubbard models using ultracold atoms and the direct observation of the superfluid-to-Mott insulator phase transition [9,10,11]. Secondly, since the interactions between neutral atoms are short-ranged, they are usually very well characterized at low temperature by a single quantity, the *scattering length*. By means of Feshbach resonances, it has become possible to tune with great freedom the scattering length, hence the interatomic interactions. This feature allowed the production of strongly interacting Bose [12], and Fermi gases [13]. We thus have at our disposal true model-systems that can be used to study many-body physics [14]. The techniques to manipulate and probe these gases are continually improving and the field has recently reached a major milestone, where it has become possible to image [15,16] and address [17] the many-body system at the single atom level.

Fermionic and Bosonic Superfluidity: the BEC-BCS crossover

Superfluidity and superconductivity are two spectacular quantum phenomena that arise on a macroscopic scale. The former was discovered in 1937 as the disappearance of viscosity in liquid ^4He , composed of bosons, below a temperature of 2.2 K. F. London first made the link between the superfluid transition in helium and the Bose-Einstein condensation predicted to occur in an ideal Bose gas [18]. The link however is only qualitative because of the importance of the interactions in liquid helium. The latter, superconductivity, was unveiled in 1911 in solid materials as a sudden drop to zero of the electric resistance below a threshold temperature. A critical step in understanding superconductivity was made by L. Cooper, who discovered that a Fermi sea is unstable in the presence of an arbitrarily weak attractive interaction, and the fermions will form bound states, the *Cooper pairs* [19]. A year later, J. Bardeen, L. Cooper and J. Schrieffer developed the *BCS* theory [20], that describes the superconducting state as an ensemble of phase-coherent Cooper pairs of electrons.

The two phenomena seem at first very different, as one occurs in a Bose liquid, the other in a Fermi system. However, D.M. Eagles and A. Leggett noticed that the BCS wavefunction was adequate for describing both the BCS superfluid of Cooper pairs in the limit of weak interactions,

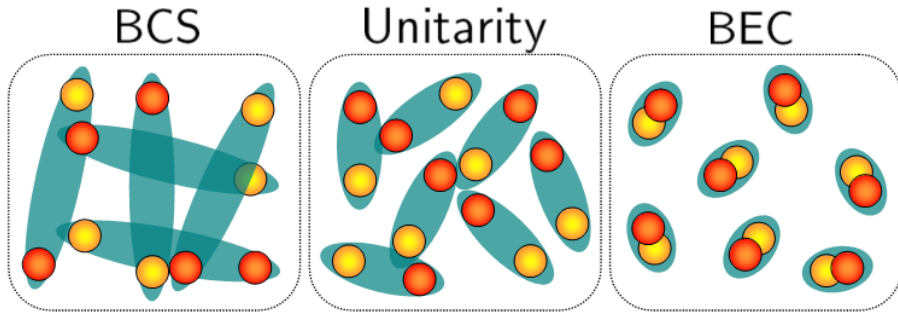


Figure 1: Sketch of the BEC-BCS crossover in a spin-1/2 attractive Fermi gas.

and a Bose-Einstein condensate (BEC) of tightly bound pairs, which are composite bosons, for strong attractive interactions [21, 22]. This smooth transition between fermionic and bosonic superfluidity is the so-called *BEC-BCS crossover* (Fig.1). The phase diagram at finite temperature was first addressed by P. Nozières and S. Schmitt-Rink, who calculated the critical temperature for the normal-to-superfluid phase transition as a function of the interaction strength [23].

Bose and Fermi gases with Feshbach resonances

However, it was not until the realization of degenerate Fermi gases in the vicinity of a Feshbach resonance in 2002 that the BEC-BCS crossover could be implemented and investigated experimentally. The tunability of the interactions allowed, for the first time, to explore in a single physical system the transition from bosonic to fermionic superfluidity. Major achievements include the observation of Bose-Einstein condensation of molecules [24, 25, 26, 27], the study of the superfluid pairing gap [28, 29], and the demonstration of superfluidity through the appearance of quantized vortices in a rotating Fermi gas [30]. Since then, theoretical and experimental work has flourished on the BEC-BCS crossover [31].

Observation of beyond-mean-field effects in atomic Bose gases was also long-sought. The early discovery of Feshbach resonances with bosonic elements in 1998 opened the possibility of increasing the interaction strength [32, 33, 34]. However, the first experiments showed a dramatic reduction of the gas lifetime in the vicinity of the resonance [35, 34, 36], due to the enhancement of three-body recombination losses [37]. While three-body losses are strongly suppressed in Fermi gases because of Pauli-blocking [38], which prevents two same-spin particles from getting close to each other, this effect is absent in Bose gases. For this reason, the early experiments on bulk Bose-Einstein condensates had the common trait of being in a regime of very weak interactions, and were thus quantitatively well explained by mean-field theories [39, 40].

One is naturally led to wonder to what extent the physics on the molecular side of the BEC-BCS crossover in a Fermi gas is similar to that of a Bose gas of pointlike bosons. One can for example investigate the ground state energy density $\mathcal{E} = E/V$ of a Bose gas, predicted in 1957 by T.D. Lee, K. Huang, and C.N. Yang, to follow an expansion in the diluteness parameter na^3 [41, 42, 43]:

$$\mathcal{E} = \mathcal{E}_{\text{MF}} \left(1 + \frac{128}{15\sqrt{\pi}} \sqrt{na^3} + \dots \right), \quad (3)$$

where n is the boson density and a the scattering length. The first term is the result of mean-field

theory (with $\mathcal{E}_{\text{MF}} = gn^2/2$). In 2004 it was predicted that the mean-field energy of a molecular Bose gas would be identical to that of a pointlike boson gas with a dimer-dimer scattering length $a_{dd} = 0.6a$ [38, 44]. The next term in the expansion, the so-called Lee-Huang-Yang correction, is due to quantum fluctuations, and is also universal in the sense that it depends on the microscopic detail of the interaction potential only through the scattering length and should be identical for all Bose gases with short-range interactions. In 2007, it was predicted that this next-order correction should also be valid for a molecular Bose gas despite the composite nature of the dimers (of size a) [45]. Signatures of beyond mean-field effects have been observed on collective modes and density profile studies of molecular Bose gases [46, 47], as well as on Bragg spectroscopy of a strongly interacting ^{85}Rb Bose gas [48]. Despite its very fundamental nature in quantum many-body physics, the Lee-Huang-Yang correction, as well as its universality had never been directly experimentally tested.

Universality and the Unitary Gas

The question of universality can be taken one step further in the expansion (3). While for pointlike bosons the next term is known to be non-universal because it involves short-range physics from the quantum-mechanical three-body problem, the equivalent for the molecular gas is currently unknown. However there is a strong belief that the BEC-BCS crossover is truly universal, in the sense that the scattering length is the only relevant interaction parameter and that any Fermi gas with short-range interactions will behave identically. A system of particular interest in the BEC-BCS crossover is the point where the scattering length diverges, the so-called *unitary limit*. If the scattering length a is the only parameter characterizing the interactions and $a \rightarrow \infty$, the system is left with no interaction energy scale. Then the only energy scale that can be built with \hbar , m and the density n is proportional to the Fermi energy $E_F = \frac{\hbar^2}{2m}(6\pi^2n)^{2/3}$ by dimensional considerations. For this reason, the Equation of State at $T = 0$ for the unitary gas should be identical to that of a free Fermi gas, up to a numerical factor:

$$\mu = \xi E_F, \quad (4)$$

and ξ being a universal number (also called the Bertsch parameter) identical to any quantum gas interacting via resonant short-range interactions [49]. This result is spectacular: while the system is subjected to strong interactions, its equation of state is formally identical to that of an ideal gas. All the many-body correlations are encapsulated in the value of ξ . We have now very good theoretical and experimental indications (for example measurements performed on different fermions, such as ^6Li and ^{40}K) that the unitary Fermi gas is indeed a universal state [31].

For a gas of bosons at unitarity, the situation is very different from the fermionic case, in particular because of the presence of the Efimov effect. The understanding of the Bose gas in the regime of strong interactions is in its infancy. The most important open question is whether a well-defined many-body state does exist at unitarity, and whether such a state has universal properties. While this system has recently generated considerable theoretical interest [50, 51, 52, 53, 54], and several works have attempted to calculate the value of ξ for the hypothetical unitary Bose gas [55, 56, 57, 58], there are still no clear indications that this system is actually well-defined and experimentally realizable.

Outline of this work: Thermodynamics of quantum gases

While the energy spectrum and eigenstates contain the whole information on a quantum many-body system, thermodynamics provides us with conceptually simple observables to compare to experiments. From a microscopic point of view, the problem reduces to the computation of the Equation of State (EoS) of the many-body system from the partition function: for example the energy E as a function of the entropy S , the number of particle N and the volume V : $E = E(S, V, N)$. From this fundamental relation it is possible to extract many quantities that are readily probed in experiments, such as the specific heat, the compressibility of the system or its pressure. In addition, the equation of state also contains information about the occurrence of phase transitions.

In this thesis, we present a general method that we developed to probe the thermodynamics of homogeneous quantum systems using trapped atomic gases. We applied it to investigate the Equation of State of Bose and Fermi gases with short-range interactions.

- In **chapter 1**, we introduce the basic concepts that are used throughout this work, the grand-canonical equation of state of the ideal quantum gases, the description of low-energy collisions through the scattering length and the phenomenon of Feshbach resonance that allows us to tune the scattering length. We will then present the technique that we implemented to extract the pressure of a homogeneous gas using a trapped sample from the in-situ density distributions. This technique allows us to directly test advanced theories of the many-body problem with our measurements.
- We will then turn in **chapter 2** to a description of our experimental setup, with which we produce degenerate Bose and Fermi gases of the two lithium isotopes, ${}^6\text{Li}$ and ${}^7\text{Li}$. The experiment involves two major stages: a magnetic trap where fermionic ${}^6\text{Li}$ is sympathetically cooled with ${}^7\text{Li}$ as a coolant, and an optical trap where the mixture is cooled to quantum degeneracy. An external magnetic field is used to tune the scattering length via a Feshbach resonance.
- The ground state of the Bose gas with tunable interactions is investigated in **chapter 3**. Using a Feshbach resonance of ${}^7\text{Li}$, we observe the onset of beyond mean-field effects in a bulk Bose gas and measure for the first time the Lee-Huang-Yang correction in a point-like Bose gas. The assumption of $T = 0$ is directly checked by comparing our results to a Quantum Monte Carlo simulation performed by S. Piatecki and W. Krauth at ENS. These results have been published in [59] (appendix B.5).
- The thermodynamic measurements on the Bose gas, presented in the chapter 3, rely on the assumption of thermal equilibrium. Because of the presence of three-body losses close to the Feshbach resonance as well as the finite duration of the interaction sweep to the strongly interacting regime, this assumption is checked via dynamic measurements on the Bose gas in **chapter 4**. Using faster sweep rates, we access the regime of strong interactions, and we infer a lower bound on the value of the universal constant ξ_B for the hypothetical unitary Bose gas which is compared to theoretical predictions. Part of these results are the subject of a publication in preparation.
- We then turn to the spin-1/2 Fermi gas of ${}^6\text{Li}$. In **chapter 5** we focus on the spin-balanced gas $N_\uparrow = N_\downarrow$. We measure the pressure of the strongly interacting gas of ${}^6\text{Li}$ as a function of temperature. Thermometry is performed using a trace of ${}^7\text{Li}$ immersed in the Fermi gas. In addition to the virial expansion at high-temperature, we observe Fermi-liquid type behavior

at low temperature and the normal-to-superfluid phase transition. We then turn to the $T = 0$ Fermi gas Equation of State as a function of interactions. In particular, on the molecular side of the BEC-BCS crossover, we measure the Lee-Huang-Yang correction which, together with the atomic Bose gas measurement presented in chapter 3, demonstrates the universality of the first beyond-mean-field correction. We directly compare our measurements of the equation of state to theories as well as to other experimental results obtained recently. The results have been published in [60] (appendix B.1), and partly in [61] (appendix B.4).

- In **chapter 6**, we present a measurement of the equation of state and phase diagram of the spin-population imbalanced Fermi gas, where $N_{\uparrow} > N_{\downarrow}$. Since fermionic superfluidity requires the pairing of two fermions, the fate of the spin-balanced superfluid subjected to spin-imbalance is an important issue, also called the Clogston-Chandrasekhar limit. We investigate the low-temperature phase diagram of the spin-imbalanced Fermi gas and measure the critical chemical potential ratio at which the superfluid breaks down to a normal phase. We show that the normal phase is well described by a weakly interacting gas of quasi-particles, the Fermi polarons. The results have been published in [62] and [63] (appendix B.2 and B).
- Finally the conclusion presents perspectives of this work. Because of the simplicity and generality of the technique presented in this work, it could readily be applied to various ultracold atomic gases currently under investigation and yield valuable information about the thermodynamics of other quantum many-body systems.

Part I

Methods to Probe the
Thermodynamics of Quantum
Gases

Chapter 1

Thermodynamics of quantum gases

In this chapter, we will present the basic concepts and tools that will be necessary throughout this thesis. First, we will review the simple thermodynamics of non-interacting Bose and Fermi gases. Then we will recall how ultracold collisions are characterized by a simple quantity, the scattering length, and how it can be tuned in dilute gases via Feshbach resonances. Finally, we will turn to the main topic of this work, the methods to measure the equation of state of quantum gases.

1.1 Ideal Quantum gases

Because of their fundamental character and central role in this work, we will first review basic facts of non-interacting gases and focus on deriving the equation of state of the ideal quantum gases that will be important for the rest of the work. In particular, we will emphasize the grand-canonical approach because of its use in this work.

1.1.1 Quantum Statistics

Quantum theory predicts that there are two categories of particle in nature: fermions and bosons. This duality stems from the principle of indistinguishability of identical quantum particles. If one writes the wavefunction of two particles $\Psi(\mathbf{r}_1, \mathbf{r}_2)$, the effect of permuting the two particles must leave the modulus square unchanged: $|\Psi(\mathbf{r}_1, \mathbf{r}_2)|^2 = |\Psi(\mathbf{r}_2, \mathbf{r}_1)|^2$. As a result, we can write the wavefunction as:

$$\Psi(\mathbf{r}_1, \mathbf{r}_2) = e^{i\theta} \Psi(\mathbf{r}_2, \mathbf{r}_1) \quad (1.1)$$

If $\theta = 0$, the wavefunction is symmetric and the particles obeying this condition are the bosons. If $\theta = \pi$, the wavefunction is antisymmetric, and the particles are fermions¹.

The thermodynamical properties of an ensemble of N fermions or bosons can be deduced from the canonical partition function:

$$Z_N(T, V) = \sum_n e^{-\beta E_n}, \quad (1.2)$$

¹The class of particles for arbitrary θ are called *anyons*, and play a central role as excitations in fractional quantum hall physics. They will not be considered in this work.

where the sum goes over all eigenstates n of the system, with energy E_n and $\beta = 1/k_B T$. For an interacting system, this sum in general cannot be performed analytically since its spectrum E_n is usually unknown. However, in some simple cases this can be done. We consider an ensemble of non-relativistic non-interacting particles of a mass m in a box, for which the Hamiltonian reads:

$$\hat{H} = \sum_{i=1}^N \frac{\hbar^2 \mathbf{k}_i^2}{2m}. \quad (1.3)$$

Since the system is non-interacting, the many-body states can be readily built from the one-body states. In a box of size L , the momentum states available are quantized and we refer to a many-body state by the number of particles $n_{\mathbf{k}}$ occupying the state of momentum \mathbf{k} (we consider here spinless particles for simplicity). For bosons, the occupation number can take any positive integer value. For fermions however, $n_{\mathbf{k}}$ can only be equal to 0 or 1, because the Pauli exclusion principle forbids two fermions to be in the same quantum state. We can calculate the partition function. However, the constraint on the total particle number makes the sum (1.2) difficult to evaluate. This constraint can be relaxed by calculating instead the partition function in the grand-canonical ensemble. In this ensemble, the atom number is fixed only in average value and the chemical potential is a new thermodynamic variable. The grand partition function is:

$$Z(\mu, T, V) = \sum_{N=0}^{\infty} e^{N\beta\mu} Z_N(T, V) \quad (1.4)$$

The sum can be easily calculated for an ideal gas, by summing on each occupation number independently [64] and one finds:

$$Z(\mu, T, V) = \begin{cases} \prod_{\mathbf{k}} \frac{1}{1 - e^{-\beta(\epsilon_{\mathbf{k}} - \mu)}} & \text{Bosons} \\ \prod_{\mathbf{k}} (1 + e^{-\beta(\epsilon_{\mathbf{k}} - \mu)}) & \text{Fermions} \end{cases} \quad (1.5)$$

The mean occupation number in the state of momentum \mathbf{k} can be computed from the partition function:

$$\langle n_{\mathbf{k}} \rangle = -k_B T \frac{\partial}{\partial \epsilon_{\mathbf{k}}} \log Z(\mu, T, V) = \frac{1}{e^{\beta(\epsilon_{\mathbf{k}} - \mu)} \pm 1}, \quad (1.6)$$

where the + is applicable for fermions and gives the Fermi-Dirac distribution. For bosons (-), we recover the Bose-Einstein statistics.

1.1.2 Bose-Einstein Condensation

We will now separate the analysis for the Bose and Fermi gases. For a Bose gas, the total atom number is:

$$N = k_B T \frac{\partial}{\partial \mu} \log Z = \sum_{\mathbf{k}} \frac{1}{e^{\beta(\epsilon_{\mathbf{k}} - \mu)} - 1}. \quad (1.7)$$

In the limit $V \rightarrow \infty$, we can replace the sum $\sum_{\mathbf{k}}$ by an integral $\frac{V}{(2\pi)^3} \int d^3 k$ if each term of the sum is small compared to N , and Eq.(1.7) then yields:

$$n \lambda_{\text{dB}}^3 = \text{Li}_{3/2}(e^{\beta\mu}) \quad (1.8)$$

where $n = N/V$ is the density, $\lambda_{\text{dB}} = \sqrt{\frac{2\pi\hbar^2}{mk_B T}}$ is the thermal de Broglie wavelength, $e^{\beta\mu}$ is the fugacity, and Li_s is the polylogarithm of order² s . The right-hand side of Eq.(1.8) has an upper-bound of $\text{Li}_{3/2}(0) = \zeta(3/2)$ (where ζ is the Riemann ζ -function, and the maximum is reached when

²The polylogarithm Li_s of order s is defined as:

$$\text{Li}_s(x) = \frac{1}{\Gamma(s)} \int_0^{\infty} \frac{u^{s-1}}{x^{-1}e^u - 1} du = \sum_{u=1}^{\infty} \frac{x^u}{u^s},$$

where Γ is the Euler function.

$\mu = 0$). This upper limit on phase-space density is a result of the assumption that each term of the sum (1.7) is small and thus the sum can be replaced by an integral. This is the expression of the *saturation* of the excited states. If additional particles are added to the system, they will accumulate in the one-body ground state (here $\mathbf{k} = 0$) and a macroscopic number of particles will share the same wavefunction, resulting in what is called a *Bose-Einstein condensate*. The textbook picture of the saturation of the excited states has recently been tested experimentally using ^{39}K with tunable interactions and it was seen that even very weak interactions dramatically change the Einstein picture of saturation but that it is recovered in the non-interacting limit [65]. Bose-Einstein condensation is a remarkable phase transition as it occurs in a non-interacting system and is solely driven by the quantum correlation due to indistinguishability of the particles.

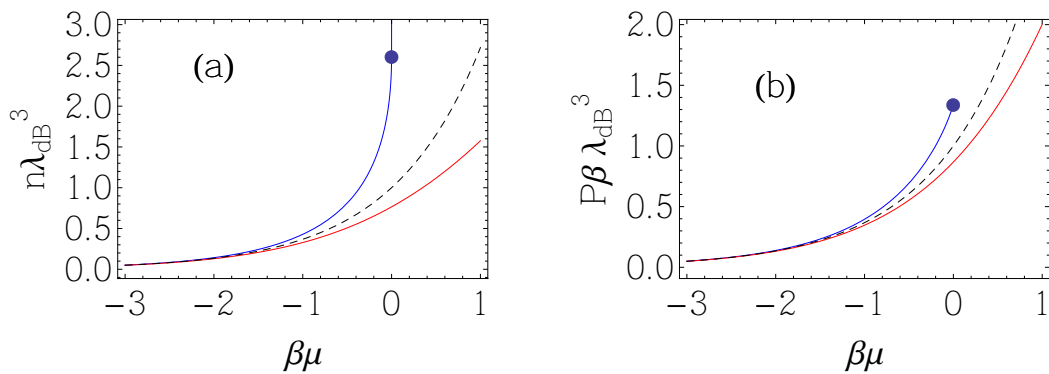


Figure 1.1: Grand-canonical equation of state of the ideal quantum gases. (a): phase space density $n\lambda_{\text{dB}}^3$ and (b) pressure $P\beta\lambda_{\text{dB}}^3$ of the Bose (blue), Fermi (red), and classical gas (dashed black). The blue circle corresponds to the Bose-Einstein transition point.

In order to describe the condensed state, it is necessary to single-out the term corresponding to $\mathbf{k} = 0$ in the sum (1.7) and the integral will describe the excited states. Instead of Eq.(1.8), we find:

$$n\lambda_{\text{dB}}^3 = \text{Li}_{3/2}(e^{\beta\mu}) + \frac{\lambda_{\text{dB}}^3}{V} \frac{e^{\beta\mu}}{1 - e^{\beta\mu}}. \quad (1.9)$$

For a non-condensed gas the second term vanishes in the thermodynamic limit, but if a Bose-condensed fraction is present ($\mu = 0$), this term remains. Solving Eq.(1.9) for μ at fixed V , and taking the limit $V \rightarrow \infty$ one finds the density of the ideal Bose gas:

$$\begin{cases} n\lambda_{\text{dB}}^3 = \text{Li}_{3/2}(e^{\beta\mu}) & \text{if } \mu < 0 \\ n\lambda_{\text{dB}}^3 > \zeta(3/2) & \text{if } \mu = 0 \end{cases} \quad (1.10)$$

Integrating the density over μ , one deduces the pressure of the ideal Bose gas:

$$\frac{P\lambda_{\text{dB}}^3}{k_B T} = \begin{cases} \text{Li}_{5/2}(e^{\beta\mu}) & (n < n_c) \\ \text{Li}_{5/2}(1) & (n > n_c), \end{cases} \quad (1.11)$$

where $\text{Li}_{5/2}(1) = \zeta(5/2) \approx 1.34$. In the grand-canonical ensemble, the equation of state $P(\mu)$ of the ideal Bose gas is peculiar because the thermodynamic variable μ cannot take any positive value. From the EoS (1.11) one can compute all the thermodynamic quantities of the Bose gas, such as the entropy, the internal energy or the specific heat.

Low and High-temperature limits

In the limit of high-temperature $k_B T \gg \mu$ (or low fugacity), the pressure can be expanded in powers of the fugacity, an expansion called the *virial expansion*:

$$P = \frac{k_B T}{\lambda_{\text{dB}}^3} \sum_{k=1}^{\infty} \tilde{b}_k e^{k\beta\mu} \quad (1.12)$$

The first virial coefficient \tilde{b}_1 must be equal to unity, in order to recover the pressure of the non-interacting classical gas in the limit $e^{\beta\mu} \rightarrow 0$:

$$P_{\text{cl}} = \frac{k_B T}{\lambda_{\text{dB}}^3} e^{\beta\mu} \quad (1.13)$$

There is a physical interpretation to the virial expansion in term of clusters [64]. Indeed one starts with the grand-partition function (see Eq.1.4) and the expression of the pressure in term of Z :

$$PV = k_B T \log(Z), \quad (1.14)$$

Then the pressure can be written as³:

$$PV = k_B T Z_1 (e^{\beta\mu} + \tilde{b}_2 e^{2\beta\mu} + \tilde{b}_3 e^{3\beta\mu} + \dots) \quad (1.15)$$

and the virial coefficients can be expressed in term of the cluster partition functions of n particles Z_n :

$$\tilde{b}_2 = (Z_2 - Z_1^2/2) / Z_1 \quad (1.16)$$

$$\tilde{b}_3 = (Z_3 - Z_1 Z_2 + Z_1^3/3) / Z_1 \quad (1.17)$$

and so on. One thus sees that in order to compute the n^{th} virial coefficient, one has to solve the n -body problem. All but the lowest virial coefficient vanish for the Boltzmann gas, because of the absence of correlations. In the case of quantum gases, this is no longer true because of the quantum correlations introduced by the indistinguishability of the particles. The virial coefficients for the ideal quantum gases can be readily obtained by Taylor-expanding the equation of state in Eq.(1.11), and we find $\tilde{b}_k = k^{-5/2}$.

The low-temperature limit is obtained from Eq.(1.11), and the pressure goes to zero as $T^{5/2}$. It is easy to show that this results in a specific heat that vanishes as $T^{3/2}$. For a linear dispersion law $\epsilon_k = \hbar ck$ instead of the quadratic of Eq.(1.3), the same calculation leads to the Debye model for phonons where $C_V \propto T^3$ at low temperature.

1.1.3 Fermi Degeneracy

We now turn to the ideal Fermi gas. Starting from the total atom number expression Eq.(1.7) and using instead the Fermi-Dirac distribution, we find:

$$n\lambda_{\text{dB}}^3 = -\text{Li}_{3/2}(-e^{\beta\mu}). \quad (1.18)$$

In contrast to the case of the gas of bosons, Eq.(1.18) provides a value of the fermionic density n for all values of μ . There is no phase transition and the transition from a classical gas to the quantum degeneracy is a smooth crossover for an ideal Fermi gas. Integrating Eq.(1.18) over chemical potential, we compute the EoS:

$$\frac{P\lambda_{\text{dB}}^3}{k_B T} = -\text{Li}_{5/2}(-e^{\beta\mu}). \quad (1.19)$$

³The validity of such an expansion is not obvious since the convergence radius of the virial expansion depends on the system studied (and is in general unknown).

Low and High-temperature limits

Let us look at the low-temperature limit of the fermionic EoS (1.18). Using the Sommerfeld expansion, we find the asymptotic expansion of the polylogarithm for large values of the fugacity⁴, and we recover to lowest order $\mu = \frac{\hbar^2}{2m}(6\pi^2 n)^{2/3} \equiv E_F$. Integrating the next term in the Sommerfeld expansion provides the expansion for the pressure:

$$P(\mu) = P_0(\mu) \left(1 + \frac{5\pi^2}{8} \left(\frac{k_B T}{\mu} \right)^2 + \dots \right) \quad (1.20)$$

where $P_0(\mu) = \frac{1}{15\pi^2} \left(\frac{2m}{\hbar^2} \right)^{3/2} \mu^{5/2}$ is the $T = 0$ Fermi pressure. The virial expansion equally applies to the ideal Fermi gas, and we immediately find $\tilde{b}_k = (-1)^{k+1} k^{-5/2}$.

1.2 Short-Range Interactions

The theory of non-interacting quantum gases is straightforward and all thermodynamic quantities can be readily computed. Obviously, most systems of interest are composed of interacting particles, to which we now turn. Usually, interacting systems are described with a binary interaction potential $V_{\text{int}}(\mathbf{r}_i - \mathbf{r}_j)$ so that the Hamiltonian of the N -body system is:

$$\hat{H} = \sum_{i=1}^N \frac{\hbar^2 \mathbf{k}_i^2}{2m} + \sum_{i<j} V_{\text{int}}(\mathbf{r}_i - \mathbf{r}_j). \quad (1.21)$$

In general the properties of the many-body system will depend on the specific form of the interaction potential V . For neutral alkali atoms, this potential has a $1/r^6$ tail (where r is the interatomic spacing) due to the electric dipole-dipole interactions (the van der Waals interaction), and a hard-core repulsion at short range when the valence electronic clouds start to overlap. The typical range of the interaction, on the order of hundreds of a_0 (where $a_0 = 0.0529$ nm is the Bohr radius), is much smaller than the typical interparticle spacing in dilute gases. For lithium for example, the van der Waals range is $r_{\text{vdW}} \sim 65 a_0$ while for densities of 10^{13} cm^{-3} (which are typically obtained in quantum degenerate gases only), the ratio of the range to the interparticle spacing $n^{1/3} r_{\text{vdW}} \sim 0.007$ is indeed much smaller than unity. Intuitively, one would thus expect the system to be nearly non-interacting, which is correct only in the classical limit. However the quantum-mechanical picture is very different because a short-range (even a zero-range, as we shall see) potential can scatter matter waves. As a result, even very dilute quantum systems can be strongly altered by weak interactions, while their classical counterpart remain only barely perturbed.

1.2.1 Reminder of scattering theory: s -wave scattering

Ultracold atomic systems offer in this respect a significant simplification of scattering processes because of the very low energies of the colliding particles. To characterize the elastic collisions at low temperatures, we have to look at the scattering of two particles, which in the frame of the center of mass is equivalent to the scattering of one particle of reduced mass in the potential

⁴ In the limit $\beta\mu \rightarrow \infty$, we have:

$$-\text{Li}_{3/2}(-e^{\beta\mu}) = \frac{4}{3\sqrt{\pi}} \left((\beta\mu)^{3/2} + \frac{\pi^2}{8} \sqrt{\beta\mu} + \dots \right)$$

$V_{\text{int}}(r) = V_{\text{int}}(|\mathbf{r}_1 - \mathbf{r}_2|)$ (assumed to be isotropic). One has to solve the Schrödinger equation⁵:

$$(\Delta + k^2)\psi(\mathbf{r}) = \frac{mV_{\text{int}}(r)}{\hbar^2}\psi(\mathbf{r}), \quad (1.22)$$

where $k^2 = 2mE/\hbar^2$ is the square of the relative momentum of the two atoms (of mass m), with the following asymptotic behavior (for r much larger than the range of the potential):

$$\psi(\mathbf{r}) \approx e^{ikz} + f(k, \theta) \frac{e^{ikr}}{r} \quad (1.23)$$

where θ is the angle between the relative momentum of the two atoms before (here assumed along the z -axis) and after the scattering. The quantity $f(k, \theta)$ is called the scattering amplitude. The differential cross-section can be deduced from it, $\frac{d\sigma}{d\Omega} = |f(k, \theta)|^2$. The assumption of the isotropy of the interaction potential can be used to expand the wavefunction in Legendre polynomials of $\cos \theta$, thanks to the axial symmetry of the problem around the z -axis of the incoming plane wave. This expansion decouples the problem of the scattering to solving a radial equation for each partial wave of order l , under the effective potential:

$$V_{\text{eff}} = V_{\text{int}}(r) + \frac{\hbar^2}{2m} \frac{l(l+1)}{r^2}, \quad (1.24)$$

where the second term is the centrifugal barrier. For sufficiently low energies of the incoming particles (or equivalently low temperatures), the barrier will prevent scattering for partial waves $l > 0$, and only the isotropic $l = 0$ wave (or s -wave) will be scattered. A quick estimate for Li shows that the height of the barrier for the $l = 1$ (or p -wave) will be $\sim k_B \times \text{mK}$ (and larger for higher partial-waves) and the particles will not explore the short-ranged part of the interaction potential (see Fig.1.2). Thus, except in the case of resonantly enhanced high-order partial wave scattering, these are strongly suppressed at the typical ($\sim \mu\text{K}$) temperatures of ultracold gases.

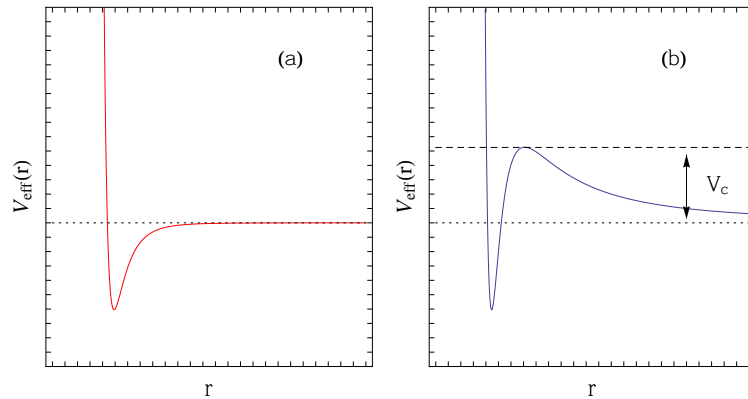


Figure 1.2: Effective interaction potential $V_{\text{eff}}(r)$ as a function of the interatomic distance r . (a): Typical interaction potential between two alkali atoms in the s -wave channel. (b): effective potential with a centrifugal barrier V_c (second term of Eq.(1.24)).

⁵For a detailed presentation, we refer the interested reader to [66]

1.2.2 The Scattering Length a and Universality

The low-energy limit of ultracold collisions can be further exploited to simplify the problem as the scattering amplitude for s -wave scattering can be expanded for low values of k [67]:

$$f_{l=0}(k) = -\frac{1}{a^{-1} + ik - \frac{1}{2}k^2 r_e + \dots}, \quad (1.25)$$

where

$$a = -\lim_{k \rightarrow 0} f_{l=0}(k) \quad (1.26)$$

is the s -wave scattering length, and r_e is the so-called effective range of the interaction. If k is sufficiently small such that the effective range is negligible ($k^2 r_e \ll a^{-1}$) the collisions are characterized by the scattering length a only. This result has far-reaching consequences: if systems consisting of different types of particles (neutrons, ${}^6\text{Li}$, ${}^{40}\text{K}$ for fermionic systems for example) with different interaction potentials have the same scattering length, they will share the same physics, a property we will refer to as *universality*. In some cases that we will also encounter in this work, the short-range physics can play a role, and different many-body systems might differ from one to another. For large values of a , the scattering amplitude is limited to $f = i/k$ and the elastic cross-section, to $\sigma = 4\pi/k^2$, the *unitary limit*.

We discussed so far the case of distinguishable particles. Indistinguishability in quantum mechanics plays an important role in the scattering process. In Fig.1.3, we show a cartoon of two possible scattering paths. Since particles 1 and 2 are indistinguishable, so are these two paths and their probability amplitude must be summed and lead to an interference. Depending on the (anti)-symmetry imposed to the wavefunction for (fermions) bosons, one can show that the differential elastic cross-section reads:

$$\frac{d\sigma}{d\Omega} = |f(k, \theta) + \epsilon f(k, \pi - \theta)| \quad (1.27)$$

where $\epsilon = 1$ (-1) for identical bosons (fermions). Since we have assumed s -wave scattering only, the scattering amplitude is independent of θ and as a result, in the low-energy limit the elastic cross-section is $\sigma = 8\pi a^2$ for bosons, and $\sigma = 0$ for fermions. The absence of s -wave collisions for polarized fermions is a consequence of the antisymmetry constraint: while the spin and radial part of the wavefunction are symmetric, the angular part must be antisymmetric, which is incompatible with isotropic scattering.

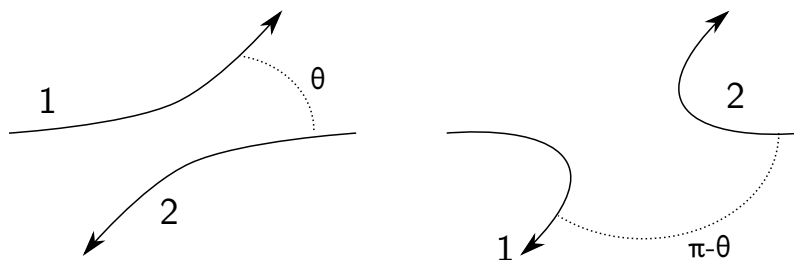


Figure 1.3: Scattering of two particles. For indistinguishable particles, the two paths drawn interfere in the calculation of the elastic cross-section, leading to a different behavior for bosons and fermions.

1.2.3 Feshbach Resonances

Scattering Resonances

One of the most attractive aspects with ultracold quantum gases is the possibility of tuning the scattering length. This is due to the existence of Feshbach resonances, which are a type of scattering resonance. In order to illustrate the concept of a scattering resonance as well as the zero-range limit and universal Feshbach bound states, we will take a look at simple textbook examples, the square-well, and the square-barrier potential of range b and amplitude V_0 . These two models will be important with respect to Monte Carlo simulations presented in this work.

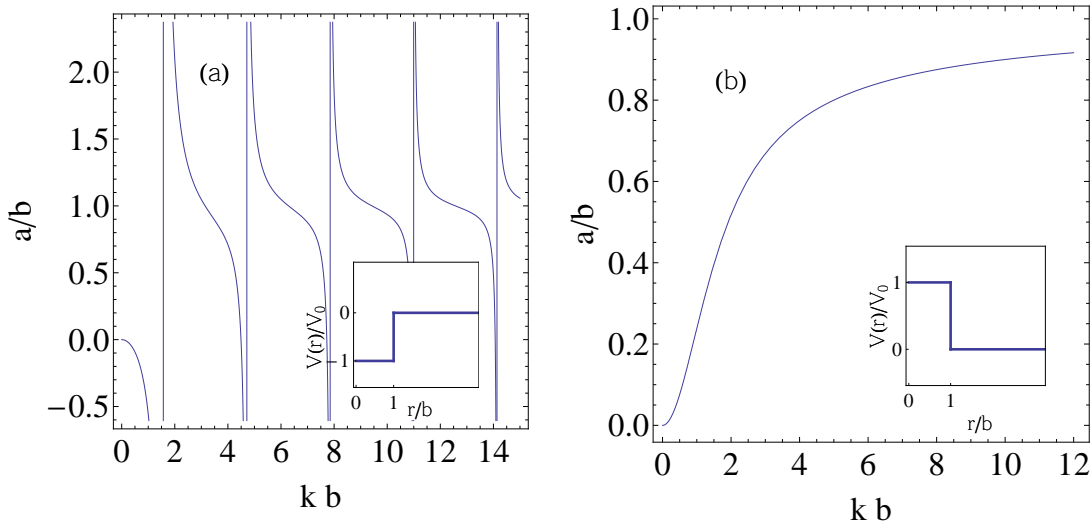


Figure 1.4: Scattering length for (a): square well potential and (b): square-barrier. The height (depth) of the barrier (well) is V_0 and its range, b . The insets represent the model potentials.

Solving the Schrödinger equation for a single-particle in the square-well by computing the zero energy solution $k \rightarrow 0$ which has the asymptotic form $1 - a/r$ for large values of the coordinate r , one finds:

$$a = b \left(1 - \frac{\tan k_0 b}{k_0 b} \right), \quad (1.28)$$

where $k_0^2 = 2mV_0/\hbar^2$. There are periodic resonant enhancements of the scattering when $k_0 b = \frac{\pi}{2}(1 + 2n)$ (where n is an integer). This condition corresponds to the appearance of a new bound state in the square-well. For the barrier potential, the expression providing the scattering length is very similar to that of the square well potential Eq.(1.28):

$$a = b \left(1 - \frac{\tanh k_0 b}{k_0 b} \right). \quad (1.29)$$

The result is very different: the scattering length is always smaller than the range b (the equality is achieved in the limit of a hard-sphere repulsion $V_0 = \infty$). The results obtained for these two basic examples are more general: for a purely repulsive potential, the scattering length will always be on the order of the range of the potential. Thus one cannot realize a system with purely repulsive binary interactions that would be both strongly interacting and dilute (in the sense that the interparticle spacing is much larger than the potential range $n^{-1/3} \gg b$). In contrast, a

potential with an attractive part can have a scattering length much larger than the range so that the strongly interacting limit $na^3 \gg 1$ is compatible with the diluteness condition $nb^3 \ll 1$. Such a system can be expected to have universal properties. However, having an attractive part in the interaction potential is delicate for numerical simulations as the system might sustain many-body bound states (clusters) that do not correspond to the metastable gaseous phase observed in the experiments.

The Zero-Range Limit

If the details of the microscopic potential do not matter, we are in principle free in our choice of model interaction potential that provides the desired scattering length. This idea constitutes a considerable theoretical simplification because inter-atomic interaction potentials are notoriously complex and accurate determination of their shape is a difficult task. This difficulty cannot be circumvented in general with dense quantum liquids such as ^4He where accurate knowledge of the interaction potential is important to obtain quantitatively satisfactory results (see for example [68]). Since in our dilute quantum gases the range of the interaction potential is usually irrelevant, it is natural to choose a model potential with no characteristic length scale and the zero-ranged 3D *pseudo-potential*⁶ is widely used to model the interactions $V_{\text{pseudo}}(\mathbf{r}_1 - \mathbf{r}_2) = g\delta(|\mathbf{r}_1 - \mathbf{r}_2|)$, where the coupling constant is $g = 4\pi\hbar^2 a/m$. An interesting property of the pseudo-potential is that it scatters only in the s -wave channel and its scattering amplitude is equal to the expansion (1.25) with $r_e = 0$.

To understand the meaning of the zero-range limit, we can take the square-well model presented above. We take the limit $V_0 \rightarrow \infty$ and $b \rightarrow 0$ such that the scattering length in Eq.(1.28) is fixed and much larger than the range b (so that $a \approx -\tan(k_0 b)/k_0$). We find that the shallowest bound state (in the limit where the depth V_0 is much larger than the energy E of this state) has an energy $E \rightarrow -\hbar^2/(ma^2)$ (where m is the mass of one particle) and a wavefunction $\psi(x) \propto e^{-|x|/a}$. These results are important: this bound state is universal, its size and energy depend on the potential only through its scattering length, not on its range. This bound state, which we will refer to as a *Feshbach molecule* will be the same for any short-ranged potential possessing a shallow bound state. In contrast, the deeply bound states will extend over a range on the order of b : they thus depend on the short-range characteristics of the potential. The zero-range pseudo-potential supports a single bound state, which is the Feshbach molecule, provided $a > 0$.

Feshbach Resonances

We have seen that by manipulating the depth of the interaction potential, we can change the scattering length. For interatomic interactions, the shape of the potential is given by the interactions between the electrons and the nuclei and cannot be modified. However, a different type of scattering resonance exists in atomic systems, called Feshbach resonance. The detailed mechanism of these resonances is rather subtle and we will only give the idea as the mechanism itself will not be

⁶Writing the pseudo-potential as a delta function is a common shortcut, but it is valid only in the Born approximation. Beyond that approximation, the delta function leads to ultraviolet divergences (for example in the calculation of the ground state energy of a BEC). A solution is to use the regularized pseudo-potential:

$$V_{\text{pseudo}}(\psi) = \frac{4\pi\hbar^2 a}{m} \delta(\mathbf{r}) \frac{\partial}{\partial r} (r\psi(\mathbf{r})). \quad (1.30)$$

Equivalently, the zero-range potential can also be replaced by contact boundary conditions (called the Bethe-Peierls conditions) on the many-body wavefunction obeying a free Schrödinger equation (see [69]).

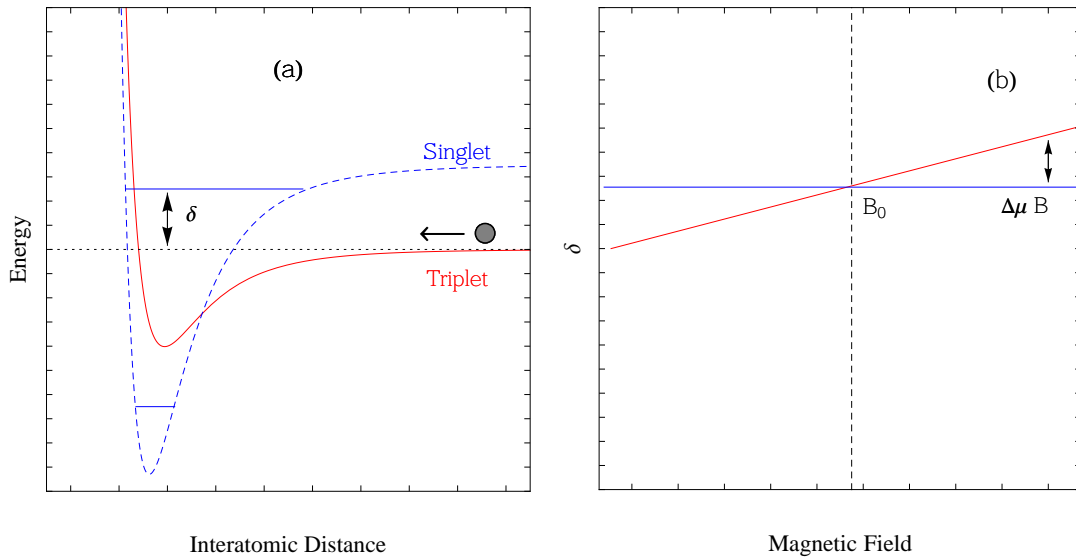


Figure 1.5: Principle of a Feshbach resonance. (a): The incoming atoms are in the open channel (full red line). Due to the coupling to the closed channel (dashed blue line), the scattering properties of the former are modified. A Feshbach resonance occurs at a magnetic field B_0 when a bound state in the closed channel is resonant with the energy in the continuum, or $\delta = 0$. (b): The energy detuning between the two potentials can be changed via a magnetic field (same color code).

relevant for the rest of this work, and extended explanations can be found elsewhere (for instance in [70]). A Feshbach resonance involves two potentials (called channels in this context). For alkali atoms, the two potentials are the singlet ($S = 0$) and triplet ($S = 1$) of electronic spin configuration (of the two valence electrons), see Fig.1.5a. Because of the hyperfine interaction, these two potentials are coupled and the scattering properties in the entrance channel can be modified. Since the magnetic moment is not the same for the two potentials (noted $\Delta\mu$ in Fig.1.5b), they can be shifted with respect to each other via an external magnetic field. A Feshbach resonance occurs at a magnetic field B_0 when a bound state in the closed channel matches the energy of the continuum in the open channel ($\delta = 0$ in Fig.1.5). In the vicinity of a s -wave Feshbach resonance, the scattering length depends dispersively on the magnetic field [71]:

$$a(B) = a_{\text{bg}} \left(1 + \frac{\Delta}{B - B_0} \right), \quad (1.31)$$

where a_{bg} is the background scattering length, B_0 is the resonance position and Δ , its width, is defined as the separation between the resonance position and the zero-crossing.

Feshbach Resonances in Lithium

Feshbach resonance were observed in cold atoms in the late '90 [33, 32, 34] and since then a large number of resonances have been identified with different elements [70]. We will focus on our system, namely ${}^7\text{Li}$ - ${}^6\text{Li}$ for which resonances had been predicted back in 1995 [71]. For fermionic ${}^6\text{Li}$, s -wave Feshbach resonances have been found in mixtures of all the three lowest Zeeman sub-states $|1\rangle, |2\rangle$ and $|3\rangle$ (see Fig.2.1 for the states labeling). The position and width of the three broad resonances have been determined by spectroscopic means [72] and are shown in Table 1.1.

Table 1.1: broad s -wave Feshbach resonances in ${}^6\text{Li}$ [72]

Mixture	a_{bg}/a_0	$B_0(G)$	$\Delta B(G)$
$ 1\rangle - 2\rangle$	-1405	834.1(1.5)	300
$ 1\rangle - 3\rangle$	-1727	690.4(5)	122.3
$ 2\rangle - 3\rangle$	-1490	811.2(1.0)	222.3

A narrow resonance in the $|1\rangle - |2\rangle$ mixture has also been found around 543 G (width of about 400 mG) [73, 74] as well as three p -wave resonances in polarized $|1\rangle$, $|2\rangle$ and in the $|1\rangle - |2\rangle$ mixture [75, 76].

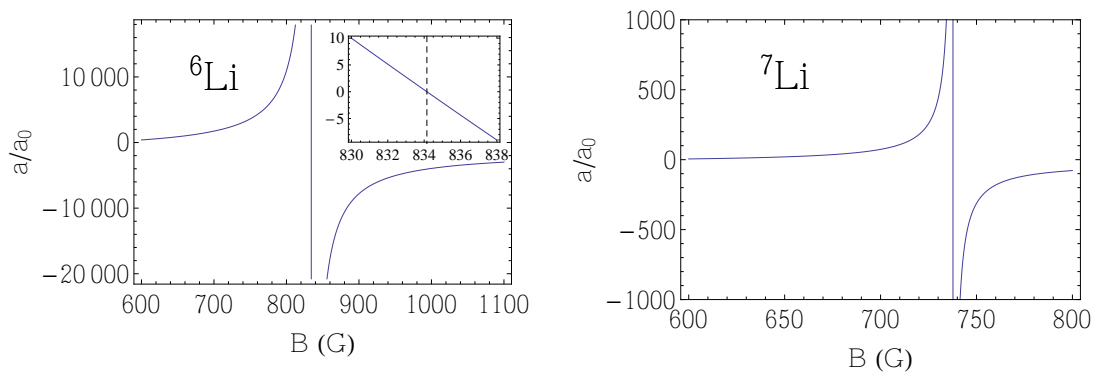


Figure 1.6: The Feshbach resonances used in this work. (a): Feshbach resonance of ${}^6\text{Li}$ in the spin-mixture $|1\rangle$ and $|2\rangle$. Inset: Zoom around the resonance: $(a/a_0)^{-1} \times 10^6$ as a function of B . (b): Resonance of ${}^7\text{Li}$ in spin state $|1\rangle$.

Bosonic ${}^7\text{Li}$ also possesses various resonances. The lowest energy state $|1\rangle$ (see Fig.2.1) has a wide Feshbach resonance at 737.8 G [77, 78, 79, 59]. This is the Feshbach resonance that we used in our experiments. There are two additional resonances in the state $|2\rangle$ that have been recently discovered: a broad one, with a width of 34 G located at 884^{+4}_{-13} G, and a narrow one (width of 7 G) at 831(4) G [80]. There are also several heteronuclear Feshbach resonances in the ${}^6\text{Li}$ - ${}^7\text{Li}$ system [81, 82, 83, 84], which makes this system very suitable for isotopic strongly interacting Bose-Fermi gas experiments, similarly to the ${}^{39}\text{K}$ - ${}^{40}\text{K}$ mixture [85].

1.3 Probing the Equation of State of Quantum Gases

We have shown that interactions between two particles in dilute quantum gases can in general be accurately described by a single parameter, the scattering length, characterizing the short-range interactions⁷. Now we are in position to ask the driving question behind this work: what are the macroscopic thermodynamic properties and the phase diagram of homogeneous quantum gases

⁷It is important to note that several ultracold systems currently studied do not fall in this category such as dipolar gases, with long-range anisotropic interactions (see [86] and references therein), or quantum gases in the vicinity of narrow resonances, where the effective range is not negligible (see for example [87, 88, 89]).

with short-range interactions ?

The Equation of State contains all the thermodynamic information about the macroscopic properties of a physical system, and many experimentally relevant quantities can be extracted from it, such as the specific heat, the compressibility or the magnetic susceptibility. In general, a phase transition will manifest itself as a singularity in the EoS. Depending on the statistical ensemble we are working with, the EoS has different expressions. Because of their use in this work, we will restrict ourselves to the canonical and grand-canonical ensembles. The canonical EoS is the equation relating the canonical thermodynamic potential, i.e. the energy E , to the entropy S (for a given volume V and particle number N)⁸:

$$E = E(S, V, N). \quad (1.32)$$

In the grand-canonical ensemble the EoS reads:

$$\Omega = \Omega(T, V, \mu), \quad (1.33)$$

relating the grand-potential Ω to the temperature T , the chemical potential μ , and the volume V . In the thermodynamic limit, these two formulations are equivalent [64] and they are related through a Legendre transform:

$$\Omega = E - TS - \mu N. \quad (1.34)$$

From the Gibbs-Duhem formula $Nd\mu = -SdT + VdP$, we relate the grand-potential to the pressure: $\Omega = -PV$. The density can be deduced from the Gibbs-Duhem relation at fixed temperature: $n = \left(\frac{\partial P}{\partial \mu}\right)_{T,V}$. The entropy is given by $S = -\left(\frac{\partial \Omega}{\partial T}\right)_{\mu,V}$.

1.3.1 Dealing with the Trapping Potential: Local Density Approximation

The ultracold atom experiments usually display an additional important feature: the atoms are confined in an external trapping potential $V(\mathbf{r})$. Even though box potentials have been realized experimentally [91] (but they require delicate tunings), most experiments are achieved in harmonic traps (or gaussian traps corresponding to the potential created by an optical dipole trap), and the gas is spatially inhomogeneous, with a local density $n(\mathbf{r})$. The relation between the properties of the trapped gas and the corresponding homogeneous system is not simple. In principle, one has to solve the many-body Hamiltonian with the additional external trapping potential, which is a different problem than the Hamiltonian of the homogeneous system alone.

The Local Density Approximation

However, the picture is considerably simplified if the trapping potential and the density of the gas are sufficiently slowly varying so that one can assume that the inhomogeneous gas can be decomposed into small volumes in which the gas can be locally considered as homogeneous, with the same properties as a uniform gas with a density $n(\mathbf{r})$. Within this approximation, called the

⁸Note that the definition of the equation of state here is different from the textbook definition [90], where the EoS are defined as the set of relationships expressing the intensive parameters in terms of the independent extensive parameters, for example $P = P(S, V, N)$, $T = T(S, V, N)$, etc. In this case, *all* equations of state are in general required to recover the fundamental equation $E = E(S, V, N)$. We will rather define the last expression as the equation of state in the canonical ensemble.

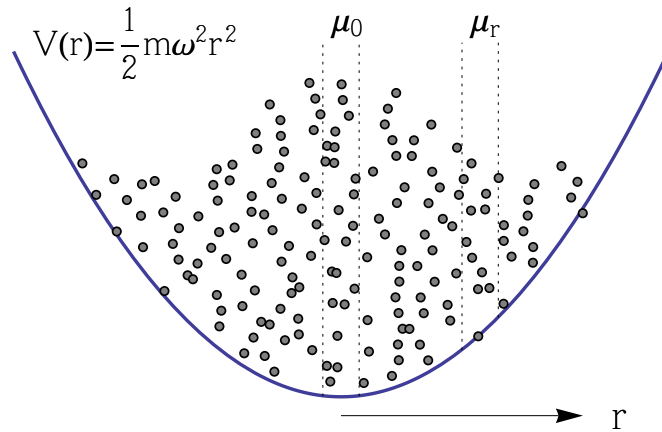


Figure 1.7: Sketch of the local density approximation. The system can be subdivided in mesoscopic volumes (dotted vertical lines) where the system has the properties of the homogeneous gas with a local chemical potential $\mu_r = \mu_0 - V(r)$, where μ_0 is the global chemical potential and $V(r)$ the trapping potential (blue solid line).

local density approximation (LDA), the trapping potential acts as an offset to the local chemical potential $\mu[n(\mathbf{r})]$ compared to the global chemical potential of the gas μ_0 :

$$\mu[n(\mathbf{r})] = \mu_0 - V(\mathbf{r}). \quad (1.35)$$

This approximation is equivalent to the mechanical equilibrium condition in hydrostatics: $\nabla P(\mathbf{r}) + n(\mathbf{r})\nabla V(\mathbf{r}) = 0$. From the Gibbs-Duhem relation at fixed temperature, we have $\nabla P = n(\mathbf{r})\nabla\mu$ and we indeed recover Eq.(1.35). In some simple cases such as the $T = 0$ weakly interacting Bose-Einstein condensate describable by the Gross-Pitaevskii equation (see section 3.1.2), the validity of the LDA can be readily verified. While it is easy to formulate necessary conditions, such as the level spacing in the trap being much smaller than the other energy scales, $\hbar\omega \ll k_B T, \mu$ in order for the LDA to be applicable, it is difficult to assess *a priori* the validity of the LDA for a strongly interacting many-body system. For instance the presence of vortices, or phase transitions can lead to sharp boundaries inside the gas, where the LDA can be locally violated.

How to measure the Equation of State within the LDA

The Local Density Approximation has very powerful consequences. Given the knowledge of the trapping potential $V(\mathbf{r})$, the LDA implies that the equation of state can be directly extracted from the in-situ density distribution. Starting from Eq.(1.35), measuring the EoS requires two steps: 1) The determination of the global chemical potential μ_0 (and possibly other variables, such as the chemical potential of other species present, the temperature T or the scattering length a , depending on the system studied). 2) The measurement of the local density $n(\mathbf{r})$, which then gives at each point \mathbf{r} , a value of the equation of state $\mu[n(\mathbf{r})]$. Each of these two steps presents significant challenges.

- The determination of the global chemical potential μ_0 from the shape of the cloud seems at first sight to require the knowledge of the EoS $n[\mu(\mathbf{r})]$ because within the LDA, μ_0 is

implicitly fixed by the total atom number N normalization:

$$\int n[\mu(\mathbf{r})]d^3r = \int n[\mu_0 - V(\mathbf{r})]d^3r = N \quad (1.36)$$

We have implemented throughout this work various techniques to determine μ_0 in a model-independent way depending on the system investigated.

- The measurement of the local density $n(\mathbf{r})$ presents different issues. For low-dimensional systems, absorption imaging in principle gives direct access to the surface density $n_{2D}(x, y)$ or the linear density $n_{1D}(z)$ ⁹ making the measurement of the EoS rather direct (see section 1.3.2). In 3D, the probe laser beam propagates along one direction in the cloud¹⁰. The integration along this line-of-sight thus gives access to the 2D-projection $\bar{n}'(x, z)$ of the three-dimensional density $n(x, y, z)$:

$$\bar{n}'(x, z) = \int dy n(x, y, z). \quad (1.37)$$

This issue can be overcome in different ways, either by performing the measurement of the global EoS for the trapped gas, or by reconstructing through numerical methods the real density from $\bar{n}'(x, z)$ (section 1.3.3). Finally, we will present the method that we have developed which actually benefits from the line-of-sight integration to extract directly the pressure from the density profiles (section 1.3.4).

1.3.2 Direct measurement of the EoS in low dimensions

The equation of state of a two-dimensional Bose gas has been extracted in C. Chin's group in Chicago [94] and J. Dalibard's group at ENS [92, 95] from an analysis of the in-situ density profiles (Fig.1.8). In this case, the EoS can be written as:

$$n\lambda_{dB}^2 = F\left(\frac{\mu}{k_B T}, \tilde{g}\right), \quad (1.38)$$

relating the phase space density $n\lambda_{dB}^2$ to the chemical potential $\mu/k_B T$ and to the 2D coupling constant $\tilde{g} = \sqrt{8\pi}a/l_z$. Here, collisions are assumed to be three-dimensional (with a scattering length a) and the harmonic oscillator length in the tightly confining direction z is $l_z = \sqrt{\hbar/m\omega_z}$. The particularity that in 2D \tilde{g} is dimensionless results in a scale invariance¹¹: at a given value of a , all density distribution obtained for any N and T should collapse in a single curve depending on $\mu/k_B T$ only (and \tilde{g} as a parameter). This approximate scale invariance was checked on 2D gases of ¹³³Cs [94] and ⁸⁷Rb [95]. The global chemical potential and temperature were obtained by fitting the wings of the each density profile with the EoS obtained from a mean-field Hartree-Fock theory.

Even though Bose-Einstein condensation does not occur in the thermodynamic limit for a homogeneous two-dimensional Bose gas because long-range order is prohibited in 2D [97, 98], a transition to superfluidity characterized by a topological order was predicted in 1973 by Berezinskii and by Kosterlitz and Thouless (BKT) [99, 100]. The entrance in the superfluid regime was

⁹Optical depth issues can make the relation between the optical density and the density less obvious than Eq.(2.8), see for example [92].

¹⁰It is however possible to image slices of a 3D cloud, using radio-frequency transitions that are locally selective by the additional presence of a magnetic-field gradient. This technique was used to image the Mott plateaus of a Bose gas in an optical lattice [93].

¹¹The scale invariance is only approximate because \tilde{g} also has logarithmic density-dependent corrections [96].

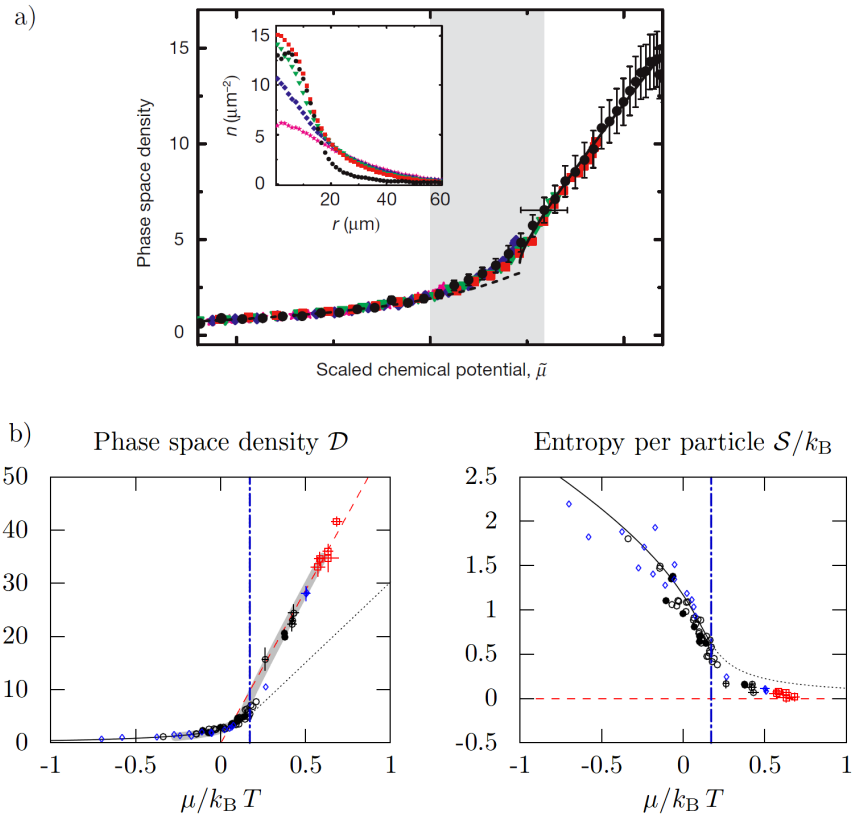


Figure 1.8: Equation of State of a 2D Bose gas. (a): Chicago group measurement of the phase space density $n\lambda_{\text{dB}}^2$ versus the chemical potential $\tilde{\mu} = \mu/k_B T$ for a coupling strength $\tilde{g} = 0.26$ [94]. (b): ENS group measurement of $n\lambda_{\text{dB}}^2$ and the entropy per particle S/Nk_B versus $\mu/k_B T$ [95] for $\tilde{g} \approx 0.1$.

interpreted by the pairing of free vortices of opposite circulation. This transition was observed as a jump in the superfluid density in a thin film of ^4He (through moment of inertia measurement) [101] and recently with ultracold atoms by interferometric measurement of the proliferation of free vortices [102] across the BKT transition. We remark that BKT transition is not followed by a sharp feature in the EoS, even though we see that the entropy drops rapidly to a value close to zero (Fig 1.8), characteristic of superfluids.

In-situ density profiles have also been measured in single one-dimensional Bose gases. Even though the equation of state has not been explicitly extracted from these, the results have been compared to the exact solution obtained from the Bethe ansatz, called the Yang-Yang thermodynamics, and the agreement is excellent [103, 104].

1.3.3 In 3D: Trapped Gas EoS and Inverse-Abel Transform

Equation of State of a Trapped Gas

In 3D, it is not possible to measure directly $n(x, y, z)$ because of the line-of-sight integration of the probe. The first thermodynamic measurements both on Fermi and Bose gases were global and resulted in quantities averaged over the trap. For example, the energy of a weakly inter-

acting trapped Bose gas was measured versus temperature T using expanding clouds showing good agreement with the thermodynamics of the ideal gas [105]. More precise measurements have shown systematic deviations due to the weak mean-field interactions [106, 107]. For Bose gases with stronger interactions, there have been no measurements of the EoS, either at zero- or finite temperature, both for the trapped or the uniform gas.

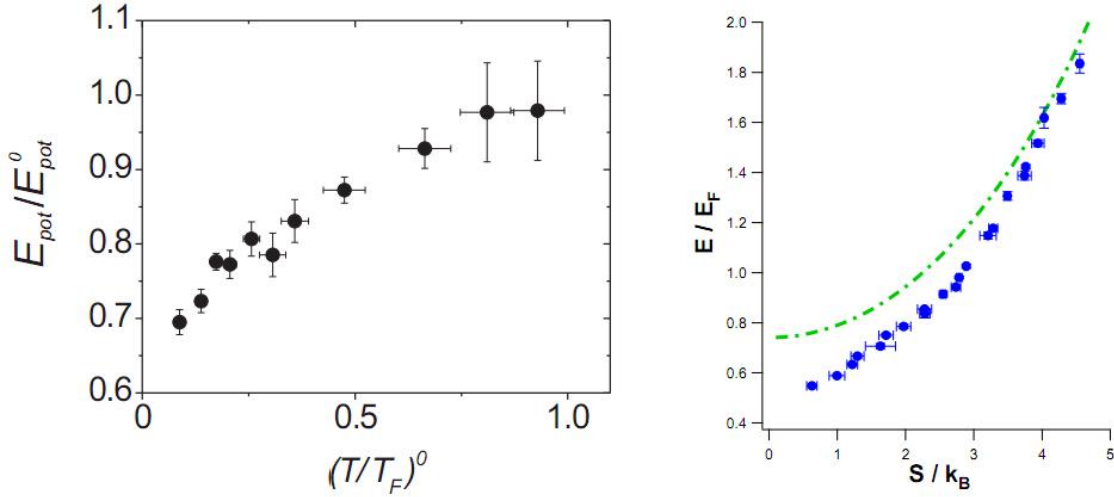


Figure 1.9: Equation of State of the trapped unitary Fermi gas. Left panel: the JILA group measured the potential energy E_{pot} of a unitary gas of ^{40}K [108]. The superscript 0 refers to the quantity measured on the non-interacting Fermi gas with the same entropy. Right panel: Duke group measured the energy E/NE_F versus entropy S/Nk_B on a unitary gas of ^6Li [109].

On the other hand, extensive thermodynamic studies on trapped Fermi gases have been performed at JILA and Duke University (see Fig.1.9). The energy could be measured in a model-independent fashion using the virial theorem verified by the unitary gas [110]. An additional difficulty with Fermi gases is that the thermometry techniques used for Bose gases, such as fitting the wings with the profiles corresponding to the weakly interacting limit, or using time-of-flight methods, are invalid because even the wings are usually strongly interacting and the expansion is strongly hydrodynamic because of the very large collision rate. Adiabatic sweeps to the weakly interacting regime were used for thermometry, measuring either the entropy [109] or the temperature [108] of the weakly interacting gas. Let us also mention that the Innsbruck group measured collective modes frequencies in the BEC-BCS crossover and that these frequencies can be related to the EoS of the trapped gas via the hydrodynamic equations [46]. The comparison between the resulting equations of state, shown in Fig.1.9, to theories of the many-body problem is rather indirect because of the effect of the trap averaging. Indeed, the energy of the trapped system (5.39) can be deduced from the energy of the uniform gas:

$$E_t = \int e[n(\mathbf{r})]d^3r \quad (1.39)$$

where $e[n(\mathbf{r})]$ is the energy density of the uniform gas with a density $n(\mathbf{r})$ (a similar expression for the entropy holds). Many numerical methods that are used to tackle the many-body problem such as the Monte-Carlo methods only calculate discrete points of the EoS (and in general few of them as it is a very time consuming task). Therefore in order to perform numerical integration of Eq.(1.39),

an additional interpolation step is required which makes the comparison with experiments less direct. In addition, the averaging will smear out sharp features (such as phase transitions) and diminish difference between theories and/or experiments.

Equation of State of a Uniform Gas

Obtaining the EoS of the uniform system instead of the trapped one is obviously more interesting because the former is a more fundamental quantity than the latter, and because it is the one that is directly computed with the various theories. Before presenting the method that we have developed to measure the EoS of a homogeneous gas, let us mention another important technique, namely the inverse Abel transform. The problem is to recover the density $n(x, y, z)$ from the 2D projection $\bar{n}'(x, z)$ of Eq.(1.37). If one assumes cylindrical symmetry for the density profile (which is usually well verified in practice) one can tomographically reconstruct $n(\mathbf{r})$ with one projection, as all projections are equivalent. This is achieved via the inverse Abel transform:

$$n(r, z) = -\frac{1}{\pi} \int_r^\infty dx \frac{d\bar{n}'(x, z)}{dx} \frac{1}{\sqrt{x^2 - r^2}}. \quad (1.40)$$

The integrand of Eq.(1.40) shows the principal drawbacks of this method: one must take the derivative of an experimental signal $\bar{n}'(x, z)$ and the other term in the integrand is singular at the lower bound of the integral. This procedure requires very low-noise data to begin with as the reconstructed density has a lower signal-to-noise than the integrated profile $n'(x, z)$. This technique to obtain the EoS was pioneered at MIT by Y. Shin, who extracted the equation of state of a homogeneous spin-polarized Fermi gas using the in-situ density profiles of a trapped system [111], following a proposal by A. Bulgac and M. Forbes [112]. A similar method was used in T. Mukaiyama's group in Tokyo to measure the EoS of the homogeneous unitary gas [113], and is currently used in M. Zwierlein's group at MIT to extract the EoS $n(\mu, T)$ of the unitary Fermi gas [114, 115].

1.3.4 Our Method: the Direct Measurement of the Local Pressure

The equation of state of the uniform gas can be obtained from the trapped density profile without relying on the inverse Abel transform, measuring the local pressure directly. The derivation of the formula is simple and starts with the doubly-integrated density profile:

$$\bar{n}(z) = \int dx dy n(x, y, z) \quad (1.41)$$

$$= 2\pi \int_0^\infty r dr n(r, z) \quad (\text{cylindric symmetry}) \quad (1.42)$$

$$= \frac{2\pi}{m\omega_r^2} \int_{-\infty}^{\mu_z} d\mu n_{\text{hom}}(\mu) \quad (\text{LDA + harmonic trapping}) \quad (1.43)$$

$$= \frac{2\pi}{m\omega_r^2} \int_{-\infty}^{\mu_z} d\mu \frac{\partial P}{\partial \mu}(\mu) \quad (\text{Gibbs-Duhem}) \quad (1.44)$$

$$= \frac{2\pi}{m\omega_r^2} P(\mu_z). \quad (1.45)$$

where $\mu = \mu_z - \frac{1}{2}m\omega_r^2 r^2$ is the local chemical potential, and $\mu_z = \mu_0 - V(z)$ is the chemical potential on the z -axis. Inverting this last expression we find the pressure formula, stating that the local pressure along the z -axis is simply proportional to the doubly-integrated density profile. This formula was derived independently in [116, 117, 118, 119] and in our group [60]. It can be

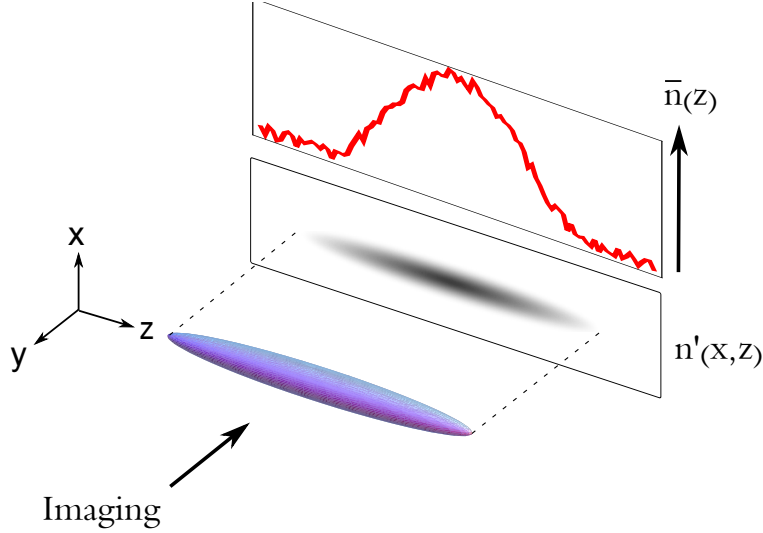


Figure 1.10: Measurement of the pressure of a three-dimensional quantum gas. The absorption imaging along the y -axis gives the 2D projected density $n'(x, z)$ (grey area). An integration along x provides the doubly-integrated density profile $\bar{n}(z)$ (in red line) which is proportional to the pressure at each point along the z -axis.

readily generalized to an arbitrary mixture of M species, each of mass m_i harmonically trapped radially with a frequency ω_{ri} :

$$P(\{\mu_{iz}\}, \lambda) = \sum_{i=1}^M \frac{m_i \omega_{ri}^2}{2\pi} \bar{n}_i(z), \quad (1.46)$$

where $\mu_{iz} = \mu_{i0} - V(z)$ is the local chemical potential of species i , and λ being additional parameters such as temperature or interaction strength.

This relation is remarkable on several grounds. Few assumptions are necessary: the local density approximation and a transverse harmonic confinement¹². Its applicability is very wide: it can be used for a gas of bosons, fermions or arbitrary mixtures of the two; it is valid at finite temperature, for any value of the scattering length, or even for long-range interactions. Most importantly, it allows the direct probing of the pressure of the locally homogeneous gas. The trapping potential is now turned into an advantage: because of the dependence of the local chemical potential with $V(z)$, the trapping scans the value of the chemical potentials and a single image provides many local samples of homogeneous systems with different chemical potentials and thus many points of the equation of state. Finally, the measurement of \bar{n} is experimentally easy and the additional integration compared to the 2D density increases the signal-to-noise for the pressure, allowing for

¹²It is easy to compute the first correction to the transverse harmonic assumption. In practice, the trapping potential are done with optical traps which have a gaussian shape: $V(r, z) = \frac{1}{2}m\omega_z^2 z^2 + U_0 \left(1 - \exp\left(-\frac{r^2}{\sigma^2}\right)\right) \approx \frac{1}{2}m\omega_z^2 z^2 + \frac{1}{2}m\omega_r^2 r^2 \left(1 - \frac{r^2}{\sigma^2}\right)$. We insert this expression in Eq.(1.42), retain the lowest order term in r^2/σ^2 and integrate by part the resulting integral to obtain:

$$\frac{m\omega_r^2}{2\pi} \bar{n}(z) = P(\mu_z) + \frac{2}{m\omega_r^2 \sigma^2} \int_0^\infty du P(\mu_z - u). \quad (1.47)$$

The pressure is then related to the integrated density profile through an integral equation. This equation is useful to estimate *a posteriori* the systematic error due to the anharmonicities of the trap.

high precision measurements.

In this work, we have applied the method of the local pressure measurement in a quantum gas to deduce the equation of state of various systems of fermions and bosons. These systems are summarized in Tab. 1.2. Each of these systems required specific methods to determine the thermodynamic variables such as the chemical potentials or the temperature, as well as the calibration of the pressure. We will present in Part II the work related to the atomic Bose gas, while Part III will be dedicated to the two-component Fermi gas.

Table 1.2: Measurement of Equations of State presented in this work.

System	Thermodynamic variables and parameters
Bose gas at $T \approx 0$ (chapter 3)	μ, a
Unitary Fermi gas with $n_{\uparrow} = n_{\downarrow}$ (chapter 5)	μ, T
Fermi gas with $n_{\uparrow} = n_{\downarrow}$ at $T \approx 0$ in the BEC-BCS crossover (chapter 5)	μ, a
Imbalanced Fermi gas at $T \approx 0$ in the BEC-BCS crossover (chapter 6)	μ_1, μ_2, a

Chapter 2

The Lithium Machine

In this chapter, we will present the experimental setup that allow us to produce quantum degenerate Bose and Fermi gases. Many technical aspects of the experiment have been described in great detail in the thesis of F. Schreck [120], L. Tarruell [84], or S. Nascimbène [121], to which we refer the interested reader. Therefore, we will deliberately focus here on a simple description of the experimental sequence and emphasize the optical trapping stage.

2.1 Trapping and Cooling the Lithium Isotopes

Lithium is the third element of the periodic table, and is a commonly used element for quantum gas experiments, with two stable isotopes, fermionic ${}^6\text{Li}$, and bosonic ${}^7\text{Li}$. The natural abundance is 92.5 % (7.5 %) for ${}^7\text{Li}$ (${}^6\text{Li}$). Lithium is a soft metal, with a melting point at 181 °C, the highest of all alkali elements. The mass of ${}^7\text{Li}$ is $1.165 \cdot 10^{-26}$ kg, while ${}^6\text{Li}$ is $0.999 \cdot 10^{-26}$ kg. Lithium is an alkali element (second lightest to hydrogen), which means that a single electron occupies the outer shell (the $2s$ shell for Li). The excitation of this electron to the $2p$ is an optical transition at 671 nm, corresponding to red light (Fig.2.1).

2.1.1 The Laser System

Several sources are available to produce, and amplify the red light at 671 nm: dye lasers, laser diodes or tapered amplifiers. Recently a solid-state laser was developed at ENS by frequency-doubling a 1342 nm laser [122]. When the experiment was rebuilt in 2005, tapered amplifier at lithium wavelength were not available and the laser system was constructed out of laser diodes alone. We use high power laser diodes (Hitachi HL6545MG), with an output power of 130 mW. Their wavelength at room temperature is 660 nm: they thus need to be heated up to 60 – 80 °C to reach the wavelength corresponding to the Li transitions. This in turn requires thermally isolated laser mounts.

As shown in Fig.2.1, hyperfine levels are not resolved in the excited state for lithium (the natural linewidth of the optical transitions is $\Gamma = 5.9$ MHz). Therefore, the cooling lines are poor cycling transitions, and lithium, in opposition to other alkali atoms (such as ${}^{87}\text{Rb}$), requires powerful repumping light (in practice as much as cooling light). Because of the small hyperfine splitting in the ground state, it would be possible in principle to derive both cooling and repumping frequencies from a single master laser for each isotope. However, there is a coincidence between the D2 line for repumping of ${}^6\text{Li}$ and the D1 line of ${}^7\text{Li}$. We thus repump ${}^6\text{Li}$ on the D1 line and

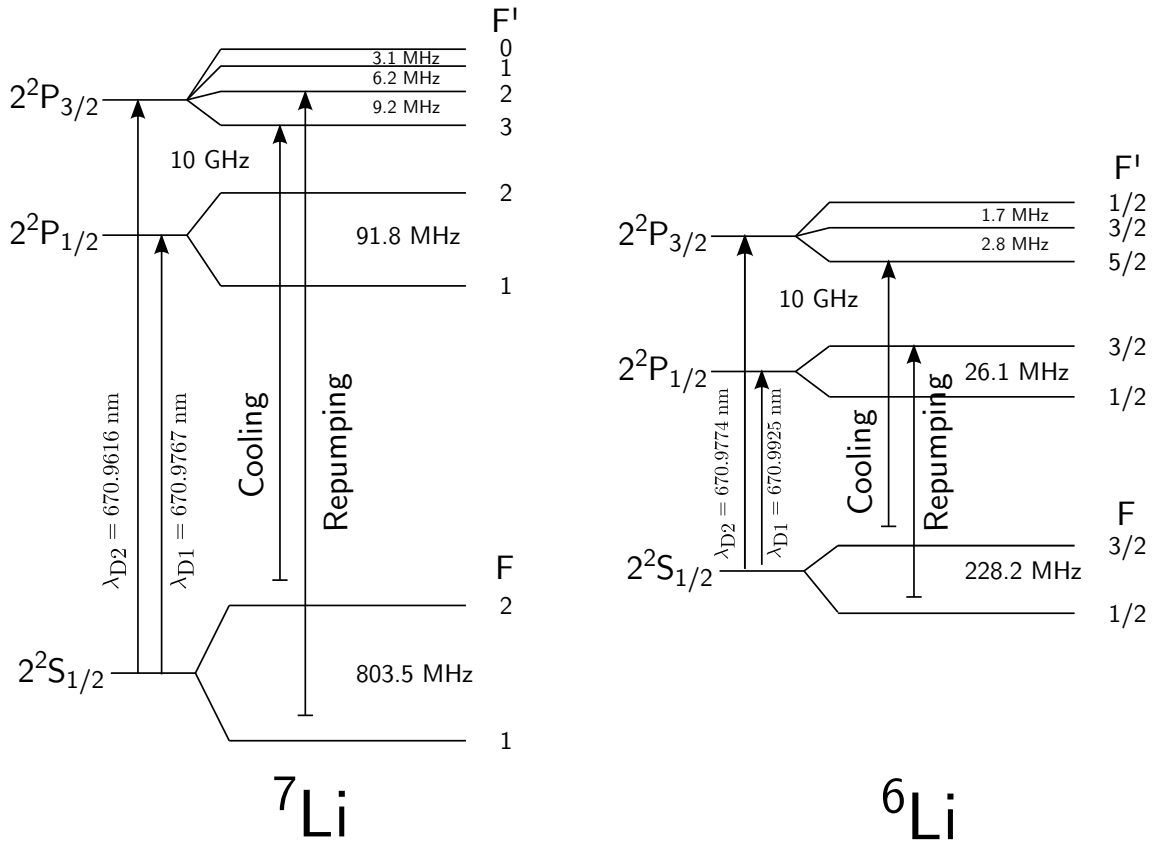


Figure 2.1: Energy levels of ${}^7\text{Li}$ and ${}^6\text{Li}$. The cooling and repumping transitions used for the MOT are also shown.

it requires an additional master laser (because of the 10 GHz difference). We have three master lasers: one for ${}^7\text{Li}$ and two for ${}^6\text{Li}$.

The master lasers are installed on a separate breadboard and are stabilized using an external cavity in Littrow configuration, from which we get about 30 mW. Their frequency is locked using Doppler-free spectroscopy on vapor lithium cells. The beams are then fiber-coupled to the main experiment breadboard and used to injection lock slave lasers. Using acousto-optic modulators (AOM) in double-pass we derive the four frequencies for the MOT (cooling and repumping laser for each isotope). Additional AOMs are used to red-detune the master light by 400 MHz in order to inject the four Zeeman slower slaves.

Operating many laser diodes at the edge of their temperature range is delicate. In particular the stability of the injection-locks is difficult to maintain over hours and appears to be the limiting factor to the automatization of an otherwise very stable experiment. We have generalized the use of fiber coupling, both acting as spatial mode filters and alignment decoupling. All master lasers are immediately fiber-coupled after going through an optical isolator. Changing the grating angle or the diode does not require to realign the spectroscopy setup. The same idea was applied to the MOT and Zeeman slaves. Even though it reduces the available power due to fiber-coupling losses, this improvement was necessary as our diodes have a short lifetime¹. We typically end up with 40 mW of light for each frequency in a TEM_{00} mode.

¹One diode has to be replaced every month at least. Changing a slave diode takes less than 30 min and has negligible effect on the experiment.

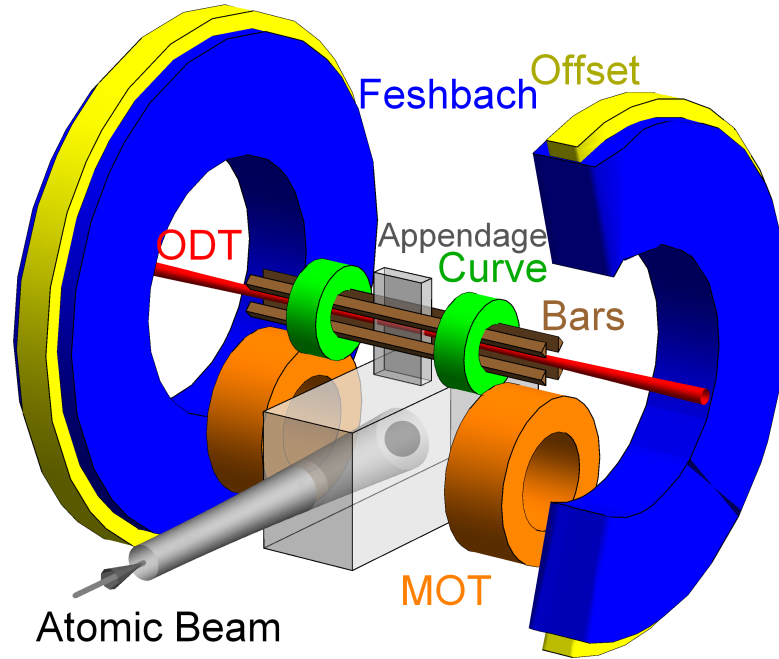


Figure 2.2: Sketch of the Experimental Apparatus. The atomic beam coming out of the oven is slowed down by a Zeeman slower (not depicted) and captured in the cell by the MOT coils (in orange), and the associated laser beams (not depicted). The cloud is then magnetically transported to the small appendage with the Feshbach (blue) coils. The gas is then loaded a Ioffe-Pritchard trap consisted by four (brown) Ioffe bars and the (green) curvature coils. After radio-frequency evaporative cooling, the gas is transferred in a far-detuned optical dipole trap (red), the Feshbach field is ramped to tune the value of the scattering length a and quantum degeneracy is achieved by a final evaporation in the optical trap.

2.1.2 The Dual Species ^7Li - ^6Li Magneto-Optical Trap

The Oven - the Zeeman Slower

Our source is a few grams of lithium heated up to 510 °C in an oven constituted by a stainless steel cylinder acting as a reservoir. A collimation tube, perpendicular to the cylinder, allows the lithium vapor to exit in the form of a collimated atomic beam. The beam has a thermal speed $\sqrt{k_B T/m}$ of about 1000 m/s. It must be first slowed down in order to be captured in the magneto-optical trap, using the pressure radiation in a 1m long Zeeman slower. The Zeeman slower compensates the Doppler shift due to the decreasing speed of the atoms using the Zeeman effect. The exit speed of the atoms is about 50 m/s, within the MOT capture velocity.

The Magneto-Optical Trap

After being slowed down, the atomic beam arrives in the lower part of the science glass cell, where it is magneto-optically trapped (Fig.2.2), centered on the MOT coils. The four frequencies (cooling and repumping transition for each isotope) are mixed on four non-polarizing beamsplitters. Three outputs provide the three pairs of trapping beams and are expanded with telescopes to a diameter of 2.5 cm. The remaining output is directed towards a Fabry-Pérot cavity. The cavity allows us to check the injection locks and also provide a spatial reference, to adjust the superposition of the trapping beams. Each beam has an intensity of about 2 mW/cm², slightly below the saturation intensity of the D2 lines $I_{\text{sat}} = 2.4 \text{ mW/cm}^2$. The beams are red-detuned by 6.7 Γ and 5.9 Γ for the cooling and repumper beam of ⁷Li, and 5.4 Γ and 2.0 Γ for ⁶Li. In about 40 seconds, we can load 10^{10} bosons and $3 \cdot 10^9$ fermions at a temperature of 2.7 mK.

Afterwards, we compress the MOT (the so-called CMOT) by ramping the frequency of the lasers in 8 ms closer to resonance, to 3.5 Γ for both cooler and repumper of ⁷Li (2 Γ and 1.5 Γ for ⁶Li). In addition, the repumping intensities are reduced to zero which leads to an almost total pumping of the atoms in the $F = 1$ and $F = 1/2$ states. After the CMOT stage, the cloud's temperature has been reduced to less than 1 mK, with 40 % of the atoms remaining. Because of the small splitting in the excited states (see Fig.2.1), there is no sub-Doppler cooling mechanisms in lithium and explains the high-temperatures observed. In order to further increase the phase space density, we load the atoms in a magnetic trap to perform evaporative cooling.

2.2 Magnetic Trapping

2.2.1 Quadrupole Trap and Magnetic Transport

The principle of magnetic trapping relies on the coupling of the magnetic moment of the atom with an external magnetic field $B(\mathbf{r})$, leading to a potential $U(\mathbf{r}) = -\boldsymbol{\mu} \cdot \mathbf{B}(\mathbf{r})$, assuming that the magnetic moment $\boldsymbol{\mu}$ follows adiabatically the direction of $\mathbf{B}(\mathbf{r})$. Depending on the relative alignment of $\boldsymbol{\mu}$ and \mathbf{B} , atoms are attracted to the low- B ($\boldsymbol{\mu} \cdot \mathbf{B} < 0$) or high- B regions ($\boldsymbol{\mu} \cdot \mathbf{B} > 0$). Since Wing's theorem forbids maxima of a static B -field, we have to prepare the atoms in a *low-field seeking* state. In addition, only stretched states are stable versus spin-relaxation. To increase the number of atoms in the $|F = 2, m_F = 2\rangle$ state of ⁷Li, we use both hyperfine (or F -) and Zeeman (m_F -) pumping on ⁷Li. As atom number is not critical for ⁶Li, we use only hyperfine pumping. The pumping is done immediately after switching off the MOT field and turning on a small guiding field. After 300 μs , the expanding cloud is recaptured in a quadrupole trap created by the MOT coils in anti-Helmholtz configuration. The overall efficiency of the loading is slightly less than 50 % for ⁷Li, and about 30 % for ⁶Li.

After the quadrupole trap is loaded, the gas is magnetically transported into the upper part of the glass cell (also called the appendage, Fig.2.2). The transport is realized by simultaneously ramping up the Feshbach coils, while ramping down the MOT coils, resulting in a vertical shift of 2.5 cm of the cloud's position. Due to the limited size of the appendage 60 % of the atoms are truncated during the transport.

2.2.2 The Ioffe-Pritchard Trap

In order to proceed to radio-frequency evaporation, we need to transfer the atoms in a trap without cancellation of the B -field. Indeed, around these regions spin-flip (also called Majorana-) losses are likely to occur, when the spin of the atom doesn't adiabatically follow the direction of \mathbf{B} anymore and flips to an untrapped state. Our Ioffe-Pritchard trap is realized with four Ioffe bars and two small curvature coils (Fig.2.2). The bars produce a quadrupole trap in the radial direction while the curvature coils (in Helmholtz configuration), the axial confinement. The appendage was designed such that the Ioffe bars can be brought very close to the atoms, leading to large gradients, which is a crucial ingredient to efficiently evaporate ${}^7\text{Li}$. Because ${}^7\text{Li}$ in the $|F = 2, m_F = 2\rangle$ state has a negative scattering length of $a_{77} = -27 a_0$, the scattering cross section strongly depends on the relative momentum of the two colliding atoms [120]. This results in a strong decrease of the elastic collision rate (typically by a factor of 3 at a temperature of 1.5 mK) and, due to the small scattering length, inhibits the runaway forced evaporation.

Doppler cooling

In order to overcome this issue and increase the collision rate before initiating the evaporative cooling, we proceed to a Doppler cooling stage in the magnetic trap. A single horizontal beam is sufficient because the cloud is already magnetically trapped and the axial confinement compensates for the radiation pressure. The cooling is initially 1D, and the other directions are cooled through thermalization of the gas due to collisions. Moreover, the bias is set to a large value of 505 G so that the σ^+ beam drives the closed transition $|F = 2, m_F = 2\rangle \rightarrow |F' = 3, m_{F'} = 3\rangle$. To avoid exciting the axial center of mass oscillation, we ramp up (and down) the beam intensity in 100 ms. We empirically found that it is more efficient to proceed to the Doppler cooling in two stages. A first cooling of 1.5s in a shallow trap ($\omega_r/2\pi = 198$ Hz, $\omega_z/2\pi = 66$ Hz) reduces the temperature from 1.5 mK to 370 μK . We then proceed to a second 1s cooling in a more tightly-confined trap ($\omega_r/2\pi = 353$ Hz, $\omega_z/2\pi = 122$ Hz), which further reduces T to about 200 μK . At this point the phase space density has increased by 50 and the elastic collision rate by 16, with about 30 % atom loss. The conditions are fulfilled to initiate a successful forced evaporation.

Radio-frequency Evaporation

Evaporative cooling relies on the removal of the most energetic particles from the trap and rethermalization of the remaining atoms. The elastic collision rate must therefore be significantly larger than the inelastic processes. After Doppler cooling, the trap is compressed by reducing the bias field. The Feshbach coils are designed to cancel exactly the large bias due to the curvature coils ($B'_0 = 2.28$ G/A) when both are supplied in series. A residual bias of 5 G is provided by independent offset coils (yellow coils on Fig.2.2). The evaporation trap frequencies are then $\omega_r/2\pi = 3.1$ kHz and $\omega_z/2\pi = 70$ Hz at the almost harmonic bottom of the Ioffe trap.

In the Ioffe trap, selective removal of atoms is easily done by flipping the spin of the atoms. Because there are no s -wave collisions in a polarized Fermi gas (and higher-order partial wave collisions are inhibited at low temperature except close to scattering resonances), it is not possible to cool a spin-polarized ${}^6\text{Li}$ gas alone. Therefore, we evaporatively cool ${}^7\text{Li}$, which in turn cools down ${}^6\text{Li}$ via boson-fermion collisions², also known as *sympathetic cooling*. Sympathetic cooling is a very suitable method to obtain cold, large-number Fermi gases because no fermions need to be lost.

²The boson-fermion scattering length between states $|2, 2\rangle$ and $|3/2, 3/2\rangle$ is $a_{6,7} = 40 a_0$.

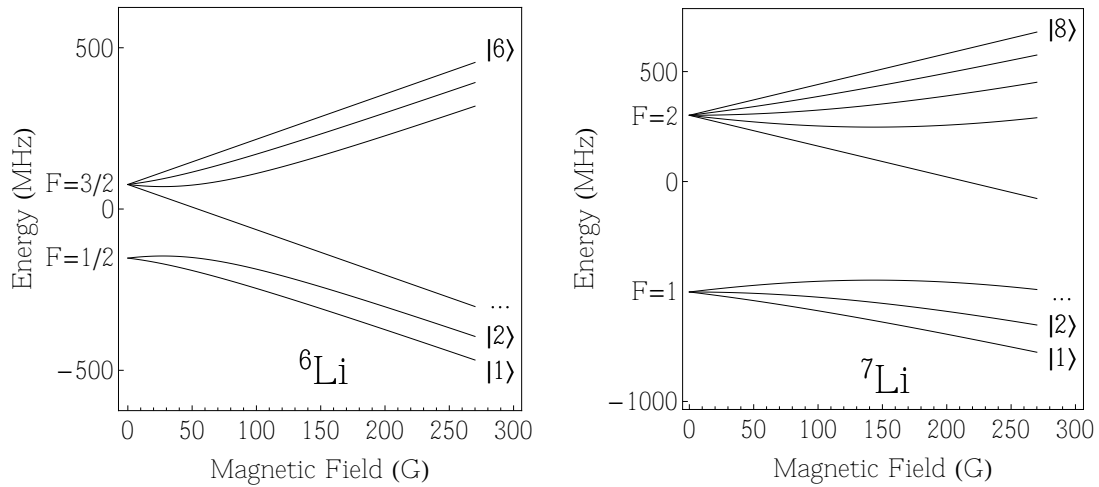


Figure 2.3: Energy levels as a function of the magnetic field for the hyperfine ground states of ${}^7\text{Li}$ and ${}^6\text{Li}$. For simplicity, energy states are labeled in the Paschen-Back limit.

Evaporation of ${}^7\text{Li}$ is done by driving the transition from $|F = 2, m_F = 2\rangle$ to $|F = 1, m_F = 1\rangle$, this latter state being magnetically expelled.

The last cooling steps in the Ioffe trap are dependent on the experiments carried out in the dipole trap. If we want to prepare an ultracold Fermi gas, we completely evaporate ${}^7\text{Li}$. The lowest temperature of ${}^6\text{Li}$ in the Ioffe trap is achieved in this way. If we want to transfer a trace of ${}^7\text{Li}$ as a thermometer of the Fermi gas, the ${}^7\text{Li}$ evaporation is stopped slightly before the RF-knife reaches the bottom of the trap. For the Bose gas experiments the final temperature has been optimized to maximize loading into the dipole trap. The conditions at the end of the Ioffe-Pritchard trap stage³ are summarized in Tab.2.1.

Table 2.1: Atom numbers and temperature at the end of the radio-frequency evaporation in the Ioffe-Pritchard trap. The first column refers to the experiment on ${}^6\text{Li}$, ${}^7\text{Li}$ being completely evaporated, and the second one refers to the evaporation of ${}^7\text{Li}$ without ${}^6\text{Li}$. T_{imag} is the temperature measured in the “imaging” trap ($\omega_r/2\pi \sim 340$ kHz and $\omega_z/2\pi \sim 30$ Hz), while $T_{\text{in-situ}}$ is the temperature in the Ioffe trap where evaporation is done ($\omega_r/2\pi = 3.1$ kHz and $\omega_z/2\pi = 70$ Hz).

	${}^6\text{Li}$	${}^7\text{Li}$
$N (\times 10^6)$	3	1.7
$T_{\text{imag}} (\mu\text{K})$	2.5	0.8
$T_{\text{in-situ}} (\mu\text{K})$	13.3	4.1

The control of inter-atomic interaction strength via a magnetic Feshbach resonance requires an

³The tightest possible Ioffe trap is used for evaporation, with maximum current of 500 A in the curvature and Feshbach coils (acting as compensation for the bias field created by the former). The latter have a very large inductance and it is not possible to switch off 500 A fast enough for time-of-flight measurements without creating dangerous overvoltages. We thus decompress in the “imaging” trap for taking the pictures.

adjustable bias field. The Ioffe-Pritchard trap is not suitable in this respect as the confinement crucially depends on the value of the bias field. Moreover, many states possessing Feshbach resonances are high-field seekers and thus cannot be magnetically trapped. For these reasons, we have to load the atoms in an optical trap.

2.3 The Hybrid Magnetic-Optical Trap

While magnetic trapping relies on the coupling of the magnetic moment of the atom with an external magnetic field, optical trapping couples the electric field of the laser to the induced dipole moment of the atom. Far from resonance, the *dipolar* interaction energy reads $U_{\text{dipole}} = -\frac{\alpha}{2} \langle E^2 \rangle$, where $\langle E^2 \rangle$ is the time-average of the oscillating electric field and α is the atomic polarizability. If the light intensity is spatially inhomogeneous, the atoms will experience a position-dependent potential. For far-detuned optical traps, the atoms will be attracted to the maxima of intensity if the oscillation frequency of the electric field ω_{OT} is red-detuned compared to the atomic transition ω , and to the minima otherwise.

In the experiment, we use a 120 W fiber laser, red-detuned to the lithium transition ($\lambda_{\text{OT}} = 1073$ nm). The gaussian beam in the TEM₀₀ produces a trapping potential that, near the focus of the laser beam can be approximated by a harmonic potential:

$$U(r, z) = -|U_0| + \frac{m}{2} (\omega_r^2 r^2 + \omega_{||}^2 z^2), \quad (2.1)$$

$$\text{where } U_0 = \frac{\hbar \Gamma^2 P}{4 I_{\text{sat}} \delta \pi w_0^2}, \quad \omega_r = \frac{2}{w_0} \sqrt{\frac{U_0}{m}}, \quad \text{and } \omega_{||} = \frac{\lambda_{\text{OT}}}{\sqrt{2} \pi w_0} \omega_r. \quad (2.2)$$

where P , w_0 , and δ are respectively the power, waist and detuning of the optical dipole trap. The intensity of the beam on the atoms is controlled by an acousto-optic modulator.

2.3.1 Loading the Optical Trap

The loading of the dipole trap is done in two steps. First, a small current of 10 A is ramped in 500 ms in the curvature coils by the independent power supply P_4 . Second, the current provided by P_1 (in series in the Feshbach and curvature coils) is reduced to zero (step 0 in Fig.2.4). This results in a decompression of the trap, with a bias increase from 5G to 23 G.

The radial confinement is then switched from magnetic to optical. We ramp down the current in the Ioffe bars in 50 ms (200 ms for ${}^6\text{Li}$ experiments) while simultaneously increasing the power in the optical trap (step 1 in Fig.2.4). The optimal power for the loading depends on the isotope used. The peak density of a classical gas in a trap scales as $n_0 \propto \left(\frac{\bar{\omega}^2}{T}\right)^{3/2}$, where $\bar{\omega} = (\omega_r^2 \omega_z)^{1/3}$ is the geometric mean trap frequency. If the tightness of a trap is adiabatically changed, the temperature varies so that $T/\bar{\omega}$ is constant. The peak density thus increases with the power of the dipole trap. At high power, the lifetime of the gas of ${}^7\text{Li}$ is reduced because of dipolar losses in the state $|F = 2, m_F = 2\rangle$ [123]. For this reason, the trap loading power is limited to $P = 5$ W. On the contrary, the gas of ${}^6\text{Li}$ behaves like an ideal gas: the transfer in the dipole trap is thus a single-particle adiabatic process. Consequently, we can load ${}^6\text{Li}$ into a high power optical trap ($P = 65$ W) and we observe no heating on a hundred-of-ms timescale. In both cases, we observe nearly unit transfer efficiency.

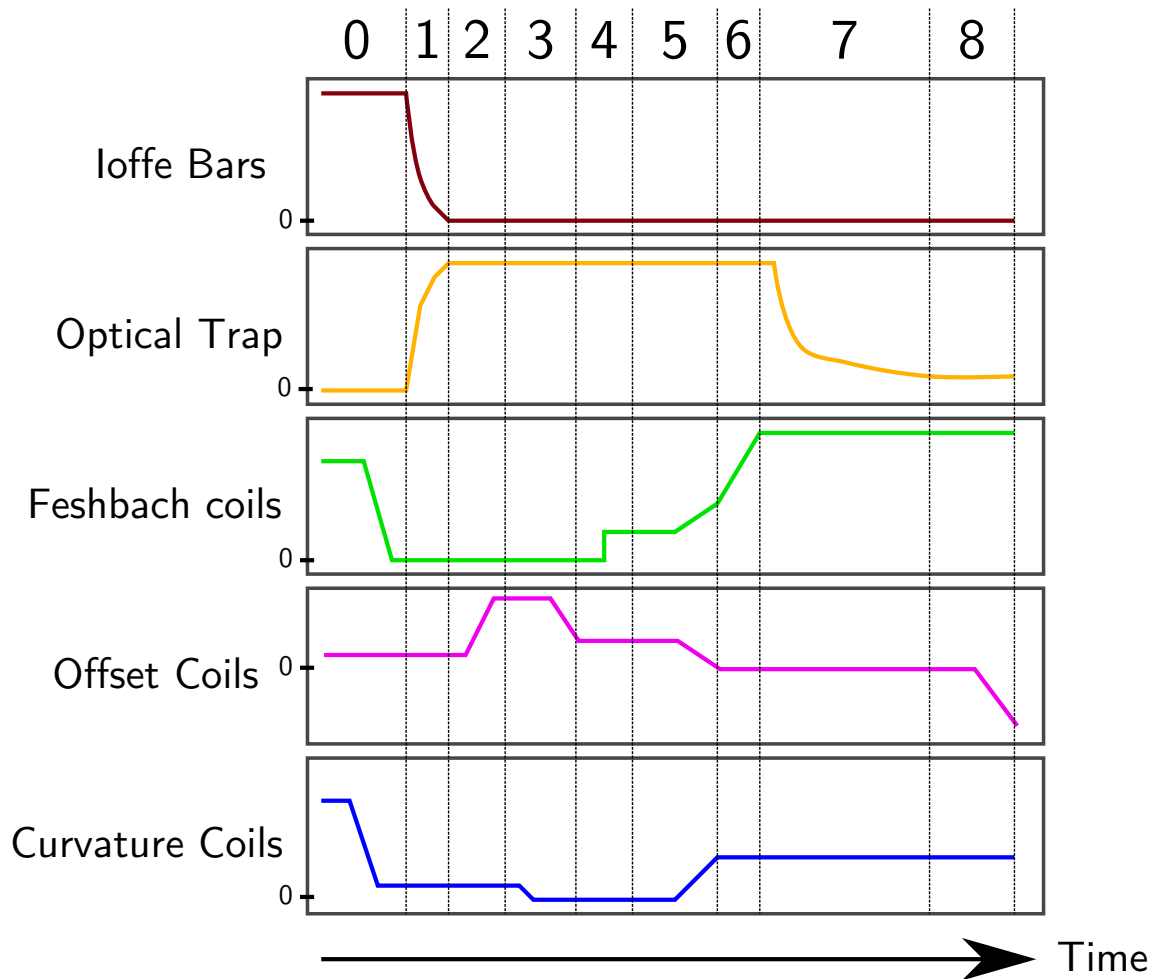


Figure 2.4: Summary of the sequence in the hybrid magnetic-optic trap (time and current not to scale). (0): At the end of the evaporation in the Ioffe-Pritchard Trap, the current in the Feshbach coils (acting as compensation of the bias produced by the curvature coils) and in the curvature coils is reduced. (1): The radial confinement is switched from the 2D quadrupolar field of the Ioffe bars to the Optical Trap. (2): Offset field is ramped up prior to the hyperfine transfer. (3): curvature coils is set to zero, the only bias remaining comes from the Offset coils. The RF is turned on and the Offset current is lowered, resulting in a transfer of the atoms in the lowest hyperfine state. (4): The bias field is flipped by rapidly increasing the current in the Feshbach coils. (5): The final curvature is set, while increasing current in the Feshbach coils (so that they always dominate the bias field). (6): The Feshbach field is ramped to tune a to its desired value prior to evaporation. (7): Forced evaporation cooling in the optical trap. (8): Final interaction ramp. For Fermi (Bose) gas experiments, this ramp is done on the Feshbach (Offset) coils.

Since all spin states are equally trapped in the optical trap, it is usually not possible to transfer the atoms in an untrapped state. In a dipole trap, the simplest method to force the evaporation is to decrease the optical trap power. This strategy has a drawback since the decreasing power leads to a decompression of the trap (see Eq.(2.2)), hence a reduced collision rate, which in turn affects the efficiency of the evaporation. In a single-beam dipole trap, this problem is exacerbated as the axial frequency is low (several Hz) even at high power (see Eq.(2.2)), and this generally forbids a runaway evaporation. A solution commonly implemented to reduce this effect is to intersect two beams, creating a tighter, *crossed* dipole trap. In our experiment we turned to a simpler solution: we use the curvature coils to provide with a magnetic axial curvature, while radial confinement is provided by the laser light.

2.3.2 Bias Flip and Magnetic Axial Curvature

The states that we use to prepare quantum gases are in the lowest hyperfine manifold $F = 1/2$ and $F = 1$, which are high-field seekers. Even though these states are not trappable in 3D by magnetic means only, we just need to produce an axial magnetic confinement. The curvature coils used in the Ioffe trap produce a saddle point that would either trap radially and anti-trap axially or the opposite, depending on the relative projection of the magnetic moment of the atom compared to the bias field direction.

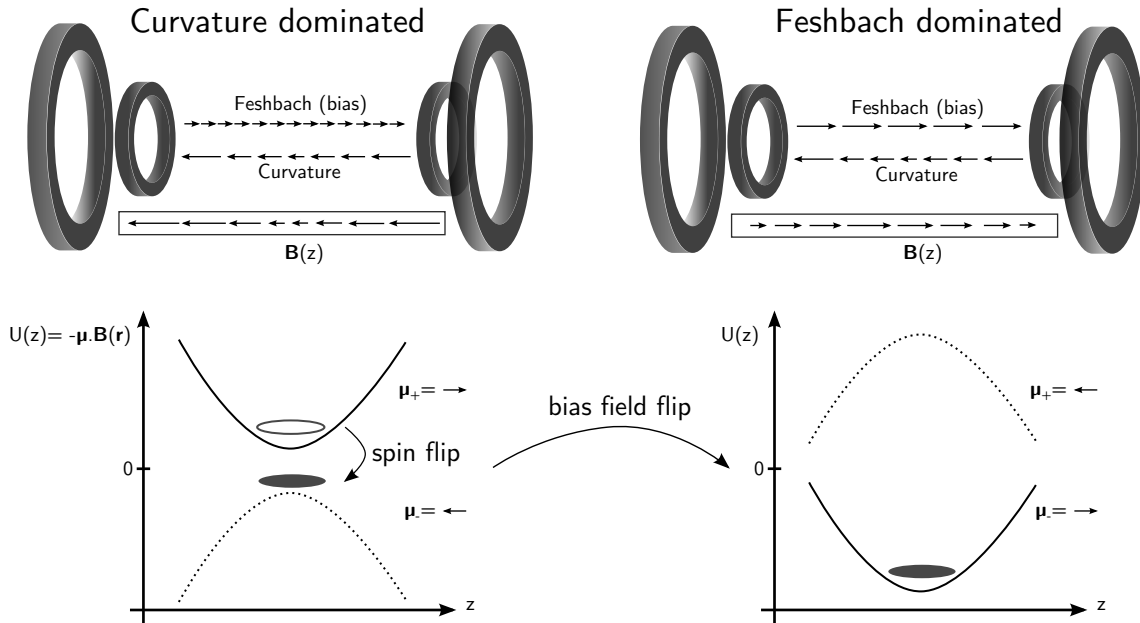


Figure 2.5: Sketch of the bias field flip. States $|+\rangle$ refer to the magnetically trappable states (magnetic moment anti-aligned to the bias field) $|F = 2, m_F = 2\rangle$ and $|3/2, 3/2\rangle$, while $|-\rangle$ refer to the ground states $|1, 1\rangle$ and $|1/2, 1/2\rangle$.

In Fig.2.5, we schematized the idea of the bias flip. First, atoms are in the magnetically trappable states (referred as $|+\rangle$) $|F = 2, m_F = 2\rangle$ and $|3/2, 3/2\rangle$. When the bias field is dominated by the curvature coils, the potential displays a minimum for $|+\rangle$, and a maximum for $|-\rangle$ ($|-\rangle$ being the ground states, $|1, 1\rangle$ and $|1/2, 1/2\rangle$). The potential can trap the $|-\rangle$ if the bias is flipped, which means that the bias field has to be dominated by the Feshbach coils. This implies that the curvature coils create an antitrapping in the radial direction, but the latter is only a small

perturbation to the optical trap confinement.

The experimental sequence is slightly more complex than the principle presented above. After the optical trap is turned on and the curvature coils set to 10 A, we ramp the offset coils current to 15 A (corresponding to 13 G bias) to prepare the bias for the transfer into the lowest hyperfine states (step 2 in Fig.2.4). Let us recall that the bias field of the offset coil points in the same direction as the curvature field. To avoid a transient axial antitrapping (the dotted potential on the left side of Fig.2.5), we ramp down the current in the curvature coils to zero (step 3 in Fig.2.4). The axial trapping is at that point completely provided by the powerful optical trap. A radio-frequency knife is switched on, at 827 MHz and 240 MHz. The offset coil bias is ramped down in 100 ms to 4 G, which results in an adiabatic passage of the ${}^7\text{Li}$ atoms (${}^6\text{Li}$) from state $|2, 2\rangle$ ($|3/2, 3/2\rangle$) to the absolute ground state $|1, 1\rangle$ ($|1/2, 1/2\rangle$) (end of step 3 in Fig.2.4).

Now that the atoms are in the appropriate states, we flip the bias field by abruptly setting the Feshbach coils' bias to 11 G (step 4 in Fig.2.4). The offset coils can then safely be switched off. In a second step, we turn on the axial magnetic curvature by increasing the current in the curvature coils, while simultaneously doing so in the Feshbach coils (step 5 in Fig.2.4). Let us recall that at all times the bias field direction must be dominated by the Feshbach coils. The value of the current in the two sets of coils allow us to adjust the trap that we need to initiate the evaporation. I_{curv} will fix the axial frequency of the trap⁴. I_{Fesh} can then be chosen to produce the desired bias field (step 6 in Fig.2.4).

2.3.3 Spin-mixture preparation in a Fermi gas

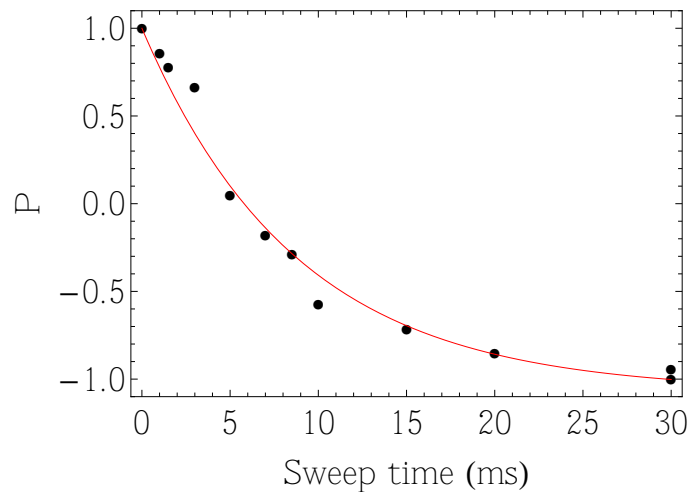


Figure 2.6: Polarization of the sample $P = \frac{N_1 - N_2}{N_1 + N_2}$ as a function of the RF sweep time. The red line corresponds to a fit of the Landau-Zener probability. The spin-mixture was prepared at a magnetic field of $B = 928$ G. The RF is swept in a window of 100 kHz around the resonance located at 76.3 MHz.

In the case of a Fermi gas, we need to prepare a spin-population mixture before starting the evaporation. We prepare it at a magnetic field of 834 G, corresponding to the Feshbach resonance in

⁴The contribution to the curvature of the Feshbach coils is about 20 smaller than the curvature coils. Though small, it can be important for very weak axial traps.

the two lowest energy states $|1\rangle$ and $|2\rangle$ (see Fig.2.3). This can easily be done by a radio-frequency Landau-Zener sweep. The Landau-Zener transition probability is given by:

$$P_{|1\rangle \rightarrow |2\rangle} = 1 - e^{-2\pi \frac{\Omega_R^2}{\dot{\omega}}}, \quad (2.3)$$

where Ω_R is the Rabi frequency (proportional to the square root of the RF power) and $\dot{\omega} = \partial\omega/\partial t$ is the sweep rate. In the limit of fast ramp $\dot{\omega} \rightarrow \infty$, no atoms are transferred while in the other limit $\dot{\omega} \rightarrow 0$, the process results in an adiabatic passage and $P_{|1\rangle \rightarrow |2\rangle} \rightarrow 1$. The rate is adjusted to prepare the desired spin-mixture, with very good reproducibility. In Fig.2.6, we plotted the polarization of the sample $P = \frac{N_1 - N_2}{N_1 + N_2}$ as a function of the sweep time. Fitting the data points with Eq.2.3, we find a Rabi frequency of $\Omega_R = 2\pi \times 0.53$ kHz. It is worthwhile to note that a Landau-Zener sweep is a coherent one-body process, thus creating a superposition of states, in this case $\alpha|1\rangle + \beta|2\rangle$. As two fermions in this state still share the same spin wavefunction, there are still no s -wave collisions. In practical, the coherence of the sample is lost within a few tens of ms because of the magnetic field inhomogeneities and the coherent superposition becomes a statistical mixture of $|1\rangle$'s and $|2\rangle$'s [124] and evaporation can be initiated.

2.3.4 Evaporation in the dipole trap

The dynamics of the forced evaporation realized by lowering the trap depth is different for the Bose and Fermi gases. Because collisions can be brought to the unitarity-limited regime in a Fermi gas (and not in a Bose gas), the dependence of the elastic cross-section $\sigma_{\text{coll}}(k)$ on the relative momentum of the two colliding atoms k (or equivalently the energy) will lead to a different behavior of the evaporation of the two isotopes.

The trapping potential can be written as $V(\mathbf{r}, t) = U(t)v(\mathbf{r})$, where $U(t)$ is the time-dependent trap depth (and $v(\mathbf{r})$ its spatial shape). The evaporation efficiency is characterized by the ratio $\eta = \frac{U}{k_B T}$ of the trap depth to the thermal energy. The higher η is, the more efficient the evaporation. Energetic atoms leave the trap after two-body collisions. If the depth is large, the escaping atom has an energy much larger than the average energy per particle, hence the temperature is strongly reduced. From simple energy considerations, it is possible to derive scaling laws for the atom number $N(t)$, phase space density $n\lambda_{\text{dB}}^3(t)$ assuming η is large (so that the potential can be assumed harmonic) and neglecting all loss processes [125]:

$$\frac{N}{N_0} = \left(\frac{U}{U_0}\right)^{\frac{3}{2} \frac{1}{\eta' - 3}} \quad (2.4)$$

$$\frac{n\lambda_{\text{dB}}^3}{n\lambda_{\text{dB}}^3(0)} = \left(\frac{N}{N_0}\right)^{4 - \eta'}, \quad (2.5)$$

where $\eta' = \eta + (\eta - 5)/(\eta - 4)$. We see that for $\eta' > 4$ the evaporation increases the phase-space density. One can also write the scaling for the elastic collision rate $\Gamma_{\text{coll}} = n\sigma_{\text{coll}}v$:

$$\frac{\Gamma_{\text{coll}}}{\Gamma_{\text{coll}}^0} = \left(\frac{U}{U_0}\right)^{\alpha'}. \quad (2.6)$$

For an energy-independent elastic cross-section, $\Gamma_{\text{coll}} \propto N\bar{\omega}^3/T$ (thermal speed scales as $U^{1/2}$) and one finds: $\alpha' = \frac{\eta'/2}{\eta' - 3}$. If σ_{coll} is unitarity limited ($\propto 1/k^2$), σ_{coll} scales as $1/U$ and the scaling law will be modified: $\alpha' = \frac{6 - \eta'}{2(\eta' - 3)}$. It is interesting to note that, in contrast to the constant cross-section case of the Bose gas (for which $\alpha' < 1$), for $\eta' > 6$ the unitary collision rate increases

($\alpha' > 1$) as the trap depth is lowered [126], a condition called *runaway* evaporation. The increase of collision rate is important as it allows one to accelerate the evaporation, an important condition because loss processes (either with the residual background gas or two-, or three-body losses) will ultimately limit the timescale for the evaporation. By means of additional optical [127] or magnetic potentials [128], it is possible to reach runaway evaporation in an optical trap, even without a unitarity limited cross-section.

Evaporation of a Bose Gas with variable interactions

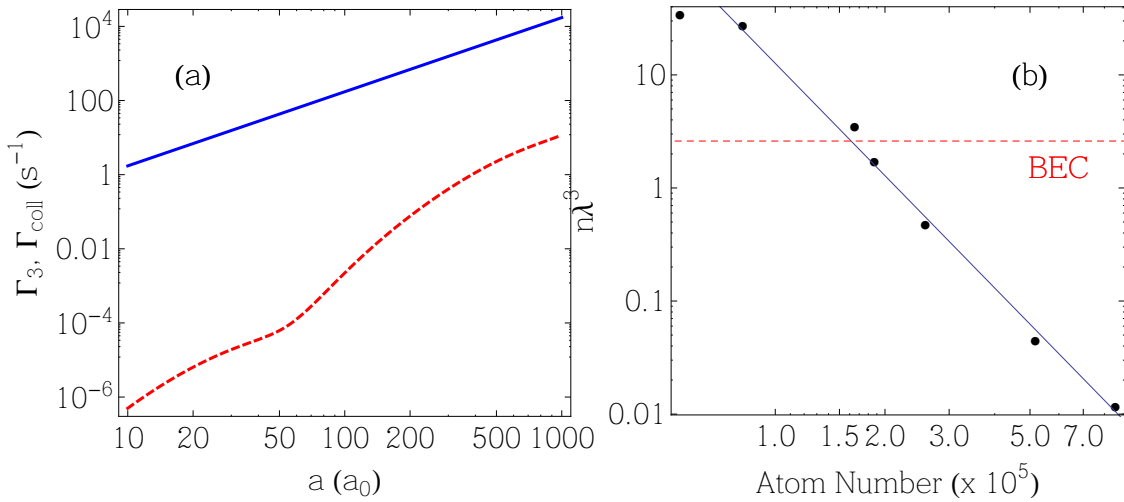


Figure 2.7: Efficiency of the evaporation of ${}^7\text{Li}$ in the dipole trap. (a): Elastic collision rate Γ_{coll} (solid blue line) and three-body loss rate Γ_3 at the beginning of the evaporation. The form of Γ_3 (including the dip at $a/a_0 \sim 50$) will be discussed in detail in section 4.1.3. (b): Phase space density at the center of the trap $n\lambda_{\text{dB}}^3$ versus the atom number N . The dashed red line corresponds to the Bose-Einstein condensation threshold $n\lambda_{\text{dB}}^3 = \zeta(3/2) \approx 2.6$. The solid blue line is a power law fit to extract η (see text).

Evaporation of ${}^7\text{Li}$ can be made much more efficient in the dipole trap, in comparison with the magnetic trap. The use of optical trapping allows us to tune freely the scattering length using a Feshbach resonance. This tuning must meet two opposite criteria. First, for dilute gases $ka \ll 1$, Γ_{coll} scales as a^2 , which favors high values of a . However, the three-body loss rate Γ_3 dramatically increases with a as well, typically a^4 [37], and is strongly density-dependent $\Gamma_3 = K_3(a)n^2$, where $K_3(a)$ is the three-body loss coefficient. In Fig.2.7a, we show the increase of Γ_{coll} and Γ_3 versus the scattering length for our typical starting conditions in the center of the trap (where $n \sim 2 \times 10^{12} \text{ cm}^{-3}$). In practice we perform the evaporation using piece-wise linear ramps of the optical trap laser intensity. The optimized value of a in our conditions is $\sim 200 a_0$. We see in Fig.2.7a that a small increase in a leads to a large increase of Γ_3 and at $500 a_0$ it is already on the order of 1 s^{-1} .

The value of degeneracy parameter $n\lambda_{\text{dB}}^3$ is plotted versus the atom number in Fig.2.7. Using

Eq.(2.3.4), we find $\eta = 6.8$, an efficient evaporation⁵. Starting from $n\lambda_{\text{dB}}^3 \sim 0.01$ we reach the Bose-Einstein condensation threshold $n\lambda_{\text{dB}}^3 = \zeta(\frac{3}{2})$ with about 2×10^5 atoms (dashed red line in Fig.2.7b). Continuing the evaporation, we produce a Bose-Einstein condensate with no discernible thermal part with $\sim 5 \times 10^4$ atoms.

Evaporation of a strongly interacting Fermi gas

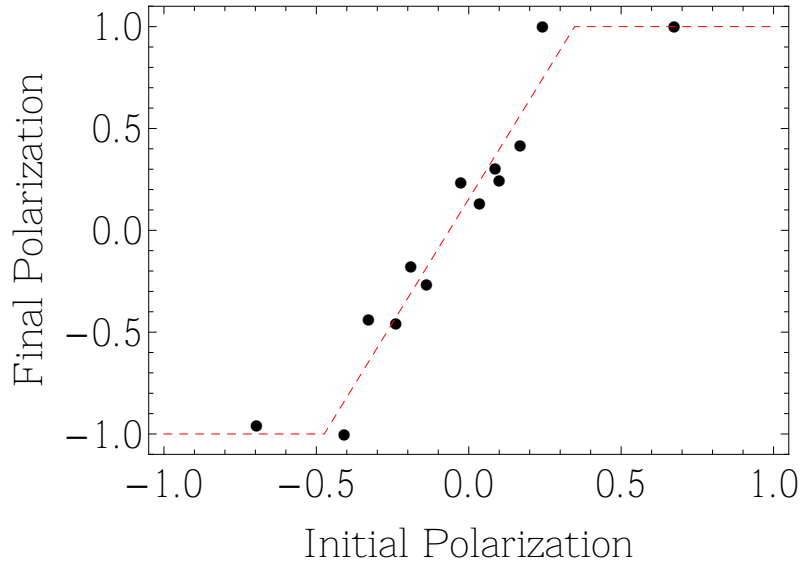


Figure 2.8: Evolution of the polarization of a Fermi gas after evaporation cooling. The polarization is plotted versus initial polarization of the gas.

A strongly interacting Fermi gas can be highly efficiently evaporated ($\eta \approx 10$ [126]) owing to the very large unitarity limited collision rate. In practice we start with about 2×10^6 atoms at $T/T_F = 3$ and exponentially lower the laser power to the final desired value with a time constant of 500 ms. We reach the deeply degenerate regime ($T/T_F \approx 0.03$) with about 10^5 atoms per spin state [121]. Evaporative cooling of a spin-imbalanced Fermi gas displays another subtlety. In addition to total atom number and temperature, the polarization P of the cloud is also a dynamical quantity, that varies during the cooling process. The variation P is highly non-monotonic and displays two opposite trends, depending on the regime:

- In the classical regime, evaporation is the result of binary collisions between spin \uparrow and spin \downarrow particles. If one particle leaves the trap, the probability is the same for each species. This means that the minority species population will, in relative value, decrease faster than the majority. Consequently, the evaporation tends to further imbalance the spin-mixture.
- In the quantum regime, the picture is different. In the case of the far BEC region, the dimers have a polarizability twice as large as that of single atoms. They thus feel a trap that is twice deeper and evaporation will selectively remove single atoms [129]. For the weakly interacting gas in the BCS regime, the minority Thomas-Fermi radius is smaller than that of the majority, and equilibration of the spin-mixture should also occur.

⁵This value is significantly higher than the one extracted from the data in the Ioffe trap [84], where $\eta \approx 5.5$.

The complexity of the dynamics of $P(t)$ comes from the fact that these two opposite trends will occur sequentially during the evaporation. In Fig.2.8, we have plotted the polarization of the gas cooled down to $1.5 \mu\text{K}$ as a function of the initial spin-mixture polarization. The large slope shows that the system is very sensitive to the initial mixture and shot-to-shot reproducibility of accurate polarizations is difficult⁶. This effect is severely amplified for the preparation of highly imbalanced mixture. In order to prepare highly imbalanced quantum gases, one has to transiently go through a state with an even higher imbalance. Of course, the gas is not allowed at any moment to become fully polarized $P = 1$, otherwise the evaporation ends. Starting the evaporation with a degenerate gas makes it simpler to prepare deterministic spin-imbalance [132], as one can already start with an almost pure Fermi sea and transfer a small amount of spin \downarrow particles. If one wants to prepare a balanced mixture, a very simple solution is to perform multiple Landau-Zener sweeps with intermediate sweep rate. In the limit of large number of sweep (in practice we do 10 sweeps), the population will tend to a 50/50 mixture.

When ${}^7\text{Li}$ is used as a thermometer of the Fermi gas, the number of bosons is much smaller than the number of fermions. Owing to this difference, the evaporation of ${}^6\text{Li}$ is only slightly degraded by the presence of ${}^7\text{Li}$. It is interesting to note at this stage that it is ${}^6\text{Li}$ that sympathetically cools down ${}^7\text{Li}$.

2.3.5 The Feshbach Field

After a degenerate quantum gas is obtained, and before an image is recorded, we sweep the magnetic field bias to the desired value. For the Fermi gas experiments, the system is not subjected to significant three-body losses in the range of magnetic field studied. The magnetic field is slowly swept, in 500 ms, and a further wait time of 1 to 1.5s is applied to let the gas thermalize. The last wait time is particularly important for the experiments involving the ${}^7\text{Li}$ as a thermometer. Indeed the boson-fermion scattering length is equal to $40 a_0$ [133], a rough estimate of the elastic collision rate for ${}^7\text{Li}$ (assuming $N_7 \ll N_6$ without taking into account Pauli blocking) is $n_6 \sigma_{6,7} v_{\text{th}} \approx 10 \text{ s}^{-1}$. This rate requires a wait time in order to ensure complete thermalization of ${}^7\text{Li}$ in contact with ${}^6\text{Li}$.

Feshbach Field Sweeps for the Bose gas experiments

In contrast to the experiments involving fermions, three-body losses are not suppressed for bosons and hence the lifetime is increasingly shorter as one approaches the Feshbach resonance. For this reason, it is crucial to spend as little time as possible at high values of a before taking the absorption image. The Feshbach coils which are usually used for the interaction sweeps are not suitable to quickly change the bias because they have a large inductance combined with a slow response time of the current servo of the precision power supply we use. The inductance of the Feshbach coils results in a measured response time of 7 ms, while the servomechanism responds in about 20 ms. Using the Feshbach coils alone, it is difficult to sweep the field to an accurate value without having to wait at least 50 ms. For high values of a , this time can already lead to significant losses.

We solved this problem by using the Offset coils (see Fig.A.2) to finely tune the magnetic field. There are several advantages to this configuration:

⁶Together with the sensitivity to initial imbalance, the dynamics of the spin-polarized Fermi gas evaporation has also shown the possibility of creating metastable many-body states [130,131]. These dynamic issues would certainly deserve further experimental investigations.

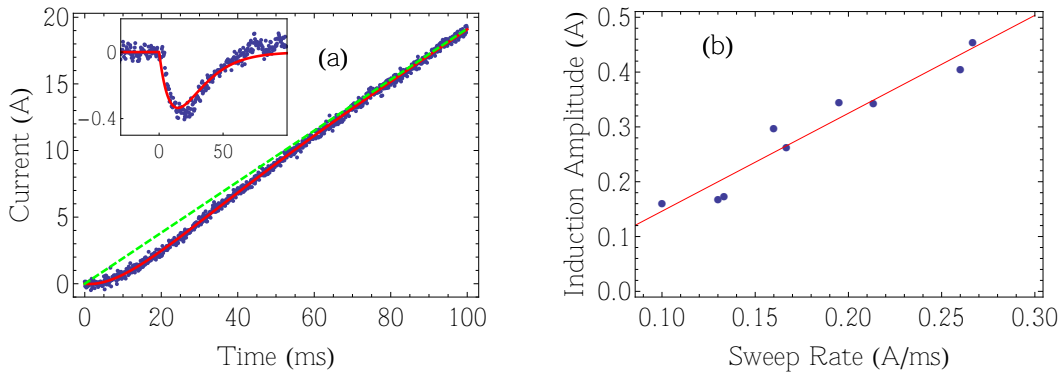


Figure 2.9: Shape of the interaction sweep. (a): Offset + Feshbach current ramp to resonance. The dashed green line is a linear ramp while the red solid line includes the effect of the induction in the Feshbach coils when current is ramped in the Offset coils. Inset: Induction in the Feshbach coils. (b): Measured amplitude of induction in the Feshbach coils as a function of the sweep rate in the Offset coils (see text).

- The largest contribution to the bias, from the Feshbach coils, is maintained constant. The power supply has an absolute stability of 5×10^{-5} , leading to fluctuations less than 40 mG at a bias of 720 G, which is sufficiently small owing to the ~ 170 G width of the bosonic Feshbach resonance.
- The absolute value of the current that needs to be stabilized in the Offset coils is about 20 A, much smaller than the bias field contribution of the Feshbach coils. Moreover, the contribution to the bias of the Offset is much lower as well (0.86 G/A compared to 2.28 G/A for the Feshbach), which results in a superior control of the magnetic field sweeps.
- Both inductance and response time of the servo for the Offset coils circuit are smaller (less than 3 ms). This allows us to realize ramps of tens of ms without a wait time and with final current values still being controlled to better than 10^{-4} . It is of critical importance when absorption images are taken immediately after the ramp.

For the experiments presented in chapter 3, especially for the dynamical measurements, it is very important to know the shape of the scattering length sweeps. For this purpose, we have monitored the currents using Hall-effect transducers in both Feshbach and Offset coils. The command of the current control of the Offset coils is linear, but we observed two effects that we have to take into account in order to properly model the interaction sweep. First, when the sweep is initiated in the Offset coils, an induction is observed in the Feshbach coils (see the inset of Fig.2.9). The total current sweep is not linear: in Fig.2.9a we plot the weighted sum of the current in the current in Feshbach and Offset coils, $I_{\text{Offset}} + \alpha I_{\text{Feshbach}}$, where $\alpha = \frac{2.28}{0.86}$ is the ratio of the bias contribution of the two sets of coils (the bias magnetic field is proportional to this quantity). The expected linear ramp is plotted in dashed green does not describe our interaction sweep. The overshoot current⁷ is well fitted by a function⁸ $A(\dot{I}) \frac{\dot{I} \times e}{\tau_F} \exp(-t/\tau_F)$, with $\tau_F = 17$ ms and the amplitude

⁷The overshoot in the inset of Fig.2.9a is initially due to the induction because of the varying flux due to the Offset coils. It is damped because the servomechanism of the Feshbach stabilize this change after a time corresponding approximately to its response time τ_F .

⁸ $e = \exp(1)$.

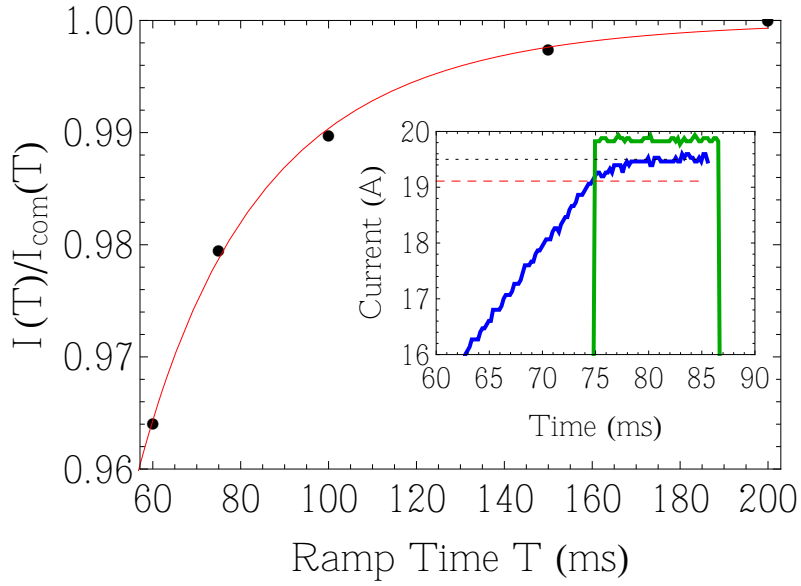


Figure 2.10: Delay of the response of the Offset Coils. Measured current $I(T)$ at the end of the ramp as a function of the sweep duration T divided by the set current $I_{\text{com}}(T)$ (measured for a ramp to $I = 19.5$ A (corresponding to $a/a_0 = 2300$). This measurement is weakly dependent on the sweep rate within the range of final currents $I = 18$ A ($a/a_0 = 1450$) to $I = 21$ A ($a/a_0 = -14400$), where this correction needs to be taken into account. The solid red line is an empirical fit to the data with a function $f_s(T)$, see text. Inset: example of an Offset sweep of 75 ms (in blue) to a value of 19.5 A. When the camera is triggered for imaging (green pulse), the current reached is 19.1 A. After the trigger, the image is taken in less than 100 μs .

$A(\dot{I})$ depends on the sweep rate \dot{I} in the Offset coils. In Fig.2.9b, we plot A as a function of \dot{I} and we observe an approximately linear behavior.

Note that when the Offset sweep is finished, the magnetic flux in the Feshbach coils is reduced and the same overshoot as in the inset of Fig.2.9) in the opposite direction occurs. This effect is dramatic when one ramps the interaction close to the Feshbach resonance as the magnetic field transiently explores values even closer to the resonance. This overshoot is damped in only 50 ms, and losses have the time to take place. We thus need to take the images right after the ramp and it is very important to know exactly the value of the Offset current when imaging is done. In the inset of Fig.2.10, we plot the end of an Offset ramp (in blue, 75 ms to 19.5 A (dotted black line)). When the camera is triggered for imaging (green pulse), the current reached is 19.1 A (dashed red line). The image is taken in less than 100 μs after the positive slope of the trigger. This measurement was repeated for various values of ramp times T and we plot in Fig.2.10 the ratio of the final measured current in the Offset coils $I(T)$ to the expected value $I_{\text{com}}(T)$. In practice, this effect needs to be taken into account only close to the resonance (typically for $a/a_0 \gtrsim 1500$) because the value of the scattering length is then increasingly sensitive to the magnetic field. Finally, we use an empirical fit to the final value of the current (red solid line in Fig.2.10). In summary, the interaction sweep ramps are shown to be well described by the following approximately linear current sweep:

$$I(t) = \frac{f_s(T)I_{\text{com}}}{T}t + A(\dot{I})\frac{t \times e}{\tau_F} \exp(-t/\tau_F), \quad (2.7)$$

where the empirical fit function is $f_s(T) = 1 - e^{-c_0 T^{c_1}}$ (with $c_0 = 0.234$ and $c_1 = 0.649$, see solid red line in Fig.2.10). The first term takes into account a small shift in the final value of the current ramp due to the response time of the Offset coil servo, and the second term, the initial induction in the Feshbach coils.

Calibration of the magnetic field

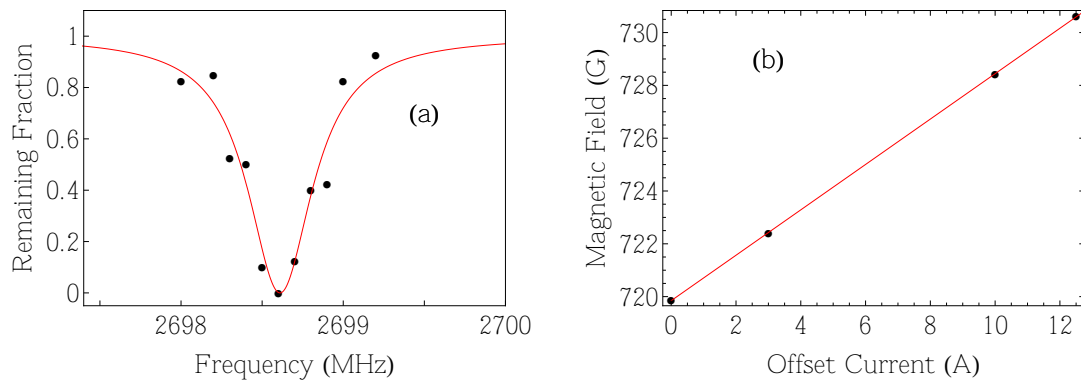


Figure 2.11: Calibration of the magnetic field using ${}^7\text{Li}$. (a): Remaining atoms in $|1\rangle$ after 50 ms of radio-frequency at a magnetic field of 730.6 G. (b): Magnetic field (determined by the position of the maximum of loss) as a function of the current in the Offset coils (with 361 A in the Feshbach coils, and 45 A in the curvature coils).

The precise knowledge of the magnetic field is of crucial importance for Feshbach resonance experiments. The calibration can simply be done by driving optical or radio-frequency transitions. Optical transitions are very convenient as they are used for absorption imaging as well. But due to the natural linewidth, their accuracy is within the MHz range which leads to ~ 1 G precision. Radio-frequency transitions are not plagued by this limitation, and much narrower linewidth can be achieved. We thus proceed by driving the ${}^7\text{Li}$ transition from state $|1\rangle$ to state $|8\rangle$ (see Fig.2.3), whose sensitivity to B is $2\mu_B$ in the Paschen-Back limit. This limit correspond to the high magnetic fields where the Zeeman effect is much larger than the hyperfine splitting and electronic and nuclear spins become decoupled. In Fig.2.11a, we plot the number of remaining atoms in state $|1\rangle$ after a radio-frequency is applied for 50 ms. As this time is comparable to the axial trapping period, atoms in $|8\rangle$ have the time to leave the trap in the axial direction. By driving transitions between two trapped states ($|1\rangle$ and $|2\rangle$ of ${}^7\text{Li}$), we have observed RF-lines as narrow as 2 kHz, compatible with a magnetic field stability better than 50 mG. Because of the large width of ${}^7\text{Li}$ and ${}^6\text{Li}$ Feshbach resonances used in this work, we do not need an additional current stabilization. In Fig.2.11b, we gather the position of the maxima of losses of various values of the Offset coils' current, from which we deduce a bias field of 0.86 G/A. A calibration of the 834 G resonance of ${}^6\text{Li}$ by optical means was shown to be consistent to a gauss with the ${}^7\text{Li}$ 730.6 G calibration.

2.4 Imaging

2.4.1 Resonant Absorption Imaging

In our experiment, we detect the atoms via resonant absorption imaging. The principle is to send a resonant probe beam (along the y -axis for example) on the atomic cloud, that will absorb part of it. We record on a CCD camera the intensity profile of the probe $I(x, z)$ after absorption by the atomic cloud. Due to the finite extent of the beam (and various imperfections on the imaging optics), the intensity profile of the beam is not perfectly uniform. In order to get rid of this inhomogeneity, we take a second image, this time without atoms, $I_0(x, z)$, to measure the intensity profile of the probe beam. The net absorption can then clearly be seen by computing the optical density $\text{OD}(x, z)$:

$$\text{OD}(x, z) = -\ln\left(\frac{I(x, z)}{I_0(x, z)}\right) = \sigma \int dy n(x, y, z), \quad (2.8)$$

where σ is the absorption cross section. The last equality in Eq.(2.8) holds if the Beer-Lambert absorption law is applicable. In several cases, Eq.(2.8) does not apply. If the intensity of the probe is comparable to the saturation intensity I_{sat} , the dependence of σ in intensity cannot be neglected. The absorption cross section is lowered at high intensities, a property that has been exploited to image dense atomic clouds [134]. In dense clouds, interactions between neighboring atoms can also lead to multiple scattering, and σ becomes density-dependent. This effect has been observed in the study of quasi-2D Bose gases and deducing the density profiles from the optical density becomes a challenging task [92]. A recurring issue in ultracold atom experiments is the accurate determination of σ and hence, the atomic density. Due to imperfections of the optical system, polarization of the probe beam, or other, it is difficult to accurately determine σ a priori. For the thermodynamic measurements presented in this work, the absolute calibration of the density is necessary to measure the pressure and we needed to implement different schemes in order to solve this problem.

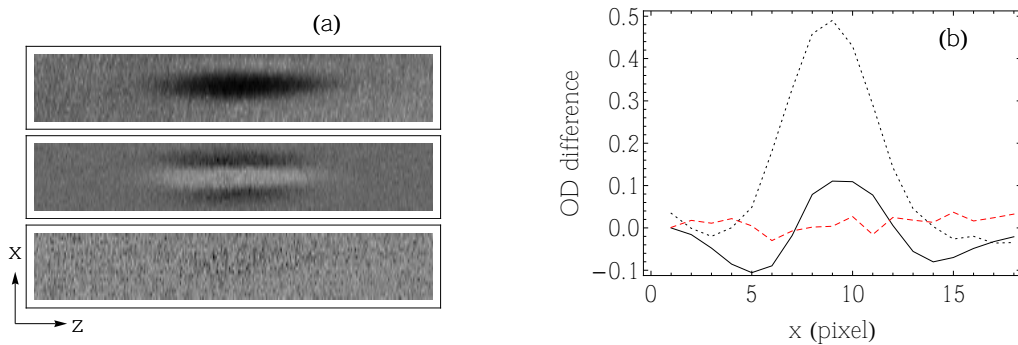


Figure 2.12: Imaging spin-balanced Fermi gases: (a) Absorption Images of the spin states $|1\rangle$ and $|2\rangle$. Up: Absorption image of spin state $|1\rangle$. Middle: Difference image with $I/I_{\text{sat}} = 0.1$. Down: Difference image with $I/I_{\text{sat}} = 0.01$. (b): vertical cuts of the absorption images of the up (dotted line), middle (solid line) and down (dashed red) images.

For our Bose gas imaging, we use two resonant pulses, one for absorption and one for reference. The intensity of the probe is reduced until further lowering does not increase the number of detected atoms, so that we reach about $I/I_{\text{sat}} \approx 0.01$. The exposure time is adjusted to see no radial broadening of the cloud due to heating from the probe. Between 50 and 100 μs the density profile

remains unchanged and the photon shot-noise ($\propto \sqrt{N_{\text{photons}}}$) is reduced by $\sqrt{2}$. Our optimum is thus at 100 μs exposure time. At 200 μs however, we observe that the gas is significantly broadened due to heating.

Imaging spin-imbalanced Fermi gases is more involved as we need to take pictures of both spin states. Two methods have been applied for this purpose: phase-contrast imaging [135, 136] and sequential absorption imaging [137].

The first technique involves non-destructive dispersive imaging of the phase shift imprinted on the beam by the cloud. Detuning the probe in between the transition for spin states $|1\rangle$ and $|2\rangle$ allows to image directly the difference of the density profiles of the two spin states [138], a very important quantity for the phase diagram of spin-imbalanced Fermi gases. However, this technique only measures the imbalance and not the absolute populations in the two spin states.

The second technique relies on the sequential absorption imaging of the two spin states. This technique is very easy to implement experimentally but one must be very careful about heating issues. Indeed, in the BEC-BCS crossover, spin \downarrow and \uparrow atoms form strongly interacting pairs. Imaging one spin-species will rapidly disturb the other species and density profiles will be distorted [137]. Hence, it is required to have the shortest pulse duration and shortest delay between the two images. We use an externally triggered pulse generator that produces two pulses of 10 μs (for the probe beams of each spin species) separated by 10 μs . Our CCD camera (PixelFly QE) works in interframing mode, allowing a separation as short as 3 μs between two subsequent images. The two reference images for each spin states are updated every ~ 10 runs. If one is interested only in the density difference, it is simply obtained via the two absorption pictures as:

$$\delta\text{OD}(x, z) = \text{OD}^{(1)} - \text{OD}^{(2)} = -\ln\left(\frac{I^{(1)}}{I_0^{(1)}}\right) + \ln\left(\frac{I^{(2)}}{I_0^{(2)}}\right) = -\ln\left(\frac{I^{(1)}}{I^{(2)}}\right) + c, \quad (2.9)$$

where $I^{(i)}$ ($I_0^{(i)}$) is the absorption (reference) image of spin state $|i\rangle$. Two simple tests can be performed to check the proper functioning of the sequential imaging.

- Perform the sequential imaging on a spin-balanced Fermi gas as shown in Fig.2.12. The optical density of spin state $|1\rangle$ (upper image in 2.12a and dotted line in 2.12b). The optical density difference should be null (lower image in 2.12a and corresponding dashed red line in 2.12b). Probe heating will lead to a residual signal due to the broadening of the second cloud imaged (middle image in 2.12a, and black solid line 2.12b). An intensity mismatch between the two probes will be identified as an offset in optical density.
- Prepare an imbalanced spin-mixture and check that the order of the pulses for the two spin-species does not affect the density profiles.

2.4.2 Probe Beams Setup

For diagnostics as well as for science purposes, we want to be able to probe the gas in two spatially separate regions (the MOT area and the center of the Ioffe trap in the appendage). Moreover, depending on whether we probe ${}^6\text{Li}$ or ${}^7\text{Li}$, at low or high bias fields, we need various probe beams at different frequencies. To satisfy these requirements, we have built a simple 4×4 beam splitter (displayed in Fig.2.13). The input beams are:

- ${}^6\text{Li}_{|F=3/2\rangle}$ and ${}^7\text{Li}_{|F=2\rangle}$ are the probes for ${}^7\text{Li}$ and ${}^6\text{Li}$ at low field (several G's bias), probing the transitions from $|F=2\rangle$ to $|F'=3\rangle$ and from $|F=3/2\rangle$ to $|F'=5/2\rangle$. They are used for the imaging of the MOT, lower quadrupole trap and the Ioffe-Pritchard trap.

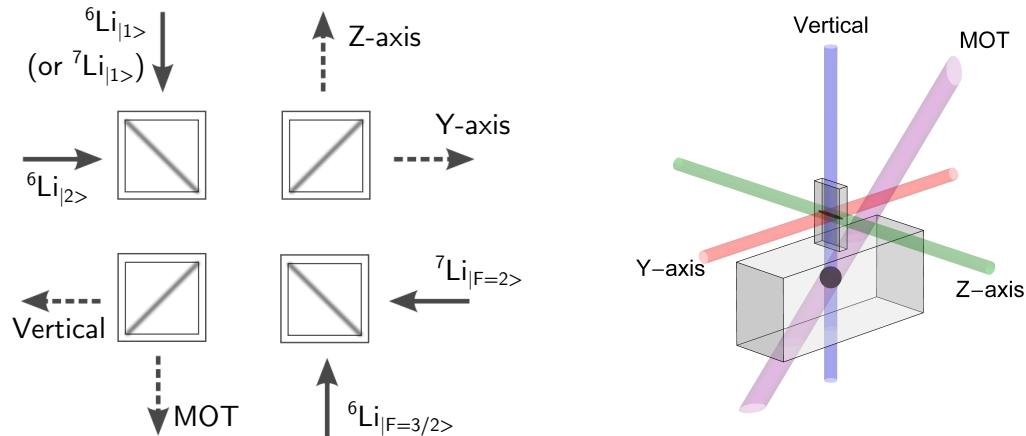


Figure 2.13: A Probe Beams splitter (left panel) distributes all frequencies used in the MOT region and along the three directions in the appendage (right panel).

- ${}^6\text{Li}_{|1\rangle}$ and ${}^6\text{Li}_{|2\rangle}$ are the probe beams of spin states $|1\rangle$ and $|2\rangle$ of ${}^6\text{Li}$ in the vicinity of the 834 G Feshbach resonance. They are used in the optical dipole trap.
- ${}^7\text{Li}_{|1\rangle}$ is used to probe ${}^7\text{Li}$ around the 740 G Feshbach resonance of ${}^7\text{Li}$ or at 834 G when used as a thermometer for strongly interacting ${}^6\text{Li}$ gases. In practice, we replaced the probe of one of ${}^6\text{Li}$ spin state by the high-field probe of ${}^7\text{Li}$.

The four non-polarizing 50/50 cubes combine these probe beams and direct them into four outputs (see Fig.2.13):

- the MOT region.
- the Z-axis along the long direction of the gas. This direction has a small numeric aperture (limited by the curvature coils) and the optical resolution is about $10\ \mu\text{m}$. However, this axis is very convenient for time-of-flight measurements, since the line-of-sight integration along the long axis allows for the detection of relatively low atom numbers. This direction was used to probe the small clouds of ${}^7\text{Li}$ in time-of-flight for thermometry. It is also used to probe large clouds during RF-evaporation in the Ioffe trap.
- the Y-axis is the “science” direction. We have access to the density profiles along the z -direction that are used to measure the equation of state. The resolution is $5\ \mu\text{m}$ standard deviation of a gaussian fit on the profile of a point object⁹.
- the Vertical direction for imaging was installed but not used. In the present setup, the radio-frequency antennas limit the aperture but with minor changes, this direction could be exploited to install a high-resolution imaging setup.

2.4.3 Probe Frequencies

The probe beams at low-fields are readily derived from the injection light to the MOT slaves. Their frequency is close to the zero-field transition from $|F = 1\rangle$ to $|F' = 2\rangle$ and $|F = 1/2\rangle$ to $|F' = 3/2\rangle$

⁹In this case, we prepare a quantum gas and compress the dipole trap so that the radial size of the gas becomes much smaller than the estimated optical resolution.

(on the D_2 line). Additional AOMs are used for fast switching and further attenuation of possible stray light.

High-field probes require slightly more work. The probing transition (leading to the excited state ($m_{J'} = -3/2$) is red-detuned by $\mu_B B$ for both ${}^6\text{Li}$ and ${}^7\text{Li}$ in the Paschen-Back regime. This results in about 1.2 GHz detuning compared to the zero-field repumping transitions (on the D_2 lines). Producing the probe for ${}^7\text{Li}$ is easy as the cooling transition light is already about 800 MHz red-detuned. An additional AOM in double-pass configuration is then sufficient to reach the desired frequency (either 110 or 200 MHz depending on whether experiments are done around 740 or 834 G). For ${}^6\text{Li}$, the hyperfine splitting provides us only with 230 MHz red-detuning and we use a high-frequency AOM in double-pass (centered around 460 MHz). Due to the poor efficiency of this AOM (less than 10 %), we need to injection-lock a slave laser from which both imaging beams for $|1\rangle$ and $|2\rangle$ states are derived.

Part II

Bosons

Chapter 3

The Ground State of an Interacting Bose Gas

The production of gaseous Bose-Einstein condensates in 1995 allowed for the first time to test in experiments the theory of weakly interacting bosons. Because of their diluteness, they can in general be well described by mean-field theory [40]. This is in contrast with the other previously known example of Bose condensate, superfluid ^4He , which is a strongly interacting quantum liquid. Reaching a regime where many-body effects become important in ultracold bulk Bose gases has been a considerable challenge, because of the increasing role of losses with interactions. In 1957, it was predicted that the ground state energy density $\mathcal{E} = E/V$ of a Bose gas follows an expansion in the diluteness parameter na^3 [41, 42, 43]:

$$\mathcal{E} = \mathcal{E}_{\text{MF}} \left(1 + \frac{128}{15\sqrt{\pi}} \sqrt{na^3} + \dots \right), \quad (3.1)$$

While the first term is the mean-field energy (with $\mathcal{E}_{\text{MF}} = gn^2/2$), the second term, also called the Lee-Huang-Yang correction, is due to the quantum fluctuations. Despite its fundamental nature in quantum many-body physics, this prediction had not been tested experimentally in dilute atomic Bose gases. In this chapter we will report on our studies of this first beyond mean-field using a low-temperature Bose gas with tunable interactions. The first section will be devoted to the preparation of the Bose condensate, and the control of interactions. The second section will present a careful characterization of the Feshbach resonance, critical for the thermodynamic study that will follow. We will then turn to our method of determining the global chemical potential of the trapped gas which is a central problem in the measurement of the equation of state. In the fourth section we will compare our experimental results with Quantum Monte Carlo calculations and in particular verify the $T = 0$ assumption made throughout this chapter. The discussions regarding the quasi-equilibrium hypothesis, including the three-body losses, and the dynamical aspect of the interaction sweep will be discussed in the next chapter.

3.1 A Bose-Einstein Condensate with Tunable Interactions

3.1.1 Obtaining a Bose-Einstein Condensate of ^7Li

Tunability of interactions in an optical trap has been exploited to reach Bose condensation with several elements: ^7Li [78, 77], ^{133}Cs [140] and ^{39}K [141]. In the case of ^{133}Cs , the attainment of BEC in a magnetic trap was prevented by large two-body losses [142] and changing the scattering

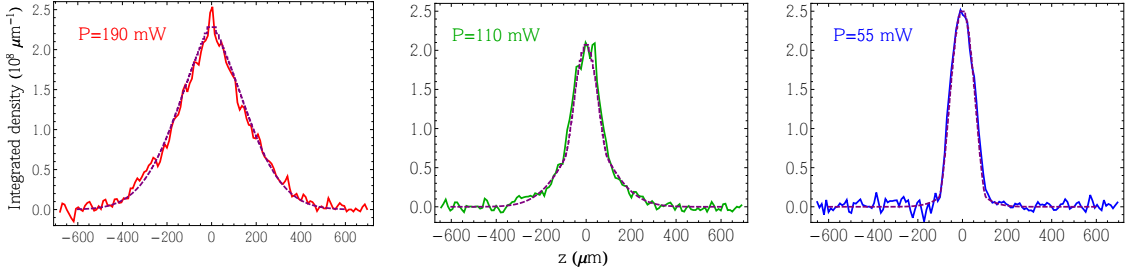


Figure 3.1: Bose-Einstein Condensation of ${}^7\text{Li}$. In-situ density profiles of a gas of ${}^7\text{Li}$ at various stages of the evaporative cooling in the optical trap, where P is the dipole trap power (from left to right) : $P = 190$ mW, 110 mW and 55 mW. The purple dashed line is a fit using a simple semi-ideal model [139]. The temperature is (from left to right): $T/T_c = 0.95$, 0.77 and 0.35.

properties in a dipole trap, involving an elaborate evaporation scheme was required to reach Bose-Einstein condensation [140]. For ${}^7\text{Li}$, the use of Feshbach resonances allows for fast production of BECs [80].

We prepare a Bose-Einstein Condensate of ${}^7\text{Li}$ through evaporative cooling in the optical dipole trap with a waist of $35 \mu\text{m}$ (see section 2.3.4). The evaporation is done at a magnetic field of about 720 G, where $a \sim 200 a_0$, found empirically to be best trade-off between a high collision rate and acceptable three-body recombination loss rate. The trap depth is reduced by a factor of about 100 in four linear steps, lasting a total of 5 s. In-situ absorption images are recorded along the Y -axis (Fig.2.13) at various stages of evaporation and are shown in Fig.3.1. The bias magnetic field is left at 720 G. At a power of 200 mW, we observe the appearance of a sharp, dense feature at the center of the cloud, corresponding to the Bose-Einstein phase transition. If the optical trap is further lowered, the number of particles in the BEC grows, the thermal wings shrink and ultimately a quasi-pure Bose-Einstein condensate is formed.

In the ideal gas picture, the Bose condensation is the collapse of a macroscopic number of particles in the one-body ground state of the system. In a harmonic trap, this corresponds to the familiar gaussian wavefunction of size $a_{\text{ho}} = \sqrt{\frac{\hbar}{m\omega}}$, the oscillator length, where ω is the frequency of the trap. For the trap used in Fig.3.1 along the z direction the frequency is $\omega_z = 2\pi 18.5$ Hz and the oscillator length in this direction is $a_{\text{ho}} \approx 9 \mu\text{m}$. It is obvious that the BEC extension is much larger than the ground state wavefunction. This is due to the repulsive interactions between the atoms. To understand this, we will now recall the most elementary description of the quantum many-body Bose system with contact interactions, the mean-field approximation.

3.1.2 Mean-Field Equation of State of a Bose-Einstein Condensate

We begin with the Hamiltonian of the Bose gas with a binary interaction potential $V_{\text{int}}(\mathbf{r})$ written in the second quantization formalism:

$$\hat{H} = \int d^3r \hat{\Psi}^\dagger(\mathbf{r}) \left(-\frac{\hbar^2}{2m} \Delta \right) \hat{\Psi}(\mathbf{r}) + \frac{1}{2} \int d^3r d^3r' \hat{\Psi}^\dagger(\mathbf{r}) \hat{\Psi}^\dagger(\mathbf{r}') V_{\text{int}}(\mathbf{r} - \mathbf{r}') \hat{\Psi}(\mathbf{r}') \hat{\Psi}(\mathbf{r}), \quad (3.2)$$

where $\hat{\Psi}(\mathbf{r})$ ($\hat{\Psi}^\dagger(\mathbf{r})$) is the bosonic destruction (creation) operator at point \mathbf{r} . The operators $\hat{\Psi}$ and $\hat{\Psi}^\dagger$ obey the bosonic commutation relations: $[\hat{\Psi}(\mathbf{r}), \hat{\Psi}(\mathbf{r}')] = 0$, $[\hat{\Psi}^\dagger(\mathbf{r}), \hat{\Psi}^\dagger(\mathbf{r}')] = 0$ and

$[\hat{\Psi}(\mathbf{r}), \hat{\Psi}^\dagger(\mathbf{r}')] = \delta(\mathbf{r} - \mathbf{r}')$. The mean-field approximation consists of assuming that all particles are in the same one-particle quantum state (the condensate). The field operator is written as:

$$\hat{\Psi}(\mathbf{r}) \approx \sqrt{n_0} \quad (3.3)$$

where $n_0 = N_0/V$ is the condensate density. If we use the contact potential $V_{\text{int}}(\mathbf{r} - \mathbf{r}') = g\delta(\mathbf{r} - \mathbf{r}')$, the energy of the system is:

$$E_0 = \frac{g N_0^2}{2 V} \quad (3.4)$$

and the equation of state:

$$\mu = \frac{\partial E}{\partial N} = gn_0. \quad (3.5)$$

This classic result was already obtained by Bogoliubov in 1947 [143]. The prescription used above is simplistic, and in particular we did not explicit yet the small parameter that controls the magnitude of the quantum fluctuations that are not included in Eq.(3.3) and to what conditions the mean-field approach is valid. However this is sufficient to understand the density profile shape in the weakly interacting regime such as in the right panel of Fig.3.1. Using the LDA prescription, we replace μ with $\mu_0 - V(\mathbf{r})$ in Eq.(3.5), and find the density distribution of a trapped Bose-Einstein condensate:

$$n(\mathbf{r}) = \frac{\mu_0 - V(\mathbf{r})}{g} \quad (3.6)$$

In the following, we assume a cylindrically symmetric trap corresponding to our physical situation: $V(\mathbf{r}) = \frac{1}{2}m\omega_z^2 z^2 + \frac{1}{2}m\omega_r^2 r^2$. The density profile has thus the shape of an inverted parabola. The quantity that we have access to is rather the doubly-integrated density as a function of the axial position z : $\bar{n}(z) = \int dx dy n(x, y, z)$. It can be obtained by direct integration of the 3D density $n(\mathbf{r})$ but it can also be readily obtained using the pressure formula. Indeed, from Gibbs-Duhem relation at fixed temperature $\partial P/\partial \mu = n$, we integrate the mean-field EoS $\mu = gn$ over μ , get the mean-field pressure

$$P_{\text{MF}} = \frac{\mu^2}{2g} \quad (3.7)$$

Using LDA prescription and $\bar{n}(z) = \frac{2\pi}{m\omega_r^2} P(\mu(z))$, we find:

$$\bar{n}_{\text{MF}}(z) = \frac{15N}{16R_{\text{TF}}^2} \left(1 - \frac{z^2}{R_{\text{TF}}^2} \right)^2, \quad (3.8)$$

The global chemical potential is $\mu_0 = \frac{1}{2}m\omega_z^2 R_{\text{TF}}^2$, where the Thomas-Fermi radius R_{TF} along the z direction is

$$R_{\text{TF}} = a_{\text{ho}} \left(15\lambda^2 N \frac{a}{a_{\text{ho}}} \right)^{1/5}, \quad (3.9)$$

where $a_{\text{ho}} = \sqrt{\frac{\hbar}{m\omega_z}}$ is the axial oscillator length, and $\lambda = \omega_r/\omega_z$ is the aspect ratio of the trap. In the mean-field regime, the radius of the cloud is a weakly increasing function of the interactions $R_{\text{TF}} \propto (Na)^{1/5}$.

Beyond the Local Density Approximation: the Gross-Pitaevskii Equation

For trapped Bose-Einstein condensates in the mean-field regime, it is easy to go beyond the local density approximation and understand its applicability. First, we add a trapping potential $V(\mathbf{r})$ to the single-particle (kinetic) term of the Hamiltonian (3.2). We write the field operator in a similar fashion as Eq.(3.3), assuming all particles occupy the same one-particle wavefunction $\phi(\mathbf{r})$:

$$\hat{\Psi}(\mathbf{r}) \approx \phi(\mathbf{r}), \quad (3.10)$$

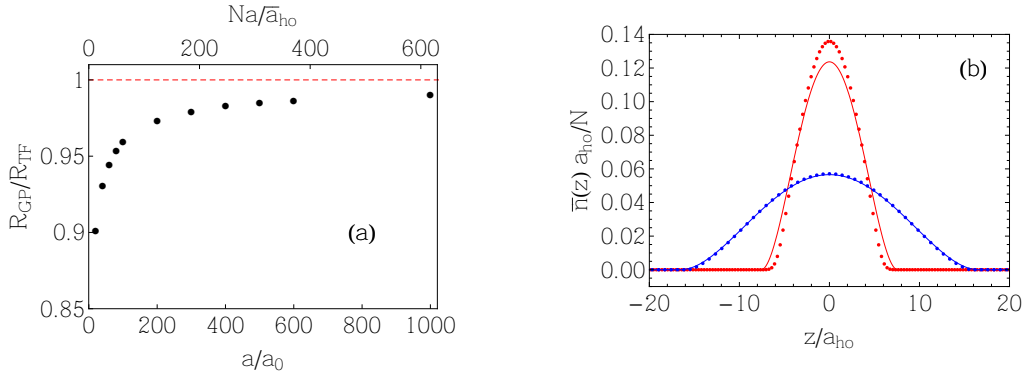


Figure 3.2: Correction to the Local Density Approximation for a weakly interacting BEC. (a): The radius predicted by the Gross-Pitaevskii equation R_{GP} is compared to the Thomas-Fermi limit R_{TF} as a function of the scattering length in a trap with $\omega_r/2\pi = 345$ Hz, $\omega_z/2\pi = 18.5$ Hz, and 4×10^4 particles. (b): Doubly integrated density distribution for $N = 4 \times 10^4$ obtained for the GP equation (for $a/a_0 = 20$ in red, $a/a_0 = 1000$ in blue) and the predicted Thomas-Fermi profile as solid lines. The stationary 3D GP equation is solved using a Fourier split-step method using imaginary-time propagation. Note that beyond-mean-field effects are not taken into account in these simulations.

where the wavefunction ϕ is normalized to the total atom number: $\int d^3r \phi(\mathbf{r}) = N$. Plugging this expression in the Hamiltonian (3.2), we obtain the energy functional $E[\phi]$. The minimization of this functional with respect to ϕ leads to the stationary Gross-Pitaevskii equation [39]:

$$\mu\phi(\mathbf{r}) = \left(-\frac{\hbar^2}{2m}\Delta + V(\mathbf{r}) + g|\phi|^2 \right) \phi(\mathbf{r}) \quad (3.11)$$

The local density approximation (3.6) (often called in this context the Thomas-Fermi (TF) limit) is recovered if the kinetic term can be neglected compared to the potential (and interaction) energy. Writing this equation dimensionlessly, it is easy to see that the ratio of the interaction to the kinetic energy is given by the parameter Na/\bar{a}_{ho} (where $\bar{a}_{ho} = \sqrt{\hbar/m\bar{\omega}}$ is the geometric mean of the oscillator lengths, and $\bar{\omega} = (\omega_r^2\omega_z)^{1/3}$ the geometric mean of the trap frequencies) [40] that controls the validity of the Thomas-Fermi approximation. We can test the validity of the LDA in our trapping conditions by solving numerically the stationary 3D GP equation¹. The simulated density profile along the z -axis is fitted with a Thomas-Fermi function, giving a radius R_{GP} that is compared to the expected value in the TF limit R_{TF} (3.9). In Fig.3.2b, we show two examples of simulated density distributions (red points for $a/a_0 = 20$, blue points for $a/a_0 = 1000$) and the expected Thomas-Fermi profile for the same value of a (solid lines). The ratio of the two radii as a function of scattering length is shown in Fig.3.2a and shows that a must be large enough ($\sim 600 a_0$) to have the LDA verified to better than 1%. This will be an important detail for the pressure calibration.

3.1.3 Increasing the interactions in a Bose-Einstein Condensate

The mean-field regime is understood, and after the pure weakly interacting BEC is formed, we ramp linearly in 150 ms (corresponding to 3 axial periods) the bias field to the desired value of the

¹The code was written by B. Rem and I. Ferrier-Barbut.

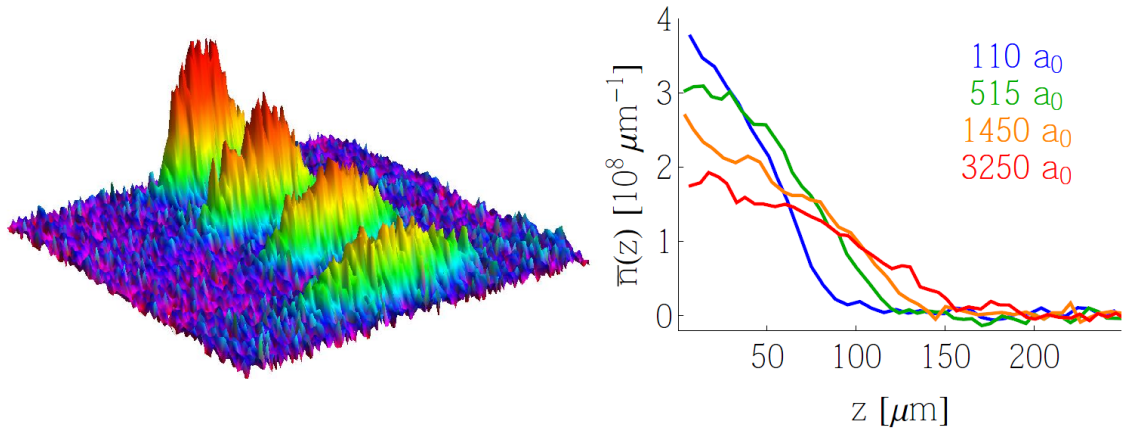


Figure 3.3: Increasing the repulsive interactions in a Bose condensate of ${}^7\text{Li}$. In-situ doubly-integrated density profiles of a gas of ${}^7\text{Li}$ for various values of the scattering length: $a/a_0 = 110$ (blue), 515 (green), 1450 (orange), and 3250 (red). The atom number is respectively 4.0, 4.6, 4.1 and 3.8×10^4 .

scattering length. The absorption image is recorded immediately after the ramp. The resulting density profiles at different values of a are displayed in Fig.3.3. In qualitative agreement with the mean-field picture, we see that for increasing values of a , the radius of the Bose condensate increases. However, the quantitative analysis of these density profiles to extract the equation of state critically requires a precise knowledge of the scattering length, to which we now turn.

3.2 The Feshbach Resonance

The position of a Feshbach resonance is hard to predict accurately because the calculation of the scattering length dramatically depends on the details of the complex atom-atom interaction potentials [70]. In practice, precision measurements around a Feshbach resonance require an experimental determination of its width and position. Interestingly, before our study was done, there were two accurate, and incompatible characterizations of the Feshbach resonance in the state $|F = 1, m_F = 1\rangle$ of ${}^7\text{Li}$, done in R. Hulet's group at Rice University and in L. Khaykovich group at Bar-Ilan University for the purpose of measuring three-body recombination rates. We thus had to proceed to an independent measurement of the Feshbach resonance properties.

In recent years, Feshbach resonances have become an essential tool to tune the interatomic interactions in ultracold gases [70]. Several methods have been devised to characterize Feshbach resonances. Inelastic loss spectroscopy is the most popular method as it is usually easy to implement. Resonant enhancement of atom number loss is observed when the scattering length is increased, due to two-body (or three-body) losses (see for example [34, 35, 144, 145]). Another possibility is to detect resonances via the elastic scattering, through thermalization rate measurements [146], collision shifts [147], mean-field interaction energy of a Bose-Einstein condensate [34, 12] or through the BEC radius measurements [148].

It is also possible to directly probe the Feshbach molecules, via radio-frequency spectroscopy. This method can lead to high precision measurements as in the universal regime, the relation

between the binding energy and the scattering length is known and model-independent. In the case of Fermi gases, molecules are long-lived and dissociation spectra are easy to measure [149, 72]. For Bose gases, where the lifetime of molecules is shorter, it is more convenient to associate them via microwave transition [150, 151] or oscillating magnetic fields [152, 79]. This method can be used in the case of narrow/broad or overlapping resonances [153].

3.2.1 A rough localization of the resonance

We have first used loss spectroscopy to provide a rough localization of the Feshbach resonance position in the $|F = 1, m_F = 1\rangle$ state of ${}^7\text{Li}$. A thermal gas is prepared slightly above T_c and the magnetic field is swept in 5 ms to the desired value (using the Feshbach coils). After a wait time of 200 ms, we sweep back the magnetic field to 719 G and wait for 100 ms before we image the remaining atoms. The curvature is left unchanged by these interaction sweeps.

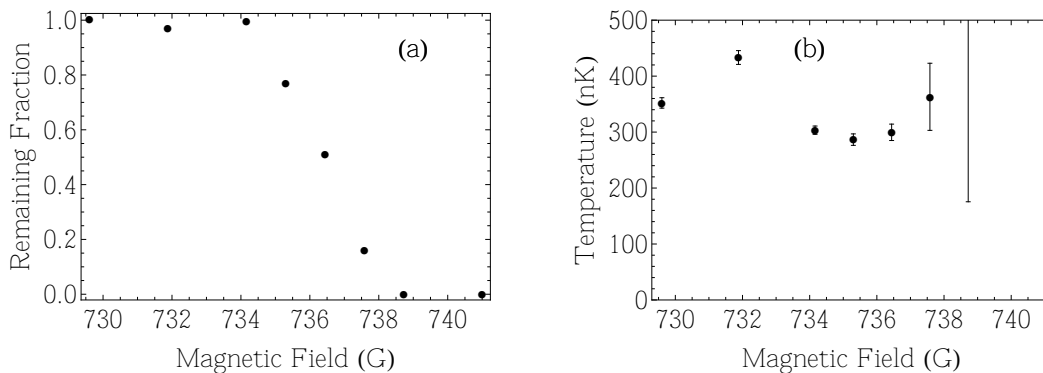


Figure 3.4: Inelastic losses around the Feshbach Resonance. (a) Remaining fraction of atoms and (b) temperature after 200 ms waiting time as a function of the magnetic field (error bars represent the fitting uncertainty only).

In Fig.3.4a, we plot the remaining fraction of atoms as a function of the magnetic field. A loss feature is readily identified for $B \sim 738$ G, in agreement with previous works [78, 77, 148, 79], even though its smoothness does not allow for an accurate localization of the resonance position (or width). It is interesting to measure the temperature of the cloud (Fig.3.4b), and we see that within our precision no significant temperature increase is observed. The inelastic loss spectroscopy is a reliable method mostly for narrow resonances, where the magnetic field sweep rate can be made fast enough. In the case of wide resonances, it is difficult to relate the properties of the Feshbach resonances to the loss features.

3.2.2 Radio-frequency association of Feshbach molecules

In order to improve our characterization of the resonance, we performed radio-frequency spectroscopy of Feshbach molecules. We stimulate formation of ${}^7\text{Li}_2$ molecules from an atomic cloud of ${}^7\text{Li}$ by modulating the bias field. When the modulation of B_0 matches the binding energy of the dimers, they are resonantly associated and rapidly lost through collisional relaxation into deeper bound states. We create the oscillating field with a linear wire positioned 3 cm above the atoms, producing a field collinear with the ~ 700 G offset. The modulation signal is generated by a synthesizer and amplified before being fed to the wire. The excitation lasts for 50 to 200 ms after

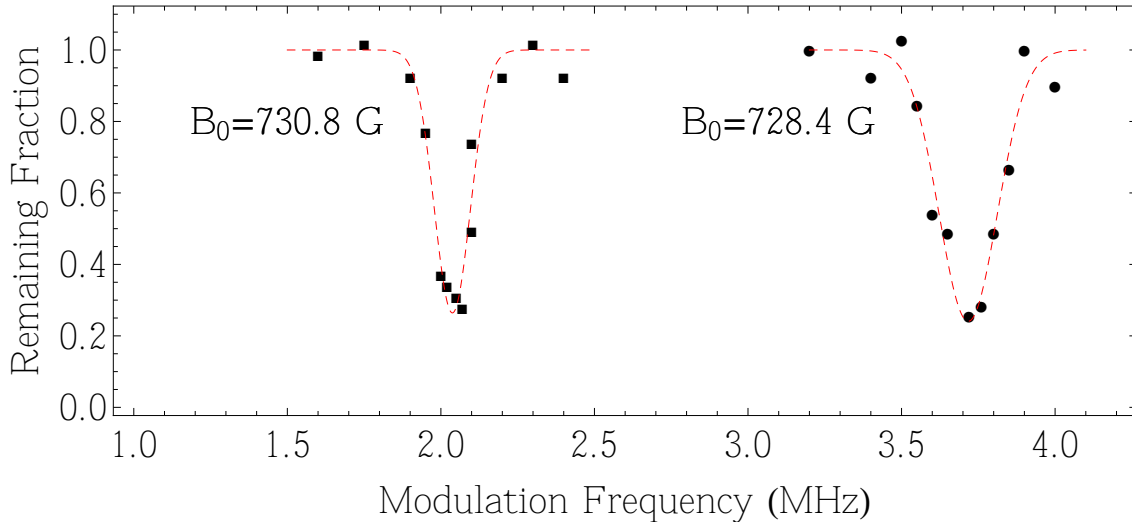


Figure 3.5: Radio-frequency association spectra of ${}^7\text{Li}_2$ molecules taken at magnetic fields of 728.4 G (circles) and 730.8 G (squares).

which the remaining atoms are imaged.

Typical association spectra are displayed in Fig.3.5 for two values of the bias field, $B_0 = 728.4$ G (circles) and 730.8 G (squares). The loss features are symmetric and we fit them with a gaussian function to locate the minimum of the feature, interpreted as the binding energy of the molecule. Gathering the binding energy measurements as a function of magnetic field, we determine the points in Fig.3.6. The sweep to the final magnetic field value is achieved either with the Feshbach coils (blue diamonds) or with the Offset coils (red squares), requiring separate magnetic field calibrations.

The last step remaining is to relate the binding energy to the scattering length. Close to the resonance the bound state energy of Feshbach molecules obeys the simple universal law (see section 1.2.3):

$$|E_b| = \frac{\hbar^2}{ma^2}. \quad (3.12)$$

This equation assumes the zero-range limit for the interactions and a wide Feshbach resonance. Finite-range correction and width correction can be taken into account to modify Eq.(3.12)². However, in order to avoid input from theoretical calculations, the scattering length extracted from the binding energy measurement will be limited to the range where the universal law applies, where a is much larger than the non-universal corrections. As $|B - B_0| \ll \Delta$, our measurement is not sensitive to a_{bg} and Δ separately but to the product $\Gamma = a_{\text{bg}}\Delta$, and Eq.(1.31) will be approximated by:

$$a(B) \approx \frac{\Gamma}{B - B_0}. \quad (3.13)$$

Fitting our data with Eqs.(3.12) and (3.13), we find: $B_0 = 737.8(2)$ G and $\Gamma = 3550(100) a_0 \cdot \text{G}$.

²The binding energy law then becomes [70] $|E_b| = \frac{\hbar^2}{m(a - \bar{a} + R^*)^2}$, where \bar{a} is a mean scattering length associated to the finite-range of the interaction potential [154], while R^* takes into account correction to the finite width of the resonance [87]. The universal law is applicable when $a \gg \bar{a}$ and $a \gg R^*$.

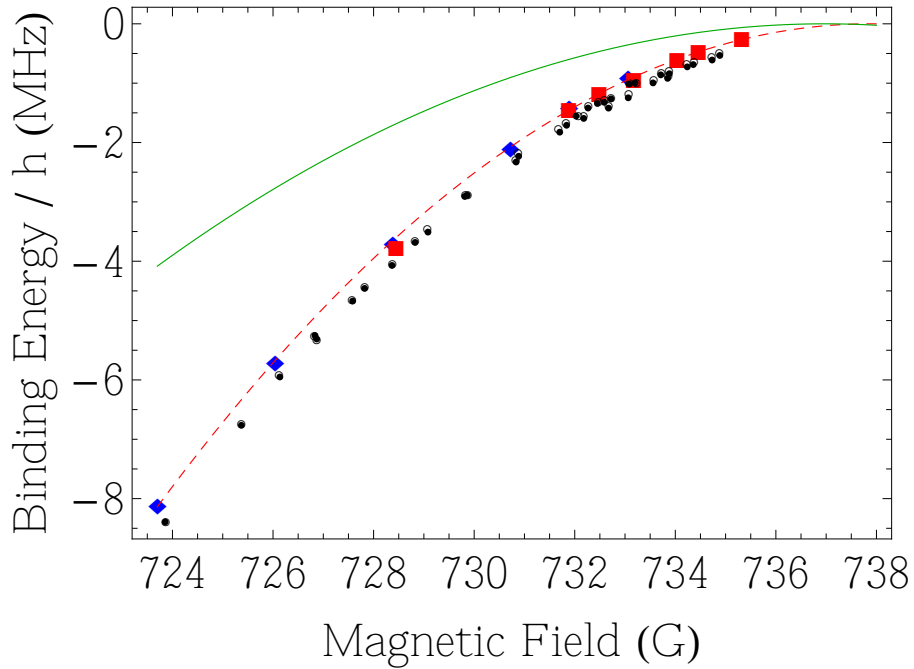


Figure 3.6: Binding energy of ${}^7\text{Li}_2$ Feshbach molecules. The final magnetic field is ramped with the Feshbach coils (blue diamond) or the Offset coils (red squares). The dashed red line is a parabolic fit of the data to the universal law Eq.(3.12) from which the scattering length is deduced. In black dots the Bar-Ilan measurement [79], in solid green line the binding energy deduced from the Feshbach resonance measurement of the Rice group [155].

For comparison, we plotted two other determinations of this Feshbach resonance: in black dots, the Bar-Ilan group RF-association measurement [79] and in solid green line, the binding energy deduced from a recent work at Rice University [155]. This last measurement was done by tuning the magnetic field and measuring the in-situ Thomas-Fermi radius of the Bose-Einstein condensate. In the mean-field regime $R_{\text{TF}} \propto (Na)^{1/5}$ and one can in principle deduce the scattering length from the BEC radius. They eventually include beyond-mean field corrections when the value of the scattering length is too large to neglect them. All the results are gathered in Tab.3.1.

Table 3.1: Properties of the Feshbach resonance in the $|F = 1, m_F = 1\rangle$ state.

	B_0 (G)	a_{bg} (a_0)	Δ (G)	Γ ($a_0 \cdot \text{G}$)
Rice (in-situ BEC size) [155]	736.97(7)	$-24.5^{+3.0}_{-0.2}$	192.3(3)	4711
Bar-Ilan (RF spectroscopy) [79]	738.3(3)	-	-	3600(150)
This work (RF spectroscopy)	737.8(2)	-	-	3550(100)
Eindhoven (coupled channel calculations) [156]	737.88(2)	-20.98	-171.0	3588

Apart from a small systematic shift of the magnetic field, our measurements are in very good agreement with Bar-Ilan group data and the properties of the resonance are fully compatible within the stated error bars (see Tab.3.1). We see however that the Rice measurement clearly differs from the two RF-spectroscopy determinations and from a coupled channel calculations. The in-situ BEC

size method is delicate because the scattering length has a sensitive dependence in R_{TF} and also subject to systematic uncertainty on N . In addition, when the scattering length becomes large, heating can be expected from three-body recombination and its effect on the radius of the BEC has to be considered for an accurate measurement.

3.3 Measurement of the Equation of State

We now turn to the quantitative analysis of the in-situ density profiles of the Bose gas. According to the pressure formula presented in section 1.3.4, we have for a single species Bose gas at zero-temperature the following relation:

$$P(\mu_z; a) = \frac{m\omega_r^2}{2\pi} \bar{n}(z) \quad (3.14)$$

between the local pressure P of the gas along the axial direction z and the doubly-integrated density $\bar{n}(z)$. This formula relies on the validity of the local density approximation, checked within mean-field theory in section 3.1.2. Knowing the value of the global chemical potential μ_0 , we can deduce the local chemical potential along the z -axis is $\mu_z = \mu_0 - V(z)$, and each pixel along the z direction gives us a point $(\mu_z, P(\mu_z))$ of the equation of state, by simply measuring the doubly-integrated density $\bar{n}(z)$. The value of a has been calibrated in the previous section. We are now left with the determination of the global chemical potential μ_0 .

3.3.1 Determination of the global chemical potential

The global chemical potential must be determined in order to deduce the local chemical potential $\mu_z = \mu_0 - V(z)$ along the z -axis. For a harmonic trap, the global chemical potential is equal to the local one at the bottom of the trap $\mathbf{r} = 0$. Determining the chemical potential directly from the density profile looks at first as a circular problem. Indeed, the absorption images give access to the density and the relation between the density and the chemical potential $n(\mu)$ is the equation of state of the system itself. However we can focus on the dilute limit, where the EoS is known: $\mu = gn$. Consequently, for vanishing density $n \rightarrow 0$, the chemical potential vanishes, $\mu \rightarrow 0$. In the harmonic trap along the z -axis, we can thus measure the chemical potential at the point where the density profile vanishes. If we note R_0 this radius (such as $\bar{n}(R_0) = 0$), the global chemical potential is simply $\mu_0 = \frac{1}{2}m\omega_z^2 R_0^2$. Let us emphasize that this reasoning is only valid at $T = 0$. As soon as we consider the finite temperature density profiles, there is no such value R_0 where the density vanishes strictly speaking. In the dilute limit the gas will behave like a classical gas and in an harmonic trap, it will result in asymptotically gaussian wings on the density profiles, and it would be necessary to determine both μ_0 and T , which is in principle possible using the classical density distribution but more difficult given the signal-to-noise ratio.

A self-consistent method to measure μ_0

The problem is now reduced to the determination of the radius R_0 at which the density profile vanishes. For density profiles with a finite signal-to-noise ratio, this task is non-trivial as in general the value of R_0 will depend on the fitting function. From the pressure formula, we know that the choice of a fitting function for the doubly-integrated density is equivalent to a choice of equation of state. We solved this problem by using a simple self-consistent scheme. Since the values of the gas parameter na^3 that can be reached in quasi-equilibrium in our experiment are still much

smaller than 1, we expect the beyond-mean-field effects to be small. As a result, determining the chemical potentials using model density profiles corresponding to the mean-field EoS (see Eq.(3.8)) is a reasonable starting point. However, this leads to an EoS that is not self-consistent because the inverted parabola assumes the MF-EoS to deduce a different EoS. One can then implement an iterative scheme to obtain a self-consistent EoS. At the first step, one starts with the density profiles $\bar{n}_i(z)$ (for $i = 1, \dots, M$) fitted with $\bar{n}^{(1)}(z) = n_0 \left(1 - \frac{z^2}{R^2}\right)^2$, and M the number of images. From the values of R_i , one deduces $\mu_{0,i}^{(1)}$ and a first step EoS $P^{(1)}(\mu)$. From this first step EoS obtained by gathering all the images, one can generate density profiles (using the pressure formula), using a fitting function for $h^{(1)}(\nu) = 2\pi\nu^2(1 + \gamma_1^{(1)}\nu + \gamma_2^{(1)}\nu^2)$. We fit again all the density profiles, this time with a fitting functions deduced from $h^{(1)}(\nu)$, to get a second set of radii, and hence a new set of chemical potentials $\mu_{0,i}^{(2)}$ for each image. This procedure is iterated until a fixed point is reached and the EoS no longer changes with additional iterations. The fixed point is a self-consistent EoS: the values of $\mu_{0,i}^{(\infty)}$ are determined using a fitting function consistent with the EoS that is deduced. The principle of the self-consistent method is simple but it is important to check that the procedure converges to the correct solution. The robustness of the convergence relative to the presence of noise is also of obvious experimental relevance. The method has been validated using simulated density profiles, and the results are shown in appendix A.1.

3.3.2 Pressure Calibration

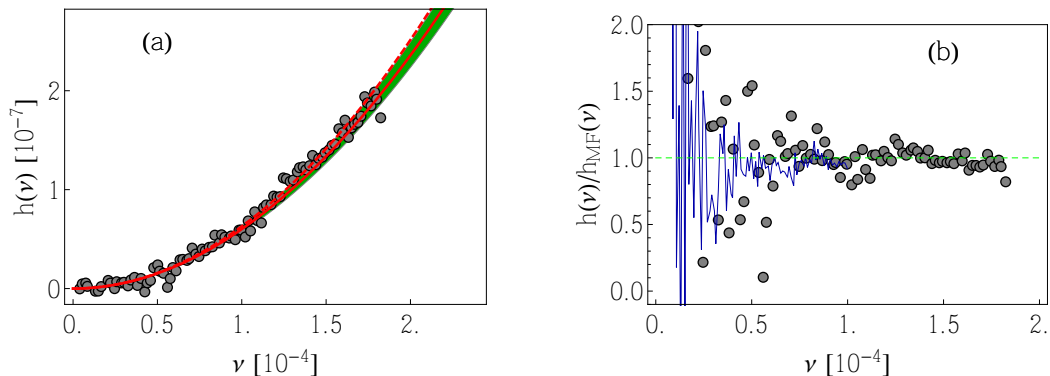


Figure 3.7: Calibration of the pressure in the mean-field regime. (a): normalized pressure $h(\nu)$ as a function of the grand-canonical gas parameter $\nu = \frac{\mu}{g}a^3$. The mean-field (Lee-Huang-Yang) pressure is plotted in red solid (dashed) line. The green area corresponds to a 5 % uncertainty on the scattering length. (b) pressure normalized to the mean-field pressure. The dots are the data at $a/a_0 = 730$, while the blue solid line, at $a/a_0 = 550$.

Now that the determination of μ_0 has been validated, we turn to the measurement of the pressure itself. In the dilute limit $na^3 \ll 1$, where the EoS is universal, the grand canonical EoS of the homogeneous Bose gas at zero temperature can dimensionally be written as

$$P(\mu, a) = \frac{\hbar^2}{ma^5} \cdot h\left(\nu \equiv \frac{\mu}{g}a^3\right), \quad (3.15)$$

where ν is the gas parameter. It is the grand-canonical analog to the usual gas parameter na^3 , since in the mean-field limit we have $\nu = na^3$. Our goal is to measure the function h . Let us recall

that in the mean-field limit, the pressure is $P = \mu^2/2g$ and we readily find $h_{\text{MF}}(\nu) = 2\pi\nu^2$.

From the pressure formula, we need only the radial trapping frequency ω_r and the integrated density profile \bar{n} . However, an absolute and precise determination of the density is notoriously difficult from absorption images, due to various parameters affecting our knowledge of the absorption cross-section, such as imperfect probe beam polarization, imaging optics, etc. (see section 2.4.1). Rather than measuring precisely this cross-section, we calibrate the pressure directly using a reference pressure, taken in the relevant experimental conditions. We write the relation of the pressure to the experimental doubly-integrated density \bar{n}_{exp} , $P(\mu_z) = \frac{m\omega_r^2}{2\pi} \xi_d \bar{n}_{\text{exp}}$, where the real density is $\bar{n} = \xi_d \bar{n}_{\text{exp}}$ and ξ_d is the detectivity of our system. In the deep mean-field regime, we can measure the pressure and adjust the detectivity ξ_d in order to recover the mean-field pressure. Two remarks can be done at this point. First, this calibration method is very convenient as it will automatically account for an error in the radial trapping frequency determination as well as for a probe detuning mismatch (provided all images are taken with the same detuning mismatch). In principle the smaller a , the better, since beyond mean-field effects will be smaller. However, there are two additional constraints. First, local density approximation should be valid and from the Gross-Pitaevskii equation we know that the Thomas-Fermi parameter Na/a_{ho} must be large (see section 3.1.2). Secondly, there are non-universal corrections to the binding energy (see the footnote after Eq.(3.12)). Therefore, we want the scattering length a to be much larger than the finite range corrections ($a \gg \delta a$ where, $\delta a \approx 20a_0$). In practice, at $a/a_0 \sim 700$, the beyond mean-field effects are smaller than 5 %. In Fig.3.7a we show the function h for images taken at $a/a_0 = 730$. Using $\xi_d = 1.55(4)$, we find excellent agreement with the mean-field prediction. We can check that we do not have important density-dependent effects altering the absorption imaging by measuring the EoS in the mean-field regime for a different values of the scattering length. In Fig.3.7b, we show the pressure normalized to h_{MF} . The points are the data at $a/a_0 = 730$, while the solid blue line is an average of 10 images taken at $a/a_0 = 550$ for which we recover the mean-field pressure to less than 5 %.

3.3.3 Observation of beyond mean-field effects in a Bose gas

Let us now turn to a regime of stronger interactions. The value of the scattering length necessary to unambiguously observe beyond mean-field effects depends on our precision in the pressure measurement. In practice we sweep the magnetic field in 150 ms, and we can reach scattering length of about $2000 a_0$ without observable losses (see chapter 4). For larger values of the scattering length, losses are visible, and it then becomes necessary to model them. The density-dependent character of three-body losses makes it subtle because the profile is distorted and a flow of atoms can exist within the cloud depending on the relative timescale of the losses and the trapping frequencies. These aspects will be discussed in chapter 4. In order to avoid these model-dependent inputs, we limit to a maximal value of $a/a_0 = 2150$. In Fig.3.8 we plot the Equation of State deduced using the self-consistent determination of the chemical potential for scattering lengths of $a/a_0 = 1400$ (Fig.3.8a) and $a/a_0 = 2150$ (Fig.3.8b). In addition, due to the finite duration of the interaction sweep, the gas has not completely reached its final size and this small systematic error is taken into account by applying a rescaling to the density profiles $\bar{n}(z) = (1 - \epsilon)^{-1} \bar{n}_0((1 - \epsilon)z)$, with $\epsilon = 1.8$ % (resp. 2.6 %) for $a/a_0 = 1400$ (resp. $a/a_0 = 2150$) (see chapter 4 for the detailed model). We see that for $a/a_0 = 1400$ even though there is a small systematic deviation to mean-field, it is within the uncertainty of 5% of the measurement. For a higher value $a/a_0 = 2150$, we observe a clear departure from the mean-field pressure. At a maximum value of $\nu \approx 2.5 \cdot 10^{-3}$, the

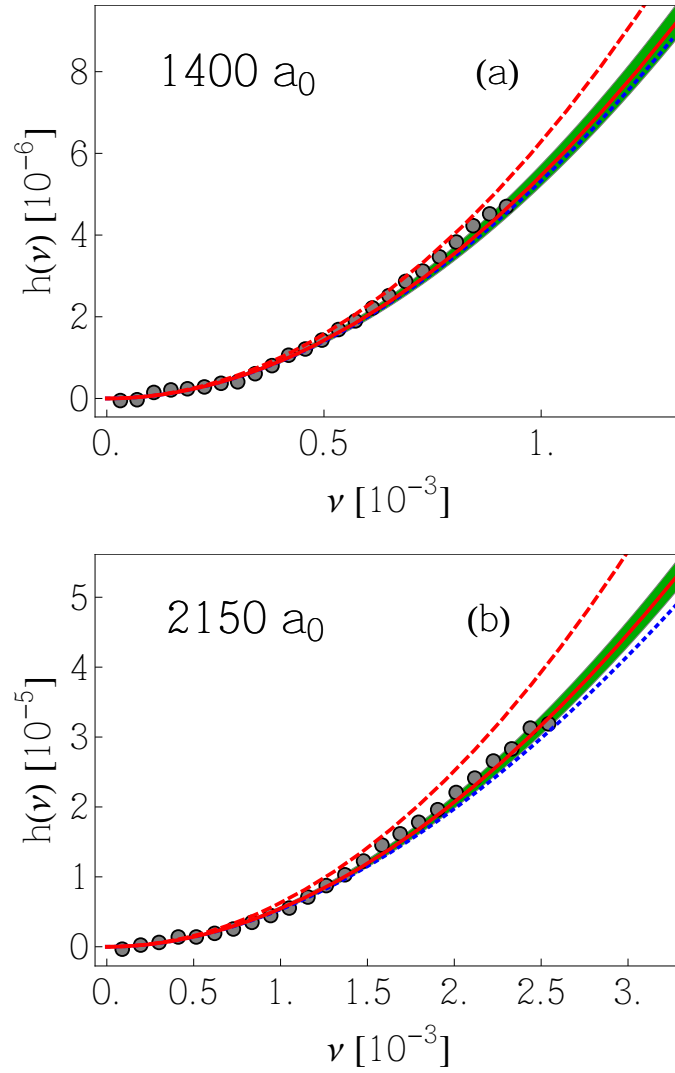


Figure 3.8: Equation of state of a low-temperature Bose gas for $a/a_0 = 1400$ (a) and $a/a_0 = 2150$ (b). In (dashed) red line, the (mean-field) Lee-Huang-Yang pressure, deduced from Eqs.(3.18), 3.23, and 3.24. The dotted blue line is the analytical Lee-Huang-Yang pressure (see text). The green area corresponds to an error of 5 % on the scattering length.

beyond mean-field effects accounts for ~ 18 % decrease of the pressure compared to the mean-field prediction.

3.3.4 Quantitative determination of the Lee-Huang-Yang correction

Our measurement presented in Fig.3.8 cannot be explained by the mean-field theory of section 3.1.2. It was shown in 1957, that the quantum fluctuations lead to a shift of the ground state energy compared to the mean-field expectation. Instead of the simple replacement (3.3), we add a small component $\delta\hat{\Psi}(\mathbf{r})$ describing the quantum fluctuations of the field operator:

$$\hat{\Psi}(\mathbf{r}) = \sqrt{n_0} + \delta\hat{\Psi}(\mathbf{r}) \quad (3.16)$$

We insert this expression in the Hamiltonian 3.2 and keep the terms at most quadratic in $\delta\hat{\Psi}$:

$$\hat{H} = E_0 + \int d^3r \delta\hat{\Psi}^\dagger(\mathbf{r}) \left(-\frac{\hbar^2}{2m} \Delta + 2gn_0 \right) \delta\hat{\Psi}(\mathbf{r}) + \frac{gn_0}{2} \int d^3r \left(\delta\hat{\Psi}^\dagger(\mathbf{r})^2 + \delta\hat{\Psi}(\mathbf{r})^2 \right), \quad (3.17)$$

where E_0 is the mean-field energy in Eq.(3.4). This Hamiltonian can be diagonalized exactly using the so-called Bogoliubov transformation and after an appropriate renormalization of the coupling constant g , the energy can be calculated and to lowest order, one finds the following expansion in powers of the gas parameter na^3 :

$$\frac{E}{V} = \frac{gn^2}{2} \left(1 + \frac{128}{15\sqrt{\pi}} \sqrt{na^3} + \dots \right). \quad (3.18)$$

The first term is the mean-field energy, obtained by Bogoliubov [143] (section 3.1.2). In 1998, it was proven that this term is a lower bound to the energy of a Bose gas with finite-range repulsive interactions [157]. The next term is the first correction beyond mean-field. It was first derived by Lee, Huang and Yang for a Bose gas with hard-sphere interactions [42, 41, 43]. More recently, the Lee-Huang-Yang formula was rigorously proven for a Bose gas with repulsive interactions described by an exponential function [158]. The Lee-Huang-Yang correction is thought to be identical for all Bose gases with short-range interactions in the dilute limit [159, 160, 161], and as such is one of the first non-trivial exact results in quantum many-body physics. The expansion (3.18) is valid provided $na^3 \ll 1$. Within the same approach, one can calculate the fraction of particles that are expelled from the condensate due to the quantum fluctuations which is $n - n_0 = \frac{8}{3\sqrt{\pi}} \sqrt{na^3}$. We see that the initial hypothesis (3.16) that few atoms are outside the condensate is controlled by the smallness of $\sqrt{na^3}$.

On the basis of the Equation of State measured in Fig.3.8, we can perform a direct quantitative comparison to the Lee-Huang-Yang calculation. In order to do so, we need to translate the expansion (3.18) into the grand-canonical ensemble, switching from $E(n)$ to $P(\mu)$. A simple approach is to start with the Lee-Huang-Yang chemical potential:

$$\mu_{\text{LHY}}(n) = gn \left(1 + \frac{32}{3\sqrt{\pi}} \sqrt{na^3} \right) \quad (3.19)$$

and invert this equation to lowest order to obtain:

$$n_{\text{LHY}}(\mu) = \frac{\mu}{g} \left(1 - \frac{32}{3\sqrt{\pi}} \sqrt{\frac{\mu}{g} a^3} \right). \quad (3.20)$$

Finally, integrating $n_{\text{LHY}}(\mu)$ yields the Lee-Huang-Yang pressure:

$$P_{\text{LHY}}(\mu) = P_{\text{MF}}(\mu) \left(1 - \frac{128}{15\sqrt{\pi}} \sqrt{\frac{\mu}{g} a^3} \right). \quad (3.21)$$

Or equivalently, the dimensionless pressure reads: $h_{\text{LHY}}(\nu) = 2\pi\nu^2 \left(1 - \frac{128}{15\sqrt{\pi}} \sqrt{\nu} \right)$. We see that apart from the sign of the correction, its magnitude in the grand-canonical variable ν is the same as in the canonical ensemble. However, if we plot this Equation of State (dotted blue lines in Fig.3.8), we see that the agreement is good only for small enough interaction strength (typically $\nu < 1.5 \cdot 10^{-3}$). For stronger interactions, our pressure is systematically slightly higher than h_{LHY} .

This apparent discrepancy can be investigated using comparison with theoretical calculations. A Diffusion Monte-Carlo (DMC) calculation was performed on the Hamiltonian for a Bose gas with binary interactions using different model potentials, whose properties were adjusted to recover the desired value of a [163]. While early Monte-Carlo studies using hard-sphere potentials

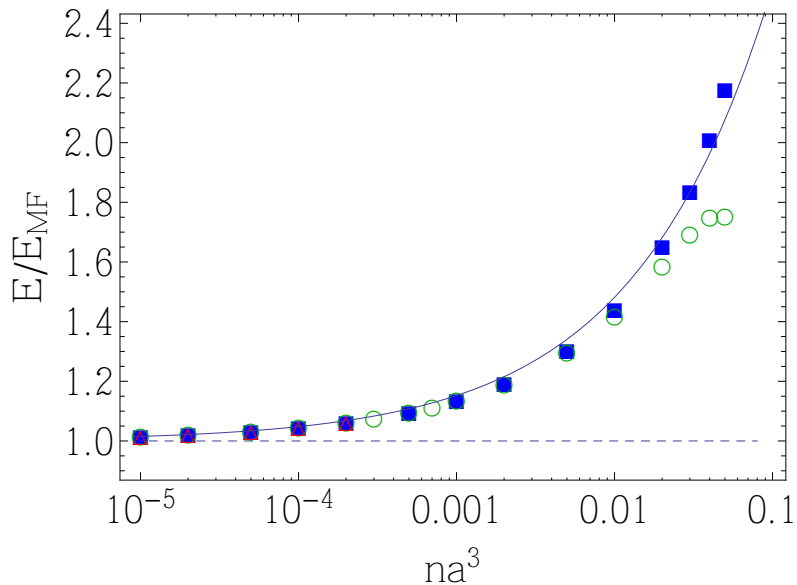


Figure 3.9: Variational Monte-Carlo calculation of the ground state energy of a Bose gas as a function of the canonical gas parameter na^3 . This energy is calculated for: hard-sphere potential (blue squares), a square-well potential with a range $R = a$ (empty green circles) and $R = 0.1a$ (empty red triangles) [162]. This set is expanded compared to the data published in [163]. The mean-field (LHY) energy (see Eq.(3.18)) is shown in dashed (solid) blue line.

were performed on very dense samples with the aim of understanding the properties of ^4He (for which $na^3 \sim 0.1$) [164,165], the work done by Giorgini *et. al.* focused on the dilute limit, which is the most relevant for ultracold gases. In Fig.3.9, we plot the ground state energy E normalized to the mean-field energy $E_{\text{MF}} = N \frac{gm}{2}$. The calculation was done for a hard-sphere potential (blue squares), a square-well potential with a range $R = a$ (empty green circles) and $R = 0.1a$ (empty red triangles). In addition to the mean-field energy (dashed blue line), we also show the Lee-Huang-Yang correction (solid blue line). We observe that universality is very well verified as all model potentials give the same ground state energy for a given value of a . Deviations start to become significant at about $na^3 \simeq 0.02$. For both hard-sphere and square-well potential (with $R = a$) the range of the potential R is on the order of a . As a consequence, for $na^3 \simeq 0.02$, the distance between particle is on the order of the range of the potential ($(nR^3)^{1/3} \sim (na^3)^{1/3} \sim 0.3$) and the details of the model potential cannot be neglected anymore (see the discussion in section 1.2.3). An unexpected result of the Monte-Carlo calculation is that the Lee-Huang-Yang EoS represents a quantitatively accurate description of the Bose gas even for gas parameter values for which the Lee-Huang-Yang contribution to the energy is not a small correction.

The numerical observation that LHY theory is valid up to high interaction strength suggests to calculate the pressure directly by applying the Legendre transform to the energy expression Eq.(3.18) rather than using the low- μ expansion (3.21). First, we define the dimensionless energy ξ :

$$\frac{E}{N} = \frac{\hbar^2}{ma^2} \xi(y \equiv na^3). \quad (3.22)$$

Combining $-PV = E - \mu N$ at zero temperature, with the Gibbs-Duhem formula $\partial P/\partial \mu = n$, we

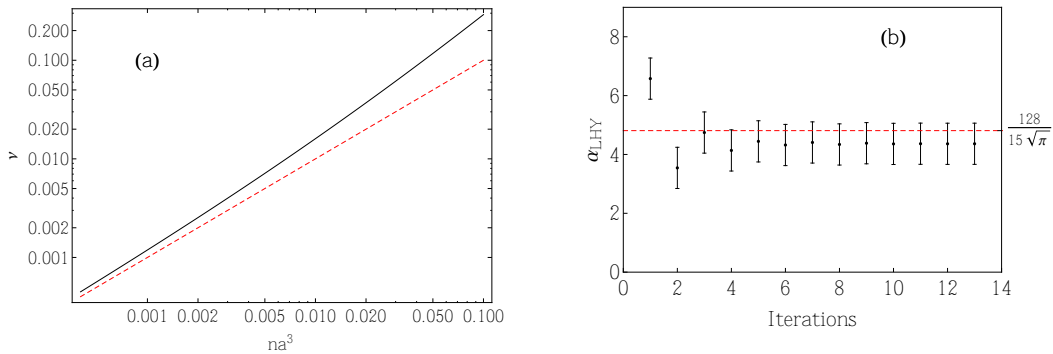


Figure 3.10: Determination of the Lee-Huang-Yang parameter. (a): correspondence between the canonical na^3 and grand-canonical ν gas parameters assuming the mean-field (LHY) EoS in black (dashed red) line. (b): fit of the Lee-Huang-Yang parameter to the data at $a/a_0 = 2150$ as a function of the iteration in the self-consistent determination of μ_0 .

find the following set of correspondence equations:

$$\nu(y, \xi) = \frac{1}{4\pi}(\xi(y) + y\xi'(y)) \quad (3.23)$$

$$h(y, \xi) = y(4\pi\nu(y, \xi) - \xi(y)) \quad (3.24)$$

The inverse transformation can be readily derived using $\partial E/\partial N = \mu$ instead of the Gibbs-Duhem relation. In Fig.3.10a we plot the relation between the canonical na^3 and grand-canonical ν gas parameters for both mean-field ($\nu = y$, solid black line) and LHY EoS ($\nu = y(1 + \frac{32}{3\sqrt{\pi}}\sqrt{y})$, dashed red line). The measured EoS, $h(\nu)$ can be used to extract the value of the Lee-Huang-Yang parameter α_{LHY} , that is defined in the canonical ensemble as: $\xi(y, \alpha_{\text{LHY}}) = 2\pi y(1 + \alpha_{\text{LHY}}y^{1/2})$. The red solid line in Fig.3.8 corresponds to $\alpha_{\text{LHY}} = \frac{128}{15\sqrt{\pi}}$. Alternatively, we can fit α_{LHY} at each iteration of the self-consistent determination of the $\mu_0^{(i)}$'s (Fig.3.10b). We notice the convergence of the EoS within a few iterations and the magnitude of the many-body effects on the pressure is found to be in very good agreement with the Lee-Huang-Yang calculation $\frac{128}{15\sqrt{\pi}} \approx 4.81$. Fitting the EoS after averaging the data taken at $1400 a_0$ and $2150 a_0$, we experimentally extract $\alpha_{\text{LHY}} = 4.5(7)$. The agreement between the experimental data taken for a gas constituted of ${}^7\text{Li}$ bosons, with a complex interatomic interaction potential, and the Lee-Huang-Yang Equation of State shows the universality of the first many-body correction to the ground state energy of a Bose gas with short-range interactions.

Non-universal effects

As the first beyond-mean-field effects have been measured, one is naturally led to wonder about the next terms in expansion (3.18) and the universality of these terms. The next terms in the expansion are [166]:

$$\frac{E}{V} = \frac{gn^2}{2} \left(1 + \frac{128}{15\sqrt{\pi}}\sqrt{na^3} + \frac{8(4\pi - 3\sqrt{3})}{3}na^3 (\log na^3 + B) - \frac{1024\sqrt{\pi}}{15} \frac{r_e}{a}(na^3)^{3/2} + \dots \right). \quad (3.25)$$

The term after the Lee-Huang-Yang contribution, in $na^3 \log na^3$ was first calculated by Wu for a hard-sphere Bose gas [167] and was later shown to be also universal [168]. The B -term however is

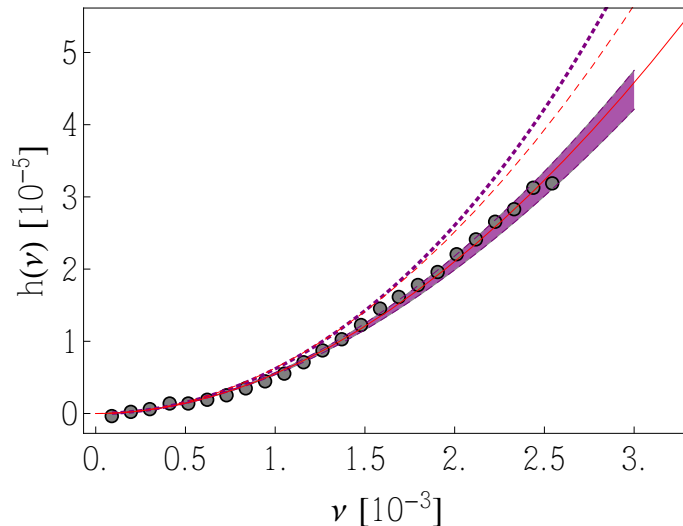


Figure 3.11: Non-universal effects in the equation of state of a $T = 0$ Bose gas. The experimental data points are plotted together with the mean-field (red dashed line) and the Lee-Huang-Yang pressure (red solid line). The log (or Wu) term is plotted in dotted purple, as well as the Wu term including the non-universal B -contribution (the shaded area corresponds to the values between $B = 5$ and $B = 9$).

non-universal and involves the scattering of three bosons [169]. It was discovered in 1961 that the three-boson problem with contact interactions is not well defined with the scattering length only and requires the introduction of an additional parameter, the *three-body parameter* Λ_* [170]. In 1971, V. Efimov discovered that the three-body system can support an infinite set of three-body bound states, with universal properties³, the Efimov trimers [2]. B was explicitly calculated for bosons with a hard-sphere interactions, yielding 8.5 [171]. In the case of bosons with short-range interactions, B was shown to be complex, the imaginary part being associated to three-body recombination. More interestingly, B depends log-periodically on the three-body parameter Λ_* , directly reflecting the presence of the Efimov trimers in the spectrum of three bosons with short-range interactions [172]. The amplitude of the log-oscillations is small and $B \approx 7.2$. The last term in Eq.(3.25) is the first correction due to the effective range r_e of the s -wave scattering [173].

We can check for possible nonuniversal effects in our measured EoS. The effective range in the $|F = 1, m_F = 1\rangle$ state is $r_e \sim 40a_0$ at our largest interaction strength [174] and we find the last term in Eq.(3.25) to be a correction of $\sim 0.04\%$ to the mean-field energy, far out of experimental reach under our conditions. The Wu and the B -terms cannot be considered separately as they are both numerically of the same order in the experimental range of na^3 explored. In addition, the logarithm term alone (as written in [163]) leads to an upshift of the ground state energy, maximum of about 3% at $na^3 \sim 10^{-4}$ and then becomes negative. This violates the Lieb-Yngvason lower energy bound [157] (see dotted purple line in Fig.3.11). Taking the value of $B = 8$, we find the third term of Eq.(3.25) to be about 10% for $na^3 = 3 \times 10^{-3}$, a large contribution, comparable to the Lee-Huang-Yang correction, while for $B = 6$ the contribution is almost zero. We can

³For example, at unitarity $a \rightarrow \infty$, the energy spectrum of the Efimov trimer contains an infinite set of states whose energies tends to zero following asymptotically a universal geometric law $E_n/E_{n+1} \rightarrow e^{2\pi/|s_0|} \approx 515$ (where $s_0 = i \times 1.00624$ is the solution of a transcendental equation).

plot the beyond-LHY contribution for values between $B = 5$ and $B = 9$ (see Fig.3.11). If we fix the value of the LHY parameter and use B as a fit parameter, we find $B = 6.8$. Attempts to extract the nonuniversal B for various model potentials on Bose gases have been done [173] based on the diffusion Monte-Carlo calculation of [163] in the very dilute limit. However, even for these precision calculations, the statistical errors prevented from inferring non-universality from the numerical data. The possibility of observing signatures of the Efimov effect directly on the Equation of State appears very challenging.

3.3.5 Comparison to Quantum Monte-Carlo calculations

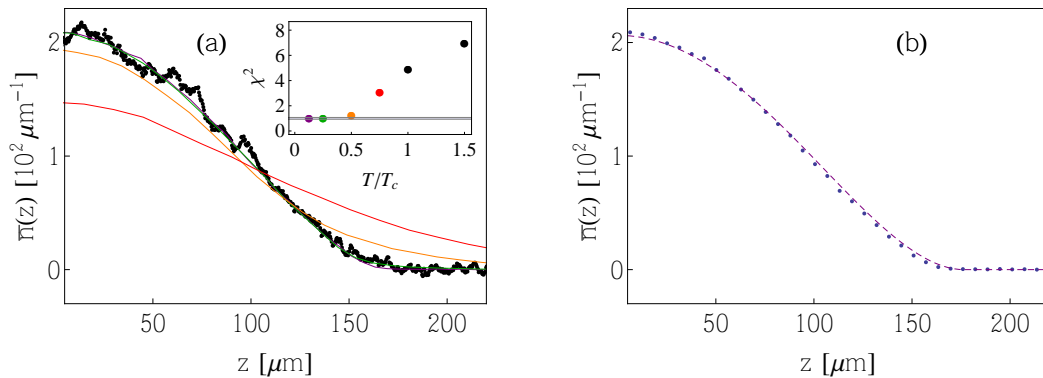


Figure 3.12: Finite-temperature effects in a Bose gas beyond mean-field. (a): In-situ density profile of a low-temperature Bose is averaged over 5 images at $a/a_0 = 2150$. The QMC calculations are performed for 38000 particles in a trap with $\omega_r/2\pi = 345$ Hz and $\omega_z/2\pi = 18.5$ Hz. The solid lines are the result of the QMC calculation at temperatures of $T/T_c^0 = 0.75$ (red), 0.5 (orange), 0.25 (green), and 0.125 (purple). (b): Comparison between the $T/T_c^0 = 0.125$ QMC density profile (blue dots) and the $T = 0$ prediction of the Lee-Huang-Yang assuming local density approximation.

All the studies realized in this chapter relied on the zero-temperature assumption. Obviously the clouds cannot be cooled to $T = 0$ and it is important to explore the role of finite-temperature effects on the equation of state measurement. For weakly interacting Bose gases, the finite-temperature corrections in the superfluid phase are small and the main feature is the presence of thermal wings outside the condensate region (see Fig.3.1) [40]. This picture was accurately confirmed experimentally using weakly interacting ^{87}Rb [106, 175]. Measuring the temperature on a weakly interacting Bose gas can thus be done on the thermal wings which can be treated classically.

The corresponding problem for a Bose gas with stronger interactions is considerably more complex. Effects of interactions on finite-temperature Bose gas is a notoriously subtle problem. Within the LDA, the density profiles simply give the equation of state. There have been several numerical studies of the finite-temperature equation of state [176, 177] but there is no simple analytical model beyond low-(or high-) temperature corrections comparable to the mean-field Hartree-Fock models [166]. In addition, the spatial separation between the Bose condensate and the thermal part is more difficult to distinguish as the Bose-Einstein condensate expands due to the increasingly repulsive interactions. In order to avoid relying on approximate models, numerical simulations were carried out by S. Piatecki and W. Krauth at ENS, using a Path-Integral Quantum Monte Carlo

(QMC) method [178]. The calculations were carried out in a cylindrically symmetric trap, in the same conditions (atom number and trapping frequency) as in the experiment. In Fig.3.12a, we plot together with an experimental density profile (averaged over 5 images with atom numbers within 5 %) the result of QMC calculations for various temperatures, in units of $T_c^0 = \hbar\bar{\omega}(N/\zeta(3/2))^{1/3}/k_B$, the critical temperature for BEC of an ideal gas in a trap of average frequency $\bar{\omega} = (\omega_r^2\omega_z)^{1/3}$. The distance to the experimental profile is quantified using a χ^2 test (see inset of Fig.3.12a) and shows that the data at $T/T_c^0 = 0.25$ and 0.125 are both within the 68 % interval of confidence. In Fig.3.12b, we compare the lowest temperature QMC calculation ($T/T_c^0 = 0.125$, blue dots) with the expected density profile assuming the Lee-Huang-Yang equation of state and the LDA (dashed purple line). The very good agreement between these two profiles, as well as with the experimental data, shows that finite-temperature effects are made negligible in our conditions and that the local density approximation is very well verified.

In this chapter, we have presented a study of the equation of state of the homogeneous Bose gas at low-temperature. We first accurately characterized the Feshbach resonance using radio-frequency association spectroscopy of $^7\text{Li}_2$ dimers. Using this Feshbach resonance, we increased the strength of the repulsive interactions and we have reached a regime where mean-field theory does not describe properly the system anymore. The first beyond-mean-field correction, due to quantum fluctuations was calculated by Lee, Huang and Yang in 1957. Our work provides the first quantitative measurement of the LHY correction in an atomic Bose gas. This beyond-mean-field is a many-body effect of fundamental importance and was shown to be universal, in the sense that it does depend on the details of the boson-boson interaction potential only through its low energy scattering properties, characterized by the scattering length. We have explored the possibility to observe non-universal effects on the equation of state. Using Quantum Monte Carlo simulations, we tested the zero-temperature assumption underlying the EoS study and find very good agreement with the lowest temperature calculations as well as with the local density approximation.

Chapter 4

Dynamics of a Bose Gas with Tunable Interactions

We now turn to the dynamics of a Bose gas subjected to an interaction sweep. The thermodynamic measurements presented in the previous chapter relied on the hypothesis of thermal equilibrium. In the first part of this chapter, we justify this assumption by studying the three-body losses close to the Feshbach resonance, and we assess the adiabaticity of the interaction sweeps for the thermodynamic measurements. We probe beyond-mean-field dynamics and propose a simple theoretical description to compare with the measurements. Finally, we use faster sweeps to access the regime of strong interactions close to the Feshbach resonance. Using a simple argument, we infer information about the hypothetical unitary Bose gas.

4.1 In quasi-equilibrium

To observe unambiguously beyond-mean-field effects in a Bose gas as presented in the previous chapter, we needed to reach values of the scattering length for which the associated three-body loss time τ_3 is not much larger than the axial trapping period, $\tau_3 \gtrsim T_{\text{ax}} (= 2\pi\omega_z^{-1})$. Because these time scales are similar, the magnetic field sweep to the strongly interacting regime cannot be made arbitrarily slow. In practice, we used $t_{\text{ramp}} \approx 3T_{\text{ax}}$, which causes slight non-equilibrium effects. Both atom losses and non-equilibrium effects can distort the density profile compared to the equilibrium profile. It is thus important to characterize the influence of the interaction sweeps, both for size and density measurements.

4.1.1 Cloud size measurements

In order to test the adiabaticity of the interaction sweeps, we measure the radius of the cloud as a function of the sweep time. For simplicity, we measure the radius using a Thomas-Fermi fitting function. As the in-situ cloud size depends on the atom number for a quantum gas, we normalize the radius to a radius¹ $R^* = a_{\text{ho}}(15\lambda^2 N)^{1/5}$. This choice is justified in the mean-field regime: if the atom number in the BEC fluctuates from shot-to-shot, the ratio R/R^* will remain constant, and the change in R/R^* would only be due to dynamical effects. However, if beyond-mean-field effects set in, the radius will not scale as $N^{1/5}$ anymore. Because most of the data is taken in a regime

¹ R^* would correspond to the mean-field Thomas-Fermi radius of a BEC with a scattering length $a = a_{\text{ho}}$.

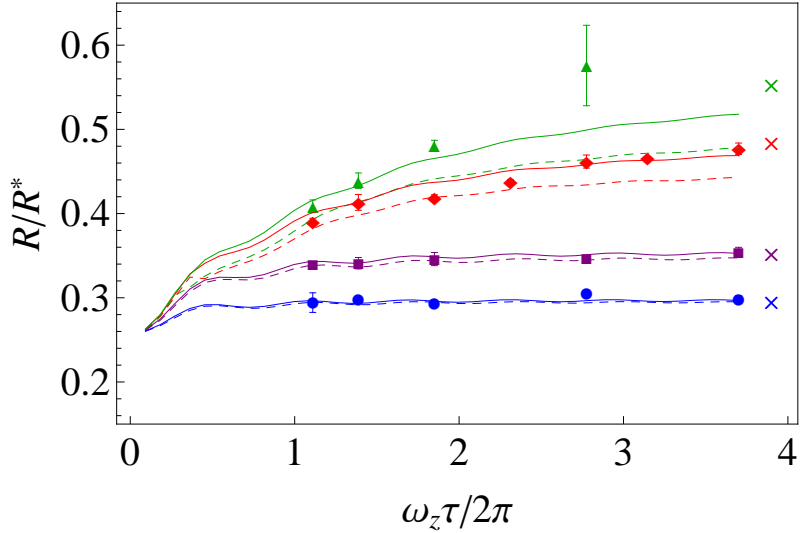


Figure 4.1: Radius R of the Bose gas as a function of the ramp duration τ of the interaction sweep. The radius R is normalized to the radius $R^* = a_{\text{ho}}(15\lambda^2 N)^{1/5}$ (where $a_{\text{ho}} = (\hbar/m\omega_z)^{1/2}$ and $\lambda = \omega_r/\omega_z$). N is the measured atom number at the end of each sweep. The final values of a/a_0 are 380 (blue dots), 840 (purple squares), 2940 (red diamonds) and 4580 (green triangles). The solid (dashed) lines show the solution of a variational hydrodynamic approach (mean-field scaling solutions), see section 4.1.2 for details. The crosses show the predicted equilibrium beyond-mean-field radii.

where beyond mean-field effects are not large, we can expect this scaling to be still approximately valid. We can test this hypothesis with the beyond-mean-field expression for the density (see Eq.3.20) and express it locally using the LDA: $n_{\text{LHY}}(\mu_0 - V(\mathbf{r}))$. Integrating this expression over the trap $4\pi \int d^3r n_{\text{LHY}}(\mu_0 - V(\mathbf{r})) = N$, we relate the atom-number $N(R)$ to the radius of the cloud $R = \sqrt{\frac{2\mu_0}{m\omega}}$. Inverting this expression to lowest order we obtain [179]:

$$R_{\text{LHY}} = R_{\text{MF}} \left(1 + \frac{1}{4\sqrt{2}} \frac{a}{a_{\text{ho}}^2} R_{\text{MF}} \right). \quad (4.1)$$

Using this expression and $R^* = R_{\text{MF}}(\frac{a}{a_{\text{ho}}})^{-1/5}$, we can compute the variation of R_{LHY}/R^* with a variation δN of atom number, due to the approximate atom number scaling. In our trap, at $3000 a_0$ a variation of 30 % in atom number around 4×10^4 leads to a relative variation of R_{LHY}/R^* of 0.5 %.

In Fig.4.1, we display the normalized radius of the cloud R/R^* as a function of the sweep time τ for different final scattering length values: $a/a_0 = 380$ (blue dots), 840 (purple squares), 2940 (red diamonds) and 4580 (green triangles). We observe that for low values of the scattering length, the ramp is adiabatic and the radius R/R^* rapidly reaches its equilibrium value (crosses in Fig.4.1). For larger values of a ($a/a_0 = 2940$), equilibrium is not ensured for short sweep rates. However, for longer ones, a plateau is noticeable and a quasi-equilibrium state is reached. For even larger scattering lengths ($a/a_0 \sim 4500$), the three-body recombination rate is faster than the axial period and there is no sweep time for which even an intermediate quasi-equilibrium is obtained. Due to the decreasing atom number, the radius R/R^* increases and no plateau is obtained.

4.1.2 Simple Theoretical Approaches

We now develop simple theoretical descriptions of the experiment presented above. We first adopt a mean-field approach, using exact scaling solutions. We then take the treatment one step further and propose a simple scaling ansatz to predict the beyond-mean-field dynamics of the Bose gas.

Mean-Field Regime: Scaling Solutions

In the limit of weak interactions, we can describe the dynamics of the BEC with a variable scattering length $a(t)$ using the time-dependent Gross-Pitaevskii equation:

$$i\hbar \frac{\partial \psi}{\partial t} = \left(-\frac{\hbar^2}{2m} \Delta + \frac{4\pi\hbar^2 a(t)}{m} |\psi|^2 + V(\mathbf{r}) \right) \psi. \quad (4.2)$$

In the Thomas-Fermi limit, the GPE can be solved using a scaling ansatz, where the spatial coordinate x_i is rescaled by a factor $\lambda_i(t)$ obeying the following set of equations [180]:

$$\ddot{\lambda}_i(t) + \omega_i^2 \lambda_i(t) = \omega_i^2 \frac{a(t)}{a(0)} \frac{1}{\lambda_i(t) \prod_j \lambda_j(t)}. \quad (4.3)$$

These equations are solved numerically and the solutions are plotted as dashed lines in Fig.4.1 for $a(t)$ corresponding to an approximately linear change in magnetic field (see section 2.3.5 for details about the ramp). This problem was also recently addressed with a simple variational gaussian ansatz [181], which was used to study non-adiabaticity and heating effects in a BEC subjected to interaction sweeps.

Beyond-Mean-Field Effects: Scaling Ansatz

As one increases the interactions in the Bose gas, it becomes necessary to go beyond-mean-field theory, as seen by the increasing discrepancy between the mean-field model (dashed lines) and the experimental data in Fig.4.1. Solving this problem beyond the framework of mean-field theory is challenging. In the Thomas-Fermi limit, the mean-field dynamics are well described by superfluid hydrodynamics (that can be deduced from the GPE) [40]. We are thus inclined to describe the beyond mean-field dynamics with the hydrodynamic equations. We start from the following Lagrangian density:

$$\mathcal{L}[n, \phi] = \frac{m}{2} n (\nabla \phi)^2 + mn \frac{\partial \phi}{\partial t} + n V_{\text{ext}}(\mathbf{r}) + e[n], \quad (4.4)$$

where \mathcal{L} depends on two functions, the density n and a phase function ϕ (whose gradient will be the velocity field), and $e[n]$ is the internal energy of the fluid considered. We are looking for the functions n and ϕ for which the action $S[n, \phi] = \int d^3r dt \mathcal{L}$ is stationary with respect to infinitesimal variations δn and $\delta \phi$: $\frac{\delta S}{\delta n} = 0$ and $\frac{\delta S}{\delta \phi} = 0$. These two conditions for the Lagrangian density (4.4) yield:

$$\frac{m}{2} (\nabla \phi)^2 + m \frac{\partial \phi}{\partial t} + V(\mathbf{r}) + \mu(n) = 0 \quad (4.5)$$

$$\frac{\partial n}{\partial t} + \nabla \cdot (n \nabla \phi) = 0. \quad (4.6)$$

We recover the hydrodynamic equations for an inviscid fluid with an equation of state $\mu(n) = \frac{\partial e}{\partial n}$. The first equation is Bernoulli's with an irrotational velocity field $\mathbf{v} = \nabla \phi$, while the second is the continuity equation. Though it is numerically possible to solve the hydrodynamic equations (4.5) and (4.6) for a given choice of EoS $\mu(n)$, it is not a simple problem as the boundary conditions

for solving these partial differential equations are mobile (the contour on which the atomic density vanishes). We have seen above that a scaling solution is valid in the mean-field limit. A simple extension is to assume a scaling ansatz:

$$n(r, z, t) = \frac{1}{\lambda_r(t)^2 \lambda_z(t)} n_0 \left(\frac{r}{\lambda_r(t)}, \frac{z}{\lambda_z(t)} \right) \quad (4.7)$$

$$\phi(r, z, t) = \phi_0(t) + \frac{a_r(t)r^2}{2} + \frac{a_z(t)z^2}{2}. \quad (4.8)$$

First, we check that the mass conservation equation (4.6) is verified for any initial density n_0 provided $a_r = \dot{\lambda}_r/\lambda_r$ and $a_z = \dot{\lambda}_z/\lambda_z$. Next, the action is written as a function of the scaling parameters $\lambda_r(t)$ and $\lambda_z(t)$ and minimized with respect to these two parameters. If one assumes the mean-field internal energy $e[n] = \frac{gn^2}{2}$, one indeed recovers the mean-field scaling equations (4.3).

Next, we take Lee-Huang-Yang expression for the internal energy:

$$e[n] = \frac{gn^2}{2} \left(1 + \frac{128}{15\sqrt{\pi}} \sqrt{na^3} \right). \quad (4.9)$$

Minimization of the action including the beyond-mean-field contribution to internal energy leads to the equations:

$$\ddot{\lambda}_r(t) = -\lambda^2 \lambda_r(t) + \frac{a(t)}{a(0)} \frac{\lambda^2}{\lambda_r^3 \lambda_z} + \left(\frac{a(t)}{a(0)} \right)^{5/2} \frac{\kappa \lambda^{12/5}}{\lambda_r^4 \lambda_z^{3/2}} \quad (4.10)$$

$$\ddot{\lambda}_z(t) = -\lambda_z(t) + \frac{a(t)}{a(0)} \frac{1}{\lambda_r^2 \lambda_z^2} + \left(\frac{a(t)}{a(0)} \right)^{5/2} \frac{\kappa \lambda^{2/5}}{\lambda_r^3 \lambda_z^{5/2}} \quad (4.11)$$

where $\kappa = \frac{105}{64\sqrt{2}} \left(\frac{a_{\text{ho}}}{a(0)} \right)^{-6/5} (15N)^{1/5}$, $\lambda = \omega_r/\omega_z$ is the aspect ratio and t is measured in units of ω_z^{-1} . Solving this set of equations numerically leads to the solid lines in Fig.4.1. We see that although this approach is variational, the agreement with the experimental data is very good, significantly improving the mean-field predictions, in particular for $a/a_0 \sim 3000$. The crosses in Fig.4.1 are the stationary solutions to Eqs.(4.11). We see however that for $a/a_0 \sim 5000$, the scaling model is accurate only for the shortest sweep rates. For longer sweep durations, the radius R/R^* is higher than predicted by the scaling ansatz, due to increasing atom losses that are not taken into account in this treatment.

4.1.3 Three-body recombination

With respect to size measurements, we have seen that for scattering lengths up to $a/a_0 \sim 3000$, a quasi-equilibrium radius is reached for intermediate sweep durations, which in turn allows for reliable measurements of the local chemical potential μ_z . Another quantity of central importance in the thermodynamic study is the (integrated) density, which gives access to the local pressure. Atom losses will distort the density distribution. In particular, three-body recombination are an important aspect of ultracold atom experiments, limiting the densities of Bose-Einstein condensates. They represent the first step towards the formation of clusters, as the gaseous phase produced in cold atom experiments is not thermodynamically stable at these ultralow temperatures: the true ground state is a solid. In most experiments involving weakly interacting Bose gases, this rate is usually sufficiently low to be neglected. However, the three-body loss rate increases dramatically with the interactions, and thus plays a crucial role in experiments exploring effects of strong interactions in Bose gases. The quantitative analysis of the in-situ density profiles in chapter 3 assumed

negligible loss and thus required a sufficiently long lifetime for the Bose gas, which we study now as a function of the scattering length.

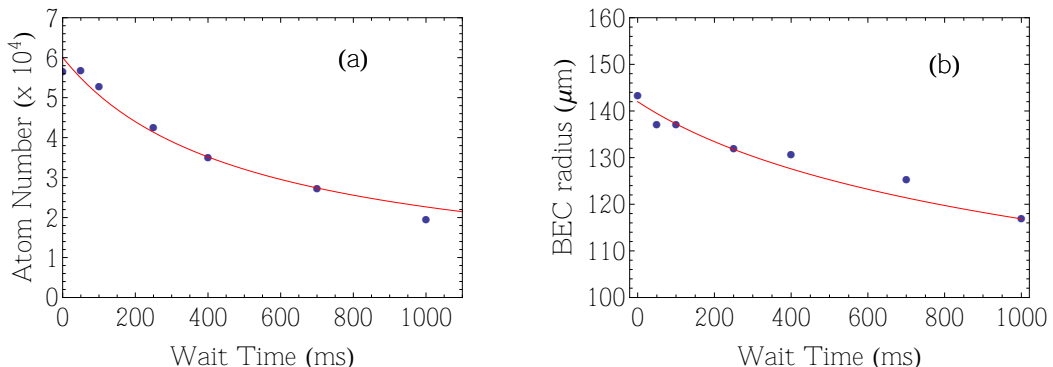


Figure 4.2: Three-body recombination in a Bose-Einstein condensate at $a = 600 a_0$. (a): Atom number versus wait time. The K_3 coefficient is deduced from the fit (red solid line), see text. (b): Thomas-Fermi radius of the BEC as a function of the wait time.

Since we work with ${}^7\text{Li}$ in its absolute ground state $|F = 1, m_F = 1\rangle$ (or $|1\rangle$ at high magnetic fields), two-body losses are suppressed. However, three-body recombination events occur, and typically two of the three incoming particles will form a dimer (either weakly or tightly bound). The energy released will be shared as kinetic energy between the third partner and the dimer. Except when the scattering length is very large, the binding energy of a weakly bound Feshbach molecule is higher than the trap depth (for example, the Feshbach molecule binding energy at $a = 1000 a_0$ is $k_B \times 25 \mu\text{K}$.) and all participants to the three-body collision are lost. Even if the Feshbach molecule remains trapped (as will happen for sufficiently high values of a), it will rapidly become subject to decay into deeper bound states when colliding with another atom (called collisional relaxation) and will thus be lost as well. The rate equation describing the three-body losses is (assuming the molecules rapidly escape from the trap):

$$\frac{dn}{dt} = -K_3 n^3, \quad (4.12)$$

where n is the density and K_3 is the three-body recombination coefficient. If we assume that the scattering length is the only relevant parameter, the following scaling is a consequence of dimensional analysis: $K_3 \propto \frac{\hbar}{m} a^4$ [37]. However, it is known that such a simple scaling is only a crude description as it neglects important three-body physics phenomena. The presence of Efimov trimers in the spectrum of the three-boson problem was shown to have a direct consequence on the a^4 scaling of K_3 , and one has to write the three-body coefficient as $K_3 = 3C(a)\frac{\hbar}{m}a^4$ where $C(a)$ is a log-periodic function of the scattering length and depends on the microscopic details of the interaction potential through Λ_* [182].

To measure the lifetime, we perform the interaction sweep with the offset coils and a systematic wait time of 50 ms is included in order to let the magnetic field stabilize. We first start in the weakly interacting regime $a = 600 a_0$, and probe the atom number (Fig.4.2a) as a function of the wait time. From Eq.(4.12), we derive an evolution equation for the total atom number $N(t)$:

$$\frac{1}{N} \frac{dN}{dt} = -\frac{g^{(3)}}{3!} K_3 \langle n^2 \rangle, \quad (4.13)$$

where $\langle X \rangle = \frac{1}{N} \int d\mathbf{r} X n(\mathbf{r})$, and $g^{(3)}$ is a spatial correlation coefficient equal to 3! for a BEC and 1 for a thermal gas [183]. In order to proceed further, we have to make an assumption about the density profile to calculate the average $\langle n^2 \rangle$. In the weakly interacting regime, we can work with a Bose-Einstein condensate. If the inverse loss rate is much larger than the trapping periods, the heating due to the three-body loss is low, the BEC will retain a Thomas-Fermi shape, and the radius will scale as $N^{1/5}$ (see Eq.(3.9)). Calculating the average in Eq.(4.13) using a TF profile, we readily obtain a closed equation for the total atom number N :

$$\frac{1}{N} \frac{dN}{dt} = -\frac{\bar{\alpha}}{3!} K_3 N^{4/5}, \quad (4.14)$$

where $\bar{\alpha} = \frac{75}{56\pi^2} 15^{-6/5} \lambda^{8/5} a_{\text{ho}}^{-24/5} a^{-6/5}$. This equation can be solved and yields the evolution of the atom number² $N(t)$:

$$N(t) = \frac{N_0}{\left(1 + \frac{4}{5} \frac{\bar{\alpha}}{3!} K_3 N_0^{4/5} t\right)^{5/4}}. \quad (4.15)$$

The assumption of quasi-equilibrium can be easily checked by measuring the Thomas-Fermi radius of the BEC as a function of time (Fig.4.2b). In red solid line, we plot the expected shrinking of the gas due to atom loss measured in Fig.4.2a, $R(t) = R(0)(N(t)/N(0))^{1/5}$ where $R(0)$ is the only fitting parameter. The very good agreement shows that even though atoms are lost, the BEC remains almost pure and can be described by the simple model derived above. Fitting the data of Fig.4.2a with the solution (4.15), we find $K_3 = 2.0(3) \times 10^{-24} \text{ cm}^6/\text{s}$, in agreement with [79] (the uncertainty is the fitting error only). We repeat this measurement for various values of the scattering length and gather the measured values of K_3 in Fig.4.3. For the two largest scattering lengths, the measurement is done with a thermal gas (empty circles in Fig.4.3). Since no appreciable heating is observed, we solve the three-body loss equation (4.12) assuming a gaussian density distribution at a fixed temperature, and the solution for the atom number decay is $N = N_0(1 + t/\tau_3)^{-1/2}$, where $\tau_3^{-1} = \frac{2\kappa}{T^3} K_3 N_0^2$ and $\kappa = \frac{1}{\sqrt{27}} \left(\frac{m\bar{\omega}^2}{2\pi k_B}\right)^3$.

In addition to our experimental data (blue points), we also show in Fig.4.3 the result for K_3 obtained in the Bar-Ilan group [79] (red solid line) and at Rice [155] (green dashed line). The observed reduction of K_3 is due to the presence of Efimov trimers in the spectrum, this oscillation is a log-periodic feature, separated by a factor 22.7 (see for example the review [185]). As the Rice determination of the Feshbach resonance disagrees with both spectroscopic methods, we have also plotted the result of Rice measurement assuming our parameters for the Feshbach resonance position and width (green solid line) and we see very good agreement with our data. For reference, an a^4 law (with an arbitrary factor) is also shown in dashed black. From these loss measurement, we can now assert the typical values of interaction that can be reached in static measurements. Indeed, the density profile equilibration necessitates a time that is on the order of the axial (weak) timescale. Our axial trapping frequency is about 20 Hz. As a consequence, the Bose condensates lifetime must be at least about 50 ms for static measurements. Using our measurement of Fig.4.3, we deduce that at the end of the interaction sweep, the lifetime of a BEC of 4.10^4 atoms in our trap geometry will be about 70 ms at $a = 2200 a_0$, while at $3000 a_0$, it is only 15 ms. This puts an upper bound to the interaction regime we can reach in these conditions, and justify the choice of $\sim 2000 a_0$ for the EoS measurement in chapter 3.

We confirm this by measuring the averaged atom number N (normalized to $N_0 = 3.8 \cdot 10^4$) for the sweep duration of 150 ms, plotted in Fig.4.4. We see that indeed up to $a/a_0 \sim 2000$ atom

²Note that in [184], the exponent of the solution (4.15) is mistyped.

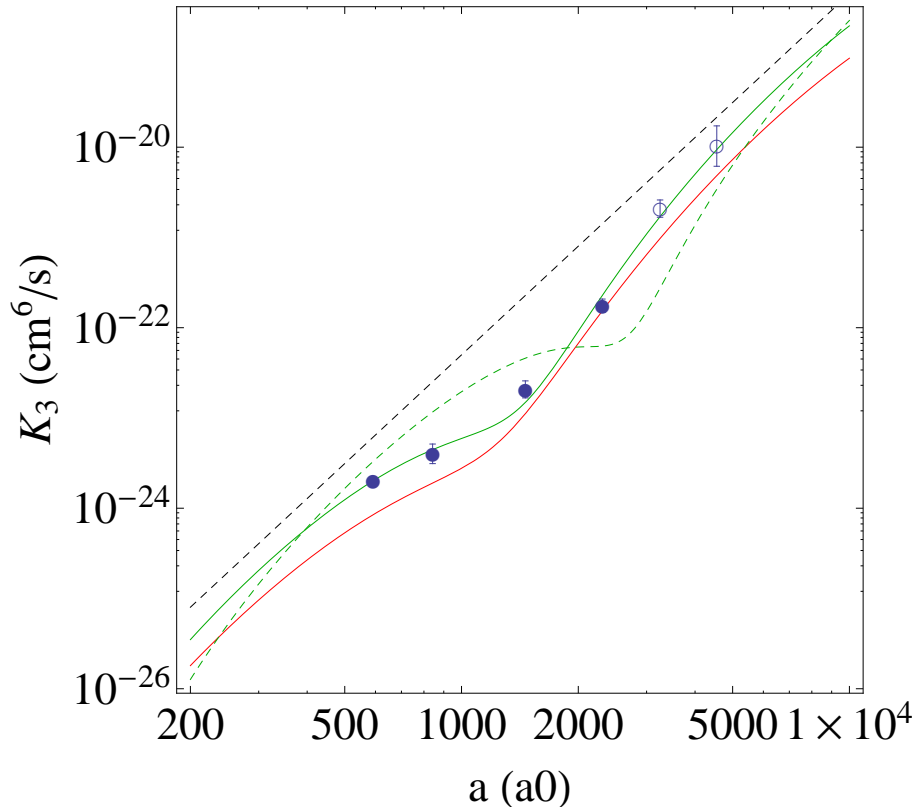


Figure 4.3: Three-body recombination coefficient K_3 as a function of the scattering length. The measurements are done on a BEC (filled circles) or a thermal gas (empty circles). The experimental measurements are shown in blue points, the Bar-Ilan group result is shown in solid red line [79], the Rice group result in dashed green line [155]. For reference, an a^4 law is plotted in dashed black line (with an arbitrary factor). Reanalyzing the Rice group data with our determination of the Feshbach resonance leads to the solid green line. The error bars represent the fitting uncertainties.

losses are negligible within our error bars. For larger scattering lengths, the losses become observable. A simple model of these losses is provided by taking the quasi-equilibrium model presented in section 4.1.3, assuming a time-dependent three-body loss coefficient $K_3(a(t))$ in Eq.(4.14), and using the experimental interaction sweep for $a(t)$. Let us recall that this model assumes that the BEC retains a Thomas-Fermi shape and that the radius of the cloud still scales as $N^{1/5}$ as the atom number is reduced. The integration of Eq.(4.14) for $N(t)$ results in the solid black line in Fig.4.4a. For $a/a_0 < 3000$ the model matches well the experimental data but at $a/a_0 \sim 3000$, the losses are slightly larger than expected (by about 5%), and this trend is reinforced for larger values of the scattering length. This is due to the fact that for these interaction strength, the loss rate becomes smaller than the axial trapping period and the density distributions do not have sufficient time to adjust to the changing scattering length. This crossover is shown in Fig.4.4b to happen between 2000 and 3000 a_0 . As the BEC radius is smaller than the equilibrium radius for the same scattering length, the peak density will be correspondingly higher and the losses faster than for the quasi-equilibrium model, as observed on the experimental data.

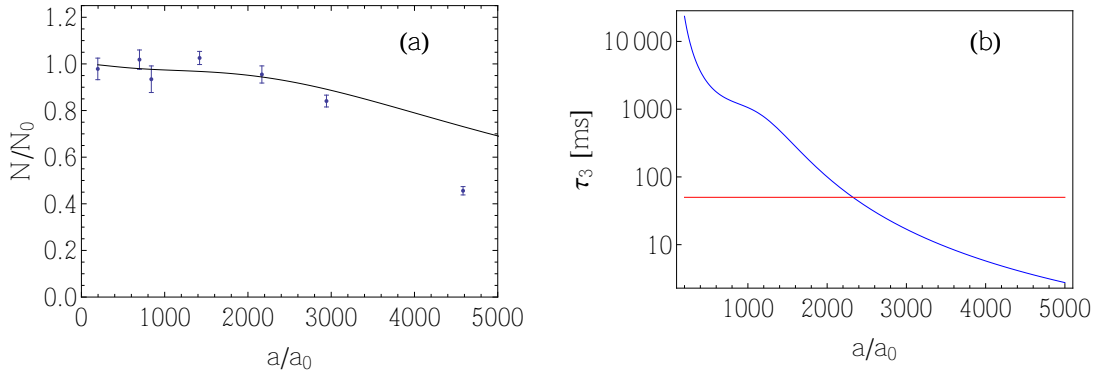


Figure 4.4: (a): Atom number measured after a sweep time of 150 ms, where $N_0 = 3.8 \cdot 10^4$ as a function of the final scattering length a/a_0 . Each experimental point is an average of about 10 shots. The black solid line is a simple model for the atomic losses in quasi-equilibrium conditions. (b): Three-body recombination time τ_3 as a function of the scattering length a/a_0 . The red solid line is the axial trapping period of 54 ms.

4.1.4 Consistency check of the Lee-Huang-Yang Equation of State

At $\sim 2000 a_0$, the losses are negligible and no model-dependent treatment of the effects of loss was necessary. We can use the above atom-loss and radii-dynamics modeling to attempt to extract the equation of state slightly beyond equilibrium and test the consistency of the LHY equation of state on the density distributions at $3000 a_0$. The raw measurement is displayed as empty blue squares in Fig.4.5a. The effect of the finite duration of the ramps as estimated using the scaling models is shown Fig.4.5b and taking it into account leads to the full black circles in Fig.4.5a. For the measurement at $2150 a_0$ the radius correction is respectively 2.3 and 2.9%³. We see on Fig.4.5b that the mean-field (dashed line) and the beyond-mean-field (solid line) models give a correction factor that are 3.5 and 5%, respectively at $3000 a_0$. We need to rely here on the beyond-mean-field model (which proved to be accurate in Fig.4.1). This reduces the predictive power of the EoS at this scattering length, but it will serve as a consistency check for the EoS measured at $2000 a_0$. The agreement obtained with the LHY equation is good, but a slight systematic downshift is observable. We see in Fig.4.4 that the atom loss at $3000 a_0$ is slightly larger than the quasi-equilibrium model prediction. As long as the quasi-equilibrium model applies, the radius of the cloud adjusts to the atom number and the density distribution (and hence the extracted equation of state) reflects the equilibrium situation. From Fig.4.4 we infer that about 5% of the atoms are lost without equilibration of the density distribution. A simple model to take this additional effect into account is to assume that a local thermal equilibrium is reached in the radial direction, while the dynamics are frozen in the axial direction. This condition is reasonably fulfilled at $3000 a_0$, where the three-body loss rate is about 67 Hz, much larger than $\nu_z = 18.5$ Hz and much smaller

³Though this difference is small, we take the average value 2.6% for the EoS extracted in chapter 4, and we check that the uncertainty introduced by this correction is within the stated error bar on the LHY coefficient, $\alpha_{\text{LHY}} = 4.5(7)$.

than $\nu_r = 345$ Hz. In this case, we can write the local chemical potential as:

$$\mu(\mathbf{r}) = \mu_z - \frac{1}{2}m\omega_r^2 r^2. \quad (4.16)$$

Due to the lack of equilibrium in the axial direction however, we cannot write μ_z as $\mu_0 - V(z)$ anymore. Integrating the density as well as the three-body loss equation (4.12) along the radial direction (assuming a Thomas-Fermi shape in this direction for simplicity) yields the following equations for $\bar{n}(z)$ and μ_z :

$$\bar{n}(z) = \frac{\pi}{g} \frac{\mu_z^2}{m\omega_r^2} \quad (4.17)$$

$$\frac{d\bar{n}}{dt}(z) = -\frac{\pi}{2} \frac{K_3}{g^3} \frac{\mu_z^4}{m\omega_r^2}. \quad (4.18)$$

Using these equations, one can predict the deformation of the density profiles due to the three-body losses. We first produce a density distribution derived with the LHY equation of state (in the same conditions as the experimental data of Fig.4.5a) and solve the equations (4.17 and 4.18) for a time corresponding to an atom-number loss of 5%. From the resulting density profile, we extract the normalized pressure and find the green solid line in Fig.4.5a, in improved agreement with the data. Even though this analysis is model-dependent, we see that the results at 3000 a_0 are also in very good quantitative agreement with the Lee-Huang-Yang equation of state.

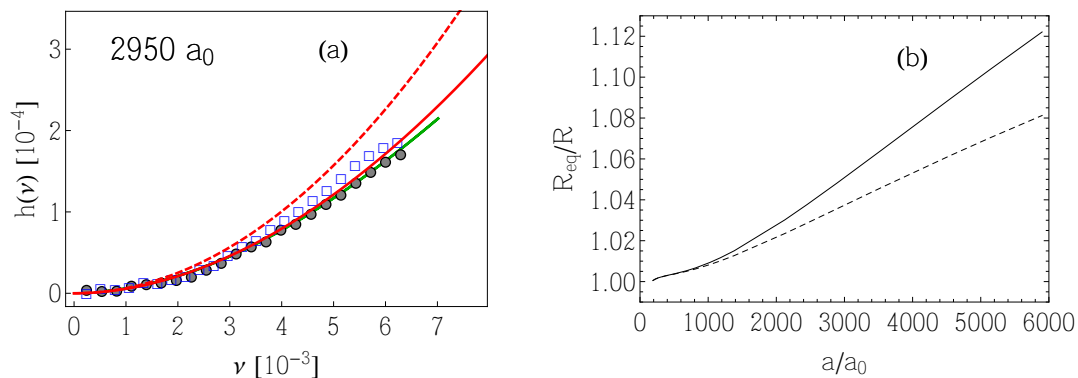


Figure 4.5: (a): Normalized pressure measured at $a/a_0 = 2950$. In red dashed (solid) line, the mean-field (Lee-Huang-Yang) EoS. The raw EoS is shown in empty blue squares; in full black circles, we include the correction due to non-equilibrium (see text). The green solid line is a simple model including the small atom losses (see text). (b): The ratio of the equilibrium radius of the BEC R_{eq} to the radius after the 150 ms sweep as a function of the final scattering length as predicted by the scaling solution for the mean-field approach (black dashed line), and including the beyond-mean-field effects through the scaling ansatz (black solid line).

4.2 Towards the Feshbach resonance

In order to access the regime of stronger interactions in a Bose gas, we cannot rely on the slow ramps used for the thermodynamic studies. A simple approach consists of using faster ramps in order to reach higher interaction strengths. This method has been used in the group of C. Wieman at JILA, where a fast magnetic field pulse (of about 10 G) was applied in tens of μs to reach

a regime of strong interactions using a Feshbach resonance with ^{85}Rb and study the atom loss dependence on the rise time of the magnetic pulse⁴ [36,188]. The time scales in both experiments are almost three orders of magnitude apart. This can be partly attributed to the comparatively low densities in our experiment (in the range 10^{12} cm^{-3} rather than 10^{13} cm^{-3}), but a more accurate measurement of K_3 as a function of a should be done on ^{85}Rb , refining the early work of [35], in order to understand this difference.

4.2.1 Atom losses close to the Feshbach resonance

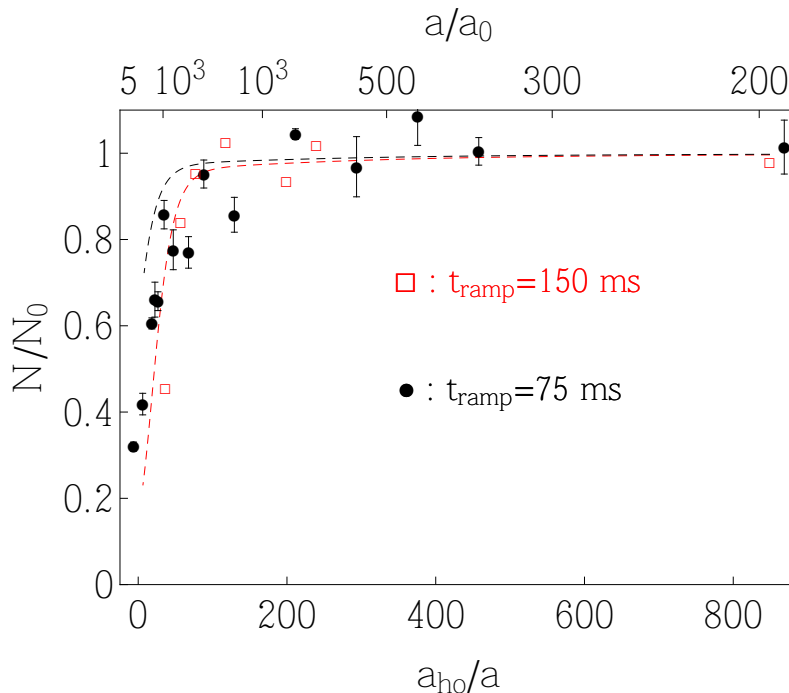


Figure 4.6: Atom number as a function of the final scattering length. In empty red squares (solid black circles), the experimental data for a ramp time of 150 ms (75 ms). The dashed lines correspond to the prediction of the quasi-equilibrium model for both ramp times. The errors bars on the black points represent the standard error of 3 to 5 shots on each point.

The three-body recombination increases dramatically in the vicinity of the Feshbach resonance. By shortening the interaction sweep, we obviously reduce the three-body losses as can be seen in Fig.4.6, allowing us to reach the resonance and slightly beyond with reasonable atom numbers. The empty red squares are the rescaled data from Fig.4.5a for a sweep of 150 ms; black points, the data for a faster sweep of 75 ms. The dashed lines correspond to the prediction of the quasi-equilibrium model for both ramp times. For the slow ramp, the agreement is much better than for the fast one. Indeed, for fast ramps we rapidly reach a regime where the density distribution does not follow the changing scattering length (as will be seen on the radii measurements in the next section). The quantitative description of the data in Fig.4.6 beyond a naive model is very challenging as we need a theoretical framework for the non-equilibrium dynamics of a strongly interacting Bose system.

⁴A similar magnetic field quench was used to study the repulsive Fermi gas, which is similarly increasingly unstable for strong interactions [186,187].

In practice, we see that we can reach the Feshbach resonance center with almost half of the atoms left.

4.2.2 Radii Measurements

Similarly, we measure the radius of the Bose gas as a function of the scattering length reached at the end of the 75-ms interaction sweep. For convenience, the radius is measured using a Thomas-Fermi fitting function and normalized to the radius R^* (see section 4.1 for details). As expected, the radius first grows as $a^{1/5}$ (static mean-field prediction in red solid line). However, for $a/a_0 \gtrsim 1000$, the experimental data starts to deviate from the mean-field expectation. The dynamical effect of the sweep is immediately observed as the deviation from the equilibrium mean-field theory is a reduction of the radius. If beyond-mean-field effects alone were present, we would expect an increase of the radius, as shown in Eq.(4.1). We can use the scaling models developed earlier in section 4.1.2 to provide with a first description of the Bose gas dynamics. With the dashed red line, we note that the scaling solutions of mean-field theory provide an improved description of the radius dynamics. For even larger scattering lengths $a/a_0 \sim 3000$, the scaling ansatz of the hydrodynamic equations using the Lee-Huang-Yang equation of state is in better agreement with the data.

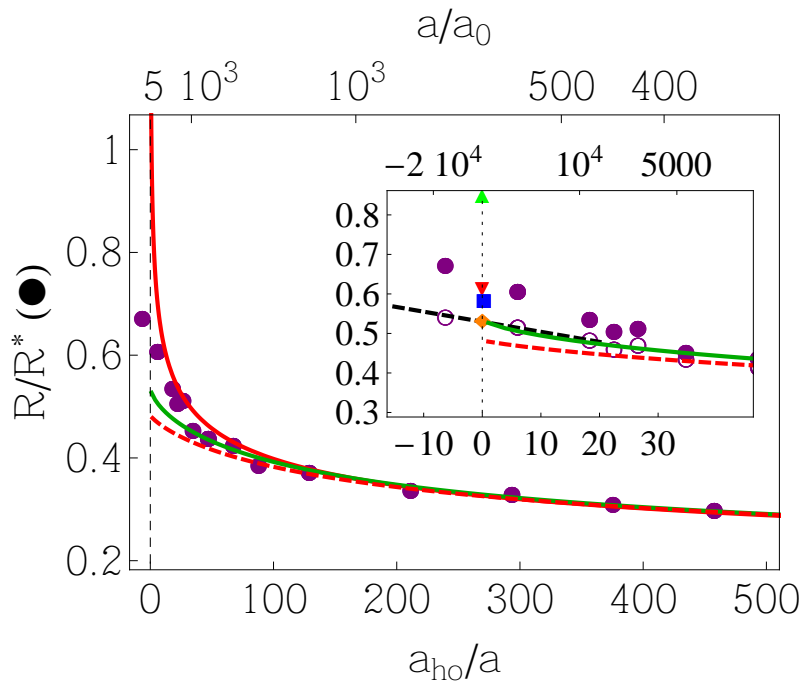


Figure 4.7: Normalized cloud radius R/R^* (filled purple circles) as a function of the inverse scattering length a_{ho}/a at the end of a 75-ms magnetic-field sweep. The static mean-field prediction is plotted in solid red line, the mean-field scaling solution in dashed red, and the beyond mean-field scaling ansatz in solid green line. Inset: Zoom around the unitary limit. Predictions for the universal constant ξ_B are shown in up green up triangle [55], red down triangle [56], blue square [57], and orange diamond [58]. The filled (empty) circles correspond to the radii normalized to the final (initial) atom number. The dotted black line is a linear interpolation at unitarity (see text).

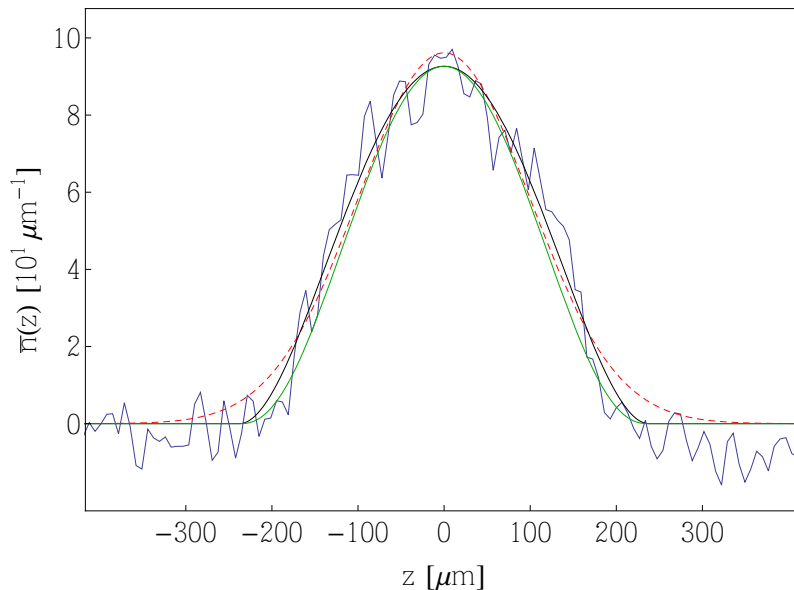
4.2.3 A Lower Bound on ξ_B 

Figure 4.8: Density profile of an out-of-equilibrium strongly interacting Bose gas with a scattering length of $a/a_0 = 2.8 \times 10^4$ after an interaction sweep of 75 ms. The peak density is $\sim 6 \times 10^{11} \text{ cm}^{-3}$, giving a gas parameter $na^3 \sim 2$. The profile is the result of an average of 5 images with a mean atom number of 2.1×10^4 atoms. The density distribution is fitted with a gaussian (dashed red line), a fermionic (solid black line), and a bosonic (solid green line) Thomas-Fermi function.

Finally, we focus on the region where the interactions are unitarity limited, and the scattering length diverges (vertical dotted line in the inset of Fig.4.7). In this region, most properties of the Bose gas are very poorly understood. First, the gas parameter $na^3 \sim 1$ and the perturbative expression 3.25 is meaningless as all the terms are of the same order. The fate of a many-body state with universal properties for a gas of bosons is currently uncertain. If one assumes that short-range physics are irrelevant to describing the low-energy collisions for all interaction strengths, there is no energy scale associated with the interactions in the limit $a \rightarrow \infty$, and the properties of the system become *universal* in the sense that the only relevant length scale is the interparticle spacing $n^{-1/3}$. It is the so-called *unitary* gas. As a consequence of dimensional analysis, the equation of state must take the form $\mu = \xi_B E_F$ where $E_F = \frac{\hbar^2}{2m} (6\pi^2 n)^{2/3}$ is the ‘‘Fermi energy’’ of the Bose gas. This is the EoS of an ideal Fermi gas, apart from a universal factor ξ_B . While the unitary Fermi gas was shown experimentally to be stable (see chapter 5) and we have good indications of its universality, the possible existence of a unitary Bose gas has attracted significant interest in the recent years, but no convincing theoretical nor experimental hints of its existence and universality has been put forward so far.

First, it is important to assess that we do not observe significant heating during the sweeps, since the radius of a classical gas is meaningless. In Fig.4.8, we display the density profile (averaged over 5 images within 5% in atom number) of a strongly interacting Bose gas. The final scattering length is $a/a_0 = 2.8 \times 10^4$ and the estimated peak density is $\sim 6 \times 10^{11} \text{ cm}^{-3}$, making the gas parameter large, $na^3 \sim 2$. If the universality conjecture applies to the Bose gas, the density distribution at unitarity should have a fermionic Thomas-Fermi shape $\bar{n}_0 \left(1 - \frac{z^2}{R^2}\right)^\gamma$ with $\gamma = 5/2$

for the doubly integrated profile (solid black line) and we compare it to a bosonic Thomas-Fermi function $\gamma = 2$ (solid green line). None of the two distributions significantly fits the data better than the other. It is not surprising since the density profile in Fig.4.8 is out-of-equilibrium and we remark that the peak density is flattened, consistent with the deformation expected from important three-body losses in the densest parts of the cloud. We observe that the density profile is highly non-gaussian (red dashed line) and the edges of the distribution are very sharp, giving a good indication that the gas is deeply degenerate. We also note that the cloud largely expanded compared to lower values of a (see for comparison the profiles in Fig.3.3).

Due to the finite response time of the gas, we can assume that the measured radius R is smaller than the equilibrium radius, $R < R_{\text{eq}}$. This reasonable assumption is verified by the scaling models. From this inequality, in the spirit of variational methods, we deduce a lower bound for the value of ξ_B by interpolating our data at unitarity, in black dashed line in the inset of Fig.4.7. The link between ξ_B and R/R^* must be established: at unitarity, the cloud radius R would scale as $N^{1/6}\xi_B^{1/4}$ (as a result of the EoS $\mu = \xi_B E_F$). The normalization radius R^* scales as $N^{1/5}$ so that $R/R^* \propto \xi_B^{1/4} N^{-1/30}$. The choice of R^* for normalization thus leads to a residual dependence on N but it is very slowly varying ($N^{-1/30}$) and results in only minor correction for our range of atom numbers (less than a percent correction) and we safely neglect it. In order to take into account the changing atom number near unitarity and obtain a conservative experimental lower bound on $\xi_B \propto (R/R^*)^4 N^{2/15}$, we minimize both R/R^* and $N^{2/15}$. This is done by taking for R/R^* the initial atom number (empty circles in the inset of Fig.4.7), and the final, for $N^{2/15}$. We then find $\xi_B > 0.44(8)$. The compressibility of the $T = 0$ unitary Bose gas has been calculated by several methods. This bound is satisfied for the predictions $\xi_B = 0.66$ [57], and a recent calculation 0.4618 [58], as well as for the upper bounds from variational calculations, 0.80 [56] and 2.93 [55]. Putting together the most stringent variational calculation and our measurement, we deduce a strong constraint on the possible value of the universal bosonic ξ_B :

$$0.44(8) < \xi_B < 0.80 \quad (4.19)$$

While this does not give direct information on the existence of the unitary Bose gas, should it exist, the stated inequality should hold. It is interesting to note that the measured radius normalized to the initial atom number (empty circles in the inset of Fig.4.7) is in very good agreement with the scaling ansatz including beyond-mean-field effects up to very high values of a (in solid green line). The choice of the proper atom number for the normalization (either initial, final or intermediate during the sweep) is a delicate issue due to the non-equilibrium state, and strongly depends on the loss rate. In the limit where the loss rate is slow, the radius follows N and the atom number at the end of the sweep is the appropriate choice. In the limit of very fast losses, the radius does not have the time to adjust to the changing atom number and the initial atom number will be the reasonable choice. This is the case in the region around unitarity and might explain the very good agreement of the experimental data (empty purple circles) up to unitarity with the beyond mean-field hydrodynamic model, though its validity is still to be demonstrated.

In this chapter, we have presented a series of experiments using a Bose gas subjected to a time-dependent sweep of the interatomic interactions. In the first part, we have shown that if the scattering length is not too large, there is a sweep rate for which the density distribution reaches a quasi-equilibrium and we justify the adiabaticity required for the thermodynamic studies of the previous chapter. We developed two simple models to describe the dynamics of the Bose gas: first by treating the interactions at the mean-field level and solving the resulting scaling equations. Sec-

only, we proposed a variational approach through a scaling ansatz to the hydrodynamic equations including the first beyond-mean-field effects in the equation of state. After a study of the atom losses as a function of the scattering length, we used these models to show that, taking into account both the dynamic aspect of the interaction sweep and the three-body losses, the density profiles at $3000 a_0$ are also in quantitative agreement with the LHY equation of state. Finally, we investigate the regime of stronger interactions using a faster sweep rate and measured both atom numbers and radii close to the unitarity limit. From these measurements, we deduced a lower bound on the universal constant ξ_B that would characterize the EoS of the unitary Bose gas.

Part III

Fermions

Chapter 5

The Strongly Interacting Fermi Gas

In this chapter, we study the thermodynamics of a strongly interacting Fermi gas. We focus here on the spin-population balanced gas: $n_{\downarrow} = n_{\uparrow}$ (the case of spin-imbalanced gases will be addressed in chapter 6). In the first section, we present the measurement of the Equation of State of the unitary ($a \rightarrow \infty$) Fermi gas as a function of temperature. In the second part, we present the measurement of the EoS for a low temperature ($T \approx 0$) Fermi gas as a function of interaction strength, and compare the molecular limit of the Fermi gas to the equation of state of the atomic Bose gas shown in chapter 3.

5.1 Universal Thermodynamics of the Unitary Fermi Gas

In 1999, before the experimental production of degenerate ultracold Fermi gases, G. Bertsch posed the following question at the 10th Many-body Conference on neutron matter (see [3]): *What are the ground state properties of the many-body system composed of spin-1/2 fermions interacting via a zero-range, infinite scattering-length contact interaction?* This question aimed at understanding a simple model for neutron matter. Indeed, in low-density neutron matter the scattering length $a \approx -18.5$ fm is much larger than the effective range $r_e \approx 2.7$ fm [189]. Despite the fact that the atom-atom and neutron-neutron interaction potentials are very different, in the low-energy limit these systems should be described by the same Hamiltonian. This idea is very profound, and it was suggested early after the production of the first ultracold Fermi gases that they could be used to quantum simulate neutron matter (see for example [190]). Indeed, as seen in chapter 1, ultracold fermions with two spin-components are accurately described by a zero-range interaction potential thanks to their diluteness (in the sense that the range of the interaction is much smaller than the interparticle spacing). The problem that G. Bertsch referred to is the limiting case where the scattering length is also much larger than the interparticle spacing $k_F a \gg 1$ (where k_F is the Fermi wavenumber), or $a \rightarrow \infty$, the *unitary limit*. In this limit, the scattering length disappears from the description of the system and there are no energy (or length) scales associated with the interactions. The only length scale left is the interparticle spacing $\sim 1/k_F$: all thermodynamic properties of the system obey simple scaling laws¹.

¹The contact interactions can also be replaced by contact boundary conditions (called the Bethe-Peierls conditions) on the many-body wavefunction obeying a free Schrödinger equation. As a result (see for instance [191]), at unitarity $1/a = 0$, the system is invariant by a scaling transformation of the spatial coordinates $\mathbf{X} \rightarrow \lambda^{-1} \mathbf{X}$ (where

However, the stability of the strongly interacting Fermi gas was uncertain until it was produced experimentally [13, 192, 149, 74, 193] using ultracold ${}^6\text{Li}$ in its two lowest spin states around the Feshbach resonance at 834 G. The universality hypothesis provides strong constraints on the thermodynamics of a unitary quantum gas [49]. In particular, due to dimensional reasons, all quantities are related to the ideal gas via universal functions. The (grand-canonical) equation of state of the unitary Fermi gas can thus be written as:

$$P(\mu, T) = \frac{1}{\beta\lambda_{\text{dB}}^3} f(\beta\mu), \quad (5.1)$$

where $\beta = 1/k_B T$, and f is a universal function. All the thermodynamic quantities can be deduced from f . For example:

$$n\lambda_{\text{dB}}^3 = f'(\beta\mu) \quad (5.2)$$

$$\frac{E}{\bar{V}} = \frac{3}{2}P, \quad (5.3)$$

relations that we will use later on. This chapter is dedicated to measuring the function f . If the local density approximation is valid, the method presented in section 1.3.4 can be applied to determine the EoS of the homogeneous unitary gas. Since the gas is equally populated in the two spin states, we have $\bar{n}_1(z) = \bar{n}_2(z) \equiv \bar{n}(z)$, and we write the total pressure of the gas as:

$$P(\mu_z, T) = \frac{m\omega_r^2}{\pi} \bar{n}(z) \quad (5.4)$$

where $\mu_z = \mu_0 - V(z)$ is the local chemical potential along the z -axis. We see that each density profile requires the determination of two parameters to obtain the pressure: the global chemical potential μ_0 and the temperature T . In a quantum gas, both μ and T determine the shape of the density profile. This is in sharp contrast to the classical non-interacting gas, where the temperature can be determined by the shape (or width) of the distribution, and the chemical potential by its amplitude. Starting from the EoS of the classical gas, and under the validity of the LDA we can write the local pressure of the gas: $P(\mathbf{r})\beta\lambda_{\text{dB}}^3 = e^{\beta\mu_0} e^{-\beta V(\mathbf{r})}$. From the pressure formula, this expression is proportional to the doubly integrated density along the z -axis \bar{n} . We see that β can be extracted from the spatial dependence of the distribution (for example the gaussian width in the case of a harmonic trap) while μ_0 is an overall factor. This decoupling of μ and T does not hold for quantum gases, not even ideal ones (as can be seen from their EoS in section 1.1). In the next two sections we present a method to determine them independently for the unitary Fermi gas.

5.1.1 Thermometry of the Strongly Interacting Fermi Gas

Thermometry is an obvious necessity for thermodynamical studies. Measuring the temperature of an ultracold gas is a fundamental problem. For weakly interacting gases, one can usually use reliable model-dependent methods to measure the temperature of a sample. In a weakly interacting gas, the wings of the density distribution can usually be well described by a classical gas EoS. If a refined treatment is necessary, interactions can be taken into account through a mean-field description (as for the 2D Bose gas studies shown in section 1.3.2 [94, 95]). Either using in-situ or time-of-flight measurement, the shape of the density (or the momentum) distribution will provide

$\mathbf{X}=(\mathbf{r}_1, \dots, \mathbf{r}_N)$, if the eigenfunction ψ_i (of energy E_i) is rescaled as $\psi_i \rightarrow \lambda^{-3N/2}\psi_i$ and $E_i \rightarrow E_i/\lambda^2$. This scaling doesn't hold for finite a (because of the boundary conditions). This can be understood in simple terms: a unitary gas remains unitary whatever its density (since $1/k_F a=0$) while at finite a , no matter how large, the system will ultimately be weakly interacting in the dilute limit.

the temperature of the sample. When strong correlations are present, thermometry becomes notoriously more difficult. Because the temperature dependence of the density distributions is usually unknown (within LDA, amounts to knowing the EoS), one cannot extract the temperature from it *a priori*. Similarly, the expansion dynamics can reveal complex phenomena (see for example [194]) and thus do not give a direct information on the temperature of the system.

It was first demonstrated at JILA [195] and by the Innsbruck group [196] that another spin state or species could be immersed in a strongly interacting gas of ${}^6\text{Li}$ and used as a thermometer probe of it. Implementing this idea on our experimental setup was fairly straightforward since we have bosonic ${}^7\text{Li}$ at our disposal as the coolant of ${}^6\text{Li}$ in the Ioffe-Pritchard trap. Instead of evaporating it completely in the magnetic trap, we keep a trace of ${}^7\text{Li}$, that is transferred together with ${}^6\text{Li}$ in the optical dipole trap. We observed no losses due to collisions between ${}^6\text{Li}$ (in equal spin-mixture of $|1/2, 1/2\rangle$ and $|1/2, -1/2\rangle$) and ${}^7\text{Li}$ atoms (in state $|1, 1\rangle$). The two-body loss rate was estimated to be $G \sim 2 \times 10^{-18} \text{ cm}^{-3}/\text{s}$ between state $|1, 1\rangle$ (of ${}^7\text{Li}$) and $|1/2, -1/2\rangle$ (of ${}^6\text{Li}$)² [133]. For a (very) conservative upper bound of $n_7 = 10^{13} \text{ cm}^{-3}$, this gives an extremely low two-body loss rate of $2 \times 10^{-5} \text{ s}^{-1}$, compatible with the observations. We wait about 1 to 1.5s at the end of the evaporation to ensure complete thermalization³ of ${}^7\text{Li}$ in contact with ${}^6\text{Li}$. Since it is an isotopic mixture, there is almost no differential gravitational sag to be compensated.

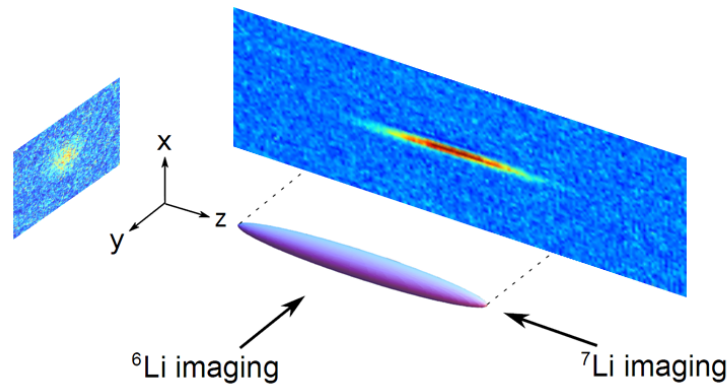


Figure 5.1: Sketch of the Imaging. The ${}^6\text{Li}$ atoms are imaged perpendicular to the long, z -axis for the pressure measurement, while the ${}^7\text{Li}$ cloud is imaged along the z -axis for thermometry.

The imaging scheme is shown in Fig.5.1. The ${}^6\text{Li}$ atoms are imaged in-situ perpendicularly to the long z -axis for the pressure measurement (see also Fig.2.13). Shortly thereafter the optical trap is switched off and the ${}^7\text{Li}$ is allowed to expand and imaged along the z -axis for a time-of-flight measurement of the momentum distribution. Because of the integration of the line-of-sight along the z -axis, imaging the Bose gas along this direction allows us to detect low atom numbers (~ 3000) with a reasonable signal-to-noise ratio. This capability is important because the number of bosons must be kept as small as possible for several reasons. First, the density of the thermometer should be kept low to avoid disturbing the Fermi gas density profile. Second, because the Bose gas is a load for the Fermi gas during the evaporative cooling, the larger the ${}^7\text{Li}$ atom number, the hotter

²For the other state of ${}^6\text{Li}$ ($|1/2, 1/2\rangle$), both isotopes are in their absolute ground state and there are no two-body loss processes.

³The boson-fermion scattering length is equal to $\sim 40 a_0$ [133], and the (classically estimated) elastic collision rate for the ${}^7\text{Li}$ atoms is about 10 s^{-1} .

the ${}^6\text{Li}$ will be at the end of the cooling.

Finally, ${}^7\text{Li}$ in state $|1, 1\rangle$ has a negative scattering length of about $-40a_0$ at a magnetic field of 834 G (see section 3.2). Consequently, due to the attractive interactions, a Bose-Einstein condensate in this state will be subject to a collapse instability above a critical atom number [197, 198]. Above a certain atom number, the attractive interactions are not compensated by the kinetic energy and collapse occurs. This critical number is written as:

$$N_c = \lambda^{-1/3} \frac{k(\lambda)}{|a|} a_{\text{ho}}, \quad (5.5)$$

where $\lambda = \omega_r/\omega_z$ is the aspect ratio of the trap, $a_{\text{ho}} = (\hbar/m\omega_z)^{1/2}$ is the axial harmonic oscillator length and $k(\lambda)$ is a factor determined numerically [199]. In our trap, $\lambda \sim 10$ and we find $N_c \sim 600$, which is much smaller than the atom numbers necessary for us to reliably measure the temperature. Our thermometer will thus be limited to a temperature above the Bose-condensation threshold. This critical temperature for BEC, T_{BEC} is approximately 90 nK (in the final trap with $\omega_r/2\pi = 420$ Hz and $\omega_z/2\pi = 37$ Hz), when one takes into account finite-size correction to T_{BEC} ⁴. This lower limit must be compared to the Fermi temperature T_F of the ${}^6\text{Li}$ gas in the same trap (we use $N_6 = 5 \times 10^4$ per spin state for this estimate):

$$\frac{T_{\text{BEC}}}{T_F} \approx 0.15 \quad (5.7)$$

where $k_B T_F = \hbar\bar{\omega}(6N)^{1/3}$ is the Fermi energy of the non-interacting trapped gas. This value is smaller than the expected superfluid/normal phase transition of the Fermi gas in the trap (see section 5.1.7). If lower temperatures need to be reached, either the ${}^7\text{Li}$ atom number must be reduced or the bosonic gas should be transferred into a state with a positive scattering length. Two additional effects have to be taken into account for accurate thermometry. First, fitting the density profile with a Bose function (Eq.(1.8) in chapter 1) close to T_{BEC} rather than with a gaussian function is important. Second, because the time-of-flight is realized in presence of the magnetic fields, the curvature coils produce an anti-trapping potential on the atoms in the radial direction. This results in a hyperbolic sine increase of the width of the distribution (rather than linear for a free-space time-of-flight in the ballistic regime). A self-consistent check of our thermometry is that our coldest samples are measured to have temperatures at most 5 % smaller than T_{BEC} , showing that the overall calibration of the magnification and atom number are accurate.

5.1.2 Determination of the chemical potential μ_0

The above determination of the temperature is a considerable simplification in the process of measuring the equation of state. We are now left only with the determination of the global chemical potential μ_0 . Let us first note that the technique used for the Bose gas in chapter 3 cannot be readily applied because at finite temperature, there is no finite radius (within the LDA) at which the density profile vanishes (since the gas will have asymptotically classical gaussian tails). In principle, we can use the known high-temperature limit of the classical gas for the equation of state to determine μ_0 on the hottest samples. However, in our range of temperature studied, the classical

⁴The shift of the critical temperature due to finite-size effects is [40]:

$$\frac{\delta T_{\text{BEC}}}{T_{\text{BEC}}^0} = -\frac{\omega' \zeta(2)}{2\bar{\omega} \zeta(3)^{2/3}} N^{-1/3}, \quad (5.6)$$

where $\bar{\omega}$ (ω') is the geometric (arithmetic) average of the trapping frequencies. For 3000 particles, the shift due to finite-size effects lowers the critical temperature by $\sim 20\%$.

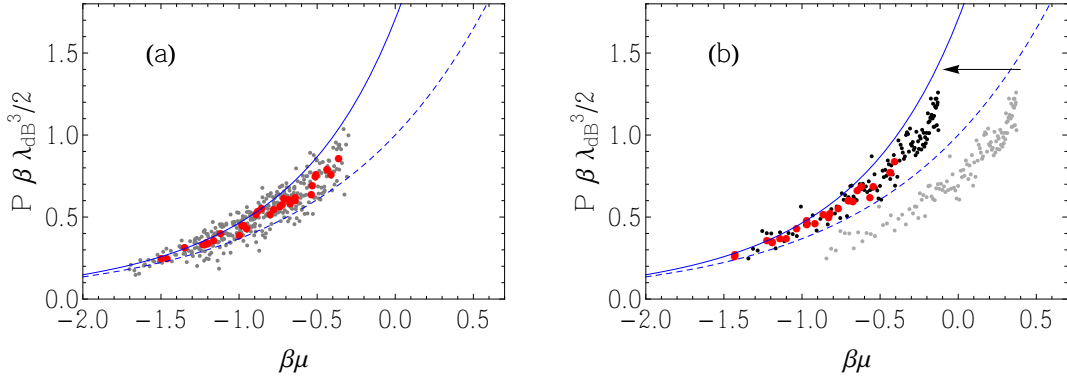


Figure 5.2: Determination of the global chemical potential μ_0 on a finite-temperature unitary Fermi gas. The normalized pressure $P\beta\lambda_{\text{dB}}^3/2$ is plotted against the normalized chemical potential $\beta\mu$. Each image has $\beta\mu_0$ as a free parameter, corresponding to a horizontal shift on these plots. (a): The global chemical potential on the high-temperature images (grey points) is fitted using the second-order virial coefficient (solid blue line) rather than the classical gas (dashed blue line) and the images are averaged to obtain a low noise EoS (red). (b): μ_0 is adjusted on lower temperature images to minimize the distance in the overlapping region of the EoS determined from the hotter samples.

gas EoS (dashed blue line in Fig.5.2) is not expected to be sufficient to describe the system and we have to include the first high-temperature correction, the second-order virial expansion (blue solid line in Fig.5.2, see section 1.1.2): $P\beta\lambda_{\text{dB}}^3/2 = e^{\beta\mu} + \tilde{b}_2 e^{2\beta\mu} + \dots$. We use the known value of \tilde{b}_2 , whose calculation will be done below, in section 5.1.4.

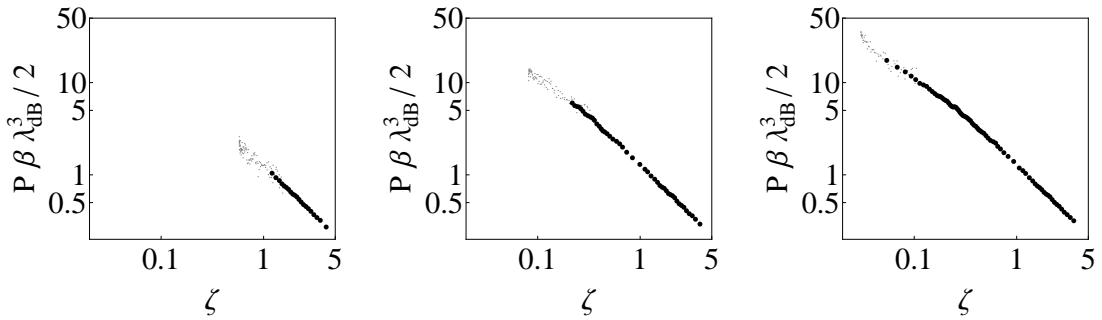


Figure 5.3: Progressive reconstruction of the EoS by patching colder and colder density profiles (grey points) on the previously averaged EoS determined by the hotter samples (full black points). The variable $\zeta = e^{-\beta\mu}$ is the inverse of the fugacity.

Each density distribution provides a parametrization (with the parameter being the position z in the trap with respect to the trap center) of the EoS with μ_0 a parameter to be determined:

$$\left\{ \beta\mu(z), \frac{P(z)\beta\lambda_{\text{dB}}^3}{2} \right\} = \left\{ \beta(\mu_0 - V(z)), \frac{\beta\lambda_{\text{dB}}^3}{2} \frac{m\omega_r^2}{\pi} \bar{n}(z) \right\} \quad (5.8)$$

First, the pressure is calibrated similarly to the procedure of chapter 3 using a reference pressure

which, in this case, is the $T = 0$ unitary Fermi gas. Since its EoS is known, $\mu = \xi_s E_F$ (with $\xi_s = 0.41$ determined independently from this calibration using spin-imbalanced mixture, see chapter 6), the density profile is a fermionic Thomas-Fermi function and provides a single-parameter calibration of the pressure, whose accuracy is estimated to be 5%. This in turn makes the determination of the radial trapping frequency ω_r irrelevant. Plotting the normalized pressure $P\beta\lambda_{\text{dB}}^3/2$ against the normalized chemical potential $\beta\mu$ gives us a piece of the EoS and changing μ_0 corresponds to a horizontal shift of the overall density profile (Fig.5.2). Using colder samples, one can in this way map out the equation of state of the unitary gas (see Fig.5.3). The result is plotted in Fig.5.4 normalized as in Eq.5.1 (the function $f(\beta\mu)/2$). With over 40 images, we have a total of about 4000 points defining the equation of state, which after averaging results in an EoS with a standard deviation of about 6 %. This is the universal pressure of the unitary Fermi gas. For comparison we also plot the pressure of a classical Boltzmann gas (dotted blue line, Eq.(1.13)) and of the ideal Fermi gas (dashed red line, Eq.(1.19)). A preliminary EoS measured at MIT is also shown (solid green line) and is in reasonable agreement, though a systematic lower shift is observable [114]. It is rather unexpected that the EoS of the unitary gas is close to the classical gas one and these differences (as well as with MIT EoS) show the necessity of normalizing the pressure in a more sensitive way. The next sections will be devoted to extracting various quantities from this function.

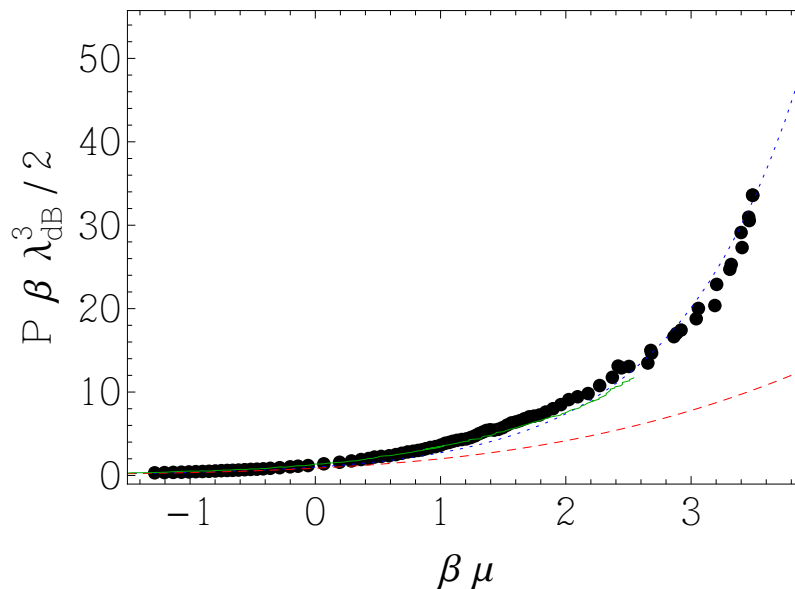


Figure 5.4: Grand-canonical Equation of State of the Unitary Fermi Gas. The ideal Fermi (Boltzmann) gas pressure is shown in red dashed (blue dotted) line. The preliminary EoS measured at MIT is shown in solid green line [114].

5.1.3 Comparison to Many-body Theories

Because of the large variation of the pressure with $\beta\mu$ in Fig.5.4, we instead normalize the pressure of the unitary gas to that of the ideal Fermi gas. We write the universal pressure as:

$$P(\mu, T) = P_1(\mu, T)h(\zeta) \quad (5.9)$$

where $P_1(\mu, T)\beta\lambda_{\text{dB}}^3 = -\text{Li}_{5/2}(-e^{\beta\mu})$ is the non-interacting Fermi gas pressure (Eq.1.19) and $\zeta = \exp(-\beta\mu)$ is the inverse of the fugacity. The h -function is universal and contains all the

thermodynamics of the spin-balanced unitary Fermi gas. We show in Fig.5.5 the measurement of $h(\zeta)$ together with various theories. We recall that the EoS of a single-component ideal Fermi gas is $h(\zeta) = 1$.

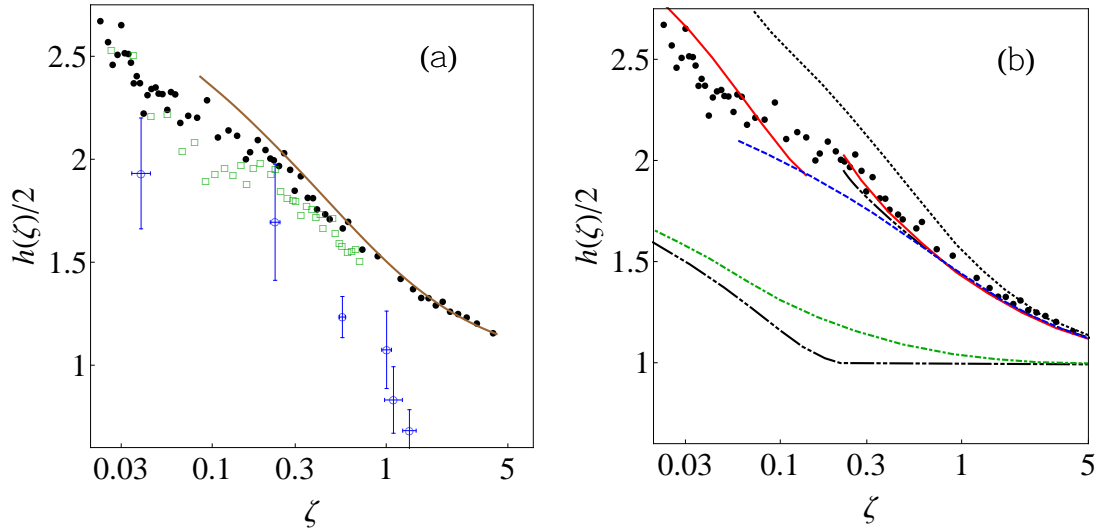


Figure 5.5: Comparison between the experimental Equation of State (black circles) and various many-body theories, (a): Monte-Carlo calculations, and (b): various analytic (or semi-analytic) calculations.

Monte Carlo simulations (Fig.5.5a)
- Blue circles: Diagrammatic MC (DMC) [200]
- Green squares: Quantum MC [201]
- Brown solid line: Recent Diagrammatic MC [115]

Analytic calculations (Fig.5.5b)
Black dotted: Self-consistent GG perturbation theory [202]
Black double-dot-dashed: BCS Mean-field theory
Green dot-dashed: Pseudo-gap model [203]
Blue dashed : GG_0 perturbation theory [203]
Red line: Gaussian pair fluctuations / Nozières-Schmitt Rink (NSR) theory [23]
Black triple-dot-dashed: Ladder diagrams approximation [204]

In Fig.5.5a, we compare the experimental result to different Monte-Carlo calculations and Fig.5.5b, to various analytic approaches (Table 5.1.3). We see that there is a wide dispersion among the theories, showing that the equation of state of the homogeneous unitary gas is a sensitive test for many-body theories. In particular BCS mean-field is strongly ruled out by our measurement. We see that the agreement is reasonably good with the Quantum Monte Carlo calculation [201] and very good with the recent diagrammatic Monte Carlo calculation of the Amherst group [115],

even though a systematic difference is observed at the lowest temperatures (or lowest ζ).

5.1.4 High-temperature Limit: Virial Expansion

We now focus on the high-temperature behavior of the EoS. We saw in section 1.1.2 that at high-temperature $k_B T \gg \mu$ or low fugacity $\zeta \gg 1$, the equation of state can be written as the virial expansion

$$P\beta\lambda_{\text{dB}}^3/2 = e^{\beta\mu} + \tilde{b}_2 e^{2\beta\mu} + \tilde{b}_3 e^{3\beta\mu} + \dots, \quad (5.10)$$

and that the calculation of the i^{th} order coefficient involves the spectrum of the i -body problem. In section 1.1.3, we computed the virial coefficients of a single component Fermi gas: $\tilde{b}_k = (-1)^{k+1} k^{-5/2}$. For convenience we define a virial expansion where we subtract the contribution of the non-interacting Fermi gas. For the function $h(\zeta)$, we write the expansion in the form:

$$\frac{h(\zeta)}{2} = \frac{\sum_{k=1}^{\infty} ((-1)^{5/2} k^{-5/2} + b_k) \zeta^{-k}}{\sum_{k=1}^{\infty} ((-1)^{5/2} k^{-5/2}) \zeta^{-k}}. \quad (5.11)$$

The b_k coefficients are non-zero only due to interactions, and the relation to the \tilde{b}_k 's in Eq.(5.10) is simply:

$$\tilde{b}_k = (-1)^{k+1} k^{5/2} + b_k \quad (5.12)$$

Calculation of the virial coefficients

Since the two-body problem is solvable, b_2 can be calculated analytically [205, 206]. It can be expressed as a function of the scattering phase shift between the two particles, the Beth-Uhlenbeck formula (see paragraph 77 of [207]):

$$\frac{b_2}{\sqrt{2}} = \sum_b e^{E_b/k_B T} + \sum_{l=0}^{\infty} \gamma_l \int_0^{\infty} \frac{dk}{\pi} \frac{d\delta_l(k)}{dk} e^{-\hbar^2 k^2/mk_B T}, \quad (5.13)$$

where $\gamma_l = 2l + 1$ and $\delta_l(k)$ is the scattering phase shift of the l^{th} order partial wave. The sum over b is done over all bound states of energy E_b . If $k \ll r_0$ (r_0 being the range of the interaction potential), the phase shift reads $\tan \delta(k) = -ka$ (we neglect finite range corrections). Performing the integral with the explicit expression of $\delta(k)$ one finds⁵:

$$\frac{b_2}{\sqrt{2}} = \sum_b e^{E_b/k_B T} - \frac{\text{sign}(a)}{2} (1 - \text{erf}(|x|)) e^{x^2} \quad (5.14)$$

where $x = \lambda_{\text{dB}}/\sqrt{2\pi}a$. Because of the $\text{sign}(a)$ term, one must be careful when taking the unitary limit $x \rightarrow 0$. On the molecular side ($a > 0$), since we neglect the deeply bound states⁶, the only term of the sum over b is the one of the Feshbach bound state. Its energy ($\sim 1/a^2$) tends to zero at unitarity and the first term of Eq.(5.14) is equal to one. On the BCS side ($a < 0$) there is no weakly two-body bound state, and the sum must be neglected. In both cases, we find:

$$b_2 = \frac{1}{\sqrt{2}}. \quad (5.15)$$

⁵The absolute value in the argument of the error function should be added in Eq.(5) for b_2 in [206].

⁶This assumption is reasonable because in general these bound states are irrelevant in the timescale of the experiments performed. However, the metastability of our gases is directly related to their existence. Decay processes in these deep bound state can happen and it releases considerable energy (the atoms are then lost) but these events are considered sufficiently rare to be neglected here.

The calculation of the third order virial coefficient is considerably more involved since it requires the solution of the quantum-mechanical three-body problem. This calculation was carried out in [208]. An interesting feature of this calculation is that they calculated the virial coefficient for three fermions in a trap. It is easy to show that the virial coefficients for the trapped (b_k^t) and homogeneous gas (b_k) are related by $b_k^t = b_k/k^{3/2}$, by writing the pressure of the trapped gas as the integral of the local pressure of the homogeneous gas and using the virial expansion for the latter [208]⁷. Using the spectrum of the three-fermion problem in a trap⁸ [209,210], b_3 was found to be -0.3551 . This result was confirmed in subsequent works [211,212,213]. Another calculation using field-theoretic methods surprisingly gives another result $b_3 = 1.05$ [214]. Recently, the daunting problem of the fourth-order virial coefficient from the four-body problem has been addressed and yielded $b_4 = -0.016(4)$ [212].

Experimental determination of the virial coefficients

The high-temperature part of the experimentally determined equation of state can be used to extract the virial coefficients. The measurement of the EoS required to use the second-order coefficient as an input parameter to fit the hottest samples (Fig.5.2). We can thus fit the data points for $h(\zeta)$ first using b_3 as a free parameter.

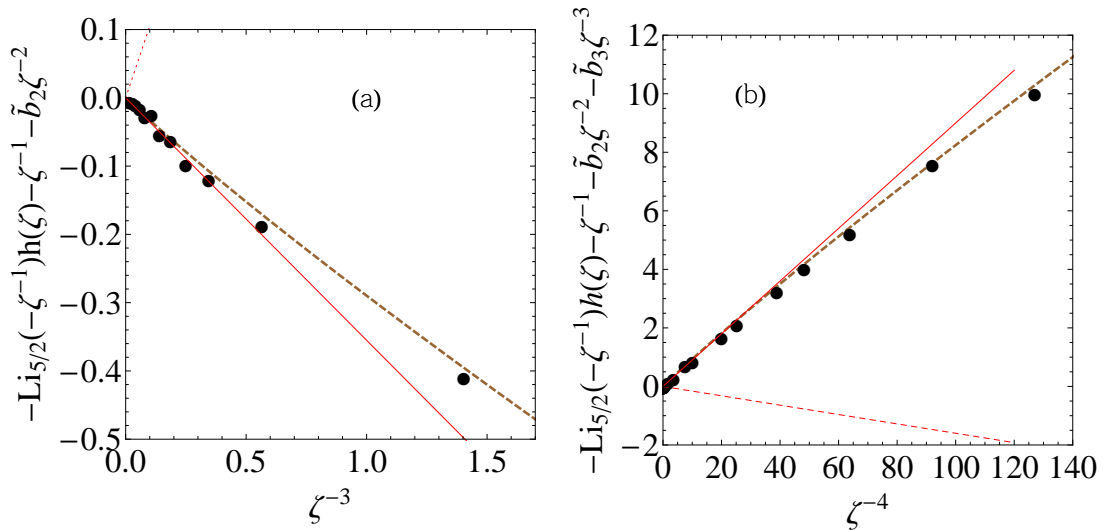


Figure 5.6: Determination of the (a) third-order and (b) fourth-order virial coefficients. The experimental data is shown as black dots and the fits to extract the coefficients are displayed as solid red lines. Theoretical calculations include a prediction for b_3 (dotted red line in (a) [214]), b_4 (dotted red line in (b) [212]) and a recent Diagrammatic Monte-Carlo calculation (brown dashed line [115]).

In order to identify b_3 , we calculate the difference between the pressure and the second order virial expansion:

$$-\text{Li}_{5/2}(-\zeta^{-1})\frac{h(\zeta)}{2} - \zeta^{-1} - \tilde{b}_2\zeta^{-2} \xrightarrow{\zeta \rightarrow \infty} \tilde{b}_3\zeta^{-3} \quad (5.16)$$

⁷The second virial coefficient of the homogeneous gas can be recovered as well by calculating b_2^t directly [121].

⁸The virial coefficients b_2 and b_3 in the BEC-BCS crossover are detailed in section 5.3.1.

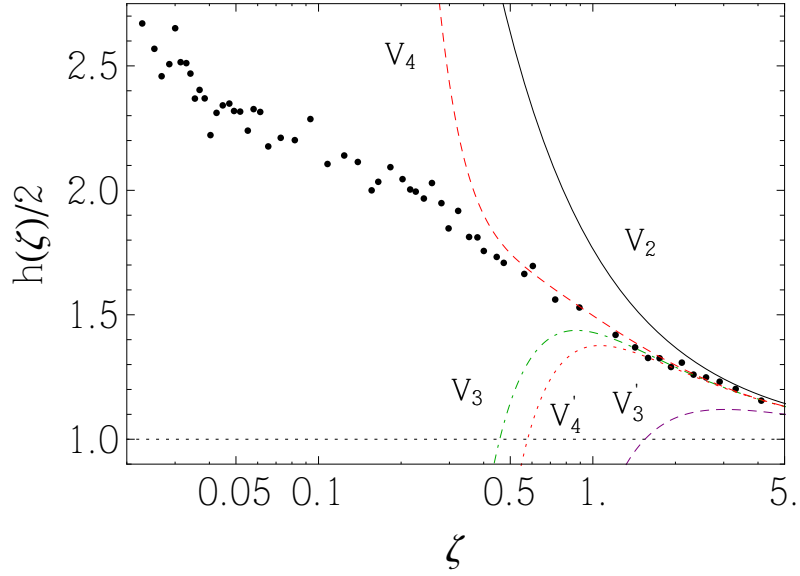


Figure 5.7: Virial expansion equations of state, V_2 (solid black line) for the second order, and higher-order deduced from the experimental data for the third V_3 (green dash-dotted line, in agreement with [208, 211, 212]) and fourth order V_4 (red dashed line) as well as the result of [214] (V_3' , dashed purple) and [212] (V_4' , dotted red).

We plot the result on Fig.5.6a as a function of ζ^{-3} and find a straight line whose slope is \tilde{b}_3 . From this fit, we find (see Eq.(5.12)):

$$b_3^{\text{exp}} = -0.35(2) \quad (5.17)$$

This experimentally confirms the theoretical predictions in [208, 211, 212] (solid red line) and rules out the result from [214] (dashed red line). We can go one step further and take the theory value for $b_3 = -0.3551$ as fixed and fit the fourth virial coefficient. Following the same procedure, we subtract up to the third order the expansion from the pressure

$$-\text{Li}_{5/2}(-\zeta^{-1}) \frac{h(\zeta)}{2} - \zeta^{-1} - \tilde{b}_2 \zeta^{-2} - \tilde{b}_3 \zeta^{-3} \xrightarrow{\zeta \rightarrow \infty} \tilde{b}_4 \zeta^{-4}, \quad (5.18)$$

and plot this quantity versus ζ^{-4} (Fig.5.6b), from which we find:

$$b_4^{\text{exp}} = 0.09(1) \quad (5.19)$$

plotted in the red solid line. The recent prediction for the fourth-order virial coefficient, $b_4 = -0.016(4)$, does not agree with this value, not even the sign of the coefficient [212]. The high-temperature limit of the DMC calculation agrees well with our value of b_4 (brown thick line in Fig.5.6b). To summarize, we plot the various virial contributions to the equation of state at high-temperature compared to the data in Fig.5.7.

5.1.5 Low-Temperature I: Fermi-liquid type behavior

We now turn to the low-temperature sector of the EoS. We will first make a brief overview of the low-temperature behavior of other known quantum systems divided in two broad families: Fermi-liquid and Non-Fermi-liquid systems.

The Normal State of Strongly Interacting Systems I: Fermi Liquids

All solid state physics textbooks introduce band theory, which is the theory of a single-electron in a periodic potential. As metals are composed of many strongly Coulomb-interacting electrons, it is remarkable that an independent-electron theory can capture many properties of metals such as the linear specific heat well below room temperature [215]. This does not mean that interactions are absent but their effect can be taken into account via a change in the properties of the free electron gas, such as a change of mass compared to the bare particle.

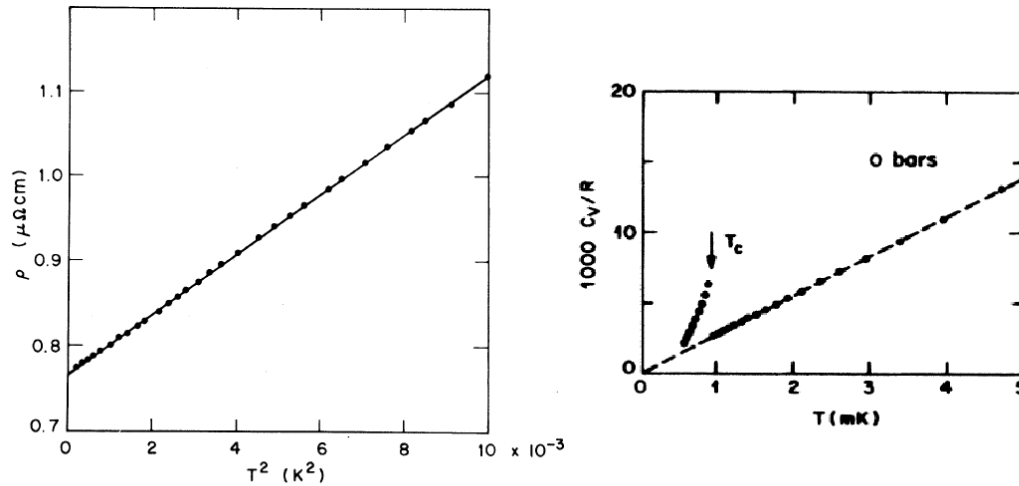


Figure 5.8: Examples of Fermi liquids. Left panel: electrical resistivity ρ as a function of T^2 of the heavy-fermion compound CeAl_3 [216]. Right panel: specific heat C_V/R as a function of temperature for liquid ^3He close to the superfluid critical temperature T_c [217].

Over time very different systems have shown those similar properties. For example, liquid ^3He also presents a linear dependence of the specific heat C_V as a function of temperature (right panel of Fig.5.8). The linearity is observed down to a critical temperature T_c [217]. This temperature marks the onset of fermionic superfluidity in ^3He and a dramatic discontinuity in specific heat is observed. Other exotic materials showing these “non-interacting Fermi gas” features were discovered in 1975. For example, the electrical resistivity was shown to scale as T^2 (left panel of Fig.5.8) in CeAl_3 , as well as the linear behavior of the specific heat [216]. The constant of proportionality A ($\rho \propto AT^2$) was observed to be unusually large. If one interprets this as the behavior of an ideal gas of particle with an effective mass m^* , they found that the excitations in these materials have gigantic effective masses, $m^* \sim 1000m$, and are called, for this reason *heavy-fermion* compounds. For comparison, the effective mass of the ^3He excitations is between 3 to 6 times the bare helium mass depending on the pressure (see Table VII in [218]).

In 1957, L. Landau developed a phenomenological theory of interacting Fermi systems [219]. Even though the ground-state properties of a material can be difficult to determine, many observables addressed in experiments such as the low-temperature properties depend only on the low-lying excitations above this ground-state. While the ground-state can be system-specific, these excitations can have very general properties. The idea of Landau’s theory is that the bare particles, such as the electrons, or ^3He atoms are *dressed* by the interactions and the system is described by

fermionic excitations that have renormalized physical characteristics compared to the bare particles: these are Landau *quasi-particles*. The theory relies on the assumption that the excited states of the interacting system are adiabatically connected to that of the non-interacting Fermi gas when one turns on the interactions. We will merely present the ideas and quote the results of Landau's Fermi liquid theory (FLT). First, the energy of a (slightly) excited state relative to the ground state energy can be Taylor-expanded:

$$F - F_0 = \sum_{\mathbf{k}\sigma} (\epsilon_{\mathbf{k}} - \mu) \delta n_{\mathbf{k}\sigma} + \frac{1}{2V} \sum_{\mathbf{k}\mathbf{k}'\sigma\sigma'} f(\mathbf{k}, \sigma; \mathbf{k}', \sigma') \delta n_{\mathbf{k}\sigma} \delta n_{\mathbf{k}'\sigma'} + \dots \quad (5.20)$$

where $F = E - \mu N$ and $\delta n_{\mathbf{k}\sigma}$ is the population of quasi-particles with wavenumber \mathbf{k} and spin σ . The dispersion relation $\epsilon_{\mathbf{k}} = \epsilon_F + \frac{\hbar^2 k_F}{m^*} (k - k_F) + \dots$ is expanded around the Fermi surface $k = k_F$, where the quasi-particles are long-lived. m^* is the effective mass of the quasi-particle. The second term describes an effective interaction between the quasi-particles. It is natural to wonder why this second term cannot be dropped altogether. This is due to the fact that the excitations are limited to a region close to the Fermi surface, where $\epsilon_{\mathbf{k}} - \mu$ is small and the first term is also of second-order, the second must thus be kept for consistency. One can show that the quasi-particles follow the same distribution as the non-interacting system, namely Fermi-Dirac statistics with an energy distribution that depends on the effective interactions. Since there is a one-to-one correspondence between the non-interacting and interacting states, the entropy has the same expression as for the non-interacting gas. Within this framework, one can calculate the entropy of a Fermi liquid to leading order in T :

$$\frac{S}{Nk_B} = \frac{\pi^2}{2} \left(\frac{2m^*}{\hbar^2} \right) \frac{T}{(6\pi^2 n)^{2/3}} = \frac{m^*}{m} \left(\frac{S}{Nk_B} \right)^0 \quad (5.21)$$

where the superscript ⁰ refers to the ideal gas. To leading order, the entropy of a Fermi liquid is the same as that of the ideal Fermi gas with a renormalized mass m^* . And so will be the specific heat as a consequence ⁹:

$$\frac{C_V}{C_V^0} = \frac{m^*}{m}, \quad (5.22)$$

Finally, the compressibility can be obtained from¹⁰:

$$\frac{\partial \mu}{\partial n} = \left(\frac{\partial \mu}{\partial n} \right)^0 \frac{1 + F_0^s}{m^*/m} \quad (5.24)$$

The quantity F_0^s is a so-called Landau parameter¹¹. Landau theory of the Fermi liquid is phenomenological in the sense that it does not state to which systems its assumptions are valid (though

⁹We recall that

$$C_V = T \left(\frac{\partial S}{\partial T} \right)_{V,N}$$

¹⁰ The isothermal compressibility is defined as:

$$\kappa_T \equiv -\frac{1}{V} \left(\frac{\partial V}{\partial p} \right)_T = \frac{1}{n^2} \left(\frac{\partial n}{\partial \mu} \right)_T \quad (5.23)$$

¹¹Because we limit to wavevectors close to the Fermi surface and we assume rotational invariance, $f(\mathbf{k}, \sigma; \mathbf{k}', \sigma')$ depends on \mathbf{k} and \mathbf{k}' only through the angle between them θ . By spin rotation symmetry, there is just one spin-parallel and antiparallel interaction and the effective interaction can be written as [220]:

$$f(\mathbf{k}, \sigma; \mathbf{k}', \sigma') = \sum_{l=0}^{\infty} (f_l^{(s)} + \sigma\sigma' f_l^{(a)}) P_l(\cos \theta) \quad (5.25)$$

From the f_l coefficients, we define dimensionless quantities: $F_l^{(s,a)} = 2g(\epsilon_F) f_l^{(s,a)}$, where $g(\epsilon_F) = m^* k_F / 2\pi \hbar^2$ is the quasi-particle density of states at the Fermi surface, and $F_l^{(s,a)}$ are the Landau parameters.

it can be justified using perturbative theory on weakly interacting systems) and does not give a framework to calculate *ab-initio* the effective mass or the Landau parameters. However, given these parameters as input (determined experimentally for example), Landau theory has proved very powerful to explain the low-temperature properties of the normal state of a broad range of systems.

The Normal State of Strongly Interacting Systems II: Non-Fermi liquids

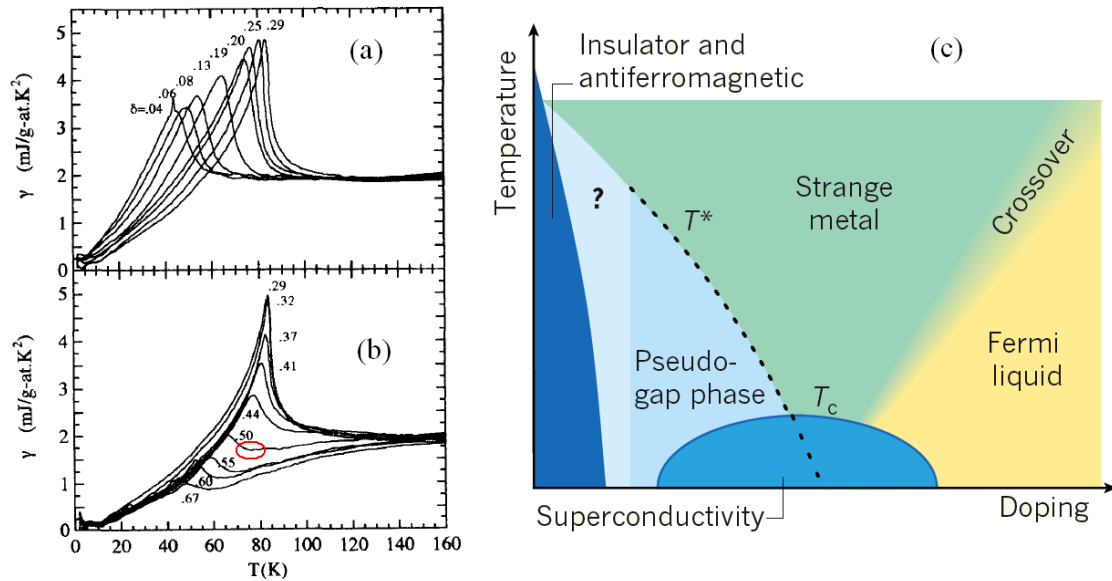


Figure 5.9: Observation of a pseudo-gap behavior in the specific heat of the $Y_{0.8}Ca_{0.2}Ba_2Cu_3O_{7-\delta}$ copper-oxide superconductor. The ratio of the electronic specific heat to the temperature $\gamma = C^{el}/T$ versus temperature is plotted in the underdoped (a) and overdoped (b) regions of the phase diagram [221]. (c): Sketch of the phase diagram versus the (hole-) doping (corresponding to $\sim 1 - \delta$ in (a) and (b)) (from [222]). Note that the definition of the doping varies and sometimes the quantity $x = 1 - \delta$ is used instead.

Some strongly interacting systems have been shown to exhibit non-Fermi-liquid behavior (see for example [223]). In this respect, high- T_c superconductors are a special family as they possess a spectacular amount of exotic features. In Fig.5.9a and Fig.5.9b, we show the measurement of the ratio of the electronic specific heat to the temperature $\gamma = C^{el}/T$ of the $Y_{0.8}Ca_{0.2}Ba_2Cu_3O_{7-\delta}$ copper-oxide¹². These measurements show a maximum corresponding to the transition to the superconducting state. T_c is the highest for $\delta = 0.29$ (the top of the superconducting “dome” on the phase diagram Fig.5.9c, see also the measurement of the dome in Fig.1 of [221]). For overdoped samples ($\delta < 0.29$) (left part of Fig.5.9c) the Fermi-liquid behavior is good for a broad range of temperatures above T_c . However, below the optimal doping ($\delta > 0.29$), a dip starts to form (red circle in Fig.5.9b) in γ before the superconducting phase transition. This depression appearing at a temperature T^* is the entrance into the *pseudo-gap* regime. The pseudo-gap corresponds to a

¹²This measurement is challenging because for the temperature range imposed by the high- T_c nature of the system, the electronic specific heat is only about 1 % of the total specific heat. A reference measurement was used to subtract the phonons contribution to the specific heat (see [224]).

depletion in the density of states around the Fermi surface that persists above T_c , and was observed with many different probes (such as photoemission or tunneling spectroscopy, see the review [225]). The disappearance of well-defined elementary excitations around the Fermi surface leads to the breakdown of a description in terms of a Fermi liquid¹³. The understanding of the pseudo-gap as a regime of pre-formed Cooper pairs that do not exhibit long-range phase coherence or an ordered phase of unknown origin, is still a highly unsettled matter (see for instance [226] and references therein).

There are other exotic features in the normal phases of cuprate superconductors. While around optimal doping, the specific heat is reasonably linear for $T > T_c$, the resistivity of the system also shows an approximately linear behavior (in contrast with the $\propto T^2$ dependence expected from a Fermi liquid), the reason for which this part of the phase diagram is coined *strange metal* (see Fig.5.9c). The Fermi liquid T^2 dependence is approximately recovered for large dopings though some strange features remain (see Fig.2 of [227] for details). The normal phases of high- T_c superconductors still lack a comprehensive theoretical description despite an enormous research effort since their discovery in 1986.

The Normal Phase of the Unitary Fermi Gas

In order to analyze the low-temperature behavior of the equation of state, and discuss its possible (non-)Fermi liquid character we change the normalization of the universal function to a normalization more appropriate around $T = 0$. We thus plot the pressure $P(\mu, T)/2$ in units of the zero-temperature pressure of a single-component Fermi gas. The thermodynamic variable is changed from ζ to $(k_B T/\mu)^2$ (we will show below that Landau Fermi theory predicts that $P \propto (T/\mu)^2$)¹⁴. This change of variable is relevant only at very low temperature, where $\mu(T) \approx \mu(0)$. Indeed, as $\mu(T)$ decreases (and goes to $-\infty$ in the high-temperature limit), the variable $k_B T/\mu$ will diverge (when $\zeta \rightarrow 1$).

The result is displayed on Fig.5.10 and we observe a clear T^2 behavior of the pressure (normalized to the $T = 0$ Fermi pressure). It is tempting to interpret this low-temperature behavior as a Fermi-liquid type behavior. This is not obvious in the grand-canonical ensemble. We saw in Eq.(5.22) that the specific heat of the Fermi liquid is linear in T , as for the ideal gas. Using usual thermodynamic relations, it is easy to show that the specific heat at constant volume is related to the pressure by:

$$\frac{C_V}{T} = \left(\frac{\partial^2 P}{\partial T^2} \right)_\mu - \left(\frac{\partial S}{\partial \mu} \right)_T \left(\frac{\partial n}{\partial \mu} \right)_T^{-1} \quad (5.28)$$

Since we expand the quantities around $T = 0$, the second term vanishes and we deduce that the pressure should indeed be quadratic in temperature to leading order, as for the Sommerfeld expansion of the ideal gas $P(\mu, T) = 2P(\mu, 0)(c_0 + \frac{5\pi^2}{8}c_1(k_B T/\mu)^2 + \dots)$. The coefficients are defined so that $c_0 = c_1 = 1$ for the non-interacting Fermi gas (see Eq.1.20). For the Fermi liquid, the only difference will be the renormalized compressibility of the gas and renormalized mass of the

¹³The destruction of the Fermi surface is anisotropic, some directions showing well-defined excitations (called Fermi arcs), others being pseudo-gapped.

¹⁴The formulas for the conversion are straightforward:

$$\left(\frac{k_B T}{\mu} \right)^2 = (\log \zeta^{-1})^{-2} \quad (5.26)$$

$$\frac{P(\mu, T)}{2P_0(\mu, 0)} = -\text{Li}_{5/2}(-\zeta^{-1}) \frac{15\sqrt{\pi}}{8} (\log \zeta^{-1})^{-5/2} \frac{h(\zeta)}{2} \quad (5.27)$$

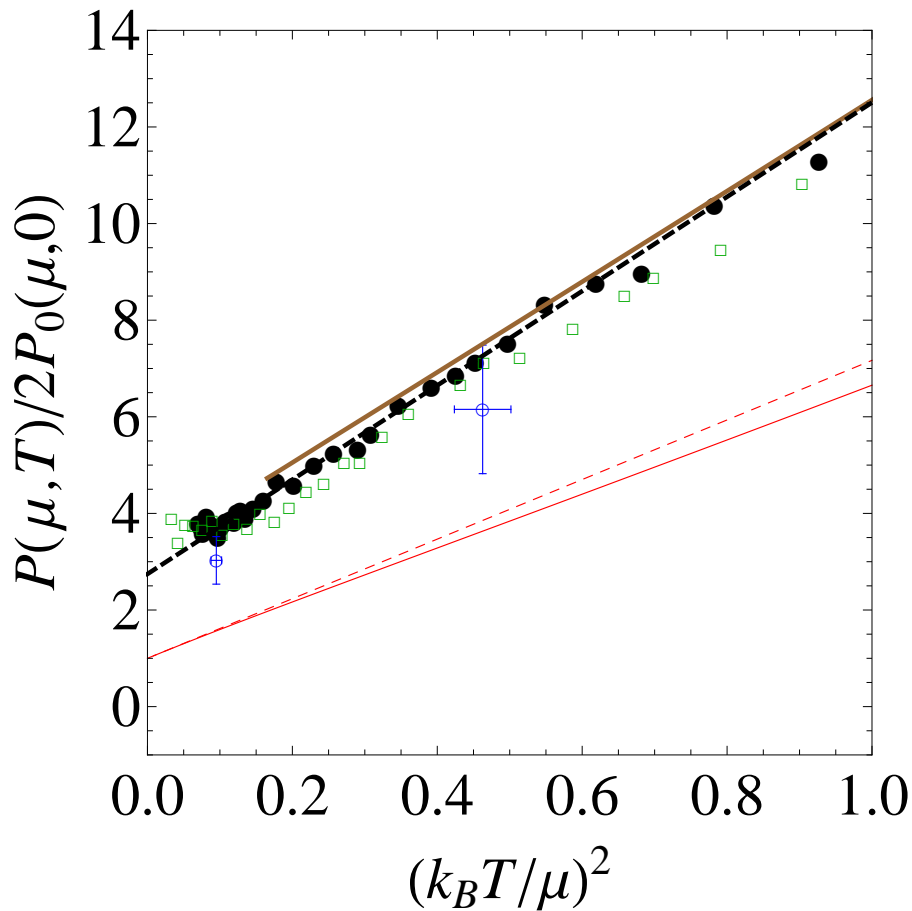


Figure 5.10: Low-temperature equation of state. The experimental data (black dots) are shown together with a linear fit in $(k_B T/\mu)^2$ (dashed black line). The ideal Fermi gas EoS is shown in solid red line (Eq.(1.19)), as well as its Sommerfeld expansion (Eq.(1.20)) in dashed red line. A Quantum Monte Carlo calculation is shown in green squares [201], and two diagrammatic Monte Carlo calculations are displayed in empty blue circles [200], and solid brown line [115] (as in Fig.5.5a).

quasi-particle that will determine the coefficients c_0 and c_1 . We write the EoS of the normal state at zero temperature as $\mu = \xi_n E_F$, so that its $T = 0$ compressibility (in units of the compressibility of the ideal two-component Fermi gas) is $\xi_n^{3/2}$, hence $c_0 = \xi_n^{-3/2}$. To determine c_1 , we use the ratio of the specific heats in Eq.(5.22). However one must be cautious as this ratio must be evaluated at constant density (not constant μ). Recalling that for the ideal gas $\mu^0 = E_F$, we find that $C_V/C_V^0 = \xi_n^{1/2} c_1$ and by equating this to m^*/m , we find the low-temperature pressure of a Fermi liquid in the grand-canonical ensemble:

$$P(\mu, T) = 2P_0(\mu, 0) \left(\xi_n^{-3/2} + \frac{5\pi^2}{8} \xi_n^{-1/2} \frac{m^*}{m} \left(\frac{k_B T}{\mu} \right)^2 + \dots \right). \quad (5.29)$$

Fitting the data shown in Fig.5.10 with Eq.(5.29), we extract the parameters of the Fermi liquid at zero-temperature¹⁵: $\xi_n = 0.51(2)$ and $m^*/m = 1.13(3)$. The compressibility is in good agreement with the fixed-Node Monte Carlo results $\xi_n = 0.54$ [228] and $\xi_n = 0.56$ [229] and the Quantum

¹⁵Or alternatively, the Landau parameters $F_0^s = \xi_n \frac{m^*}{m} - 1 = -0.42$ and $F_1^s = 3(\frac{m^*}{m} - 1) = 0.39$.

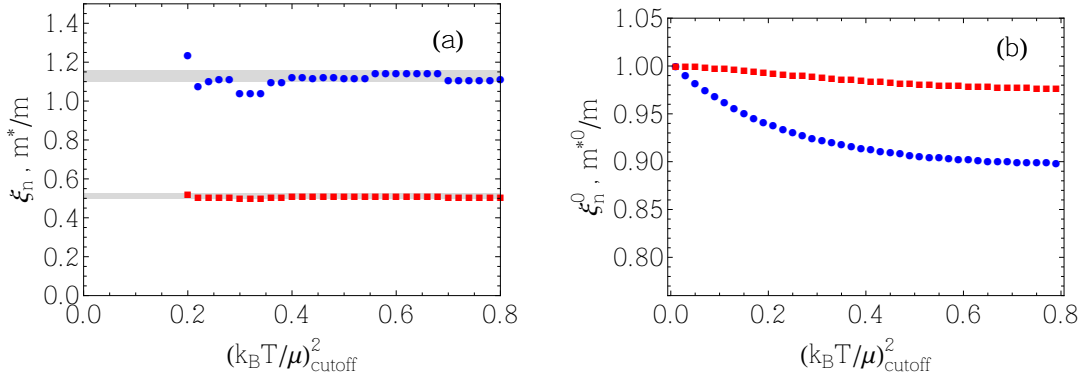


Figure 5.11: Compressibility ξ_n (red squares) and effective mass m^*/m (blue circles) of the (a) normal phase of the unitary gas, (b): the ideal Fermi gas (see Eq.5.29).

Monte Carlo calculation $\xi_n = 0.52$ [230]. The value for the effective mass has not been predicted yet. Note that there is possibly a source of systematic error in this determination. In principle, the expansion (5.29) is valid only in the $T \rightarrow 0$ limit (though we must have $T > T_c$). It is instructive to compare the Sommerfeld expansion (dashed red line in Fig.5.10) of the ideal gas to its exact EoS (solid red line in the same figure). A small deviation is observed. We compare the fitted parameters extracted for the ideal Fermi gas (Fig.5.11a) and for the unitary gas (Fig.5.11b) as a function of the cutoff value for $(k_B T/\mu)^2$. The ideal gas values $\xi_n^0 = 1$ and $m^{*0}/m = 1$ are indeed recovered in the low-temperature limit $(k_B T/\mu)_{\text{cutoff}} \rightarrow 0$ but a systematic downshift is observed at intermediate values. Since the exact EoS of the unitary gas is unknown, it is not clear that a similar effect is present for the thermal excitation of the unitary gas and a systematic upshift correction should be applied. Assuming this is the case, for $(k_B/\mu)_{\text{cutoff}} = 0.3$, the compressibility is downshifted by 1 % (small compared to the error bar) but the effective mass of the ideal fermion requires a 9 % correction, and for the unitary Fermi liquid, one would then find $m^*/m = 1.23(4)$, a value remarkably close to the Fermi-polaron mass (see section 6.1.2). Whether this is an appropriate correction or a numerical coincidence requires further investigation. We now use our observation of Fermi liquid behavior to make a prediction on the photoemission spectra of the unitary gas.

Using Fermi Liquid Theory: Comparison with the Photoemission Spectra from JILA

The nature of the normal phase of the unitary gas is currently debated. As far as the thermodynamics are concerned, we have seen that the low-temperature properties of the unitary gas are well described by Landau's Fermi liquid theory. However, recent photoemission spectroscopy experiments performed at JILA on a strongly interacting Fermi gas of ^{40}K have been interpreted with pseudo-gap models [232, 233]. The goal of these experiments is to extract the spectral function $A(k, \omega)$, a fundamental quantity characterizing the single-particle excitations of a many-body system¹⁶. In photoemission spectroscopy experiments, an RF photon with a frequency ν is used to expel an atom from the gas with a momentum \mathbf{k} . This allows one to measure the energy of the single-particle state E_s :

$$E_s = \epsilon_{\mathbf{k}} + \phi - h\nu \quad (5.30)$$

¹⁶For example the signature of a quasi-particle in $A(k, \omega)$ is a narrow peak, whose width will be related to its lifetime. The position of the peak maximum in k and ω will provide the dispersion relation of the excitation $\hbar\omega_k = E_s(k)$.

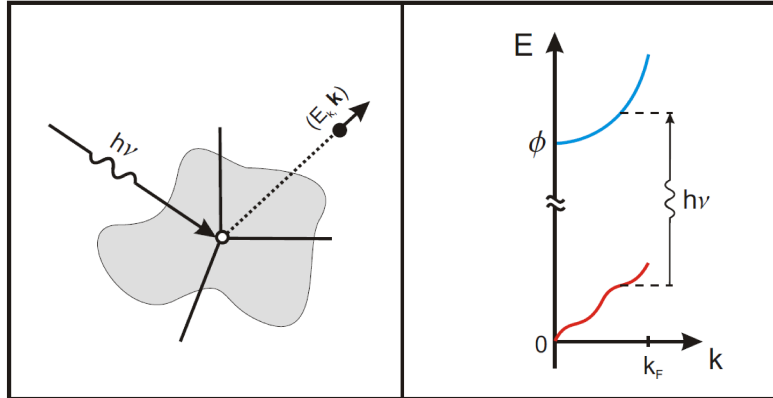


Figure 5.12: Principle of momentum-resolved photoemission spectroscopy. An RF photon with an energy $h\nu$ is used to extract an atom from the sample and allows one to measure the single particle excitation energy (Figure from [231])

where $\epsilon_{\mathbf{k}} = \hbar^2 k^2 / 2m$, and ϕ is the work function of the surface (see Fig.5.12). Experimentally the spectroscopy is achieved by applying an RF field on the unitary gas and measuring the shell of particles transferred to another state after time-of-flight, using an Abel reconstruction of the three-dimensional momentum distribution, to obtain \mathbf{k} . The RF-outcoupling is done on the transition from state $|9/2, -7/2\rangle$ to state $|9/2, -5/2\rangle$ and in the absence of final state effects¹⁷ the function ϕ is given by the Zeeman splitting between these two states. However, the relation between the measured signal and E_s contains additional subtleties. First, the finite energy resolution of the measurement broadens the spectral function $A(k, \omega)$ (where $\omega = 2\pi\nu$). Secondly, one has to convolve the spectral function with a finite-temperature Fermi-Dirac distribution. Finally, the signal must be integrated over the trap because the measurement address the trapped sample as a whole and is not spatially resolved. As a result the measured Energy Distribution Curves (EDC) are related to the spectral function by [233]:

$$\text{EDC}(k, \omega) = \frac{48k^2}{\pi^2} \int d^3r \frac{A(k, \omega - \mu(\mathbf{r})/\hbar)}{\exp[\beta(\hbar\omega - \mu(\mathbf{r}))] + 1} \quad (5.31)$$

where $\beta = 1/k_B T$. In order to calculate this integral, we consider long-lived quasi-particles, and we would take for $A(k, \omega - \mu)$ a delta function $\delta(\omega - \omega_k)$ with the excitation spectrum of the Fermi liquid:

$$\hbar\omega_k = \mu + \frac{\hbar^2(k^2 - k_F^2)}{2m^*} \quad (5.32)$$

However, to take into account the experimental resolution, due to the finite duration of the RF-pulse, we take instead a gaussian function with a width of $\sigma = 0.25 E_F/\hbar$ for ω [233]. The integral (5.31) requires calculation of the local Fermi wavenumber $k_F(\mathbf{r})$ from the in-trap density distribution. Since the experiments at JILA are done at T_c , we take a central value of the chemical potential corresponding to the critical one: $(k_B T/\mu)_c = 0.32(3)$ (see next section) and use our measured equation of state $h(\zeta)$ to calculate $k_F(\mathbf{r})$.

¹⁷For these states of ^{40}K , final state effects are indeed small. Early RF-spectroscopy studies on ^6Li used the traditional mixture $|1\rangle - |2\rangle$ (around 834 G) and outcoupling to state $|3\rangle$ where final effects were important, making the interpretation of the RF-spectra difficult [28, 234, 235]. This issue was solved in subsequent works using resonant $|1\rangle - |3\rangle$ mixtures (around 690 G) and outcoupling to state $|2\rangle$ [236, 29].

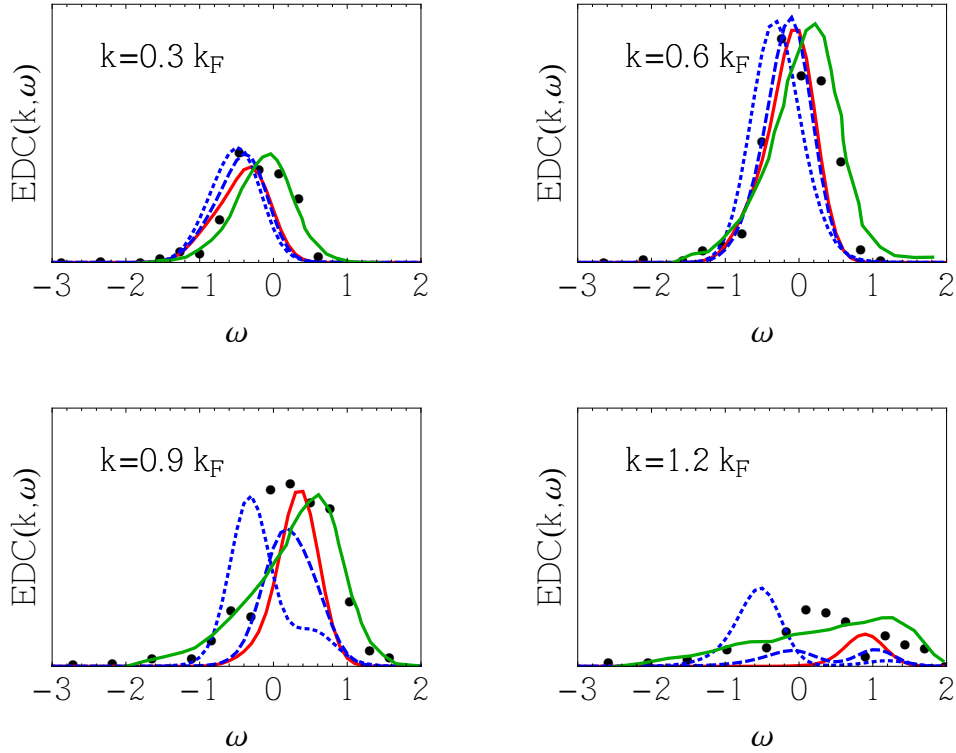


Figure 5.13: Spectral function of a trapped unitary gas at $T = T_c$ for $k = 0.3, 0.6, 0.9$ and $1.2 k_F$ (where ω is in units of $E_F/\hbar = \bar{\omega}(3N)^{1/3}$). The data from JILA [233] is shown in black dots. The spectral functions predicted by Fermi liquid theory is shown in red line, the prediction from a t-matrix pairing-fluctuation approach in green line [233]. In dashed (dotted) blue line, a simple BCS model with a pseudo-gap $\Delta_{pg}/E_F = 0.3$ (0.8), see text.

We show in Fig.5.13 several spectra for different values of momenta k of the $EDC(k, \omega)$ as predicted for a Fermi liquid (red line) together with the experimental data from JILA (black points). A t-matrix pairing-fluctuation calculation is shown in green line [233]. Apart from a global normalization factor (the same normalization is used in all panels of Fig.5.13), the prediction from FLT has no adjustable parameter. In particular, in the region around k_F where FLT is applicable (and where the infinite quasi-particles lifetime assumption is most valid), the agreement with the experimental data is very good. We see that at $0.6 k_F$, close to the most probable wavevector k (as measured by the area under the RF-signal), the FLT spectrum reproduces well the width of the experimental data, showing that the width of the lines is probably limited by the measurement resolution or trap inhomogeneity broadening rather than the lifetime of the quasi-particles. We see that the t-matrix calculation, predicting the existence of a pseudo-gap is not in significantly better agreement with the data compared to the prediction of FLT.

Instead of the Fermi liquid dispersion relation (5.32), we can use a simple pseudo-gap model in the form of a BCS-like dispersion relation [237, 238]: $\hbar\omega_k^\pm = \mu \pm \sqrt{(\frac{\hbar^2}{2m}(k^2 - k_F^2))^2 + \Delta_{pg}^2}$. The spectral function is given by $A(k, \omega) = u_k^2\delta(\omega - \omega_k^+) + v_k^2\delta(\omega - \omega_k^-)$, and the u_k, v_k are the standard coefficients from the BCS theory. We replace the superfluid pairing gap Δ by the pseudo-gap Δ_{pg} .

Integrating the spectral functions, we find the dashed (dotted) blue line for $\Delta_{\text{pg}}/E_F = 0.3$ (0.8) in Fig.5.13. We see that qualitatively the pseudo-gap appears as an onset of a second peak close to $k = k_F$ distant from the first one by Δ_{pg} (for the uniform case). They further separate for increasing values of k as was seen in ARPES experiment on high- T_c superconductors [239]. This results in a “back-bending” feature on the one-particle excitation spectrum, that is the maxima $E(k)$ of the spectral function $A(k, \omega)$. However, it is difficult to interpret the BCS-like back-bending as proposed by the JILA group [232] since it occurs in the region where the spectral weight collapses for $k > k_F$.

The JILA group interpreted their photoemission spectra as evidence for a pseudo-gap regime. However we conclude that the smoothening effect due to the trap averaging makes unambiguous interpretation of the photoemission spectra difficult and their data is equally well described by a Fermi liquid theory with no adjustable parameters. Quantitative data on the pseudo-gap magnitude and corresponding depletion of the density of states remain to be obtained. Let us note that the $P \propto (T/\mu)^2$ behavior was also recovered using a pseudo-gap theory [233]. Direct proof of Fermi liquid (or pseudo-gap) character of the normal phase could be given by a spatially resolved measurement of the spectral function, which would allow the observation of the existence (or absence) of long-lived excitations in the vicinity of the Fermi surface (provided sufficient energy resolution to access the quasi-particles lifetime). Experiments on two-dimensional Fermi gases by photoemission spectroscopy, ongoing in M. Köhl group, could also shine some light on the effect of the dimensionality on the normal phase, and the quasi-particle behavior.

5.1.6 Low-Temperature II: Normal to Superfluid Phase Transition

The description in term of a Fermi liquid, and in particular the $T = 0$ equation of state of the normal phase $\mu = \xi_n E_F$ is not expected to be valid down to very low temperatures. Indeed, the unitary gas possesses a phase transition to a superfluid state. By further zooming on the lowest temperatures of Fig.5.10, we observe a systematic deviation of the coldest data points compared to the Fermi liquid behavior. We interpret this deviation as the onset of the superfluid phase. There are several reasons to back up this interpretation.

First, we observe that within the noise of our data, the pressure is saturating. The robustness of the superfluid to thermal excitations is expected (as for Bose gases, for example). Indeed, there are two types of excitations, single-particle gapped fermionic excitations, which are exponentially suppressed, and collective phononic excitations, which scale as T^4 [244]. Simple models of those two excitations show that the pressure should not vary by more than $\sim 3\%$ up to the transition point (see [121] for details). Unfortunately, our data is limited by the collapse of the cloud of ^7Li used as a thermometer, which did not allow us to explore colder regions.

Second, the value at which the pressure saturates is found to be¹⁸ $\xi_s \approx 0.415$, which is in very good agreement with various low-temperature determinations of ξ_s (see section 5.2.4). It is interesting to investigate the energy difference between the superfluid and the normal phase at $T = 0$, given by: $\delta E = E_S - E_N = \frac{3}{5} N E_F (\xi_s - \xi_n)$. Since $\delta E < 0$, the superfluid is the stable phase, and δE is the so-called *condensation* energy. The BCS theory predicts that the condensation energy is related to the single-particle excitation gap Δ through

$$\delta E_{\text{BCS}} = \frac{3N}{8} \frac{\Delta^2}{E_F}. \quad (5.33)$$

¹⁸We recall that at $T = 0$ the equation of state of the superfluid unitary Fermi gas reads $\mu = \xi_s E_F$.

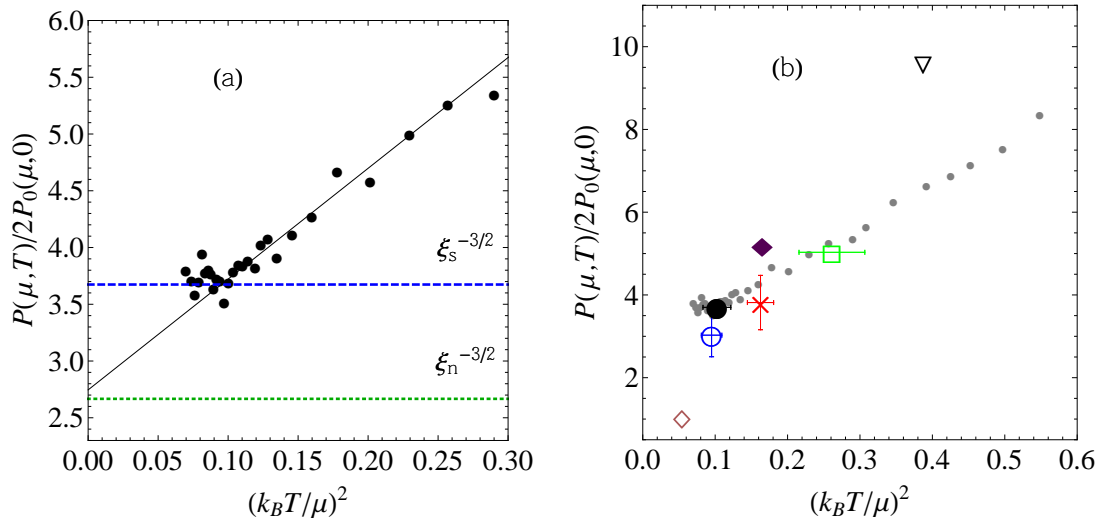


Figure 5.14: Normal/superfluid phase transition in the unitary Fermi gas. (a): Low-temperature deviation to the Fermi liquid behavior. The $T = 0$ compressibility of the superfluid (normal fluid) ξ_s (ξ_n) is shown in dashed blue line (dotted green line). (b): Comparison between the experimental critical point (black dot) and theoretical predictions: $1/N$ expansion (brown diamond [240]), Diagrammatic Monte-Carlo calculations from Burovski *et. al.* (blue circle [241]) and Goulko *et. al.* (red cross [242]), Quantum Monte Carlo (green square [230]), self-consistent diagrammatic approach (solid purple diamond [202]), a Borel-Padé approximation connecting a ϵ -expansion (black down triangle [243]) (the result for the $\epsilon = 1$ of the $\epsilon = 4 - d$ expansion is off range [243]).

Taking $\xi_s \approx 0.41$ and $\xi_n = 0.51$, we find that the condensation energy of the unitary gas per particle (in units of the Fermi energy) is $3(\xi_s - \xi_n)/5 \approx -0.06$. Using the value of Δ measured by radio-frequency spectroscopy to be $0.44 E_F$ [29], the BCS theory predicts a condensation energy $\delta E/(NE_F) \approx -0.07$, remarkably close to our determination.

Now, the simplest way of pinpointing the transition point is to fit the pressure in Fig.5.14 by a two-piece linear function. In this way, we find the value of the critical point for the superfluid transition:

$$\left(\frac{k_B T}{\mu}\right)_c = 0.32(3). \quad (5.34)$$

Physically, the two-piece linear function is not satisfactory as it would mean that there would be a jump in the density at the phase transition, which would then be first-order. However, the transition is expected to be second order [241, 245]. A more refined modelization of the critical region (using the appropriate critical behavior for the pressure) does not change the value of the critical point beyond the error bars (see [246]).

The measurement of the critical point for the homogeneous unitary gas allows a direct comparison with several predictions from advanced many-body theories. Usually the results are given in the canonical ensemble, stating the quantities T_c/T_F , μ/E_F and E/NE_F for the critical point (as

well as the entropy, see for example Table II of [202])¹⁹. The critical values are plotted in Fig.5.14b and compared to the experimental data point (black dot). The dispersion of the various predictions is spectacular and except for the reasonable agreement with the Diagrammatic Monte-Carlo calculation [241], the other predictions are quite far from the experimental determination.

It is also instructive to extract the critical temperature T_c/T_F in units of the Fermi temperature. Since $k_B T_F = \frac{\hbar^2}{2m}(3\pi^2 n)^{2/3}$ (where n is the total density), it requires the relation giving the chemical potential μ as a function of n , that is, the equation of state. Since the density verifies the Gibbs-Duhem formula $n = (\partial P/\partial \mu)_T$, we have to calculate the slope of the pressure at the critical point. Given the feature in Fig.5.14a, we can calculate this slope both on the lower side (where $P/2P_0$ is approximately constant) and upper side, which will give us lower and upper bound on the value of T_c/T_F . First, on the lower side, we have $\mu \approx \xi_s E_F$, hence $T_c/T_F = \xi_s (k_B T/\mu)_c$. Reaching the transition from above, we use the Fermi-liquid EoS Eq.(5.29), from which we deduce:

$$\frac{T_c}{T_F} = \left(\frac{k_B T}{\mu} \right)_c \left[\xi_n^{-3/2} - \frac{5\pi^2}{8} \xi_n^{-1/2} \frac{m^*}{m} \left(\frac{k_B T}{\mu} \right)_c^2 \right]^{-1} \quad (5.37)$$

so that we find:

$$0.13 < \frac{T_c}{T_F} < 0.18 \quad (5.38)$$

which is in good agreement with 0.152(7) [241], 0.173(3) [242], 0.16 [202], in marginal agreement with 0.136 [240] and 0.183 [243] and in disagreement with 0.23 [230], 0.225 [247] and 0.249 (also in [243]). It is also in agreement with the extrapolation at the spin-population balanced limit of a measurement of the phase diagram of the spin-imbalanced Fermi gas at MIT, where they found $T_c/T_F \approx 0.15$ [248]. This makes the resonantly interacting Fermi gas the *highest- T_c* superfluid known, in units of T_F . Indeed, in most metals, the Fermi temperature is several ten thousands of kelvins. For conventional superconductors ($T_c \sim 10$ K), we have $T_c/T_F \sim 10^{-4}$. For high- T_c superconductors this ratio can reach 0.05, still significantly below the unitary Fermi gas value ~ 0.15 . The role of the strong interactions in the dramatic increase of the critical temperature is clear.

5.1.7 Equation of State of the Trapped Unitary Gas

The pioneering works on the thermodynamics of the unitary Fermi gas done at Duke University [249], at JILA [108], and at ENS [250, 27] measured global quantities of the gas, such as its total energy or entropy. For example, in the experiment of the Duke group, they measured the energy of the trapped gas E_t through the size of the density distribution in model-independent way by using the virial theorem [110]:

$$E_t = 3m\omega_z^2 \langle z^2 \rangle, \quad (5.39)$$

where $\langle X \rangle = \frac{1}{N} \int d^3r X n(\mathbf{r})$ is the average over the density distribution. By using an adiabatic sweep deep in the BCS regime (at a magnetic field of 1200 G), they measured the entropy of the system assuming it is a weakly interacting Fermi gas (correcting for the large background scattering

¹⁹It is straightforward to calculate the critical point in the plane $\{(k_B T/\mu)^2, P/2P_0\}$:

$$\left(\frac{k_B T}{\mu} \right)_c = \left(\frac{T_c}{T_F} \frac{E_F}{\mu_c} \right) \quad (5.35)$$

$$\frac{P_c(\mu_c, T_c)}{2P_0(\mu_c)} = \frac{5}{3} \frac{E}{N E_F} \left(\frac{\mu_c}{E_F} \right)^{-5/2} \quad (5.36)$$

where we used that $PV = 2E/3$.

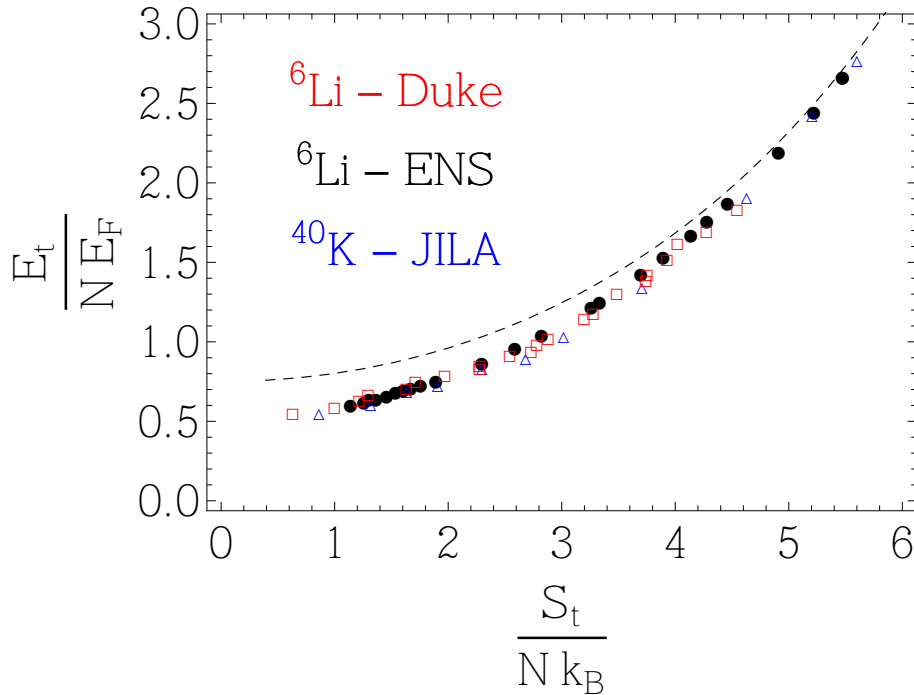


Figure 5.15: Universality of the unitary Fermi gas: the equation of state in the canonical ensemble for the trapped gas. The energy $E_t/N E_F$ is plotted versus the entropy per particle $S_t/N k_B$. The data from Duke University on ${}^6\text{Li}$ (red squares, [249]) and JILA on ${}^{40}\text{K}$ (blue triangles, [108]) are plotted together with the EoS deduced from our measurement on ${}^6\text{Li}$ of the homogeneous EoS (black dots). The ideal gas EoS is shown in dashed black line.

length). In this way, they extracted the relation between the energy E_t and the entropy S_t of the unitary gas, the canonical equation of state of the trapped gas (right panel of Fig.1.9). The JILA group probed the potential energy of the unitary gas as a function of the ideal gas temperature $(T/T_F)^0$ (left panel of Fig.1.9). They used a gas of ${}^{40}\text{K}$ around a Feshbach resonance at 202 G. This resonance has a nice feature: there is a zero crossing at 209.9 G on the BCS side of the resonance. They could thus normalize the potential energy of the unitary to the measured potential energy of the ideal one, after an adiabatic sweep to the zero-crossing. We can convert this set of data to the $E(S)$ representation by converting the abscissa using the relation $S_{t0} \left(\frac{T}{T_F}\right)^0$ for the ideal gas²⁰, and using the virial theorem, we convert $E_{\text{pot}}/E_{\text{pot}}^0$ (where the superscript ⁰ refers to the quantity measured on the non-interacting Fermi gas with the same entropy) to $E_t(S_t)$ by multiplying the ratio by the relation $E_{t0}(S_{t0})$ for the harmonically trapped non-interacting gas.

We compare our EoS to the results from Duke and JILA by calculating the relation $E_t(S_t)$ from the homogeneous pressure $h(\zeta)$ using the local density approximation. For example, the total atom number is obtained by integrating the local density:

$$N = \int d^3r n(\mathbf{r}) = \int d^3r \left(\frac{\partial P}{\partial \mu} \right)_T (\mu(\mathbf{r})) \quad (5.40)$$

Using the definition of h and replacing the integration over position \mathbf{r} by the integration over ζ

²⁰Calculating the $S_{t0}(T/T_F)$ relation, as well as $\mu_{t0}(T/T_F)$ using the density of states in a harmonic trap can easily be done numerically and the details can be found in section 5.1.1 of [251].

(and recalling that $\zeta(\mathbf{r}) = \exp(-\beta(\mu_0 - V(\mathbf{r})))$), we find:

$$N = -\frac{2}{\sqrt{\pi}} \left(\frac{k_B T}{\hbar \omega} \right)^3 \int_{\zeta_0}^{\infty} d\zeta \frac{d\sqrt{\log(\zeta/\zeta_0)}}{d\zeta} \text{Li}_{5/2}(-\zeta^{-1}) h(\zeta) \quad (5.41)$$

where $\omega = (\omega_r^2 \omega_z)^{1/3}$. Similar expressions can be derived for E_t/NE_F (using $PV = 2E/3$) and S_t/Nk_B (through $-PV = E - TS - \mu N$). These normalized quantities do not depend on ω and can be calculated parametrically with the inverse fugacity at the center of the trap ζ_0 . E_F here is the Fermi energy of the trapped gas, $E_F = \hbar \omega (3N)^{1/3}$. The integral in Eq.(5.41) is discretized and the sum runs over the experimental data. We thus avoid relying on an interpolation function²¹. The results are gathered in Fig.5.15 and we see the excellent agreement between the three measurements. This is even more remarkable because the measurement at JILA (blue triangles) is done on ⁴⁰K, while the others on ⁶Li. This shows the universality of the unitary Fermi gas [252]. However, because of the smoothening effect of the trap average, this is not a test as stringent as the homogeneous gas EoS would be. For example, while there are (small) differences between the experimental data and the quantum Monte Carlo calculation on the uniform gas EoS (green squares of Fig.5.5), the agreement between the latter and the Duke EoS is excellent (see Fig.2 of [201]).

The superfluid transition in the trapped gas happens when the atoms at the bottom of the trap become superfluid. We can thus estimate the critical point for the trapped system by setting ζ_0 to ζ_c . Calculating the trapped quantities, we deduce that $T_c/T_F = 0.19(2)$, $(S_t/Nk_B)_c = 1.5(1)$ and $(E_t/NE_F)_c = 0.67(5)$. These critical parameters can be compared to the various theories (usually using the LDA to integrate their EoS in a trap) (see Table II of [249] for example), and also to experimental determinations. Our measurement of T_c/T_F is in good agreement with a previous thermodynamic determination 0.21(1) [249], a condensate fraction technique 0.21(2) [113, 253] or via the quenching of the momentum of inertia 0.2 [254], but somewhat lower than previous thermodynamic measurements from the Duke group 0.29(3) [109], 0.27 [255] and 0.35 [256].

5.1.8 Comparison with the Tokyo Canonical Equation of State

Almost simultaneously to our work, the group led by M. Ueda and T. Mukaiyama also presented the measurement of the EoS of the homogeneous unitary Fermi gas by a different method. Assuming mechanical equilibrium, we can write the following equation (which is a restatement of the local density approximation):

$$\nabla P(\mathbf{r}) + n(\mathbf{r}) \nabla V(\mathbf{r}) = 0 \quad (5.42)$$

At unitary, we write the local internal energy $\mathcal{E} = n \epsilon_F f_E(T/T_F)$ (where f_E is a universal dimensionless function) and $P(\mathbf{r}) = 2\mathcal{E}(\mathbf{r})/3$. The in-situ density distribution was inferred from time-of-flight images using the assumption of hydrodynamic expansion (and the corresponding scaling solutions). By using the inverse Abel transform, the local density $n(\mathbf{r})$ was deduced from the column density. Eq.(5.42) was used to measure $\mathcal{E}(\mathbf{r})$, using an additional assumption for the shape of the density profile (with three fitting parameters adjusted to each local density data $n(\mathbf{r})$). This method does not require the determination of the global chemical potential, since the measurement is entirely done in the canonical ensemble but the temperature must still be known. The Japanese group performed the thermometry by measuring the size of the density profile and made use of the virial theorem Eq.(5.39) and the trapped energy measurement of the Duke group $E_t(T)$ [249] (red solid

²¹However, it is necessary to complete the data at high-temperature with the second-order virial coefficient in order to have proper convergence of the sums.

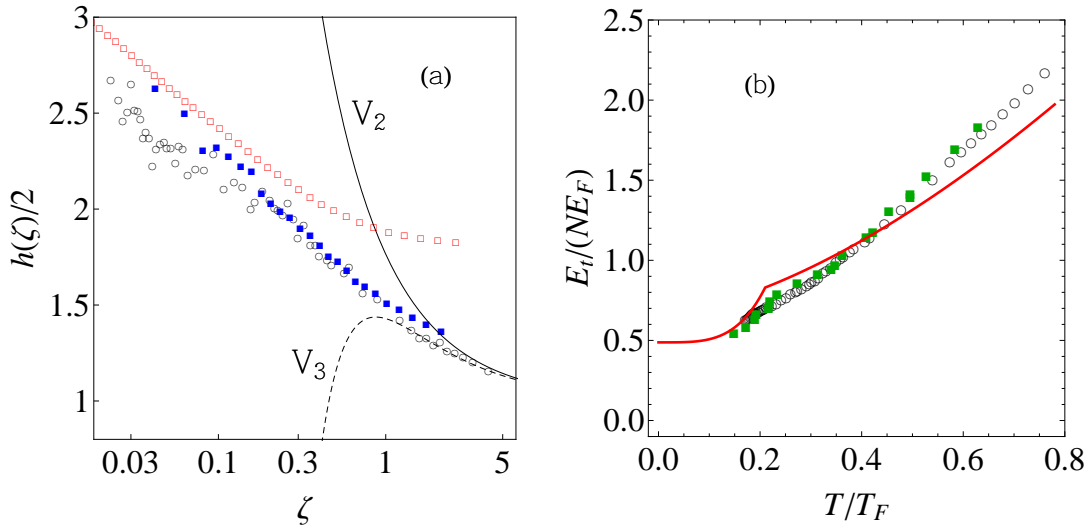


Figure 5.16: Comparison with the Tokyo group equation of state [113]. (a): h -function deduced from the Tokyo measurement, the red empty squares are obtained by using the previous $E(T)$ Duke thermometry calibration (red solid line in (b)), the full blue squares by using our $E(T)$ calibration (black empty dots in (b)). Our curve for $E(T)$ is in good agreement with a recent revised $E(T)$ curve from the Duke group (full green squares in (b)) [257].

line in Fig.5.16b). We see in Fig.5.16 that there is an important discrepancy between our h -function (black empty circles) and the Japanese EoS (red empty squares)²². However, the Tokyo EoS does not recover the virial expansion at high temperature. It was noted that the calibration curve from the Duke work is not in agreement with the $E_t(T)$ deduced from our h -function (black points in Fig.5.16b). In a subsequent work, the Duke group presented a revised curve²³ [257] (green squares in Fig.5.16b) which is in very satisfactory agreement with our data. In light of this change, the data from the Tokyo EoS was reanalyzed with the new temperature calibration resulting in the blue squares in Fig.5.16b [258], which is in considerably better agreement with our data.

5.2 The Low-Temperature Fermi Gas with Tunable Interactions

In the preceding section, we have studied the EoS for a unitary gas $a = \infty$ as a function of temperature T . It is then natural to extend this measurement as a function of interaction strength. As a first step towards this direction, we have studied the thermodynamics of a Fermi gas at very

²²Since the Japanese group provided us both the function f_E and the chemical potential $\mu = \epsilon_F f_\mu(T/T_F)$, it is easy to convert their EoS in the grand-canonical ensemble:

$$\zeta = \exp\left(-\frac{T_F}{T} f_\mu\right) \quad (5.43)$$

$$\frac{h(\zeta)}{2} = \frac{8}{9\sqrt{\pi}} \frac{(T/T_F)^{-5/2} f_E}{-\text{Li}_{5/2}(-\zeta^{-1})} \quad (5.44)$$

²³The initial $E_t(T)$ curve published in [249] used the ideal gas approximation, this was corrected in [257], yielding the green squares in Fig.5.16b, see comment [37] in [257].

low temperature with variable scattering length. As we have shown in chapter 1, we can measure the pressure through the doubly-integrated density profiles, as the pressure formula requires no specific assumptions about the scattering length (except the validity of LDA).

For the sake of clarity, the EoS of the $T = 0$ Fermi gas in the BEC-BCS crossover is presented in this chapter even though it has been measured using spin-population imbalanced mixtures (see chapter 6). The imbalance proved very convenient to extract the EoS of the spin-balanced gas using the central, fully paired region of a spin-imbalanced sample. The technicalities related to the determination of the chemical potential required for the EoS determination are specific to spin-imbalanced gases and since it is irrelevant for the physics of the unpolarized superfluid described in this section, we will describe the procedure in section 6.2.3 as well as the $T \approx 0$ assumption that will be made throughout this section.

5.2.1 The Equation of State of a Fermi gas in the BEC-BCS crossover

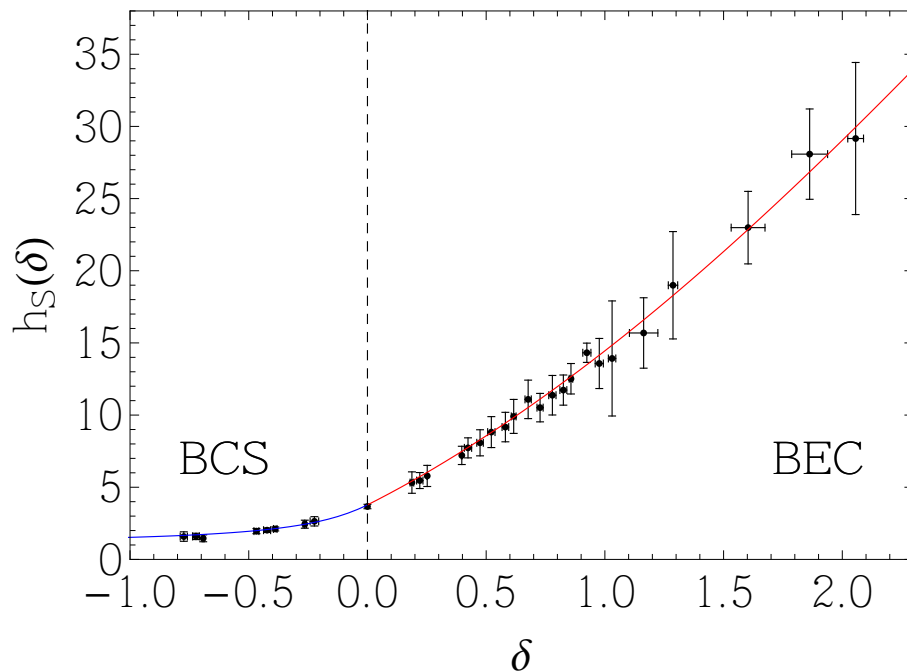


Figure 5.17: Equation of state of a low-temperature Fermi gas in the BEC-BCS crossover. The blue and red lines are the Padé approximants on the BCS and BEC side of the resonance, used to extract several physical quantities as well as to convert the EoS into the canonical EoS (see text).

Usually, the interaction strength in a Fermi gas is characterized by the parameter $1/k_F a$ where $k_F = (3\pi^2 n)^{1/3}$ (where n is the total density), that compares the inter-particle spacing to the scattering length (similarly to na^3 for the Bose gas). Since we work in the grand-canonical ensemble, we characterize the interaction strength using the chemical potential instead of the density as we have done it for the Bose gas (section 3.3.2). Different choices can be made and they are not equally convenient in particular as the properties turn from those a Fermi gas (on the BCS side) to a Bose gas (on the BEC side of the resonance). Here, we favor a Fermi gas normalization, and the grand-canonical interaction parameter is defined as $\delta = \hbar/\sqrt{2m\tilde{\mu}}a$, where we subtract the binding energy per particle to the chemical potential on the BEC side, $\tilde{\mu} = \mu + \Theta(a)\hbar^2/2ma^2$, so that $\tilde{\mu} > 0$

everywhere. δ is related to $1/k_F a$ through the EoS $\mu(n)$ and this interpretation is straightforward on the BCS side, as we have in this limit $\mu \rightarrow E_F$ and thus $\delta \rightarrow 1/k_F a$. Similarly, the pressure of the two-component $T = 0$ Fermi gas with tunable interactions can be written as:

$$P(\mu; a) = 2P_0(\tilde{\mu})h_S(\delta). \quad (5.45)$$

$P_0(\tilde{\mu})$ is the $T = 0$ pressure of a single-component Fermi gas. The h_S -function is a universal dimensionless function, that we measured and show in black dots on Fig.5.17. The pressure normalization in Eq.(5.45) is also a fermionic normalization. While appropriate on the BCS side (where $h_S \rightarrow 1$), this normalization gives a less intuitive result on the molecular side, as seen by the linear divergence of h_S . This can be understood very simply: far in the BEC regime, one expects a mean-field Bose gas equation of state $P \propto \mu^2$, which in Eq.(5.45) result in $h_S \propto \mu^{-1/2} \propto \delta$.

5.2.2 Comparison with many-body theories

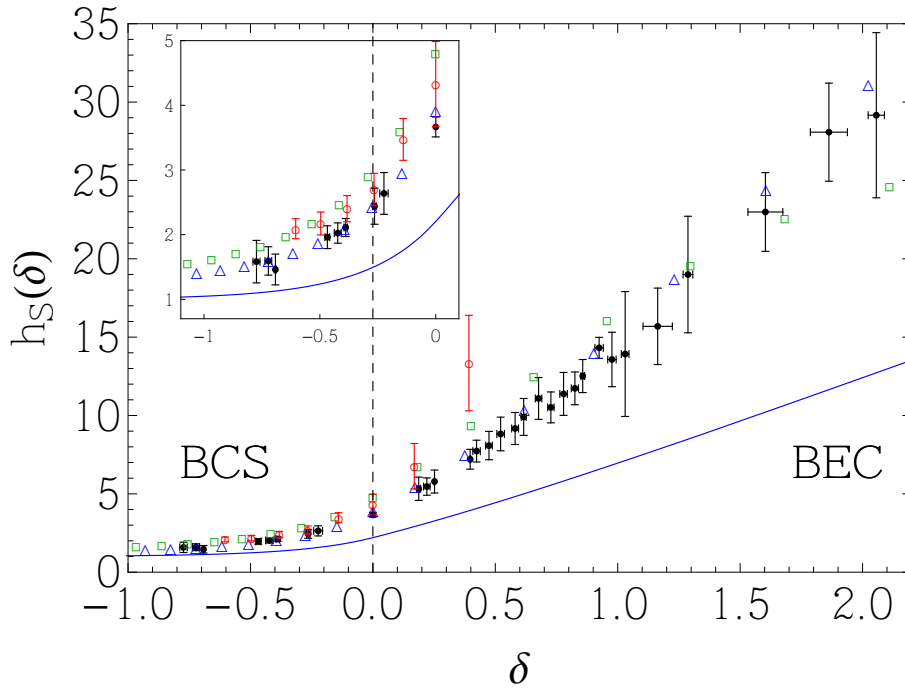


Figure 5.18: Equation of state of a low-temperature Fermi gas in the BEC-BCS crossover. The experimental data (black dots) are compared to different zero-temperature theories: a Quantum Monte Carlo calculation (red circles [230]), a self-consistent t-matrix approach (green squares [202]), a Nozières-Schmitt Rink approximation (blue triangles [259]), and the BCS-mean-field theory (blue solid line [21,22]). Inset: Zoom on the BCS side of the resonance ($\delta < 0$).

We can directly compare this measurement to many-body theories (Fig.5.18). The agreement is very good with a Nozières-Schmitt Rink (NSR) approximation (blue triangles [259]) while small differences can be observed with the Quantum Monte Carlo (red circles [230]) and the self-consistent t-matrix approach (green squares [202]). Note that the two latter are zero-temperature extrapolations of finite-temperature calculations. The BCS mean-field theory²⁴ is completely ruled out and

²⁴From the standard number and gap equations of BCS mean-field theory, one can readily calculate the gap Δ/E_F ,

shows again that the EoS is a sensitive probe of beyond mean-field effects.

Several calculations of the $T = 0$ EoS have been performed using the fixed-Node Monte Carlo method, where the energy is calculated as a function of $1/k_F a$. In order to compare our measurement to the calculations of the canonical EoS, we need to proceed to the grand-canonical to canonical transformation. This is done by the following correspondence equations:

$$x(\delta) = \frac{\delta}{(h(\delta) - \frac{\delta}{5}h'(\delta))^{1/3}} \quad (5.47)$$

$$\xi(\delta) = \frac{h(\delta) - \frac{\delta}{3}h'(\delta)}{(h(\delta) - \frac{1}{5}\delta h'(\delta))^{5/3}}, \quad (5.48)$$

where the canonical variable $x = 1/k_F a$ and the dimensionless energy ξ is defined as:

$$E - \Theta(x) \frac{NE_b}{2} = \frac{3}{5}NE_F\xi(x) \quad (5.49)$$

where we subtract to the energy the binding energy of the Feshbach molecules $E_b = -\hbar^2/ma^2$ on the BEC side of the resonance (Θ is the Heaviside step function). Eq.(5.47) follows from the Gibbs-Duhem relation $\partial P/\partial\mu = n$, while Eq.(5.48) is derived from the Legendre transform $-PV = E - \mu N$. Thus knowing $h(\delta)$ we can parametrically plot $\xi(x)$. Since Eqs.(5.47) and (5.48) involve the derivative of $h(\delta)$, we need to parametrize our data with analytical functions. This is conveniently done using Padé approximants, that will be detailed in the next sections (blue and red lines in Fig.5.17) and in the appendix A.2.

In this way, we compute the thick black line of Fig.5.19 and we compare it to many-body calculations (Fig.5.19). The agreement is excellent with the Fixed-Node Monte Carlo calculations of Pilati and Giorgini (green triangles [261]), and Chang *et. al.* (red squares [262]) as well as with Astrakharchik *et. al.* (blue points [44]). For the latter a small deviation can be observed in the BCS region, where the trial wavefunction is changed from a BCS wavefunction to a Jastrow-Slater wavefunction (see Fig.1 in [44]), and this region is less reliable. In the more recent Monte Carlo work by Gandolfi *et. al.* (purple empty circles [263]) an improved *ansatz* is used for the variational calculation, and the result is systematically lower than our measurement. Another important quantity that can be computed from our fits is the chemical potential in the BEC-BCS crossover:

$$\frac{\mu}{E_F} = x(\delta)^2 \left(\frac{1}{\delta^2} - \Theta(\delta) \right). \quad (5.50)$$

and is plotted in Fig.5.20b. The link between the usual interaction parameter $1/k_F a$ and the grand-canonical one δ is shown in Fig.5.20a. In order to extract the physical content from our EoS, we now focus on well-controlled analytical limits of the crossover.

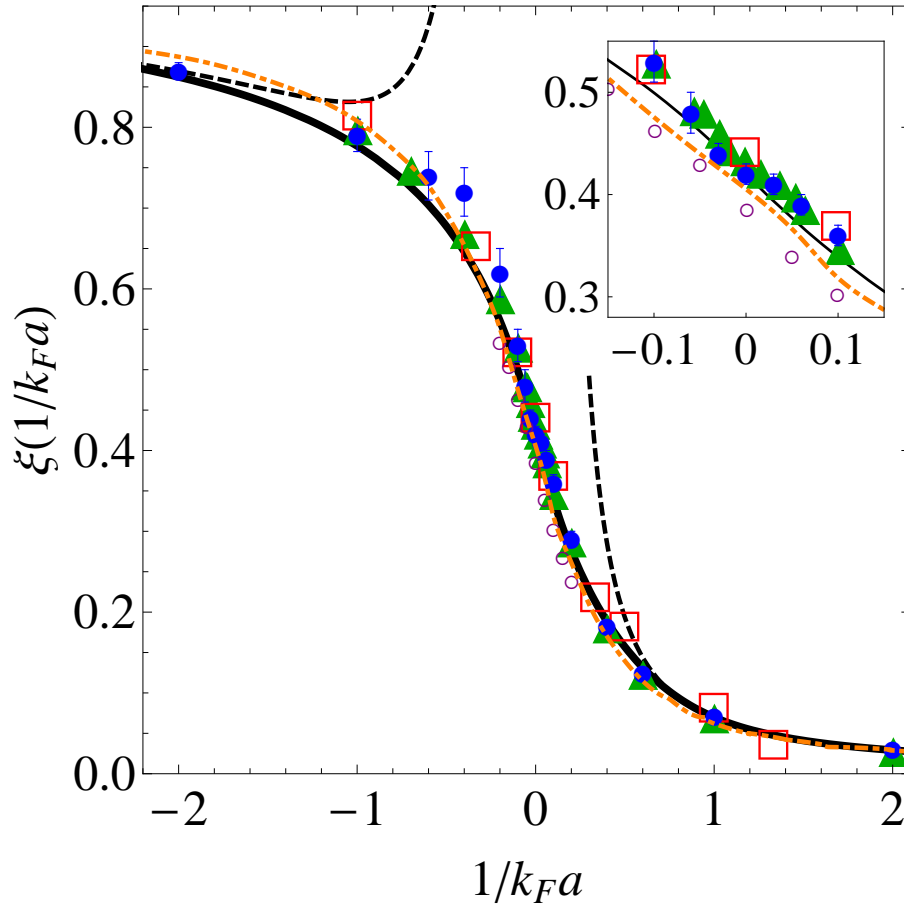


Figure 5.19: Energy of the low-temperature spin-1/2 Fermi gas in the BEC-BCS crossover. The dimensionless energy ξ is defined in Eq.(5.49). The curve deduced from the experimental data is plotted in black thick line and compared to Fixed-Node Monte Carlo calculations by Astrakharchik *et. al.* (blue points [44]), by Pilati and Giorgini (green triangles [261]), by Chang *et. al.* (red squares [262]), by Gandolfi *et. al.* (purple empty circles [263]), and a Nozières-Schmitt Rink approximation (orange dash-dotted line [259]). The BCS mean-field theory is shown in dotted blue line and the dashed black lines are the analytic expansions in the dilute BEC and BCS limits (see text). Right panel: Zoom around the unitary limit.

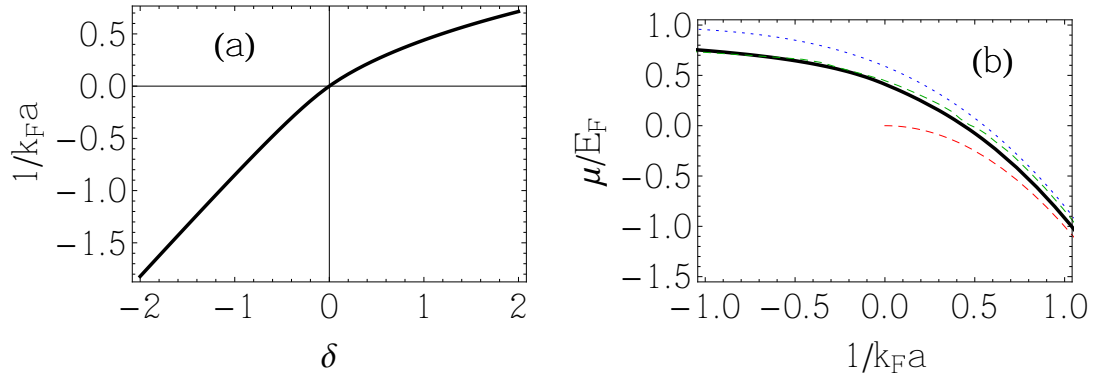


Figure 5.20: (a): Conversion between the canonical ($1/k_F a$) and grand-canonical (δ) interaction parameters. (b): Chemical potential deduced from the measured h_S (black thick line), compared to BCS mean-field theory (dotted blue line), and to a t-matrix theory (dashed green line [264]). Half the binding energy of a molecule $\hbar^2/2ma^2$ is plotted on the BEC side (dashed red line).

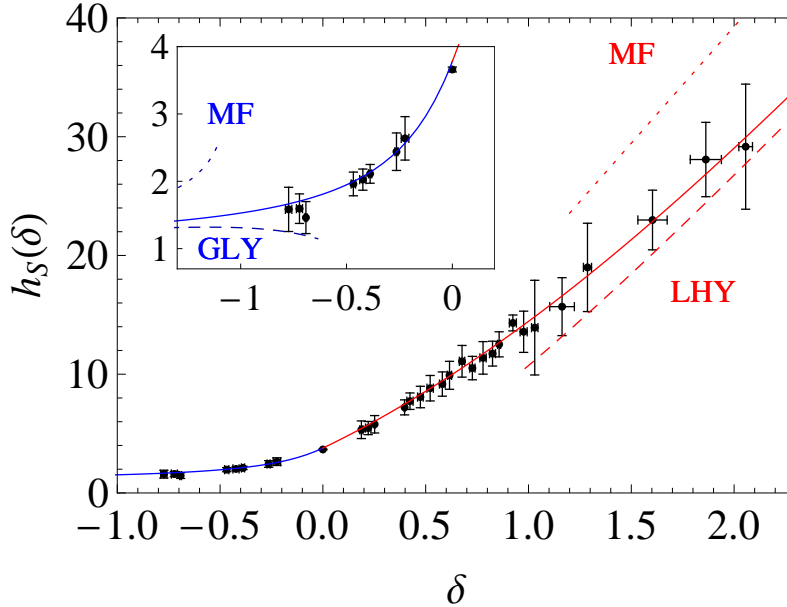


Figure 5.21: Asymptotic behaviors in the BEC (main panel) and in the BCS (inset) limits are shown. The mean-field (Galitskii-Lee-Yang) EoS is shown in dotted (dashed) blue line on the BCS side, the mean-field (the Lee-Huang-Yang) EoS is shown in dotted (dashed) red line on the molecular side.

5.2.3 Asymptotics I: the BCS-limit of a Weakly Interacting Fermi Gas

For a weakly interacting repulsive Fermi gas, the energy of the system was shown in 1958 by Galitskii [265], Lee and Yang [42] to obey a perturbative expansion, in powers of $k_F a$:

$$E = \frac{3}{5} N E_F \left(1 + \frac{10}{9\pi} k_F a + \alpha_{GLY} (k_F a)^2 + \alpha_B (k_F a)^3 + \dots \right) \quad (5.51)$$

or the chemical potential μ/E_F as a function of $1/k_F a$ (which can be expressed in terms of elliptic functions [260]). The resulting chemical potential is shown in dotted blue line in Fig.5.20b. We can calculate the dimensionless energy ξ (defined in Eq.(5.49)):

$$\xi(x) = 5x^5 \int_x^{\text{sign}(a)\infty} \frac{du}{u^6} \tilde{\mu}(u) + \Theta(x) \frac{5}{3} x^2, \quad (5.46)$$

where $\tilde{\mu} = \mu/E_F$, $x = 1/k_F a$ and displayed in dotted blue in Fig.5.19. In particular, we recover that BCS theory

The term proportional to $k_F a$ is the mean-field shift to the ideal gas energy, while the $(k_F a)^2$ -term is due to the quantum fluctuations. The applicability of the Galitskii-Lee-Yang expansion to our problem is not obvious. It was calculated for a repulsive Fermi gas while our gas is subjected to attractive interactions²⁵. In particular, in the limit of weak interactions $a \rightarrow 0^-$, the system is of paramount importance in condensed matter physics as it is subjected to the *Cooper* instability of the Fermi sea towards pairing of fermions, in the presence of arbitrarily weak attractive interactions, leading to the formation of the BCS superfluid. The energy difference between the BCS and the normal state is exponentially small since BCS theory predicts that it is proportional to Δ^2 (Eq.5.33), and $\Delta \propto \exp(-\pi/2k_F|a|)$. However, it was shown that the quantum fluctuations of the superfluid BCS state, also lead to the Galitskii-Lee-Yang expansion (apart from the condensation energy) [266]. It is notorious that the BCS mean-field theory does not verify the Galitskii-Lee-Yang expansion and only contains the condensation energy, and we see that the theory (dotted blue line in Fig.5.19) tends to unity on the BCS side much faster than expected. We can quantitatively test this expansion by fitting our data on the BCS side with a rational function that has the appropriate asymptotic behavior for small values of $k_F a$, and that is regular around unitarity²⁶:

$$h_S^{\text{BCS}}(\delta) = \frac{\delta^2 + \alpha_1 \delta + \alpha_2}{\delta^2 + \alpha_3 \delta + \alpha_4} \quad (5.52)$$

This function by construction satisfies the non-interacting limit: $h_S^{\text{BCS}}(\delta) \rightarrow 1$ when $\delta \rightarrow -\infty$. Two additional constraints on the α_i parameters are added: first, the value of the mean-field shift is fixed because our data do not explore the deep BCS limit; secondly, the value at unitarity $h(\delta = 0) = \xi_s^{-3/2}$ is assumed, leaving two fitting parameters that are determined on our data for $\delta < 0.2$. Using the correspondence equations, we can relate the coefficients of the Galitskii-Lee-Yang expansion to the α_i and we find:

$$\alpha_{GLY} = 0.18(2) \quad (5.53)$$

which is in very good agreement with the predicted value of $4(11 - \log 2)/21\pi^2 \approx 0.186$. Further, assuming this value, we can fit the next term in the expansion, and find $\alpha_B = 0.03(2)$ that is also compatible with the calculated value of 0.030 [267]. This expansion up to $(k_F a)^2$ is plotted as a dashed black line on the BCS side in Fig.5.19.

5.2.4 Asymptotics II: the Unitary Limit

Next, we focus on the strongly interacting limit. Around unitarity, where $1/k_F a \rightarrow 0$, we write the dimensionless energy as:

$$\xi \left(\frac{1}{k_F a} \right) = \xi_s - \frac{\zeta_C}{k_F a} \quad (5.54)$$

The first term is the compressibility of the unitary gas ξ_s , the Bertsch parameter. The second parameter ζ_C is defined here²⁷ as the derivative of the energy with respect to $1/k_F a$. This parameter appears to have a deep physical interpretation that connects microscopic and macroscopic observables of the unitary gas.

predicts $\xi = 0.59$ at unitarity. The h -function predicted by BCS mean-field theory can be computed either from ξ by inverting the correspondence equations (5.47) and (5.48), or directly from $x = x(\bar{\mu})$, by integrating the Gibbs-Duhem relation: $P = \int d\mu n(\mu)$.

²⁵A repulsive Fermi gas can be prepared in so-called higher *branches*, such as the repulsive Bose gas, but it is increasingly unstable to decay to lower branches. The BEC-BCS crossover as described here is occurring in the lower branch.

²⁶Details about the Padé approximants can be found in appendix A.2.

²⁷Not to be confused with the inverse critical fugacity $\zeta_c = e^{-(\beta\mu)_c}$ of the previous section !

The Contact ζ_C

In 2005, S. Tan derived a set of remarkable universal relations holding for the two-component Fermi gas with short-range interactions [268, 269, 270]. He showed that the momentum distribution $n_{\mathbf{k}\sigma}$ decreases for large momenta as $1/k^4$ such that it is possible to define a quantity \mathcal{I} : $\mathcal{I} = \lim_{\mathbf{k} \rightarrow \infty} k^4 n_{\mathbf{k}\sigma}$. In addition the pair correlation function diverges at short distances $r \rightarrow 0$ as $\mathcal{I}/16\pi r^2$. These properties are very general, and are valid for any many-body state, at zero or finite temperature, in the superfluid or normal state [268]. Tan later showed that the contact is related to the energy of the system by the *adiabatic sweep theorem* [269]:

$$\frac{dE}{d(-1/a)} = \frac{\hbar^2}{4\pi m} \mathcal{I}, \quad (5.55)$$

For homogeneous systems, it is convenient to define the contact density $C = \mathcal{I}/V$ (where V is the volume), so that the quantity ζ_C defined in Eq.(5.54) is the dimensionless contact density:

$$C = \frac{2\zeta_C}{5\pi} k_F^4 \quad (5.56)$$

Moreover, the virial theorem can be generalized away from unitarity with an additional term that is proportional to the contact. It is remarkable that the contact C relates microscopic properties (probability of finding two fermions close to each other²⁸), to macroscopic observables (the derivative of the energy). Using the equation of state together with the Padé approximants, we determine the value of ζ_C from the adiabatic sweep theorem:

$$\zeta_C = 0.93(5). \quad (5.57)$$

We can compare our measurement to various calculations: Quantum Monte Carlo calculation of the pair correlation function yields $\zeta_C = 0.95$ [272], or the static structure factor $\zeta_C = 0.90$ [273]. It also agrees well with a Nozières-Schmitt Rink approximation 0.89 [274], but is somewhat larger than a self-consistent diagrammatic calculation 0.80 [275] and a t-matrix approximation 0.86 [276]. A recent fixed-node calculation compared the contact obtained by the adiabatic sweep theorem $\zeta_C = 0.901(2)$ and by the pair-correlation function 0.897(2) [263], both in very good agreement with our determination.

Several groups have measured the contact by different means. The number of closed-channel molecules was measured in the group of R. Hulet [278], and it was later shown that this amounted to measuring the contact [280]. In the group of P. Hannaford, the static structure factor was probed via Bragg spectroscopy [279] and the large momentum behavior yields the contact. Finally, the group of D. Jin tested several of the Tan universal relations, by measuring the contact both through the large momentum part of the momentum distribution (by a fast magnetic field sweep technique and photoemission spectroscopy) and the large frequency tail of the RF lineshape, as well as testing the generalized virial theorem [277]. All these measurements were global probes of the trapped gas and thus yielded the trap-averaged contact. Similarly to what has been done in section 5.1.7, we can use our uniform gas EoS in order to predict the trap-averaged contact measured in the above experiments. The contact is the integral over the trap of the contact density:

$$\mathcal{I}_t = \int d^3r C(\mathbf{r}) = \frac{2}{5\pi} \int d^3r \zeta_C \left(\frac{1}{k_F a} \right) k_F(\mathbf{r})^4 = \frac{2}{5\pi} (3\pi^2)^{1/3} \int d^3r \zeta_C \left(\frac{1}{k_F a} \right) n(\mathbf{r})^{4/3} \quad (5.58)$$

²⁸This interpretation is made more quantitative in section 3.1 of [271]

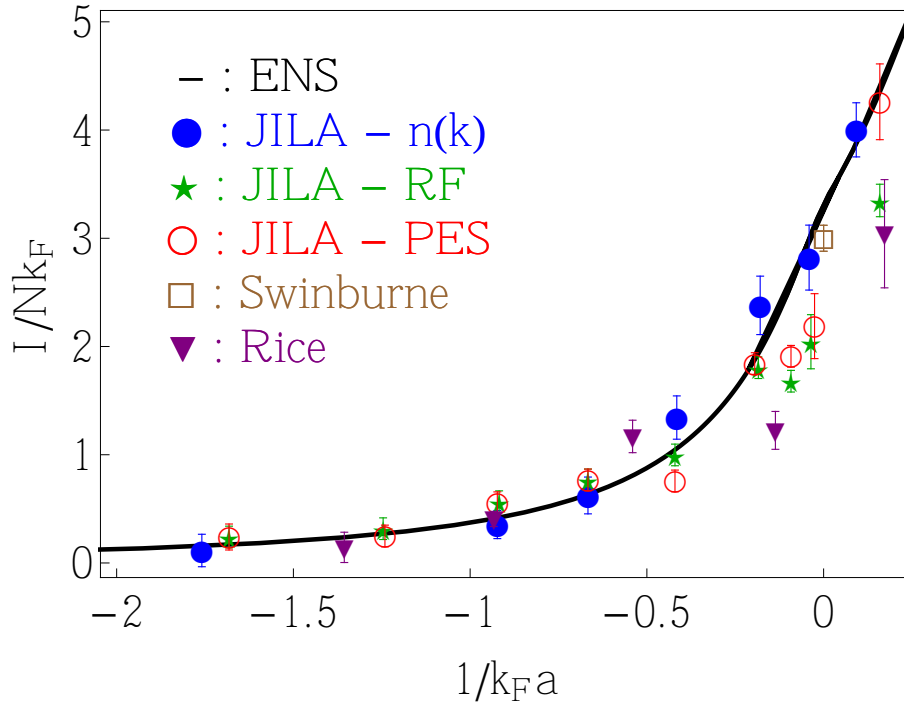


Figure 5.22: Integrated Contact in the trap \mathcal{I}_t/Nk_{Ft} in the BEC-BCS crossover. The curve deduced from our equation of state (solid black line) is compared to three measurements done at JILA: large momentum-tail of the momentum distribution using a fast magnetic field sweep (solid blue circles) and photoemission spectroscopy (red empty circles), and the large frequency tail of the RF lines (green stars) [277]. We also plot the measurement using the number of closed-channel molecules at Rice (purple down triangles) [278]), and the Bragg spectroscopy measurement at Swinburne University (brown empty square) [279].

The density profile $n(\mathbf{r})$ is deduced from the equation of state, under the assumption of the local density approximation. This integral can be calculated analytically at unitarity, since the EoS (and thus the density profile) is exactly known and depends only on ξ_s (see next section):

$$n(\mathbf{r}) = n_0 \left(1 - \frac{r^2}{R_{\text{TF}}^2}\right)^{3/2}, \quad (5.59)$$

where $R_{\text{TF}} = a_{\text{ho}}\xi_s^{1/4}(24N)^{1/6}$, $a_{\text{ho}} = \sqrt{\hbar/m\omega}$, and $n_0 = 8N/\pi^2 R_{\text{TF}}^3$. We assumed an isotropic trap for convenience (with trapping frequency ω). This is not a necessary assumption, since the end result will be normalized in such a way to be independent of the trap frequencies. Evaluating the integral, we find:

$$\frac{\mathcal{I}_t}{Nk_{Ft}} = \frac{512}{175\xi_s^{1/4}}\zeta_C \quad (5.60)$$

where $\zeta_C = \zeta_C(0)$, and $k_{Ft} = \sqrt{2}a_{\text{ho}}^{-1}(3N)^{1/3}$ is the Fermi wavenumber of the trapped gas. The quantity in the left-hand side of Eq.(5.60) has been measured to be 3.00(12) using Bragg spectroscopy [279] close to our value of 3.40(18) (with $\xi_s = 0.41$), determined via the energy of the system, which provides an experimental evidence of the Tan relations.

Our EoS can also be compared to the experiments performed in the BEC-BCS crossover. Deducing the integrated contact \mathcal{I}_t/Nk_{Ft} from the equation of state away from unitarity is slightly

more involved. The contact can readily be expressed in the grand-canonical ensemble since²⁹

$$\left(\frac{\partial E}{\partial(-1/a)}\right)_{S,V,N} = \left(\frac{\partial \Omega}{\partial(-1/a)}\right)_{T,V,\mu}, \quad (5.61)$$

where $\Omega = -PV$ is the grand-potential. We then calculate \mathcal{I}_t , N , and k_{Ft} , as function of δ_0 and we plot the parametric curve $\{1/k_{Ft}a(\delta_0), \mathcal{I}_t/Nk_{Ft}(\delta_0)\}$ in Fig.5.22 as a solid black line³⁰. We gather all the measurements in Fig.5.22 and the overall agreement between the various measurements makes a strong case, both for universality (as the JILA measurements are done on ⁴⁰K, the others on ⁶Li) as well as for a verification of the Tan relations.

The Bertsch parameter ξ_s

Because of the divergence of a at unitarity, there is no energy scale associated to the interactions and the $T = 0$ thermodynamics of the unitary gas are formally identical to those of an ideal gas except for the universal number ξ_s . It is remarkable that all the complexity of the maximally interacting unitary Fermi gas is encapsulated in a single universal number. Obviously, while the form of the EoS can simply be deduced on dimensional grounds only, the *ab-initio* calculation of ξ_s requires to solve the fermion many-body problem and is a formidable theoretical challenge, that is still unsettled. Averaging our data at unitarity gives a result of 0.41(1). These measurements were taken at a magnetic field of 835.5 G. The comparison with the result expected at 834.1 is studied in section 5.3. Correcting for the 1.4 G shift using the contact and taking into account the uncertainty on the Feshbach resonance position ($B_0 = 834.1 \text{ G} \pm 1.5 \text{ G}$ [72]), we find $\xi_s = 0.40(2)$.

5.2.5 Asymptotics III: the BEC-limit of a Weakly Interacting Bose Gas

In the limit where $a \rightarrow 0^+$, the two-body potential sustains a bound state that is spatially localized (with a size $\sim a$). The dimers can thus be considered as pointlike bosons, and the Fermi gas will have the properties of a Bose gas of ⁶Li₂ dimers. It is then natural to wonder whether the ground-state energy of the system can be expanded in powers of the gas parameter as for a Bose gas (see chapter 3). First, the mean-field energy $g_{dd}n_d^2/2$ (where n_d is the dimer density) will depend on the dimer-dimer scattering length. This scattering length was determined by solving the scattering four-body problem and it was found that $a_{dd} = 0.6a$ [38], in sharp contrast with the BCS mean-field prediction $a_{dd} = 2a$. Fitting the energy deeply in the BEC regime, G. Astrakharchik *et al.* found that the EoS was well described by a mean-field energy with a effective scattering length of $a_{dd} = 0.62(1)$ [44], thus confirming that the first term of the energy expansion is valid provided the $g_{dd} = 2\pi\hbar^2 a_{dd}/m$ (where m is the fermion mass, half the mass of the dimer).

²⁹See section 5.3.2 for details.

³⁰As an example, the calculation on the BCS side gives:

$$\mathcal{I}(\delta_0) = \frac{128\sqrt{2}}{15} \int_0^1 du u^2(1-u^2)^2 h'(\delta(u)) \quad (5.62)$$

$$N(\delta_0) = \frac{16}{15\pi} \int_0^1 du u^2(1-u^2)^{3/2} (5h(\delta(u)) - \delta(u)h'(\delta(u))) \quad (5.63)$$

$$\frac{1}{k_{Ft}a} = \frac{\delta_0}{(6N(\delta_0))^{1/6}} \quad (5.64)$$

where $\delta(u) = \delta_0/\sqrt{1-u^2}$. The calculation on the BEC side is similar except that care must be taken for the shift of the binding energy in the chemical potential. Interestingly, the calculation is more straightforward than the same calculation performed in the canonical ensemble, in the appendix C of [280].

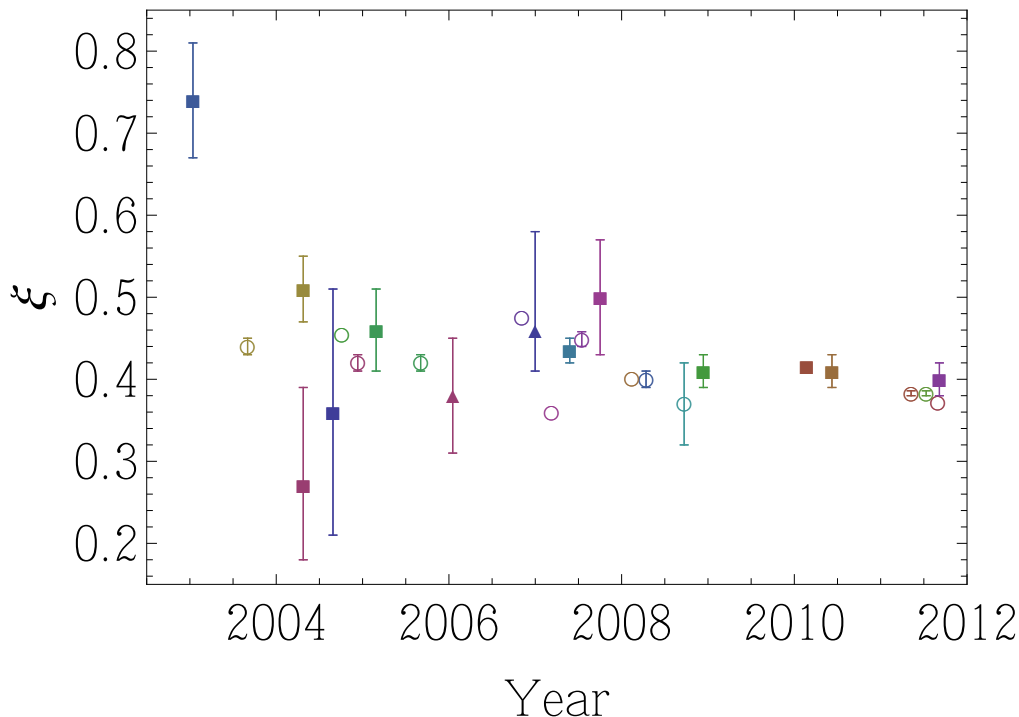


Figure 5.23: Predictions and measurements of the Bertsch parameters ξ_s . From left to right, the measurements on ${}^6\text{Li}$ are shown in full squares: [13], [255] (up) [281] (down), [27, 137, 282, 235, 249, 113, 62], and this work. In full triangles, the works on ${}^{40}\text{K}$: [283, 108]. The open circles are theoretical calculations: [228, 284, 44, 285, 286, 202, 287, 259, 189, 230, 263, 288, 289]. The value predicted from BCS mean-field theory is $\xi_s = 0.59$ [23].

X. Leyronas and R. Combescot showed afterwards that this intuitive replacement is also correct for the first beyond mean-field term, the Lee-Huang-Yang correction [45]. It is remarkable that the composite nature of the dimer does not show up in the energy expansion up to this order. We can test this expansion, assuming the mean-field energy:

$$\frac{E}{V} = nE_b + \frac{g_{dd}n^2}{2} \left(1 + \alpha_{\text{LHY}} \sqrt{na_{dd}^3} + \dots \right), \quad (5.65)$$

where the first term accounts for the binding energy of the molecular Bose gas. Fitting the Padé approximant on the BEC side³¹ with Eq.5.65, we find $\alpha_{\text{LHY}} = 4.4(5)$, in good agreement with the calculation by Lee, Huang and Yang: $128/15\sqrt{\pi} \approx 4.81$.

Going beyond the LHY correction for the Bose gas of Feshbach molecules is a delicate problem. The simplest approach would be to assume that the expansion for molecules can be derived from that of a Bose gas (see Eq.3.25), provided we replace a by a_{dd} , m by $2m$, and n by $n/2$. In the same spirit of section 3.3.4, we assume the LHY coefficient and fit the parameter B , for which we find $B \approx 7$. It is interesting to note that this value is close both to the calculation for a hard-sphere Bose gas ($B = 8.5$ [171]), for a Bose gas with contact interactions ($B \approx 7.2$ [172]) as well as the value $B = 6.8$ estimated on the EoS for the Bose gas in chapter 3. It is however important to keep in my mind that it is unknown whether the energy expansion is still valid up to

³¹Details about the Padé approximants can be found in appendix A.2.

that order for a gas of dimers. This raises an interesting question: while it is known that B is not universal for pointlike bosons (as it involves the three-body problem, which in turn depends on short-range physics [172]), we can expect this parameter to be truly universal for a Fermi gas. First, the hypothesis of universality of the BEC-BCS crossover would imply that B cannot depend on another parameter than a . Second, the short-range physics of dimers can in principle be described by the a only, because the internal structure of the molecules is also given by the scattering length. These questions would be answered by solving the three-dimer or six-fermion problem.

5.2.6 Universality of the Lee-Huang-Yang correction

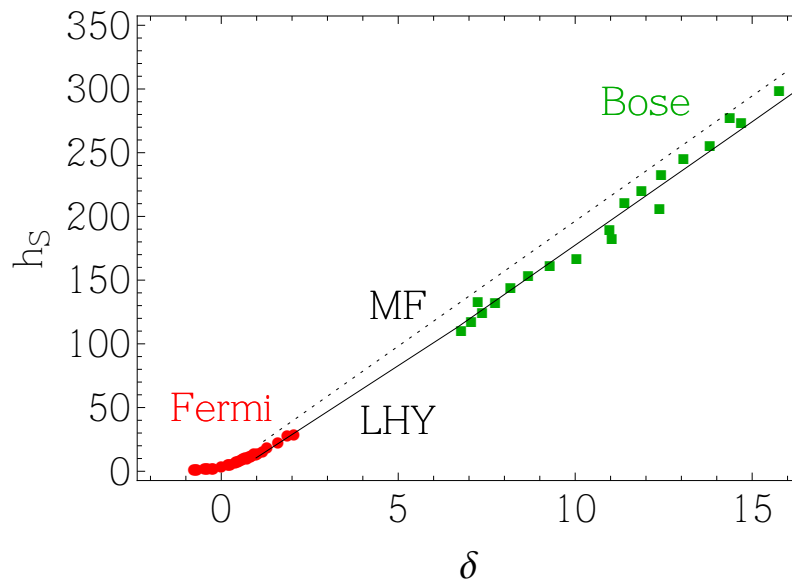


Figure 5.24: Low-temperature Equations of State of the atomic Bose (green squares at large $\delta > 0$, rescaling the bosonic a to the dimer-dimer a_{dd}) and spin-1/2 Fermi gases (red circles at small δ) with short-range interactions. The mean-field (Lee-Huang-Yang) EoS is shown in dotted (solid) black line.

Finally, it is instructive to gather the low-temperature equations of state obtained on the bosonic ${}^7\text{Li}$ (in chapter 3) and on the fermionic ${}^6\text{Li}$ (in the present chapter), as shown in Fig.5.24. The Bose (Fermi) gas EoS is shown in green squares (red circles). In order to plot the bosonic EoS on the Fermi gas representation, it is important to keep in mind that the two Bose gases interact via different scattering lengths. To find the appropriate rescaling, we write the EoS of the molecular Bose gas in the BEC limit (see appendix A.2.4 for details): $h_S \rightarrow \frac{15}{4} \frac{a}{a_{dd}} \delta$ (when $\delta \rightarrow +\infty$) and rescale it so that the EoS of the atomic Bose gas in the mean-field limit is identical provided one replaces a_{dd} by a_B . The fact that both measurements fall on the Lee-Huang-Yang EoS shows that despite the two Bose gases have very different interaction potentials, the first beyond mean-field correction depends only on the scattering length. It is obviously interesting to explore the region in between the two measurements. However, it is difficult due to stability issues: for the molecular Bose, weakening the interactions make the dimers smaller, and the gas is increasingly unstable due to collisional relaxation losses as the dimers are no longer Pauli-protected against three-body recombination into deeply bound states. The Bose gas on the other hand becomes unstable due to increasing three-body losses. Nonetheless, even if these losses could be prevented, it is not clear

that the two curves would join since we know that the term beyond the Lee-Huang-Yang correction is non-universal for a Bose gas with short-range interaction. In addition, these systems should belong to different many-body branches: attractive Fermi gas for one (lower-branch), repulsive Bose gas for the second one (upper-branch), and different crossover physics might be expected [290].

5.3 Finite Scattering Length Corrections

Subsequent refined magnetic field calibration have shown that our data at unitarity have been most likely taken at a magnetic field of 835.5 G, rather than 834.1 G³². The current most precise determination of the Feshbach resonance, $B_0 = 834.1(1.5)$ G does not discriminate between these two values. However, since most other experiments are reported at 834.1 G, it is instructive to estimate the effect of the finite scattering length on the previously obtained results, mostly the Bertsch parameter ξ_s and the EoS $h(\zeta)$ of the unitary gas. First, $\delta(1/a) = \delta B/\Gamma$ where the width of the resonance for ⁶Li is $\Gamma = a_{bg}\Delta = 4.2 \times 10^5 a_0 \cdot \text{G}$. For a shift of 1.4G we find $\delta(1/a) = -3.3 \times 10^{-6} a_0^{-1}$. If the center of the resonance is at 834.1 G, the scattering length is $a/a_0 = -3 \times 10^5$ at 835.5 G, very large but not infinite.

Taking a conservative lower bound for k_F (at the edge of the superfluid region in the spin-imbalanced mixture), $1/k_F \approx 300$ nm, we have a deviation of at most $|1/k_F a| = 0.02$ from the resonance, which given a contact density $\zeta_C = 0.93$ determined in section 5.2.4, would lead to a maximum down shift of 0.02 for ξ_s . However, as we shall see in chapter 6, this is an upper bound to the error committed since the local value of the interaction parameter δ varies in the trap. Taking this into account on the spin-polarized gas analysis, a more realistic correction of the systematic error assuming the resonance position at 834.1 G leads to $\xi_s = 0.40(2)$ (see section 6.2.5). We now investigate the effects of finite- a corrections on the equation of state of the unitary gas determined in chapter 5.

5.3.1 The virial coefficients b_2 and b_3 in the BEC-BCS crossover

The virial expansion, which is an expansion in powers of the fugacity $e^{\beta\mu}$ can be extended beyond unitarity:

$$P(\mu, T, a)\beta\lambda_{dB}^3/2 = e^{\beta\mu} + \tilde{b}_2(T, a)e^{2\beta\mu} + \tilde{b}_3(T, a)e^{3\beta\mu} + \dots, \quad (5.66)$$

where the virial coefficients \tilde{b}_j depend on T and a . By dimensional analysis, the virial coefficients at unitarity are independent of temperature, since the \tilde{b}_j are dimensionless. Away from unitarity, the coefficients can depend on T and a only through a/λ_{dB} . In particular, the two first virial coefficients \tilde{b}_2 and \tilde{b}_3 were calculated as a function of $1/k_F a$ for various temperatures T/T_F in Fig.3 of [208]. However, we found that the curves at different temperatures collapse on a single universal function of a/λ_{dB} for each coefficient. The result is shown in Fig.5.25. In order to obtain a conservative estimate, we take for $\lambda_{dB}(T)$ an intermediate temperature of 1 μK , for which the deviation from unitarity in term of a/λ_{dB} is about 0.04. Both b_2 and b_3 vary by less than 5 %, well within the error bar stated in Eq.(5.17), and this is an upper bound.

³²The refined calibration has been performed more than a year after the original data taking and it is thus not excluded that the magnetic trap has slightly moved, leading to a possible minute change in the bias field, for the same set of currents in the coils as in the original experiment.

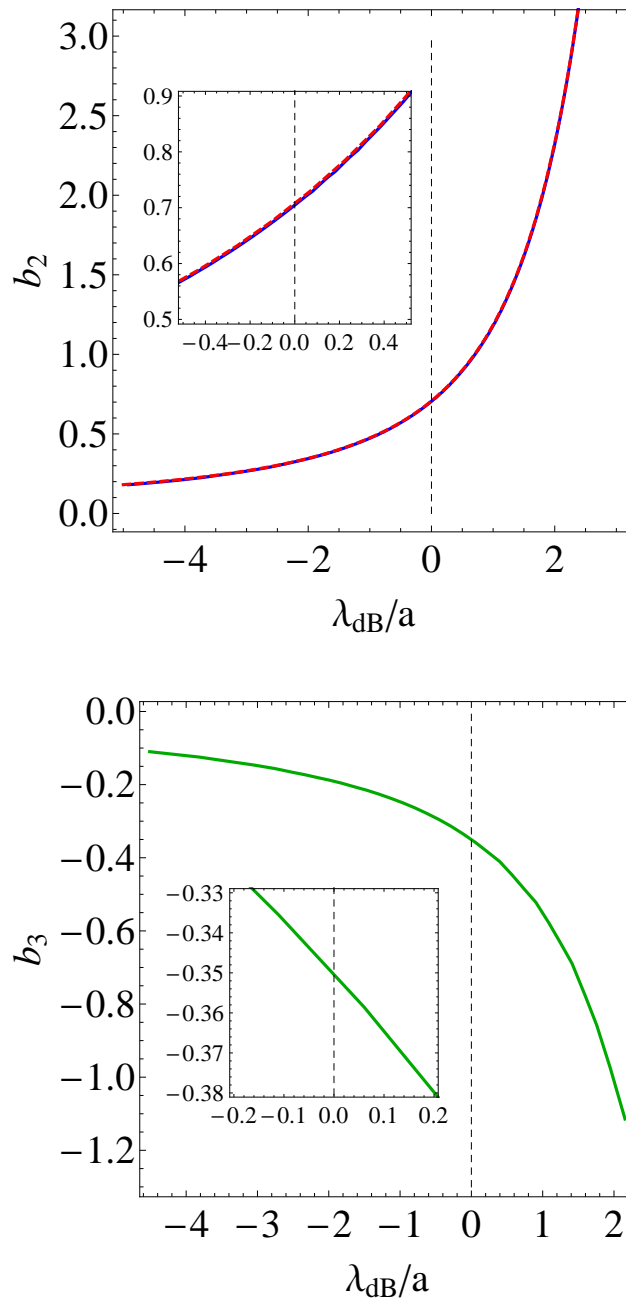


Figure 5.25: Virial coefficients b_2 (upper) and b_3 (lower panel) in the BEC-BCS crossover, as a function of a/λ_{dB} . Zoom around unitarity are shown in insets. The Beth-Uhlenbeck formula (5.13) is shown in dashed red for b_2 . The calculation of b_2 from the coefficient b_2^t for the trapped gas is in near perfect agreement with the Beth-Uhlenbeck formula as expected.

5.3.2 Tan Contact at Finite Temperature

Following an idea of the Amherst-MIT collaboration [115], we can calculate the correction away from unitarity using the Tan contact at finite temperature. We recall that the contact is defined

as:

$$\frac{dE}{d(-1/a)} = \frac{\hbar^2}{4\pi m} \mathcal{I}, \quad (5.67)$$

The contact can be expressed in the grand-canonical ensemble using the relation

$$\left(\frac{\partial E}{\partial(-1/a)} \right)_{S,V,N} = \left(\frac{\partial \Omega}{\partial(-1/a)} \right)_{T,V,\mu} \quad (5.68)$$

where $\Omega = -PV$ is the grand-potential³³. Using the contact density $C = \mathcal{I}/V$, we can write to lowest order in a^{-1} :

$$P(\mu, T, a^{-1}) = P(\mu, T, 0) + a^{-1} \frac{\hbar^2}{4\pi m} C(\mu, T, 0) \quad (5.72)$$

where the contact density at unitarity is a function of $\beta\mu$. We can thus write the finite a correction to the universal h -function:

$$h(\zeta) - h_a(\zeta) = \frac{1}{8\pi^2} \frac{\lambda_{\text{dB}}}{a} \frac{\tilde{C}(\zeta)}{\text{Li}_{5/2}(-\zeta^{-1})} \quad (5.73)$$

where $h_a(\zeta)$ is the pressure away from unitarity, $\tilde{C}(\zeta) = C\lambda_{\text{dB}}^4$ is the dimensionless contact density. In order to calculate the correction, we need both the contact density $\tilde{C}(\zeta)$, and λ_{dB}/a . Differentiating the virial expansion of the grand-potential Eq.(5.66) with respect to $1/a$ (with Eqs.(5.67) and (5.68)) we find a virial expansion for the contact density:

$$C\lambda_{\text{dB}}^4 = 16\pi^2 (c_2 e^{2\beta\mu} + c_3 e^{3\beta\mu} + \dots) \quad (5.74)$$

with

$$c_j = \frac{\partial b_j}{\partial(\lambda_{\text{dB}}/a)}. \quad (5.75)$$

Since the first coefficient b_1 is constant, the virial expansion for the contact starts at the second-order in fugacity. The c_2 coefficient can be readily calculated from the explicit expression of b_2 from Beth-Uhlenbeck formula in Eq.(5.14) and we find $c_2 = 1/\pi$ [291]. The derivative of b_3 at unitarity (see Fig.5.25b) provides the third virial coefficient for the contact: $c_3 = -0.141$ [274].

The contact has otherwise been calculated at finite temperature by analytical [276, 274], and Quantum Monte Carlo methods [292] but these calculations normalize the contact to the density C/k_F^4 and we thus also need the equation of state $n\lambda_{\text{dB}}^3(\beta\mu)$ to convert the contact to the normalization $C\lambda_{\text{dB}}^4(\zeta)$. A DMC calculation of $C\lambda_{\text{dB}}^4(\zeta)$ was directly performed by the Amherst group (blue circles in Fig.5.26) and we will use this one for the correction [115]. On Fig.5.26, we also

³³The relation (5.68) can be easily demonstrated by proving the same relation first for the Helmholtz free energy $F(T, V, N)$ and differentiating the relation $F = E - TS$ (V is fixed):

$$\left(\frac{\partial E}{\partial(-1/a)} \right)_{S,N} = \left(\frac{\partial F}{\partial(-1/a)} \right)_{S,N} + S \left(\frac{\partial T}{\partial(-1/a)} \right)_{S,N} \quad (5.69)$$

We use a common formula for changing the variable that is kept fixed:

$$\left(\frac{\partial F}{\partial(-1/a)} \right)_{S,N} = \left(\frac{\partial F}{\partial(-1/a)} \right)_{T,N} + \left(\frac{\partial F}{\partial T} \right)_{a,N} \left(\frac{\partial T}{\partial(-1/a)} \right)_{S,N} \quad (5.70)$$

Since $\left(\frac{\partial F}{\partial T} \right)_{a,N} = -S$, we find that:

$$\left(\frac{\partial E}{\partial(-1/a)} \right)_{S,V,N} = \left(\frac{\partial F}{\partial(-1/a)} \right)_{T,V,N} \quad (5.71)$$

Using the same relation with the additional Legendre transform $\Omega = F - \mu N$, Eq.5.68 is recovered.

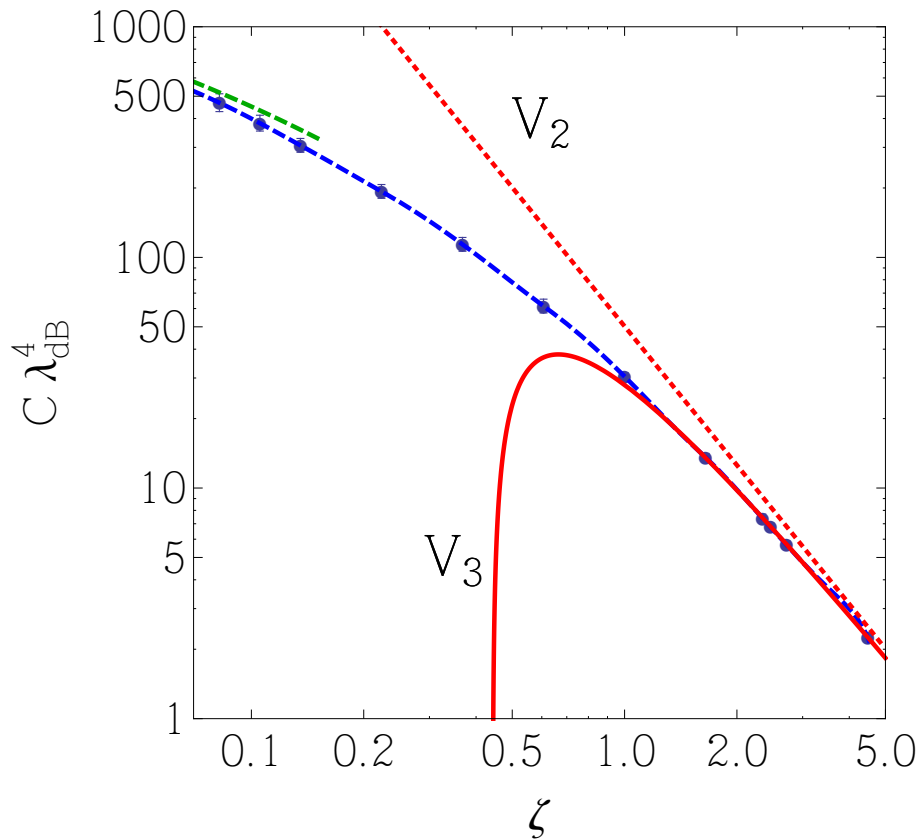


Figure 5.26: Finite-temperature contact $C\lambda_{\text{dB}}^4$ versus ζ . The DMC calculation is shown in blue circles [115], the interpolation function used in the text, in dashed blue line. The second-order (third-order) virial expansion is plotted in red dashed (solid) line. The $T = 0$ contact determined in chapter 5 is plotted in dashed green.

show the second-order (third-order) expansion of the contact in red dashed (solid) line. The $T = 0$ limit of the contact can be displayed on this plot, though it requires the EoS, since we have:

$$C\lambda_{\text{dB}}^4 = \frac{2\zeta_C}{5\pi} (3\pi^2)^{4/3} (n\lambda_{\text{dB}}^3)^{4/3}, \quad (5.76)$$

where the contact in the zero-temperature limit is $C/k_F^4 = 2\zeta_C/5\pi$. Since the DMC calculations are limited to $\zeta > \zeta_c = 0.05$ (where ζ_c is the critical inverse fugacity for the superfluid transition), we can use the Fermi-liquid parametrization of the pressure from Eq.(5.29) to deduce the phase-space density in Eq.(5.76) at low temperature. Using $\zeta_C = 0.93$ found in section 5.2.4, we compute $C\lambda_{\text{dB}}^4(\zeta)$ at zero temperature (dashed green line on Fig.5.26).

5.3.3 Estimate of the Correction for the Equation of State $h(\zeta)$

The value of λ_{dB}/a is estimated by measuring the temperature of the gas obtained as a function of the fugacity for which it contributes (we take here ζ_0). This is shown in gray points on Fig.5.27, together with an empirical fit $\lambda_{\text{dB}} = (0.647\mu\text{m}) \times \zeta^{-0.275}$ in red solid line³⁴. Using this estimate

³⁴Let us recall that the images are taken at various depth, trap frequencies and atom number and as such, images at different temperatures could contribute for a same window of ζ . The relation between $\lambda_{\text{dB}}(T)$ and ζ is thus only

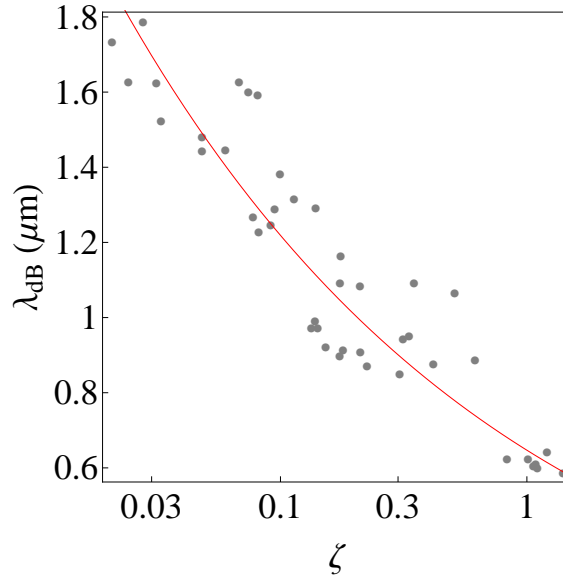


Figure 5.27: Estimation of the average value of λ_{dB}/a for a data set (gray circles) and an empirical fit $\lambda_{dB} = (0.647\mu\text{m}) \times \zeta^{-0.275}$ in red solid line.

for λ_{dB}/a , we calculate the shift from our original EoS (black empty circles) and estimate the EoS at 834.1 G from Eq.(5.73) and obtain the full red circles. The largest systematic error occurs at the lowest temperatures, where the upshift is 4 %. We see that the agreement between our EoS estimated at 834.1 G (red circles), the reanalyzed EoS from the Tokyo group (empty blue squares), and the Amherst Diagrammatic Monte Carlo calculation (brown solid line) is slightly improved in the low-temperature regime above T_c . The very good agreement between the experiments and theory for a strongly correlated many-body system almost down to T_c is remarkable.

The state of art techniques to probe quantum many-body physics with ${}^6\text{Li}$ have now reached a level of accuracy that requires an improved determination of the position (and width) of the Feshbach resonance (in particular for the measurement of ξ_s). Previous characterizations of the wide resonance on the $|1\rangle - |2\rangle$ spin-mixture of ${}^6\text{Li}$ include a thermodynamic determination ($B_0 = 800(40)$ G, [250]), dissociation of molecules ($B_0 = 822\dots 834$ G, [76]), and molecular radio-frequency spectroscopy ($B_0 = 834.1(1.5)$ G [72]). This last method is generally considered as the most reliable one. However, the regime where $k_F a \gg 1$ is very extended and the RF-association (or dissociation) of Feshbach molecules can only be performed very far from the resonance (about 100 G below) in order to avoid important many-body effects. This is due to the very large width of the resonance. We can compare here the case of ${}^6\text{Li}$ and ${}^7\text{Li}$. The spectroscopic determination of the Feshbach resonance on state $|F = 1, m_F = 1\rangle$ of ${}^7\text{Li}$ was shown in chapter 3 and a scattering length $a/a_0 = 2000$ (where beyond mean-field start to become important) is reached about 2 G below the resonance, for which the Feshbach binding energy is $E_b = h \times 150$ kHz. The same scattering length for ${}^6\text{Li}$ is reached about 110 G below the resonance³⁵.

an estimate but we see that the dispersion around the fit is reasonably small (less than 20 % on the value of the correction, whose absolute value is at most of 4 %). A more rigorous approach would be to perform the correction image per image, and then only, fitting μ_0 for the patching.

³⁵The relevant quantity is not the width Δ of the resonance but the product $\Gamma = a_{bg}\Delta$. While the widths are similar $\Delta_6 = 300$ G and $\Delta_7 = 170$ G, the products are not: $\Gamma_7 = 3550$, $\Gamma_6 = 4.2 \times 10^5$ (in units of $a_0\text{G}$), owing to

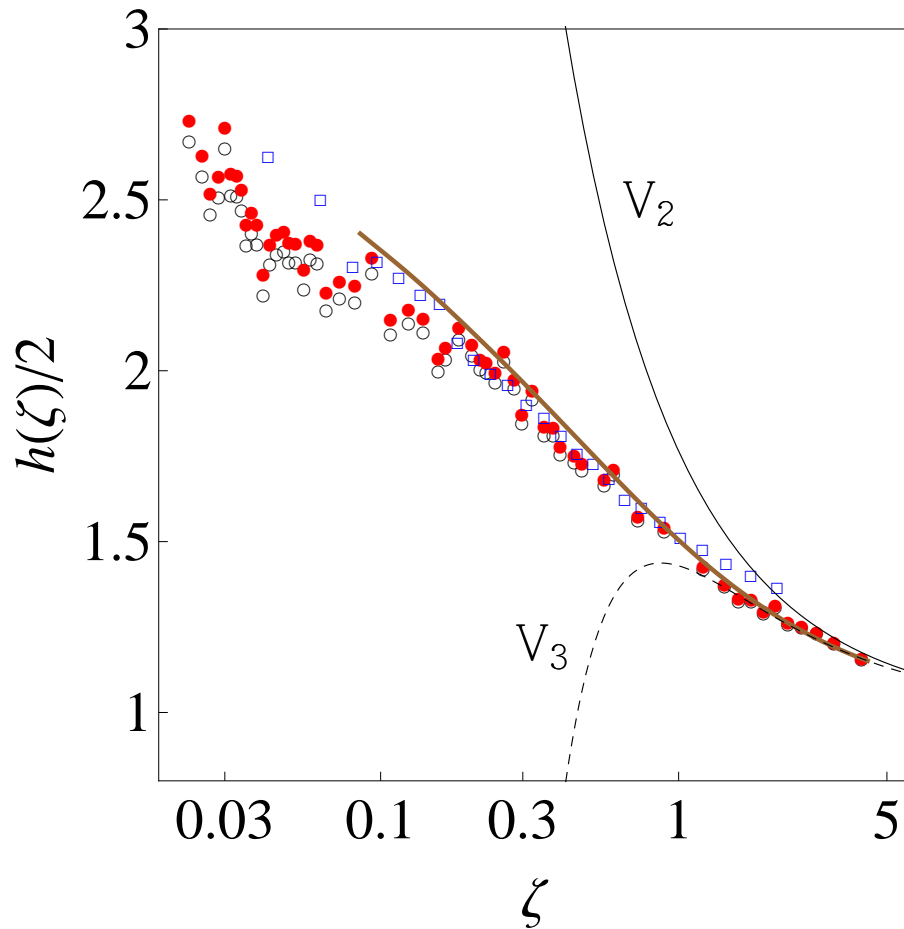


Figure 5.28: Finite-temperature correction on the equation of state using the contact. Together with our measurement (empty black circles), we plot the EoS estimated at 834 G (red circles), the reanalyzed Tokyo EoS (empty blue squares) and the DMC (brown solid line).

Methods to determine more accurately the Feshbach resonance position (and width) without theoretical input (as was required in [72] for example) remain to be devised. A possibility could be to measure the dissociation spectra in time-of-flight on a gas of molecules, and extrapolate the binding energy in the dilute limit $n \rightarrow 0$. Since the deterministic preparation of trapped few-fermion systems is now experimentally achievable [293], it would be possible to measure the binding energy of a single trapped molecule, in which case many-body effects would obviously be inexistent. An elegant determination of the Feshbach resonance position would be to directly observe the scale invariance of the unitary gas, for example by proving that all quantities depend only on the local Fermi energy E_F of the system. For example, the measurement of ξ_s should be shown to be independent of the gas density (or equivalently, of k_F). This wouldn't be true away from unitarity, where an energy scale associated with a is also involved.

In conclusion, we have measured in this chapter the equation of state of the spin-balanced Fermi gas. In a first part, we studied the finite-temperature thermodynamics of the uniform unitary Fermi

the very large background scattering length of ${}^6\text{Li}$ in the mixture of states |1) and |2).

gas, allowing for a direct comparison with many-body theories. We measured the virial expansion at high-temperature, and observed a Fermi-liquid type behavior at low-temperature. Using the parameters of the Fermi liquid, we have predicted the spectral functions, that are in good agreement with photoemission spectroscopy experiments performed at JILA. In the second part, we measured the equation of state of the low-temperature Fermi gas in the BCS-BCS crossover. In the asymptotic limit, we have shown the universality of the Lee-Huang-Yang correction, identical for atomic and molecular Bose gases. In addition to the asymptotic limits, we have compared the prediction of our equation of state to measurements of the contact in a trapped gas.

In spite of the intense research effort, much work is still necessary to have a full quantitative understanding of the thermodynamics of the unitary Fermi gas. In addition, there are many open questions. First, the scale invariance of the unitary gas has never been directly tested. Secondly, increasing the accuracy on the measurement of ξ would now be desirable to provide extremely stringent benchmarks for theories. This in turn will require an improved precision on the determination of the Feshbach resonance position as seen above. The exact nature of the normal phase also needs to be clarified. New methods should be devised to address the ongoing pseudo-gap/Fermi liquid debate, such as spatially resolved photoemission spectroscopy, and could also allow to describe recent spin-transport [294] and viscosity [194] measurements performed in the normal phase. In addition, the thermodynamic study presented here should be extended in the BEC-BCS crossover, and would yield the critical temperature T_c of the homogeneous gas as a function of interaction strength, one of the most fundamental quantity of the BEC-BCS crossover physics.

Chapter 6

The Spin-Polarized Fermi Gas

The fundamental question of fermionic superfluidity with spin-population imbalance $n_{\downarrow} \neq n_{\uparrow}$ has been studied since the early 1960's and the work by Clogston and Chandrasekhar [295,296]. Despite important efforts in condensed matter physics [297], the first unambiguous experimental evidence for the robustness of the unpolarized superfluid to spin-imbalance came with ultracold Fermi gas experiments performed at MIT and Rice University in 2006 [137,298]. In these experiments, it was observed that the trapped unitary gas phase-separates and adopts a shell-like structure. In the center of the trap, an unpolarized ($n_{\downarrow} = n_{\uparrow}$) superfluid accommodates spin-imbalance by expelling the excess atoms in a surrounding polarized normal shell. These experiments triggered a rush of interest in the rich phase diagram of the system at low temperature, and searches for predicted exotic phases.

In this last chapter, we address the thermodynamics of the spin-population imbalanced Fermi gas. First, we will review basic facts about the phase diagram and the physics that arises from the spin imbalance. We then present the implementation of the equation of state measurement scheme in the case of spin-imbalanced systems, allowing us to explore the phase diagram of the system. Finally we compare our equation of state with previous measurements performed on trapped samples and with the canonical equation of state obtained for the uniform gas at MIT.

6.1 Overview of the Phase Diagram

We introduce the main concepts of spin-imbalanced Fermi gas physics, starting with the Clogston-Chandrasekhar limit of superfluidity. We will then expose the theory of highly-imbalanced gases and the Fermi polaron, a quasi-particle composed of a single minority atom immersed in a Fermi sea of majority atoms that is of central relevance to the normal phase of the imbalanced Fermi gas.

6.1.1 The Clogston-Chandrasekhar Limit

As the key ingredient for BCS superconductivity is the Cooper pairing of spin \uparrow and \downarrow particles with opposite momenta, the question naturally arises whether the unpolarized superfluid can survive if a spin-polarizing field is applied. This is related to the energy competition between the gain in flipping the spin of one particle and the cost of breaking a pair. In the grand-canonical ensemble, the ground state is obtained by minimizing the grand-potential:

$$\Omega(\mu_{\uparrow}, \mu_{\downarrow}) = E - \mu_{\uparrow}N_{\uparrow} - \mu_{\downarrow}N_{\downarrow} = E - HM - \bar{\mu}N, \quad (6.1)$$

where $M = N_\uparrow - N_\downarrow$ is the polarization, $N = N_\uparrow + N_\downarrow$ the total atom number, $\bar{\mu} = (\mu_\uparrow + \mu_\downarrow)/2$ the mean chemical potential, and $H = (\mu_\uparrow - \mu_\downarrow)/2$ the effective “magnetic” (or spin-polarizing) field¹. The robustness of the unpolarized superfluid state was first addressed very soon after the discovery of BCS theory by Clogston and Chandrasekhar [295, 296]. They compared the energy of the superconducting state to that of the normal state and they showed that the BCS superconducting state has a lower energy provided the effective magnetic field H is smaller than a critical value $H < H_c = \Delta/\sqrt{2}$, where $\Delta = 8e^{-2} \exp(-1/2k_F|a|)$ is the pairing gap. The BCS superfluid will be exponentially fragile in $1/k_F a$ to spin-imbalance. Since $H_c < \Delta$, the transition to a normal state occurs before the superfluid becomes polarized². Because the unpolarized superfluid is still a local minimum in the energy landscape (see for instance [299]), the transition is first-order. Deep in the BEC region, the picture is different. The energy cost to flip a spin is essentially the bound state energy of a dimer, \hbar^2/ma^2 , and this energy is increasingly large in the BEC limit. The system will be robust to the presence of an effective magnetic field. In this case however, the unpolarized superfluid is not a local minimum anymore and a second-order transition to a polarized superfluid occurs [300]³. The gas is then a molecular Bose gas immersed in a Fermi sea of unpaired excess atoms.

6.1.2 The $N + 1$ body problem: the Fermi Polaron

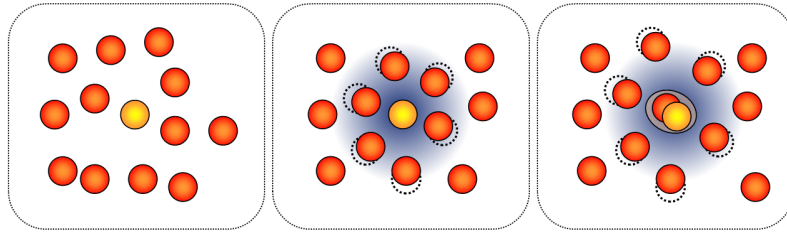


Figure 6.1: Sketch of the impurity \downarrow particle in a Fermi sea of \uparrow atoms (left panel). The interactions with the majority atoms lead to a dressing of the minority atom, the Fermi polaron (middle panel). If the interactions are further increased, the \downarrow -atom binds with a single \uparrow -atom forming a molecule that interacts with the rest of the Fermi sea.

Another important limiting case is that of highly-imbalanced samples, namely a single minority \downarrow particle immersed in a Fermi sea of \uparrow atoms. In the phase diagram, this corresponds to the line between the fully polarized phase at large effective field and a partially polarized phase (either normal or superfluid). This question was first addressed analytically in [112, 301]. F. Chevy proposed an intuitive variational ansatz describing the scattering of the \downarrow particle, creating one

¹The effective field is usually written h in the literature but we avoid this notation because of the h -pressure function.

²The system becomes polarized when it is energetically favored to flip a spin. We calculate the variation of the grand-potential $\delta\Omega$ for flipping one atom from Eq.(6.1): $\delta M = 2$ (and $\delta N = 0$). If the system is paired, this results in breaking a pair: $\delta E = 2\Delta$. The unpolarized system is protected as long as $\delta\Omega > 0$, or $H < \Delta$.

³A simple mean-field model of this picture can be found in [300], and one finds:

$$\frac{H_c}{E_F} = \frac{1}{(k_F a)^2} + \frac{1}{2\pi k_F a} \left(a_{ad} - \frac{a_{dd}}{6} \right), \quad (6.2)$$

where a_{ad} (a_{dd}) is the atom-dimer (dimer-dimer) scattering length.

particle-hole excitation in the \uparrow Fermi sea [301]:

$$|\psi\rangle = \phi_{\mathbf{k}_0} |\mathbf{k}_0, \text{FS}\rangle + \sum_{\mathbf{k}, \mathbf{q}} \phi_{\mathbf{k}, \mathbf{q}} a_{\mathbf{k}\uparrow}^\dagger a_{\mathbf{q}\uparrow} |\mathbf{k}_0 + \mathbf{q} - \mathbf{k}, \text{FS}\rangle \quad (6.3)$$

where $|\mathbf{k}_0, \text{FS}\rangle$ is the Fermi sea of \uparrow and the \downarrow particle has a momentum \mathbf{k}_0 . The second term describes the particle-hole excitations, with a majority atom of the Fermi sea of momentum \mathbf{q} ($q < k_F$) being excited to a momentum \mathbf{k} ($k > k_F$), and to conserve momentum, the minority particle acquires a momentum $\mathbf{k}_0 + \mathbf{q} - \mathbf{k}$. To determine the properties of the minority atom interacting with the Fermi sea, one finds the ϕ_0 and $\phi_{\mathbf{k}, \mathbf{q}}$ parameters which minimize the expectation value of the Hamiltonian describing a two-component Fermi gas with short-range interactions:

$$\hat{H} = \sum_{\mathbf{k}\sigma} \epsilon_{\mathbf{k}} a_{\mathbf{k}\sigma}^\dagger a_{\mathbf{k}\sigma} + \frac{g_0}{V} \sum_{\mathbf{k}, \mathbf{k}', \mathbf{q}} a_{\mathbf{k}+\mathbf{q}\uparrow}^\dagger a_{\mathbf{k}'-\mathbf{q}\downarrow}^\dagger a_{\mathbf{k}'\downarrow} a_{\mathbf{k}\uparrow} \quad (6.4)$$

where $\epsilon_{\mathbf{k}} = \hbar^2 k^2 / 2m$, $a_{\mathbf{k}\sigma}$ is the annihilation operator of particle of spin σ and momentum \mathbf{k} , and g_0 is the bare coupling constant. The minimization leads to an implicit equation for the energy of the minority particle:

$$E = \epsilon_{\mathbf{k}_0} + \frac{1}{V} \sum_{q < k_F} \frac{1}{g_0} + \frac{1}{V} \sum_{k > k_F} \frac{1}{\epsilon_{\mathbf{k}} - \epsilon_{\mathbf{q}} + \epsilon_{\mathbf{k}_0 + \mathbf{q} - \mathbf{k}} - E} \quad (6.5)$$

This expression requires a renormalization of the bare coupling constant g_0 , that needs to be replaced by the scattering length, using the Lippman-Schwinger equation $\frac{1}{g_0} = \frac{m}{4\pi\hbar^2 a} - \frac{1}{V} \sum_{\mathbf{k}} \frac{1}{2\epsilon_{\mathbf{k}}}$. At low momenta, the dispersion relation of the impurity can be expanded as:

$$E(\mathbf{k}_0) = AE_F + \frac{\hbar^2 k_0^2}{2m^*} + \dots \quad (6.6)$$

The minority atom becomes dressed by the interaction with the Fermi sea and the resulting quasi-particle is called the *Fermi polaron*. The polaron has two important properties: a binding energy AE_F and an effective mass m^* . For a free particle, one would have $A = 0$ and $m^* = m$. To determine these quantitatively, we replace the sums in Eq.(6.5) by integrals, and solve Eq.(6.5) for the energy. At unitarity $1/a = 0$ we find $A = -0.607$ and $m^*/m = 1.17$. This calculation can be performed as a function of $1/k_F a$ [302], and the result is shown by the dashed black line in Fig.6.2. The polaron characteristics have been determined accurately by more advanced approaches: two Fixed-Node calculations find $A = 0.58(1)$ and $m^*/m = 1.04(3)$ [229] (black triangle in Fig.6.2b), and $A = 0.59(1)$ and $m^*/m = 1.09(2)$ [261] (green diamonds in Fig.6.2). An analytical approach taking into account two particle-hole excitations yields $A = 0.6156$ and $m^*/m = 1.20(2)$ [303] (blue circles in Fig.6.2b). A Diagrammatic Monte Carlo calculation yields $A = 0.615$ and $m^*/m = 1.225(50)$ [304, 305, 306] (red squares in Fig.6.2). It is remarkable that the simple variational treatment (6.3) gives a quantitatively reasonable picture of the Fermi polaron. All theoretical calculations are in reasonable agreement for the binding energy of the polaron, together with the measurement at MIT, $A = -0.58(5)$ [132]. On the other hand, there are important quantitative differences concerning the effective mass, together with the experimental measurements from MIT, using a density profile analysis ($m^*/m = 1.06$) [111], and from our group, using a collective modes study ($m^*/m = 1.17(10)$) [63]. Nevertheless, all determinations agree that the effective mass of the Fermi polaron is close to unity and is thus surprisingly barely modified by the interactions, contrary to other strongly interacting systems such as ^4He (see section 5.1.5).

The Polaron-to-Molecule Transition

The properties of the Fermi polaron can be calculated in the BEC-BCS crossover, giving the line in the phase diagram between the fully polarized and a partially polarized normal phase. Indeed,

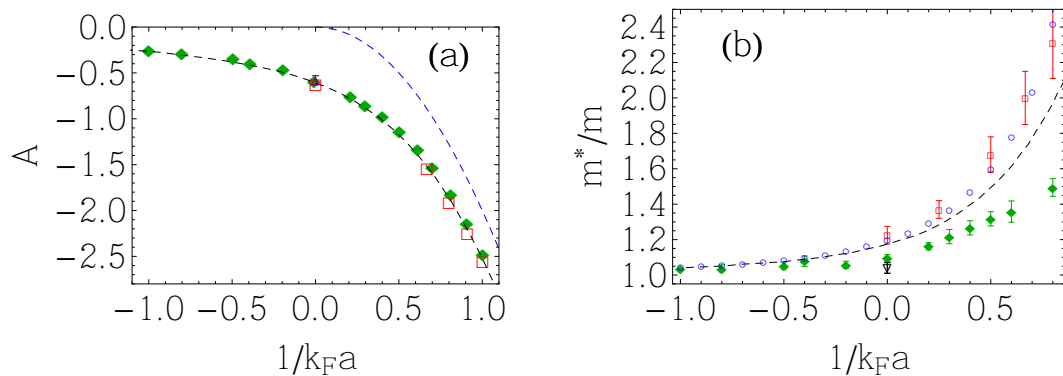


Figure 6.2: Properties of the Fermi Polaron. (a): The binding energy A of the Fermi polaron (where $E = AE_F$). Theoretical predictions: the single particle-hole ansatz (dashed black line [302]), a Diagrammatic Monte Carlo calculation (red squares [304]), and a Fixed-Node Monte Carlo (green diamonds [261]). A RF-spectroscopy measurement is in agreement with the calculations at unitarity $A = -0.58(5)$ (purple triangle [132]). The binding energy on the BEC side is shown in dashed blue line. (b): The effective mass m^*/m as predicted by a one-particle-hole (dashed black line [302]), and two-particle-hole analytical calculation (blue circles [303]), together with a Fixed-Node result at unitarity (black triangle [229]). The Fixed-Node Monte Carlo calculation from [261] is shown in green diamonds.

in this case $H_s/E_F = (\mu_\uparrow - \mu_\downarrow)/2E_F = (1 - A)/2$ (since $\mu_\uparrow = E_F$) where A is a function of $1/k_F a$ (Fig.6.2a). However, it is expected that far in the BEC regime, the Fermi polaron will not be stable as the minority atom will tend to bind with a single \uparrow particle. In this case, the trial wavefunction (6.3) is not appropriate to describe a $\uparrow\downarrow$ molecule interacting with the Fermi sea of \uparrow . In particular, the calculation of the effective mass leads to a diverging behavior in the BEC limit (see Fig.6.2b), while we expect the effective mass to tend to $2m$ because of the formation of a molecule. The energy of the molecule was calculated using a Diagrammatic Monte Carlo method [304], an analytic theory involving two particle-hole excitations [307] and a molecular variational ansatz in the spirit of the variational wavefunction [308, 300]. These studies revealed that the energy of the polaron and the molecule crosses, leading to a sharp transition between the polaron and the molecular state for a value of $1/k_F a \approx 0.9$.

6.1.3 A Qualitative Phase Diagram

We now show in Fig.6.3 a qualitative phase diagram of the spin-imbalanced Fermi gas. The M -point is the polaron-to-molecule transition. The splitting point S is the point where the superfluid-to-normal transition turns from first-order to second-order. Deep in the BEC regime, the critical effective field will turn the unpolarized superfluid SF into a polarized superfluid SF_p rather than a normal phase. The system is then composed of a Bose-Einstein condensate of molecules immersed in a weakly interacting gas of unpaired majority atoms. However, for large enough interactions, the atom-dimer mixture is unstable against demixion (a mean-field calculation provides a critical value $1/k_F a \approx 1.7$). Monte-Carlo simulations have shown that between $1/k_F a \approx 0.73$ and $1/k_F a \approx 1.7$, the H_s -line indeed becomes first-order [261] (not depicted in Fig.6.3), where the molecules and the unpaired atoms are phase-separated, and the polarized superfluid disappears with a finite density-jump. Because the M -point is expected to sit inside this first-order line, it cannot be observed for a

finite amount of minority atoms, since the pairs will phase-separate before the polaron-to-molecule transition occurs. This phase diagram is however not completely understood. It is predicted for example that in the BCS regime, the balanced superfluid has a transition to a phase with a spatially varying order parameter, the Fulde-Ferrel-Larkin-Ovchinnikov (FFLO) phase [309, 310]. Other exotic phases have been proposed such as the deformed Fermi surface, or Sarma phase (see for instance the reviews [311, 312]). The transition from the normal partially polarized phase to the polarized superfluid (region marked by “?”) is also discussed, with a possible splitting of H_c in two lines (see for instance Fig.2 in [312]) with an unstable region up to the tricritical point (not shown) at $1/k_F a \approx 1.7$ where the SF, SF_p and FP phases join.

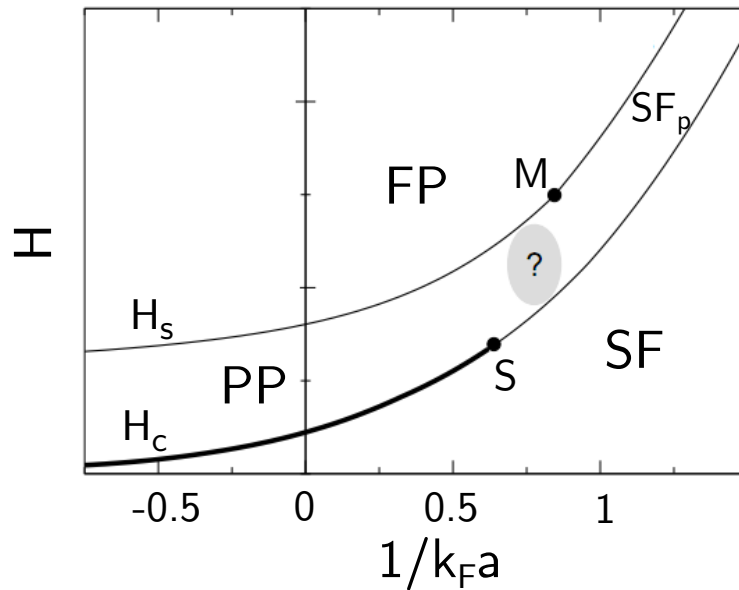


Figure 6.3: Qualitative Phase Diagram of the Spin-Polarized Fermi Gas in the BEC-BCS crossover (figure adapted from [300]). The phases indicated are the fully polarized normal phase (FP), the partially polarized normal phase (PP), the unpolarized superfluid (SF) and the polarized superfluid (SF_p).

6.1.4 Experimental investigations

Because of the ubiquitous presence of Fermi systems in nature, the search for the Clogston-Chandrasekhar limit was undertaken in various fields of physics, ranging from astrophysics, to quantum chromodynamics and solid state physics [297]. In most superconductors, it is hard to observe the CC-limit as the necessary magnetic fields are usually above the critical field for the quench of the superconducting phase, in addition to the difficulty of addressing the electron spins rather than their orbital motion (see chapter VI in [297]). Though experimental hints of the existence of the FFLO phase have been gathered in heavy-fermion compounds [297], a clear experimental observation remains elusive. In ultracold atoms, because of the stability of the Zeeman spin-mixture, it is experimentally easy to produce chemical potential imbalance in dilute Fermi gases. When our work was initiated, two groups had performed pioneering experiments on spin-polarized Fermi gases, observing the robustness of the unpolarized superfluid but with different scenarios. The group of W. Ketterle at MIT had observed phase-separation of an unpolarized superfluid core

surrounded by a partially polarized normal phase and a fully polarized outer rim [298]. Above a critical polarization $P_c = (N_1 - N_2)/(N_1 + N_2) \approx 75\%$ the superfluid core disappeared. The group of R. Hulet at Rice University observed a qualitatively different picture [137, 313]: the unpolarized superfluid core was surrounded by a fully polarized shell only. As a consequence, it was always present regardless of the spin-imbalance, thus giving $P_c = 100\%$.

The discrepancy sparked an intense theoretical effort. The two experiments were performed in very different atom number and trap aspect-ratio conditions and this was considered as a possible explanation for the differences observed in the experiments [314]. In addition, clear LDA-violating features were observed in the Rice experiment, and surface tension effects were considered to explain them [315, 316]. Understanding this discrepancy was an important source of motivation for our early experiments.

6.2 Measurement of the Equation of State

The equation of state of the low-temperature two-component imbalanced Fermi gas can be measured using the technique introduced in the previous chapters, since the pressure formula is also valid for unequal spin populations. In this case, the pressure of the system will read $P(\mu_1, \mu_2, a)$ where μ_1 and μ_2 are the chemical potential of both spin species (by convention label “1” will refer to the majority component), and a the scattering length. Assuming that the local density approximation is verified, the pressure is measured from the sum of the doubly-integrated density profiles of the two spin components:

$$P(\mu_{1z}, \mu_{2z}, a) = \frac{m\omega_r^2}{2\pi} (\bar{n}_1(z) + \bar{n}_2(z)). \quad (6.7)$$

where $\mu_{iz} = \mu_i^0 - V(z)$ is the local chemical potential of species i along the z -axis. As usual, we introduce dimensionless quantities. First, the new variables introduced are the dimensionless spin-imbalance η , and interaction strength δ_1 :

$$\eta = \frac{\mu_2}{\mu_1} \quad (6.8)$$

$$\delta_1 = \frac{\hbar}{\sqrt{2m\mu_1}a}. \quad (6.9)$$

Secondly, the pressure is normalized to the pressure of a single-component non-interacting gas of majority atoms $P_0(\mu_1) = 1/15\pi^2(2m/\hbar^2)^{3/2}\mu_1^{5/2}$:

$$P(\mu_1, \mu_2, a) = P_0(\mu_1)h(\eta, \delta_1). \quad (6.10)$$

The aim of this chapter is the measurement of the universal function $h(\eta, \delta_1)$. The interaction strength δ_1 is similar to the interaction strength introduced in chapter 5, except that it refers to the majority spin component⁴. Similarly to what was encountered in the previous chapters, the trap scans different local values of both η and δ_1 , and the main issue is to determine the global chemical potential of each spin species μ_1^0 and μ_2^0 .

In the experimental sequence, we prepare the spin-mixture following the procedure in section 2.3.3, and the interaction strength is varied by slowly ramping the Feshbach coils to the desired final magnetic field value, while evaporating the mixture using an exponential ramp of 5 s (with

⁴In the interaction range explored, we will show later that $\mu_1 > 0$ so that δ_1 is well defined.

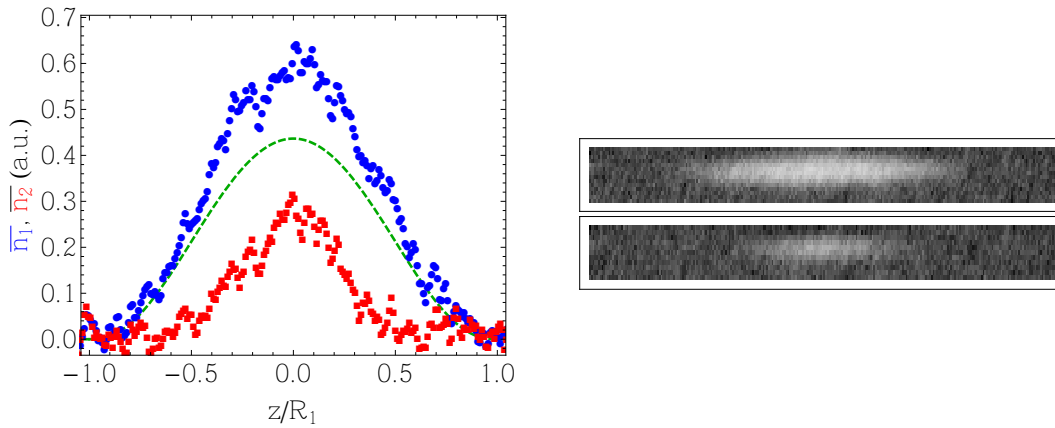


Figure 6.4: Raw *in-situ* doubly-integrated density profiles (left panel) and absorption images (right panel) of a spin-imbalanced Fermi gas at the unitary limit. Both images are taken with an exposure time of $10 \mu\text{s}$, separated by a $10 \mu\text{s}$ delay. The pressure calibration using the fully polarized outer shell is shown in dashed green (see text). The vertical size of each absorption image (right panel) is $45 \mu\text{m}$.

a characteristic time of 500 ms) towards a final laser trap intensity before taking the images. The density profiles $\bar{n}_1(z)$ and $\bar{n}_2(z)$ are recorded using absorption imaging, imaged successively on a spin-imbalanced mixture (see section 2.4.1). An example of raw density profiles of a spin-imbalanced gas at the unitarity limit is shown in Fig.6.4. The majority (minority) component is shown in blue circles (red squares), together with the absorption images (right panel).

6.2.1 Pressure Calibration and Determination of the Chemical Potentials

The local population imbalance and interaction strength along the z -axis (denoted by η_z and δ_{1z}) vary according to:

$$\eta_z = \frac{\eta_0 - V(z)/\mu_1^0}{1 - V(z)/\mu_1^0} \quad (6.11)$$

$$\delta_{1z} = \frac{\hbar}{\sqrt{2m(\mu_1^0 - V(z))}a}, \quad (6.12)$$

We thus have to determine μ_2^0 and μ_1^0 (and hence, $\eta_0 = \mu_2^0/\mu_1^0$). In addition, the pressure formula requires an absolute measurement of the doubly-integrated density profiles 6.7, together with an accurate determination of the radial trapping frequency ω_r . As we have seen in the previous chapters, several tricks can be used to calibrate the pressure to a reference pressure. In the case of imbalanced spin-mixtures, an elegant solution to the calibration issue can be implemented, as first presented in [111]. The h -function as defined in Eq.(6.10) is normalized to the pressure of the non-interacting Fermi gas of majority with the same chemical potential. In the range of interaction strength explored in this work, we always observe an outer rim consisting of majority atoms only. Because p -wave interactions are negligible, this fully polarized gas at the rim is a non-interacting gas and its density profile in a trap corresponds to the fermionic Thomas-Fermi distribution. As a consequence, the global chemical potential of the majority spin species μ_1^0 is readily given by the

Thomas-Fermi radius R_1 fitted in the outer shell⁵:

$$\mu_1^0 = \frac{1}{2}m\omega_z^2 R_1^2. \quad (6.13)$$

At each point on the z -axis, the fitted Thomas-Fermi profile $\bar{n}_1^0(z) = A_0(1 - z^2/R_1^2)^{5/2}$ is the pressure of the non-interacting gas with the same local chemical potential μ_{1z} than the interacting majority component. This pressure is precisely the normalization of h . We can thus rewrite Eq.(6.10), together with the pressure formula (6.7):

$$h(\eta, \delta_1) = \frac{P(\mu_1, \mu_2, a)}{P_0(\mu_1)} = \frac{\bar{n}_1(z) + \bar{n}_2(z)}{\bar{n}_1^0(z)}. \quad (6.14)$$

We note that the fully polarized shell acts as a reference pressure for the whole density distribution. This is a very convenient normalization as it is self-included in each absorption picture. Importantly, the self-normalization contained in the factor A_0 cancels various systematic errors: it makes accurate knowledge of the radial trapping frequency irrelevant, as well as a probe detuning mismatch (provided it is the same for both spin species) or image magnification error.

Finally, the determination of the minority global chemical potential μ_2^0 can be achieved with the minority density profile. We saw in section 6.1.2 that the dilute limit, where $\bar{n}_2 \rightarrow 0$, the problem reduces to a single impurity in a (local) Fermi sea of majority atoms, the Fermi polaron. Hence, in this limit the minority chemical potential is related to the majority one by $\mu_2 = A\mu_1$, with A being the dimensionless polaron binding energy and μ_2^0 given by the radius R_2 at which the minority density distribution vanishes:

$$\mu_{2z}(z = R_2) = A\mu_{1z}(z = R_2) \iff \eta_0 = A + \left(\frac{R_2}{R_1}\right)^2 (1 - A) \quad (6.15)$$

This approach thus requires one to use A as an input parameter⁶. Finding R_2 is still subject to the choice of the fitting function, as for the case of the $T = 0$ Bose gas of chapter 3. Fixed-Node Monte Carlo calculations first observed that the normal partially polarized state appeared to behave like a weakly interacting gas of quasi-particles [229]. This was later confirmed experimentally at MIT [111], and established analytically [317], justifying the simple choice of a fermionic Thomas-Fermi distribution⁷ to fit R_2 .

6.2.2 The Equation of State of the Spin-Imbalanced Gas in the BEC-BCS crossover

In order to make an intuitive link between the density distributions, the phase diagram and the grand-canonical equation of state that we will extract from them, we first present the measurement at unitarity $1/a = 0$. In addition, it will allow us to introduce the main features observed in the region of the BEC-BCS crossover that we investigated.

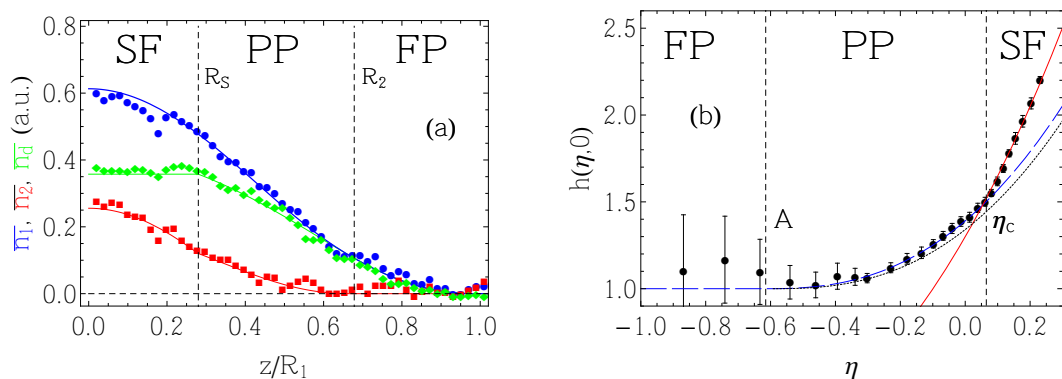


Figure 6.5: Equation of state of the two-component unitary ($\delta_1 = 0$) Fermi gas as a function of spin-imbalance η . (a): In-situ density profiles of the majority $\bar{n}_1(z)$ (blue circles), minority spin-component $\bar{n}_2(z)$ (red squares), and the difference $\bar{n}_d(z) = \bar{n}_1(z) - \bar{n}_2(z)$ (green diamonds). R_S (R_2) is the superfluid (minority) radius. The solid lines are guides to the eye. (b): h -function extracted from the density distributions showing the three phases: the superfluid (SF), normal partially polarized (PP), and fully polarized phase (FP). We also show the equation of state for the PP phase predicted by a Fixed-Node Monte Carlo (dotted black line [229]) and using a Fermi-liquid EoS together with the polaron properties extracted the two particle-hole excitations (dashed blue line [303]), see section 6.2.4. The transition FP-PP is given by the polaron binding energy $\eta = A$, while the PP-SF transition occurs for $\eta = \eta_c$.

Density Profiles and Phase Diagram of the Spin-Imbalanced Unitary Gas

In Fig.6.5a, we show the in-situ density profiles of the majority $\bar{n}_1(z)$ (blue circles), minority spin-component $\bar{n}_2(z)$ (red squares), and the difference $\bar{n}_d(z) = \bar{n}_1(z) - \bar{n}_2(z)$ (green diamonds). We first note that there is an outer region where the majority is present without minority atoms, composing the fully polarized (FP) phase. According to the normalization of h Eq.(6.10), this corresponds to:

$$h_{\text{FP}}(\eta) = 1. \quad (6.16)$$

The first minority atoms appear at a radius R_2 , when the minority chemical potential $\mu_2 = A\mu_1$, or $\eta = A$, marking the separation between the fully polarized and the normal partially polarized phase (PP). Finally, we observe that $\bar{n}_d(z)$ saturates below a radius R_S . As we will see in section 6.2.3, within LDA, it is a direct signature of a fully paired core, the unpolarized superfluid phase (SF). The critical chemical potential imbalance for the normal-to-superfluid transition η_c is simply related to the superfluid radius R_S by:

$$\eta_c = \frac{\eta_0 - (R_S/R_1)^2}{1 - (R_S/R_1)^2}. \quad (6.17)$$

⁵From Eq.(6.13), $\mu_{1z} > 0$ for all z and δ_1 in Eq.(6.9) is well defined.

⁶An alternative option is to use ξ_s as an input, which in turn fixes η^0 .

⁷This procedure, though simple, is sensitive to the fitted radius R_2 . In order to make it robust, about 20 images are averaged before determining η_0 . We first start with a reference image, with some unknown $\eta_0^{(1)}$. A second image is patched to it by adjusting its value $\eta_0^{(2)}$. Both are averaged and a third image is patched, and so on, recursively. At the end, we obtain a low-noise averaged profile whose η_0 can be determined accurately (the interested reader is referred to the Appendix B.1 of [121] for details).

Moreover, an abrupt change is seen in the slope of \bar{n}_d at $z = R_S$, which is clearer in the averaged pressure on Fig.6.5b at $\eta = \eta_c$ and is the signature of a first-order phase transition, as we will see in section 6.2.3.

The Equation of State in the BEC-BCS crossover

Applying the pressure method for density profiles taken at different values of the magnetic fields comprised between 766 and 981 G (about 20 images are taken for each magnetic field value), we measure the function $h(\eta, \delta_1)$, for which several examples are shown in Fig.6.6. Let us first note that, while it is clear that the measurements of h for each magnetic field are convenient to plot in this way, they represent curved lines in the parameter space of interaction strength and spin imbalance (δ_1, η). If one takes into account the variation of these parameters in the trap, Eqs.(6.11) and (6.12), they are locally related one to each other by:

$$\delta_{1z} = \delta_1^0 \sqrt{\frac{1 - \eta_z}{1 - \eta_0}} \quad (6.18)$$

Each absorption image thus scans the parameter space (δ_1, η) from a central value of (δ_1^0, η_0) along the line 6.18 down to $\delta_1 \rightarrow \text{sign}(a)\infty$ and $\eta \rightarrow -\infty$ (in the limit of infinite signal-to-noise ratio)⁸.

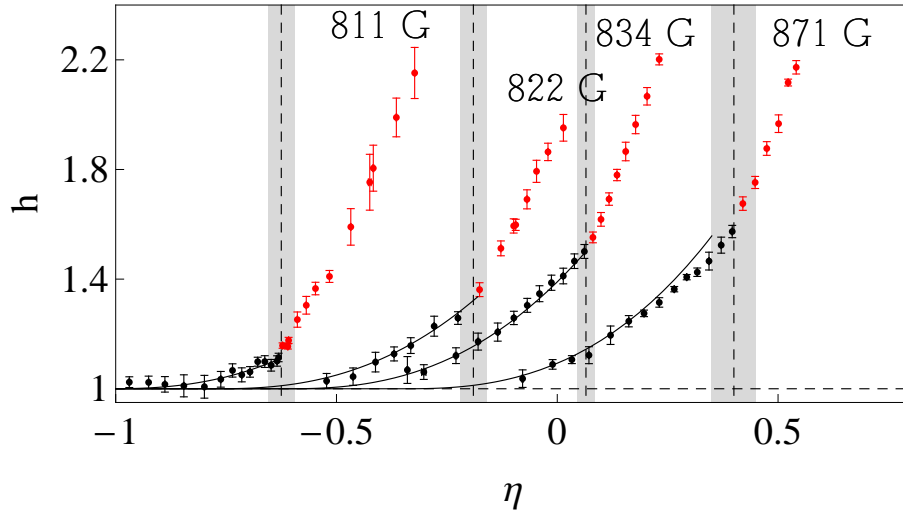


Figure 6.6: Equation of state h of an imbalanced Fermi gas as a function of spin-imbalance η for different values of the magnetic field. The superfluid (normal) phase is shown in red (black) points. The critical spin-imbalance for the superfluid transition η_c is shown in vertical dashed lines together with the uncertainty in grey shaded area. The fits to extract the effective mass m^*/m using a Fermi-liquid type EoS are shown in black solid lines.

⁸Except for the unitary limit, where all images belong to the line $(0, \eta)$ and thus can be patched together, various images at different polarization for a given magnetic field will not necessarily belong to the same curve $(\delta_1, \eta(\delta_1))$ and cannot be patched in principle. We estimated the systematic error of patching together images at a given magnetic field by comparing the EoS obtained by averaging the M simulated profiles with the same values of $(\delta_1^{0(i)}, \eta_0^{(i)})$ (where $i = 1, 2, \dots, M$) as the set of data patched and observed a deviation of at most 5% compared to the EoS expected for the averaged value $(\langle \delta_1^{0(i)} \rangle, \langle \eta_0^{(i)} \rangle)$, thanks to the fact that the images selected have similar total atom number and polarization conditions.

6.2.3 The Normal/Superfluid Phase Transition

For all values of interaction strength explored in this work ($-1 < \delta_1 < 0.6$), we observe in the center of the trap a flat-top feature in the doubly-integrated difference of the density profiles (see green diamonds on Fig.6.5a at unitarity). Assuming the LDA (and a harmonic trap), we can simply relate the local density on the z -axis $n(0, 0, z)$ to $\bar{n}(z)$. We start with the Gibbs-Duhem relation $n = \partial P / \partial \mu$ and use the pressure formula to replace P by \bar{n} . We then use the LDA: $\partial / \partial \mu = -(m\omega_z^2 z)^{-1} \partial / \partial z$ to find:

$$n(0, 0, z) = -\frac{\lambda^2}{2\pi} \frac{1}{z} \frac{d\bar{n}}{dz}, \quad (6.19)$$

where $\lambda = \omega_r / \omega_z$ is the trap aspect ratio. This relation is valid for any of the spin species and by linearity, for the density difference as well. We thus deduce from Eq.(6.19) that $d\bar{n}_d/dz = 0$ implies $n_1 = n_2$. The plateau is a direct indication of a fully paired inner core. Though strong evidence, the full pairing character is not a direct proof of superfluidity. This proof came by setting an imbalanced gas in rotation and observing the appearance of quantized vortices only in the fully paired core, not in the outside normal regions [298]. Another important consequence of Eq.(6.19) is that a discontinuity in the derivative of h represents a jump in the density n .

At Unitarity...

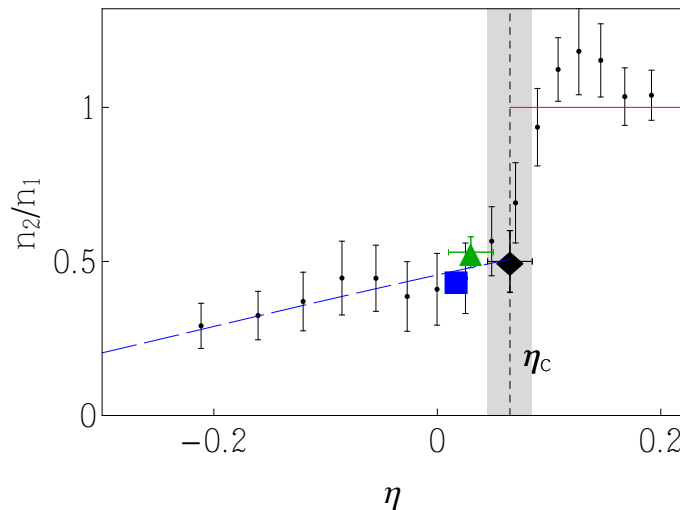


Figure 6.7: Minority concentration n_2/n_1 as a function of chemical potential spin-imbalance η for the unitary gas. The critical point was determined experimentally (black diamond) and is compared to a density profile analysis at MIT (green triangle [111]), as well as to a Fixed-Node Monte Carlo study (blue square [229]).

At unitarity, the minority concentration n_2/n_1 can be readily calculated from $h(\eta)$ (here $\delta_1 =$

0)⁹:

$$\frac{n_2}{n_1} = \frac{h'}{\frac{5}{2}h - \eta h'} \quad (6.22)$$

where $' = d/d\eta$. The discontinuity in h' at $\eta = \eta_c$ on Fig.6.5b thus leads to a jump in the minority concentration. Using the value of h measured as well as a three-point finite difference derivative, we can extract n_2/n_1 from our data at unitarity (Fig.6.7). For $\eta > \eta_c$, $n_2/n_1 \approx 1$ as expected for the balanced superfluid. From the equality of densities we deduce that the pressure depends on μ_1 and μ_2 through $\bar{\mu}$ only, and we can write¹⁰:

$$P_{\text{SF}} = \frac{2}{15\pi^2} \left(\frac{2m}{\xi_s \hbar^2} \right)^{3/2} \bar{\mu}^{5/2} \quad (6.24)$$

where $\bar{\mu} = (\mu_1 + \mu_2)/2$. This pressure is plotted in a red solid line in Fig.6.5b. Below η_c the density abruptly jumps, marking a first-order quantum phase transition to the normal state with a critical concentration $(n_2/n_1)_c = 0.5(1)$ and $\eta_c = 0.065(20)$ (black diamond in Fig.6.7). This phase separation was first observed at MIT [138] using the inverse Abel transform, and from a subsequent density profile study Y. Shin extracted $\eta_c = 0.03(2)$ and $(n_2/n_1)_c = 0.53(5)$ (green triangle in Fig.6.7) [111]. Our result is in agreement both with the MIT analysis as well as with a Fixed-Node calculation $\eta_c = 0.017$ and $(n_2/n_1)_c = 0.44$ (blue square) [229].

...and beyond

Similarly, we can pinpoint the location of the transition from the kink on the pressure as shown in vertical dashed lines in Fig.6.6 for the different values of the interaction parameter δ_1 . We show in Fig.6.8 the critical effective field $H_c/\mu_1 = (1 - \eta_c)/2$ in the BEC-BCS crossover¹¹. In particular we see that the two lines between the FP-PP and the PP-SF transition are joining on the BEC side, which marks the disappearance of the partially polarized normal phase. This point was determined experimentally at MIT and found at $1/k_{F1}a = 0.74(4)$ [47] (green filled rectangle in Fig.6.8)¹², consistent with our phase diagram.

For the superfluid to remain unpolarized, it is necessary that the effective field $H = (\mu_1 - \mu_2)/2$ be smaller than the single-particle excitation gap Δ . Indeed, as we have seen before, if $H > \Delta$ it is energetically favorable to flip the particle spins, and the system becomes polarized. We then have a transition either to a normal or a superfluid polarized phase. Since we investigated a region where

⁹ Starting from the definition $P(\mu_1, \mu_2) = P_0(\mu_1)h(\eta)$, Gibbs-Duhem relation for each spin species yields:

$$E_{F1}^{3/2} = \frac{2}{5}\mu_1^{3/2}\left(\frac{5}{2}h - \eta h'\right) \quad (6.20)$$

$$E_{F2}^{3/2} = \frac{2}{5}\mu_1^{3/2}h', \quad (6.21)$$

where $E_{Fi} = \frac{\hbar^2}{2m}(6\pi^2 n_i)^{2/3}$ is the Fermi energy of species i .

¹⁰Or:

$$h_{\text{SF}}(\eta) = (2\xi_s)^{-3/2}(1 + \eta)^{5/2}. \quad (6.23)$$

¹¹The analysis on the density jump is not as easily extendable outside the unitary limit. Indeed the calculation of n_2/n_1 involves not only the derivative of h versus η but also versus δ_1 . Our measurement is not sufficiently dense to estimate the latter from the experimental data points (see right panel of Fig.6.8) but it is still possible to extract n_2/n_1 from the density profiles knowing from Eq.(6.19) that $n_2/n_1 = d\bar{n}_2/d\bar{n}_1$. This analysis is undertaken in section 5.3.2 of [121].

¹²The horizontal width represents the error bar, the vertical position and size are chosen for clarity.

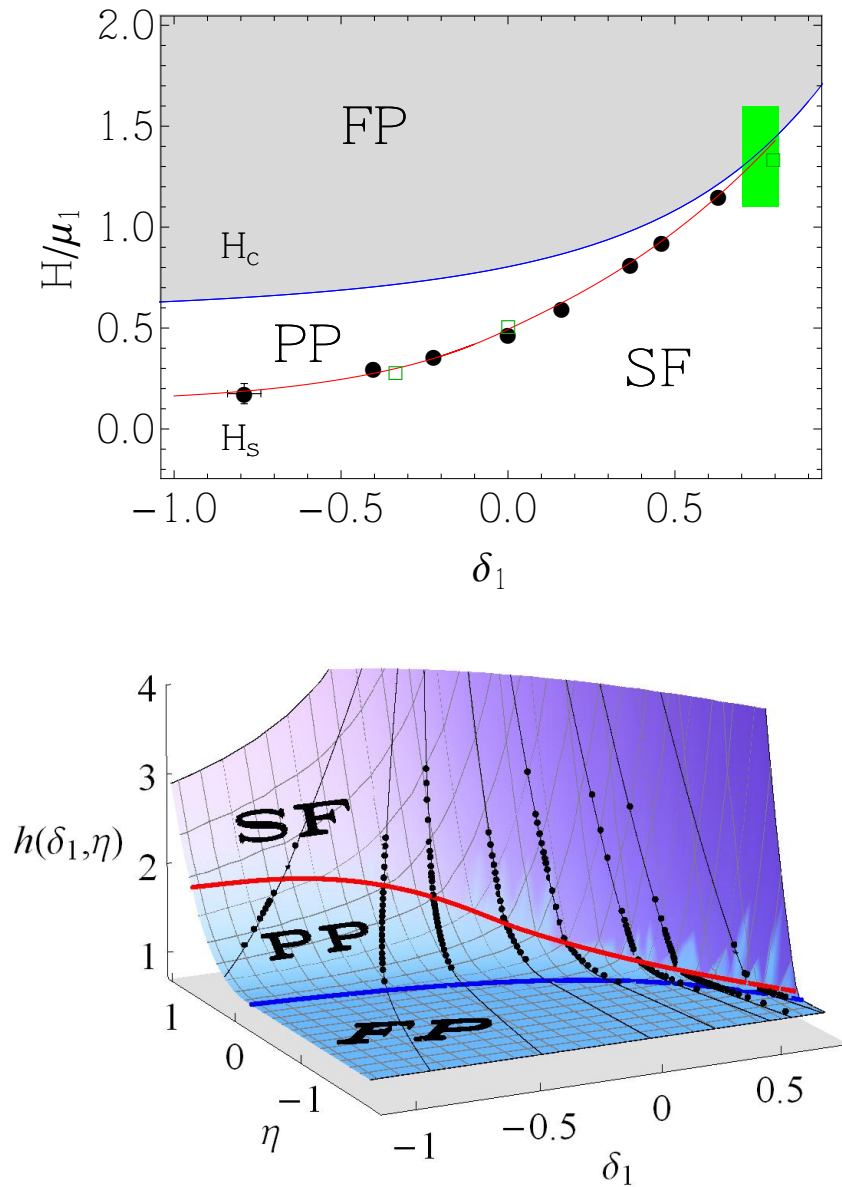


Figure 6.8: Phase Diagram of the spin-imbalanced Fermi gas. The three phases present are the superfluid phase (SF), the normal partially polarized phase (PP) and the fully polarized phase (FP). Upper panel: The experimental data points for the critical field H_c/μ_1 for the superfluid-to-normal phase transition are shown together with a guide to the eye (red solid line), as well as the transition line between the FP to PP phase (blue solid line). The upper bounds provided by RF-spectroscopy of the pairing gap are shown in green squares [29]. Lower panel: EoS $h(\delta_1, \eta)$ together with the data points (black dots) and the transition lines. The solid black lines are the curves (δ_{1z}, η_z) scanned by an image in the trap (see Eq.(6.18)).

the superfluid is unpolarized, the gap provides us with an upper bound to the value of the critical field. We plot on the phase diagram Fig.6.8 the bound provided by the MIT measurement of the

pairing gap using radio-frequency spectroscopy [29] (green squares). Our value of H_c seems to saturate the upper bound in the interaction regime explored here rather than verify the Clogston expression $H_c = \Delta/\sqrt{2}$ which should ultimately be reached in the BCS limit. This shows the remarkable robustness of the strongly interacting superfluid Fermi gas to population imbalance. This point was already suggested in a Monte Carlo calculation [285].

Zero-Temperature Assumption

We have throughout this chapter assumed that our measurements were done at $T = 0$. It is important, as in chapter 3, to check the validity of this assumption. For an imbalanced spin-mixture a remarkable solution for the problem of thermometry of strongly interacting systems has been proposed and implemented in [248]: since the fully polarized phase of majority atoms is a non-interacting gas, its thermodynamics is exactly known, and it is in thermal contact with the inner strongly correlated region. It thus fulfills the requirement of an ideal thermometer and the temperature can be fitted using finite-temperature Thomas-Fermi distributions on the fully polarized wings. From our unitarity gas density profiles (see Fig.6.5a for example), we find an upper bound on the temperature of $T < 0.06T_F$, where $k_B T_F = \mu_1^0$. This method is also efficient on the BEC side and leads to the same upper bound. On the BCS side, where the fully polarized shell is smaller, the fit is less reliable and we obtain a less stringent upper bound of $T < 0.13T_F$.

We also have an independent check on this bound because we observe a kink, hence a first-order phase transition between the superfluid and the normal phase. It was determined experimentally that at unitarity this transition becomes second order above the temperature of a tricritical point $T_{\text{tri}} = 0.07T_F$ [248], in agreement with mean-field calculations [318,319] and they predicted that T_{tri} is about half the critical temperature for superfluidity on the BCS side. We thus have T_{tri} as an upper bound for all our values of interaction strength.

The Superfluid Phase

We recall that the unpolarized superfluid, where $n_1 = n_2$, depends only on the mean chemical potential $\bar{\mu} = (\mu_1 + \mu_2)/2$. In this phase, we can also write the pressure symmetrically:

$$P(\mu_1, \mu_2, a) = 2P_0(\bar{\mu})h_S(\delta) \quad (6.25)$$

where the symmetric interaction strength is defined as:

$$\delta = \frac{\hbar}{\sqrt{2m(\bar{\mu} - E_b/2)a}}. \quad (6.26)$$

We subtract to the mean chemical potential the binding energy on the BEC side of the resonance $E_b = -\hbar^2/ma^2$ for $a > 0$ and zero otherwise in order to avoid negative chemical potentials. Using the points in the superfluid phase (red points in Fig.6.6), we have a direct measurement of the EoS of the balanced superfluid in the BEC-BCS crossover, presented in section 5.2.

6.2.4 A Gas of Polarons

Let us focus on the normal partially polarized phase. The critical value for the appearance of the normal phase is dictated by the problem of a single impurity in a Fermi sea, and the transition between the fully polarized and the partially polarized phase occurs for $\eta = A(\delta_1)$. However, going beyond this picture is not trivial and computing the EoS of the normal phase requires, in principle,

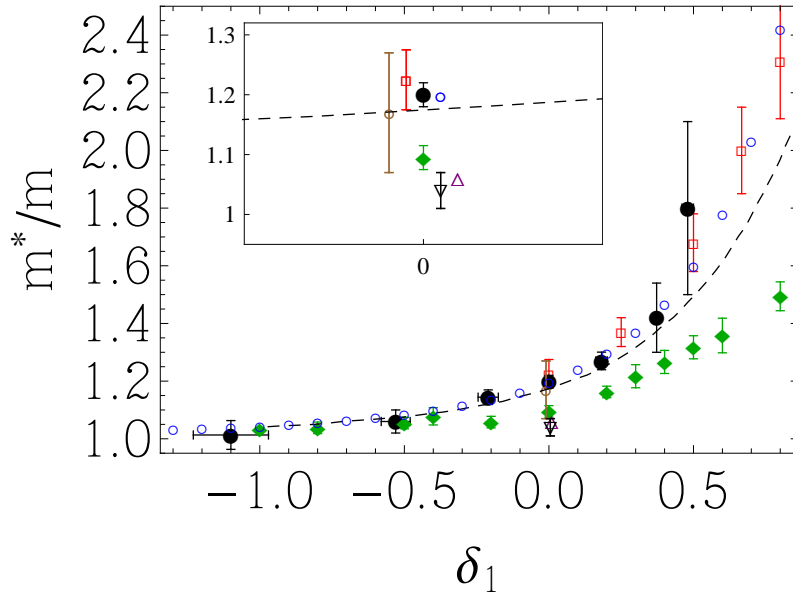


Figure 6.9: Effective mass of the Fermi Polaron in the BEC-BCS crossover (our data is shown as black points). Other experimental measurements: a density profile analysis at MIT $m^*/m = 1.06$ (down black triangle [111]) and a measurement we performed using collective modes $m^*/m = 1.17(10)$ (brown empty circle [63]). Theoretical predictions: a one-particle (dashed black line [302]), and two particle-hole analytical calculation (blue circles [303]), together with a Fixed-Node result (black triangle [229]). The Fixed-Node Monte Carlo calculation from [261] is shown in green diamonds. Inset: Zoom around unitarity. The various measurements are slightly shifted from the unitary limit for clarity.

to solve the problem of a finite number of minority atoms immersed in a Fermi sea of majority atoms. This cannot be done analytically and Fixed-Node Monte Carlo methods have been used to address this problem. It was observed numerically [229, 320], and later justified analytically [317] that at finite concentration $x = n_2/n_1$, the small amount of Fermi polarons would form a degenerate gas describable by a Landau-Pomeranchuk equation of state:

$$E = \frac{3}{5}N_1 E_{F1} \left(1 - \frac{5}{3}Ax + \frac{m}{m^*}x^{5/3} + Fx^2 + \dots\right) \quad (6.27)$$

where the quadratic F -term represents interactions between polarons. In order to test this behavior, we need to translate the Fermi-liquid EoS in the grand-canonical ensemble. We suggested writing the pressure in the normal phase as [60]:

$$P(\mu_1, \mu_2) = \frac{1}{15\pi^2} \left(\left(\frac{2m}{\hbar^2}\right)^{3/2} \mu_1^{5/2} + \left(\frac{2m^*}{\hbar^2}\right)^{3/2} (\mu_2 - A\mu_1)^{5/2} \right). \quad (6.28)$$

Using the canonical to grand-canonical correspondence equations Eqs.(6.37) and (6.38), it is easy to show that to lowest order Eq.(6.28) is equivalent to the canonical expression Eq.(6.27), provided $F = 5A^2/9$. Using the value of A at unitarity, we deduce $F = 0.21$, in reasonable agreement with the estimate $F = 0.14$ from the Fixed-Node calculation [261]. It was later shown by C. Mora and F. Chevy that this relation is a particular case of the exact relation $F = \frac{5}{9} \left(\frac{d\mu_p}{d\mu_1}\right)^2$ (where $\mu_p = A(\delta_1)\mu_1$) valid in the BEC-BCS crossover (as long as the Fermi polaron is stable) [317]. The gas of polaron is thus assumed to be a weakly-interacting gas of quasi-particles with a renormalized

mass m^* and a shifted chemical potential $\mu_2 - A\mu_1$ due to the binding to the Fermi sea. In the crossover, we simply generalize the pressure from Eq.(6.28) as:

$$h_{\text{PP}}(\eta, \delta_1) = 1 + \left(\frac{m^*(\delta_1)}{m} \right)^{3/2} (\eta - A(\delta_1))^{5/2} \quad (6.29)$$

In Fig.6.5b we use Eq.(6.29) with the parameters $A(0) = -0.61$ and $m^*(0) = 1.2m$ determined at unitarity from the Diagrammatic Monte Carlo [304] (or the two particle-hole calculation [303]) and we obtain the blue dashed line in the PP phase. The predictions from the Fixed-Node Monte Carlo [229] result in the dotted black line on the same figure. We see that while the first one is in excellent agreement with our EoS in the normal phase, the second one is slightly but systematically below our data. Alternatively, we can use A as the only input parameter, and leave m^*/m as a free fitting parameter. Doing so in the BEC-BCS crossover, we obtain the solid black lines in Fig.6.6 and we can directly measure the effective mass of the Fermi polaron in the BEC-BCS crossover as shown in Fig.6.9. It is remarkable that, except for the data points in the BCS regime (EoS at 871 G in Fig.6.6) the description of the normal phase as a weakly interacting gas of polarons is very successful even up to the critical point η_c , despite the fact that the minority concentration n_2/n_1 reaches 0.5, and the picture of a dilute gas of polarons might be expected to break down.

6.2.5 Comparison to other experiments

Critical Polarization of a Trapped Fermi gas

As was already demonstrated in the previous chapters, the EoS of the homogeneous gas can be used to deduce information on trapped samples, provided the LDA is verified. Early experiments on spin-polarized Fermi gases measured global quantities, most importantly the critical polarization at which the superfluid core vanishes. For example, the MIT group has measured the critical polarization via the condensate fraction, by using the fast-sweep-projection technique [321, 322] and observing a bimodal distribution after expansion (blue triangles [298] and red squares [138] in Fig.6.10). We plot the critical polarization $P = (N_1 - N_2)/(N_1 + N_2)$ as a function of the global majority interaction strength $1/k_F a$, where $k_F^2 = \frac{2m}{\hbar^2} \hbar\bar{\omega} (6N_1)^{1/3}$. For $P < P_c$, a superfluid core is present at the center of the trap while for $P > P_c$ the cloud is completely normal. In early experiments performed in the Rice group, a superfluid was always seen regardless of the imbalance, thus setting the Clogston-Chandrasekhar limit to 1 (empty black square [137]).

We can determine P_c from the full h -function shown in the right panel of Fig.6.8. The critical polarization is reached when the critical spin-imbalance η_c is obtained at the center of the trap. The global polarization is obtained by calculating the total atom number of each spin-species in the trap:

$$N_i = \int d^3r n_i(\mu_1^0 - V(r), \mu_2^0 - V(r)) \quad (6.30)$$

where the trap is considered isotropic. This is not an additional assumption since the LDA is assumed for this calculation and the normalized result will not depend on the trap frequencies. Finally the interaction strength in the trap must also be computed:

$$\frac{1}{k_F a} = \frac{R_1}{a} \frac{1}{(6N_1)^{1/6}} = \frac{\delta_1^0}{(6N_1)^{1/6}} \quad (6.31)$$

The total atom numbers are calculated as a function of δ_1^0 , the grand-canonical interaction strength

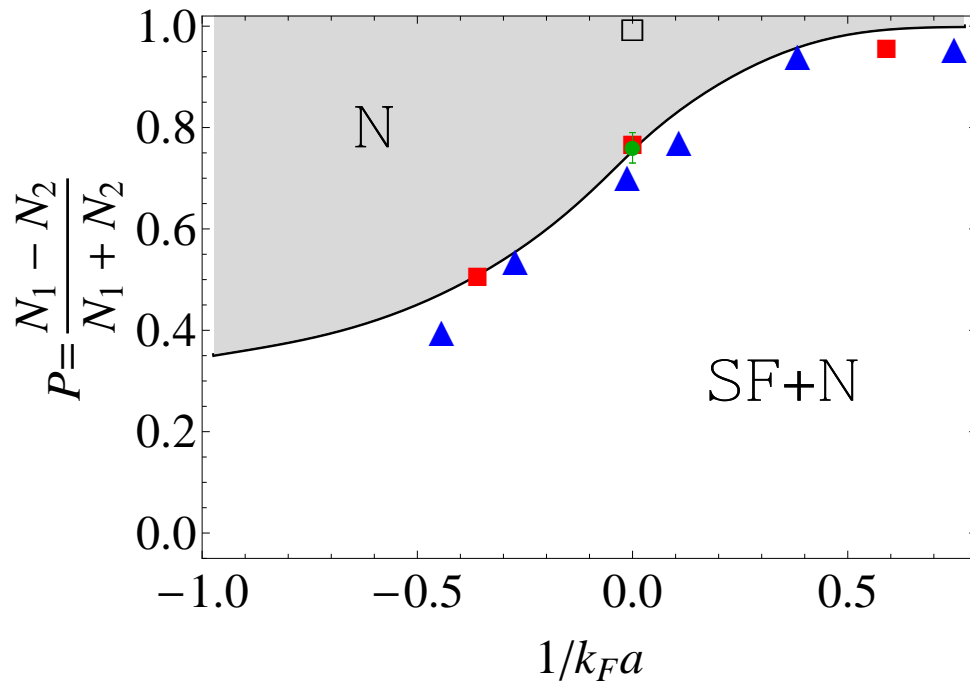


Figure 6.10: Critical polarization $P = (N_1 - N_2)/(N_1 + N_2)$ for a trapped imbalanced Fermi gas versus the majority interaction parameter $1/k_F a$. Below the critical polarization $P_c(1/k_F a)$ a superfluid SF is present in the center of the trap surrounded by a normal phase shell N (SF+N). The calculation in the trap using our experimentally determined EoS for the homogeneous gas is shown in thick black line and compared to two measurements at MIT (blue triangles [298] and red squares [138]), one in our group at unitarity (green circle [63]) and one from the Rice group (empty black square [137]).

at the center of the trap¹³. The central spin-imbalance is constrained to $\eta_0 = \eta_c(\delta_1^0)$. We show in thick black line the curve $\{1/k_F a(\delta_1^0), P(\delta_1^0)\}$ in Fig.6.10. The agreement with the MIT measurement is excellent, as well as with a previous determination of P_c from the density profiles at unitarity from our group (green circle [63]). It is however incompatible with the Rice experiment. The fact that we quantitatively confirmed the MIT scenario using experimental conditions (trap aspect ratio and atom number) close to the Rice experiment further thickened the mystery. In a subsequent work, the Rice group has reported that the maximal Clogston-Chandrasekhar limit observed in their early experiments was probably due to non-equilibrium evaporative depolarization which lead to a long-lived metastable state [131], possibly explaining the discrepancy.

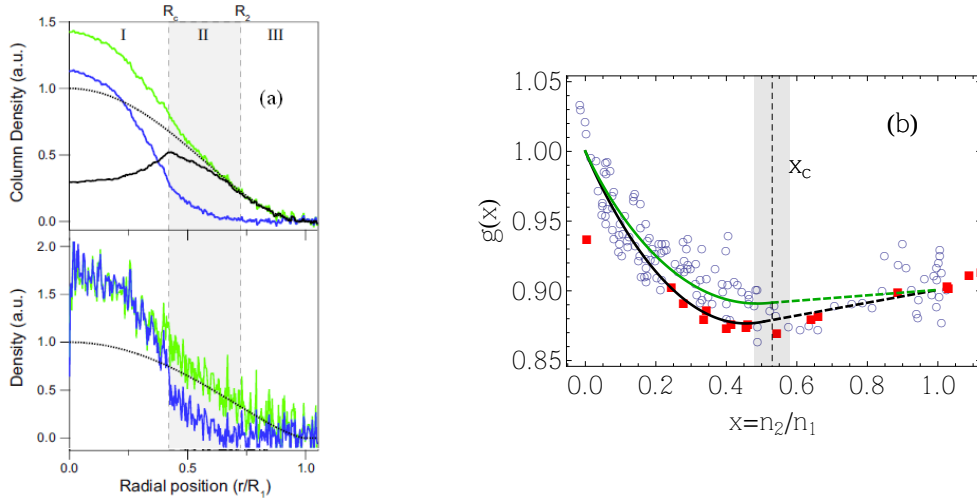


Figure 6.11: Canonical Equation of State of the Unitary Spin-Polarized Fermi Gas. (a): Radial (upper) and Abel-reconstructed (lower) MIT density profiles. (b): Universal $g(x)$ function obtained at MIT (empty blue circles [111]) and calculated from our h -function (red squares) together with the Landau-Pomeranchuk fits for both EoS (in green for the MIT EoS, in black for ours). The critical concentration x_c above which the system phase-separates is shown in grey shaded area and the fits are shown in dashed lines in the thermodynamically unstable region.

Comparison with the MIT Canonical EoS for the Spin-Polarized Unitary Gas

A measurement of the equation of state of a homogeneous spin-polarized Fermi gas using the in-situ density profiles of a trapped system was performed at MIT [111]. The quantity measured is the universal dimensionless energy $g(x)$ defined by

$$\mathcal{E}(n_1, n_2) = \frac{3}{5} \alpha (n_1 g(x))^{5/3} \quad (6.34)$$

where $\mathcal{E} = E/V$ is the energy density, $\alpha = (6\pi^2)^{2/3} \hbar^2 / 2m$ and $x = n_2/n_1$. The function $g(x)$ is measured using the relation $\mu_i = \partial \mathcal{E} / \partial n_i$ which yields:

$$g(x)^{5/3} = \frac{\mu_1}{E_{F1}} (1 + x\eta). \quad (6.35)$$

The local density approximation is assumed to determine the spatial variation of μ_1 and η and the local densities n_1 and n_2 are computed using an inverse Abel transform (bottom image in Fig.6.11a) on the radial density profiles (top image). The measurement of the local densities comes at a cost of a significant decrease in signal-to-noise ratio on the density distributions. The resulting EoS is shown in empty blue circles in Fig.6.11b. The solid green line represents a fit using a modified

¹³More precisely, we find:

$$N_1 = \frac{32}{15\pi^2} \int_0^1 du u^2 (1-u^2)^{3/2} \left(\frac{5}{2} h - \eta h_\eta - \frac{1}{2} \delta_1 h_{\delta_1} \right) \quad (6.32)$$

$$N_2 = \frac{32}{15\pi^2} \int_0^1 du u^2 (1-u^2)^{3/2} h_\eta \quad (6.33)$$

where $u = r/R_1$, $R_1 = \sqrt{2\mu_1^0/m\omega^2}$ being the majority radius, the function h and its derivatives $h_{\delta_1} = \partial h / \partial \delta_1$ and $h_\eta = \partial h / \partial \eta$ are all evaluated at the local value $\eta(u) = (\eta_c(\delta_1^0) - u^2)/(1-u^2)$ and $\delta_1(u) = \delta_1^0 / \sqrt{1-u^2}$.

Landau-Pomeranchuk EoS [111]:

$$g(x)^{5/3} = 1 + \frac{5}{3}Ax + \frac{1+cx}{m^*}x^\gamma, \quad (6.36)$$

which yielded $m^*/m = 1.06$, $A = -0.58$, $c = -0.019$, and $\gamma = 1.6$. The fact that $\gamma \approx 3/2$ shows that the polaron gas is weakly interacting (c being a correction to the Fermi liquid behavior). We can compare this measurement to our grand-canonical equation of state. Using Eq.(6.35), together with Eq.(6.22) for the minority concentration and the expression of the majority Fermi energy in Eq.(6.20), we find:

$$x = \frac{h'}{\frac{5}{2}h - \eta h'} \quad (6.37)$$

$$g = \frac{h^{3/5}}{h - \frac{2}{5}\eta h'}. \quad (6.38)$$

Using our data points for $h(\eta)$ (black points in Fig.6.5b), we compute the g -function (full red squares in Fig.6.11b). Alternatively, we can use the analytical form for the function $h(\eta)$ and we deduce the black line. Note that the curves are shown in dashed in the region $x > x_c$ where the system is unstable and phase-separates. We see that the agreement is reasonable.

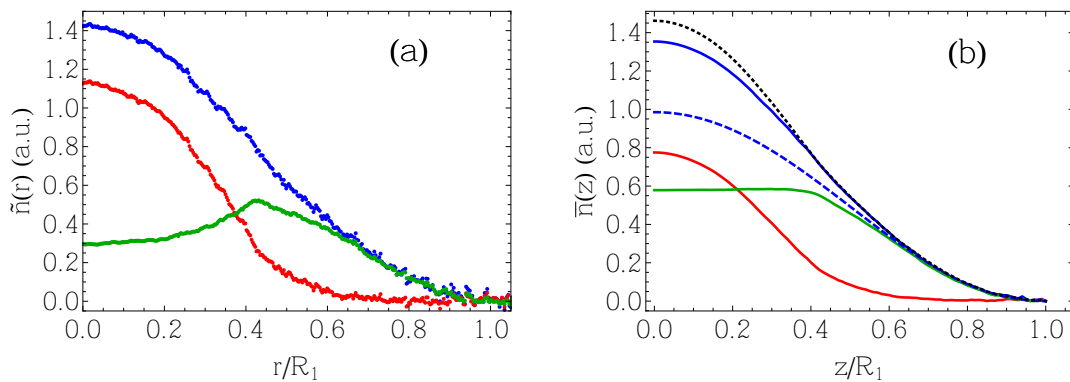


Figure 6.12: Density profiles of the unitary imbalanced Fermi gas measured at MIT [248]. (a): Radial density profiles $\tilde{n}_i(r)$, obtained by absorption imaging. (b): the numerically-integrated radial distribution, giving the doubly-integrated profiles $\tilde{n}_i(z)$ (solid lines). The blue dashed line is the normalization $\tilde{n}_1^0(z)$ (see text), and the dotted black line is $\tilde{n}_1^0(z) - A\tilde{n}_2(z)$ (see text). (b):

Grand-Canonical analysis of MIT density profiles

It is striking that using density profiles with a signal-to-noise ratio lower than MIT's¹⁴, we can measure an EoS with an equivalent or even higher precision. This demonstrates the power of the grand-canonical pressure analysis, and in what follows we use the pressure method to analyze the MIT density distributions, assuming harmonic trapping as in [111]. Since the raw data consists of the radial density distributions $\tilde{n}_i(r)$ (Fig.6.12a) measured in [248]¹⁵, we first use interpolation

¹⁴Typical atom numbers in the MIT experiment is 10 to 50 times larger than in our (or most other) experiment because of the very efficient cooling of ^6Li , using a large BEC of ^{23}Na as a coolant in a magnetic trap [323].

¹⁵The radial distribution are obtained using absorption imaging and are related to the real 3D density by an integration along the line-of-sight y : $\tilde{n}_i(r) = \int dy n(\sqrt{y^2 + r^2})$. We assume here that each direction has been rescaled according to the trap aspect ratio (which can be done provided the LDA is verified).

functions of the data to compute the doubly-integrated density profiles $\bar{n}_i(z) = \int dx \tilde{n}_i(\sqrt{x^2 + z^2})$, plotted in Fig.6.12b. We notice the clear flat-top feature on $\bar{n}_d(z)$. We then determine the reference calibration density $\bar{n}_1^0(z)$ using the fit on the fully polarized shell (see Eq.6.14), shown in dashed blue line in Fig.6.12b.

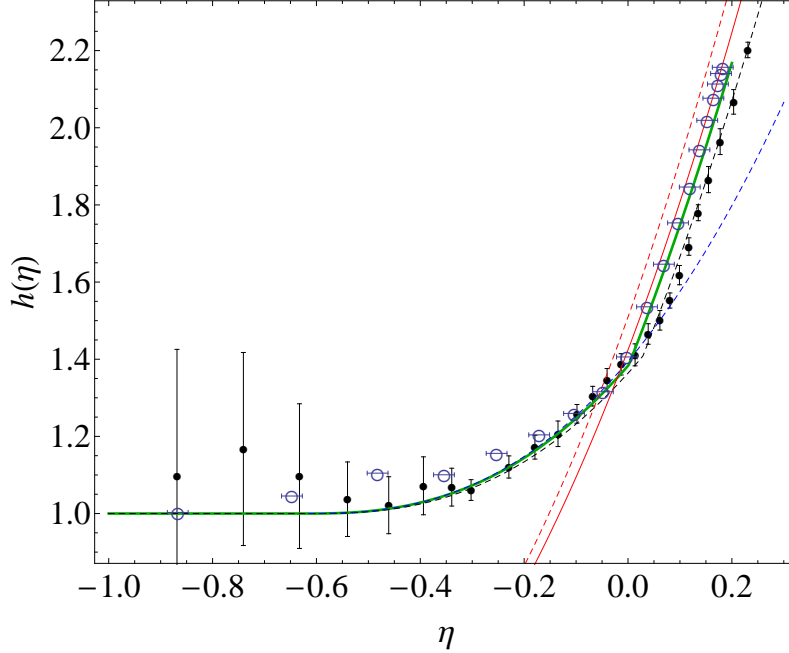


Figure 6.13: Universal function $h(\eta)$ extracted from the MIT data (in empty blue circles). The error bars are an estimate on the uncertainty on the determination of η_0 . The solid (dashed) red line is the superfluid EoS with $\xi_s = 0.395$ (0.38). The dashed blue line is the EoS of the polaron gas (Eq.6.28). Our measurement is shown in filled black circles. We also plot the function $h(\eta, \delta_1^{0a})$ in solid green line, corresponding to a down shift of 1.4 G between the magnetic fields of the two measurements.

We also plot the quantity $\bar{n}_1^0(z) - A\bar{n}_2(z)$ (dotted black line) and notice that it is equal to $\bar{n}_1(z)$ to less than 1 % in the whole partially polarized phase. These profiles thus seem to verify the following functional relation¹⁶

$$\frac{\partial P}{\partial \mu_1} = \frac{\partial P_0}{\partial \mu_1} - A \frac{\partial P}{\partial \mu_2} \quad (6.39)$$

from which we deduce that the pressure in the normal phase should read $P(\mu_1, \mu_2) = P_0(\mu_1) + f(\mu_2 - A\mu_1)$. For dimensional reasons, the unknown f -function can only be the pressure of the non-interacting Fermi gas times a constant that can be recast in a renormalization of the mass. Hence, we deduce from the profiles that the EoS in the normal phase is, to very good precision, equal to the pressure that we proposed for the polaron gas in Eq.(6.28). Finally, fitting the minority radius (and using A as an input parameter), we deduce the chemical potential ratio η_0 and we plot the resulting EoS in empty blue circles in Fig.6.13. We find very good agreement between our EoS and the one extracted from MIT density profiles in all three phases, though a small

¹⁶We differentiate with respect to z the relation $\bar{n}_1(z) = \bar{n}_1^0(z) - A\bar{n}_2(z)$, and use Eq.(6.19) in a harmonic trap. We deduce that $n_1(\mathbf{r}) = n_1^0(\mathbf{r}) - An_2(\mathbf{r}) + c$, with $c = 0$ since $n_1(\mathbf{r}) = n_1^0(\mathbf{r})$ if $|\mathbf{r}|$ is larger than the minority radius. Using the Gibbs-Duhem formula in this last expression leads to Eq.(6.39).

systematic shift is seen in the superfluid phase, that might be explained by a small difference in magnetic field between the two measurements (see section 5.3). For comparison, we displayed in a dashed red line the expected EoS for the superfluid with the most recent Fixed-Node upper bound $\xi_s < 0.38$ [263, 288], which is different from both EoS¹⁷. It is remarkable that such an analysis can be undertaken on a single density profile. Two points could easily be improved in this study. First, an average over several profiles would further reduce the noise on the data. Secondly and more importantly, the measurement of the EoS could be made more accurate by preparing the largest possible normal phase, with still a small superfluid core (to pinpoint η_c), adjusting the imbalance so that η_0 is just slightly above η_c .

Finite Scattering Length correction on ξ_s

As performed in section 5.3, we can estimate the EoS at a magnetic field of 834.1 G, given the fact that our data were likely taken at $B = 835.5$ G. A simple estimate is given by evaluating the value of the interaction parameter at the center of the trap $\delta_1^{0a} = \hbar/\sqrt{2m\mu_1^0}a$, with the value of a given above, and a typical value $\mu_1^0 = 630$ nK. Using our parametrization of the EoS $h(\eta, \delta_1)$ (see Fig.6.8), we plot in Fig.6.13 $h(\eta, \delta_{az})$ (solid green line) together with $h(\eta, 0)$ (dashed black line), where $\delta_{az} = \delta_1^{0a}/\sqrt{1 - z^2/R_1^2}$. The resulting EoS is slightly shift in the superfluid phase, and we note that the small systematic shift between our EoS and the one deduced from the MIT density profiles seems to be well explained by the small magnetic field shift. The change in the normal phase is even smaller because the change of the polaron energy A and effective mass are tiny, leading to minute changes in the partially polarized phase EoS. This analysis leads to a value of the Bertsch parameter of

$$\xi_s = 0.40(2). \quad (6.40)$$

The current uncertainty on the resonance position is an important source of systematic error on the determination of ξ_s .

To conclude this chapter, we have measured the equation of state of the uniform spin-1/2 Fermi gas as a function of spin-population imbalance and interaction strength. We have measured the critical line marking the separation between the unpolarized superfluid and the partially polarized normal phase phase diagram. This was observed to be a first-order quantum phase transition. From the unpolarized phase, we have extracted the equation of state of the balanced superfluid in the BEC-BCS crossover. We saw that the EoS in the normal phase was well described by the pressure of a weakly interacting gas of polarons. We used our measurement to compare with previous works done both in a trap and on the homogeneous gas. Our work should be extended in the deep molecular regime, where many questions remain opened on the phase diagram, in particular the change from the partially polarized normal phase to the polarized superfluid, and the detection of exotic phases, such as the FFLO phase. However, in the BEC regime, a new method to determine μ_2 in the absence of the partially polarized phase should be devised.

¹⁷One can assume this value of ξ_s and fit η_0 to match the data in the superfluid phase. However, we notice in this case that the data points for the EoS are systematically above unity for $\eta \approx A$. This would be in contradiction with the single-polaron physics, expecting to constraint the appearance of the minority atoms at $\eta = A$. More investigations are required to clarify this point.

Conclusion

Summary

In this work, we have developed and implemented a new method to probe the thermodynamics of homogeneous 3D quantum gases using harmonically trapped samples. This method is based on an elementary relation that links the local pressure of the gas to the doubly-integrated density profile. This technique is very powerful: it requires only very general assumptions, namely the validity of the local density approximation and an external harmonic trapping. Because it makes no additional assumptions on the system itself, this method can be equally applied to systems of interacting bosons, fermions, or arbitrary mixtures. It is valid at finite temperature and for arbitrary, short- or long-range interactions. In this work, we have applied this method to measure the equation of state of Bose and Fermi gases with short-range interactions. We benefited from Feshbach resonances on fermionic ^6Li and bosonic ^7Li and used them to study the many-body physics of these systems with tunable interactions. The equation of state of the homogeneous gas is a central quantity in the characterization of the many-body system, since it condenses all the thermodynamic information of the system. Furthermore it can be calculated by advanced many-body theories and thus allows direct comparison between theory and experiment, providing benchmarks for theoretical models.

We first presented our study of the pointlike Bose gas. Using a cloud of ^7Li , we measured the pressure as a function of the interaction strength. For sufficiently large interactions, we observed the onset of beyond mean-field effects. We made a quantitative comparison with the seminal calculation performed by T.D. Lee, K. Huang and C.N. Yang in 1957 and found excellent agreement. The increase of three-body losses with interactions required a study of non-equilibrium effects to support the assumption of thermal equilibrium, as well as a direct comparison with a Quantum Monte Carlo calculation to verify the zero-temperature assumption. Using faster sweep rates, we have explored the regime of strong interactions, and we inferred a lower bound on the value of the universal constant ξ_B that would characterize the hypothetical unitary Bose gas. This lower bound was compared to theoretical predictions.

In the second part, we explored the thermodynamics of a two-component Fermi gas. We first addressed the finite-temperature thermodynamics of the unitary Fermi gas. Thermometry of the strongly interacting system was performed using a trace of bosonic ^7Li as a thermometer. Besides the virial expansion, and the superfluid-to-normal phase transition, we observed that the normal phase thermodynamics of the unitary gas is well described by Landau's Fermi liquid theory. Using the Landau parameters extracted from our EoS, we predicted the spectral function of the system. Photoemission experiments performed at JILA have been interpreted using pseudo-gap models but we find that our description in terms of a Fermi liquid accounts well for their current observations,

with no adjustable parameters.

We then turned to the low-temperature Fermi gas in the BEC-BCS crossover, from which we extracted various well-controlled asymptotic behaviors. In particular, we used our measured EoS to compute the contact for a trapped gas and compare it to several other measurements on ^6Li and ^{40}K , providing strong indication of universality of the BEC-BCS crossover. In the molecular limit, we recover the Lee-Huang-Yang correction for a gas of bosonic dimers, illustrating the universality of the first beyond-mean-field correction in a Bose gas.

Finally, we investigated the phase diagram of a two-component Fermi gas with spin-population imbalance. We confirmed that the unpolarized superfluid is very robust with respect to chemical potential imbalance, and is present at the center of the trapped sample. Above a critical chemical potential ratio η_c , a first-order quantum phase transition to a normal state occurs and we mapped out the phase diagram. We showed that the normal phase is well described by a Fermi-liquid equation of state of Fermi polarons, the quasi-particle resulting from a single minority atom dressed by the interactions with the Fermi sea majority atoms.

Perspectives

The work presented in this thesis could be extended in various directions. In what follows, we first focus on ideas that could readily be implemented on our existing ^6Li - ^7Li setup.

Bose gases

A possible extension to our $T = 0$ study would be the measurement of another fundamental prediction of weakly interacting Bose gases. Bogoliubov theory predicts that due to interactions, some particles are expelled from the condensate (state $\mathbf{k} = 0$ for a homogeneous Bose gas) and possess a finite momentum, the so-called *quantum depletion*. The quantum depleted fraction of a Bose-Einstein condensate is predicted to be [143]:

$$1 - \frac{N_0}{N} = \frac{8}{3\sqrt{\pi}} \sqrt{na^3} \quad (6.41)$$

A central example of strongly interacting quantum liquid, superfluid ^4He , was measured to have a quantum depletion of about 90 % [324], for which the gas parameter is $na^3 \sim 0.1$ and Bogoliubov theory is not expected to be quantitatively accurate. For the largest interaction strengths reached in quasi-equilibrium in this work ($na^3 \sim 3 \times 10^{-3}$), Eq. (6.41) predicts a quantum depletion of about 8 %. This can be contrasted with the quantum depletion for typical ^{87}Rb or ^{23}Na condensates of 0.1-0.5 %. First measurements of quantum depletion in an ultracold Bose gas were achieved by loading a BEC in a deep optical lattice, which effectively increased the interactions [325]. Bragg spectroscopy could be used to probe the momentum distribution of the depleted Bose-Einstein condensate [326]. One can also employ a Feshbach resonance to switch off the interactions just prior to switching off the trap and measure the momentum distribution using the time-of-flight technique. This method allowed for the detection of a condensed fraction as low as 2 % on ^{39}K [327].

The problem of the strongly interacting Bose gas is largely open and it would be important to investigate whether a unitary limit $na^3 \rightarrow \infty$ can be well defined, and whether the properties of this unitary Bose gas could be universal or if it would depend on additional parameters besides the

scattering length a (such as the three-body parameter Λ_*). In order to avoid the collapse instability, numerical simulations have been limited either to weak interactions, or potentials without two-body bound states [163]. However, we saw in chapter 1 that in order to be simultaneously short-ranged ($nb^3 \ll 1$, b being the range of the potential) and strongly interacting ($na^3 \gg 1$), and thus expect universal properties, one needs an interaction potential with an attractive part. A simulation with such a potential that would reject the two- (and possibly N -) body bound states in order to simulate the gaseous phase, could explore the strongly correlated regime. From an experimental perspective, the three-body losses are the main obstacle in achieving a strongly interacting Bose gas. However, it was proposed that immersing the Bose gas (at low filling factors) in an optical lattice could lead to an effective three-body repulsion and would prevent the collapse in deeply bound states, thus stabilizing the “lower branch” [328]. If the stability issues were solved, it might be possible to investigate a type of BEC-BCS crossover predicted to occur in pointlike Bose gases, from atomic to molecular superfluids [50, 51, 52, 53].

The finite-temperature thermodynamics of the Bose gas is a very rich subject as well. In particular, the effect of interactions on the Bose-Einstein transition is a notoriously subtle problem and has been the center of considerable attention for many years. An important motivation is to understand why the critical temperature for the λ -transition of liquid ^4He , $T_c = 2.2$ K is smaller than the Bose-Einstein condensation temperature $T_c^0 = 3.1$ K for an ideal gas of helium atoms with the same density ($n = 2.2 \times 10^{22} \text{ cm}^{-3}$). This problem was tackled theoretically as early as the 1950’s and a Monte-Carlo calculation on a hard-sphere Bose gas showed highly non-trivial interaction-strength dependence of T_c , first *increasing* at low density compared to T_c^0 , then becoming smaller above $na^3 \sim 0.1$ [329]. The low-density limit was addressed with various methods, leading to a large number of different predictions, both in dependence on a and even sign¹⁸ ! It is now generally believed that the critical shift for a homogeneous Bose gas is to leading order $\Delta T_c/T_c^0 = c(na^3)^{1/3}$, with $c \approx 1.3$ [331, 332]. The interest in the study of strongly interacting Bose gases has been considerably revived in the last years [48, 148]. Very recently, the observation of the critical shift for BEC in a trapped Bose gas of ^{39}K as well as the condensate fraction behavior close to the critical point have been reported [327, 333]. The equation of state $P(\mu, a)$ as a function of the parameter a/λ_{dB} could be measured with our method (μ_0 and T being determined using a mean-field theory on the thermal wings), exploring for instance the critical chemical potential shift, the role of the Bogoliubov quasi-particles [334] in the finite-temperature thermodynamics of the superfluid phase, the possible role of the Efimov effect in the virial expansion [205], or a breakdown of universality at large scattering lengths [176].

Fermi gases

The finite-temperature thermodynamic study of the unitary gas could be extended in the BEC-BCS crossover. Using a/λ_{dB} as the interaction parameter (rather than a local interaction parameter such as δ), it should be possible to scan the parameter space $(\beta\mu, a/\lambda_{dB})$ along lines of fixed a/λ_{dB} , owing to the fact that T is homogeneous in the trapped sample, by adjusting the scattering length to the temperature of the gas obtained. In this way, the same patching method used in chapter 5 could be readily applied to reconstruct the EoS of the finite-temperature balanced Fermi gas, using the virial coefficients calculated in the BEC-BCS crossover (shown in the appendix 5.3). The stakes are high: the critical temperature T_c for the superfluid transition of the homogeneous gas is one of

¹⁸For a historical perspective of these predictions, see the introduction in [330].

the most important quantities to be measured for the crossover physics. The exact nature of the normal phase is still to be clarified, with a crossover between a normal phase described by Fermi liquid theory in the BCS side and at unitarity, and a bosonic normal phase with preformed pairs on the BEC side of the resonance. The phase diagram of the imbalanced Fermi gas is even richer. The phase diagram in the molecular regime contains many open questions and deserves further investigation. Moreover, a tri-critical point was observed at finite-temperature for the imbalanced unitary gas [248], where the unpolarized superfluid/normal phase transition turns from first-order to second-order. The temperature dependence of the tri-critical point as a function of interactions could be measured.

In addition to the attractive Fermi gas discussed above, the repulsive Fermi gas (on the “upper branch”) has attracted considerable attention. A recent experiment suggested that the Fermi gas undergoes a phase transition to a ferromagnetic state at a critical value of $(k_F a)_c = 1.9(2)$ [186]. However, with similarities to the repulsive Bose gas studied in chapter 3, this system is metastable for increasing interactions (with a decay to the “lower branch”), and since there was no direct observation of ferromagnetic domains or divergence of the magnetic susceptibility, the interpretation of the MIT measurements in terms of the ferromagnetic Stoner instability is challenged (see for instance [335]). The equation of state of the repulsive Fermi gas could be measured, and should follow the Galitskii-Lee-Yang expansion in the dilute limit. It is not sure, however, that reaching sufficiently high values of $k_F a$ will be possible, due to stability issues [187]. Finally, the two-component Fermi gas in the vicinity of a narrow resonance could allow us to study a system with a non-negligible effective range r_e , a situation closely resembling the one of medium-density neutron matter [189]. This could be done with the resonance located at 543 G for the $|1\rangle - |2\rangle$ mixture of ${}^6\text{Li}$.

Bose-Fermi mixtures

The ${}^6\text{Li}$ - ${}^7\text{Li}$ system provides us with a very convenient isotopic mixture to study strongly interacting Bose-Fermi mixtures (reminiscent of the ${}^4\text{He}$ - ${}^3\text{He}$ system), which are predicted to have similarities with dense QCD matter (see for instance [336]). The ${}^6\text{Li}$ - ${}^7\text{Li}$ is predicted to have several wide heteronuclear resonances in various spin-mixture combinations [133]. The limitation due to the collapse of ${}^7\text{Li}$ at the BEC threshold (because of its negative scattering length) encountered in chapter 5 can be solved using two different spin-combinations. One can use ${}^6\text{Li}$ in the $|1\rangle - |3\rangle$ mixture (around $B = 690$ G) and ${}^7\text{Li}$ in state $|1\rangle$ (the state used for our Bose gas experiments), whose Feshbach resonance is at 738 G. Another possibility is the fermion gas in the $|1\rangle - |2\rangle$ mixture (around $B = 834$ G) and ${}^7\text{Li}$ in state $|2\rangle$. This last Bose-Fermi mixture might exhibit unusual features because both Feshbach resonances occur at almost the same magnetic field ($B_0 = 831(4)$ for ${}^7\text{Li}$ in state $|2\rangle$). Using one of these mixtures, we could probe the very-low temperature physics of the strongly interacting Fermi gas, as well as creating mixtures of bosonic and fermionic superfluids.

Other systems

In addition to these perspectives applicable to our ${}^6\text{Li}$ - ${}^7\text{Li}$ system, virtually any (harmonically) trapped cold atomic system could benefit from the pressure measurement method. Indeed, there are many intriguing systems under active investigation whose thermodynamics could yield very valuable information. For example Fermi-Fermi mixtures with mass imbalance in the strongly interacting regime have been realized [145, 337], and have mismatched Fermi surfaces (similarly to the spin-imbalanced gas). They are predicted to have a rich phase diagram (see for instance [338])

and references therein), including a crystalline phase transition [339]. Quantum gases of ground state polar molecules are now prepared near quantum degeneracy [340, 341], and would allow the study of systems with long-range anisotropic interactions. Bosons and/or fermions in optical lattices present a major interest in simulating quantum magnetism [14], and studying their phase diagram, described by the Bose- or Fermi-Hubbard model [8] using our thermodynamic method would be possible as well. Because of its simplicity, and its wide applicability, we believe that the pressure method we have developed could be a valuable tool to probe the thermodynamics of novel strongly correlated ultracold systems.

Appendix A

Technical details

A.1 Testing the self-consistent determination of μ_0 on a Bose gas

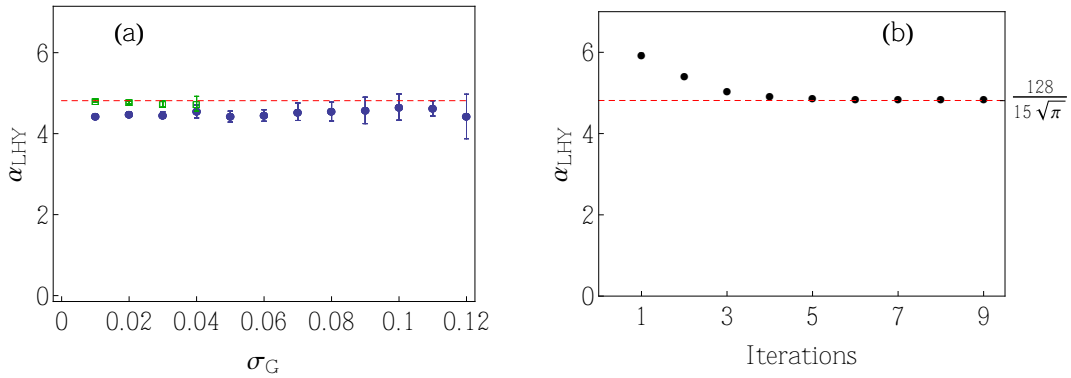


Figure A.1: Test of the self-consistent determination of μ_0 . (a): The LHY coefficient α_{LHY} is plotted as a function of the gaussian noise (measured in standard deviation of σ_G with respect to the peak density). In blue circles (green squares) the result using a polynomial interpolation function (the exact LHY function). The experimental data correspond to $\sigma_G \sim 0.07$. (b): An example of convergence of the EoS towards the fixed point, by fitting α_{LHY} at each fitting iteration.

We test the self-consistent determination of μ_0 on the Bose gas presented in chapter 3 by generating realistic density profiles for our trap geometry ($\omega_r/2\pi = 345$ Hz, $\omega_z/2\pi = 18.5$ Hz) and typical atom numbers, using the beyond-mean-field EoS predicted by Lee, Huang and Yang Eq.(3.1). We add a gaussian noise of standard deviation σ_G , normalized to the peak density. We use the generic polynomial interpolation function presented above, and after averaging over 15 profiles, we fit the Lee-Huang-Yang coefficient α_{LHY} , defined by $\mathcal{E} = \mathcal{E}_{\text{MF}}(1 + \alpha_{\text{LHY}}\sqrt{na^3})$ (and using the correspondence equations (3.23) and (3.24) to translate the energy into pressure) to find the blue circles in Fig.A.1a. This shows that apart from a small shift, the method converges towards the correct equation of state. By plotting α_{LHY} at each iteration (Fig.A.1b), we see the necessity of the self-consistent determination as the first value is incorrect. We recall that the

mean-field EoS correspond to $\alpha_{\text{LHY}} = 0$. The systematic shift is due to the choice of interpolation function, and can be made arbitrarily small if one assumes the correct power for the first beyond mean-field correction, for example $h(\nu)^{(1)} = 2\pi\nu^2(1 + \gamma_1\nu^{1/2} + \gamma_2\nu)$ (green squares Fig.A.1a), but it is currently not a limiting factor given our experimental accuracy.

A.2 Padé approximants

In this section, we detail the Padé approximants used in section 5.2, and show how the various asymptotic behaviors and the related physical quantities (such as the Galitskii-Lee-Yang or the Lee-Huang-Yang coefficients) are extracted. The Padé approximants are used to parametrize our equation of state $h_S(\delta)$ of the spin-balanced $T = 0$ Fermi gas in the BEC-BCS crossover and have two uses. First, it allows us to translate the grand-canonical EoS (the pressure) $h(\delta)$, in the canonical one (the energy) $\xi(x)$ using the Legendre transform, which involves derivative of the EoS (see Fig.5.19 for instance). Next, it allows us to extract physically relevant quantities in the BEC, the BCS and the unitary limit. Since our measurements are limited to a range where the interactions are not weak $k_F|a| \gtrsim 1$, it is useful to fit the data with functions that can be expanded in powers of $k_F a$ and that are regular around unitarity.

We want to relate the perturbative expansion coefficients of the ξ function (in the canonical ensemble) by the one found from the function $h(\delta)$ in the grand-canonical language. The definitions are:

$$\xi\left(x \equiv \frac{1}{k_F a}\right) = \frac{E/N - E_b/2}{E_{FG}} \quad (\text{A.1})$$

where E_b is the molecular binding energy ($E_b = -\hbar^2/ma^2$ when $a > 0$, 0 otherwise), N the total atom number and $E_{FG} = \frac{3}{5}E_F$ the energy of a non-interacting Fermi gas. The function h is defined as:

$$h(\delta) = \frac{P(\mu, a)}{2P_0(\mu)} \quad (\text{A.2})$$

where $\tilde{\mu} = \mu - E_b/2$, $\delta = \frac{\hbar}{a\sqrt{2m\tilde{\mu}}}$,

A.2.1 Relation between ξ and h

From Canonical to Grand-Canonical

Using the standard Legendre transform for the fully paired superfluid $E/V = -P + \mu n$ (where n is the total atomic density), the Gibbs-Duhem relationship $dP = nd\mu$ and the appropriate normalization for the dimensionless functions ξ and h , one finds the following equations related the two EoS in the two ensembles (from Canonical to Grand-Canonical, using the canonical variable x):

$$G(x) = \xi(x) - \Theta(x)\frac{5}{3}x^2 \quad (\text{A.3})$$

$$\mu(x) = G(x) - \frac{x}{5}G'(x) + \Theta(x)x^2 \quad (\text{A.4})$$

$$\delta(x) = \frac{x}{\sqrt{\mu(x)}} \quad (\text{A.5})$$

$$h(x) = \frac{G(x) - \frac{x}{2}G'(x)}{\mu(x)^{5/2}} \quad (\text{A.6})$$

h can thus be plotted as a function of its natural variable δ through a parametric plot $(\delta(x), h(x))$. The terms with $\Theta(x)$ account for the molecular binding energy on the BEC side ($x > 0$).

From Grand-Canonical to Canonical

The EoS in the reverse direction is given by:

$$x(\delta) = \frac{\delta}{(h(\delta) - \frac{\delta}{5}h'(\delta))^{1/3}} \quad (\text{A.7})$$

$$\xi(\delta) = \frac{h(\delta) - \frac{\delta}{3}h'(\delta)}{(h(\delta) - \frac{\delta}{5}h'(\delta))^{5/3}} \quad (\text{A.8})$$

Moreover, we can write down the expression of the chemical potential (in units of the Fermi energy):

$$\mu(\delta) = x(\delta)^2 \left(\frac{1}{\delta^2} - \Theta(\delta) \right) \quad (\text{A.9})$$

A.2.2 The BCS side

We write the expansion on the BCS side:

$$\xi(x) = 1 + \alpha_{MF}x^{-1} + \alpha_{LHY}x^{-2} + \alpha_Bx^{-3}, \quad (\text{A.10})$$

where α_{MF} is the mean-field shift, α_{LHY} the fermionic Lee-Huang-Yang correction and α_B the first beyond-LHY coefficient, computed by Baker. We start from the grand-canonical Padé approximant on the BCS side:

$$h(\delta) = \frac{\delta^2 + \alpha_1\delta + \alpha_2}{\delta^2 + \alpha_3\delta + \alpha_4} \quad (\text{A.11})$$

By expanding this expression in powers of δ^{-1} , and using the correspondence equations we obtain the coefficients of the power-expansion of h as a function of $\alpha_{MF}, \alpha_{LHY}$ and α_B , and we can relate them to the α_i 's of Eq.(A.11):

$$\alpha_{MF} = \frac{2}{3}(\alpha_3 - \alpha_1) \quad (\text{A.12})$$

$$\alpha_{LHY} = -\frac{2}{3}(\alpha_2 - \alpha_1\alpha_3 + \alpha_3^2 - \alpha_4 - \frac{6}{5}(\alpha_3 - \alpha_1)^2) \quad (\text{A.13})$$

$$\alpha_B = -\frac{2}{3}(-\alpha_2\alpha_3 + \alpha_1\alpha_3^2 - \alpha_3^3 - \alpha_1\alpha_4 + 2\alpha_3\alpha_4) + \frac{21}{5}\alpha_{LHY}\alpha_{MF} - \frac{18}{5}\alpha_{MF}^3 \quad (\text{A.14})$$

The four fitting parameters α_i 's are reduced to two using two constraints, the value at unitarity $\alpha_2/\alpha_4 = \xi_s^{-3/2}$ and the value of the mean-field correction $\alpha_{MF} = \frac{10}{9\pi}$.

A.2.3 The Contact

The Tan contact is defined as:

$$C = -\frac{4\pi m}{\hbar^2} \frac{\partial \mathcal{E}}{\partial(1/a)}, \quad (\text{A.15})$$

where \mathcal{E} is the energy density. It is more convenient to write it in the form : $C = \frac{2\zeta_C}{5\pi} k_F^4$ where k_F is the Fermi momentum and ζ_C is a dimensionless number. It is easy to see that $\zeta_C = -\xi'(0)$. Using instead the function $h(\delta)$ we have: $\zeta_C = \frac{2\xi_s^2}{3} h'(0)$. It follows:

$$\zeta_C = \frac{2}{3\xi_s\alpha_2} \left((\xi_s^{3/2} - 1)\alpha_1 - \frac{5}{3\pi} \right) \quad (\text{A.16})$$

A.2.4 The BEC side

The function $\xi(x)$ on the BEC side is written as:

$$\xi(x) = \alpha_{MF} x^{-1} (1 + \alpha_{LHY} x^{-3/2} + x^{-3} (\alpha_W \log(x^{-1}) + \alpha_B)), \quad (\text{A.17})$$

We find the following expansion for h in the deep BEC regime (in powers of δ^{-1}):

$$h(\delta) = \frac{25}{24\alpha_{MF}} \left(\delta^{-1} - \frac{\sqrt{\frac{5}{6}} \alpha_{LHY}}{\alpha_{MF}^{1/2}} \right) + O(\delta) \quad (\text{A.18})$$

We use the following approximant:

$$h(\delta) = \frac{\beta_1 + \beta_2 \delta + \beta_3 \delta \log(1 + \delta) + \beta_4 \delta^2 + \beta_5 \delta^3}{1 + \beta_6 \delta^2} \quad (\text{A.19})$$

The Lee-Huang-Yang correction

We fit the data for $\delta > 0$ with the approximant (A.19) and we add two constraints: the value at unitarity : $\beta_1 = \xi_s^{-3/2}$ and the known mean-field coefficient. To do so, we develop (A.19) in powers of δ^{-1} :

$$h(\delta) = \frac{\beta_5}{\beta_6} \left(\delta^{-1} + \frac{\beta_4}{\beta_5} \right) + O(\delta) \quad (\text{A.20})$$

Thus, identifying the powers in (A.18) and (A.20), we fix a coefficient, $\beta_6 = \frac{24\alpha_{MF}\beta_5}{25}$, by using the mean-field coefficient (for simplicity the dimer-dimer scattering length a_{dd} is in unit of the atomic scattering length a) $\alpha_{MF} = \frac{5a_{dd}}{18\pi}$. From β_4 and the constraint on β_6 we can readily extract the LHY correction :

$$\alpha_{LHY} = \frac{\beta_4}{\beta_6} \frac{24\alpha_{MF}^{3/2}}{25} \sqrt{\frac{6}{5}} \quad (\text{A.21})$$

Wu parameter

We go one step further to determine the three-body parameter α_B . To do so, we use additional constraints: we fix the value of the checked LHY correction and the Wu coefficient α_W ¹:

$$\alpha_W = \frac{a_{dd}^3}{6\pi^2} (8(4\pi - 3\sqrt{3})) = \frac{a_{dd}^3}{2\pi^2} W, \quad (\text{A.22})$$

where $W = \frac{8}{3}(4\pi - 3\sqrt{3}) \approx 19.65$. And for the B coefficient:

$$\alpha_B = \frac{a_{dd}^3}{6\pi^2} \left(W \log \left(\frac{a_{dd}^3}{6\pi^2} \right) + BW \right) \quad (\text{A.23})$$

We fix the parameters in the Padé expression by pursuing the development (A.18) and simplifying with the known expression of the MF and LHY terms:

$$h(\delta) = \frac{15\pi}{4a_{dd}} \delta - 16\sqrt{2} + \left(\frac{640a_{dd}}{3\pi} - \frac{15a_{dd}W}{8} \log \left(\frac{a_{dd}^2}{2\pi} \right) - \frac{15a_{dd}BW}{8} \right) \frac{1}{\delta} + \frac{15a_{dd}}{4} W \frac{\log(\delta)}{\delta} \quad (\text{A.24})$$

¹Note that the 1/3 factor is missing compared to the traditional Wu coefficient because the expansion (A.17) is usually written in powers of in powers of na_{dd}^3 (see Eq. (5) in the paper), hence the argument of the log is x^{-3} .

To fit B , we fix use five constraints: ξ_s , ζ , the MF and LHY coefficients, and the Wu parameter. Thus:

$$\beta_1 = \xi_s^{-3/2} \quad (\text{A.25})$$

$$\beta_2 = \frac{3\zeta}{2\xi_s^2} \quad (\text{A.26})$$

$$\beta_6 = \frac{4a_{dd}}{15\pi}\beta_5 \quad (\text{A.27})$$

$$\beta_4 = -32\sqrt{\frac{3}{5}}\beta_6 \quad (\text{A.28})$$

$$\beta_3 = \frac{15a_{dd}}{4}W\beta_6 \approx 44.22\beta_6 \quad (\text{A.29})$$

Using all the preceding, we extract B through the only fitting parameter β_5 :

$$B = \frac{8}{15a_{dd}W} \left(-\frac{\beta_2\beta_6 - \beta_5}{\beta_6^2} + \frac{640a_{dd}}{3\pi} - \frac{15a_{dd}W}{8} \log \left(\frac{a_{dd}^2}{2\pi} \right) \right) \quad (\text{A.30})$$

A.2.5 Parameters for the Padé approximants

The best fit parameters to our total data for $h_S(\delta)$ are gathered in Tab.A1

	α_1	α_2	α_3	α_4		
	-1.137	0.533	-0.606	0.141		
	β_1	β_2	β_3	β_4	β_5	β_6
	3.78	8.22	8.22	-4.21	3.65	0.186

Table A.1: Padé-type approximants coefficients α_i and β_i fitted from our data.

A.3 The Magnetic Circuit

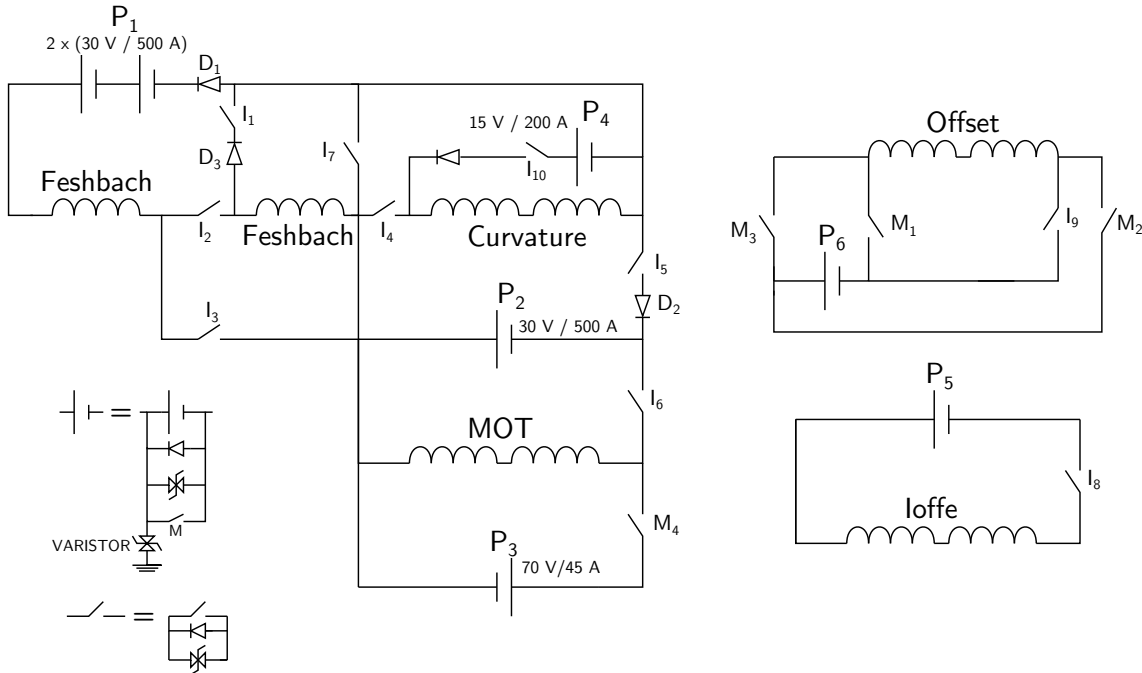


Figure A.2: Electric circuit of the experimental setup. High power supplies are noted P_i , IGBT switches I_i , power diodes D_i , and MOSFET switches M_i . Each power supply is protected by a diode in inverse and a high-voltage varistor (as the IGBT's). An additional MOSFET in parallel is used to unload the capacitors of the power supply to have smooth start ramps.

The magnetic trapping (Fig.2.2) involves several stages detailed in chapter 2. As the coils of our setup are often used in various configurations, the electric circuit (pictured in Fig.A.2) was designed (and modified) to be able to switch between these modes².

- In the MOT, Quadrupole Trap and Magnetic Transport: P_1 supplies the Feshbach coils in quadrupole (I_1 and I_3 closed, and I_2 open) and P_2 for the MOT coils (I_6 closed). At the end of the transport, the cloud is pushed slightly further by reversing the current in the MOT coils using P_3 (and M_4 closed).
- In the Ioffe-Pritchard trap, P_1 supplies the Feshbach and Curvature coils in series (I_2 and I_4 closed). Their bias fields cancel and makes the bias very robust to current fluctuations while the axial curvature is achieved by the curvature coils. The Ioffe bars are supplied by an independent circuit. During Doppler cooling, an additional large bias field (~ 500 G) is provided by P_2 in the curvature coils (I_5 closed). In the tight trap for RF evaporation, the (small) bias field is provided by the Offset coils (I_9 and M_3 closed).
- In the optical trap, the Feshbach and curvature coils are supplied separately, by P_1 and P_4 respectively (I_2 , I_7 and I_{10} closed). The Offset coils provide a fine tuning of the Feshbach

²Note that this setup is not optimal and in particular the circuit configuration used in the optical trap could be achieved with P_2 only, though we currently use P_4 in this stage as well. P_4 was added in a subsequent upgrade of the electric circuit in order to leave the working setup as is, without changing its characteristics in the previous MOT and Ioffe trap stages.

field in reverse (to match the Feshbach coils bias direction) by closing M_1 and M_2 (and opening M_3 and I_9).

Appendix B

Publications

Collective Oscillations of an Imbalanced Fermi Gas: Axial Compression Modes and Polaron Effective Mass

S. Nascimbène, N. Navon, K. J. Jiang, L. Tarruell, M. Teichmann, J. McKeever, F. Chevy, and
C. Salomon

Physical Review Letters **103**, 170402 (2009)

Collective Oscillations of an Imbalanced Fermi Gas: Axial Compression Modes and Polaron Effective Mass

S. Nascimbène, N. Navon, K. J. Jiang, L. Tarruell,^{*} M. Teichmann,[†] J. McKeever,[‡] F. Chevy, and C. Salomon

Laboratoire Kastler Brossel, CNRS, UPMC, École Normale Supérieure, 24 rue Lhomond, 75231 Paris, France

(Received 15 July 2009; revised manuscript received 2 October 2009; published 20 October 2009)

We investigate the low-lying compression modes of a unitary Fermi gas with imbalanced spin populations. For low polarization, the strong coupling between the two spin components leads to a hydrodynamic behavior of the cloud. For large population imbalance we observe a decoupling of the oscillations of the two spin components, giving access to the effective mass of the Fermi polaron, a quasiparticle composed of an impurity dressed by particle-hole pair excitations in a surrounding Fermi sea. We find $m^*/m = 1.17(10)$, in agreement with the most recent theoretical predictions.

DOI: 10.1103/PhysRevLett.103.170402

PACS numbers: 03.75.Ss, 05.30.Fk, 32.30.Bv, 67.60.Fp

The study of the low-lying excitation modes of a complex system can be a powerful tool for investigation of its physical properties. For instance, Earth's structure has been probed using the propagation of seismic waves in the mantle, and the ripples in space-time propagated by gravitational waves can be used as probes of extreme cosmic phenomena. In ultracold atomic gases, the measurement of low energy modes of bosonic or fermionic systems has been used to probe superfluidity effects [1], to measure the angular momentum of vortex lattices [2], and to characterize the equation of state of fermionic superfluids [3,4].

In this Letter, we study the excitation spectrum of an ultracold Fermi gas with imbalanced spin populations. This topic was initiated in the 1960s by the seminal works of Clogston and Chandrasekhar [5,6] and only recently found experimental confirmation thanks to the latest developments in ultracold Fermi gases [7,8]. These dramatic experiments have observed that when a fermionic superfluid is polarized through imbalance of spin populations, the trapped atomic cloud forms a shell structure. The energy gap associated with pairing maintains a superfluid core where the two spin densities are equal, while the outer shell is composed by a normal gas with imbalanced spin densities (see Fig. 1). Here, we extend this work to the unexplored dynamical properties of these systems and we focus on the regime of strong interactions, where the scattering length a is infinite. We show, in particular, that the study of the axial breathing mode provides valuable insight on the dynamical properties of a quasiparticle, the Fermi polaron, that was introduced recently to describe the normal component occupying the outer shell of the cloud [9–14]. The Fermi polaron is composed of an impurity (labeled 2) immersed in a noninteracting Fermi sea (labeled 1), and is analogous to the polaron of condensed matter physics, i.e., an electron immersed in a bath of noninteracting (bosonic) phonons. Understanding the static and dynamic properties of impurities immersed in an external bath is a paradigm of many-body systems. In addition

to polaron physics, famous examples include the Kondo effect, Higgs mechanism, or the dressed atom. Despite its apparent simplicity, this problem remains today very challenging in the limit of strong interactions.

According to the Landau theory of the Fermi liquid, the low energy spectrum of the polaron is similar to that of a free particle and can, in the local density approximation (LDA), be recast as

$$E_2(\mathbf{r}, \mathbf{p}) = AE_{F1}(\mathbf{r}) + V(\mathbf{r}) + \frac{p^2}{2m^*} + \dots \quad (1)$$

where V is the trapping potential, $E_{F1}(\mathbf{r}) = E_{F1}(0) - V(\mathbf{r})$

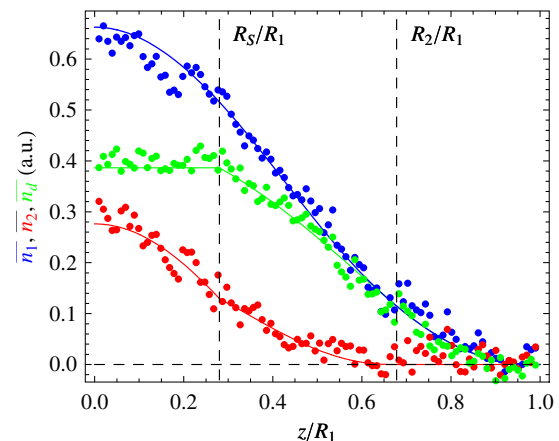


FIG. 1 (color online). Integrated density profiles of an imbalanced Fermi gas. Blue (dark gray): majority atoms $\bar{n}_1(z)$; Red (medium gray): minority atoms $\bar{n}_2(z)$; Green (light gray): difference $\bar{n}_d = \bar{n}_1 - \bar{n}_2$. In this latter case, the flat-top feature signals a cancellation of the density difference at the center of the trap, characteristic of the existence of a fully paired superfluid core. The superfluid (resp. minority) radius R_S (resp. R_2) are marked by vertical dashed lines. The solid color lines correspond to the prediction of Monte Carlo theories [20], the only fit parameters being the number of atoms in each spin state, $N_1 = 8.0 \times 10^4$, $N_2 = 2.4 \times 10^4$ for this image. The axial (radial) trap frequency is 18.6 Hz (420 Hz).

is the local Fermi energy of the majority species, A is a dimensionless quantity characterizing the attraction of the impurity by the majority atoms, and m^* is the effective mass of the Fermi polaron. For $a = \infty$, $A = -0.61$ has been determined both experimentally [14] and theoretically [9–13], while slight disagreements still exist on the value of the effective mass. Fixed node Monte Carlo suggests $m^*/m = 1.09(2)$ [15], systematic diagrammatic expansion yields $m^*/m = 1.20$ [11], and analysis of density profiles (such as Fig. 1) gives $m^*/m = 1.06$ [16].

From Eq. (1), the quasiparticle evolves in an effective potential $V^*(\mathbf{r}) = (1 - A)V(\mathbf{r})$. Assuming $V(\mathbf{r})$ to be harmonic with frequency ω , the polaron is trapped in an effective potential of frequency ω^* [9]:

$$\frac{\omega^*}{\omega} = \sqrt{\frac{1 - A}{m^*/m}}. \quad (2)$$

In this Letter we explore the compression mode properties and determine the effective mass through the measurement of the oscillation frequency ω^* in the axial direction (labeled z) of a cylindrically symmetric trap.

Our experimental setup is an upgraded version of the one presented in [17]. 7×10^6 ${}^6\text{Li}$ atoms in the hyperfine state $|F = 3/2, m_F = +3/2\rangle$ are loaded into a mixed magnetic or optical trap at $100 \mu\text{K}$. The optical trap uses a single beam of waist $w_0 = 35 \mu\text{m}$ and maximum power $P = 60 \text{ W}$ operating at a wavelength $\lambda = 1073 \text{ nm}$. The atoms are transferred into the hyperfine ground state $|1/2, 1/2\rangle$, and a spin mixture is created by a radio-frequency sweep across the hyperfine transition $|1/2, 1/2\rangle \rightarrow |1/2, -1/2\rangle$. By varying the rate of this sweep, we control the sample's degree of polarization $P \equiv (N_1 - N_2)/(N_1 + N_2)$, where N_1 (resp. N_2) is the atom number of the majority (resp. minority) spin species. The mixture is then evaporatively cooled in 6 s by reducing the laser power to 70 mW. This is done at a magnetic field $B = 834 \text{ G}$, which corresponds to the position of the broad Feshbach resonance in ${}^6\text{Li}$ where the scattering length is infinite and where further experiments are performed. Typical radial frequencies are $\omega_x = \omega_y \sim 2\pi \times 400 \text{ Hz}$. The axial confinement of the dipole trap is enhanced by the addition of a magnetic curvature, leading to an axial frequency $\omega_z \sim 2\pi \times 30 \text{ Hz}$. Our samples contain $\sim 8 \times 10^4$ atoms in the majority spin state at a temperature $T \lesssim 0.09T_F$. The temperature is evaluated by fitting the wings of the majority density profile outside the minority radius. In this region, the gas is noninteracting, allowing unambiguous thermometry of the inner, strongly interacting part of the cloud [18]. Here, T_F is defined as the Fermi temperature of an ideal gas whose density profile overlaps the majority one in the fully polarized rim.

The two spin states are imaged sequentially using *in situ* absorption imaging. To prevent heating from the scattered photons and the strong interactions between the two species, the duration of the two imaging pulses as well as their separation must be short ($10 \mu\text{s}$ each). By reversing the

order in which we image the two spin components, we checked that imaging of the first species did not significantly influence the second. Typical integrated density profiles of the atom cloud $\bar{n}(z) = \int dx dy n(x, y, z)$, where $n(x, y, z)$ is the 3D atom density, are presented in Fig. 1. These profiles display the characteristic features already observed by the MIT group [18]: a flat-top structure in the superfluid region confirming the existence of a fully paired core satisfying the LDA [19], an intermediate phase where the two spin species are present with unequal densities, and an outer rim containing only majority atoms. Following [20], we compare our density profiles to the prediction for the equation of state of the different phases and find fairly good agreement. In particular, we observe that the superfluid core disappears for polarizations $P > 0.76(3)$. This limit agrees well with the measurement of the MIT group [7] but differs from the Rice group value [8]. Our data also show no evidence for surface tension effects [8,21].

We excite the axial breathing mode by switching off the axial magnetic trapping field for 1 ms. The effect of this excitation is twofold: in addition to nearly suppressing the axial confinement, the bias field is increased up to 1050 G, where $k_F a \sim -1$, so that the gas is no longer strongly interacting. This scheme provides a spatially selective excitation of the cloud. Indeed, while the reduction of the trapping frequency perturbs the whole cloud, the modification of the scattering length only acts in the region where the two spin components overlap. In the regime of strong polarization, these two regions are well separated, leading to a differential excitation of the two spin components.

Let us first focus on the oscillations of the majority spin species presented in Fig. 2. Typical dynamics of the outer radius $R_1(t)$ of the majority component are exemplified by Fig. 2(a). For each polarization, this time evolution is fitted using an exponentially damped sinusoid, with $R_1(t) = R_1^{(0)}[1 + A_1 \cos(\omega_1 t + \varphi)e^{-\gamma_1 t}]$, and the variations of ω_1 and γ_1 as a function of P are displayed in Figs. 2(b) and 2(c). One remarkable feature of this graph is the frequency plateau for polarizations $P \lesssim 0.7$, corresponding approximately to the domain where a superfluid core is present in the cloud. Although in this range of parameters, the dynamics of the system is fairly complex due to the strong coupling between the superfluid and normal components, a simple argument based on a sum rule approach generalizing the result of [22] allows us to understand this property.

We describe the system by the Hamiltonian $H = \sum_i p_i^2/2m + U(\mathbf{r}_1, \mathbf{r}_2, \dots)$, where \mathbf{r}_i (resp. \mathbf{p}_i) is the position (resp. momentum of particle i), m is the mass of the atoms and U includes both trapping potential and interatomic interaction. The compression of the trapping frequency in the z direction is associated with the operator $F = \sum_i z_i^2$. Let us introduce the moments of the spectral distribution associated with F and defined by

$$m_k = \sum_{n \neq 0} (E_n - E_0)^k \langle 0|F|n\rangle^2,$$

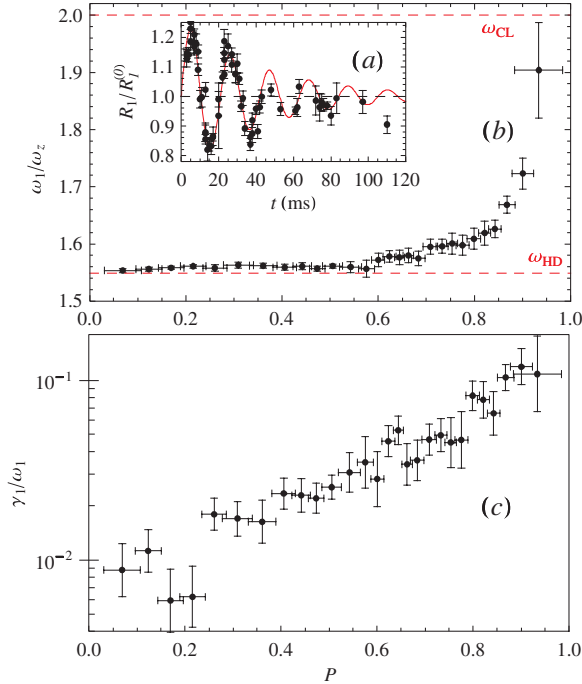


FIG. 2 (color online). (a) Oscillations of the axial radius of the majority component, for a population imbalance $P = 0.85(2)$, beyond the Clogston limit. The solid line corresponds to a fit by an exponentially damped sinusoid. (b) Frequency of the breathing mode ω_1 normalized to the axial trapping frequency ω_z versus polarization. The superfluid (resp. collisionless) limits $\omega_1 = \sqrt{12/5}\omega_z$ (resp. $2\omega_z$) are indicated by the dashed red lines. The axial (radial) trap frequency is $28.9(1)$ Hz (420 Hz). (c) Damping rate γ_1 versus polarization (in log scale). Note that our data are limited to $P < 0.95$ due to the small minority atom number ($N_2 \lesssim 2 \times 10^3$) at such high polarizations.

where the $|n\rangle$ are the eigenstates of H associated with the eigenvalue E_n , and $|0\rangle$ is the many-body ground state. We assume that the operator F mainly couples $|0\rangle$ to one excited state $|1\rangle$. In this case, the frequency of the breathing mode excited by the axial compression of the trap is given by $\omega_1 = (E_1 - E_0)/\hbar \simeq \sqrt{m_1/m_{-1}}/\hbar$. An explicit calculation of these two moments leads to the following expression:

$$\omega_1^2 \simeq -2\langle z^2 \rangle / \frac{\partial \langle z^2 \rangle}{\partial \omega_z^2}. \quad (3)$$

For a unitary gas, LDA imposes that the mean radius of the cloud is given by $\langle z^2 \rangle = R_{\text{TF}}^2 f(P)$, where R_{TF} is the radius of an ideal Fermi gas in the same trap and with the same atom number and f is some universal function of the polarization [23]. Using this assumption, the calculation of the oscillation frequency is straightforward and yields $\sqrt{12/5}\omega_z = 1.55\omega_z$, i.e., the hydrodynamic prediction [3,24] for $P = 0$, regardless of the polarization of the sample. This argument is in good agreement with our experimental findings [Fig. 2(b)].

At larger polarizations the frequency sharply increases towards the collisionless value. The damping rate, very small in the balanced superfluid, increases by a factor ~ 20 for higher imbalances [25]. Interestingly, as seen in Fig. 3, this behavior is consistent with a general argument about relaxation processes in fluid dynamics [26]. Indeed, one can relate ω_1 and γ_1 through

$$\omega^2 = \omega_{\text{CL}}^2 + \frac{\omega_{\text{HD}}^2 - \omega_{\text{CL}}^2}{1 + i\omega\tau}, \quad (4)$$

where $\omega = \omega_1 + i\gamma_1$, $\omega_{\text{HD}} = \sqrt{12/5}\omega_z$ (resp. $\omega_{\text{CL}} = 2\omega_z$) is the hydrodynamic (resp. collisionless) frequency and τ is an effective relaxation rate.

Measurements of ω_1/ω_z in three different traps of aspect ratios 8.2, 9.0, and 14.5 give identical results (within 3%) for all polarizations. By contrast, the effect of temperature is more pronounced: for instance at $0.12(1)T_F$, $\omega_1(P)$ remains equal to the hydrodynamic prediction at all attainable polarizations with $P_{\text{max}} = 0.95$, for a cloud of $N_1 \sim 2 \times 10^5$ majority atoms held in a trap of aspect ratio 22. This illustrates the role of Pauli blocking at the lowest temperatures which favors collisionless behavior. This is in contrast with the balanced gas case where the collisionless regime was observed at higher temperature ($T \gtrsim T_F$) [27].

Let us now consider the dynamics of the minority cloud (we recall that subscript 2 refers to the impurity atoms). We observe that for polarizations smaller than $P \sim 0.75$, the oscillation frequencies and damping rates of the two spin species are equal, indicating a strong coupling between them. By contrast, for $P > 0.75$, a Fourier spectrum of $R_2(t)$ reveals two frequencies [Fig. 4(a)], a generic feature of systems with multiple phases [28,29]. The lower frequency ω_{2a} is equal to the majority oscillation frequency ω_1 . We interpret the higher frequency ω_{2b} , whose weight increases with polarization, as the axial breathing of the minority atoms out of phase with the majority cloud. A linear extrapolation of this frequency to $P = 1$ gives the oscillation frequency of a dilute gas of weakly interacting polarons inside a Fermi sea at rest, $\omega_{2b}(P \rightarrow 1) = 2.35(10)\omega_z$ [Fig. 4(b)]. The uncertainty represents the standard deviation of a linear fit taking into account the

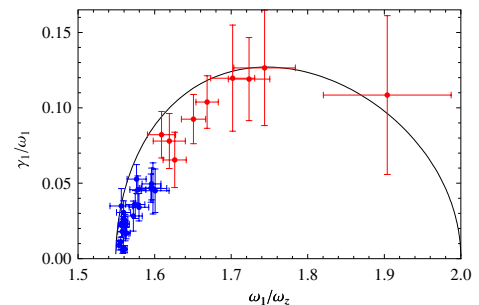


FIG. 3 (color online). Comparison of our experimental results with the parametric curve $(\omega_1(\tau)/\omega_z, \gamma_1(\tau)/\omega_1(\tau))$ deduced from prediction (4). The data in blue (dark gray) [red (medium gray)] correspond to polarizations $P < 0.8$ [$P > 0.8$].

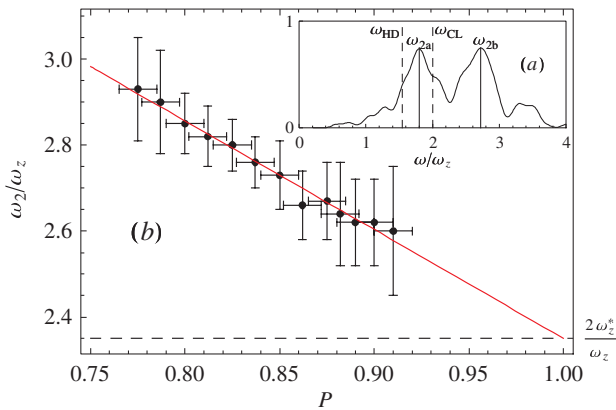


FIG. 4 (color online). (a) Frequency power spectrum of the minority spin state for $P = 0.90(2)$. The peak between ω_{HD} and ω_{CL} corresponds to the oscillation in phase with the majority, the other one to the polaron oscillation. (b) Frequency of the polaron component as a function of polarization. All frequencies are normalized to ω_z .

statistical uncertainties of the ω_{2b} measurements for each polarization.

By identifying the breathing mode frequency ω_{2b} as $2\omega_z^*$ and using (2), we deduce the mass of the quasiparticle: $m^*/m = 1.17(10)$. This is the first dynamic measurement of the polaron effective mass, in good agreement with the most recent theoretical predictions [11,15]. The previous measurement of m^* through analysis of density profiles required an approximate equation of state for the polaron gas, with uncontrolled accuracy [16]. Extrapolating $\omega_{2b}(P)$ to $P = 1$ allows us to overcome this issue. m^* is close to m (albeit different), a surprising feature for a system at unitarity.

In conclusion, we have studied the low frequency breathing modes of an elongated Fermi gas with imbalanced spin populations. In the presence of a superfluid core, the majority and minority components oscillate in phase with a frequency that is largely independent of the spin polarization. At strong polarizations, the minority atom oscillation reveals a second frequency, that we interpret as the Fermi polaron breathing mode. Further investigations will extend our work to all values of the scattering length. In particular, they should provide a clear signature of the polaron-molecule transition [14,30]. The role of interactions between polarons and damping phenomena should also be clarified [31].

We are grateful to S. Stringari, A. Recati, C. Lobo, M. Zwierlein, J. Dalibard, and Y. Castin for fruitful discussions as well as K. Magalhães and G. Duffy for experimental support. We acknowledge support from ESF (FerMix), SCALA, ANR FABIOLA, Région Ile de France (IFRAF), ERC and Institut Universitaire de France.

*Present address: Institute for Quantum Electronics, ETH Zurich, 8093 Zurich, Switzerland.

- [†]Present address: Max-Born-Institut, Max-Born-Strasse 2 A, 12489 Berlin, Germany.
- [‡]Present address: IOS, CQIQC and Department of Physics, University of Toronto, Canada.
- [1] S. Giorgini, L. Pitaevskii, and S. Stringari, *Rev. Mod. Phys.* **80**, 1215 (2008).
 - [2] F. Chevy, K. W. Madison, and J. Dalibard, *Phys. Rev. Lett.* **85**, 2223 (2000).
 - [3] M. Bartenstein, A. Altmeyer, S. Riedl, S. Jochim, C. Chin, J. Denschlag, and R. Grimm, *Phys. Rev. Lett.* **92**, 203201 (2004).
 - [4] J. Kinast, S. Hemmer, M. Gehm, A. Turlapov, and J. Thomas, *Phys. Rev. Lett.* **92**, 150402 (2004).
 - [5] A. Clogston, *Phys. Rev. Lett.* **9**, 266 (1962).
 - [6] B. S. Chandrasekhar, *Appl. Phys. Lett.* **1**, 7 (1962).
 - [7] M. Zwierlein, A. Schirotzek, C. Schunck, and W. Ketterle, *Science* **311**, 492 (2006).
 - [8] G. Partridge, W. Li, R. Kamar, Y. Liao, and R. Hulet, *Science* **311**, 503 (2006).
 - [9] C. Lobo, A. Recati, S. Giorgini, and S. Stringari, *Phys. Rev. Lett.* **97**, 200403 (2006).
 - [10] F. Chevy, *Phys. Rev. A* **74**, 063628 (2006).
 - [11] R. Combescot and S. Giraud, *Phys. Rev. Lett.* **101**, 050404 (2008).
 - [12] R. Combescot, A. Recati, C. Lobo, and F. Chevy, *Phys. Rev. Lett.* **98**, 180402 (2007).
 - [13] N. Prokof'ev and B. Svistunov, *Phys. Rev. B* **77**, 125101 (2008).
 - [14] A. Schirotzek, C.-H. Wu, A. Sommer, and M. W. Zwierlein, *Phys. Rev. Lett.* **102**, 230402 (2009).
 - [15] S. Pilati and S. Giorgini, *Phys. Rev. Lett.* **100**, 030401 (2008).
 - [16] Y. Shin, *Phys. Rev. A* **77**, 041603 (2008).
 - [17] T. Bourdel, L. Khaykovich, J. Cubizolles, J. Zhang, F. Chevy, M. Teichmann, L. Tarruell, S. Kokkelmans, and C. Salomon, *Phys. Rev. Lett.* **93**, 050401 (2004).
 - [18] Y. Shin, C. Schunck, A. Schirotzek, and W. Ketterle, *Nature (London)* **451**, 689 (2008).
 - [19] M. Haque and H. Stoof, *Phys. Rev. A* **74**, 011602 (2006).
 - [20] A. Recati, C. Lobo, and S. Stringari, *Phys. Rev. A* **78**, 023633 (2008).
 - [21] T. De Silva and E. Mueller, *Phys. Rev. Lett.* **97**, 070402 (2006).
 - [22] L. Vichi and S. Stringari, *Phys. Rev. A* **60**, 4734 (1999).
 - [23] F. Chevy, *Phys. Rev. Lett.* **96**, 130401 (2006).
 - [24] M. Amoruso, I. Meccoli, A. Minguzzi, and M. Tosi, *Eur. Phys. J. D* **7**, 441 (1999).
 - [25] The damping rate is expected to vanish in the truly collisionless limit, a regime difficult to access experimentally.
 - [26] L. Landau and E. Lifshitz, *Fluid Mechanics*, Course of Theoretical Physics Vol. 6 (Butterworth-Heinemann, Oxford, 1987).
 - [27] S. Riedl, E. Sánchez Guajardo, C. Kohstall, A. Altmeyer, M. Wright, J. Denschlag, R. Grimm, G. Bruun, and H. Smith, *Phys. Rev. A* **78**, 053609 (2008).
 - [28] M. Urban, *Phys. Rev. A* **78**, 053619 (2008).
 - [29] G. Bruun and B. Mottelson, *Phys. Rev. Lett.* **87**, 270403 (2001).
 - [30] N. Prokof'ev and B. Svistunov, *Phys. Rev. B* **77**, 020408 (2008).
 - [31] G. Bruun, A. Recati, C. Pethick, H. Smith, and S. Stringari, *Phys. Rev. Lett.* **100**, 240406 (2008).

Exploring the thermodynamics of a universal Fermi gas

S. Nascimbène*, N. Navon*, K. J. Jiang, F. Chevy, and C. Salomon

Nature **463**, 1057 (2010)

Exploring the thermodynamics of a universal Fermi gas

S. Nascimbène¹, N. Navon¹, K. J. Jiang¹, F. Chevy¹ & C. Salomon¹

One of the greatest challenges in modern physics is to understand the behaviour of an ensemble of strongly interacting particles. A class of quantum many-body systems (such as neutron star matter and cold Fermi gases) share the same universal thermodynamic properties when interactions reach the maximum effective value allowed by quantum mechanics, the so-called unitary limit^{1,2}. This makes it possible in principle to simulate some astrophysical phenomena inside the highly controlled environment of an atomic physics laboratory. Previous work on the thermodynamics of a two-component Fermi gas led to thermodynamic quantities averaged over the trap^{3–5}, making comparisons with many-body theories developed for uniform gases difficult. Here we develop a general experimental method that yields the equation of state of a uniform gas, as well as enabling a detailed comparison with existing theories^{6–15}. The precision of our equation of state leads to new physical insights into the unitary gas. For the unpolarized gas, we show that the low-temperature thermodynamics of the strongly interacting normal phase is well described by Fermi liquid theory, and we localize the superfluid transition. For a spin-polarized system^{16–18}, our equation of state at zero temperature has a 2 per cent accuracy and extends work^{19,20} on the phase diagram to a new regime of precision. We show in particular that, despite strong interactions, the normal phase behaves as a mixture of two ideal gases: a Fermi gas of bare majority atoms and a non-interacting gas of dressed quasi-particles, the fermionic polarons^{10,18,20–22}.

In this Letter we study the thermodynamics of a mixture of the two lowest spin states ($i = 1, 2$) of ⁶Li prepared at a magnetic field $B = 834$ G (see Methods), where the dimensionless number $1/k_F a$ characterizing the s -wave interaction is equal to zero, the unitary limit. (Here k_F is the Fermi momentum and a the scattering length.) Understanding the universal thermodynamics at unitarity is a challenge for many-body theories because of the strong interactions between particles. Despite this complexity at the microscopic scale, all the macroscopic properties of an homogeneous system are encapsulated within a single equation of state (EOS), $P(\mu_1, \mu_2, T)$, that relates the pressure P of the gas to the chemical potentials μ_i of the species i and to the temperature T . In the unitary limit, this relationship can be expressed as¹:

$$P(\mu_1, \mu_2, T) = P_1(\mu_1, T) h\left(\eta = \frac{\mu_2}{\mu_1}, \zeta = \exp\left(\frac{-\mu_1}{k_B T}\right)\right) \quad (1)$$

where $P_1(\mu_1, T) = -k_B T \lambda_{\text{dB}}^{-3}(T) f_{5/2}(-\zeta^{-1})$ is the pressure of a single component non-interacting Fermi gas. Here k_B is the Boltzmann constant, $\lambda_{\text{dB}}(T)$ is the de Broglie wavelength and $f_{5/2}(z) = \sum_{n=1}^{\infty} z^n / n^{5/2}$. $h(\eta, \zeta)$ is a universal function which contains all the thermodynamic information of the unitary gas (Fig. 1). In cold atomic systems, the inhomogeneity due to the trapping potential makes the measurement of $h(\eta, \zeta)$ challenging. However, this inhomogeneity of the trap can be turned into an advantage, as shown in refs 20 and 23.

We directly probe the local pressure of the trapped gas using *in situ* images, following a recent proposal²³. In the local density approximation, the gas is locally homogeneous with local chemical potentials:

$$\mu_i(\mathbf{r}) = \mu_i^0 - V(\mathbf{r}) \quad (2)$$

here μ_i^0 is the chemical potential at the bottom of the trap for species i and $V(\mathbf{r})$ is the trapping potential. Then a simple formula relates the pressure P to the doubly-integrated density profiles²³:

$$P(\mu_{1z}, \mu_{2z}, T) = \frac{m\omega_r^2}{2\pi} (\bar{n}_1(z) + \bar{n}_2(z)) \quad (3)$$

where $\bar{n}_i(z) = \int n_i(x, y, z) dx dy$, n_i being the atomic density. ω_r and ω_z are respectively the transverse and axial angular frequency of a cylindrically symmetric trap (see Fig. 2), m is the ⁶Li mass, and $\mu_{iz} = \mu_i(0, 0, z)$ is the local chemical potential along the z axis. From a single image, we thus measure the EOS, equation (1), along the parametric line $(\eta, \zeta) = (\mu_{2z}/\mu_{1z}, \exp(-\mu_{1z}/k_B T))$; see below.

The interest of this method is straightforward. First, one directly measures the EOS of the uniform gas. Second, each pixel row z_i gives a point $h(\eta(z_i), \zeta(z_i))$ whose signal to noise ratio is essentially given by that of $\bar{n}_1(z) + \bar{n}_2(z)$; typically one experimental run leads to ~ 100 points with a signal to noise ratio between 3 and 10. With about 40 images one gets $\sim 4,000$ points $h(\eta, \zeta)$, which after averaging provides a low-noise EOS of standard deviation $\sigma = 2\%$. In the following we illustrate the efficiency of our method on two important sectors of the parameter space (η, ζ) in Fig. 1: the balanced gas at finite temperature $(1, \zeta)$ and the zero-temperature imbalanced gas $(\eta, 0)$.

We first measure the EOS of the unpolarized unitary gas at finite temperature, $P(\mu_1, \mu_2, T) = P(\mu, T)$. The measurement of $h(1, \zeta)$ through the local pressure, equation (3), can be done provided one knows the temperature T of the cloud and its central chemical potential μ^0 .

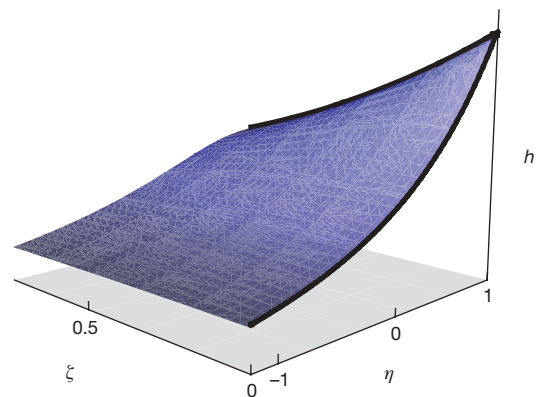


Figure 1 | Schematic representation of the universal function $h(\eta, \zeta)$. It fully describes the thermodynamics of the unitary gas as a function of chemical potential imbalance $\eta = \mu_2/\mu_1$ and of the inverse of the fugacity $\zeta = \exp(-\mu_1/k_B T)$. In this paper we measure the function h over the black lines $(1, \zeta)$ and $(\eta, 0)$, which correspond to the balanced unitary gas at finite temperature and to the spin-imbalanced gas at zero temperature, respectively.

¹Laboratoire Kastler Brossel, CNRS, UPMC, École Normale Supérieure, 24 rue Lhomond, 75231 Paris, France.

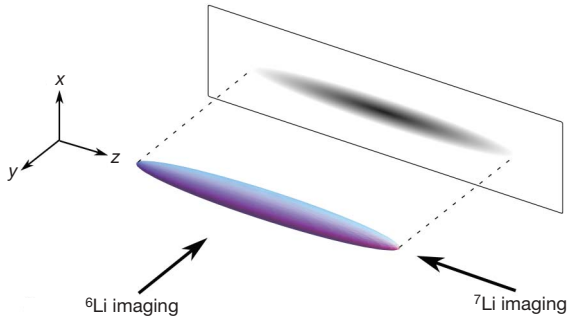


Figure 2 | Schematic representation of our atomic sample. The ${}^6\text{Li}$ atomic cloud is imaged in the direction y ; the column density is then integrated along the direction x to give $\bar{n}(z)$. The ${}^7\text{Li}$ atoms are imaged after a time of flight along the z direction.

In the balanced case, model-independent thermometry is notoriously difficult because of the strong interactions. Inspired by ref. 24, we overcome this issue by measuring the temperature of a ${}^7\text{Li}$ cloud in thermal equilibrium with the ${}^6\text{Li}$ mixture (see Methods).

The central chemical potential μ^0 is fitted on the hottest clouds so that the EOS agrees in the classical regime $\zeta \gg 1$ with the second-order virial expansion $h(1, \zeta) \approx 2(1 + \zeta^{-1}/\sqrt{2})$ (ref. 25). For colder clouds we proceed recursively. The EOS of an image recorded at temperature T has some overlap with the previously determined EOS from all images with $T' > T$. In this overlap region, μ^0 is fitted to minimize the distance between the two EOSs. This provides a new portion of the EOS at lower temperature. Using 40 images of clouds prepared at different temperatures, we thus reconstruct a low-noise EOS from the classical part down to the degenerate regime, as shown in Fig. 3a.

We now comment on the main features of the EOS. At high temperature, the EOS can be expanded in powers of ζ^{-1} as a virial expansion¹¹:

$$\frac{h(1, \zeta)}{2} = \frac{\sum_{k=1}^{\infty} \left((-1)^{k+1} k^{-5/2} + b_k \right) \zeta^{-k}}{\sum_{k=1}^{\infty} (-1)^{k+1} k^{-5/2} \zeta^{-k}}$$

where b_k is the k^{th} virial coefficient. As we have $b_2 = 1/\sqrt{2}$ in the measurement scheme described above, our data provide for the first time the experimental values of b_3 and b_4 . $b_3 = -0.35(2)$ is in excellent agreement with the recent calculation $b_3 = -0.291 - 3^{-5/2} = -0.355$ from ref. 11, but not with $b_3 = 1.05$ from ref. 12. $b_4 = 0.096(15)$ involves the four-fermion problem at unitarity and could interestingly be computed along the lines of ref. 11.

Let us now focus on the low-temperature regime of the normal phase $\zeta \ll 1$. As shown in Fig. 3b, we observe a T^2 dependence of the pressure with temperature. This behaviour is reminiscent of a Fermi liquid, and indicates that pseudogap effects expected for strongly interacting Fermi superfluids²⁶ do not show up at the thermodynamic level within our experimental precision. In analogy with ${}^3\text{He}$ or heavy-fermion metals, we fit our data with the EOS:

$$P(\mu, T) = 2P_1(\mu, 0) \left(\zeta_n^{-3/2} + \frac{5\pi^2}{8} \zeta_n^{-1/2} \frac{m^*}{m} \left(\frac{k_B T}{\mu} \right)^2 \right) \quad (4)$$

Here $P_1(\mu, 0) = 1/15\pi^2 (2m/\hbar^2)^{3/2} \mu^{5/2}$ is the pressure of a single-component Fermi gas at zero temperature, m^* is the quasi-particle mass, and ζ_n^{-1} is the compressibility of the normal gas extrapolated to zero temperature, and normalized to that of an ideal gas of same density. We deduce two new parameters $m^*/m = 1.13(3)$ and $\zeta_n = 0.51(2)$. Despite the strong interactions, m^* is close to m , unlike the weakly interacting ${}^3\text{He}$ liquid for which $2.7 < m^*/m < 5.8$, depending on pressure. Our ζ_n value is in agreement with the variational fixed-node Monte Carlo calculations $\zeta_n = 0.54$ in ref. 27 and

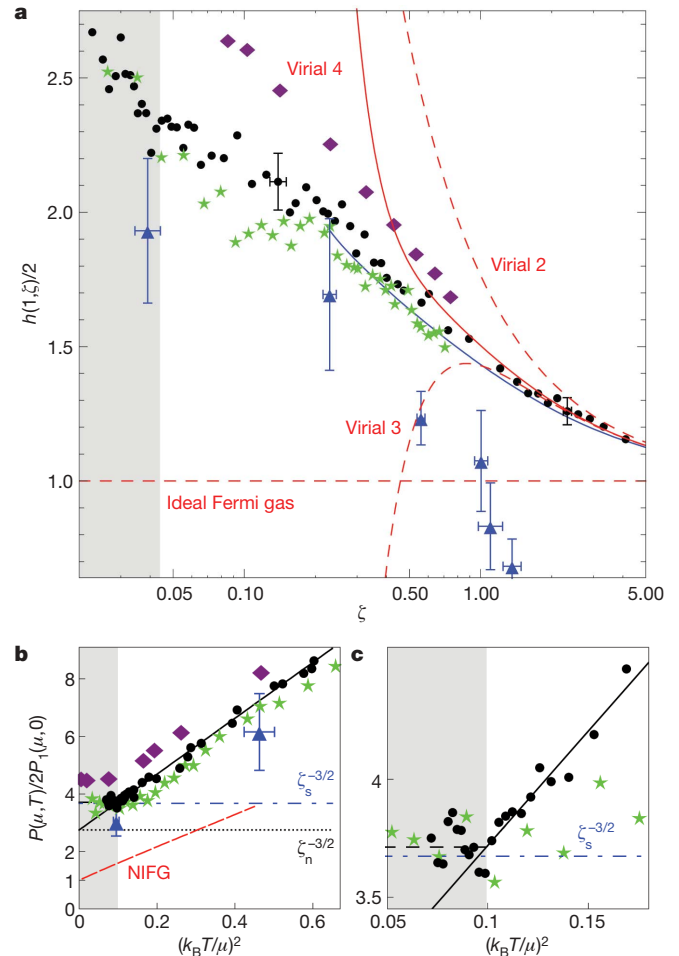


Figure 3 | Equation of state of a spin-balanced unitary Fermi gas. **a**, Finite-temperature equation of state (EOS) $h(1, \zeta)$ (black dots). The error bars represented at $\zeta = 0.14$ and $\zeta = 2.3$ indicate the 6% accuracy in ζ and h of our EOS. The red curves are the successive virial expansions up to fourth order. The blue triangles are from ref. 6, the green stars from ref. 7, the purple diamonds from ref. 8, and the blue solid line from ref. 9. The grey region indicates the superfluid phase. **b**, EOS $P(\mu, T)/2P_1(\mu, 0)$ as a function of $(k_B T/\mu)^2$, fitted by the Fermi liquid EOS, equation (4). The red dashed line is the non-interacting Fermi gas (NIFG). The horizontal dot-dashed and dotted lines indicate respectively the zero-temperature pressure of the superfluid phase $\propto \zeta_s^{-3/2}$ and that of the normal phase $\propto \zeta_n^{-3/2}$. **c**, Expanded view of **b** near T_c . The sudden deviation of the data from the fit occurs at $(k_B T/\mu)_c = 0.32(3)$ that we interpret as the superfluid transition. The black dashed line indicates the mean value of the data points below T_c .

$\zeta_n = 0.56$ in ref. 10, and with the quantum Monte Carlo calculation $\zeta_n = 0.52$ in ref. 28. This yields the Landau parameters $F_0^s = \zeta_n m^*/m - 1 = -0.42$ and $F_1^s = 3(m^*/m - 1) = 0.39$.

In the lowest temperature points (Fig. 3c) we observe a sudden deviation of the data from the fitted equation (4) at $(k_B T/\mu)_c = 0.32(3)$ (see Supplementary Information). We interpret this behaviour as the transition from the normal phase to the superfluid phase. This critical ratio has been extensively calculated in recent years. Our value is in close agreement with the diagrammatic Monte Carlo calculation $(k_B T/\mu)_c = 0.32(2)$ of ref. 6 and with the quantum Monte Carlo calculation $(k_B T/\mu)_c = 0.35(3)$ of ref. 28; but it differs from the self-consistent approach in ref. 8 that gives $(k_B T/\mu)_c = 0.41$, from the renormalization group prediction 0.24 in ref. 29, and from several other less precise theories. From equation (4) we deduce the total density $n = n_1 + n_2 = \partial P(\mu_i = \mu, T)/\partial \mu$ and the Fermi energy $E_F = k_B T_F = \hbar^2/2m(3\pi^2 n)^{2/3}$ at the transition point. We obtain $(\mu/E_F)_c = 0.49(2)$ and $(T/T_F)_c = 0.157(15)$, in very good agreement with ref. 6. Our measurement is the first direct determination of $(\mu/E_F)_c$

and $(T/T_F)_c$ in the homogeneous gas. It agrees with the extrapolated value of the MIT measurement¹⁹.

Below T_c , advanced theories^{7,8} predict that $P(\mu, T)/2P_1(\mu, 0)$ is nearly constant (Fig. 3b). Therefore at $T = T_c$, $P/2P_1 \approx \xi_s^{-3/2} \approx 3.7$, and is consistent with our data. Here $\xi_s = 0.42(1)$ is the fundamental parameter characterizing the EOS of the balanced superfluid at zero temperature, a quantity extensively measured and computed in recent years².

Our data are compared at all temperatures with the calculations from refs 6–9 in Fig. 3a. The agreement with ref. 7 is very good for a large range of temperatures. Concerning ref. 6, the deviation from our data is about one error bar of the Monte Carlo method below $\zeta = 0.2$, and the deviation increases with temperature (Fig. 3a). Furthermore, we show in the Supplementary Information that $h(1, \zeta)/2$ must be greater than 1, an inequality violated by the two hottest Monte Carlo points of ref. 6.

From our homogeneous EOS we can deduce the EOS of the harmonically trapped unitary gas by integrating $h(1, \zeta)$ over the trap (see Supplementary Information). In particular, we find a critical temperature for the trapped gas $(T/T_F)_c = 0.19(2)$, where $T_F = h(3\omega_r^2\omega_z N)^{1/3}$ and N is the total atom number. This value agrees very well with the recent measurement of ref. 30, and with less precise measurements^{5,31,32}.

Let us now explore a second line in the universal diagram $h(\eta, \zeta)$ (Fig. 1) by considering the case of the $T = 0$ spin-imbalanced mixture $\mu_2 \neq \mu_1$, that is, $\eta \neq 1$. Previous work^{16–18} has shown that phase separation occurs in a trap. Below a critical population imbalance a fully paired superfluid occupies the centre of the trap. It is surrounded by a normal mixed phase and an outer rim consisting of an ideal gas of the majority component. In two out of the three previous experiments including ours^{16,18}, the local density approximation has been carefully checked. We are therefore justified in using equation (3) to analyse our data.

As in the previous case, the relationship between the pressure and the EOS requires the knowledge of the chemical potentials μ_1^0 and μ_2^0 at the centre of the trap. μ_1^0 is determined using the outer shell of the majority spin component ($i = 1$). The pressure profile $P(\mu_{1\geq}, \mu_{2\geq}, 0)$ corresponds to the Fermi–Dirac distribution and is fitted with the Thomas–Fermi formula $P_1 = \alpha(1 - z^2/R_1^2)^{5/2}$, providing $\mu_1^0 = \frac{1}{2}m\omega_z^2 R_1^2$. Using P_1 for the calculation of $h = P/P_1$ cancels many systematic effects on the absolute value of the pressure. Moreover, fitting the outer shell using a finite-temperature Thomas–Fermi profile¹⁹, we measure a temperature $k_B T = 0.03(3)\mu_1^0$. μ_2^0 is fitted by comparison in the superfluid region with the superfluid EOS at zero temperature²¹:

$$h(\eta, 0) = (1 + \eta)^{5/2} / (2\xi_s)^{3/2} \quad (5)$$

Our measured EOS $h(\eta, 0)$ is displayed in Fig. 4. By construction our data agree for $\eta \geq 0.1$ with equation (5). In Fig. 4 the slope of $h(\eta, 0)$ displays an obvious discontinuity for $\eta = \eta_c = 0.065(20)$. This is a signature of a first-order quantum phase transition to the partially polarized normal phase. The error bar is dominated by the uncertainty on ξ_s . This value is slightly higher than the prediction $\eta_c = 0.02$ given by the fixed-node Monte Carlo¹⁰ and than the value $\eta_c = 0.03(2)$ measured in ref. 19.

From the relations $n_i = \partial P / \partial \mu_i$, we deduce from $h(\eta, 0)$ the density ratio n_2/n_1 (Fig. 4 inset). This ratio is discontinuous at the phase transition, from a maximum value in the normal phase $(n_2/n_1)_c = 0.5(1)$ to $n_2 = n_1$ in the superfluid phase. Our value is close to the zero-temperature calculation 0.44 (ref. 10) and agrees with the coldest MIT samples^{19,20}. It confirms that the temperature is much smaller than the tricritical point temperature $T = 0.07T_F$ (ref. 19) where the discontinuity vanishes, justifying our $T = 0$ assumption made above.

For $\eta < \eta_c$ our data display a good agreement with a simple polaron model, based on the pioneering work in ref. 10. A polaron is a quasi-particle describing a single minority atom immersed in the majority Fermi sea^{15,18,21,22}. It is characterized¹⁰ by a renormalized

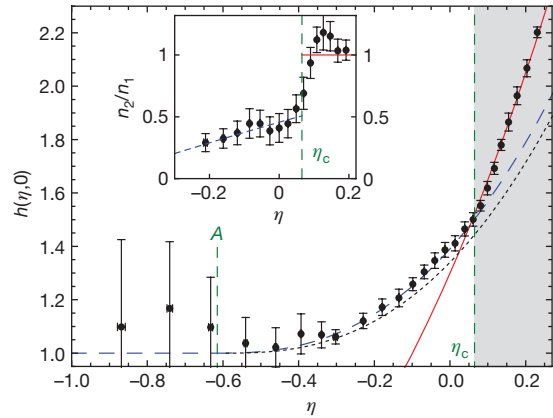


Figure 4 | Equation of state of the zero-temperature spin-imbalanced unitary gas $h(\eta, 0)$. The EOS is shown as filled black circles; error bars are equal to one standard error. The red solid line is the superfluid EOS, the blue dashed line is the ideal Fermi liquid, equation (7), with $A = -0.615$, $m^* = 1.20m$ and the black dotted line is the Monte Carlo calculation from ref. 10. Inset, local density ratio n_2/n_1 as a function of η . The red solid line $n_2/n_1 = 1$ corresponds to the fully paired superfluid and blue dashed line to the model, equation (7).

chemical potential $\mu_2 - A\mu_1$ and an effective mass m_p^* . Following this picture, we write the pressure as the sum of the Fermi pressures of ideal gases of majority atoms and of polarons:

$$P = \frac{1}{15\pi^2} \left(\frac{2m}{\hbar^2} \right)^{3/2} \left(\mu_1^{5/2} + \left(\frac{m_p^*}{m} \right)^{3/2} (\mu_2 - A\mu_1)^{5/2} \right) \quad (6)$$

which can be written as:

$$h(\eta, 0) = 1 + \left(\frac{m_p^*}{m} \right)^{3/2} (\eta - A)^{5/2} \quad (7)$$

A and m_p^* have recently been calculated exactly^{14,15}: $A = -0.615$, $m_p^*/m = 1.20(2)$, and with these values inserted in equation (7) the agreement with our data is perfect. Note that our data lie slightly above the variational fixed-node Monte Carlo calculation¹⁰. We therefore conclude that interactions between polarons are not visible at this level of precision.

Alternatively, we can fit our data with m_p^*/m as a free parameter in equation (7). We obtain $m_p^*/m = 1.20(2)$. The uncertainty combines the standard error of the fit and the uncertainty on ξ_s . This value agrees with our previous measurement¹⁸ $m_p^*/m = 1.17(10)$ (with a fivefold improvement in precision), with the theoretical value^{14,15} $m_p^*/m = 1.20(2)$, and with the variational calculation¹³. It differs from the values 1.09(2) in ref. 33, 1.04(3) in ref. 10, and from the experimental value 1.06 in ref. 20.

We arrive at a simple physical picture of the $T = 0$ spin-polarized gas: the fully paired superfluid is described by an ideal gas EOS renormalized by a single coefficient ξ_s ; the normal phase is nothing but two ideal gases, one of bare majority particles and one of polaronic quasiparticles.

In conclusion, we have introduced a powerful method for the measurement of the EOS of the unitary and homogeneous Fermi gas that enables direct comparison with theoretical models and provides a set of new parameters shown in Table 1. The method

Table 1 | Table of quantities measured in this work

Parameter	b_3	b_4	$(k_B T/\mu)_c$	$(\mu/E_F)_c$	$(T/T_F)_c$
Value	-0.35(2)	0.096(15)	0.32(3)	0.49(2)	0.157(15)
Parameter	ξ_n	m^*/m	η_c	$(n_2/n_1)_c$	m_p^*/m
Value	0.51(2)	1.13(3)	0.065(20)	0.5(1)	1.20(2)

can readily be extended to any multi-component cold atom gas in three dimensions that fulfils the local density approximation (see Supplementary Discussion). We have shown that the normal phase of the unitary Fermi gas is a strongly correlated system whose thermodynamic properties are well described by Fermi liquid theory, unlike high- T_c copper oxides.

Note added in proof: Since this paper was accepted for publication, we have become aware of the measurement of a similar equation of state for the balanced unitary Fermi gas at finite temperature by different methods³⁴.

METHODS SUMMARY

Our experimental set-up is presented elsewhere¹⁸. We load into an optical dipole trap and evaporate a mixture of ^6Li in the $|1/2, \pm 1/2\rangle$ states and of ^7Li in the $|1, 1\rangle$ state at 834 G. The cloud typically contains $N_6 = (5-10) \times 10^4$ atoms of ^6Li in each spin state and $N_7 = (3-20) \times 10^3$ atoms of ^7Li at a temperature from $T = 150$ nK to 1.3 μK . The ^6Li trap frequencies are $\omega_x/2\pi = 37$ Hz, $\omega_y/2\pi$ varying from 830 Hz to 2.20 kHz, and the trap depth is 25 μK for our hottest samples, with $T \approx 2T_F$. ^6Li atoms are imaged *in situ* using absorption imaging, while ^7Li atoms are imaged after time of flight, providing the temperature in the same experimental run (Fig. 4). As the scattering length describing the interaction between ^7Li and ^6Li atoms, $a_{67} = 2$ nm, is much smaller than k_F^{-1} , the ^7Li thermometer has no influence on the ^6Li density profiles. The ^7Li - ^6Li collision rate, $\Gamma_{67} = 10$ s $^{-1}$, is large enough to ensure thermal equilibrium between the two species.

Full Methods and any associated references are available in the online version of the paper at www.nature.com/nature.

Received 2 November 2009; accepted 6 January 2010.

- Ho, T.-L. Universal thermodynamics of degenerate quantum gases in the unitarity limit. *Phys. Rev. Lett.* **92**, 090402 (2004).
- Inguscio, M., Ketterle, W. & Salomon, C. (eds) *Proc. Int. School of Physics Enrico Fermi* (Course CLXIV, IOS Press, Amsterdam, 2006).
- Stewart, J., Gaebler, J., Regal, C. & Jin, D. Potential energy of a ^40K Fermi gas in the BCS-BEC crossover. *Phys. Rev. Lett.* **97**, 220406 (2006).
- Luo, L., Clancy, B., Joseph, J., Kinast, J. & Thomas, J. Measurement of the entropy and critical temperature of a strongly interacting Fermi gas. *Phys. Rev. Lett.* **98**, 080402 (2007).
- Luo, L. & Thomas, J. Thermodynamic measurements in a strongly interacting Fermi gas. *J. Low Temp. Phys.* **154**, 1-29 (2009).
- Burovski, E., Prokofev, N., Svistunov, B. & Troyer, M. Critical temperature and thermodynamics of attractive fermions at unitarity. *Phys. Rev. Lett.* **96**, 160402 (2006).
- Bulgac, A., Drut, J. & Magierski, P. Spin 1/2 fermions in the unitary regime: a superfluid of a new type. *Phys. Rev. Lett.* **96**, 090404 (2006).
- Haussmann, R., Rantner, W., Cerrito, S. & Zwirger, W. Thermodynamics of the BCS-BEC crossover. *Phys. Rev. A* **75**, 023610 (2007).
- Combescot, R., Alzetto, F. & Leyronas, X. Particle distribution tail and related energy formula. *Phys. Rev. A* **79**, 053640 (2009).
- Lobo, C., Recati, A., Giorgini, S. & Stringari, S. Normal state of a polarized Fermi gas at unitarity. *Phys. Rev. Lett.* **97**, 200403 (2006).
- Liu, X., Hu, H. & Drummond, P. Virial expansion for a strongly correlated Fermi gas. *Phys. Rev. Lett.* **102**, 160401 (2009).
- Rupak, G. Universality in a 2-component Fermi system at finite temperature. *Phys. Rev. Lett.* **98**, 090403 (2007).
- Combescot, R., Recati, A., Lobo, C. & Chevy, F. Normal state of highly polarized Fermi gases: simple many-body approaches. *Phys. Rev. Lett.* **98**, 180402 (2007).
- Combescot, R. & Giraud, S. Normal state of highly polarized Fermi gases: full many-body treatment. *Phys. Rev. Lett.* **101**, 050404 (2008).
- Prokofev, N. & Svistunov, B. Fermi-polaron problem: diagrammatic Monte Carlo method for divergent sign-alternating series. *Phys. Rev. B* **77**, 020408 (2008).
- Shin, Y., Zwierlein, M., Schunck, C., Schirotzek, A. & Ketterle, W. Observation of phase separation in a strongly interacting imbalanced Fermi gas. *Phys. Rev. Lett.* **97**, 030401 (2006).
- Partridge, G., Li, W., Kamar, R., Liao, Y. & Hulet, R. Pairing and phase separation in a polarized Fermi gas. *Science* **311**, 503-505 (2006).
- Nascimbene, S. *et al.* Collective oscillations of an imbalanced Fermi gas: axial compression modes and polaron effective mass. *Phys. Rev. Lett.* **103**, 170402 (2009).
- Shin, Y., Schunck, C., Schirotzek, A. & Ketterle, W. Phase diagram of a two-component Fermi gas with resonant interactions. *Nature* **451**, 689-693 (2008).
- Shin, Y. Determination of the equation of state of a polarized Fermi gas at unitarity. *Phys. Rev. A* **77**, 041603 (2008).
- Chevy, F. Universal phase diagram of a strongly interacting Fermi gas with unbalanced spin populations. *Phys. Rev. A* **74**, 063628 (2006).
- Schirotzek, A., Wu, C.-H., Sommer, A. & Zwierlein, M. W. Observation of Fermi polarons in a tunable Fermi liquid of ultracold atoms. *Phys. Rev. Lett.* **102**, 230402 (2009).
- Ho, T.-L. & Zhou, Q. Obtaining phase diagram and thermodynamic quantities of bulk systems from the densities of trapped gases. *Nature Phys.* **6**, 131-134 (2010).
- Spiegelhalder, F. *et al.* Collisional stability of ^40K immersed in a strongly interacting Fermi gas of ^6Li . *Phys. Rev. Lett.* **103**, 223203 (2009).
- Ho, T.-L. & Mueller, E. High temperature expansion applied to fermions near Feshbach resonance. *Phys. Rev. Lett.* **92**, 160404 (2004).
- Chen, Q., Stajic, J., Tan, S. & Levin, K. BCS-BEC crossover: from high temperature superconductors to ultracold superfluids. *Phys. Rep.* **412**, 1-88 (2005).
- Carlson, J., Chang, S., Pandharipande, V. & Schmidt, K. Superfluid Fermi gases with large scattering length. *Phys. Rev. Lett.* **91**, 050401 (2003).
- Bulgac, A., Drut, J. & Magierski, P. Quantum Monte Carlo simulations of the BCS-BEC crossover at finite temperature. *Phys. Rev. A* **78**, 023625 (2008).
- Gubbels, K. & Stoof, H. Renormalization group theory for the imbalanced Fermi gas. *Phys. Rev. Lett.* **100**, 140407 (2008).
- Riedl, S., Guajardo, E., Kohstall, C., Denschlag, J. & Grimm, R. Superfluid quenching of the moment of inertia in a strongly interacting Fermi gas. Preprint at (<http://arXiv.org/abs/0907.3814>) (2009).
- Greiner, M., Regal, C. & Jin, D. Emergence of a molecular Bose-Einstein condensate from a Fermi gas. *Nature* **426**, 537-540 (2003).
- Inada, Y. *et al.* Critical temperature and condensate fraction of a fermion pair condensate. *Phys. Rev. Lett.* **101**, 180406 (2008).
- Pilati, S. & Giorgini, S. Phase separation in a polarized Fermi gas at zero temperature. *Phys. Rev. Lett.* **100**, 030401 (2008).
- Horikoshi, M., Nakajima, S., Ueda, M. & Mukaiyama, T. Measurement of universal thermodynamic functions for a unitary Fermi gas. *Science* **327**, 442-445 (2010).

Supplementary Information is linked to the online version of the paper at www.nature.com/nature.

Acknowledgements We are grateful to R. Combescot, X. Leyronas, Y. Castin, A. Recati, S. Stringari, S. Giorgini, M. Zwierlein and T. Giamarchi for discussions and to C. Cohen-Tannoudji, J. Dalibard, F. Gerbier and G. Shlyapnikov for critical reading of the manuscript. We acknowledge support from ESF (Euroquam), SCALA, ANR FABIOLA, Région Ile de France (IFRAF), ERC and Institut Universitaire de France.

Author Contributions S.N. and N.N. contributed equally to this work. S.N., N.N. and K.J.J. took the experimental data, and all authors contributed to the data analysis and writing of the manuscript.

Author Information Reprints and permissions information is available at www.nature.com/reprints. The authors declare no competing financial interests. Correspondence and requests for materials should be addressed to S.N. (sylvain.nascimbene@ens.fr).

METHODS

Construction of the EOS by successive patches. A typical image at high temperature provides about 100 pixels corresponding to ζ values varying from 2 at the trap centre to 6 at the edges, with a signal-to-noise from 3 to 10. Seven such images are fitted in the wings using the second-order virial expansion and averaged to obtain a low-noise EOS up to $\zeta = 2$. Then images of clouds where the evaporation has been pushed to a slightly lower temperature are recorded. They show about 75% overlap in ζ with the previous EOS. After minimization of the distance between a new image and the previously determined EOS in the overlap region, we obtain the value of μ^0 for a single image with 3% statistical uncertainty. This process is repeated for six successive trap depths. When averaging one image with typically 10 previous images, we obtain a new EOS with an error on ζ of about $0.03/\sqrt{10} \approx 1\%$. The EOS experiences a random walk error on the 40 images of $0.01 \times \sqrt{40} \approx 5\%$ for the coldest data. An independent check of the maximum error is provided by the good agreement with the superfluid EOS for temperatures lower than T_c (refs 7, 8).

Evaluation of the systematic uncertainties. For the measurement of $h(1, \zeta)$, the combined uncertainties on the radial frequency of the trap, trap anharmonicity, magnification of our imaging system, and atom counting affect the pressure measurement given in equation (3) at $\sim 20\%$ level. However, two measurements, one at relatively high temperature and one at very low temperature, enable us to show that the overall error does not exceed 6%. In the temperature range $\zeta > 0.5$, the agreement between the experimental value $b_3 = -0.35(2)$ and the theoretical value $b_3 = -0.355$ of the third virial coefficient indicates that the global systematic error is smaller than 6%. Second, at very low temperature, theory^{7,8} predicts that the variation of $P/2P_1$ as a function of $k_B T/\mu$ in the superfluid phase remains smaller than 5%. Our value of $P/2P_1 = 3.75$ below the critical point is within 5% of the $T = 0$ prediction $\xi_s^{-3/2} = 3.7(2)$. This confirms that systematic errors for our coldest samples are also smaller than 6%.

For the determination of the critical transition to superfluidity we fit the low-temperature data $P(\mu, T)/2P_1(\mu, 0)$ with a variable horizontal line for $T < T_c$ and

with the Fermi-liquid equation (4) for $T > T_c$. The result of the fit is the dashed black line in Fig. 3c, which intersects equation (4) at $(k_B T/\mu)_c = 0.315(8)$. This statistical error is negligible compared to the error induced by the 6% systematic uncertainty discussed above, justifying our very simplified fit procedure. Indeed a 6% error on the pressure induces a 10% error on μ for images recorded in the vicinity of the critical temperature, leading to $(k_B T/\mu)_c = 0.32(3)$.

For the measurement of $h(\eta, 0)$, the fit of the fully polarized wings of the cloud serves as a pressure calibration for the rest of the cloud, cancelling many systematic effects.

In order to estimate temperature effects in the polarized gas, let us first remark that in the superfluid phase corrections scale as T^4 for the bosonic excitations and are exponentially suppressed by the gap for the fermionic ones⁷. So in our temperature range $k_B T = 0.03\mu_1^0$ their contributions will be very small. On the other hand, in the partially polarized normal phase, we expect a typical Fermi liquid T^2 scaling. In order to obtain an estimate of the error on the EOS, we develop the following simple model. In equation (6) which describes a mixture of zero-temperature ideal gases, we replace the Fermi pressures by the finite-temperature pressures of ideal gases (see equation (1)):

$$P(\mu_1, \mu_2, T) = P_1(\mu_1, T) + \left(\frac{m_p^*}{m}\right)^{3/2} P_1(\mu_2 - A\mu_1, T)$$

and run the analysis described in the main text. At $T = 0.05\mu_1^0$, the correction on h is less than 1%, half of our current error bar.

Limit of ^7Li thermometry. As the scattering length between the ^7Li atoms, $a_{77} = -3$ nm is negative, the ^7Li cloud becomes unstable when a BEC forms. This occurs at $T \approx 150$ nK with typically 3,500 atoms. Precise thermometry with lower atom numbers becomes difficult. For the measurement of the zero-temperature EOS of the imbalanced gas, we do not use ^7Li thermometry but rather the fit of the wings of the majority spin component.

The Equation of State of a Low-Temperature Fermi Gas with Tunable Interactions

N. Navon*, S. Nascimbene*, F. Chevy, and C. Salomon

Science **328**, 729 (2010)

43210, USA. ¹²Istituto Nazionale di Fisica Nucleare, Sezione di Perugia, I-06123 Perugia, Italy. ¹³Dipartimento di Fisica, Università degli Studi di Perugia, I-06123 Perugia, Italy. ¹⁴Dipartimento di Fisica "M. Merlin" dell'Università e del Politecnico di Bari, I-70126 Bari, Italy. ¹⁵Istituto Nazionale di Fisica Nucleare, Sezione di Bari, 70126 Bari, Italy. ¹⁶Laboratoire Leprince-Ringuet, École polytechnique, CNRS/IN2P3, Palaiseau, France. ¹⁷Department of Physics, University of Washington, Seattle, WA 98195–1560, USA. ¹⁸Institut de Ciències de l'Espai (IEEC-CSIC), Campus UAB, 08193 Barcelona, Spain. ¹⁹Istituto Nazionale di Astrofisica (INAF)–Istituto di Astrofisica Spaziale e Fisica Cosmica, I-20133 Milano, Italy. ²⁰Agenzia Spaziale Italiana Science Data Center, I-00044 Frascati (Roma), Italy. ²¹NASA Goddard Space Flight Center, Greenbelt, MD 20771, USA. ²²Center for Research and Exploration in Space Science and Technology and NASA Goddard Space Flight Center, Greenbelt, MD 20771, USA. ²³Department of Physics and Center for Space Sciences and Technology, University of Maryland Baltimore County, Baltimore, MD 21250, USA. ²⁴George Mason University, Fairfax, VA 22030, USA. ²⁵Laboratoire de Physique Théorique et Astroparticules, Université Montpellier 2, CNRS/IN2P3, Montpellier, France. ²⁶Department of Physics and Astronomy, Sonoma State University, Rohnert Park, CA 94928–3609, USA. ²⁷Department of Physics, Stockholm University, AlbaNova, SE-106 91 Stockholm, Sweden. ²⁸The Oskar Klein Centre for Cosmoparticle Physics, AlbaNova, SE-106 91 Stockholm, Sweden. ²⁹Dipartimento di Fisica, Università di Udine and Istituto Nazionale di Fisica Nucleare, Sezione di Trieste, Gruppo Col-

legato di Udine, I-33100 Udine, Italy. ³⁰Université de Bordeaux, Centre d'Études Nucléaires Bordeaux Gradignan, UMR 5797, Gradignan, 33175, France. ³¹CNRS/IN2P3, Centre d'Études Nucléaires Bordeaux Gradignan, UMR 5797, Gradignan, 33175, France. ³²Department of Physical Sciences, Hiroshima University, Higashi-Hiroshima, Hiroshima 739-8526, Japan. ³³Department of Astronomy and Astrophysics, Pennsylvania State University, University Park, PA 16802, USA. ³⁴Department of Physics and Department of Astronomy, University of Maryland, College Park, MD 20742, USA. ³⁵INAF Istituto di Radioastronomia, 40129 Bologna, Italy. ³⁶Max-Planck-Institut für Radioastronomie, Auf dem Hügel 69, 53121 Bonn, Germany. ³⁷Center for Space Plasma and Aeronomic Research, University of Alabama in Huntsville, Huntsville, AL 35899, USA. ³⁸Department of Physics, Royal Institute of Technology, AlbaNova, SE-106 91 Stockholm, Sweden. ³⁹Waseda University, 1-104 Totsukamachi, Shinjuku-ku, Tokyo, 169-8050, Japan. ⁴⁰Department of Physics, Tokyo Institute of Technology, Meguro City, Tokyo 152-8551, Japan. ⁴¹Cosmic Radiation Laboratory, Institute of Physical and Chemical Research (RIKEN), Wako, Saitama 351-0198, Japan. ⁴²Centre d'Étude Spatiale des Rayonnements, CNRS/UPS, BP 44346, F-30128 Toulouse Cedex 4, France. ⁴³Istituto Nazionale di Fisica Nucleare, Sezione di Roma "Tor Vergata," I-00133 Roma, Italy. ⁴⁴Department of Physics and Astronomy, University of Denver, Denver, CO 80208, USA. ⁴⁵Max-Planck Institut für Extraterrestrische Physik, 85748 Garching, Germany. ⁴⁶Institut für Astro- und Teilchenphysik and Institut für Theoretische Physik, Leopold-Franzens-Universität Innsbruck, A-6020 Innsbruck,

Austria. ⁴⁷Space Sciences Division, NASA Ames Research Center, Moffett Field, CA 94035–1000, USA. ⁴⁸NYCB Real-Time Computing, Lattingtown, NY 11560–1025, USA. ⁴⁹Astronomical Observatory, Jagiellonian University, 30-244 Kraków, Poland. ⁵⁰Department of Chemistry and Physics, Purdue University Calumet, Hammond, IN 46323–2094, USA. ⁵¹Institute of Space and Astronautical Science, Japanese Aerospace Exploration Agency, 3-1-1 Yoshinodai, Sagami-hara, Kanagawa 229-8510, Japan. ⁵²Institució Catalana de Recerca i Estudis Avançats, Barcelona, Spain. ⁵³Consorzio Interuniversitario per la Fisica Spaziale, I-10133 Torino, Italy. ⁵⁴Dipartimento di Fisica, Università di Roma "Tor Vergata," I-00133 Roma, Italy. ⁵⁵School of Pure and Applied Natural Sciences, University of Kalmar, SE-391 82 Kalmar, Sweden. ⁵⁶Centre for Astrophysics Research, University of Hertfordshire, College Lane, Hatfield AL10 9AB, UK.

Supporting Online Material

www.sciencemag.org/cgi/content/full/science.1184656/DC1
Materials and Methods
SOM Text
Figs. S1 to S3
Tables S1 to S3
References

13 November 2009; accepted 19 March 2010
Published online 1 April 2010;
10.1126/science.1184656
Include this information when citing this paper.

The Equation of State of a Low-Temperature Fermi Gas with Tunable Interactions

N. Navon,[†] S. Nascimbène,^{*} F. Chevy, C. Salomon

Interacting fermions are ubiquitous in nature, and understanding their thermodynamics is an important problem. We measured the equation of state of a two-component ultracold Fermi gas for a wide range of interaction strengths at low temperature. A detailed comparison with theories including Monte-Carlo calculations and the Lee-Huang-Yang corrections for low-density bosonic and fermionic superfluids is presented. The low-temperature phase diagram of the spin-imbalanced gas reveals Fermi liquid behavior of the partially polarized normal phase for all but the weakest interactions. Our results provide a benchmark for many-body theories and are relevant to other fermionic systems such as the crust of neutron stars.

Recently, ultracold atomic Fermi gases have become a tool of choice to study strongly correlated quantum systems because of their high controllability, purity, and tunability of interactions (*I*). In the zero-range limit, interactions in a degenerate Fermi system with two spin-components are completely characterized by a single parameter $1/k_F a$, where *a* is the *s*-wave scattering length and $k_F = (6\pi^2 n)^{1/3}$ is the Fermi momentum (*n* is the density per spin state). In cold atom gases, the value of $|a|$ can be tuned over several orders of magnitude using a Feshbach resonance; this offers an opportunity to entirely explore the so-called BCS-BEC crossover, that is, the smooth transition from Bardeen-Cooper-Schrieffer (BCS) superfluidity at small

negative values of *a* to molecular Bose-Einstein Condensation (BEC) at small positive values of *a* (*I*, 2). Between these two well-understood limiting situations, *a* diverges, leading to strong quantum correlations. The description of this system is a challenge for many-body theories, as testified by the large amount of work in recent years (*I*). The physics of the BEC-BCS crossover is relevant for very different systems, ranging from neutron stars to heavy nuclei and superconductors.

In the grand-canonical ensemble and at zero temperature, dimensional analysis shows that the Equation of State (EoS) of a two-component Fermi gas, relating the pressure *P* to the chemical potentials μ_1 and μ_2 of the spin components can be written as

$$P(\mu_1, \mu_2, a) = P_0(\mu_1) h\left(\delta_1 \equiv \frac{\hbar}{\sqrt{2m\mu_1} a}, \eta \equiv \frac{\mu_2}{\mu_1}\right) \quad (1)$$

where $P_0(\mu_1) = 1/15\pi^2 (2m/\hbar^2)^{3/2} \mu_1^{5/2}$ is the pressure of a single-component ideal Fermi gas,

m is the atom mass, \hbar is the Planck constant divided by 2π , and δ_1 is the grand-canonical analog of the dimensionless interaction parameter $1/k_F a$. The indices 1 and 2 refer to the majority and minority spin components, respectively. From the dimensionless function $h(\delta_1, \eta)$, it is possible to deduce all the thermodynamic properties of the gas, such as the compressibility, the magnetization, or the existence of phase transitions. The aim of this paper is to measure $h(\delta_1, \eta)$ for a range of interactions (δ_1) and spin imbalances (η) and discuss its physical content. Because it contains the same information as Eq. 1, the function *h* will also be referred to as the EoS in the rest of the text.

In situ absorption images of harmonically trapped gases are particularly suited to investigate the EoS, as first demonstrated in (3) and (4). In the particular case of the grand-canonical ensemble, a simple formula relates the local pressure *P* at a distance *z* from the center of the trap along the *z* axis to the doubly integrated density profiles \bar{n}_1 and \bar{n}_2 (5).

$$P(\mu_1(z), \mu_2(z), a) = \frac{m\omega_r^2}{2\pi} (\bar{n}_1(z) + \bar{n}_2(z)) \quad (2)$$

Here, we define the local chemical potentials $\mu_i(z) = \mu_i^0 - \frac{1}{2} m\omega_z^2 z^2$, where μ_i^0 is the chemical potential of the component *i* at the bottom of the trap, assuming local density approximation. ω_r and ω_z are the transverse and axial angular frequencies of a cylindrically symmetric trap, respectively, and $\bar{n}_i(z) = \int n_i(x, y, z) dx dy$ is the atomic density n_i of the component *i*, doubly integrated over the transverse *x* and *y* directions. In a single experimental run at a given magnetic field, two images are recorded, providing $\bar{n}_1(z)$ and $\bar{n}_2(z)$ (fig. S4); the *z*-dependence of the chemical potentials then enables the measurement of *P* along a curve in the (δ_1, η) plane (6). This method was validated in (4) for the particular case of the

Laboratoire Kastler Brossel, CNRS, Université Pierre et Marie Curie, École Normale Supérieure, 24 rue Lhomond, 75231 Paris, France.

^{*}These authors contributed equally to this work.
[†]To whom correspondence should be addressed. E-mail: navon@ens.fr

unitary limit $a = \infty$. Deducing the function h from the doubly integrated profiles further requires a precise calibration of ω_z and the knowledge of the central chemical potentials μ_i^0 (6).

Our experimental setup is presented in (7). We prepared an imbalanced mixture of ^6Li in the two lowest internal spin states, at the magnetic field of 834 G (where $a = \infty$), and trapped it in a hybrid magnetic-optical dipole trap. We then performed evaporative cooling by lowering the optical trap power, while the magnetic field was ramped to the final desired value for a . The cloud typically contained $N = 2$ to 10×10^4 atoms in each spin state at a temperature of $0.03(3) T_F$, justifying our $T = 0$ assumption (6). The final trap frequencies are $\omega_x/2\pi \sim 30$ Hz and $\omega_y/2\pi \sim 1$ kHz. Below a critical spin population imbalance, our atomic sample consists of a fully paired superfluid occupying the center of the trap, surrounded by a normal mixed phase and an outer rim of an ideal gas of majority component atoms (4, 7, 8).

For a given magnetic field, 10 to 20 images are taken, leading after averaging to a low-noise EoS along one line in the (δ_1, η) plane. Measurements at different magnetic fields chosen between 766 G and 981 G give a sampling of the surface $h(\delta_1, \eta)$ in the range $-1 < \delta_1 < 0.6$ and $-2 < \eta < 0.7$ (Fig. 1). Let $A(\delta_1)$ be the limiting value of the ratio of chemical potentials $\mu_1(z)/\mu_2(z)$ below which the minority density vanishes. At fixed δ_1 and $\eta < A(\delta_1)$, $h(\delta_1, \eta)$ represents the EoS of an ideal Fermi gas of majority atoms and is equal to 1. For $\eta > A(\delta_1)$, it slowly rises and corresponds to the normal mixed phase, where both spin components are present. At a critical value $\eta = \eta_c(\delta_1)$, the slope of h abruptly changes (6), the signature of a first-order phase transition from the normal phase (for $A < \eta < \eta_c$) to a superfluid phase with a lower chemical potential imbalance ($\eta > \eta_c$). We notice that the discontinuity is present for all values of δ_1 we investigated, and this feature is more pronounced on the BEC side.

Let us first consider the EoS of the superfluid phase, $\eta > \eta_c$. Each of our in situ images has, along the z axis, values of the chemical potential ratio $\eta(z) = \mu_2(z)/\mu_1(z)$ both lower and greater than η_c . In the region where $\eta(z) > \eta_c$, the doubly integrated density difference $\bar{n}_1(z) - \bar{n}_2(z)$ is constant within our signal-to-noise ratio (fig. S4). This is the signature of equal densities of the two species in the superfluid core, that is, the superfluid is fully paired. Using Gibbs-Duhem relation $n_i = \frac{\partial P}{\partial \mu_i}$, equal densities $n_1 = n_2$ imply that $P(\mu_1, \mu_2, a)$ is a function of μ and a only, where $\mu \equiv (\mu_1 + \mu_2)/2$. For the balanced superfluid, we then write the EoS symmetrically.

$$P(\mu_1, \mu_2, a) = 2P_0(\tilde{\mu})h_S\left(\tilde{\delta} \equiv \frac{h}{\sqrt{2m\tilde{\mu}a}}\right) \quad (3)$$

To avoid using negative chemical potentials, we define here $\tilde{\mu} = \mu - E_b/2$, where E_b is the molecular binding energy $E_b = -\hbar^2/m\tilde{a}^2$ for $a > 0$ (and 0 for $a \leq 0$). $h_S(\tilde{\delta})$ is then a single-variable function. It fully describes the ground-state

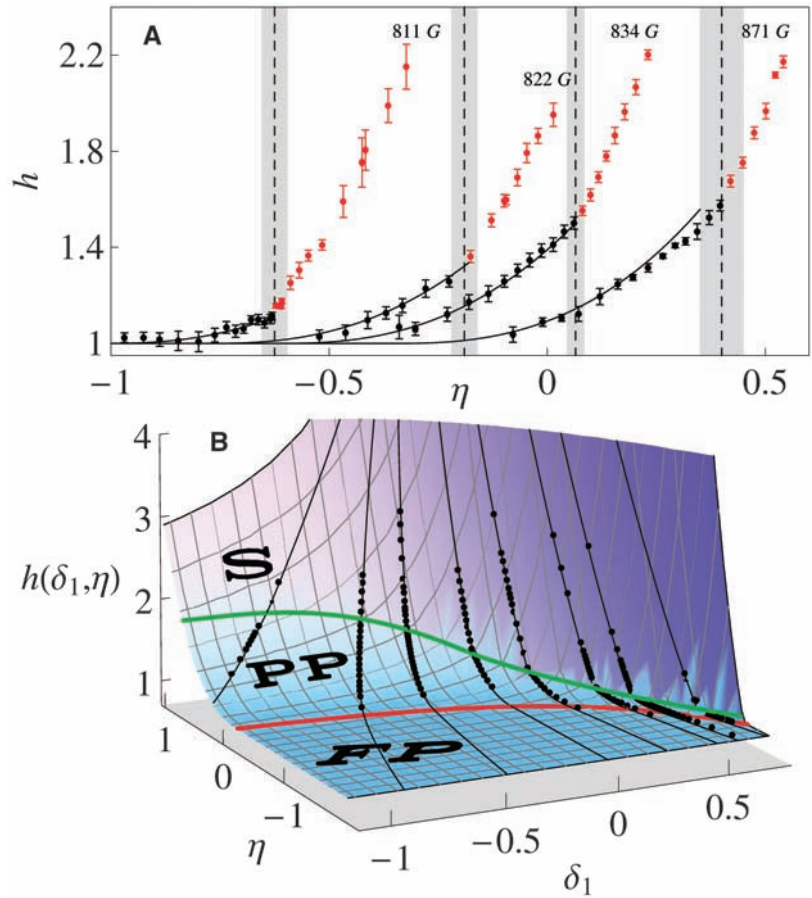


Fig. 1. $h(\delta_1, \eta)$ of a zero-temperature two-component Fermi gas in the BEC-BCS crossover. **(A)** Samples of the data for different magnetic fields. The black (red) data points correspond to the normal (superfluid) phase and are separated at $\eta_c(\delta_1)$ by a clear kink in the local slope of h . Solid black lines are the predictions of the polaron ideal gas model (Eq. 8). The scattering length corresponding to each curve is (from left to right): (1.7, 3.4, ∞ , and -1.3) in units of $10^4 a_0$, where a_0 is the Bohr radius. **(B)** $h(\delta_1, \eta)$. The black dots are data recorded for each magnetic field value (as in Fig. 1A). The black lines correspond to the parametric curves $[\delta_1(\eta), \eta]$ scanned by the density inhomogeneity in the harmonic trap (6). The red line is $A(\delta_1)$, the frontier between the fully polarized (FP) ideal gas $h = 1$ and the normal partially polarized (PP) phase. The green line is $\eta_c(\delta_1)$, marking the phase transition between the normal and superfluid (S) phases. The surface is the parametrization of $h(\delta_1, \eta)$ given in the text.

Fig. 2. $h_S(\tilde{\delta})$ of the $T = 0$ balanced superfluid in the BEC-BCS crossover (black dots). The blue solid line is the fit $h_S^{\text{BCS}}(\tilde{\delta})$ on the BCS side of the resonance; the red solid line is the fit $h_S^{\text{BEC}}(\tilde{\delta})$ on the BEC side. The dotted (dashed) red line is the mean-field (LHY) theory (32). (Inset) Zoom on the BCS side. The dotted and dashed blue lines are the EoS, including the mean-field and LHY terms, respectively. The systematic uncertainties on the x and y axes are about 5%. The errors bars represent the standard deviation of the statistical uncertainty.

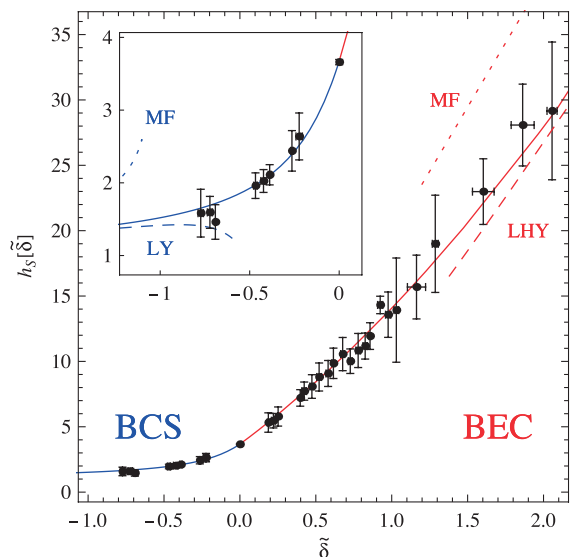
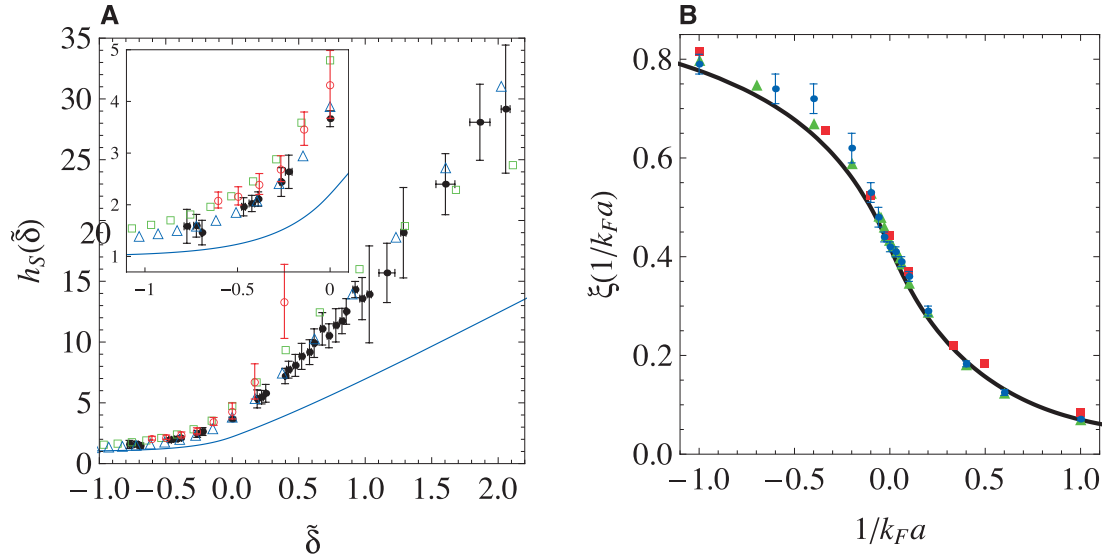


Fig. 3. Comparison with many-body theories. **(A)** Direct comparison of $h_S(\delta)$ with a quantum Monte-Carlo calculation [red open circles (22)], a diagrammatic method [green open squares (23)], a Nozières-Schmitt-Rink approximation [blue open triangles (21)], and the BCS mean-field theory (solid blue line). (Inset) Zoom on the BCS side. **(B)** EoS in the canonical ensemble $\xi(1/k_F a)$ (solid black line) deduced from the Padé-type approximants to the experimental data h_S^{BCS} and h_S^{BEC} plotted in Fig. 2. Fixed-Node Monte-Carlo theories: red squares (24), blue circles (25), and green triangles (26).



macroscopic properties of the balanced superfluid in the BEC-BCS crossover and is displayed in Fig. 2 as black dots.

To extract relevant physical quantities, such as beyond mean-field corrections, it is convenient to parametrize our data with analytic functions. In this pursuit, we use Padé-type approximants (6), interpolating between the EoS measured around unitarity and the well-known mean-field expansions on the BEC and BCS limits. The two analytic functions, h_S^{BCS} and h_S^{BEC} , are respectively represented in blue and red solid lines in Fig. 2 and represent our best estimate of the EoS in the whole BEC-BCS crossover.

On the BCS side, ($\delta < 0$), h_S^{BCS} yields the following perturbative expansion of the energy in series of $k_F a$

$$E = \frac{3}{5} N E_F \left(1 + \frac{10}{9\pi} k_F a + 0.18(2)(k_F a)^2 + 0.03(2)(k_F a)^3 + \dots \right) \quad (4)$$

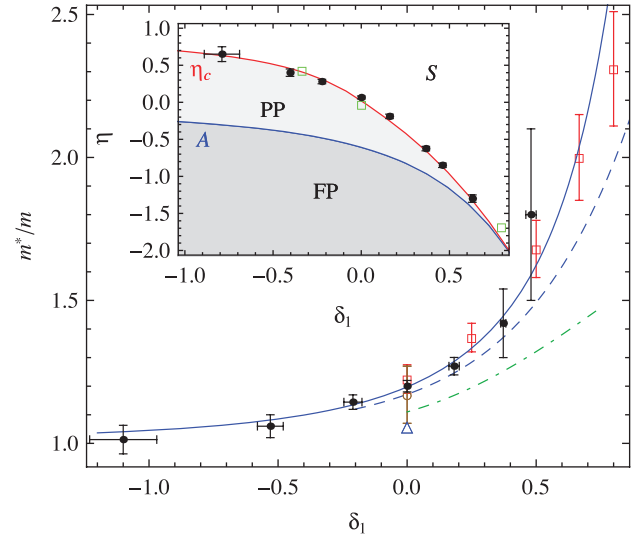
where N is the total number of atoms, E_F is the Fermi energy, and where by construction of h_S^{BCS} , the mean-field term (proportional to $k_F a$) is fixed to its exact value $10/9\pi$. We obtain beyond mean-field corrections up to the third order. The term proportional to $(k_F a)^2$ agrees with the Lee-Yang (9, 10) theoretical calculation $4(11-2\log 2)/21\pi^2 \cong 0.186$. The third-order coefficient also agrees with the value 0.030 computed in (11).

Around unitarity, the energy expansion yields

$$E = \frac{3}{5} N E_F \left(\xi_s - \zeta \frac{1}{k_F a} + \dots \right) \quad (5)$$

We find the universal parameter of the unitary $T = 0$ superfluid, $\xi_s = 0.41(1)$ with 2% accuracy. This value is in agreement with recent calculations and measurements (1). Our thermodynamic measurement $\zeta = 0.93(5)$ can be compared with a recent experimental value $\zeta = 0.91(4)$ (12), as well as the theoretical value $\zeta = 0.95$ (13), both of them

Fig. 4. Effective mass m^*/m of the polaron in the BEC-BCS crossover (black dots). The blue dashed line is a calculation from (29), red open squares (30), green dot-dashed line (26), and blue solid line (31). Measurements at unitarity through density profile analysis [blue triangle (3)] and collective modes study [brown empty circle (7)] are also displayed. (Inset) Phase diagram of a zero-temperature imbalanced Fermi gas in the BEC-BCS crossover. The blue line is the theoretical value of A (26, 29, 30) that sets the separation between the partially polarized (PP) and the fully polarized (FP) phases. Black dots are the measured values of η_c (as in Fig. 1A), which set the separation between the superfluid (S) phase and the partially polarized phase. The red line is the calculation of η_c using our EoS of the superfluid and the model (Eq. 8) for the normal phase. The green squares are lower bounds of η_c given by the values of the gap measured in (33); see (6).



obtained through the study of the pair correlation function. This experimental agreement confirms the link between the macroscopic thermodynamic properties and the microscopic short-range pair correlations, as shown theoretically in (14).

In the BEC limit, the energy of the superfluid is that of a weakly interacting Bose-Einstein condensate of molecules (9, 15)

$$E = \frac{N}{2} E_b + N \frac{\pi \hbar^2 a_{dd}}{2m} \times n \left(1 + \frac{128}{15\sqrt{\pi}} \sqrt{na_{dd}^3} + \dots \right) \quad (6)$$

where $a_{dd} = 0.6a$ is the dimer-dimer scattering length (1) and n is the dimer density. The term in $\sqrt{na_{dd}^3}$ is the well-known Lee-Huang-Yang (LHY) correction to the mean-field interaction

between molecules (9, 15). Signatures of beyond mean-field effects were previously observed through a pioneering study of collective modes (16) and density profile analysis (17), but no quantitative comparison with Eq. 6 was made. Fitting our data in the deep BEC regime with Eq. 6, we measure the bosonic LHY coefficient $4.4(5)$, in agreement with the exact value $128/15\sqrt{\pi} \cong 4.81$ calculated for elementary bosons in (9) and recently for composite bosons in (15).

Having checked this important beyond mean-field contribution, we can go one step further in the expansion. The analogy with point-like bosons suggests that the next term should be written as $\frac{8}{3}(4\pi - 3\sqrt{3})na_{dd}^3(\log(na_{dd}^3) + B)$ (6, 18, 19). Using $h_S^{\text{BEC}}(\delta)$ (Fig. 2) (6), we deduce the effective three-body parameter for composite bosons $B = 7(1)$. Interestingly, this value is close

to the bosonic hard-sphere calculation $B = 8.5$ (20) and to the value $B \approx 7.2$ for point-like bosons with large scattering length (19).

Our measurements also allow direct comparison with advanced many-body theories developed for homogeneous gases in the strongly correlated regime. As displayed in Fig. 3A, our data are in agreement with a Nozières-Schmitt-Rink approximation (21) but show significant differences from a quantum Monte-Carlo calculation (22) and a diagrammatic approach (23). The measured EoS strongly disfavors the prediction of BCS mean-field theory.

Comparison with Fixed-Node Monte-Carlo theories requires the calculation of the EoS $\xi(1/k_F a)$ in the canonical ensemble

$$\xi\left(\frac{1}{k_F a}\right) \equiv \frac{E - \frac{N}{2}E_b}{\frac{3}{5}NE_F} \quad (7)$$

that is deduced from $h_S^{\text{BCS}}(\tilde{\delta})$ and $h_S^{\text{BEC}}(\tilde{\delta})$ (6). As shown in Fig. 3B, the agreement with theories (24–26) is very good.

We now discuss the EoS of the partially polarized normal phase (black points in Fig. 1). At low concentrations, we expect the minority atoms to behave as noninteracting quasiparticles, the fermionic polarons (27). The polarons are dressed by the majority Fermi sea through a renormalized chemical potential $\mu_2 - A(\delta_1)\mu_1$ (28) and an effective mass $m^*(\delta_1)$ (26, 29, 30). Following a Fermi liquid picture, we propose to express the gas pressure as the sum of the Fermi pressure of the bare majority atoms and of the polarons (4).

$$h(\delta_1, \eta) = 1 + \left(\frac{m^*(\delta_1)}{m}\right)^{3/2} (\eta - A(\delta_1))^{5/2} \quad (8)$$

Our measured EoS agrees with this model at unitarity and on the BEC side of the resonance (Fig. 1), where for $m^*(\delta_1)$ we use the calculations from (30, 31). On the BCS side of the resonance, however, we observe at large minority concentrations an intriguing deviation to Eq. 8. In the BCS regime, the superfluid is less robust to spin imbalance. Consequently, the ratio of the two densities n_1/n_2 in the normal phase becomes close to unity near the superfluid/normal boundary η_c . The polaron ideal gas picture then fails.

Alternatively, we can let the effective mass m^* be a free parameter in the model in Eq. 8 in the fit of our data around $\eta = A$. We obtain the value of the polaron effective mass in the BEC-BCS crossover (Fig. 4).

An important consistency check of our study is provided by the comparison between our direct measurements of $\eta_c(\delta_1)$ (from Fig. 1, black dots in the inset of Fig. 4) and a calculated $\eta_c(\delta_1)$ from Eq. 8 and the EoS of the superfluid h_S . Assuming negligible surface tension, the normal/superfluid boundary is given by equating the pressure and chemical potential in the two phases. This procedure leads to the solid red line in the inset of Fig. 4, in excellent agreement with

the direct measurements. In addition, by integrating our measured EoS of the homogeneous gas over the trap, one retrieves the critical polarization for superfluidity of a trapped gas, in agreement with most previous measurements (6).

We have measured the equation of state of a two-component Fermi gas at zero temperature in the BEC-BCS crossover. Extensions of our work include exploring the thermodynamics of the far BEC region of the phase diagram where a new phase associated with a polarized superfluid appears (17, 26), mapping the EoS as a function of temperature, and investigating the influence of finite interaction range, which is playing a key role in higher-density parts of neutron stars.

References and Notes

- M. Inguscio, W. Ketterle, C. Salomon, Eds. *Ultra-cold Fermi Gases: Proceedings of the International School of Physics "Enrico Fermi", Course CLXIV, Varenna, 20 to 30 June 2006* (IOS Press, Amsterdam, 2008).
- A. J. Leggett, in *Modern Trends in the Theory of Condensed Matter*, A. Pekalski, R. Przystawa, Eds. (Springer-Verlag, Berlin, 1980), pp. 13–27.
- Y. Shin, *Phys. Rev. A* **77**, 041603 (2008).
- S. Nascimbène, N. Navon, K. J. Jiang, F. Chevy, C. Salomon, *Nature* **463**, 1057 (2010).
- T. Ho, Q. Zhou, *Nat. Phys.* **6**, 131 (2009).
- Materials and methods are available as supporting material on Science Online.
- S. Nascimbène *et al.*, *Phys. Rev. Lett.* **103**, 170402 (2009).
- Y. Shin, M. Zwierlein, C. Schunck, A. Schirotzek, W. Ketterle, *Phys. Rev. Lett.* **97**, 30401 (2006).
- T. D. Lee, C. N. Yang, *Phys. Rev.* **105**, 1119 (1957).
- R. B. Diener, R. Sensarma, M. Randeria, *Phys. Rev. A* **77**, 023626 (2008).
- G. Baker Jr., *Rev. Mod. Phys.* **43**, 479 (1971).
- H. Hu *et al.*, "Universal structure of a strongly interacting Fermi superfluid," <http://arxiv.org/abs/1001.3200> (2010).
- C. Lobo, I. Carusotto, S. Giorgini, A. Recati, S. Stringari, *Phys. Rev. Lett.* **97**, 100405 (2006).
- S. Tan, *Ann. Phys.* **323**, 2971 (2008).
- X. Leyronas, R. Combescot, *Phys. Rev. Lett.* **99**, 170402 (2007).
- A. Altmeyer *et al.*, *Phys. Rev. Lett.* **98**, 040401 (2007).
- Y. I. Shin, A. Schirotzek, C. H. Schunck, W. Ketterle, *Phys. Rev. Lett.* **101**, 070404 (2008).
- T. Wu, *Phys. Rev.* **115**, 1390 (1959).
- E. Braaten, H. W. Hammer, T. Mehen, *Phys. Rev. Lett.* **88**, 040401 (2002).
- S. Tan, *Phys. Rev. A* **78**, 013636 (2008).
- H. Hu, X. Liu, P. Drummond, *Europhys. Lett.* **74**, 574 (2006).
- A. Bulgac, J. Drut, P. Magierski, *Phys. Rev. A* **78**, 023625 (2008).
- R. Haussmann, W. Rantner, S. Cerrito, W. Zwerger, *Phys. Rev. A* **75**, 023610 (2007).
- S. Chang, V. Pandharipande, J. Carlson, K. Schmidt, *Phys. Rev. A* **70**, 043602 (2004).
- G. E. Astrakharchik, J. Boronat, J. Casulleras, A. S. Giorgini, *Phys. Rev. Lett.* **93**, 200404 (2004).
- S. Pilati, S. Giorgini, *Phys. Rev. Lett.* **100**, 030401 (2008).
- C. Lobo, A. Recati, S. Giorgini, S. Stringari, *Phys. Rev. Lett.* **97**, 200403 (2006).
- A. Schirotzek, C.-H. Wu, A. Sommer, M. W. Zwierlein, *Phys. Rev. Lett.* **102**, 230402 (2009).
- R. Combescot, A. Recati, C. Lobo, F. Chevy, *Phys. Rev. Lett.* **98**, 180402 (2007).
- N. Prokof'ev, B. Svistunov, *Phys. Rev. B* **77**, 020408 (2008).
- R. Combescot, S. Giraud, X. Leyronas, *Europhys. Lett.* **88**, 60007 (2009).
- In the BEC limit, the grand-canonical EoS expands as $h_S(\tilde{\delta}) \approx 15\pi a/4a_{eff}\tilde{\delta} - 16\sqrt{2}$; the first term is the mean-field interaction and the second is the LHY correction asymptotic behavior.
- A. Schirotzek, Y. I. Shin, C. H. Schunck, W. Ketterle, *Phys. Rev. Lett.* **101**, 140403 (2008).
- We thank K. Jiang for participation in the early phase of the experimental work. We are grateful to X. Leyronas, C. Mora, Y. Castin, F. Werner, R. Combescot, J. Dalibard, F. Gerbier, and G. Shlyapnikov for stimulating discussions and critical comments on the manuscript. We thank S. Giorgini, P. Drummond, J. Drut, R. Haussmann, and W. Zwerger for providing us with their data. We acknowledge support from European Research Council, European Science Foundation (Euroquam), SCALA (Scalable Quantum Computing with Light and Atoms), Agence Nationale de la Recherche FABIOLA (Fermions and Bosons in Optical Lattices), Région Ile de France Institut Francilien de Recherche sur les Atomes Froids, and Institut Universitaire de France.

Supporting Online Material

www.sciencemag.org/cgi/content/full/science.1187582/DC1
Materials and Methods
Figs. S1 to S4
References

27 January 2010; accepted 30 March 2010
Published online 15 April 2010;
10.1126/science.1187582
Include this information when citing this paper.

Nanoscale Three-Dimensional Patterning of Molecular Resists by Scanning Probes

David Pires,¹ James L. Hedrick,² Anuja De Silva,³ Jane Frommer,² Bernd Gotsmann,¹ Heiko Wolf,¹ Michel Despont,¹ Urs Duerig,¹ Armin W. Knoll^{1*}

For patterning organic resists, optical and electron beam lithography are the most established methods; however, at resolutions below 30 nanometers, inherent problems result from unwanted exposure of the resist in nearby areas. We present a scanning probe lithography method based on the local desorption of a glassy organic resist by a heatable probe. We demonstrate patterning at a half pitch down to 15 nanometers without proximity corrections and with throughputs approaching those of Gaussian electron beam lithography at similar resolution. These patterns can be transferred to other substrates, and material can be removed in successive steps in order to fabricate complex three-dimensional structures.

To date, a wide variety of techniques has been available for nanofabrication (1), including electron beam lithography (EBL) and scanning probe lithography (SPL) (2–4) as direct-write methods. Although EBL is used in critical applications such as the fabrication of

**The equation of state of ultracold Bose and Fermi gases: a
few examples**

S. Nascimbène, N. Navon, F. Chevy, and C. Salomon

New. J. Phys. **12**, 103026 (2010)

The equation of state of ultracold Bose and Fermi gases: a few examples

Sylvain Nascimbène¹, Nir Navon, Frédéric Chevy and
Christophe Salomon

Laboratoire Kastler Brossel, CNRS, UPMC, École Normale Supérieure,
24 rue Lhomond, 75231 Paris, France
E-mail: sylvain.nascimbene@lkb.ens.fr

New Journal of Physics **12** (2010) 103026 (14pp)

Received 16 June 2010

Published 15 October 2010

Online at <http://www.njp.org/>

doi:10.1088/1367-2630/12/10/103026

Abstract. We describe a powerful method for determining the equation of state of an ultracold gas from *in situ* images. The method provides a measurement of the local pressure of a harmonically trapped gas and we give several applications to Bose and Fermi gases. We obtain the grand-canonical equation of state of a spin-balanced Fermi gas with resonant interactions as a function of temperature (Nascimbène *et al* 2010 *Nature* **463** 1057). We compare our equation of state with an equation of state measured by the Tokyo group (Horikoshi *et al* 2010 *Science* **327** 442), which reveals a significant difference in the high-temperature regime. The normal phase, at low temperature, is well described by a Landau Fermi liquid model, and we observe a clear thermodynamic signature of the superfluid transition. In a second part, we apply the same procedure to Bose gases. From a single image of a quasi-ideal Bose gas, we determine the equation of state from the classical to the condensed regime. Finally, the method is applied to a Bose gas in a three-dimensional optical lattice in the Mott insulator regime. Our equation of state directly reveals the Mott insulator behavior and is suited to investigate finite-temperature effects.

¹ Author to whom any correspondence should be addressed.

Contents

1. Introduction	2
2. Measurement of the local pressure inside a trapped gas	3
3. Thermodynamics of a Fermi gas with resonant interactions	3
3.1. Grand-canonical equation of state	3
3.2. Canonical equation of state	5
3.3. Fermi liquid behavior in the normal phase	5
3.4. Superfluid transition	6
4. Thermodynamics of a weakly interacting Bose gas	7
4.1. Determination of the equation of state	7
4.2. Analysis of the equation of state	8
5. Mott insulator behavior of a Bose gas in a deep optical lattice	8
5.1. Realization of the Bose–Hubbard model with ultracold gases	9
5.2. Determination of the equation of state	9
5.3. Observation of Mott insulator behavior	10
5.4. Estimation of finite-temperature effects	10
6. Summary and concluding remarks	11
Acknowledgments	11
Appendix. Validity of local density approximation (LDA)	12
References	12

1. Introduction

Ultracold gases are a privileged tool for the simulation of model Hamiltonians relevant in the fields of condensed matter, astrophysics or nuclear physics in the laboratory [3]. As an example, thanks to the short-range character of interactions, ultracold Fermi mixtures prepared around a Feshbach resonance mimic the behavior of neutron matter in the outer crust of neutron stars [4, 5]. For cold atoms, the density inhomogeneity induced by the trapping potential has long made the connection between the Hamiltonian of a homogeneous system and an ultracold gas indirect. Early experimental thermodynamic studies have provided global quantities averaged over the whole trapped gas, such as total energy and entropy [6, 7], collective mode frequencies [8] or radii of the different phases that may be observed in an imbalanced Fermi gas [9]–[11]. Reconstructing the equation of state of the homogeneous gas then requires deconvolving the effect of the trapping potential, a delicate procedure that has not been done so far. However, the gas can often be considered as locally homogeneous (local density approximation (LDA)), and careful analysis of *in situ* density profiles can directly provide the equation of state of a homogeneous gas [1], [12]–[14]. In the case of two-dimensional (2D) gases, *in situ* images taken along the direction of tight confinement obviously give access to the surface density [15]–[18] and thus to the equation of state [19]. For three-dimensional (3D) gases, imaging leads to an unavoidable integration along the line of sight. As a consequence, inferring local quantities is not straightforward. Local density profiles can be computed from a cloud image using an inverse Abel transform for radially symmetric traps [20]. A more powerful method was suggested in [13] and implemented in [1, 14]: as explained below, for a harmonically trapped gas, the local pressure is simply proportional to the integrated *in situ*

absorption profile. Using this method, the low-temperature superfluid equation of state for balanced and imbalanced Fermi gases was studied as a function of interaction strength [1, 14]. In this paper, we describe in more detail the procedure used to determine the equation of state of a spin-unpolarized Fermi gas in the unitary limit [1]. We compare our data with recent results from the Tokyo group [2], and show a significant discrepancy in the high-temperature regime. In the second part, we apply the method to ultracold Bose gases. From an *in situ* image of ^7Li , we obtain the equation of state of a weakly interacting Bose gas. Finally, analyzing the experimental profiles of a Bose gas in a deep optical lattice [21], we observe clear thermodynamic signatures of the Mott insulator phases.

2. Measurement of the local pressure inside a trapped gas

In the grand-canonical ensemble, all thermodynamic quantities of a macroscopic system can be derived from the equation of state $P = f(\mu, T)$ relating the pressure P to the chemical potential μ and the temperature T . P can be straightforwardly deduced from integrated *in situ* images.

Consider first a single-species ultracold gas, held in a cylindrically symmetric harmonic trap whose frequencies are labeled $\omega_x = \omega_y \equiv \omega_r$ in the transverse direction and ω_z in the axial direction. Provided that the LDA is satisfied, the gas pressure along the z -axis is given by [13]

$$P(\mu_z, T) = \frac{m\omega_r^2}{2\pi} \bar{n}(z), \quad (1)$$

where $\bar{n}(z) = \int dx dy n(x, y, z)$ is the doubly integrated density profile, $\mu_z = \mu^0 - \frac{1}{2}m\omega_z^2 z^2$ is the local chemical potential on the z -axis and μ^0 is the global chemical potential. $\bar{n}(z)$ is obtained from an *in situ* image taken along the y -axis, by integrating the optical density along the x -axis (see figure 1). As described below, if one independently determines temperature T and chemical potential μ^0 , then each pixel row of the absorption image at a given position z provides an experimental data point for the grand-canonical equation of state $P(\mu_z, T)$ of the *homogeneous* gas. The large number of data obtained from several images allows one to perform an efficient averaging, leading to a low-noise equation of state.

This formula is also valid in the case of a two-component Fermi gas with equal spin populations if $\bar{n}(z)$ is the total integrated density. The method can be generalized to multicomponent Bose and Fermi gases, as first demonstrated on spin-imbalanced Fermi gases in [1, 14].

3. Thermodynamics of a Fermi gas with resonant interactions

In this section, we describe the procedure used in [1] to determine the grand-canonical equation of state of a homogeneous and unpolarized Fermi gas with resonant interactions ($a = \infty$). We also compare our data with recent measurements from the Tokyo group [1, 2]. We then study the physical content of the equation of state at low temperature.

3.1. Grand-canonical equation of state

In the grand-canonical ensemble, the equation of state of a spin-unpolarized Fermi gas in the unitary limit can be written as

$$P(\mu, T) = P^{(0)}(\mu, T)h_T(\zeta), \quad (2)$$

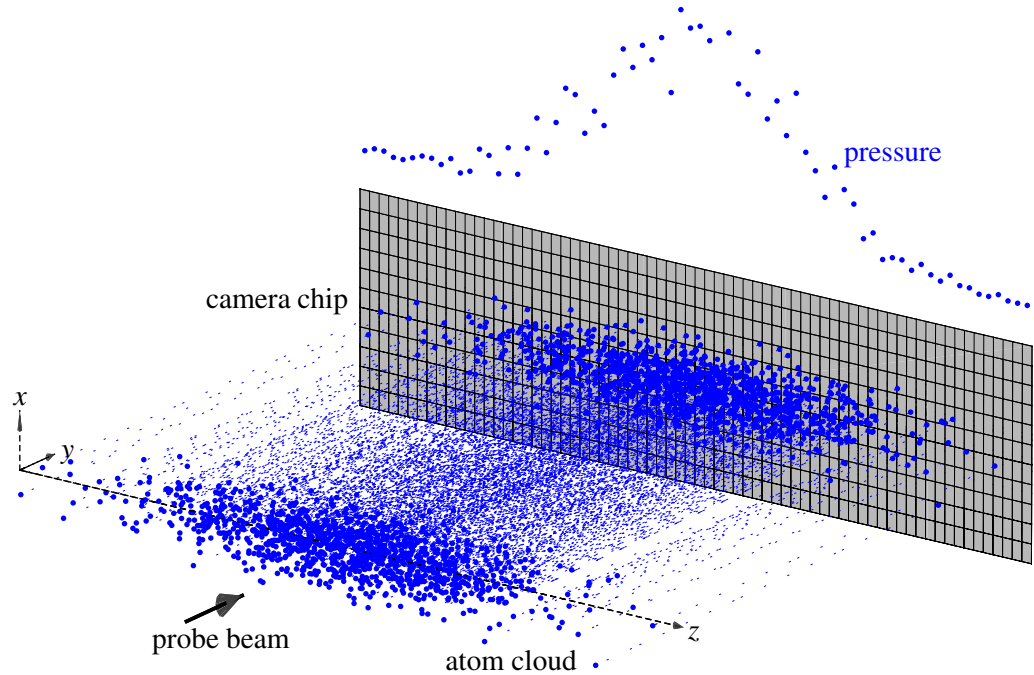


Figure 1. Scheme of the local pressure measurement: the absorption of a probe beam propagating along the y -direction provides a 2D image on the CCD camera. Integration of this image along the x -axis provides the doubly integrated density profile $\bar{n}(z)$ and, using equation (1), the pressure profile along the z -axis.

where $P^{(0)}(\mu, T)$ is the pressure of a non-interacting two-component Fermi gas and $\zeta = \exp(-\mu/k_B T)$ is the inverse fugacity. Since $P^{(0)}(\mu, T)$ is known, the function $h_T(\zeta)$ completely determines the equation of state $P(\mu, T)$. Let us now describe the procedure used to measure it. The pressure profile of the trapped gas along the z -axis is directly derived from its *in situ* image using equation (1). The effect of the trap anharmonicity of the optical dipole trap on the pressure measurement is expected to be less than 5%. One still has to know the value of the temperature T and the global chemical potential μ^0 in order to infer $h_T(\zeta)$. We use a small number of ^7Li atoms, at thermal equilibrium in the ^6Li component, as a thermometer. We then extract μ^0 from the pressure profile, by comparison in the cloud's wings with a reference equation of state. For high-temperature clouds ($k_B T > \mu^0$), we choose μ^0 so that the wings of the pressure profile match the second-order virial expansion [22] (see figure 2(a)):

$$P(\mu, T) = \frac{2k_B T}{\lambda_{\text{dB}}^3(T)} \left(e^{\mu/k_B T} + \frac{4}{3\sqrt{2}} e^{2\mu/k_B T} + \dots \right). \quad (3)$$

For colder clouds, the signal-to-noise ratio is not good enough, in the region where (3) is valid, to extract μ^0 using the same procedure. We thus rather use the equation of state determined from all images previously treated as a reference, since it is accurate over a wider parameter range than (3) (see figure 2(b)). We then iterate this procedure at lower and lower temperatures, eventually below the superfluid transition. By gathering the data from all images and statistical averaging, we obtain a low-noise equation of state in the range $0.02 < \zeta < 5$ (see figure 3(a)).

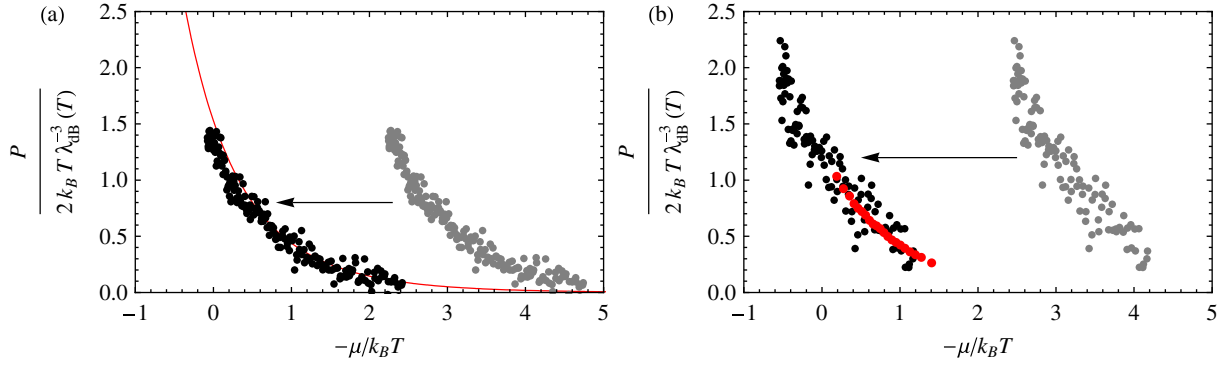


Figure 2. Determination of μ^0 : we plot the data from an *in situ* image as $P/2k_B T \lambda_{\text{dB}}^{-3}$ versus $-\mu/k_B T = V(z)/k_B T - \mu^0/k_B T$ (black points). A wrong choice of μ^0 in this representation corresponds to a translation of the data in abscissa. We adjust μ^0 so that the wings of the pressure profile match a reference equation of state (in red). (a) For high-temperature clouds, we use the second-order virial expansion (3). (b) For a lower temperature pressure profile, we minimize its distance with the averaged equation of state deduced from higher temperature images (in red) in the overlap region.

3.2. Canonical equation of state

In [2], a canonical equation of state $E(n, T)$ expressing energy E as a function of density and temperature was measured using fits of absorption images taken after a short time-of-flight. *In situ* density profiles were deduced by assuming a hydrodynamic expansion. The temperature was extracted from the cloud's total potential energy at unitarity, using the experimental calibration made in [7]. In figure 3(b), data from [2] are plotted as $E(n, T)/E^{(0)}(n, T)$ as a function of $\theta = T/T_F$, where n is the total atom density, T_F is the Fermi temperature and $E^{(0)}(n, T)$ is the energy of a non-interacting Fermi mixture.

The comparison between the two equations of state requires expressing our data in the canonical ensemble. The density $n = \partial P / \partial \mu|_T$ is calculated by taking a discrete derivative, and we obtain the black points in figure 3(b). While the two sets of data are in satisfactory agreement in the low-temperature regime $T/T_F < 0.4$, they clearly differ in the high-temperature regime. The disagreement of the data from [2] with the second- and third-order virial expansions calculated in [22, 23] indicates a systematic error in this regime. This is possibly due to a breakdown of hydrodynamics during the time-of-flight as expected at high temperature.

3.3. Fermi liquid behavior in the normal phase

Above the superfluid transition and in the low-temperature regime $0.05 < \zeta < 0.5$, our data are well modeled by a Fermi liquid equation of state

$$P^{\text{FL}}(\mu, T) = \frac{2}{15\pi^2} \left(\frac{2m}{\hbar^2} \right)^{3/2} \mu^{5/2} \left(\xi_n^{-3/2} + \frac{5\pi^2}{8} \xi_n^{-1/2} \frac{m^*}{m} \left(\frac{k_B T}{\mu} \right)^2 \right), \quad (4)$$

where $\xi_n = 0.51(1)$ and $m^* = 1.12(3)m$ respectively characterize the compressibility of the normal phase extrapolated to zero temperature and the effective mass of the low-lying excitations. The agreement with (4) is better than 5% in a large parameter range $0.33 \mu < k_B T < 2 \mu$. Our value of ξ_n is in agreement with the variational fixed-node Monte Carlo calculations

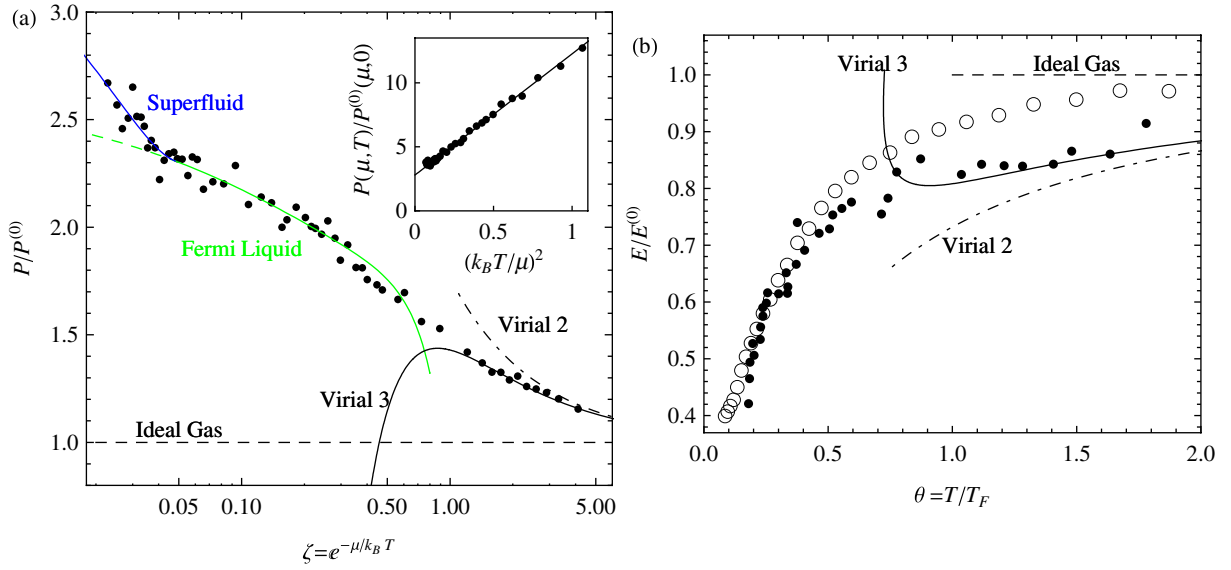


Figure 3. (a) Grand-canonical equation of state of a two-component Fermi gas with resonant interactions from [1] (black dots). Inset: equation of state expressed as $P(\mu, T)/P^{(0)}(\mu, 0)$ as a function of $(k_B T/\mu)^2$. The solid line is the Fermi liquid equation of state (4). (b) Canonical equation of state from the Tokyo group [2] (open circles) and from the ENS group (black dots). The dashed black line is the ideal gas equation of state, the dot-dashed (solid) black line is the second- (third-) order virial expansion, the solid green line is the Fermi liquid equation (4) and the solid blue line is the fit function (5) in the superfluid phase. The superfluid transition occurs at $\zeta = 0.05$.

$\xi_n = 0.54$ in [24], $\xi_n = 0.56$ in [25], and with the quantum Monte Carlo calculation $\xi_n = 0.52$ in [26]. It is surprising that the quasi-particle mass m^* is quite close to the free fermion mass, despite the strongly interacting regime. Note also that this mass is close to the effective mass $m^* = 1.20 m$ of a single spin-down atom immersed in a Fermi sea of spin-up particles (the Fermi polaron) [1, 11, 12, 25], [27]–[30].

3.4. Superfluid transition

The deviation of the experimental data from (4) for $\zeta < 0.05$ signals the superfluid phase transition. This transition belongs to the $U(1)$ universality class, and the critical region is expected to be wide [31] in the unitary limit. Assuming that our low-temperature data belong to the critical region, we fit our data with a function

$$P(\mu, T) = P^{\text{FL}}(\mu, T) + A(\zeta_c - \zeta)^{2-\alpha} H(\zeta_{rmc} - \zeta), \quad (5)$$

where H is the Heaviside function and $\alpha \simeq -0.013$ is the specific heat critical exponent, measured with a very good accuracy on liquid ^4He [32]. We obtain the position of the superfluid transition $\zeta_c = 0.05$, or $k_B T_c/\mu = 0.33$, in agreement with the value $k_B T_c/\mu = 0.32(3)$ extracted in [1] using a simpler fit function. We thus confirm more rigorously our previous determination of the superfluid transition. In the appendix, we discuss the validity of LDA around the superfluid transition. Under our current experimental conditions, the deviation from LDA is very small.

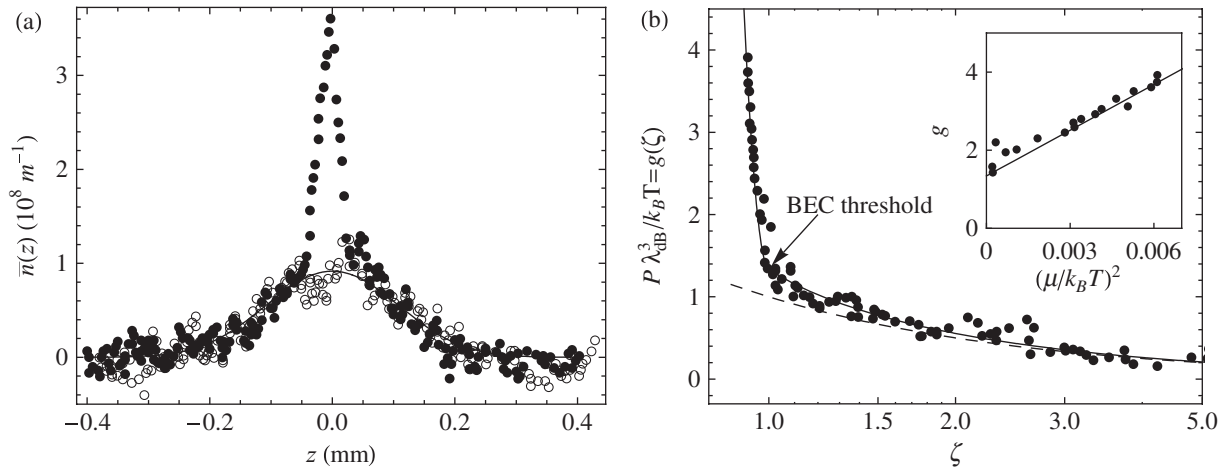


Figure 4. (a) Integrated density profiles $\bar{n}(z)$ for the ^7Li component (black dots) and the ^6Li component (open circles). The solid line is a fit of the ^6Li component with a finite-temperature Thomas–Fermi profile, yielding $T = 1.6(1) \mu\text{K}$. (b) Thermodynamic function $g(\zeta)$ determined from the ^7Li profile. The solid line is a fit of the data with a Bose function in the non-condensed region and a mean-field equation of state in the condensed region (see text). The dashed line is the equation of state of a classical gas $g(\zeta) = \zeta^{-1}$. The difference between the dashed and solid lines around $\zeta = 1$ is a consequence of Bose statistics. Inset: equation of state in the condensed phase expressed as g as a function of $(\mu/k_B T)^2$. The solid line is the Thomas–Fermi equation of state (5).

4. Thermodynamics of a weakly interacting Bose gas

In this section, we apply equation (1) to the case of trapped Bose gases. Firstly, we test the method by determining the equation of state of a weakly interacting Bose gas [33, 34]. We use an *in situ* absorption image of a ^7Li gas taken from [35] (see figure 4(a)). ^7Li atoms are polarized in the internal state $|F = 1, m_F = -1\rangle$, and held in an Ioffe–Pritchard magnetic trap with $\omega_r/2\pi = 4970 \text{ Hz}$ and $\omega_z/2\pi = 83 \text{ Hz}$, in a bias field $B_0 \simeq 2 \text{ G}$. The anharmonicity of this magnetic trap is negligible. Thermometry is provided by a gas of ^6Li atoms, prepared in $|F = \frac{1}{2}, m_F = -\frac{1}{2}\rangle$, and in thermal equilibrium with the ^7Li cloud.

4.1. Determination of the equation of state

The equation of state of a weakly interacting Bose gas can be expressed, in the grand-canonical ensemble, as

$$P(\mu, T) = \frac{k_B T}{\lambda_{\text{dB}}^3(T)} g(\zeta),$$

where $\zeta = e^{-\mu/k_B T}$ is the inverse fugacity and $\lambda_{\text{dB}}(T) = \sqrt{2\pi\hbar^2/mk_B T}$ is the thermal de Broglie wavelength. The pressure profile is calculated using (1). We aim here at measuring $g(\zeta)$. We

obtain the global chemical potential value $\mu^0 = 0.10 k_B T$ by fitting the ^7Li profile in the non-condensed region $|z| > 50 \mu\text{m}$ with a Bose function:

$$P(\mu_z, T) = \frac{k_B T}{\lambda_{\text{dB}}^3(T)} g_{5/2}(\zeta_z), \quad \zeta_z = e^{-\mu^0/k_B T} \exp\left(\frac{m\omega_z^2 z^2}{2k_B T}\right), \quad g_{5/2}(z) = \sum_{k=1}^{\infty} \frac{z^{-k}}{k^{5/2}}.$$

Combining the measurement of the pressure profile, the cloud's temperature T and the global chemical potential μ^0 , we obtain the thermodynamic function $g(\zeta)$ plotted in figure 4(b).

4.2. Analysis of the equation of state

In the region $\zeta > 1$, the data agree with the Bose function $g(\zeta) = g_{5/2}(\zeta)$ expected for a weakly interacting Bose gas. The departure from the thermodynamic function of a classical gas $g(\zeta) = \zeta^{-1}$, and especially the fact that $g(\zeta) > 1$ above the condensation threshold, is the thermodynamic signature of a bosonic bunching effect, as observed in [36]–[38]. The sudden and fast increase of our data for $\zeta \lesssim 1$ indicates the Bose–Einstein condensation threshold. In the LDA framework, the chemical potential of a weakly interacting Bose–Einstein condensate reads as follows:

$$\mu = \frac{4\pi \hbar^2 a_{77}}{m_7} n,$$

where m_7 is the ^7Li atom mass and a_{77} is the scattering length describing s-wave interactions between ^7Li atoms. We neglect thermal excitations in the condensed region. Integrating the Gibbs–Duhem relation at a fixed temperature $dP = nd\mu$ between the condensation threshold ζ_c and $\zeta < \zeta_c$, and imposing continuity at $\zeta = \zeta_c$, we obtain the equation of state in the condensed phase:

$$g(\zeta) = g_{5/2}(\zeta_c) + \frac{\lambda_{\text{dB}}(T)}{4 a_{77}} (\log^2 \zeta - \log^2 \zeta_c). \quad (6)$$

Fitting our data with the function $g(\zeta)$ given by (6) for $\zeta < \zeta_c$ and with $g_{5/2}(\zeta)$ for $\zeta > \zeta_c$, we obtain $\zeta_c = 1.0(1)$ and $a_{77} = 8(4) a_0 = 0.4(2) \text{ nm}$. The uncertainties take into account the fit uncertainty and the uncertainty related to the temperature determination. The condensation threshold is in agreement with the value $\zeta_c = 1$ expected for an ideal Bose gas, the mean-field correction being of the order of 1% [39, 40]. Our measurement of the scattering length is in agreement with the most recent calculations $a_{77} = 7(1) a_0$ [41].

Extending this type of measurement to larger interaction strength Bose gases prepared close to a Feshbach resonance would reveal more complex beyond-mean-field phenomena, provided thermal equilibrium is reached for strong enough interactions.

5. Mott insulator behavior of a Bose gas in a deep optical lattice

Here we extend our grand-canonical analysis to the case of a ^{87}Rb gas in an optical lattice in the Mott insulator regime. By comparing experimental data with advanced Monte Carlo techniques, it has been shown that in many circumstances the LDA is satisfied in such a system [42]. We analyze the integrated density profiles of the Munich group (see figure 2 of [21]).

5.1. Realization of the Bose–Hubbard model with ultracold gases

Atoms are held in a trap consisting of the sum of a harmonic potential $V_h(x, y, z)$ and a periodic potential,

$$V_0(\sin^2(kx) + \sin^2(ky) + \sin^2(kz)),$$

created by three orthogonal standing waves of red-detuned laser light at the wavelength $\lambda = 2\pi/k = 843$ nm. The atoms occupy the lowest Bloch band and realize the Bose–Hubbard model [43]:

$$\hat{H} = -J \sum_{\langle i,j \rangle} \hat{a}_i^\dagger \hat{a}_j + \frac{U}{2} \sum_i (\hat{a}_i^\dagger \hat{a}_i - 1) \hat{a}_i^\dagger \hat{a}_i, \quad (7)$$

with a local chemical potential $\mu(\mathbf{r}) = \mu^0 - V_h(\mathbf{r})$. The index i refers to a potential well at position \mathbf{r}_i , J is the tunneling amplitude between nearest neighbors, and U is the on-site interaction, U and J being a function of the lattice depth [3]. The slow variation of $V_h(\mathbf{r})$ compared with the lattice period $\lambda/2$ justifies the use of LDA.

We consider here the case of a large lattice depth $V_0 = 22E_r$, for which $J \simeq 0.003 U \sim 0$, and assume that the temperature is much smaller than U . In this regime, the gas is expected to form a Mott insulator: in the interval $\mu \in [(p-1)U, pU]$, where p is an integer, the atom number per site remains equal to p , and the density is equal to $n = p(2/\lambda)^3$. Integrating the Gibbs–Duhem relation between 0 and μ , we obtain that the pressure P is a piecewise linear function of μ :

$$P(\mu, T=0) = \left(\frac{2}{\lambda}\right)^3 \left(\mu - \frac{p-1}{2}U\right) p, \quad \text{where } (p-1)U < \mu < pU.$$

5.2. Determination of the equation of state

We use a series of three images from [21], labeled a , b and c , with different atom numbers $N_a = 1.0 \times 10^5$, $N_b = 2.0 \times 10^5$ and $N_c = 3.5 \times 10^5$ (see figure 5(a)). The integrated profiles $\bar{n}(z)$ are not obtained using *in situ* absorption imaging but rather using a tomographic technique, providing $\sim 1 \mu\text{m}$ resolution. The pressure profile is then obtained using equation (1).

Each image $i = a, b$ and c plotted as P as a function of $-\frac{1}{2}m\omega_z^2 z^2$ provides the equation of state $P(\mu)$ translated by the unknown global chemical potential μ_i^0 . By imposing that all images correspond to the same equation of state (in the overlapping μ/U region), we deduce the chemical potential differences between the different images $\mu_b^0 - \mu_a^0 = 0.56 U$ and $\mu_c^0 - \mu_b^0 = 0.61 U$ (see figure 5(b)). Gathering the data from all images, we thus obtain a single equation of state, translated by μ_a^0 , which is still unknown. We fit these data with a function translated by μ_a^0 from the following function, capturing the Mott insulator physics:

$$\begin{aligned} \frac{P}{U(\lambda/2)^{-3}} &= 0, \quad \text{for } \mu < 0 \\ &= n_1 \frac{\mu}{U} \quad \text{for } 0 < \mu < \delta\mu_1 \\ &= n_1 \frac{\delta\mu_1}{U} + n_2 \frac{\mu - \delta\mu_1}{U} \quad \text{for } \delta\mu_1 < \mu < \delta\mu_1 + \delta\mu_2 \\ &= n_1 \frac{\delta\mu_1}{U} + n_2 \frac{\delta\mu_2}{U} + n_3 \frac{\mu - \delta\mu_1 - \delta\mu_2}{U} \quad \text{for } \delta\mu_1 + \delta\mu_2 < \mu, \end{aligned}$$

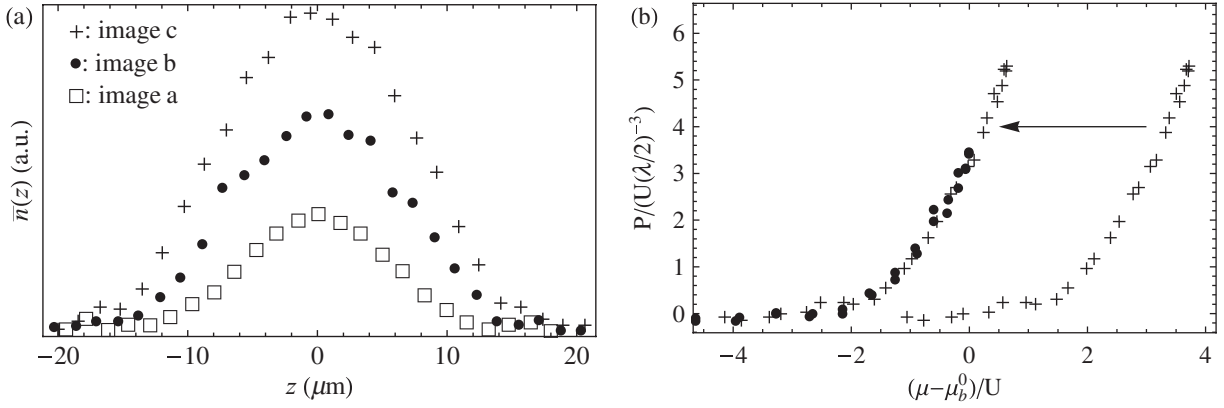


Figure 5. (a) Integrated density profiles $\bar{n}(z)$ corresponding to images *a* (open squares), *b* (black dots) and *c* (crosses) from [21]. (b) Determination of the global chemical potential difference $\mu_c^0 - \mu_b^0$ by superposing the equations of states given by each image.

with μ_a^0 , $\delta\mu_1$, $\delta\mu_2$, n_1 , n_2 and n_3 as free parameters. The value $\mu_a^0 = 1.51 U$ yielded by the fit thus corresponds to the condition $P \rightarrow 0$ when $\mu \rightarrow 0$. Once it is determined, we obtain the equation of state of the Bose–Hubbard model in the Mott regime, plotted in figure 6.

5.3. Observation of Mott insulator behavior

After fitting the value of μ_a^0 , the other parameters resulting from the fit exhibit the characteristic features of incompressible Mott phases. The occupation number in the first Mott region is $n_1 = 0.9(1)$ atom per site and the size is $\delta\mu_1 = 0.9(1)U$. The second Mott region occupation number is $n_2 = 2.0(1)$ and its size is $\delta\mu_2 = 1.1(1)U$. Finally, the third Mott region occupation number is $n_3 = 3.1(1)$. These values agree with the theoretical values $n_i = i$ and $\delta\mu_i = U$, in the $T = 0$ and $J = 0$ limits.

5.4. Estimation of finite-temperature effects

The equation of state deduced from the experimental data is also suited for investigating finite-temperature effects. Since sites are decoupled in the regime $J \ll U$, $k_B T$ considered in this study, the finite-temperature equation of state is easily calculated from the thermodynamics of a single site [44, 45]:

$$P(\mu, T) = \frac{k_B T}{(\lambda/2)^3} \log \left(\sum_{p=0}^{\infty} \exp \left(-\frac{Up(p-1)/2 - \mu p}{k_B T} \right) \right). \quad (8)$$

Fitting now the experimental data with (8) and T and μ_a^0 as free parameters, we deduce

$$k_B T = 0.09_{-0.09}^{+0.04} U.$$

This value is in agreement with a direct fit of the density profiles and number statistics measurements [46]. Firstly, this temperature is significantly smaller than the temperature $k_B T^* \simeq 0.2 U$ at which the Mott insulator is expected to melt [44]. Secondly, this temperature should be considered as an upper limit because of its uncertainty on the low-temperature side.

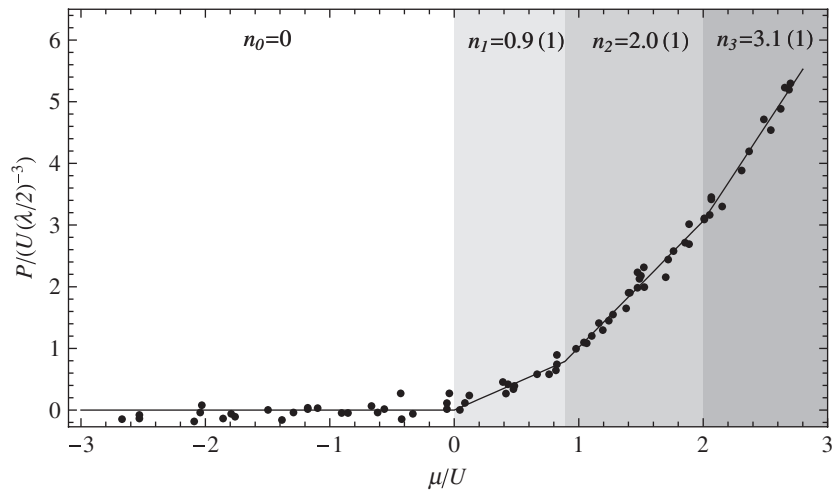


Figure 6. Equation of state of a Bose gas in an optical lattice, in the Mott insulator regime. The solid line is a fit with a piecewise linear function capturing the Mott insulator behavior. The slope $dP/d\mu$ provides the density in each of the Mott zones, $n_1 = 0.9(1)$, $n_2 = 2.0(1)$ and $n_3 = 3.1(1)$.

Indeed, the finite resolution of the images tends to smear out the sharp structure associated with Mott insulator boundaries, leading to an overestimation of the actual temperature. To overcome this limit, the spin-gradient thermometry proposed in [47] could be employed.

6. Summary and concluding remarks

To summarize, we have shown on various examples of Fermi and Bose gas systems how *in situ* absorption images can provide the grand-canonical equation of state of the homogeneous gas. This equation of state is obtained up to a global shift in chemical potential and we have given several examples for its determination. The method relies on the LDA, which is satisfied in many situations, but notable exceptions exist such as the case of the ideal Bose gas. The equation of state given by this procedure allows a direct comparison with many-body theories. Although we have here illustrated this method on a single-component Bose gas and a spin-balanced Fermi gas, it can easily be generalized to multi-component gases. For instance, the phase diagram and the superfluid equation of state of spin-imbalanced Fermi gases were obtained in [1, 14]. We expect this method to be very useful in the investigation of Bose–Bose, Bose–Fermi and Fermi–Fermi mixtures. Finally, the equation of state of a Bose gas close to a Feshbach resonance may reveal thermodynamic signatures of beyond-mean-field behavior in Bose–Einstein condensates [48].

Acknowledgments

We are grateful to Fabrice Gerbier and Kenneth Guenter for stimulating discussions. We acknowledge support from ERC (Ferlodim), ESF (Euroquam Fermix), ANR FABIOLA, Région Ile de France (IFRAF) and Institut Universitaire de France.

Appendix. Validity of local density approximation (LDA)

Let us now discuss the validity of LDA around the superfluid transition in our experiment. Along the z -axis, the correlation length ξ diverges around the transition point $z = z_c$ according to $\xi \sim k_F^{-1} |(z - z_c)/z_c|^{-\nu}$, where $\nu = 0.67$ is the correlation length critical exponent, directly measured in [49], and in agreement with $\nu = (2 - \alpha)/3$. LDA is expected to become inaccurate in the region $z_c - \delta z < z < z_c + \delta z$, where δz is given by [31, 50]

$$\delta z \sim \xi(z_c + \delta z), \quad \text{i.e.} \quad \delta z \sim z_c (k_F z_c)^{-1/(1+\nu)}.$$

z_c is of the order of the cloud size along z , and is much larger than k_F^{-1} , which is of the order of the inter-particle distance. Given the parameters of our experiments, $(k_F z_c)^{-1/(1+\nu)} \sim 1\%$ and the size δz where LDA is invalid is very small. Given the noise of our data (a few per cent), the deviation from LDA is thus negligible. Investigating the critical behavior at the superfluid transition, such as measuring the critical exponent α , would be an interesting development for this method, as proposed in [50].

References

- [1] Nascimbène S, Navon N, Jiang K J, Chevy F and Salomon C 2010 Exploring the thermodynamics of a universal Fermi gas *Nature* **463** 1057
- [2] Horikoshi M, Nakajima S, Ueda M and Mukaiyama T 2010 Measurement of universal thermodynamic functions for a unitary Fermi gas *Science* **327** 442
- [3] Bloch I, Dalibard J and Zwirger W 2008 Many-body physics with ultracold gases *Rev. Mod. Phys.* **80** 885–964
- [4] *The many-body challenge problem* formulated by G F Bertsch, see Bishop R F 2001 *Int. J. Mod. Phys. B* **15**(10–11) iii
- [5] Gezerlis A and Carlson J 2008 Strongly paired fermions: cold atoms and neutron matter *Phys. Rev. C* **77** 32801
- [6] Stewart J T, Gaebler J P, Regal C A and Jin D S 2006 Potential energy of a ^{40}K Fermi gas in the BCS–BEC crossover *Phys. Rev. Lett.* **97** 220406
- [7] Luo L, Clancy B, Joseph J, Kinast J and Thomas J E 2007 Measurement of the entropy and critical temperature of a strongly interacting Fermi gas *Phys. Rev. Lett.* **98** 80402
- [8] Altmeyer A, Riedl S, Kohstall C, Wright M J, Geursen R, Bartenstein M, Chin C, Denschlag J H and Grimm R 2007 Precision measurements of collective oscillations in the BEC–BCS crossover *Phys. Rev. Lett.* **98** 40401
- [9] Partridge G B, Li W, Kamar R I, Liao Y and Hulet R G 2006 Pairing and phase separation in a polarized Fermi gas *Science* **311** 503–5
- [10] Zwierlein M W, Schunck C H, Schirotzek A and Ketterle W 2006 Direct observation of the superfluid phase transition in ultracold Fermi gases *Nature* **442** 54–8
- [11] Nascimbène S, Navon N, Jiang K, Tarruell L, Teichmann M, Mckeever J, Chevy F and Salomon C 2009 Collective oscillations of an imbalanced Fermi gas: axial compression modes and polaron effective mass *Phys. Rev. Lett.* **103** 170402
- [12] Shin Y 2008 Determination of the equation of state of a polarized Fermi gas at unitarity *Phys. Rev. A* **77** 041603
- [13] Ho T L and Zhou Q 2009 Obtaining the phase diagram and thermodynamic quantities of bulk systems from the densities of trapped gases *Nat. Phys.* **6** 131–4
- [14] Navon N, Nascimbène S, Chevy F and Salomon C 2010 The equation of state of a low-temperature Fermi gas with tunable interactions *Science* **328** 729
- [15] Hadzibabic Z, Kruger P, Cheneau M, Battelier B and Dalibard J 2006 Berezinskii–Kosterlitz–Thouless crossover in a trapped atomic gas *Nature* **441** 1118–21

- [16] Cladé P, Ryu C, Ramanathan A, Helmerson K and Phillips W D 2009 Observation of a 2D Bose gas: from thermal to quasicondensate to superfluid *Phys. Rev. Lett.* **102** 170401
- [17] Gemelke N, Zhang X, Hung C L and Chin C 2009 *In situ* observation of incompressible Mott-insulating domains in ultracold atomic gases *Nature* **460** 995–8
- [18] Bakr W S, Gillen J I, Peng A, Fölling S and Greiner M 2009 A quantum gas microscope for detecting single atoms in a Hubbard-regime optical lattice *Nature* **462** 74–7
- [19] Rath S P, Yefsah T, Günter K J, Cheneau M, Desbuquois R, Holzmann M, Krauth W and Dalibard J 2010 The equilibrium state of a trapped two-dimensional Bose gas *Phys. Rev. A* **82** 013609
- [20] Shin Y, Schunck C H, Schirotzek A and Ketterle W 2008 Phase diagram of a two-component Fermi gas with resonant interactions *Nature* **451** 689–93
- [21] Fölling S, Widera A, Müller T, Gerbier F and Bloch I 2006 Formation of spatial shell structure in the superfluid to Mott insulator transition *Phys. Rev. Lett.* **97** 60403
- [22] Ho T L and Mueller E J 2004 High temperature expansion applied to fermions near Feshbach resonance *Phys. Rev. Lett.* **92** 160404
- [23] Liu X J, Hu H and Drummond P D 2009 Virial expansion for a strongly correlated Fermi gas *Phys. Rev. Lett.* **102** 160401
- [24] Carlson J, Chang S Y, Pandharipande V R and Schmidt K E 2003 Superfluid Fermi gases with large scattering length *Phys. Rev. Lett.* **91** 50401
- [25] Lobo C, Recati A, Giorgini S and Stringari S 2006 Normal state of a polarized Fermi gas at unitarity *Phys. Rev. Lett.* **97** 200403
- [26] Bulgac A, Drut J E and Magierski P 2008 Quantum Monte Carlo simulations of the BCS–BEC crossover at finite temperature *Phys. Rev. A* **78** 23625
- [27] Chevy F 2006 Universal phase diagram of a strongly interacting Fermi gas with unbalanced spin populations *Phys. Rev. A* **74** 063628
- [28] Combescot R, Recati A, Lobo C and Chevy F 2007 Normal state of highly polarized Fermi gases: simple many-body approaches *Phys. Rev. Lett.* **98** 180402
- [29] Prokof'ev N and Svistunov B 2008 Fermi-polaron problem: diagrammatic Monte Carlo method for divergent sign-alternating series *Phys. Rev. B* **77** 020408
- [30] Combescot R and Giraud S 2008 Normal state of highly polarized Fermi gases: full many-body treatment *Phys. Rev. Lett.* **101** 050404
- [31] Taylor E 2009 Critical behavior in trapped strongly interacting Fermi gases *Phys. Rev. A* **80** 23612
- [32] Lipa J A and Chui T C P 1983 Very high-resolution heat-capacity measurements near the lambda point of helium *Phys. Rev. Lett.* **51** 2291–4
- [33] Caracanhas M A, Seman J A, Ramos E R F, Henn E A L, Magalhães K M F, Helmerson K and Bagnato V S 2009 Finite temperature correction to the Thomas–Fermi approximation *J. Phys. B: At. Mol. Opt. Phys.* **42** 145304
- [34] Romero-Rochín V 2005 Equation of state of an interacting Bose gas confined by a harmonic trap: the role of the harmonic pressure *Phys. Rev. Lett.* **94** 130601
- [35] Schreck F, Khaykovich L, Corwin K L, Ferrari G, Bourdel T, Cubizolles J and Salomon C 2001 Quasipure Bose–Einstein condensate immersed in a Fermi sea *Phys. Rev. Lett.* **87** 80403
- [36] Yasuda M and Shimizu F 1996 Observation of two-atom correlation of an ultracold neon atomic beam *Phys. Rev. Lett.* **77** 3090–3
- [37] Fölling S, Gerbier F, Widera A, Mandel O, Gericke T and Bloch I 2005 Spatial quantum noise interferometry in expanding ultracold atom clouds *Nature* **434** 481–4
- [38] Schellekens M, Hoppeler R, Perrin A, Gomes J V, Boiron D, Aspect A and Westbrook C I 2005 Hanbury Brown Twiss effect for ultracold quantum gases *Science* **310** 648
- [39] Giorgini S, Pitaevskii L P and Stringari S 1996 Condensate fraction and critical temperature of a trapped interacting Bose gas *Phys. Rev. A* **54** 4633–6
- [40] Giorgini S, Pitaevskii L P and Stringari S 1997 Thermodynamics of a trapped Bose-condensed gas *J. Low Temp. Phys.* **109** 309–55

- [41] Kokkelmans S 2010 private communication
- [42] Trotzky S, Pollet L, Gerbier F, Schnorrberger U, Bloch I, Prokof'ev N V, Svistunov B and Troyer M 2009 Suppression of the critical temperature for superfluidity near the Mott transition: validating a quantum simulator arXiv:0905.4882
- [43] Jaksch D, Bruder C, Cirac J I, Gardiner C W and Zoller P 1998 Cold bosonic atoms in optical lattices *Phys. Rev. Lett.* **81** 3108–11
- [44] Gerbier F 2007 Boson Mott insulators at finite temperatures *Phys. Rev. Lett.* **99** 120405
- [45] Capogrosso-Sansone B, Prokof'ev N V and Svistunov B V 2007 Phase diagram and thermodynamics of the three-dimensional Bose–Hubbard model *Phys. Rev. B* **75** 134302
- [46] Gerbier F 2010 private communication
- [47] Weld D M, Medley P, Miyake H, Hucul D, Pritchard D E and Ketterle W 2009 Spin gradient thermometry for ultracold atoms in optical lattices *Phys. Rev. Lett.* **103** 245301
- [48] Papp S B, Pino J M, Wild R J, Ronen S, Wieman C E, Jin D S and Cornell E A 2008 Bragg spectroscopy of a strongly interacting ^{85}Rb Bose–Einstein condensate *Phys. Rev. Lett.* **101** 135301
- [49] Donner T, Ritter S, Bourdel T, Ottl A, Kohl M and Esslinger T 2007 Critical behavior of a trapped interacting Bose gas *Science* **315** 1556
- [50] Pollet L, Prokofev N V and Svistunov B V 2010 Criticality in trapped atomic systems *Phys. Rev. Lett.* **104** 245705

Fermi-Liquid Behavior of the Normal Phase of a Strongly Interacting Gas of Cold Atoms

S. Nascimbène, N. Navon, S. Pilati, F. Chevy, S. Giorgini, A. Georges, and C. Salomon

Physical Review Letters **106**, 215303 (2011)

Fermi-Liquid Behavior of the Normal Phase of a Strongly Interacting Gas of Cold Atoms

S. Nascimbène,^{1,*} N. Navon,¹ S. Pilati,² F. Chevy,¹ S. Giorgini,³ A. Georges,^{4,5} and C. Salomon¹

¹Laboratoire Kastler Brossel, CNRS, UPMC, École Normale Supérieure, 24 rue Lhomond, 75231 Paris, France

²Theoretische Physik, ETH Zurich, CH-8093 Zurich, Switzerland

³Dipartimento di Fisica, Università di Trento and INO-CNR BEC Center, I-38050 Povo, Trento, Italy

⁴Centre de Physique Théorique, CNRS, Ecole Polytechnique, route de Saclay, 91128 Palaiseau Cedex, France

⁵Collège de France, 11 place Marcellin Berthelot, 75005 Paris, France

(Received 26 January 2011; revised manuscript received 6 April 2011; published 27 May 2011)

We measure the magnetic susceptibility of a Fermi gas with tunable interactions in the low-temperature limit and compare it to quantum Monte Carlo calculations. Experiment and theory are in excellent agreement and fully compatible with the Landau theory of Fermi liquids. We show that these measurements shed new light on the nature of the excitations of the normal phase of a strongly interacting Fermi gas.

DOI: 10.1103/PhysRevLett.106.215303

PACS numbers: 67.85.Lm, 67.10.Db

In 1956 Landau developed an elegant description of interacting Fermi systems at low temperature relying on the existence of long-lived quasiparticles. While this Fermi-liquid theory (FLT) describes well Helium 3 and many solid-state materials above the superfluid temperature, there exist notable exceptions such as underdoped cuprates [1], where despite tremendous theoretical and experimental efforts, the nature of the normal phase is not yet understood. Similarly to high-critical temperature superconductors, the properties of the normal phase of strongly correlated atomic fermionic gases and the nature of its excitations are still debated. This issue was addressed recently for spin-balanced gases above the superfluid transition, through the measurement of equations of state [2–5], the study of the single-particle excitation spectrum [6,7], or of spin fluctuations [8]. On the one hand, recent photoemission spectroscopy experiments near the critical temperature were interpreted using a pseudogap model [7]. On the other hand, measurement of the temperature dependence of the specific heat displayed a linear behavior compatible with Fermi liquid's prediction [2]. All these experimental probes give access to the properties of the normal phase of the unpolarized normal phase above the critical temperature T_c . This limitation can be overcome by stabilizing the normal state at $T < T_c$ by imposing a spin population imbalance in the trapped gas [9–11] and extrapolating its properties to zero imbalance. Previous works focused on the highly polarized limit where minority atoms behave as impurities: $n_2 \ll n_1$, where n_i is the density for species i [2,12–20]. Here, we interpret the spin imbalance as the application of an effective magnetic field to the unpolarized normal gas at very low temperature and using a combination of Monte Carlo simulations and experimental results, we extract from the equation of state the magnetic spin response of the normal phase in the limit $T \ll T_c$. We show that our results are compatible with a Fermi-liquid description of the normal phase, and we

extract the Fermi-liquid parameters in the universal unitary limit where scattering length is infinite. The relationship between these parameters and the properties of low-lying excitations of the system allow us to quantitatively interpret spectroscopic data from [6,7].

The polarization dependence of the energy E of the system directly reflects the presence of spin-singlet dimers in the sample. Indeed, the presence of a gap in the spin excitation spectrum implies a linear dependence of the energy E with polarization $p = (N_1 - N_2)/(N_1 + N_2)$ at low temperature, and hence a zero spin susceptibility. We have performed quantum Monte Carlo simulations of the partially polarized Fermi gas at $T = 0$ in the BEC-BCS crossover. We make use of the fixed-node diffusion Monte Carlo method that was employed in earlier studies of polarized Fermi gases [14,18]. The state of the system is forced to be in the normal phase by imposing the nodal surface of a many-body wave function incompatible with off-diagonal long-range order. A simple way to implement this requirement is by choosing the trial function of the Jastrow-Slater form

$$\psi_T(\mathbf{R}) = \prod_{i,i'} f(r_{ii'}) D(N_1) D(N_2), \quad (1)$$

where $\mathbf{R} = (\mathbf{r}_1, \dots, \mathbf{r}_N)$ is the spatial configuration vector of the N particles and D denotes the Slater determinant of plane waves in a cubic box of size L with periodic boundary conditions. The positive Jastrow correlation term $f(r)$ is determined as described in Ref. [14]: at short distances it corresponds to the lowest-energy solution of the two-body problem, while it satisfies the boundary condition on its derivative $f'(r = L/2) = 0$.

The results for the canonical equation of state $E(N_1, N_2)$ are shown in Fig. 1. They are well fitted by the energy functional

$$E(p) = \frac{3}{5} N E_F (\xi_N + \frac{5}{9} \tilde{\chi}^{-1} p^2 + \dots), \quad (2)$$

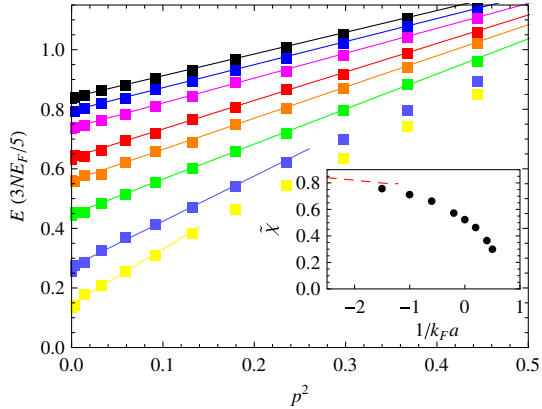


FIG. 1 (color online). Canonical equation of state of a two-component Fermi gas calculated using quantum Monte Carlo simulation, for $1/k_F a = -1.5, -1, -0.6, -0.2, 0, 0.2, 0.4, 0.5$ (from top to bottom). The solid lines are fits of the low-polarization data with Eq. (2). Inset: Extracted values of the susceptibility $\tilde{\chi}$ as a function of $1/k_F a$. The dashed red line is the result of a perturbation expansion valid up to order $(k_F a)^2$.

holding for a spin polarizable system at low temperature, where both ξ_N and the dimensionless spin susceptibility $\tilde{\chi}$ (in units of the susceptibility of an ideal Fermi gas $3n/2E_F$) depend on $1/k_F a$, where $k_F = (3\pi^2 n)^{2/3}$. The Monte Carlo method indicates the absence of spin gap, and thus of preformed molecules in the normal phase for $1/k_F a \lesssim 0.5$. Note that the extracted values of $\tilde{\chi}$ reported in the inset of Fig. 1 show a rapid drop for positive values of a when entering the BEC side of the Feshbach resonance. A likely explanation is the binding of fermions into spin-singlet pairs for some positive value of the interaction strength $1/k_F a$. Monte Carlo calculations for values of $1/k_F a \geq 0.7$ show that $E(p)$ is indeed linear rather than quadratic in p , indicating the emergence of a gap. However, pairing fluctuations play a major role for such values of the coupling and the nodal surface of the Jastrow-Slater state (see the supplemental material [21]) is no longer sufficient to enforce the normal phase. This behavior is reminiscent of the pairing transition investigated in the framework of BCS theory [22], as well as in the normal phase of the attractive Hubbard model, extrapolated to a temperature range below the superfluid transition [23,24], while in our work the extrapolation is made towards a small spin imbalance.

We now compare these simulations with the grand-canonical equation of state (EOS) of a homogeneous system obtained experimentally in Refs. [2,12]. We prepare a deeply degenerate mixture of the two lowest internal states of ${}^6\text{Li}$, held in a cylindrically symmetric hybrid optical-magnetic trap, of radial (axial) frequency ω_r (ω_z , respectively). The bias magnetic field B_0 is chosen between 822 and 981 G, allowing us to tune the strength of interactions $-1 < 1/k_F a < 0.2$. The final atom number is 2 to 10×10^4 atoms per spin state, and the gas temperature is

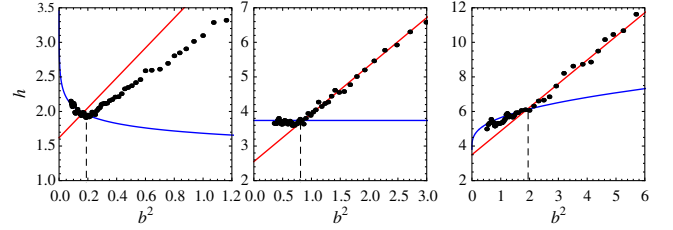


FIG. 2 (color online). Thermodynamic function $h(b)$ measured at different magnetic fields $B_0 = 871, 834, 822$ G. The blue lines correspond to the superfluid equation of state $h_S(\delta)$ measured in [12]. The red line is a linear fit of the data in the normal phase, $b > b_c$. The dashed line indicates the superfluid/normal phase transition ($b = b_c$).

smaller than $0.06T_F$, as measured from the fully polarized wings of a trapped gas [25]. From dimensional analysis, the EOS of a spin-imbalanced Fermi gas can be written as

$$P(\mu_1, \mu_2, a) = P_0(\mu)h\left(\delta = \frac{\hbar}{\sqrt{2m\mu a}}, b = \frac{\mu_1 - \mu_2}{\mu_1 + \mu_2}\right),$$

where $\mu = (\mu_1 + \mu_2)/2$ is the mean chemical potential and $P_0(\mu)$ is the pressure of a noninteracting unpolarized Fermi gas. δ is a grand-canonical analog of the interaction parameter $1/k_F a$, and b is a dimensionless number proportional to the “spin-polarizing field” $\mu_1 - \mu_2$.

At all values of the scattering length addressed in this work, the equation of state exhibits a clear discontinuity of its derivative at the critical field $b_c(\delta)$ (See Fig. 2), indicating a first-order phase transition from a superfluid state for $b < b_c$ to a normal state for $b > b_c$, where h is linear in b^2 . [10,12]. The equation of state of the superfluid phase has been discussed in a previous work [12] and we focus here on the properties of the normal phase. We write

$$h(\delta, b) = h_N(\delta)(1 + \frac{15}{8}\tilde{\chi}^{\text{GC}}(\delta)b^2 + O(b^4)). \quad (3)$$

$h_N(\delta)$ is the grand-canonical equation of state in the normal state, extrapolated to a spin-symmetric configuration. $\tilde{\chi}^{\text{GC}}(\delta)$ is a grand-canonical magnetic susceptibility. For an ideal two-component Fermi gas, the functions h_N and $\tilde{\chi}^{\text{GC}}$ are equal to 1. Fitting our data in the normal phase with (3), we obtain the parameters $h_N(\delta)$ and $\tilde{\chi}^{\text{GC}}(\delta)$ in the BEC-BCS crossover shown in Fig. 3 where we compare their values to the predictions of the Monte Carlo simulations. To this end, we fit the dependence with $1/k_F a$ of the parameters ξ_N and $\tilde{\chi}$ determined by Monte Carlo simulations, and perform a Legendre transform to obtain the grand-canonical EOS $h_N(\delta)$ of the normal phase and magnetic susceptibility $\tilde{\chi}^{\text{GC}}(\delta)$ measured experimentally. In the investigated parameter range, the agreement between theory and experiment is excellent. We also remark that our value for the susceptibility of the normal phase at unitarity is about twice larger than the value measured in [8] on a gas with a 35% condensate fraction, confirming a significant

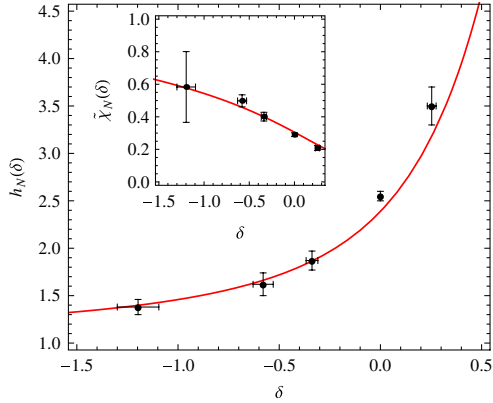


FIG. 3 (color online). Fermi-liquid equation of state extrapolated to a spin-symmetric configuration $h_N(\delta)$. The black dots are the experimental data, and the red line is calculated from the Monte Carlo data. Inset: Grand-canonical susceptibility $\tilde{\chi}^{\text{GC}}(\delta)$ of a Fermi gas in the BEC-BCS crossover.

suppression of the spin susceptibility in the superfluid phase.

Our findings demonstrate that for $1/k_F a \lesssim 0.5$, the spin excitations of the system are not gapped in the normal phase which therefore does not support “true” molecules. However, a certain class of theories predicts a reminiscence of this gap in the form of a dip in the density of states over a range Δ^* around the Fermi level [26]. Δ^* is often called the pseudogap, in relationship to some features of high-critical temperature superconductors. These theories predict a departure of $E(p)$ from its quadratic behavior when the Fermi levels of the two spin species reach the edges of the dip, $\mu_2 - \mu_1 \simeq \Delta^*$. (see Auxiliary Materials). The absence of such an anomaly in Fig. 1 and 2, and in the whole range $-1 < 1/k_F a < 0.5$ thus suggests that the dip is either extremely narrow or very broad: the density of state remains flat over the range of polarizations and interaction strength studied in our work. For instance, at unitarity this range covers $0 < b^2 < 3$. If a sizeable dip existed, then its width cannot be smaller than $\simeq (\mu_1 + \mu_2)\sqrt{3} \simeq 1.4E_F$ where we have used the unitary equation of state, $\mu = 0.41E_F$ [12]. Such a large pseudogap is not compatible with the photoemission data of [7] (See below). Furthermore, we would expect on physical grounds that Δ^* becomes smaller on the BCS side of the resonance. This is observed neither in the experimental data of Fig. 2 nor in the quantum Monte Carlo results of Fig. 1.

On the contrary, Landau’s theory of Fermi liquids is fully compatible with our observations. This theory assumes the existence of long-lived fermionic excitations above the Fermi surface. Combining the measurement of the low-temperature compressibility κ and specific heat C_v of [2] with the data presented here, we can fully characterize the parameters of the theory at the unitary limit. From the magnetic response of the $T = 0$ gas, we obtain here its

magnetic susceptibility and another determination of κ . The two determinations of κ coincide within 5%, showing that the two approaches indeed probe the same Fermi liquid. From this set of thermodynamic quantities we derive, according to Landau’s Fermi-liquid theory, a complete characterization of the low-lying excitations of the unitary gas: besides their effective mass $m^* = 1.13m$ and Landau parameters $F_0^s = -0.42$, $F_1^s = 0.39$ found in [2], we recover here $F_0^s = -0.40$ and obtain the new parameter $F_0^a = m^*/m\tilde{\chi}(0)^{-1} - 1 = 1.1(1)$. Note that $F_0^a > 0$ corresponds to magnetic correlations which do favor the singlet configuration.

We can finally test FLT on the single-particle photoemission spectrum obtained at the unitary limit and at the onset of superfluidity from Ref. [7]. The experimental signal $\bar{A}(k, \omega)$ is directly proportional to the spectral function $A(k, \omega - \mu)$ averaged over the trap that we estimate using the following procedure: In the vicinity of the Fermi surface, the dispersion relation of the Fermi-liquid quasiparticles reads $\hbar\omega_k = \mu + \hbar^2(k^2 - k_F^2)/2m^*$ where $m^* = 1.13m$. Assuming long-lived quasiparticles, we approximate $A(k, \omega)$ by $\delta(\omega - \omega_k)$ and perform the integration over the trap to obtain $\bar{A}(k, \omega)$ given by [7]

$$\bar{A}(k, \omega) = \frac{48k^2}{\pi^2} \int d^3r \frac{A(k, \omega - \mu(\mathbf{r})/\hbar)}{1 + \exp\frac{\hbar\omega - \mu(\mathbf{r})}{k_B T}}, \quad (4)$$

where $\mu(\mathbf{r})$ is the local chemical potential at position \mathbf{r} . In order to calculate the integrated spectral function $\bar{A}(k, \omega)$ of a Fermi liquid, we replace the spectral function by $\delta(\omega - \omega_k)$, and perform the integration in Eq. (4). $k_F(r)$ is calculated from the equation of state of the unitary gas determined in [2]. The temperature is chosen at the onset of superfluidity $k_B T/\mu^0 = 0.32$ [2,27]. In order to make a direct comparison with the experimental data, we finally convolve our result with the experimental resolution in ω [7], equal to $0.25E_F/\hbar$ and results for various values of k are shown in Fig. 4.

With no free parameter in the theory, FLT well reproduces the experimental spectra for $\bar{A}(k, \omega)$ in the region $k < k_F$, with an excellent agreement in the region $0.3k_F \leq k \leq k_F$ close to the most probable Fermi level in the trap ($\simeq 0.7k_F$) where FLT is expected to be more accurate. Interestingly, we observe that the width of the peak at $k/k_F = 0.6$ is well reproduced by our model meaning that the broadening of the line is not limited by the lifetime of the quasiparticles, but rather by trap inhomogeneity and measurement resolution. Significant deviations between experiment and FLT appear for $k > 1.1k_F$, far from the most probable Fermi wave vector. However, in this region the energy spectrum signal is very broad and weak, corresponding to an incoherent background in the spectral function. Our Fermi-liquid description thus accounts for the coherent part of the excitation spectrum from [7].

In conclusion we have shown that the magnetic and thermal responses of the unitary Fermi gas support a

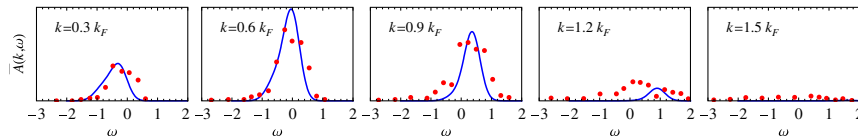


FIG. 4 (color online). Energy distribution data $\bar{A}(k, \omega)$ from [7] (red dots), compared with the prediction of Fermi-liquid theory (blue lines), for $k/k_F = 0.3, 0.6, 0.9, 1.2, 1.5$.

description of the normal phase in terms of Fermi-liquid theory despite the fact that this system exhibits a high-critical temperature for superfluidity. This behavior is in contrast with underdoped cuprate high T_c materials displaying anomalous magnetic susceptibility or pseudogap physics in the normal phase. Recent quantum oscillation experiments on cuprates in high magnetic fields, aiming at studying the incipient normal state (somewhat analogously to the present work) do suggest long-lived quasiparticles [28]. The drop of the susceptibility on the BEC side of the resonance for $1/k_F a \gtrsim 0.5$ indicates the appearance of a spin gap in this regime that deserves further investigations. Finally, the magnetic susceptibility could be a key observable for characterizing the onset of itinerant ferromagnetism in a repulsive Fermi gas [29,30].

We are grateful to G. Bruun, C. Lobo, P. Massignan, S. Stringari, T. Giamarchi, and R. Combescot for insightful comments. We thank D. Jin, T. Drake, and J. Gaebler for providing us experimental data on radio-frequency spectroscopy. We acknowledge support from ESF (FerMix), ANR FABIOLA, Région Ile de France (IFRAF), ERC Ferlodim, and IUF. S.P. acknowledges support from the Swiss National Science Foundation, S.P. and A.G. from the Army Research Office with funding from the DARPA OLE program.

*To whom correspondence should be addressed.

Present address: Ludwig-Maximilians Universität, Schellingstr. 4, 80799 München, Germany.
sylvain.nascimbene@physik.uni-muenchen.de

- [1] P. Lee, N. Nagaosa, and X. Wen, *Rev. Mod. Phys.* **78**, 17 (2006).
- [2] S. Nascimbène *et al.*, *Nature (London)* **463**, 1057 (2010).
- [3] J. Stewart, J. Gaebler, C. Regal, and D. Jin, *Phys. Rev. Lett.* **97**, 220406 (2006).
- [4] L. Luo *et al.*, *Phys. Rev. Lett.* **98**, 80402 (2007).
- [5] M. Horikoshi, S. Nakajima, M. Ueda, and T. Mukaiyama, *Science* **327**, 442 (2010).
- [6] J. Gaebler *et al.*, *Nature Phys.* **6**, 569 (2010).
- [7] A. Perali *et al.*, *Phys. Rev. Lett.* **106** 060402 (2011).
- [8] C. Sanner, E. Su, A. Keshet, W. Huang, and W. Ketterle, *Phys. Rev. Lett.* **106** 010402 (2011).
- [9] G. Partridge, W. Li, R. Kamar, Y. Liao, and R. Hulet, *Science* **311**, 503 (2006).
- [10] M. Zwierlein, A. Schirotzek, C. Schunck, and W. Ketterle, *Science* **311**, 492 (2006).
- [11] S. Nascimbène *et al.*, *Phys. Rev. Lett.* **103**, 170402 (2009).
- [12] N. Navon, S. Nascimbène, F. Chevy, and C. Salomon, *Science* **328**, 729 (2010).
- [13] F. Chevy, *Phys. Rev. A* **74**, 063628 (2006).
- [14] C. Lobo, A. Recati, S. Giorgini, and S. Stringari, *Phys. Rev. Lett.* **97**, 200403 (2006).
- [15] R. Combescot, A. Recati, C. Lobo, and F. Chevy, *Phys. Rev. Lett.* **98**, 180402 (2007).
- [16] Y.I. Shin, *Phys. Rev. A* **77**, 041603 (2008).
- [17] N. Prokof'ev and B. Svistunov, *Phys. Rev. B* **77**, 020408 (2008).
- [18] S. Pilati and S. Giorgini, *Phys. Rev. Lett.* **100**, 030401 (2008).
- [19] A. Schirotzek, C.-H. Wu, A. Sommer, and M.W. Zwierlein, *Phys. Rev. Lett.* **102**, 230402 (2009).
- [20] C. Mora and F. Chevy, *Phys. Rev. Lett.* **104**, 230402 (2010).
- [21] See supplemental material at <http://link.aps.org/supplemental/10.1103/PhysRevLett.106.215303>.
- [22] R. Combescot, *Eur. Phys. J. D* **32**, 69 (2004).
- [23] M. Capone, C. Castellani, and M. Grilli, *Phys. Rev. Lett.* **88**, 126403 (2002).
- [24] A. Toschi, P. Barone, M. Capone, and C. Castellani, *New J. Phys.* **7**, 7 (2005).
- [25] Y. Shin, C. Schunck, A. Schirotzek, and W. Ketterle, *Nature (London)* **451**, 689 (2008).
- [26] Q.J. Chen, J. Stajic, S.N. Tan, and K. Levin, *Phys. Rep.* **412**, 1 (2005).
- [27] E. Burovski, N. Prokofev, B. Svistunov, and M. Troyer, *Phys. Rev. Lett.* **96**, 160402 (2006).
- [28] L. Taillefer, *J. Phys. Condens. Matter* **21**, 164212 (2009).
- [29] G. Jo *et al.*, *Science* **325**, 1521 (2009).
- [30] S. Pilati, G. Bertaina, S. Giorgini, and M. Troyer, *Phys. Rev. Lett.* **105**, 030405 (2010).

Dynamics and Thermodynamics of the Low-Temperature Strongly Interacting Bose Gas

N. Navon, S. Piatecki, K. Gunter, B. Rem, T. Nguyen, F. Chevy, W. Krauth, and C. Salomon

Physical Review Letters **107**, 135101 (2011)

Dynamics and Thermodynamics of the Low-Temperature Strongly Interacting Bose Gas

Nir Navon,^{1,*} Swann Piatecki,^{2,†} Kenneth Günter,¹ Benno Rem,¹ Trong Canh Nguyen,¹
Frédéric Chevy,¹ Werner Krauth,² and Christophe Salomon¹

¹Laboratoire Kastler Brossel, CNRS, UPMC, École Normale Supérieure, 24 rue Lhomond, 75005 Paris, France

²Laboratoire de Physique Statistique, École Normale Supérieure, UPMC, Université Paris Diderot,
CNRS, 24 rue Lhomond, 75005 Paris, France

(Received 15 March 2011; revised manuscript received 21 June 2011; published 19 September 2011)

We measure the zero-temperature equation of state of a homogeneous Bose gas of ^7Li atoms by analyzing the *in situ* density distributions of trapped samples. For increasing repulsive interactions our data show a clear departure from mean-field theory and provide a quantitative test of the many-body corrections first predicted in 1957 by Lee, Huang, and Yang [*Phys. Rev.* **106**, 1135 (1957)]. We further probe the dynamic response of the Bose gas to a varying interaction strength and compare it to simple theoretical models. We deduce a lower bound for the value of the universal constant $\xi > 0.44(8)$ that would characterize the universal Bose gas at the unitary limit.

DOI: 10.1103/PhysRevLett.107.135301

PACS numbers: 67.85.-d, 05.30.Jp, 32.30.Bv, 67.60.Fp

From sandpiles to neuronal networks, electrons in metals, and quantum liquids, one of the greatest challenges in modern physics is to understand the behavior of strongly interacting systems. A paradigmatic example is superfluid ^4He , the understanding of which has resisted theoretical analysis for decades. Early attempts to address the problem of the strongly interacting Bose liquid focused on the dilute limit. A seminal result for the thermodynamics of the dilute Bose gas was the expansion of the ground state energy (per volume V), first obtained in the late 1950s [1]:

$$\frac{E}{V} = \frac{gn^2}{2} \left(1 + \frac{128}{15\sqrt{\pi}} \sqrt{na^3} + \dots \right), \quad (1)$$

where n is the density of the gas, $g = 4\pi\hbar^2 a/m$ is the coupling constant for particles with mass m , and a is the s -wave scattering length, which characterizes the low-energy interactions. The first term in Eq. (1) is the mean-field energy, while the Lee-Huang-Yang (LHY) correction, proportional to $\sqrt{na^3}$, is due to quantum fluctuations [1]. Up to this order, the expansion is *universal*, in the sense that it depends solely on the gas parameter na^3 and not on microscopic details of the interaction potential [2–4].

Despite its fundamental importance, this expansion was never checked experimentally before the advent of ultracold quantum gases, where it became possible to tune the value of the scattering length using magnetic Feshbach resonances [5,6]. A first check of the LHY prediction was provided by recent experiments on strongly correlated Fermi gases [7–9] that behave as a gas of tightly bound dimers in the limit of small and positive values of a [10–12]. By contrast, early studies of Bose gases in the strongly interacting regime were plagued by severe inelastic atom loss [13], but recent experiments at JILA and Rice have revived interest in these systems and showed the onset of beyond mean-field effects [14,15]. Here we report on a quantitative measurement of the thermodynamic equation

of state (EOS) of a strongly interacting atomic Bose gas in the low-temperature limit. We show that the EOS follows the expansion (1), and the comparison with fermionic systems illustrates the universality of the LHY correction.

In the first part, we restrict ourselves to a moderately interacting gas with negligible 3-body atom loss: $a/a_0 \sim 2000$, a_0 being the Bohr radius. In this regime our EOS reveals the Lee-Huang-Yang correction due to quantum fluctuations. We perform quantum Monte Carlo (QMC) simulations to support our zero-temperature approximation. We then test our assumption of thermal equilibrium by dynamically bringing the gas into a more strongly interacting regime where atom loss is no longer negligible. Finally, we explore the unitary regime where the scattering length is infinite.

Our experimental setup was described in [16]. Starting from a ^7Li cloud in a magneto-optical trap, we optically pump the atoms into the $|F = 2, m_F = 2\rangle$ hyperfine state and transfer them into a magnetic Ioffe trap. After evaporative cooling to a temperature of $\sim 4 \mu\text{K}$, the atoms are loaded into a hybrid magnetic/optical trap and then transferred to the $|F = 1, m_F = 1\rangle$ state. The radial optical confinement of the trap is provided by a single laser beam of $35 \mu\text{m}$ waist operating at a wavelength of 1073 nm, while the weak axial confinement is enhanced by an additional magnetic-field curvature. We apply a homogeneous magnetic field to tune the interaction strength by means of a wide Feshbach resonance that we locate at 737.8(2) G. The final stage of evaporation in the optical trap is carried out at a bias field of 717 G, where the scattering length has a value of about $200a_0$, and results in a Bose-Einstein condensate of $\sim 6 \times 10^4$ atoms with no discernible thermal part. In the final configuration the trapping frequencies are given by $\omega_r = 2\pi \times 345(20)$ Hz in the radial and $\omega_z = 2\pi \times 18.5(1)$ Hz in the axial direction. The magnetic bias field is then adiabatically ramped

to the vicinity of the Feshbach resonance in 150 ms and the density distribution is recorded using *in situ* absorption imaging (Fig. 1). As the EOS critically depends on the scattering length, a precise knowledge of the latter close to the Feshbach resonance is essential. In view of the discrepancy between two recent works [15,17], we have independently calibrated the scattering length $a(B)$ as a function of magnetic field B by radio-frequency molecule association spectroscopy [18], as described in the Supplemental Material [19].

For the measurement of the EOS, we follow the method of [9,20–23]. Accordingly, the local pressure $P(z)$ along the symmetry axis of a harmonically trapped gas is related to the doubly integrated *in situ* density profile $\bar{n}(z) = \int dx dy n(x, y, z)$:

$$P(\mu_z) = \frac{m\omega_z^2}{2\pi} \bar{n}(z). \quad (2)$$

This formula relies on the local-density approximation in which the local chemical potential is defined as $\mu_z = \mu_0 - \frac{1}{2}m\omega_z^2 z^2$, where μ_0 is the global chemical potential of the gas.

To measure the pressure at different interaction strengths we have selected images with atom numbers in the range of $3\text{--}4 \times 10^4$ in order to avoid high optical densities during absorption imaging while keeping a good signal-to-noise ratio. A total of 50 images are used, spanning values of a/a_0 from 700 to 2150. We calibrate the relation between the integrated optical density and the pressure of the gas at weak interaction, well described by mean-field theory (inset of Fig. 2). The density profiles then generate the

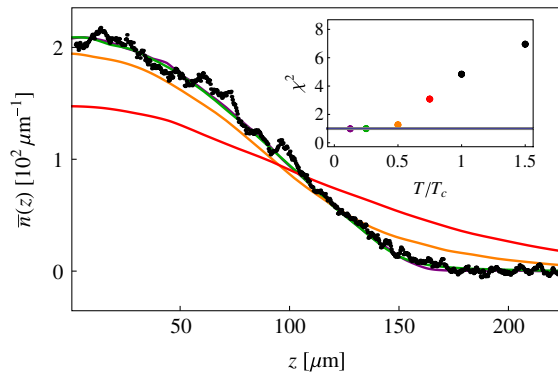


FIG. 1 (color online). Doubly integrated density profile of a trapped Bose gas at a scattering length $a/a_0 = 2150$, used to measure the LHY expansion (1). The average over 5 experimental images is shown in black points. The QMC predictions for 3.9×10^4 atoms are plotted in a solid line for $T/T_c = 0.75$ in red, 0.5 in orange, 0.25 in green, and 0.125 in purple (solid lines from bottom to top). Inset: χ^2 deviation per degree of freedom of a single experimental density profile with QMC results at different temperatures. The excellent agreement between experimental profiles and QMC validates the zero-temperature assumption for the EOS measurement.

EOS (2). The global chemical potential μ_0 remains to be determined. For this work, we infer μ_0 self-consistently in a model-independent way from the density profiles (see the Supplemental Material [19]).

In the dilute limit $na^3 \ll 1$, where the EOS is universal, dimensional analysis can be used to write the grand canonical EOS of the homogeneous Bose gas at zero temperature in the form

$$P(\mu, a) = \frac{\hbar^2}{ma^5} h(\nu), \quad (3)$$

where $\nu \equiv \mu a^3/g$ is the (grand canonical) gas parameter and $h(\nu)$ is the normalized pressure. This EOS contains all thermodynamic macroscopic properties of the system. For example, the energy can be deduced from the pressure using a Legendre transform detailed in the Supplemental Material [19], and in particular, its LHY asymptotic expansion (1). According to the above definition of h , the mean-field EOS simply reads $h(\nu) = 2\pi\nu^2$. These predictions for $h(\nu)$ are compared to the experimental data points in Fig. 2, and to our QMC calculation. We observe a clear departure of the EOS from the mean-field prediction [dashed gray line (dashed red online)]. At the largest measured value of $\nu = 2.8 \times 10^{-3}$ our data show a reduction of 20% of the pressure with respect to the mean-field result.

We observe that LHY theory accurately describes our experimental data and is hardly distinguishable from the

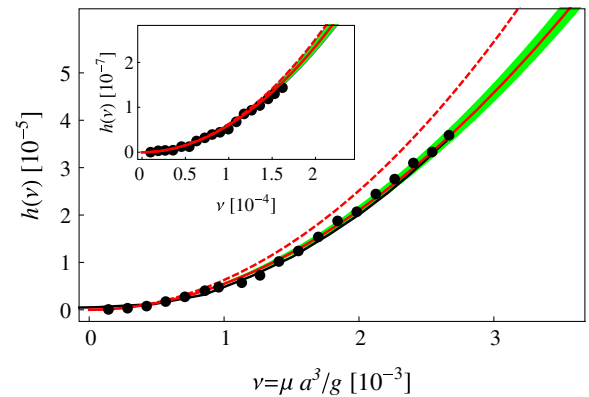


FIG. 2 (color online). Equation of state of the homogeneous Bose gas expressed as the normalized pressure h as a function of the gas parameter ν . The gas samples for the data shown in the main panel (inset) have been prepared at scattering lengths of $a/a_0 = 1450$ and 2150 ($a/a_0 = 700$). The gray (red online) solid line corresponds to the LHY prediction, and the gray (red online) dashed line to the mean-field EOS $h(\nu) = 2\pi\nu^2$. In the weakly interacting regime the data are well described by mean-field theory (inset), in opposition to stronger interactions where beyond-mean-field effects are important (main panel). The QMC EOS at $T/T_c = 0.25$ (solid black line) is nearly indistinguishable from the LHY EOS. The shaded (green online) area delimits the uncertainty of 5% on the value of a .

QMC in the studied range of interaction strength, a point already put forward in a diffusion Monte Carlo simulation at even higher values of the gas parameter [24]. We can quantify the deviation of our data from mean-field theory by fitting the measured EOS with a function that includes a correction of order $\sqrt{na^3}$. For this purpose we convert the energy $E/N = [2\pi\hbar^2/(ma^2)]na^3[1 + \alpha(na^3)^{1/2}]$ to the grand canonical EOS (see the Supplemental Material [19]) and use α as a fit parameter in the resulting pressure $P(\mu)$. The fit yields the value $\alpha = 4.5(7)$, which is in excellent agreement with the theoretical result $128/(15\sqrt{\pi}) \approx 4.81$ in Eq. (1). Together with the measurement with composite bosons of [9], this provides a striking check of the universality predicted by the expansion (1) up to order $\sqrt{na^3}$ [11].

In the above interpretation we assumed that the zero-temperature regime has effectively been reached. To check this crucial assumption, we have performed finite-temperature path-integral quantum Monte Carlo simulations [25] in the anisotropic harmonic trap geometry of the experiment with continuous space variables. The experimental atom number can be reached without difficulty and pair interactions are described by a pseudopotential. All thermodynamic properties of the gas at finite temperature are obtained to high precision and without systematic errors. As seen in Fig. 1, we find good agreement between the experimental density distributions and the QMC profiles at temperatures up to $0.25T_c$, where T_c is the condensation temperature of the ideal Bose gas. This shows that thermal effects are negligible and lead to an error in the EOS much smaller than the statistical error bars in Fig. 2.

We now assess the adiabaticity of the interaction sweep in the measurements described above. A violation of adiabaticity could lead to nonequilibrium density profiles that distort the measured EOS. We study the dynamics of the Bose gas subjected to time-dependent interaction sweeps into increasingly strongly interacting regimes, where the enhanced three-body loss rate limits the practical duration of the sweep. In Fig. 3 we plot the axial cloud size determined by a Thomas-Fermi fit as a function of the sweep duration. The magnetic field is ramped approximately linearly in time, sweeping a/a_0 from an initial value of 200 to different final values. Besides the experimental data we present theoretical results from a mean-field scaling solution [26,27] and from a solution of the hydrodynamic equations incorporating the LHY EOS based on a variational scaling ansatz [28]. The latter shows a remarkable agreement with our experimental data for $a \leq 3000a_0$. For scattering lengths $a/a_0 \leq 840$ the radius is nearly constant for sweep durations $\tau\omega_z/(2\pi) > 1.5$ ($\tau > 80$ ms), indicating that the cloud follows the interaction strength adiabatically. For the largest value used in the EOS study ($a/a_0 = 2150$), the atom loss is less than 4% and the cloud size after the $\tau = 150$ ms sweep [$\tau\omega_z/(2\pi) \approx 2.8$] is 2.5%

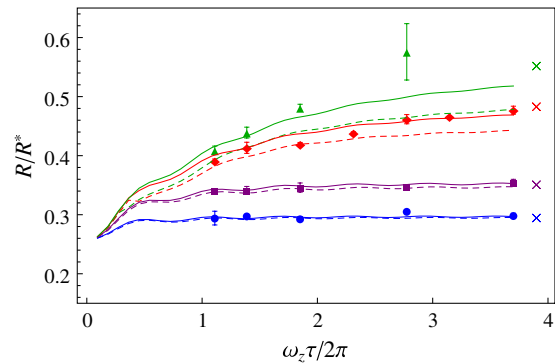


FIG. 3 (color online). Radius R of the Bose gas as a function of the duration τ of the interaction sweep. The radius R is normalized to the radius $R^* = a_{\text{ho}}(15\lambda^2 N)^{1/5}$ [where $a_{\text{ho}} = (\hbar/m\omega_z)^{1/2}$ and $\lambda = \omega_r/\omega_z$]. N is the measured atom number at the end of each sweep. The final values of a/a_0 are 380 (blue dots), 840 (purple squares), 2940 (red diamonds), and 4580 (green triangles). The solid (dashed) lines show the solution of a variational hydrodynamic approach (mean-field scaling solutions). The crosses show the predicted equilibrium beyond-mean-field radii.

smaller than the equilibrium value. We have corrected for this systematic effect by rescaling the measured density n_0 for the determination of the EOS, $\bar{n} = \eta^{-1}\bar{n}_0(\eta z)$ (with $\eta = 0.975$ for $a/a_0 = 2150$).

The properties of the Bose gas for very large values of na^3 constitute a challenging open problem. Because of the

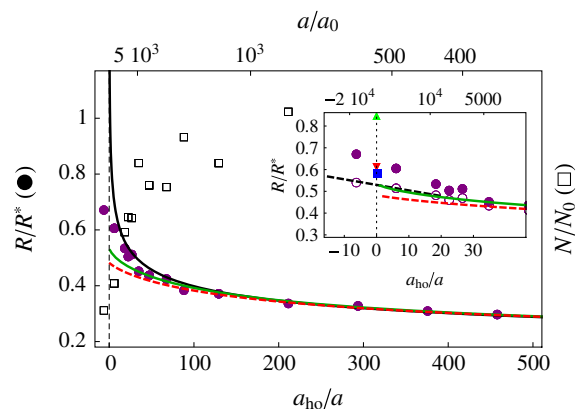


FIG. 4 (color online). Normalized cloud radius R_{TF}/R^* (filled purple circles) and normalized atom number (open black squares) as a function of the inverse scattering length a_{ho}/a at the end of a 75-ms magnetic-field sweep. The static mean-field prediction is plotted in a solid black line, the mean-field scaling solution in a dashed red line, and the beyond mean-field scaling ansatz in a solid gray line (green online). Inset: Zoom around the unitary limit. Predictions for the universal constant ξ are shown in an up triangle [34], down triangle [33], and square [32]. The filled (empty) circles correspond to the radii normalized to the final (initial) atom number (see [31]). The dashed black line is the linear interpolation at unitarity.

experimental limitation imposed by three-body recombination, we access this region with a shorter sweep of duration $\tau\omega_z/(2\pi) = 1.35$ ($\tau \approx 75$ ms). In Fig. 4 we plot the normalized radius of the Bose gas as a function of the inverse scattering length a_{ho}/a . Deep in the mean-field regime ($a \lesssim 800a_0$) the ramp is adiabatic as the data match the equilibrium Thomas-Fermi prediction. As the scattering length is increased, both nonadiabaticity and beyond mean-field effects become important. A departure from the equilibrium result becomes evident above a scattering length of $\approx 2000a_0$. Taking into account the mean-field dynamics gives an improved description of our data (red dashed line). Even better agreement (up to values of $a/a_0 \approx 5000$) is obtained with the variational approach incorporating the LHY correction as presented above [gray solid line (green online)] [28]. Probing larger values of the scattering length enables us to gain further insight into the unitary Bose gas, $a = \infty$. Because of the low densities of our samples, only half of the atoms are lost at the end of the sweep to the resonance (see squares in Fig. 4). Universal thermodynamics at unitarity have been conjectured for quantum gases [29] and successfully checked experimentally for Fermi gases [30]. In the case of bosonic atoms the existence of a many-body universal state at unitarity is still unknown. Under the assumption of universality, the only relevant length scale should be the interparticle spacing $n^{-1/3}$ and the EOS would take the form $\mu \propto \frac{\hbar^2}{m} n^{2/3}$. Up to a numerical factor, this EOS is identical to that of an ideal Fermi gas and we can write $\mu = \xi E_F$ [where $E_F = \hbar^2/2m(6\pi^2 n)^{2/3}$]. As we increase the scattering length towards the unitarity regime, the cloud is expected to grow in size. Because of the finite response time of the gas, it is reasonable to assume that the measured radius R is smaller than the equilibrium radius. From this inequality, in the spirit of variational methods, we deduce a lower bound for the value of ξ by interpolating our data at unitarity [black dashed line in the inset of Fig. 4]: $\xi > 0.44(8)$ [31]. This bound is satisfied for the predictions $\xi = 0.66$ [32] and for the upper bounds from variational calculations, 0.80 [33] and 2.93 [34].

Future work could focus on the measurement of the condensate fraction since the quantum depletion is expected to be as large as $\sim 8\%$ for our most strongly interacting samples in equilibrium, and on finite-temperature thermodynamic properties [35]. Our measurements on resonance as well as future theoretical studies should give crucial insights on the unitary Bose gas.

We are grateful to Y. Castin, F. Werner, X. Leyronas, S. Stringari, S. Giorgini, S. Pilati, and A. Grier for discussions and to C. Lancien, I. Lahlou, S. El-Ghazzal, T. Vu, and L. Bernard for experimental assistance. We thank J. Dalibard and S. Nascimbène for useful comments on the manuscript. We acknowledge support from ESF Euroquam (FerMix), ANR FABIOLA, Région Ile de France (IFRAF), ERC, and Institut Universitaire de France.

*navon@ens.fr

†swann.piatecki@ens.fr

- [1] T. D. Lee, Kerson Huang, and C. N. Yang, *Phys. Rev.* **106**, 1135 (1957).
- [2] K. Brueckner and K. Sawada, *Phys. Rev.* **106**, 1117 (1957).
- [3] S. Beliaev, *JETP* **7**, 289 (1958).
- [4] E. Lieb, *Phys. Rev.* **130**, 2518 (1963).
- [5] S. Inouye *et al.*, *Nature (London)* **392**, 151 (1998).
- [6] J. Roberts *et al.*, *Phys. Rev. Lett.* **85**, 728 (2000).
- [7] A. Altmeyer *et al.*, *Phys. Rev. Lett.* **98**, 40401 (2007).
- [8] Y. Shin *et al.*, *Phys. Rev. Lett.* **101**, 070404 (2008).
- [9] N. Navon *et al.*, *Science* **328**, 729 (2010).
- [10] G. Astrakharchik *et al.*, *Phys. Rev. Lett.* **93**, 200404 (2004).
- [11] X. Leyronas and R. Combescot, *Phys. Rev. Lett.* **99**, 170402 (2007).
- [12] H. Hu *et al.*, *Europhys. Lett.* **74**, 574 (2006).
- [13] P. Fedichev *et al.*, *Phys. Rev. Lett.* **77**, 2921 (1996).
- [14] S. Papp *et al.*, *Phys. Rev. Lett.* **101**, 135301 (2008).
- [15] S. Pollack *et al.*, *Phys. Rev. Lett.* **102**, 90402 (2009).
- [16] S. Nascimbene *et al.*, *Phys. Rev. Lett.* **103**, 170402 (2009).
- [17] N. Gross *et al.*, *Phys. Rev. Lett.* **105**, 103203 (2010).
- [18] J. Zirbel *et al.*, *Phys. Rev. A* **78**, 13416 (2008).
- [19] See Supplemental Material at <http://link.aps.org/supplemental/10.1103/PhysRevLett.107.135301> for technical details about the density profiles analysis and Feshbach resonance calibration.
- [20] C. H. Cheng and S. K. Yip, *Phys. Rev. B* **75**, 14526 (2007).
- [21] Y. I. Shin, *Phys. Rev. A* **77**, 41603 (2008).
- [22] T. Ho and Q. Zhou, *Nature Phys.* **6**, 131 (2009).
- [23] S. Nascimbene *et al.*, *Nature (London)* **463**, 1057 (2010).
- [24] S. Giorgini, J. Boronat, and J. Casulleras, *Phys. Rev. A* **60**, 5129 (1999).
- [25] W. Krauth, *Phys. Rev. Lett.* **77**, 3695 (1996).
- [26] Y. Castin and R. Dum, *Phys. Rev. Lett.* **77**, 5315 (1996).
- [27] Y. Kagan, E. L. Surkov, and G. V. Shlyapnikov, *Phys. Rev. Lett.* **79**, 2604 (1997).
- [28] The details of the time-dependent analysis will be published elsewhere.
- [29] T. L. Ho, *Phys. Rev. Lett.* **92**, 90402 (2004).
- [30] M. Inguscio, W. Ketterle, and C. Salomon, *Proceedings of the International School of Physics Enrico Fermi, Course CLXIV* (IOS Press, Amsterdam, 2006).
- [31] At unitarity, the cloud radius R would scale as $N^{1/6}\xi^{1/4}$. The normalization R^* used in Fig. 4 scales as $N^{1/5}$ so that $R/R^* \propto \xi^{1/4}N^{-1/30}$ very slowly depends on the atom number. In order to take into account the changing atom number near unitarity and obtain a safe experimental lower bound on $\xi \propto (R/R^*)^4 N^{2/15}$, we minimize both R/R^* and $N^{2/15}$. This is done by taking for R/R^* the initial atom number (empty circles in the inset of Fig. 4), and the final, for $N^{2/15}$.
- [32] Y.-L. Lee and Y.-W. Lee, *Phys. Rev. A* **81**, 063613 (2010).
- [33] J. L. Song and F. Zhou, *Phys. Rev. Lett.* **103**, 25302 (2009).
- [34] S. Cowell *et al.*, *Phys. Rev. Lett.* **88**, 210403 (2002).
- [35] R. Smith, R. Campbell, N. Tammuz, and Z. Hadzibabic, *Phys. Rev. Lett.* **106**, 250403 (2011).

Condensation energy of a spin-1/2 strongly interacting Fermi gas

N. Navon, S. Nascimbène, X. Leyronas, F. Chevy, and C. Salomon

Physical Review A **88**, 063614 (2013)

Condensation energy of a spin-1/2 strongly interacting Fermi gas

N. Navon,^{1,*} S. Nascimbène,¹ X. Leyronas,^{2,†} F. Chevy,¹ and C. Salomon¹

¹Laboratoire Kastler Brossel, CNRS, UPMC, Ecole Normale Supérieure, 24 rue Lhomond, 75231 Paris, France

²Laboratoire de Physique Statistique, Ecole Normale Supérieure, UPMC Université Paris 06, Université Paris Diderot, CNRS, 24 rue Lhomond, 75005 Paris, France

(Received 4 April 2013; revised manuscript received 15 October 2013; published 6 December 2013)

We report a measurement of the condensation energy of a two-component Fermi gas with tunable interactions. From the equation of state of the gas, we infer the properties of the normal phase in the zero-temperature limit. By comparing the pressure of the normal phase at $T = 0$ to that of the low-temperature superfluid phase, we deduce the *condensation energy*, i.e., the energy gain of the system upon being in the superfluid rather than the normal state. We compare our measurements to a ladder approximation description of the normal phase and to a fixed-node Monte Carlo approach, finding excellent agreement. We discuss the relationship between condensation energy and pairing gap in the BEC-BCS crossover.

DOI: [10.1103/PhysRevA.88.063614](https://doi.org/10.1103/PhysRevA.88.063614)

PACS number(s): 03.75.Ss, 05.30.Fk, 34.50.-s

I. INTRODUCTION

From a thermodynamic point of view, a superconducting state is favored compared to a normal state when the free energy of the former (E_S) is lower than that of the latter (E_N). This energy difference, called the *condensation energy*, is a central concept in the BCS theory of conventional superconductivity. For example, in the weakly interacting regime the condensation energy is related to the superfluid pairing gap Δ by

$$E_c = E_N - E_S = N_f \frac{\Delta^2}{2}, \quad (1)$$

where N_f is the density of states at the Fermi energy [1]. For superconductors, the condensation energy is obtained from the measurement of the critical magnetic field H_c at which superconductivity is quenched,

$$E_c = \mu_0 \frac{H_c^2}{2}, \quad (2)$$

where μ_0 is the vacuum magnetic permeability [1]. While BCS theory [and relation (1)] have proven very successful to explain conventional superconductivity, a similar description to explain exotic forms of superconductivity, such as encountered in cuprate or iron-compound materials, is still lacking. In particular, the role of the condensation energy in high- T_c superconductors is thought to give insight into the mechanism that could be responsible for driving the superconducting transition (see, e.g., [2–5], and references therein), though its extraction from experimental data or even its relevance is still a hotly debated issue [6–8].

Ultracold atoms are now increasingly used as test beds to experimentally explore quantum many-body physics, owing to their high degree of control [9]. It has become possible to simulate Hamiltonians from various fields of physics, such as neutron matter or condensed matter physics in simple systems.

Moreover, interactions between ultracold atoms, characterized by the s -wave scattering length a , can be tuned via magnetic Feshbach resonances, giving access to the regime of strong interactions.

In this article, we investigate the condensation energy of a dilute spin-1/2 strongly interacting Fermi gas with a variable interaction strength. We show that the condensation energy can be measured by applying a chemical potential imbalance between the two spin states which is the analog of a magnetic field in superconductors. In contrast to superconductors, we explore a regime where the effective Zeeman energy is of the order of the Fermi energy. We compare our experimental results to a diagrammatic theory, finding excellent agreement.

II. NORMAL-STATE PRESSURE

The experimental setup was presented in [13]. Our system is a quantum gas of ^6Li prepared in a mixture of its two lowest energy spin states.

The gas is loaded into a single-beam dipole trap, providing a radial (strong) confinement, while the axial (weak) confinement (z axis) is provided by magnetic coils. This results in a cigar-shaped trap. The interactions are tuned using a pair of coils in the Helmholtz configuration in order to create a large homogeneous bias field to tune the scattering length a via the 832.18-G Feshbach resonance [10]. The mixture is cooled to quantum degeneracy by lowering the trap depth, and absorption images perpendicular to the weak direction are recorded to obtain the *in situ* density distributions along the z axis. Previous theoretical [11,12] and experimental [13,14] studies have demonstrated that the density profiles of a trapped spin-imbalanced Fermi gas can be used to extract the equation of state (EoS) of the corresponding homogeneous system via the pressure formula, $P(\mu_1, \mu_2, T) = \frac{m\omega_r^2}{2\pi} [\bar{n}_1(z) + \bar{n}_2(z)]$, where ω_r is the radial trapping frequency, and $\bar{n}_i(z) = \int d^2r n_i(r, z)$ is the doubly integrated density distribution of spin species i ($i = 1, 2$).

At unitarity, where the scattering length a diverges, we previously measured the pressure of the spin-balanced gas as a function of the reduced temperature $t = k_B T / \mu$ (where $2\mu = \mu_1 + \mu_2$) [13], as well as the pressure of the spin-imbalanced

*Present address: Cavendish Laboratory, University of Cambridge, J. J. Thomson Avenue, Cambridge CB3 0HE, United Kingdom; nn270@cam.ac.uk

[†]leyronas@lps.ens.fr

gas at $t \approx 0$ as a function of the spin-polarizing field $b = \frac{\mu_1 - \mu_2}{\mu_1 + \mu_2}$. We suggested that the low-temperature properties of the normal phase of the Fermi gas were consistent with a Fermi-liquid behavior [19]. As a result, the low-temperature and low-imbalance limit of the pressure of the unitary gas can be written as

$$h(t, b) = \frac{P(\mu_1, \mu_2, T)}{2P_0(\bar{\mu})} \simeq \xi_N^{-3/2} + \frac{\tilde{\chi} b^2}{2} + \frac{\tilde{c}_V t^2}{2}, \quad (3)$$

where $P_0(\mu) = \frac{1}{15\pi^2} (\frac{2m}{\hbar^2})^{3/2} \mu^{5/2}$ is the ideal Fermi-gas pressure. The response coefficient to temperature t is the dimensionless specific heat \tilde{c}_V , while the response to the polarizing field b is the dimensionless magnetic susceptibility $\tilde{\chi}$ (equal to $5\pi^2/8$ and $15/4$, respectively, for the ideal Fermi gas). The magnetic susceptibility has been the subject of a previous work [18], and we focus here on the measurement of the pressure of the normal phase $\xi_N^{-3/2}$ in the $t = 0$ and $b = 0$ limits. In the (t, b) plane, our measurements of the EoS of the unitary gas have been performed along two directions: the unpolarized gas as a function of temperature $h(t, b = 0)$ (Fig. 1) and the low-temperature polarized gas versus the chemical potential imbalance $h(t = 0, b)$ [Fig. 2(a)]. The quadratic behavior of the pressure versus both b and t supports the Fermi-liquid interpretation of the low-temperature thermodynamic properties of the normal phase. However, the

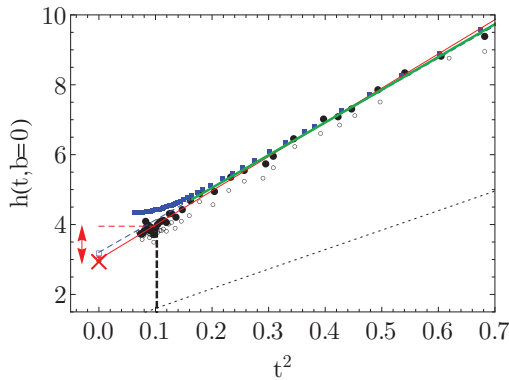


FIG. 1. (Color online) Reduced pressure $h(t, b) = P(\mu_1, \mu_2, T)/2P_0(\bar{\mu})$ of the spin-1/2 unitary Fermi gas, where P_0 is the $T = 0$ Fermi pressure of an ideal gas, t the reduced temperature $k_B T/\mu$, and $b = 0$ the unpolarized gas. Open black circles are data from [13] taken at $B = 834$ G, while filled black circles include a small correction due to a recently determined downshift of the Feshbach resonance [10]. This correction is estimated using Tan's contact calculated by the bold diagrammatic Monte Carlo (bDMC [16]) (see Appendix B for details). The Fermi-liquid fit is shown as the solid red line, and the extrapolated zero-temperature pressure of the normal state $\xi_N^{-3/2}$ is represented by the (red) X. MIT data from [15] are represented by (blue) squares; the corresponding fit, by the dashed (blue) line; and the extrapolation at $t = 0$, by the open (blue) square. The bDMC calculation [16] is shown by the solid green line. The agreement with the bDMC data is excellent, while a small discrepancy from the MIT data is visible near the superfluid-to-normal transition around $t_c = 0.40$ [15] or $t_c = 0.33$ here [17] (the latter represented by the dashed vertical line). The dashed horizontal (red) line corresponds to the superfluid pressure; the dotted black line, to the ideal gas.

system will ultimately undergo a second-order phase transition to a superfluid state, and below the temperature $t_c \sim 0.33$, the pressure of the spin-balanced gas deviates from the t^2 behavior. In contrast, at $t = 0$, the spin-imbalanced gas ($\mu_1 \neq \mu_2$) undergoes a first-order phase transition to an unpolarized superfluid phase when $h_S(0, 0) = h_N(0, 0) + \tilde{\chi} b^2/2$. This condition is the analog of Eq. (2), and at unitarity it yields the critical chemical potential imbalance $b_c \approx \sqrt{0.8}$ [see Fig. 2(a)]. This is demonstrated by the discontinuity in the slope of h vs b^2 . From Eq. (3), and extrapolating the Fermi-liquid behavior to the zero-temperature and spin-balanced limits, we measure the $T = 0$ dimensionless pressure of the spin-balanced unitary gas in the normal phase $\xi_N^{-3/2}$. In the first limit ($t \rightarrow 0, b = 0$) we find $\xi_N = 0.48(2)$, while in the second one ($t = 0, b \rightarrow 0$), we extract $\xi_N = 0.53(2)$ [see (red) X's in Figs. 1 and 2(a)]. The proximity of these values, taken for two very different limiting regimes, is remarkable and further supports the accurate

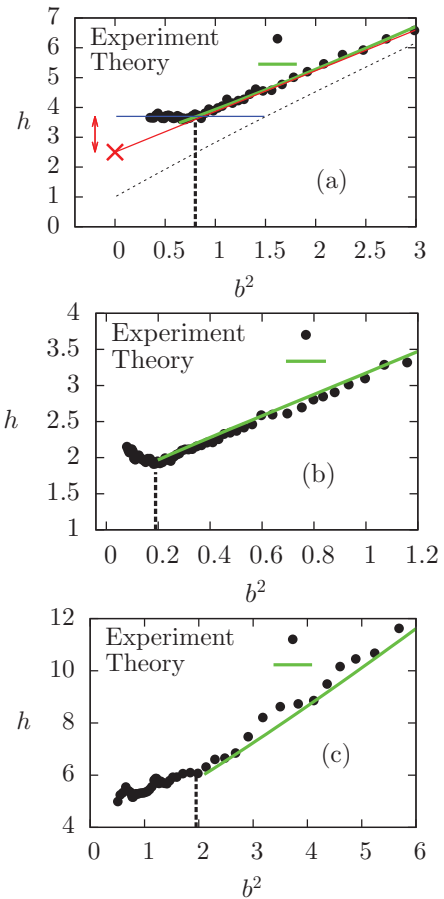


FIG. 2. (Color online) Pressure of the spin-imbalanced gas in the BEC-BCS crossover at $t = 0$. The position of the first-order phase transition to the superfluid is shown by the vertical dashed black line. (a) Unitary limit. The Fermi-liquid fit is shown by the solid red line; the $t = 0$ equation of state in the superfluid phase, by the solid horizontal blue line. The pressure of the noninteracting gas is displayed as the dotted gray line. The $t = 0$ and $b = 0$ extrapolation of the normal phase pressure is shown by the (red) X; the condensation pressure, by the double-headers. (a-c) Results of the ladder approximation for the normal phase are shown in green for $\delta = 0, -0.58$, and $+0.2$, respectively.

description of the normal phase of the unitary gas as a Fermi liquid. This value is in good agreement with the experimental value, 0.46(1) [15], and close to the values calculated using Monte Carlo methods: 0.54 [19], 0.56, [20], and 0.52 [21].

III. COMPARISON TO THE LADDER APPROXIMATION THEORY

The problem of the zero-temperature balanced superfluid Fermi gas has been the subject of thorough theoretical investigations [22]. However, much less work has been devoted to the EoS of the zero-temperature normal phase [20]. We show below that our experimental results can be quantitatively reproduced using the ladder approximation [23,24]. This theory includes the repeated two-body scattering between particle 1 and particle 2 described by the scattering length a . In particular, for $a^{-1} > 0$, it contains the physics of a molecular state. We use the finite-temperature formalism and take the zero-temperature limit. The self-energy for particles 2, which physically describes the effect of interaction between particles, is given by (we take $\hbar = 1$)

$$\Sigma_2(k, i\omega) = \int \frac{d^3\mathbf{K}}{(2\pi)^3} \int_{i\mathbb{R}} \frac{d\Omega}{2\pi i} \frac{\Gamma(K, \Omega)}{\left[\Omega - i\omega + \mu_1 - \frac{(\mathbf{K}-\mathbf{k})^2}{2m}\right]}, \quad (4)$$

where the two-particle vertex Γ is given by

$$\Gamma(K, \Omega)^{-1} = \frac{m}{4\pi a} + \Pi(K, \Omega), \quad (5)$$

where $\Pi(K, \Omega)$ is the pair bubble [24]. At zero temperature, $\Pi(K, \Omega)$ can be calculated analytically. The pairing instability, signaling a second-order phase transition, is found using the Thouless criterion $\Gamma^{-1}(0,0) = 0$. For given μ_1 and a , this happens for a critical value of the chemical potential μ_{2c} of particles 2. In order to stay in the normal phase, we have performed our calculations for $\mu_2 < \mu_{2c}$. The integration on Ω can be performed by deforming the integration contour in the half-plane $\text{Re}(\Omega) < 0$. In this way, we pick the singularities of the integrand in Eq. (4) and get three contributions corresponding to the pole of $(\Omega - i\omega + \mu_1 - \frac{(\mathbf{K}-\mathbf{k})^2}{2m})^{-1}$ (Σ_L), the branch cut of $\Gamma(K, \Omega)$ (Σ_Γ), and the molecular pole $\Omega_0(K)$ (for $a^{-1} > 0$) of $\Gamma(K, \Omega)$ (Σ_m) [24]. $\Omega_0(K) + 2\mu$ represents physically the energy of a molecule of momentum \mathbf{K} . We find that in the normal phase $\Omega_0(K) > 0$. As a consequence, when we deform the integration contour in $\text{Re}(\Omega) < 0$, we do not get any contribution from the molecular pole of Γ , and therefore we have $\Sigma_m = 0$. This is consistent with the physical argument in favor of the absence of molecules in the normal phase. Indeed, if we had some molecules in the system, they would be condensed at zero temperature. Therefore the system would be superfluid, and we would no longer be entitled to use Eq. (4). We deduce the minority density n_2 using the Fermi-liquid-type relation due to Landau,

$$\mu_2 = \frac{k_{F,2}^2}{2m} + \Sigma_2(k_{F,2}, 0), \quad (6)$$

where, by definition, $k_{F,2} \equiv (6\pi^2 n_2)^{1/3}$, is the Fermi wave vector of particles of type 2. For given μ_1, μ_2 , and a , this is an implicit equation for $k_{F,2}$ and, hence, n_2 . Another approach to calculation of the minority density relies on the interpretation

of the momentum distribution obtained from the self-energy, Eq. (4). These two methods give very similar results (see Appendix A for details). As found in [25], we find a no zero density n_2 for a chemical potential μ_2 larger than the polaron [25,26] chemical potential $\mu_p(\mu_1)$. In practice, we fix $\mu_1 > 0$, then solve Eq. (6) for a given $\mu_2 \geq \mu_p(\mu_1)$. The pressure is determined by integrating the density using the Gibbs-Duhem relation,

$$P(\mu_1, \mu_2) = P_0(\mu_1) + \int_{\mu_p}^{\mu_2} d\mu'_2 \frac{1}{6\pi^2} [k_{F,2}(\mu_1, \mu'_2)]^3. \quad (7)$$

For a fixed μ_1 , we calculate the minority density for increasing minority chemical potential between $\mu_p(\mu_1)$ and μ_2 . For a sufficiently large chemical potential difference, the system is normal (the pairing susceptibility does not diverge). For sufficiently low b , we calculate the dimensionless EoS $h(\delta, b)$, where δ is the grand-canonical interaction strength, $\delta = \hbar/\sqrt{2m\mu}a$. For all values of $\delta \leq 0$, we find a linear behavior of h as a function of b^2 . The comparison between experiment and theory is shown for $\delta = 0$ (unitary limit), $\delta = -0.58$ (BCS side of the crossover), and $\delta = 0.2$ (BEC side) in Figs. 2(a), 2(b), and 2(c), respectively. The agreement is very good. However, for increasing $a^{-1} > 0$, the values of b in the normal phase become larger and larger, and as a consequence, the linear fit of h as a function of b^2 , valid at low b , is worse. Still, for $\delta = 0.2$ the experimental EoS $h(\delta, b)$ is in good agreement with the ladder approximation calculation above b_c [diagonal (green) line in Fig. 2(c)]. Within the ladder approximation we have determined the critical spin polarizing field b_c at which a pole appears in the vertex function Γ at zero frequency and zero wave vector (Thouless criterion). We found that b_c was always *smaller* than the experimental value of the first-order transition. Our calculation is therefore free of any instability singularity in the normal phase. For the spin susceptibility, we also find a good agreement among the ladder approximation, experiments, and Monte Carlo simulations of [18].

Gathering the results from Fig. 2, we now extract the zero-temperature dimensionless pressure h_N of the normal phase as a function of δ [18]. The resulting EoS of the normal phase $h_N(\delta)$ is plotted in Fig. 3 as open (red) squares together with the ladder approximation calculation [thick lower solid (green) line], showing excellent agreement in the explored crossover. For comparison, the previously measured EoS of the low-temperature gas in the superfluid phase $h_S(\delta)$ is shown as the blue points and upper solid (blue) line fit [14]. The difference between the superfluid and the normal pressure at $T = 0$ thus represents the *condensation pressure*. The superfluid pressure is higher than the normal phase pressure, $h_S(\delta) > h_N(\delta)$, hence the grand potential is lower and the superfluid state is the stable phase at low temperature. Turning to the canonical ensemble the superfluid and normal phase energies ξ_S and ξ_N as a function of the canonical interaction strength $1/k_F a$ can be computed from the pressure measurement in Fig. 3 using a Legendre transform [27]. The measured condensation energy $\xi_N - \xi_S$ is shown as the solid black line in Fig. 4.

IV. COMPARISON TO THE BCS RESULT

In the BCS regime, the condensation energy E_c can be explicitly calculated from the energy of the superconducting and normal states, yielding the well-known result $E_c = \frac{3}{8} N \frac{\Delta^2}{E_F}$,

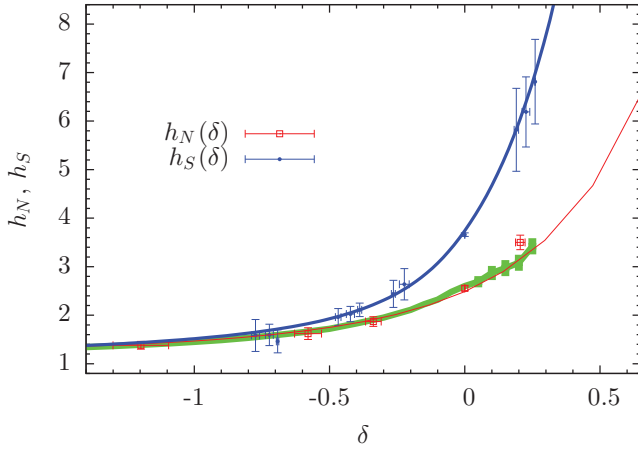


FIG. 3. (Color online) Pressure of the normal h_N [open (red) squares] and superfluid h_S [filled (blue) circles] phases at low temperature in the BEC-BCS crossover measured in [14]. The thick lower solid (green) line is the result of the ladder approximation. The upper solid (blue) line is a guide for the eye, while the lower solid (red) line is the result of fixed-node Monte Carlo calculations [18]. The difference between the blue and the red or green lines is the condensation pressure.

where Δ is the single-particle excitation gap, and E_F the Fermi energy. Since $E = \frac{3}{5}NE_F\xi_\alpha(1/k_Fa)$ (where $\alpha = S, N$), the BCS equation becomes

$$\xi_N - \xi_S = \frac{5}{8} \left(\frac{\Delta}{E_F} \right)^2. \quad (8)$$

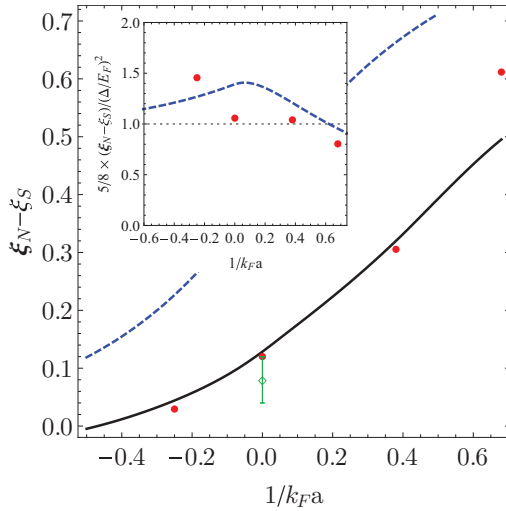


FIG. 4. (Color online) Relation between the condensation energy and the superfluid pairing gap. Dimensionless condensation energy $\xi_N - \xi_S$ versus interaction strength $1/k_Fa$ extracted from the $b \rightarrow 0$ extrapolation (solid black line). Filled (red) circles represent the BCS expression, (8), using the values of Δ measured in [28]. The prediction from mean-field BCS theory is shown by the dashed (blue) line, and the open (green) circle with a vertical bar is the $t \rightarrow 0$ extrapolation of Fig. 1. A fixed-node Monte Carlo calculation [18] coincides with the solid black line. Inset: Rratio of the condensation energy $\xi_N - \xi_S$ to $\frac{5}{8}(\frac{\Delta}{E_F})^2$.

Strictly speaking, this formula is valid only in the weakly attractive limit $\Delta \rightarrow 0$. For an arbitrary interaction, the condensation energy is given by a more involved function of the gap, and based on dimensional arguments, it should be written as

$$\xi_N - \xi_S = \frac{5}{8} \left(\frac{\Delta}{E_F} \right)^2 F(\Delta/E_F), \quad (9)$$

where F is a (yet) unknown function with $F(0) = 1$ to satisfy the BCS prediction. In the spirit of Landau's theory, the $U(1)$ invariance suggests that F can be expanded with $(\Delta/E_F)^2$ instead of k_Fa , and as such, the first beyond-BCS correction should be proportional to $|\Delta/E_F|^2$. At unitarity, where $\Delta \simeq 0.5E_F$ [19], this leads to a moderate 25% correction to the BCS prediction, which suggests that the range of validity of Eq. (8) should extend beyond the strict weakly interacting limit [21].

In order to test the BCS expression, (8), in the BEC-BCS crossover, we compare our measurement of the condensation energy to $\frac{5}{8}(\frac{\Delta}{E_F})^2$ using the values of Δ measured by radio-frequency spectroscopy in [28] [filled (red) circles in Fig. 4]. The agreement shown in Fig. 4 indicates that, even in the strongly interacting regime, the BCS expression is remarkably valid. A more stringent test is provided by plotting the ratio between the left-hand and the right-hand sides of Eq. (8) (inset in Fig. 4), and we indeed find a ratio close to unity. Note that calculating this ratio using BCS mean-field theory provides a reasonable estimate [dashed (blue) line in Fig. 4 inset], even though the absolute values of the condensation energy [dashed (blue) line in Fig. 4] or of the pairing gap are both quantitatively inaccurate in the strongly interacting regime.

V. CONCLUSION

In summary, we have measured the condensation energy of a two-component Fermi gas with tunable interactions. The temperature and spin-polarizing field dependence of the normal phase pressure are in good agreement with a Fermi-liquid description. A simple ladder approximation calculation quantitatively reproduces experimental data at zero temperature in the normal phase. Future work will explore the critical region and search for exotic phases such as the FFLO phase [22].

ACKNOWLEDGMENTS

We thank M. Ku and M. Zwierlein for providing their experimental data and F. Werner for the bold diagrammatic Monte Carlo calculations. We acknowledge support from Institut de France (Louis D.), Région Ile de France (IFRAF-C'nano), ERC Ferlodim, and Institut Universitaire de France.

APPENDIX A: CALCULATION OF THE MINORITY DENSITY

Another way to calculate the minority density n_2 is to integrate on the frequency and wave vector the one-particle Green's function,

$$n_{\mathbf{k},2} = \int_{i\mathbb{R}} \frac{d\omega}{2\pi i} e^{\omega\delta} \frac{1}{\left[\omega + \mu_2 - \frac{k^2}{2m} - \Sigma_2(k, \omega) \right]}, \quad (A1)$$

$$n_2 = \frac{1}{2\pi^2} \int_0^{+\infty} k^2 dk n_{\mathbf{k},2}, \quad (\text{A2})$$

where $n_{\mathbf{k},2}$ is the occupation number of minority fermions at wave vector \mathbf{k} , $\delta \rightarrow 0^+$, and we have used the isotropy of $n_{\mathbf{k},2}$. In practice, in order to have a more rapidly converging integral, we add and subtract the free particle Green's function, and we calculate analytically the free particle occupation number. This method is of course much more lengthy than the Landau method, since one has to perform two additional integrations. In the case of a negative chemical potential of the minority particles $\mu_2 < 0$, we find that the Green's function has, for $\text{Re}(\omega) < 0$, a single quasiparticle pole at an energy $E_k < 0$ with a residue Z_k . Therefore we find $n_{\mathbf{k},2} = Z_k$ for $E_k < 0$ or, equivalently, $k < k_{F,2}$ and $n_{\mathbf{k},2} = 0$ for $k > k_{F,2}$. This transforms the integration on frequency into finding a root E_k and computing $Z_k = [1 - \partial \Sigma_2(k, \omega = E_k) / \partial \omega]^{-1}$, which is easier numerically.

Furthermore, we find that for $\mu_2 < 0$, $\Sigma_2(k, \omega; \mu_1, \mu_2, a^{-1}) = F(k, \omega + \mu_2; \mu_1, a^{-1})$. This can be shown by studying the location of the singularities of $\Gamma(K, \Omega)$ in the complex Ω plane and by deforming the integration contour in Eq.(4). As a consequence, the residue Z_k does not depend on μ_2 . This simplifies the calculation of the pressure in Eq. (7). Indeed we find

$$\begin{aligned} P(\mu_1, \mu_2; a^{-1}) - P_0(\mu_1) &= \int_{\mu_P}^{\mu_2} d\mu'_2 n_2(\mu_1, \mu'_2; a^{-1}) \\ &= \int_{\mu_P}^{\mu_2} d\mu'_2 \int_0^{k_{F,2}(\mu'_2)} \frac{dk}{2\pi^2} k^2 Z_k \\ &= \int_0^{k_{F,2}(\mu_2)} \frac{dk}{2\pi^2} k^2 Z_k (\mu_2 - \mu_F(k)), \end{aligned}$$

where we have permuted the integration order between the second and the third lines. We have defined $\mu_F(k)$ such that $\mu_F(k) = k^2/(2m) + \Sigma_2(k, \omega = 0; \mu_1, \mu_2 = \mu_F(k))$ (μ_F is basically the inverse function of $k_{F,2}$). We are left with a single integral and numerical calculation of μ_F and Z_k . The quantities μ_P (polaron chemical potential), $n_2(\mu'_2)$ (minority density), $k_{F,2}(\mu'_2)$ (minority Fermi wave vector), and Z_k (quasiparticle residue) depend on the majority chemical potential μ_1 and the inverse scattering length a^{-1} .

For the unitary limit, we show in Fig. 5 the results for the reduced EoS $h(b)$ using the two methods [Landau and Eqs. (A1) and (A2)]. We see that the difference between the two methods is small. Due to its simplicity, we therefore use the Landau method.

APPENDIX B: SCATTERING LENGTH CORRECTION OF THE EQUATION OF STATE

While the original data were taken at a magnetic field of 834 G, corresponding to a previous determination of the position of the wide Feshbach resonance between the two lowest energy states of ^6Li [29], a more refined measurement involving radio-frequency spectroscopy of a few molecules led to a small downshift of the resonance position, to $B_0 = 832.18(8)$ [10]. The influence of this scattering length change on the thermodynamics can be estimated using the Tan contact \mathcal{I} , since it verifies the following relation (the so-called

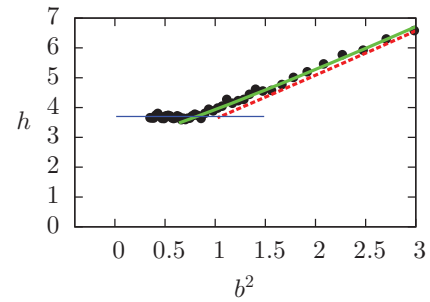


FIG. 5. (Color online) Dimensionless pressure of the spin-imbalanced gas in the unitary limit ($\delta = 0$). Experimental results are shown as filled black circles. The theory using Eq. (6) (Landau's method) is shown by the thick solid (green) line, while the result of Eqs. (A1) and (A2) is shown as the dashed (red) line. The horizontal (blue) line shows the value of the dimensionless pressure in the superfluid state.

adiabatic sweep theorem):

$$\frac{dE}{d(-1/a)} = \frac{\hbar^2}{4\pi m} \mathcal{I}. \quad (\text{B1})$$

The contact can be expressed in the grand-canonical ensemble using the relation

$$\left(\frac{\partial E}{\partial(-1/a)} \right)_{S,V,N} = \left(\frac{\partial \Omega}{\partial(-1/a)} \right)_{T,V,\mu}, \quad (\text{B2})$$

where $\Omega = -PV$ is the grand potential. Using the contact density $C = \mathcal{I}/V$, we can write to lowest order in a^{-1} ,

$$P(\mu, T, a^{-1}) = P(\mu, T, 0) + a^{-1} \frac{\hbar^2}{4\pi m} C(\mu, T, 0), \quad (\text{B3})$$

where the contact density at unitarity is a function of $\beta\mu$ only. We can thus write the finite a correction to the dimensionless

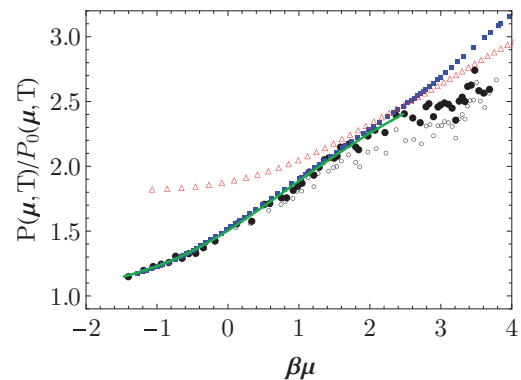


FIG. 6. (Color online) Pressure of the unpolarized unitary Fermi gas. The original data taken at 834 G are shown as open black circles [13], while the corrected EoS at 832.18 G is displayed as filled black circles (see text). Measurements from MIT and Tokyo are shown as filled (blue) squares [15] and open (red) triangles [31], respectively, and the bDMC calculation from Amherst, as the solid (green) line [16]. At the lowest temperatures, we find a corrected Bertsch parameter, $\xi_S = 0.40(2)$.

pressure,

$$\frac{P(\mu, T)}{P_0(\mu, T)} = \frac{P(\mu, T, a^{-1})}{P_0(\mu, T)} + \frac{1}{8\pi^2} \frac{\lambda_{\text{dB}}}{a} \frac{\tilde{C}(\beta\mu)}{\text{Li}_{5/2}(-\exp(\beta\mu))}, \quad (\text{B4})$$

where $P_0(\mu, T)$ is the pressure of the noninteracting Fermi gas, and $\tilde{C}(\beta\mu) = C\lambda_{\text{dB}}^4$ is the dimensionless contact density. $\tilde{C}(\beta\mu)$ has recently been calculated by the diagrammatic Monte Carlo method [30]. We compute the small a cor-

rection by applying Eq. (B4) to the pressure extracted from each ^6Li density profile used in the measurement of the EoS. The temperature in Eq. (B4) is determined from the ^7Li thermometer, and the full EoS is reconstructed by first adjusting μ_0 for each high-temperature image to match the virial expansion and then progressively connecting lower temperature images to high- $\beta\mu$ ones, as originally done in [13]. The result for the pressure is shown in Fig. 6.

-
- [1] J. Schrieffer, *Theory Of Superconductivity* (Perseus Books, New York, 1999).
- [2] A. Leggett, *Science* **274**, 587 (1996).
- [3] E. Demler and S. Zhang, *Nature* **396**, 733 (1998).
- [4] D. J. Scalapino and S. R. White, *Phys. Rev. B* **58**, 8222 (1998).
- [5] R. Haslinger and A. V. Chubukov, *Phys. Rev. B* **68**, 214508 (2003).
- [6] S. Chakravarty, H.-Y. Kee, and E. Abrahams, *Phys. Rev. B* **67**, 100504(R) (2003).
- [7] D. Van der Marel, A. J. Leggett, J. W. Loram, and J. R. Kirtley, *Phys. Rev. B* **66**, 140501(R) (2002).
- [8] S. Chakravarty, H.-Y. Kee, and E. Abrahams, *Phys. Rev. Lett.* **82**, 2366 (1999).
- [9] I. Bloch, J. Dalibard, and W. Zwerger, *Rev. Mod. Phys.* **80**, 885 (2008).
- [10] G. Zürn, T. Lompe, A. N. Wenz, S. Jochim, P. S. Julienne, and J. M. Hutson, *Phys. Rev. Lett.* **110**, 135301 (2013).
- [11] C.-H. Cheng and S.-K. Yip, *Phys. Rev. B* **75**, 014526 (2007).
- [12] T. Ho and Q. Zhou, *Nat. Phys.* **6**, 131 (2009).
- [13] S. Nascimbène, N. Navon, K. Jiang, F. Chevy, and C. Salomon, *Nature* **463**, 1057 (2010).
- [14] N. Navon, S. Nascimbène, F. Chevy, and C. Salomon, *Science* **328**, 729 (2010).
- [15] M. Ku, A. Sommer, L. Cheuk, and M. Zwierlein, *Science* **335**, 563 (2012).
- [16] K. Van Houcke, F. Werner, E. Kozik, N. Prokof'ev, B. Svistunov, M. Ku, A. Sommer, L. Cheuk, A. Schirotzek, and M. Zwierlein, *Nat. Phys.* **8**, 366 (2012).
- [17] S. Nascimbène, N. Navon, F. Chevy, and C. Salomon, *New J. Phys.* **12**, 103026 (2010).
- [18] S. Nascimbène, N. Navon, S. Pilati, F. Chevy, S. Giorgini, A. Georges, and C. Salomon, *Phys. Rev. Lett.* **106**, 215303 (2011).
- [19] J. Carlson, S.-Y. Chang, V. R. Pandharipande, and K. E. Schmidt, *Phys. Rev. Lett.* **91**, 050401 (2003).
- [20] C. Lobo, A. Recati, S. Giorgini, and S. Stringari, *Phys. Rev. Lett.* **97**, 200403 (2006).
- [21] A. Bulgac, J. E. Drut, and P. Magierski, *Phys. Rev. A* **78**, 023625 (2008).
- [22] Edited by W. Zwerger, *The BEC-BCS Crossover and the Unitary Fermi Gas, Lecture Notes in Physics, Vol. 836* (Springer, Berlin, 2012).
- [23] P. Pieri and G. C. Strinati, *Phys. Rev. B* **61**, 15370 (2000); A. Perali, P. Pieri, G. C. Strinati, and C. Castellani, *ibid.* **66**, 024510 (2002); A. Perali, P. Pieri, and G. C. Strinati, *Phys. Rev. Lett.* **93**, 100404 (2004); P. Perali, P. Pieri, L. Pisani, and G. C. Strinati, *ibid.* **92**, 220404 (2004).
- [24] R. Combescot, X. Leyronas, and M. Yu. Kagan, *Phys. Rev. A* **73**, 023618 (2006).
- [25] R. Combescot, A. Recati, C. Lobo, and F. Chevy, *Phys. Rev. Lett.* **98**, 180402 (2007).
- [26] F. Chevy, *Phys. Rev. A* **74**, 063628 (2006); N. V. Prokof'ev and B. V. Svistunov, *Phys. Rev. B* **77**, 020408 (2008); R. Combescot and S. Giraud, *Phys. Rev. Lett.* **101**, 050404 (2008); R. Combescot, S. Giraud, and X. Leyronas, *Europhys. Lett.* **88**, 60007 (2009).
- [27] The correspondence formulas from the canonical to the grand-canonical ensemble can be found in the Supplementary Material to [14]. Since the formulas involve derivatives, it is convenient to parametrize the data points with rational functions (solid lines in Fig. 3).
- [28] A. Schirotzek, Y.-il Shin, C. H. Schunck, and W. Ketterle, *Phys. Rev. Lett.* **101**, 140403 (2008).
- [29] M. Bartenstein, A. Altmeyer, S. Riedl, R. Geursen, S. Jochim, C. Chin, J. H. Denschlag, R. Grimm, A. Simoni, E. Tiesinga, C. J. Williams, and P. S. Julienne, *Phys. Rev. Lett.* **94**, 103201 (2005).
- [30] K. Van Houcke, F. Werner, E. Kozik, N. Prokof'ev, and B. Svistunov, [arXiv:1303.6245](https://arxiv.org/abs/1303.6245).
- [31] M. Horikoshi, S. Nakajima, M. Ueda, and T. Mukaiyama, *Science* **327**, 442 (2010).

Bibliography

- [1] P. Anderson, More Is Different, *Science* **177**(4), 393 (1972).
- [2] V. Efimov, Weakly-bound states of three resonantly-interacting particles, *Sov. J. Nucl. Phys* **12**, 589 (1971).
- [3] G. Baker, The Many-Body Challenge Competition: A neutron matter model, in *Recent progress in many-body theories: the proceedings of the 10th international conference, Seattle, USA, September 10-15, 1999*, volume 3, page 15, World Scientific Pub Co Inc, 2000.
- [4] R. Feynman, Simulating physics with computers, *International Journal of Theoretical Physics* **21**(6), 467–488 (1982).
- [5] M. Anderson, J. Ensher, M. Matthews, C. Wieman, and E. Cornell, Observation of Bose-Einstein condensation in a dilute atomic vapor, *Science* **269**(5221), 198 (1995).
- [6] K. Davis, M. Mewes, M. Andrews, N. Van Druten, D. Durfee, D. Kurn, and W. Ketterle, Bose-Einstein condensation in a gas of sodium atoms, *Phys. Rev. Lett.* **75**(22), 3969–3973 (1995).
- [7] B. DeMarco and D. Jin, Onset of Fermi degeneracy in a trapped atomic gas, *Science* **285**(5434), 1703 (1999).
- [8] D. Jaksch, C. Bruder, J. Cirac, C. Gardiner, and P. Zoller, Cold bosonic atoms in optical lattices, *Phys. Rev. Lett.* **81**(15), 3108–3111 (1998).
- [9] M. Greiner, O. Mandel, T. Esslinger, T. Hansch, and I. Bloch, Quantum phase transition from a superfluid to a Mott insulator in a gas of ultracold atoms, *Nature* **415**, 39–44 (2002).
- [10] R. Jordens, N. Strohmaier, K. Gunter, H. Moritz, and T. Esslinger, A Mott insulator of fermionic atoms in an optical lattice, *Nature* **455**(7210), 204–207 (2008).
- [11] U. Schneider, L. Hackermuller, S. Will, T. Best, I. Bloch, T. Costi, R. Helmes, D. Rasch, and A. Rosch, Metallic and insulating phases of repulsively interacting fermions in a 3D optical lattice, *Science* **322**(5907), 1520 (2008).
- [12] S. Cornish, N. Claussen, J. Roberts, E. Cornell, and C. Wieman, Stable ^{85}Rb Bose-Einstein Condensates with Widely Tunable Interactions, *Phys. Rev. Lett.* **85**(9), 1795–1798 (2000).
- [13] K. O'Hara, S. Hemmer, M. Gehm, S. Granade, and J. Thomas, Observation of a strongly interacting degenerate Fermi gas of atoms, *Science* **298**(5601), 2179 (2002).
- [14] I. Bloch, J. Dalibard, and W. Zwerger, Many-body physics with ultracold gases, *Rev. Mod. Phys.* **80**(3), 885–964 (2008).

- [15] W. Bakr, J. Gillen, A. Peng, S. Folling, and M. Greiner, A quantum gas microscope for detecting single atoms in a Hubbard-regime optical lattice, *Nature* **462**(7269), 74–77 (2009).
- [16] J. Sherson, C. Weitenberg, M. Endres, M. Cheneau, I. Bloch, and S. Kuhr, Single-atom-resolved fluorescence imaging of an atomic Mott insulator, *Nature* **467**(7311) (2010).
- [17] C. Weitenberg, M. Endres, J. Sherson, M. Cheneau, P. Schaus, T. Fukuhara, I. Bloch, and S. Kuhr, Single-spin addressing in an atomic Mott insulator, *Nature* **471**(7338), 319–324 (2011).
- [18] F. London, The-phenomenon of liquid helium and the Bose-Einstein degeneracy, *Nature* **141**(3571), 643–644 (1938).
- [19] L. Cooper, Bound electron pairs in a degenerate Fermi gas, *Phys. Rev.* **104**(4), 1189 (1956).
- [20] J. Bardeen, L. Cooper, and J. Schrieffer, Theory of superconductivity, *Phys. Rev.* **108**(5), 1175 (1957).
- [21] D. Eagles, Possible pairing without superconductivity at low carrier concentrations in bulk and thin-film superconducting semiconductors, *Phys. Rev.* **186**(2), 456 (1969).
- [22] A. Leggett, *Modern trends in the theory of condensed matter*, 1980.
- [23] P. Nozières and S. Schmitt-Rink, Bose condensation in an attractive fermion gas: From weak to strong coupling superconductivity, *J. Low. Temp. Phys.* **59**(3), 195–211 (1985).
- [24] S. Jochim, M. Bartenstein, A. Altmeyer, G. Hendl, S. Riedl, C. Chin, J. Hecker Denschlag, and R. Grimm, Bose-Einstein condensation of molecules, *Science* **302**(5653), 2101 (2003).
- [25] M. Greiner, C. Regal, and D. Jin, Emergence of a molecular Bose-Einstein condensate from a Fermi gas, *Nature* **426**(6966), 537–540 (2003).
- [26] M. Zwierlein, C. Stan, C. Schunck, S. Raupach, S. Gupta, Z. Hadzibabic, and W. Ketterle, Observation of Bose-Einstein condensation of molecules, *Phys. Rev. Lett.* **91**(25), 250401 (2003).
- [27] T. Bourdel, L. Khaykovich, J. Cubizolles, J. Zhang, F. Chevy, M. Teichmann, L. Tarruell, S. Kokkelmans, and C. Salomon, Experimental Study of the BEC-BCS Crossover Region in Lithium 6, *Phys. Rev. Lett.* **93**(5), 050401 (2004).
- [28] C. Chin, M. Bartenstein, A. Altmeyer, S. Riedl, S. Jochim, J. Denschlag, and R. Grimm, Observation of the pairing gap in a strongly interacting Fermi gas, *Science* **305**(5687), 1128 (2004).
- [29] A. Schirotzek, Y. Shin, C. Schunck, and W. Ketterle, Determination of the superfluid gap in atomic fermi gases by quasiparticle spectroscopy., *Phys. Rev. Lett.* **101**(14), 140403 (2008).
- [30] M. Zwierlein, J. Abo-Shaeer, A. Schirotzek, C. Schunck, and W. Ketterle, Vortices and superfluidity in a strongly interacting Fermi gas, *Nature* **435**(7045), 1047–1051 (2005).
- [31] M. Inguscio, W. Ketterle, and C. Salomon, *Ultracold Fermi Gases*, Proceedings of the International School of Physics “Enrico Fermi”, Course CLXIV, Varenna (2006).

- [32] J. Roberts, N. Claussen, J. Burke Jr, C. Greene, E. Cornell, and C. Wieman, Resonant Magnetic Field Control of Elastic Scattering in Cold ^{85}Rb , *Phys. Rev. Lett.* **81**(23), 5109–5112 (1998).
- [33] P. Courteille, R. Freeland, D. Heinzen, F. Van Abeelen, and B. Verhaar, Observation of a Feshbach resonance in cold atom scattering, *Phys. Rev. Lett.* **81**(1), 69–72 (1998).
- [34] S. Inouye, M. Andrews, J. Stenger, H. Miesner, D. Stamper-Kurn, and W. Ketterle, Observation of Feshbach resonances in a Bose–Einstein condensate, *Nature* **392**(6672), 151–154 (1998).
- [35] J. Roberts, N. Claussen, S. Cornish, and C. Wieman, Magnetic field dependence of ultracold inelastic collisions near a Feshbach resonance, *Phys. Rev. Lett.* **85**(4), 728–731 (2000).
- [36] N. Claussen, E. Donley, S. Thompson, and C. Wieman, Microscopic dynamics in a strongly interacting Bose-Einstein condensate, *Phys. Rev. Lett.* **89**(1), 10401 (2002).
- [37] P. Fedichev, M. Reynolds, and G. Shlyapnikov, Three-body recombination of ultracold atoms to a weakly bound s level, *Phys. Rev. Lett.* **77**(14), 2921–2924 (1996).
- [38] D. Petrov, C. Salomon, and G. Shlyapnikov, Weakly bound dimers of fermionic atoms, *Phys. Rev. Lett.* **93**(9), 90404 (2004).
- [39] C. Pethick and H. Smith, *Bose-Einstein condensation in dilute gases*, Cambridge University Press, 2002.
- [40] F. Dalfovo, S. Giorgini, L. Pitaevskii, and S. Stringari, Theory of Bose-Einstein condensation in trapped gases, *Rev. Mod. Phys.* **71**(3), 463 (1999).
- [41] T. Lee, K. Huang, and C. Yang, Eigenvalues and eigenfunctions of a Bose system of hard spheres and its low-temperature properties, *Phys. Rev.* **106**(6), 1135–1145 (1957).
- [42] T. D. Lee and C. N. Yang, Many-Body Problem in Quantum Mechanics and Quantum Statistical Mechanics, *Phys. Rev.* **105**(3), 1119–1120 (1957).
- [43] T. Lee and C. Yang, Low-temperature behavior of a dilute Bose system of hard spheres. I. Equilibrium properties, *Phys. Rev.* **112**(5), 1419 (1958).
- [44] G. Astrakharchik, J. Boronat, J. Casulleras, and S. Giorgini, Equation of state of a Fermi gas in the BEC-BCS crossover: A quantum Monte Carlo study, *Phys. Rev. Lett.* **93**(20), 200404 (2004).
- [45] X. Leyronas and R. Combescot, Superfluid equation of state of dilute composite bosons, *Phys. Rev. Lett.* **99**(17), 170402 (2007).
- [46] A. Altmeyer, S. Riedl, C. Kohstall, M. J. Wright, R. Geursen, M. Bartenstein, C. Chin, J. H. Denschlag, and R. Grimm, Precision Measurements of Collective Oscillations in the BEC-BCS Crossover, *Phys. Rev. Lett.* **98**(4), 040401 (2007).
- [47] Y. Shin, A. Schirotzek, C. Schunck, and W. Ketterle, Realization of a strongly interacting Bose-Fermi mixture from a two-component Fermi gas, *Phys. Rev. Lett.* **101**(7), 070404 (2008).

- [48] S. Papp, J. Pino, R. Wild, S. Ronen, C. Wieman, D. Jin, and E. Cornell, Bragg Spectroscopy of a Strongly Interacting ^{85}Rb Bose-Einstein Condensate, *Phys. Rev. Lett.* **101**(13), 135301 (2008).
- [49] T. Ho, Universal thermodynamics of degenerate quantum gases in the unitarity limit, *Phys. Rev. Lett.* **92**(9), 90402 (2004).
- [50] Y. Lee and Y. Lee, Quantum phase transition in an atomic Bose gas near a Feshbach resonance, *Phys. Rev. B* **70**(22), 224506 (2004).
- [51] M. Romans, R. Duine, S. Sachdev, and H. Stoof, Quantum phase transition in an atomic Bose gas with a Feshbach resonance, *Phys. Rev. Lett.* **93**(2), 20405 (2004).
- [52] L. Radzihovsky, P. Weichman, and J. Park, Superfluidity and phase transitions in a resonant Bose gas, *Annals of Physics* **323**(10), 2376–2451 (2008).
- [53] A. Koetsier, P. Massignan, R. Duine, and H. Stoof, Strongly interacting Bose gas: Nozières and Schmitt-Rink theory and beyond, *Phys. Rev. A* **79**(6), 063609 (2009).
- [54] F. Cooper, C. Chien, B. Mihaila, J. Dawson, and E. Timmermans, Nonperturbative predictions for cold atom Bose gases with tunable interactions, *Phys. Rev. Lett.* **105** (2010).
- [55] S. Cowell, H. Heiselberg, I. Mazets, J. Morales, V. Pandharipande, and C. Pethick, Cold Bose gases with large scattering lengths, *Phys. Rev. Lett.* **88**(21), 210403 (2002).
- [56] J. Song and F. Zhou, Ground State Properties of Cold Bosonic Atoms At Large Scattering Lengths, *Phys. Rev. Lett.* **103**(2), 25302 (2009).
- [57] Y.-L. Lee and Y.-W. Lee, Universality and stability for a dilute Bose gas with a Feshbach resonance, *Phys. Rev. A* **81**(6), 063613 (2010).
- [58] J. Diederix, T. van Heijst, and H. Stoof, Ground state of a resonantly interacting Bose gas, arXiv:1107.1369 (2011).
- [59] N. Navon, S. Piatecki, K. Günter, B. Rem, T. Nguyen, F. Chevy, W. Krauth, and C. Salomon, Dynamics and Thermodynamics of the Low-Temperature Strongly Interacting Bose Gas, *Physical Review Letters* **107**(13), 135301 (2011).
- [60] S. Nascimbene, N. Navon, K. Jiang, F. Chevy, and C. Salomon, Exploring the thermodynamics of a universal Fermi gas, *Nature* **463**, 1057–1060 (2010).
- [61] S. Nascimbène, N. Navon, S. Pilati, F. Chevy, S. Giorgini, A. Georges, and C. Salomon, Fermi-Liquid Behavior of the Normal Phase of a Strongly Interacting Gas of Cold Atoms, *Phys. Rev. Lett.* **106**(21), 215303 (2011).
- [62] N. Navon, S. Nascimbene, F. Chevy, and C. Salomon, The Equation of State of a Low-Temperature Fermi Gas with Tunable Interactions, *Science* **328**(5979), 729 (2010).
- [63] S. Nascimbene, N. Navon, K. Jiang, L. Tarruell, M. Teichmann, J. McKeever, F. Chevy, and C. Salomon, Collective Oscillations of an Imbalanced Fermi Gas: Axial Compression Modes and Polaron Effective Mass, *Phys. Rev. Lett.* **103**(17), 170402 (2009).
- [64] K. Huang, *Statistical Mechanics*, John Wiley & Sons Inc (1963).

- [65] N. Tammuz, R. Smith, R. Campbell, S. Beattie, S. Moulder, J. Dalibard, and Z. Hadzibabic, Can a Bose gas be saturated?, *Phys. Rev. Lett.* **106**(23), 230401 (2011).
- [66] J. Sakurai, *Modern quantum mechanics*, Addison Wesley (1985).
- [67] L. Landau and E. Lifshitz, *Quantum Mechanics*, Pergamon Press, Oxford, UK, 1980.
- [68] D. Ceperley, Path integrals in the theory of condensed helium, *Rev. Mod. Phys.* **67**(2), 279 (1995).
- [69] F. Werner, Trapped cold atoms with resonant interactions : unitary gas and three-body problem, Ph.D Thesis (2008).
- [70] C. Chin, R. Grimm, P. Julienne, and E. Tiesinga, Feshbach resonances in ultracold gases, *Rev. Mod. Phys.* **82**(2), 1225 (2010).
- [71] A. Moerdijk, B. Verhaar, and A. Axelsson, Resonances in ultracold collisions of ${}^6\text{Li}$, ${}^7\text{Li}$, and ${}^{23}\text{Na}$, *Phys. Rev. A* **51**, 4852–4861 (1995).
- [72] M. Bartenstein, A. Altmeyer, S. Riedl, R. Geursen, S. Jochim, C. Chin, J. Denschlag, R. Grimm, A. Simoni, E. Tiesinga, et al., Precise Determination of ${}^6\text{Li}$ Cold Collision Parameters by Radio-Frequency Spectroscopy on Weakly Bound Molecules, *Phys. Rev. Lett.* **94**(10), 103201 (2005).
- [73] K. Dieckmann, C. Stan, S. Gupta, Z. Hadzibabic, C. Schunck, and W. Ketterle, Decay of an ultracold fermionic lithium gas near a Feshbach resonance, *Phys. Rev. Lett.* **89**(20), 203201 (2002).
- [74] K. Strecker, G. Partridge, and R. Hulet, Conversion of an atomic Fermi gas to a long-lived molecular Bose gas, *Phys. Rev. Lett.* **91**(8), 80406 (2003).
- [75] J. Zhang, E. Van Kempen, T. Bourdel, L. Khaykovich, J. Cubizolles, F. Chevy, M. Teichmann, L. Tarruell, S. Kokkelmans, and C. Salomon, P-wave Feshbach resonances of ultracold ${}^6\text{Li}$, *Phys. Rev. A* **70**(3), 030702 (2004).
- [76] C. Schunck, M. Zwierlein, C. Stan, S. Raupach, W. Ketterle, A. Simoni, E. Tiesinga, C. Williams, and P. Julienne, Feshbach resonances in fermionic ${}^6\text{Li}$, *Phys. Rev. A* **71**(4), 045601 (2005).
- [77] K. Strecker, G. Partridge, A. Truscott, and R. Hulet, Formation and propagation of matter-wave soliton trains, *Nature* **417**(6885), 150–153 (2002).
- [78] L. Khaykovich, F. Schreck, G. Ferrari, T. Bourdel, J. Cubizolles, L. Carr, Y. Castin, and C. Salomon, Formation of a matter-wave bright soliton, *Science* **296**(5571), 1290 (2002).
- [79] N. Gross, Z. Shotan, S. Kokkelmans, and L. Khaykovich, Nuclear-spin-independent short-range three-body physics in ultracold atoms, *Phys. Rev. Lett.* **105**, 103203 (2010).
- [80] N. Gross and L. Khaykovich, All-optical production of ${}^7\text{Li}$ Bose-Einstein condensation using Feshbach resonances, *Phys. Rev. A* **77**(2), 023604 (2008).
- [81] E. Kempen, B. Marcelis, and S. Kokkelmans, Formation of fermionic molecules via interisotope Feshbach resonances, *Phys. Rev. A* **70**(5), 050701 (2004).

- [82] J. Zhang, E. Van Kempen, T. Bourdel, L. Khaykovich, J. Cubizolles, F. Chevy, M. Teichmann, L. Tarruell, S. Kokkelmans, and C. Salomon, Expansion of a lithium gas in the BEC-BCS crossover, in *Proceedings of the International Conference on Atomic Physics, ICAP 2004*, 2005.
- [83] M. Teichmann, Ultracold Lithium-6 Atoms in the BEC-BCS Crossover: Experiments and the Construction of a New Apparatus, Ph.D Thesis (2007).
- [84] L. Tarruell, Superfluidité dans un gaz de fermions ultrafroids, Ph.D Thesis (2008).
- [85] C. Wu, I. Santiago, J. Park, P. Ahmadi, and M. Zwierlein, Strongly Interacting Isotopic Bose-Fermi Mixture Immersed in a Fermi Sea, arXiv:1103.4630 (2011).
- [86] T. Lahaye, C. Menotti, L. Santos, M. Lewenstein, and T. Pfau, The physics of dipolar bosonic quantum gases, *Rep. Prog. Phys.* **72**, 126401 (2009).
- [87] D. Petrov, Three-boson problem near a narrow Feshbach resonance, *Phys. Rev. Lett.* **93**(14), 143201 (2004).
- [88] S. Simonucci, P. Pieri, and G. Strinati, Broad vs. narrow Fano-Feshbach resonances in the BCS-BEC crossover with trapped Fermi atoms, *Europhys. Lett.* **69**, 713 (2005).
- [89] T. Ho and X. Cui, Alternative Route to Strong Interaction: Narrow Feshbach Resonance, arXiv:1105.4627 (2011).
- [90] H. Callen, *Thermodynamics and an Introduction to Thermostatistics*, John Wiley & Sons Inc (1985).
- [91] T. Meyrath, F. Schreck, J. Hanssen, C. Chuu, and M. Raizen, Bose-Einstein condensate in a box, *Phys. Rev. A* **71**(4), 041604–1 (2005).
- [92] S. Rath, T. Yefsah, K. Gunter, M. Cheneau, R. Desbuquois, M. Holzmann, W. Krauth, and J. Dalibard, Equilibrium state of a trapped two-dimensional Bose gas, *Phys. Rev. A* **82**, 013609 (2010).
- [93] S. Folling, A. Widera, T. Muller, F. Gerbier, and I. Bloch, Formation of spatial shell structure in the superfluid to Mott insulator transition, *Phys. Rev. Lett.* **97**(6), 60403 (2006).
- [94] C. Hung, X. Zhang, N. Gemelke, and C. Chin, Observation of scale invariance and universality in two-dimensional Bose gases, *Nature* **470**(7333), 236–239 (2011).
- [95] T. Yefsah, R. Desbuquois, L. Chomaz, K. Gunter, and J. Dalibard, Exploring the thermodynamics of a two-dimensional Bose gas, arXiv:1106.0188 (2011).
- [96] D. Petrov, M. Holzmann, and G. Shlyapnikov, Bose-Einstein condensation in quasi-2D trapped gases, *Phys. Rev. Lett.* **84**(12), 2551–2555 (2000).
- [97] N. Mermin and H. Wagner, Absence of ferromagnetism or antiferromagnetism in one- or two-dimensional isotropic Heisenberg models, *Phys. Rev. Lett.* **17**(22), 1133–1136 (1966).
- [98] P. Hohenberg, Existence of long-range order in one and two dimensions, *Phys. Rev.* **158**(2), 383–386 (1967).

- [99] V. Berezinskii, Destruction of long-range order in one-dimensional and two-dimensional systems possessing a continuous symmetry group. II. Quantum systems, *Sov. Phys. JETP* **34**, 610 (1972).
- [100] J. Kosterlitz and D. Thouless, Ordering, metastability and phase transitions in two-dimensional systems, *J. Phys. C* **6**, 1181 (1973).
- [101] D. Bishop and J. Reppy, Study of the Superfluid Transition in Two-Dimensional ^4He Films, *Phys. Rev. Lett.* **40**(26), 1727–1730 (1978).
- [102] Z. Hadzibabic, P. Krüger, M. Cheneau, B. Battelier, and J. Dalibard, Berezinskii–Kosterlitz–Thouless crossover in a trapped atomic gas, *Nature* **441**(7097), 1118–1121 (2006).
- [103] A. Van Amerongen, J. Van Es, P. Wicke, K. Kheruntsyan, and N. Van Druten, Yang-Yang thermodynamics on an atom chip, *Phys. Rev. Lett.* **100**(9), 90402 (2008).
- [104] J. Armijo, T. Jacqmin, K. Kheruntsyan, and I. Bouchoule, Mapping out the quasicondensate transition through the dimensional crossover from one to three dimensions, *Phys. Rev. A* **83**(2), 021605 (2011).
- [105] J. Ensher, D. Jin, M. Matthews, C. Wieman, and E. Cornell, Bose-Einstein condensation in a dilute gas: Measurement of energy and ground-state occupation, *Phys. Rev. Lett.* **77**(25), 4984–4987 (1996).
- [106] F. Gerbier, J. Thywissen, S. Richard, M. Hugbart, P. Bouyer, and A. Aspect, Experimental study of the thermodynamics of an interacting trapped Bose-Einstein condensed gas, *Phys. Rev. A* **70**(1), 013607 (2004).
- [107] F. Gerbier, J. Thywissen, S. Richard, M. Hugbart, P. Bouyer, and A. Aspect, Critical temperature of a trapped, weakly interacting Bose gas, *Phys. Rev. Lett.* **92**(3), 30405 (2004).
- [108] J. Stewart, J. Gaebler, C. Regal, and D. Jin, Potential Energy of a ^{40}K Fermi Gas in the BCS-BEC Crossover, *Phys. Rev. Lett.* **97**(22), 220406 (2006).
- [109] L. Luo, B. Clancy, J. Joseph, J. Kinast, and J. Thomas, Measurement of the entropy and critical temperature of a strongly interacting Fermi gas, *Phys. Rev. Lett.* **98**(8), 80402 (2007).
- [110] J. Thomas, J. Kinast, and A. Turlapov, Virial theorem and universality in a unitary Fermi gas, *Phys. Rev. Lett.* **95**(12), 120402 (2005).
- [111] Y. Shin, Determination of the equation of state of a polarized Fermi gas at unitarity, *Phys. Rev. A* **77**(4), 041603 (2008).
- [112] A. Bulgac and M. McNeil Forbes, Zero Temperature Thermodynamics of Asymmetric Fermi Gases at Unitarity, *Phys. Rev. A* **75**, 031605 (2007).
- [113] M. Horikoshi, S. Nakajima, M. Ueda, and T. Mukaiyama, Measurement of universal thermodynamic functions for a unitary Fermi gas, *Science* **327**(5964), 442 (2010).
- [114] A. Schirotzek, Radio-Frequency of Ultracold Atomic Fermi Gases, Ph.D Thesis (2010).
- [115] M. Ku, A. Sommer, L. Cheuk, A. Schirotzek, M. Zwierlein, K. Van Houcke, F. Werner, E. Kozik, N. Profok'ev, and B. Svistunov, In preparation.

- [116] J. Fuchs, X. Leyronas, and R. Combescot, Hydrodynamic modes of a one-dimensional trapped Bose gas, *Phys. Rev. A* **68**(4), 043610 (2003).
- [117] T. De Silva and E. Mueller, Profiles of near-resonant population-imbalanced trapped Fermi gases, *Phys. Rev. A* **73**(5) (2006).
- [118] C. Cheng and S. Yip, Trapped resonant fermions above the superfluid transition temperature, *Phys. Rev. B* **75**(1), 14526 (2007).
- [119] T. Ho and Q. Zhou, Obtaining the phase diagram and thermodynamic quantities of bulk systems from the densities of trapped gases, *Nat. Phys.* **6**, 131 (2009).
- [120] F. Schreck, Mixtures of ultracold gases: Fermi sea and Bose-Einstein condensate of lithium isotopes, Ph.D Thesis (2002).
- [121] S. Nascimbène, Thermodynamics of ultracold Fermi gases, Ph.D Thesis (2010).
- [122] U. Eismann, F. Gerbier, C. Canalias, A. Zukauskas, G. Tréneç, J. Vigué, F. Chevy, and C. Salomon, An all-solid-state laser source at 671 nm for cold atom experiments with lithium, arXiv:1103.5841 (2011).
- [123] J. Gerton, C. Sackett, B. Frew, and R. Hulet, Dipolar relaxation collisions in magnetically trapped ^7Li , *Phys. Rev. A* **59**(2), 1514 (1999).
- [124] M. Zwierlein, Z. Hadzibabic, S. Gupta, and W. Ketterle, Spectroscopic insensitivity to cold collisions in a two-state mixture of fermions, *Phys. Rev. Lett.* **91**(25), 250404 (2003).
- [125] K. O'Hara, M. Gehm, S. Granade, and J. Thomas, Scaling laws for evaporative cooling in time-dependent optical traps, *Phys. Rev. A* **64**(5), 051403 (2001).
- [126] L. Luo, B. Clancy, J. Joseph, J. Kinast, A. Turlapov, and J. Thomas, Evaporative cooling of unitary Fermi gas mixtures in optical traps, *New J. Phys.* **8**, 213 (2006).
- [127] J. Clement, J. Brantut, M. Robert-de Saint-Vincent, R. Nyman, A. Aspect, T. Bourdel, and P. Bouyer, All-optical runaway evaporation to Bose-Einstein condensation, *Phys. Rev. A* **79**(6), 061406 (2009).
- [128] C. Hung, X. Zhang, N. Gemelke, and C. Chin, Accelerating evaporative cooling of atoms into Bose-Einstein condensation in optical traps, *Phys. Rev. A* **78**(1), 011604 (2008).
- [129] R. Grimm, Ultracold Fermi gases in the BEC-BCS crossover: a review from the Innsbruck perspective, Proceedings of the International School of Physics 'Enrico Fermi', Course CLXIV, Varenna (2006).
- [130] M. Parish and D. Huse, Evaporative depolarization and spin transport in a unitary trapped Fermi gas, *Phys. Rev. A* **80**(6), 063605 (2009).
- [131] Y. Liao, M. Revelle, T. Paprotta, A. Rittner, W. Li, G. Partridge, and R. Hulet, Metastability in Spin-Polarized Fermi Gases, arXiv:1105.6369 (2011).
- [132] A. Schirotzek, C. Wu, A. Sommer, and M. Zwierlein, Observation of Fermi polarons in a tunable Fermi liquid of ultracold atoms, *Phys. Rev. Lett.* **102**(23), 230402 (2009).
- [133] S. Kokkelmans, private communication.

- [134] G. Reinaudi, T. Lahaye, Z. Wang, and D. Guéry-Odelin, Strong saturation absorption imaging of dense clouds of ultracold atoms, *Opt. Lett.* **32**(21), 3143–3145 (2007).
- [135] M. Andrews, M. Mewes, N. Van Druten, D. Durfee, D. Kurn, and W. Ketterle, Direct, nondestructive observation of a Bose condensate, *Science* **273**(5271), 84 (1996).
- [136] W. Ketterle, D. Durfee, and D. Stamper-Kurn, Making, probing and understanding Bose-Einstein condensates, *Proceedings of the International School of Physics 'Enrico Fermi'*, Course CXL, Varenna (1999).
- [137] G. Partridge, W. Li, R. Kamar, Y. Liao, and R. Hulet, Pairing and phase separation in a polarized Fermi gas, *Science* **311**(5760), 503–505 (2006).
- [138] Y. Shin, M. Zwierlein, C. Schunck, A. Schirotzek, and W. Ketterle, Observation of phase separation in a strongly interacting imbalanced Fermi gas, *Phys. Rev. Lett.* **97**(3), 30401 (2006).
- [139] M. Naraschewski and D. Stamper-Kurn, Analytical description of a trapped semi-ideal Bose gas at finite temperature, *Phys. Rev. A* **58**(3), 2423 (1998).
- [140] T. Weber, J. Herbig, M. Mark, H. Nagerl, and R. Grimm, Bose-Einstein condensation of cesium, *Science* **299**(5604), 232 (2003).
- [141] G. Roati, M. Zaccanti, C. D'Errico, J. Catani, M. Modugno, A. Simoni, M. Inguscio, and G. Modugno, ^{39}K Bose-Einstein Condensate with Tunable Interactions, *Phys. Rev. Lett.* **99**(1), 10403 (2007).
- [142] J. Soding, D. Guéry-Odelin, P. Desbiolles, G. Ferrari, and J. Dalibard, Giant spin relaxation of an ultracold cesium gas, *Phys. Rev. Lett.* **80**(9), 1869–1872 (1998).
- [143] N. Bogoliubov, On the theory of superfluidity, *J. Phys.(USSR)* **11**(23), 4–2 (1947).
- [144] A. Marte, T. Volz, J. Schuster, S. Durr, G. Rempe, E. Van Kempen, and B. Verhaar, Feshbach resonances in rubidium 87: Precision measurement and analysis, *Phys. Rev. Lett.* **89**(28), 283202 (2002).
- [145] E. Wille, F. Spiegelhalder, G. Kerner, D. Naik, A. Trenkwalder, G. Hendl, F. Schreck, R. Grimm, T. Tiecke, J. Walraven, et al., Exploring an Ultracold Fermi-Fermi Mixture: Interspecies Feshbach Resonances and Scattering Properties of ^6Li and ^{40}K , *Phys. Rev. Lett.* **100**(5), 53201 (2008).
- [146] V. Vuletic, A. Kerman, C. Chin, and S. Chu, Observation of low-field feshbach resonances in collisions of cesium atoms, *Phys. Rev. Lett.* **82**(7), 1406–1409 (1999).
- [147] H. Marion, S. Bize, L. Cacciapuoti, D. Chambon, F. Pereira Dos Santos, G. Santarelli, P. Wolf, A. Clairon, A. Luiten, M. Tobar, et al., First observation of Feshbach resonances at very low magnetic field in a ^{133}Cs fountain, in *Frequency and Time Forum, 2004. EFTF 2004. 18th European*, pages 49–55, IET, 2004.
- [148] S. Pollack, D. Dries, M. Junker, Y. Chen, T. Corcovilos, and R. Hulet, Extreme Tunability of Interactions in a ^7Li Bose-Einstein Condensate, *Phys. Rev. Lett.* **102**(9), 90402 (2009).
- [149] C. Regal, C. Ticknor, J. Bohn, and D. Jin, Creation of ultracold molecules from a Fermi gas of atoms, *Nature* **424**(6944), 47–50 (2003).

- [150] M. Mark, F. Ferlaino, S. Knoop, J. Danzl, T. Kraemer, C. Chin, H. Nagerl, and R. Grimm, Spectroscopy of ultracold trapped cesium Feshbach molecules, *Phys. Rev. A* **76**(4), 042514 (2007).
- [151] J. Zirbel, K. Ni, S. Ospelkaus, T. Nicholson, M. Olsen, P. Julienne, C. Wieman, J. Ye, and D. Jin, Heteronuclear molecules in an optical dipole trap, *Phys. Rev. A* **78**(1), 13416 (2008).
- [152] S. Papp and C. Wieman, Observation of Heteronuclear Feshbach Molecules from a ^{85}Rb - ^{87}Rb Gas, *Phys. Rev. Lett.* **97**(18), 180404 (2006).
- [153] A. Lange, K. Pilch, A. Prantner, F. Ferlaino, B. Engeser, H. Nagerl, R. Grimm, and C. Chin, Determination of atomic scattering lengths from measurements of molecular binding energies near Feshbach resonances, *Phys. Rev. A* **79**(1), 013622 (2009).
- [154] G. Gribakin and V. Flambaum, Calculation of the scattering length in atomic collisions using the semiclassical approximation, *Phys. Rev. A* **48**(1), 546–553 (1993).
- [155] S. Pollack, D. Dries, and R. Hulet, Universality in Three- and Four-Body Bound States of Ultracold Atoms, *Science* **326**(5960), 1683 (2009).
- [156] N. Gross, Z. Shotan, O. Machtey, S. Kokkelmans, and L. Khaykovich, Study of Efimov physics in two nuclear-spin sublevels of ^7Li , *Comptes Rendus Physique* (2011).
- [157] E. Lieb and J. Yngvason, Ground state energy of the low density Bose gas, *Phys. Rev. Lett.* **80**(12), 2504–2507 (1998).
- [158] A. Giuliani and R. Seiringer, The Ground State Energy of the Weakly Interacting Bose gas at High Density, *J. Stat. Phys.* **135**(5), 915–934 (2009).
- [159] K. Brueckner and K. Sawada, Bose-Einstein gas with repulsive interactions: General theory, *Phys. Rev.* **106**(6), 1117–1127 (1957).
- [160] S. Beliaev, Application of the methods of quantum field theory to a system of bosons, *Sov. Phys. JETP* **7**, 289–299 (1958).
- [161] E. Lieb, Simplified approach to the ground-state energy of an imperfect Bose gas, *Phys. Rev.* **130**(6), 2518–2528 (1963).
- [162] S. Giorgini, unpublished, (2011).
- [163] S. Giorgini, J. Boronat, and J. Casulleras, Ground state of a homogeneous Bose gas: A diffusion Monte Carlo calculation, *Phys. Rev. A* **60**(6), 5129–5132 (1999).
- [164] M. Kalos, D. Levesque, and L. Verlet, Helium at zero temperature with hard-sphere and other forces, *Phys. Rev. A* **9**(5), 2178 (1974).
- [165] J. Hansen, D. Levesque, and D. Schiff, Fluid-solid phase transition of a hard-sphere Bose system, *Phys. Rev. A* **3**, 776–780 (1971).
- [166] J. Andersen, Theory of the weakly interacting Bose gas, *Rev. Mod. Phys.* **76**(2), 599 (2004).
- [167] T. Wu, Ground state of a Bose system of hard spheres, *Phys. Rev.* **115**(6), 1390–1404 (1959).
- [168] N. Hugenholtz and D. Pines, Ground-state energy and excitation spectrum of a system of interacting bosons, *Phys. Rev.* **116**(3), 489 (1959).

- [169] E. Braaten and A. Nieto, Quantum corrections to the energy density of a homogeneous Bose gas, *Eur. Phys. J. B* **11**(1), 143–159 (1999).
- [170] G. Danilov, On the three-body problem in the case of short-range forces, *Sov. Phys. JETP* .
- [171] S. Tan, Three-boson problem at low energy and implications for dilute Bose-Einstein condensates, *Phys. Rev. A* **78**(1), 013636 (2008).
- [172] E. Braaten, H. Hammer, and T. Mehen, Dilute Bose-Einstein condensate with large scattering length, *Phys. Rev. Lett.* **88**(4), 40401 (2002).
- [173] E. Braaten, H. Hammer, and S. Hermans, Nonuniversal effects in the homogeneous Bose gas, *Phys. Rev. A* **63**(6), 063609 (2001).
- [174] S. Kokkelmans, unpublished, (2010).
- [175] R. Meppelink, R. Rozendaal, S. Koller, J. Vogels, and P. van der Straten, Thermodynamics of Bose-Einstein-condensed clouds using phase-contrast imaging, *Phys. Rev. A* **81**(5), 053632 (2010).
- [176] S. Pilati, K. Sakkos, J. Boronat, J. Casulleras, and S. Giorgini, Equation of state of an interacting Bose gas at finite temperature: A path-integral Monte Carlo study, *Phys. Rev. A* **74**(4), 043621 (2006).
- [177] B. Capogrosso-Sansone, S. Giorgini, S. Pilati, L. Pollet, N. Prokof'ev, B. Svistunov, and M. Troyer, The Beliaev technique for a weakly interacting Bose gas, *New J. of Phys.* **12**, 043010 (2010).
- [178] W. Krauth, Quantum Monte Carlo calculations for a large number of bosons in a harmonic trap, *Phys. Rev. Lett.* **77**(18), 3695–3699 (1996).
- [179] E. Timmermans, P. Tommasini, and K. Huang, Variational Thomas-Fermi theory of a nonuniform Bose condensate at zero temperature, *Phys. Rev. A* **55**(5), 3645 (1997).
- [180] Y. Kagan, E. Surkov, and G. Shlyapnikov, Evolution and global collapse of trapped Bose condensates under variations of the scattering length, *Phys. Rev. Lett.* **79**(14), 2604–2607 (1997).
- [181] F. Zimmer and M. Haque, Interaction ramps in a trapped Bose condensate, arXiv:1012.4492 (2010).
- [182] E. Braaten and H. Hammer, Universality in few-body systems with large scattering length, *Phys. Rep.* **428**(5-6), 259–390 (2006).
- [183] Y. Kagan, B. Svistunov, and G. Shlyapnikov, Effect of Bose condensation on inelastic processes in gases, *Sov. Phys. JETP* **42**(4) (1985).
- [184] M. Zaccanti, B. Deissler, C. D'Errico, M. Fattori, M. Jona-Lasinio, S. Muller, G. Roati, M. Inguscio, and G. Modugno, Observation of an Efimov spectrum in an atomic system, *Nat. Phys.* **5**(8), 586–591 (2009).
- [185] E. Braaten and H. Hammer, Efimov physics in cold atoms, *Annals of Physics* **322**(1), 120–163 (2007).

- [186] G. Jo, Y. Lee, J. Choi, C. Christensen, T. Kim, J. Thywissen, D. Pritchard, and W. Ketterle, Itinerant ferromagnetism in a Fermi gas of ultracold atoms, *Science* **325**(5947), 1521 (2009).
- [187] C. Sanner, E. Su, W. Huang, A. Keshet, J. Gillen, and W. Ketterle, Correlations and Pair Formation in a Repulsively Interacting Fermi Gas, arXiv:1108.2017 (2011).
- [188] R. Duine and H. Stoof, Dynamics of a Bose-Einstein condensate near a Feshbach resonance, *Phys. Rev. A* **68**(1), 013602 (2003).
- [189] A. Gezerlis and J. Carlson, Strongly paired fermions: Cold atoms and neutron matter, *Phys. Rev. C* **77**(3), 032801 (2008).
- [190] H. Heiselberg, Fermi systems with long scattering lengths, *Phys. Rev. A* **63**(4), 043606 (2001).
- [191] Y. Castin and F. Werner, The Unitary Gas and its Symmetry Properties, arXiv:1103.2851, in "BCS-BEC Crossover and the Unitary Fermi Gas" edited by W. Zwerger, Springer, in press (2011).
- [192] J. Cubizolles, T. Bourdel, S. Kokkelmans, G. Shlyapnikov, and C. Salomon, Production of Long-Lived Ultracold ${}^6\text{Li}_2$ Molecules from a Fermi Gas, *Phys. Rev. Lett.* **91**(24), 240401 (2003).
- [193] S. Jochim, M. Bartenstein, A. Altmeyer, G. Hendl, C. Chin, J. Denschlag, and R. Grimm, Pure gas of optically trapped molecules created from fermionic atoms, *Phys. Rev. Lett.* **91**(24), 240402 (2003).
- [194] C. Cao, E. Elliott, J. Joseph, H. Wu, J. Petricka, T. Schafer, and J. Thomas, Universal Quantum Viscosity in a Unitary Fermi Gas, *Science* **331**(6013), 58 (2011).
- [195] D. Jin and C. Regal, Fermi gas experiments, Proceedings of the International School of Physics 'Enrico Fermi', Course CLXIV, Varenna (2006).
- [196] F. Spiegelhalder, A. Trenkwalder, D. Naik, G. Hendl, F. Schreck, and R. Grimm, Collisional Stability of ${}^{40}\text{K}$ Immersed in a Strongly Interacting Fermi Gas of ${}^6\text{Li}$, *Phys. Rev. Lett.* **103**, 223203 (2009).
- [197] P. Ruprecht, M. Holland, K. Burnett, and M. Edwards, Time-dependent solution of the nonlinear Schrodinger equation for Bose-condensed trapped neutral atoms, *Phys. Rev. A* **51**(6), 4704 (1995).
- [198] C. Bradley, C. Sackett, and R. Hulet, Bose-Einstein condensation of lithium: Observation of limited condensate number, *Phys. Rev. Lett.* **78**(6), 985–989 (1997).
- [199] A. Gammal, T. Frederico, and L. Tomio, Critical number of atoms for attractive Bose-Einstein condensates with cylindrically symmetrical traps, *Phys. Rev. A* **64**(5), 055602 (2001).
- [200] E. Burovski, N. Prokof'ev, B. Svistunov, and M. Troyer, Critical temperature and thermodynamics of attractive fermions at unitarity, *Phys. Rev. Lett.* **96**(16), 160402 (2006).
- [201] A. Bulgac, J. Drut, and P. Magierski, Thermodynamics of a trapped unitary fermi gas, *Phys. Rev. Lett.* **99**(12), 120401 (2007).

- [202] R. Haussmann, W. Rantner, S. Cerrito, and W. Zwerger, Thermodynamics of the BCS-BEC crossover, *Phys. Rev. A* **75**(2), 23610 (2007).
- [203] H. Hu, X. Liu, and P. Drummond, Universal thermodynamics of a strongly interacting Fermi gas: theory versus experiment, *New J. Phys.* **12**, 063038 (2010).
- [204] R. Combescot, F. Alzetto, and X. Leyronas, Particle distribution tail and related energy formula, *Phys. Rev. A* **79**(5), 053640 (2009).
- [205] P. Bedaque and G. Rupak, Dilute resonating gases and the third virial coefficient, *Phys. Rev. B* **67**(17), 174513 (2003).
- [206] T. Ho and E. Mueller, High temperature expansion applied to fermions near Feshbach resonance, *Phys. Rev. Lett.* **92**(16), 160404 (2004).
- [207] L. Landau and E. Lifshitz, *Statistical Physics*, Pergamon Press, Oxford, UK, 1980.
- [208] X. Liu, H. Hu, and P. Drummond, Virial expansion for a strongly correlated Fermi gas, *Phys. Rev. Lett.* **102**(16), 160401 (2009).
- [209] F. Werner and Y. Castin, Unitary quantum three-body problem in a harmonic trap, *Phys. Rev. Lett.* **97**(15), 150401 (2006).
- [210] J. Kestner and L. Duan, Level crossing in the three-body problem for strongly interacting fermions in a harmonic trap, *Phys. Rev. A* **76**(3), 033611 (2007).
- [211] D. Kaplan and S. Sun, A new field theoretic method for the virial expansion, arXiv:1105.0028 (2011).
- [212] D. Rakshit, K. Daily, and D. Blume, Thermodynamics of two-component Fermi gas with large scattering length: Fourth- and higher-order virial coefficients, arXiv:1106.5958 (2011).
- [213] X. Leyronas, In preparation.
- [214] G. Rupak, Universality in a 2-Component Fermi System at Finite Temperature, *Phys. Rev. Lett.* **98**(9), 90403 (2007).
- [215] N. Ashcroft and N. Mermin, *Solid State Physics*, (1976).
- [216] K. Andres, J. Graebner, and H. Ott, 4f-Virtual-Bound-State Formation in CeAl₃ at Low Temperatures, *Phys. Rev. Lett.* **35**(26), 1779–1782 (1975).
- [217] D. Greywall, ³He specific heat and thermometry at millikelvin temperatures, *Phys. Rev. B* **33**(11), 7520 (1986).
- [218] D. S. Greywall, Specific heat of normal liquid ³He, *Phys. Rev. B* **27**(5), 2747–2766 (1983).
- [219] L. Landau, The theory of a Fermi liquid, *Sov. Phys. JETP* **3**(6), 920–925 (1957).
- [220] D. Pines and P. Nozières, *The Theory of Quantum Liquids, vol. I: Normal Fermi Liquids*, WA Benjamin, New York, 1966.
- [221] J. Loram, K. Mirza, J. Cooper, and J. Tallon, Superconducting and normal state energy gaps in Y_{0.8}Ca_{0.2}Ba₂Cu₃O_{7- δ} from the electronic specific heat, *Physica C* **282**, 1405–1406 (1997).

- [222] C. Varma, High-temperature superconductivity: Mind the pseudogap, *Nature* **468**(7321), 184–185 (2010).
- [223] H. Schultz, Fermi liquids and non-Fermi liquids, in the Proceedings of Les Houches Summer School LXI, ed. E. Akkermans, G. Montambaux, J. Pichard, et J. Zinn-Justin (Elsevier, Amsterdam) (1995).
- [224] J. Loram, K. Mirza, J. Cooper, and W. Liang, Electronic specific heat of $\text{YBa}_2\text{Cu}_3\text{O}_{6+x}$ from 1.8 to 300 K, *Phys. Rev. Lett.* **71**(11), 1740–1743 (1993).
- [225] T. Timusk and B. Statt, The pseudogap in high-temperature superconductors: an experimental survey, *Rep. Prog. Phys.* **62**, 61 (1999).
- [226] J. Hoffman, High-temperature superconductivity: To pair or not to pair?, *Nat. Phys.* **6**, 404 (2010).
- [227] N. Hussey, Phenomenology of the normal state in-plane transport properties of high-Tc cuprates, *J. Phys. : Condensed Matter* **20**, 123201 (2008).
- [228] J. Carlson, S. Chang, V. Pandharipande, and K. Schmidt, Superfluid Fermi gases with large scattering length, *Phys. Rev. Lett.* **91**(5), 50401 (2003).
- [229] C. Lobo, A. Recati, S. Giorgini, and S. Stringari, Normal state of a polarized Fermi gas at unitarity, *Phys. Rev. Lett.* **97**(20), 200403 (2006).
- [230] A. Bulgac, J. Drut, and P. Magierski, Quantum Monte Carlo simulations of the BCS-BEC crossover at finite temperature, *Phys. Rev. A* **78**(2), 23625 (2008).
- [231] J. Stewart, J. Gaebler, and D. Jin, Using photoemission spectroscopy to probe a strongly interacting Fermi gas., *Nature* **454**(7205), 744 (2008).
- [232] J. Gaebler, J. Stewart, T. Drake, D. Jin, A. Perali, P. Pieri, and G. Strinati, Observation of pseudogap behaviour in a strongly interacting Fermi gas, *Nat. Phys.* **6**(8), 569–573 (2010).
- [233] A. Perali, F. Palestini, P. Pieri, G. Strinati, J. Stewart, J. Gaebler, T. Drake, and D. Jin, Evolution of the Normal State of a Strongly Interacting Fermi Gas from a Pseudogap Phase to a Molecular Bose Gas, *Phys. Rev. Lett.* **106**(6), 60402 (2011).
- [234] C. Schunck, Y. Shin, A. Schirotzek, M. Zwierlein, and W. Ketterle, Pairing without superfluidity: The ground state of an imbalanced Fermi mixture, *Science* **316**(5826), 867 (2007).
- [235] Y. Shin, C. Schunck, A. Schirotzek, and W. Ketterle, Tomographic rf spectroscopy of a trapped Fermi gas at unitarity, *Phys. Rev. Lett.* **99**(9), 90403 (2007).
- [236] C. Schunck, Y. Shin, A. Schirotzek, and W. Ketterle, Determination of the fermion pair size in a resonantly interacting superfluid., *Nature* **454**(7205), 739 (2008).
- [237] T. Dao, I. Carusotto, and A. Georges, Probing quasiparticle states in strongly interacting atomic gases by momentum-resolved Raman photoemission spectroscopy, *Phys. Rev. A* **80**(2), 023627 (2009).
- [238] F. Palestini, A. Perali, P. Pieri, and G. Strinati, Dispersions, weights, and widths of the single-particle spectral function in the normal phase of a Fermi gas, arXiv:1106.6193 (2011).

- [239] M. Norman, H. Ding, M. Randeria, J. Campuzano, T. Yokoya, T. Takeuchi, T. Takahashi, T. Mochiku, K. Kadowaki, P. Guptasarma, et al., Destruction of the Fermi surface in underdoped high-Tc superconductors, *Nature* **392**(6672), 157–160 (1998).
- [240] P. Nikolic and S. Sachdev, Renormalization-group fixed points, universal phase diagram, and $1/N$ expansion for quantum liquids with interactions near the unitarity limit, *Phys. Rev. A* **75**(3), 033608 (2007).
- [241] E. Burovski, E. Kozik, N. Prokof'ev, B. Svistunov, and M. Troyer, Critical Temperature Curve in BEC-BCS Crossover, *Phys. Rev. Lett.* **101**(9), 90402 (2008).
- [242] O. Goulko and M. Wingate, Thermodynamics of balanced and slightly spin-imbalanced Fermi gases at unitarity, *Phys. Rev. A* **82**(5), 053621 (2010).
- [243] Y. Nishida, Unitary Fermi gas at finite temperature in the ϵ -expansion, *Phys. Rev. A* **75**(6), 063618 (2007).
- [244] A. Bulgac, J. Drut, and P. Magierski, Spin 1/2 fermions in the unitary regime: A superfluid of a new type, *Phys. Rev. Lett.* **96**(9), 90404 (2006).
- [245] E. Taylor, Critical behavior in trapped strongly interacting Fermi gases, *Phys. Rev. A* **80**(2), 023612 (2009).
- [246] S. Nascimbène, N. Navon, F. Chevy, and C. Salomon, The equation of state of ultracold Bose and Fermi gases: a few examples, *New. J. Phys.* **12**, 103026 (2010).
- [247] H. Hu, X. Liu, and P. Drummond, Temperature of a trapped unitary Fermi gas at finite entropy, *Phys. Rev. A* **73**(2), 023617 (2006).
- [248] Y. Shin, C. Schunck, A. Schirotzek, and W. Ketterle, Phase diagram of a two-component Fermi gas with resonant interactions, *Nature* **451**(4), 689–693 (2008).
- [249] L. Luo and J. Thomas, Thermodynamic Measurements in a Strongly Interacting Fermi Gas, *J. Low Temp. Phys.* **154**(1), 1–29 (2009).
- [250] T. Bourdel, J. Cubizolles, L. Khaykovich, K. Magalhaes, S. Kokkelmans, G. Shlyapnikov, and C. Salomon, Measurement of the Interaction Energy near a Feshbach Resonance in a ^6Li Fermi Gas, *Phys. Rev. Lett.* **91**(2), 20402 (2003).
- [251] L. Luo, Entropy and superfluid critical parameters of a strongly interacting Fermi gas, Ph.D Thesis (2008).
- [252] H. Hu, P. Drummond, and X. Liu, Universal thermodynamics of strongly interacting Fermi gases, *Nat. Phys.* **3**(7), 469–472 (2007).
- [253] Y. Inada, M. Horikoshi, S. Nakajima, M. Kuwata-Gonokami, M. Ueda, and T. Mukaiyama, Critical temperature and condensate fraction of a fermion pair condensate, *Phys. Rev. Lett.* **101**(18), 180406 (2008).
- [254] S. Riedl, E. Sanchez Guajardo, C. Kohstall, J. Hecker Denschlag, and R. Grimm, Superfluid quenching of the moment of inertia in a strongly interacting Fermi gas, *New J. Phys.* **13**, 035003 (2011).
- [255] J. Kinast, A. Turlapov, J. Thomas, Q. Chen, J. Stajic, and K. Levin, Heat capacity of a strongly interacting Fermi gas, *Science* **307**(5713), 1296 (2005).

- [256] J. Kinast, A. Turlapov, and J. Thomas, Damping of a unitary Fermi gas, *Phys. Rev. Lett.* **94**(17), 170404 (2005).
- [257] C. Cao, E. Elliott, H. Wu, and J. Thomas, Searching for Perfect Fluids: Quantum Viscosity in a Universal Fermi Gas, arXiv:1105.2496 (2011).
- [258] T. Mukaiyama, private communication.
- [259] H. Hu, X. Liu, and P. Drummond, Equation of state of a superfluid Fermi gas in the BCS-BEC crossover, *Europhys. Lett.* **74**, 574 (2006).
- [260] M. Marini, F. Pistolesi, and G. Strinati, Evolution from BCS superconductivity to Bose condensation: analytic results for the crossover in three dimensions, *Eur. Phys. J. B.* **1**(2), 151–159 (1998).
- [261] S. Pilati and S. Giorgini, Phase separation in a polarized Fermi gas at zero temperature, *Phys. Rev. Lett.* **100**, 030401 (2008).
- [262] S. Chang, V. Pandharipande, J. Carlson, and K. Schmidt, Quantum Monte Carlo studies of superfluid Fermi gases, *Phys. Rev. A* **70**(4), 043602 (2004).
- [263] S. Gandolfi, K. Schmidt, and J. Carlson, BEC-BCS crossover and universal relations in unitary Fermi gases, *Phys. Rev. A* **83**(4), 041601 (2011).
- [264] P. Pieri, L. Pisani, and G. Strinati, Comparison between a diagrammatic theory for the BCS-BEC crossover and quantum Monte Carlo results, *Phys. Rev. B* **72**(1), 12506 (2005).
- [265] V. Galitskii, The energy spectrum of a non-ideal Fermi gas, *Sov. Phys. JETP* **34**(7), 104–112 (1958).
- [266] R. Diener, R. Sensarma, and M. Randeria, Quantum fluctuations in the superfluid state of the BCS-BEC crossover, *Phys. Rev. A* **77**(2), 023626 (2008).
- [267] G. Baker Jr, Singularity structure of the perturbation series for the ground-state energy of a many-fermion system, *Rev. Mod. Phys.* **43**(4), 479 (1971).
- [268] S. Tan, Energetics of a strongly correlated Fermi gas, *Annals of Physics* **323**(12), 2952–2970 (2008).
- [269] S. Tan, Large momentum part of a strongly correlated Fermi gas, *Annals of Physics* **323**(12), 2971–2986 (2008).
- [270] S. Tan, Generalized virial theorem and pressure relation for a strongly correlated Fermi gas, *Annals of Physics* **323**(12), 2987–2990 (2008).
- [271] E. Braaten, Universal Relations for Fermions with Large Scattering Length, arXiv:1008.2922 (2010).
- [272] C. Lobo, I. Carusotto, S. Giorgini, A. Recati, and S. Stringari, Pair correlations of an expanding superfluid Fermi gas, *Phys. Rev. Lett.* **97**(10), 100405 (2006).
- [273] R. Combescot, S. Giorgini, and S. Stringari, Molecular signatures in the structure factor of an interacting Fermi gas, *Europhys. Lett.* **75**, 695 (2006).
- [274] H. Hu, X. Liu, and P. Drummond, Universal contact of strongly interacting fermions at finite temperatures, *New J. Phys.* **13**, 035007 (2011).

- [275] R. Haussmann, M. Punk, and W. Zwerger, Spectral functions and rf response of ultracold fermionic atoms, *Phys. Rev. A* **80**(6), 063612 (2009).
- [276] F. Palestini, A. Perali, P. Pieri, and G. Strinati, Temperature and coupling dependence of the universal contact intensity for an ultracold Fermi gas, *Phys. Rev. A* **82**(2), 021605 (2010).
- [277] J. Stewart, J. Gaebler, T. Drake, and D. Jin, Verification of universal relations in a strongly interacting Fermi gas, *Phys. Rev. Lett.* **104**(23), 235301 (2010).
- [278] G. Partridge, K. Strecker, R. Kamar, M. Jack, and R. Hulet, Molecular probe of pairing in the BEC-BCS crossover, *Phys. Rev. Lett.* **95**(2), 20404 (2005).
- [279] E. Kuhnle, H. Hu, X. Liu, P. Dyke, M. Mark, P. Drummond, P. Hannaford, and C. Vale, Universal behavior of pair correlations in a strongly interacting Fermi gas, *Phys. Rev. Lett.* **105**(7), 70402 (2010).
- [280] F. Werner, L. Tarruell, and Y. Castin, Number of closed-channel molecules in the BEC-BCS crossover, *Euro. Phys. J. D.* **68**(3), 401–415 (2009).
- [281] M. Bartenstein, A. Altmeyer, S. Riedl, S. Jochim, C. Chin, J. Denschlag, and R. Grimm, Collective excitations of a degenerate gas at the BEC-BCS crossover, *Phys. Rev. Lett.* **92**, 203201 (2004).
- [282] J. Joseph, B. Clancy, L. Luo, J. Kinast, A. Turlapov, and J. Thomas, Measurement of sound velocity in a Fermi gas near a Feshbach resonance, *Phys. Rev. Lett.* **98**(17), 170401 (2007).
- [283] C. Regal, M. Greiner, S. Giorgini, M. Holland, and D. Jin, Momentum distribution of a Fermi gas of atoms in the BCS-BEC crossover, *Phys. Rev. Lett.* **95**(25), 250404 (2005).
- [284] A. Perali, P. Pieri, and G. Strinati, Quantitative comparison between theoretical predictions and experimental results for the BCS-BEC crossover, *Phys. Rev. Lett.* **93**(10), 100404 (2004).
- [285] J. Carlson and S. Reddy, Asymmetric two-component fermion systems in strong coupling, *Phys. Rev. Lett.* **95**(6), 60401 (2005).
- [286] O. Juillet, Sign-free stochastic mean-field approach to strongly correlated phases of ultracold fermions, *New J. Phys.* **9**, 163 (2007).
- [287] Y. Nishida and D. Son, ϵ -expansion for a Fermi gas at infinite scattering length, *Phys. Rev. Lett.* **97**(5), 50403 (2006).
- [288] M. Forbes, S. Gandolfi, and A. Gezerlis, Resonantly interacting fermions in a box, *Phys. Rev. Lett.* **106**(23), 235303 (2011).
- [289] J. Carlson, S. Gandolfi, K. Schmidt, and S. Zhang, Auxiliary Field quantum Monte Carlo for Strongly Paired Fermions, arXiv:1107.5848 (2011).
- [290] H. Heiselberg, Crossovers in Unitary Fermi Systems, arXiv:1008.5086, in "BCS-BEC Crossover and the Unitary Fermi Gas" edited by W. Zwerger, Springer, in press (2010).
- [291] Z. Yu, G. Bruun, and G. Baym, Short-range correlations and entropy in ultracold-atom Fermi gases, *Phys. Rev. A* **80**(2), 023615 (2009).
- [292] J. Drut, T. Lahde, and T. Ten, Momentum Distribution and Contact of the Unitary Fermi gas, *Phys. Rev. Lett.* **106**(20), 205302 (2011).

- [293] F. Serwane, G. Zurn, T. Lompe, T. Ottenstein, A. Wenz, and S. Jochim, Deterministic preparation of a tunable few-fermion system, *Science* **332**(6027), 336 (2011).
- [294] A. Sommer, M. Ku, G. Roati, and M. Zwierlein, Universal spin transport in a strongly interacting Fermi gas, *Nature* **472**(7342), 201–204 (2011).
- [295] A. Clogston, Upper limit for the critical field in hard superconductors, *Phys. Rev. Lett.* **9**(6), 266–267 (1962).
- [296] B. S. Chandrasekhar, A Note On The Maximum Critical Field of High-Field Superconductors, *App. Phys. Lett.* **1**(1), 7–8 (1962).
- [297] R. Casalbuoni and G. Nardulli, Inhomogeneous superconductivity in condensed matter and QCD, *Rev. Mod. Phys.* **76**(1), 263 (2004).
- [298] M. Zwierlein, A. Schirotzek, C. Schunck, and W. Ketterle, Fermionic superfluidity with imbalanced spin populations, *Science* **311**(5760), 492–496 (2006).
- [299] P. Bedaque, H. Caldas, and G. Rupak, Phase separation in asymmetrical fermion superfluids, *Phys. Rev. Lett.* **91**(24), 247002–247002 (2003).
- [300] M. Punk, P. Dumitrescu, and W. Zwerger, Polaron-to-molecule transition in a strongly imbalanced Fermi gas, *Phys. Rev. A* **80**(5), 053605 (2009).
- [301] F. Chevy, Universal phase diagram of a strongly interacting Fermi gas with unbalanced spin populations, *Phys. Rev. A* **74**(6), 063628 (2006).
- [302] R. Combescot, A. Recati, C. Lobo, and F. Chevy, Normal state of highly polarized Fermi gases: simple many-body approaches, *Phys. Rev. Lett.* **98**(18), 180402 (2007).
- [303] R. Combescot and S. Giraud, Normal state of highly polarized Fermi gases: full many-body treatment., *Phys. Rev. Lett.* **101**(5), 050404 (2008).
- [304] N. Prokof'ev and B. Svistunov, Fermi-polaron problem: Diagrammatic Monte Carlo method for divergent sign-alternating series, *Phys. Rev. B* **77**(2), 020408 (2008).
- [305] N. Prokof'ev and B. Svistunov, Bold diagrammatic Monte Carlo: A generic sign-problem tolerant technique for polaron models and possibly interacting many-body problems, *Phys. Rev. B* **77**, 125101 (2008).
- [306] N. Prokof'ev and B. Svistunov, private communication.
- [307] R. Combescot, S. Giraud, and X. Leyronas, Analytical theory of the dressed bound state in highly polarized Fermi gases, *Europhys. Lett.* **88**, 60007 (2009).
- [308] C. Mora and F. Chevy, Ground state of a tightly bound composite dimer immersed in a Fermi Sea, *Phys. Rev. A* **80**(3), 033607 (2009).
- [309] P. Fulde and R. Ferrell, Superconductivity in a strong spin-exchange field, *Phys. Rev.* **135**(3A), A550–A563 (1964).
- [310] A. Larkin and Y. Ovchinnikov, Inhomogeneous state of superconductors, *Sov. Phys. JETP* **20**, 762 (1965).
- [311] F. Chevy and C. Mora, Ultra-cold polarized Fermi gases, *Rep. Prog. Phys.* **73**, 112401 (2010).

- [312] L. Radzihovsky and D. Sheehy, Imbalanced Feshbach-resonant Fermi gases, *Rep. Prog. Phys.* **73**, 076501 (2010).
- [313] G. Partridge, W. Li, Y. Liao, R. Hulet, M. Haque, and H. Stoof, Deformation of a trapped Fermi gas with unequal spin populations, *Phys. Rev. Lett.* **97**(19), 190407 (2006).
- [314] M. Tezuka, Y. Yanase, and M. Ueda, Elongated Fermi superfluid: absence of critical imbalance enhancement at equilibrium, arXiv:0811.1650 (2008).
- [315] T. De Silva and E. Mueller, Surface tension in unitary fermi gases with population imbalance., *Phys. Rev. Lett.* **97**(7), 070402 (2006).
- [316] S. Baur, S. Basu, T. De Silva, and E. Mueller, Theory of the normal-superfluid interface in population-imbalanced Fermi gases, *Phys. Rev. A* **79**(6), 063628 (2009).
- [317] C. Mora and F. Chevy, Normal phase of an imbalanced fermi gas, *Phys. Rev. Lett.* **104**(23), 230402 (2010).
- [318] M. Parish, F. Marchetti, A. Lamacraft, and B. Simons, Finite-temperature phase diagram of a polarized Fermi condensate, *Nat. Phys.* **3**(2), 124–128 (2007).
- [319] R. Combescot and C. Mora, Transition to Fulde-Ferrel-Larkin-Ovchinnikov phases near the tricritical point: an analytical study, *Eur. Phys. J. B.* **28**(4), 397–406 (2002).
- [320] S. Pilati and S. Giorgini, Phase separation in a polarized Fermi gas at zero temperature, *Phys. Rev. Lett.* **100**(3), 30401–30401 (2008).
- [321] C. Regal, M. Greiner, and D. Jin, Observation of resonance condensation of fermionic atom pairs, *Phys. Rev. Lett.* **92**(4), 40403 (2004).
- [322] M. Zwierlein, C. Stan, C. Schunck, S. Raupach, A. Kerman, and W. Ketterle, Condensation of pairs of fermionic atoms near a Feshbach resonance, *Phys. Rev. Lett.* **92**(12), 120403 (2004).
- [323] Z. Hadzibabic, S. Gupta, C. Stan, C. Schunck, M. Zwierlein, K. Dieckmann, and W. Ketterle, Fiftyfold improvement in the number of quantum degenerate fermionic atoms, *Phys. Rev. Lett.* **91**(16), 160401 (2003).
- [324] V. Sears, E. Svensson, P. Martel, and A. Woods, Neutron-Scattering Determination of the Momentum Distribution and the Condensate Fraction in Liquid ^4He , *Phys. Rev. Lett.* **49**(4), 279–282 (1982).
- [325] K. Xu, Y. Liu, D. Miller, J. Chin, W. Setiawan, and W. Ketterle, Observation of strong quantum depletion in a gaseous Bose-Einstein Condensate, *Phys. Rev. Lett.* **96**(18), 180405 (2006).
- [326] J. Stenger, S. Inouye, A. Chikkatur, D. Stamper-Kurn, D. Pritchard, and W. Ketterle, Bragg spectroscopy of a Bose-Einstein condensate, *Phys. Rev. Lett.* **82**(23), 4569–4573 (1999).
- [327] R. Smith, R. Campbell, N. Tammuz, and Z. Hadzibabic, Effects of Interactions on the Critical Temperature of a Trapped Bose Gas, *Phys. Rev. Lett.* **106**(25), 250403 (2011).
- [328] A. Daley, J. Taylor, S. Diehl, M. Baranov, and P. Zoller, Atomic three-body loss as a dynamical three-body interaction, *Phys. Rev. Lett.* **102**(4), 40402 (2009).

- [329] P. Gruter, D. Ceperley, and F. Laloe, Critical temperature of Bose-Einstein condensation of hard-sphere gases, *Phys. Rev. Lett.* **79**(19), 3549–3552 (1997).
- [330] G. Baym, J. Blaizot, M. Holzmann, F. Laloe, and D. Vautherin, Bose-Einstein transition in a dilute interacting gas, *Eur. Phys. J. B.* **24**(1), 107–124 (2001).
- [331] P. Arnold and G. Moore, BEC transition temperature of a dilute homogeneous imperfect Bose gas, *Phys. Rev. Lett.* **87**(12), 120401 (2001).
- [332] V. Kashurnikov, N. Prokof'ev, and B. Svistunov, Critical temperature shift in weakly interacting Bose gas, *Phys. Rev. Lett.* **87**(12), 120402 (2001).
- [333] R. Smith, N. Tammuz, R. Campbell, M. Holzmann, and Z. Hadzibabic, Condensed Fraction of an Atomic Bose Gas Induced by Critical Correlations, [arXiv:1106.6295](https://arxiv.org/abs/1106.6295) (2011).
- [334] J. Steinhauer, R. Ozeri, N. Katz, and N. Davidson, Excitation spectrum of a Bose-Einstein condensate, *Phys. Rev. Lett.* **88**(12), 120407 (2002).
- [335] D. Pekker, M. Babadi, R. Sensarma, N. Zinner, L. Pollet, M. Zwierlein, and E. Demler, Competition between pairing and ferromagnetic instabilities in ultracold Fermi gases near Feshbach resonances, *Phys. Rev. Lett.* **106**(5), 50402 (2011).
- [336] K. Maeda, G. Baym, and T. Hatsuda, Simulating dense QCD matter with ultracold atomic boson-fermion mixtures, *Phys. Rev. Lett.* **103**(8), 85301 (2009).
- [337] A. Trenkwalder, C. Kohstall, M. Zaccanti, D. Naik, A. Sidorov, F. Schreck, and R. Grimm, Hydrodynamic Expansion of a Strongly Interacting Fermi-Fermi Mixture, *Phys. Rev. Lett.* **106**(11), 115304 (2011).
- [338] I. Bausmerth, A. Recati, and S. Stringari, Chandrasekhar-Clogston limit and phase separation in Fermi mixtures at unitarity, *Phys. Rev. A* **79**(4), 043622 (2009).
- [339] D. Petrov, G. Astrakharchik, D. Papoular, C. Salomon, and G. Shlyapnikov, Crystalline phase of strongly interacting Fermi mixtures, *Phys. Rev. Lett.* **99**(13), 130407 (2007).
- [340] J. Danzl, E. Haller, M. Gustavsson, M. Mark, R. Hart, N. Bouloufa, O. Dulieu, H. Ritsch, and H. Nagerl, Quantum gas of deeply bound ground state molecules, *Science* **321**(5892), 1062 (2008).
- [341] K. Ni, S. Ospelkaus, M. De Miranda, A. Pe'er, B. Neyenhuis, J. Zirbel, S. Kotochigova, P. Julienne, D. Jin, and J. Ye, A high phase-space-density gas of polar molecules, *Science* **322**(5899), 231 (2008).

Résumé

Le problème à N -corps quantique est au centre de quelques-uns des plus importants problèmes ouverts de la physique moderne, comme le mécanisme de la supraconductivité à haute température critique, ou le comportement des étoiles à neutrons. Les gaz quantiques ultrafroids sont maintenant utilisés pour simuler des hamiltoniens modèles de la physique de la matière condensée ou de la physique nucléaire, dans un environnement très bien contrôlé. Dans cette thèse, nous avons développé une nouvelle méthode pour sonder la thermodynamique de systèmes quantiques homogènes en utilisant des gaz ultrafroids piégés. Nos mesures peuvent être directement comparées aux prédictions des théories du problème à N -corps quantique. Nous avons appliqué cette technique au gaz de fermions à deux composantes de spin et au gaz de Bose atomique avec des interactions à courte portée. Grâce au ^6Li fermionique, nous avons exploré une partie de l'espace de paramètres du système, en changeant la force des interactions, le déséquilibre de population de spin ou la température du gaz. Ce système présente une physique remarquablement riche, avec une transition normale/superfluide (qui peut être de nature thermique ou quantique) ou un comportement de type liquide de Fermi à basse température. Nous avons également utilisé cette méthode pour sonder le gaz de Bose atomique, constitué d'atomes de ^7Li au voisinage d'une résonance de Feshbach. Nous avons mesuré l'équation d'état du gaz de bosons en fonction de la force des interactions à très basse température et avons déterminé la première correction au-delà du champ moyen, dite correction de Lee-Huang-Yang, à l'énergie de l'état fondamentale du système, prédite pour la première fois en 1957. Nous avons comparé nos résultats à des simulations Monte Carlo quantique. Nous avons étendu cette étude à la dynamique hors d'équilibre du gaz de bosons en interaction forte, donnant une première indication sur les propriétés de l'hypothétique gaz de Bose unitaire.

Abstract

The quantum many-body problem is at the heart of some of the most formidable open problems in modern physics, such as high- T_c superconductivity or the behaviour of neutron stars. Ultracold atomic systems can now be used to simulate model Hamiltonians of condensed matter or nuclear physics, in very well-controlled environment. In this thesis, we have developed a general method to probe the thermodynamics of homogeneous quantum systems using trapped atomic gases. These measurements are directly compared to the predictions of theories of the quantum many-body problem. We have applied this technique to the spin-1/2 Fermi gas and the Bose with short-range interactions. Using fermionic ^6Li , we explored a part of the wide parameter space by changing the interaction strength, the spin-population imbalance or the temperature of the gas. This system exhibits remarkably rich physics, such as normal/superfluid phase transitions (that can be of thermal or quantum character) or a Fermi liquid-type behaviour of the normal phase. We have also used this method to probe a Bose gas of ^7Li atoms close to a Feshbach resonance. We have measured the Equation of State of the Bose gas as a function of interactions at very low temperature. For the first time, we measured quantitatively the Lee-Huang-Yang beyond mean-field correction to the ground-state energy of the system, first predicted in 1957. We compared the experimental results to Quantum Monte-Carlo calculations. We have extended this study using out-of-equilibrium measurements of the Bose gas in the strongly interacting regime, which gives a first hint on the properties of the hypothetical unitary Bose gas.